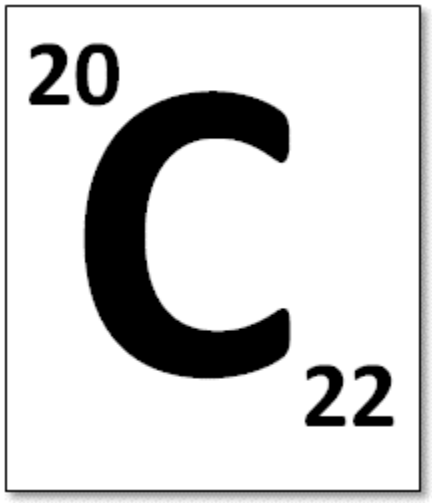


**Carbon 2022**

# The World Conference on Carbon
# 'Carbon for a Cleaner Future'

**3rd July – 8th July 2022**
**at**
**Imperial College London**
**UNITED KINGDOM**

# Extended Abstract Book

www.carbon2022.org

organised under the auspices of
The British Carbon Group

The
British Carbon Group

Carbon 2022 is organised by the British Carbon Group. The British Carbon Group is a special interest group of the Royal Society of Chemistry, the Institute of Physics and the Society of Chemical Industry devoted to the advancement of carbon science. It is also a member of the European Carbon Association.

# Preface

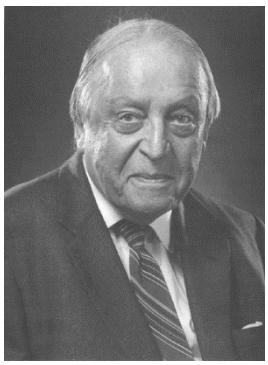

After a 2-year absence, the British Carbon Group was delighted to organise the 21st edition of the World Conference on Carbon at Imperial College London. Since the first World Conference on Carbon in 2000, scientists from around the globe have met annually to discuss and celebrate advancements in the field of carbon science - together in-person - and we continued that tradition in 2022. It was especially appropriate that we met at Imperial College London. This was the institution where Professor A. R Ubbelohde established his Carbon Research Laboratory and organised the First UK Industrial Carbon and Graphite Conference (one of the precursors to the World Conference on Carbon), held in 1957 in London – 65 years ago.

*Alfred R. J. P. Ubbelohde*

The United Kingdom has a long history of carbon science starting with the 'discovery' of plumbago (natural graphite) in Cumbria in 1564 during the reign of Elizabeth I – the word graphite didn't really exist until several centuries later when proposed by Werner and Harsten in 1879. Carbon science in the UK has a long tradition associated with the rich coal fields found in the North of England and through this led to many achievements including Rosalind Franklin's very influential work on graphitizing and non-graphitizing carbons. Certainly, the familiarity with industrial carbon materials influenced the UK's decision to focus on graphite-moderated civil nuclear power since the 1940s. This era of the Advanced Gas-cooled fleet of nuclear electricity generation is coming to an end which creates new challenges. Indeed, the UK has had a long association with industrial carbons, from major production of anode carbons in Sheffield until the 1990s, to modern composites technology especially in sports such as Formula One. Later the work by Sir Harry Kroto and colleagues on Buckminsterfullerene led to the 1996 Nobel Prize, with a second Nobel prize in 2010 for Sir Andre Geim and Sir Konstantin Novoselov, for their work on graphene. Carbon science has a rich and influential history, but this conference showed it has a bright future too.

We had over 300 registered attendees with 45 countries represented, and over 200 talks and 150 posters presented. This extended abstract book represents a summary of some of the excellent work seen over the week. We look forward to the discussions continuing in 2023 in Mexico!

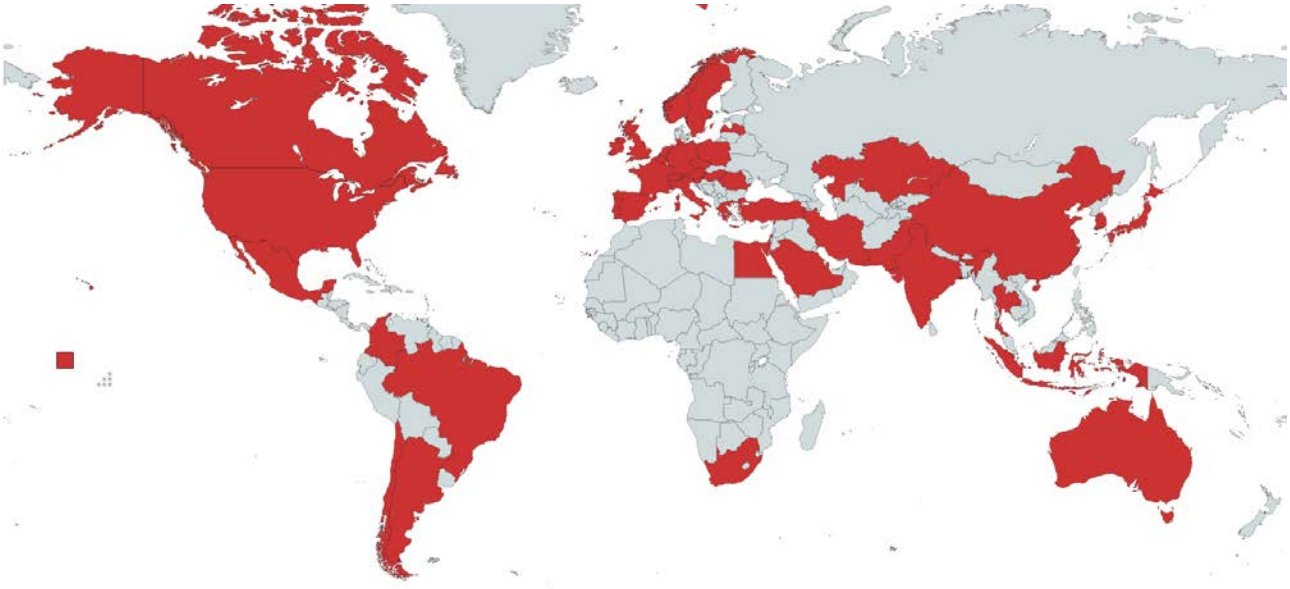

# ACKNOWLEDGEMENTS & SPONSORS

The organising committee and the British Carbon Group would like to thank the following organisations for financial support for this meeting

- Attonuclei
- Advanced Material Development
- Alvatek
- Beilstein Journal of Nanotechnology
- BioLogic
- Elsevier Carbon Journal
- Hiden
- Horiba
- Ingevity
- Institute of Physics
- MDPI C – Journal of Carbon research
- National Nuclear Laboratory
- Royal Society of Chemistry
- Society of Chemical Industry
- Surface Measurement Systems
- Verder Scientific

## Organising Committee

| | |
|---|---|
| Geoff Fowler | Conference Chair |
| Chris Ewels | Vice Chair |
| Izabela Jurewicz | Hon. Treasurer |
| Gareth Neighbour | Programme Chair |
| Samantha Wilkinson | Sponsorship Co-ordinator |
| Peter C. Minshall | Secretary |
| Natalia Martsinovich | Programme Vice-Chair |
| Sergey Mikhalovsky | |
| Maria-Magdalena Titirici | |
| Norman Parkyns | |
| Manasi R Mulay | Conference Officer |

## International Advisory Board

| | |
|---|---|
| Rodney Andrews | University of Kentucky |
| Alberto Bianco | CNRS Strasbourg |
| Hui-Ming Chen | Shenyang National Laboratory |
| Yuan Chen | University of Sydney |
| Deborah Chung | University of Buffalo |
| Jonathan Coleman | Trinity College Dublin |
| Luiz Depine de Castro | Centro Tecnologico do Exercito |
| Morinobu Endo | Shinshu University |
| Elżbieta Frąckowiak | Poznan University of Technology |
| Nidia Gallego | ORNL |
| Hiroaki Hatori | AIST |
| Robert Hurt | Brown University |
| Nathalie Job | University of Liege |
| Marc Monthioux | CEMES, CNRS, Toulouse |
| Emilia Morallon | University of Alicante |
| Chong Rae Park | Seoul National University |
| Rodney Ruoff | University of Ulsan |
| Michael Strano | MIT |
| Juan M. D. Tascon | INCAR, CSIC |
| Mauricio Terrones | Penn State University |
| Matthew Weisenberger | University of Kentucky |
| Aiden Westwood | Leeds University |

# C2022 Summary Programme

| | Morning | | Afternoon | | Evening |
|---|---|---|---|---|---|
| | 09:00 - 10:10 | 10:40 - 13:00 | 14:00 - 15:00 | 15:30 - 17:30 | |
| **Sunday 3rd July** | | | | | |
| Queens Tower Rooms | | | | Registration, Exhibition Set-Up | Welcome Reception (16:00-18:30) |
| **Monday 4th July** | | | | | |
| **Session** | | 1 | 2 | 3 | |
| **A** Great Hall | 08:30 Opening Ceremony, Plenary & Brian Kelly Award | Carbon in Energy | Nanoscale Carbons | Carbon in Energy | SCI Drinks Reception at Belgrave Square (19:00) |
| **B** Pippard | | Graphite | Innovative Carbons for Sustainability | Carbon in Biology, Medicine & Health | |
| C Read | | Physicochemical Carbon Properties | Environmental Carbon | Heterocarbons | |
| QT Rooms | | Set-up Posters (Session 1) | | | |
| **Tuesday 5th July** | | | | | |
| **Session** | | 4 | 5 | 6 | |
| **A** Great Hall | Plenary & French Carbon Group Awards | Carbon in Energy | Carbon in Energy | Elsevier Carbon Journal Workshop | |
| **B** Pippard | | Nanoscale Carbons *(sponsored by C Journal)* | Carbon in Biology, Medicine & Health *(sponsored by C Journal)* | | |
| C Read | | Nuclear Graphite *(sponsored by NNL Ltd)* | Carbon Fibres & Composites | Nanoscale Carbons | |
| QT Rooms | | | | Poster Session 1 | |
| **Wednesday 6th July** | | | | | |
| **Session** | | 7 | 8 | 9 | |
| **A** Great Hall | Plenary & Attonuclei Prize | Carbon in Energy | Carbon in Energy | Carbon in Energy | |
| **B** Pippard | | Carbon Fibres & Composites | Graphite | Amorphous Carbons | |
| C Read | | Environmental Carbon | Nanoscale Carbons | Nanoscale Carbons | |
| QT Rooms | | Set-up Posters (Session 2) | | | |
| **Thursday 7th July** | | | | | |
| **Session** | | 10 | 11 | 12 | |
| **A** Great Hall | Plenary & ECA Award | Carbon in Energy | French Carbon Group Awards (SFEC2020-22) | Miscellaneous Carbons | Conference Banquet at Butler's Wharf (19:15 for 19:30 departure) |
| **B** Pippard | | Innovative Carbons for Sustainability | Innovative Carbons for Sustainability | | |
| C Read | | Environmental Carbon | Environmental Carbon | | |
| QT Rooms | | | | Poster Session 2 | |
| **Friday 8th July** | | | | | |
| **Session** | | 13 | 14 | 15 | |
| **A** Great Hall | Plenary (Presentation C2023) | Carbon in Energy | Carbon in Energy | Carbon in Energy | |
| **B** Pippard | | Innovative Carbons for Sustainability | Physicochemical Carbon Properties | Nanoscale Carbons | |
| C Read | | Environmental Carbon | Nanoscale Carbons | Carbon Fibres & Composites | |

Abstracts are listed alphabetically by presenting author.

Carbon 2022

# Evaluating the electrocatalytic activity towards OER and ORR of nanostructured carbons produced via PW11Co@ZIF-67 carbonization.

**Víctor K. Abdelkader-Fernández[1], Diana M. Fernandes[2], Salete S. Balula[2], Luís Cunha-Silva[2], Manuel J. Pérez-Mendoza[1] and Cristina Freire[2]**

Email: victorkarim@ugr.es

[1]Departamento de Química Inorgánica, Facultad de Ciencias, Universidad de Granada (UGR), Avenida de Fuente Nueva, s/n, 18071 Granada, Spain
[2]REQUIMTE/LAQV, Departamento de Química e Bioquímica, Faculdade de Ciências da Universidade de Porto, Rua do Campo Alegre, 4169-007 Porto, Portugal

**Keywords**
Guest@host nanocomposites, zeolitic imidazolate frameworks (ZIFs), polyoxometalates (POMs), MOF-derived nanocarbons, carbonization, electrocatalysis, oxygen evolution reaction (OER), oxygen reduction reaction (ORR).

## INTRODUCTION

The oxygen reduction and the oxygen evolution reactions (ORR and OER, respectively) are crucial energy-related processes that take place in fuel cell and electrolyzer systems, correspondingly. In addition, for the development of affordable and efficient unitized regenerative fuel cell (URFC) devices (**FIGURE 1**) —systems that can act as electrolyzer or fuel cell depending on the energy requirements in each period—, electrocatalysts (ECs) must present bifunctionality towards these two processes (Freire, 2018). Thereby, regarding the real implementation of these devices, new materials —alternative to the expensive state-of-the-art benchmarks: Pt/C for ORR, and $RuO_2$ and $IrO_2$ for OER— are required, stimulating the quest for candidates to bifunctional EC during the last years. In this context, nanostructured carbons obtained from metal-organic frameworks pyrolysis, *i. e.*, MOF-derived nanocarbons, have recently attracted a lot of attention due to their remarkable structural and electrochemical features: carbon-embedded and well dispersed metal-containing nanoparticles (NPs), presence of heteroatoms in the carbon matrix, and significant conductivity and stability (Abdelkader-Fernández, 2019). Taking advantage of guest@host polyoxometalate (POM)@MOF nanocomposites —previously developed in our group (Abdelkader-Fernández, 2020; Abdelkader-Fernández, 2020)— with good performances towards the catalysis of the OER process, but insufficient ORR activity, we have produced a set of POM@MOF-derived nanocarbons. Thus, we present a study focused on the carbonization of a POM@MOF nanocomposite in which the POM units ($PW_{11}Co$) are individually confined inside the MOF (a cobalt-containing zeolitic imidazole framework, ZIF-67) cavities.

## EXPERIMENTAL

***In-situ* synthesis of guest@host $PW_{11}Co$@ZIF-67 nanocomposite.** $Co(NO_3)_2{\cdot}6H_2O$ methanolic solution was mixed with a $PW_{11}Co$ aqueous solution and stirred for 30 min. Next, 2-methylimidazole methanolic solution was added, resulting in a violet mixture. After additional stirring for 2.5 h, the purple fine powder was collected by centrifugation, washed with water and methanol, and dried. **Preparation of nanostructured materials derived from $PW_{11}Co$@ZIF-67.** $PW_{11}Co$@ZIF-67 was employed as a sacrificial precursor/template to produce a set of five derived samples via thermal treatments performed in a tubular furnace, and using different hold temperatures (200, 400, 500,

600, and 950 °C) for 2 h, under $N_2$ flow. **Physicochemical characterization.** The changes produced by the thermal treatments on $PW_{11}Co$@ZIF-67 composition/structure were assessed by using coupled plasma optical emission spectrometry (ICP-OES), CHNS analysis, X-ray photoelectron spectroscopy (XPS), attenuated total reflection Fourier transform infrared (ATR-FTIR) spectroscopy, powder X-ray diffraction (PXRD), Raman spectroscopy, $N_2$ and $CO_2$ adsorption/desorption measurements, and transmission electron microscopy (TEM) with energy-dispersive X-ray spectroscopy (EDS). **Electrochemical characterization.** Electrocatalytically active surface areas (ECSA), intrinsic electrochemistry, and electrocatalytic performances toward ORR and OER were evaluated via the acquisition of the corresponding cyclic and linear sweep voltammetry (CV and LSV, respectively) plots utilizing a standard 3-electrode cell setup coupled to a potentiostat/galvanostat station by modifying the glassy carbon working electrode with the selected sample (EC) ink.

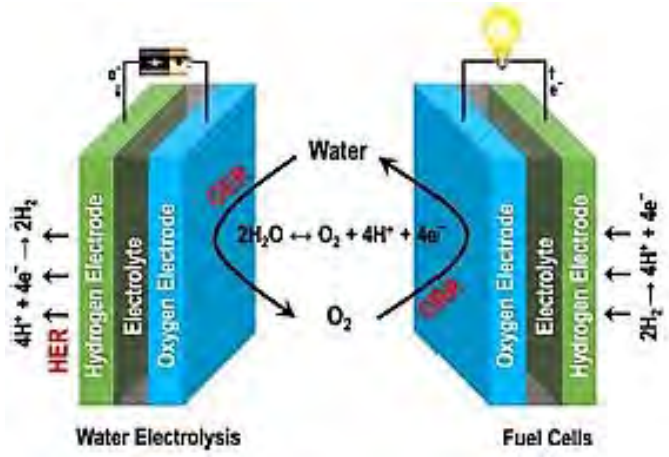


**FIGURE 1**: Schematic illustration of a hydrogen/air fuel cell and electrolyzer principle of operation (Freire, 2018).

**RESULTS**

The two first derivatives —D200 and D400— show the same nanoarrangement that $PW_{11}Co$@ZIF-67, although with incipient signs of both POM and ZIF-67 structural decompositions. Then, the following samples —D500, D600, and D950— exhibit a carbonaceous nature consisting of C-embedded compositionally complex nanoparticles that involve Co and W presented in diverse species —metallic/oxide/phosphate/phosphide—. See the evolution of Raman profile in **FIGURE 2a**. Regarding their electrocatalytic performances toward both OER and ORR processes, the corresponding polarization curves obtained via LSV measurements in alkaline electrolyte are collected in **FIGURE 2b**.

**CONCLUSIONS**

The D200 and D400 samples undergo very limited modifications in both ZIF-67 skeleton and confined $PW_{11}Co$ units. These concurrent POM/ZIF partial decompositions probably compromise their electronic interaction, deteriorating their electrochemical/catalytical features. Noteworthily, D500 exhibits finely dispersed few nm-sized Co-enriched NPs embedded in a highly disordered C matrix. In contrast, in D600 and D950, the higher treatment T generate two types of large-sized NPs, one enriched in Co and one enriched in W —with low amounts of phosphates and phosphides derived from $PW_{11}Co$—. As a consequence of the increasing T, these two samples show more ordered C matrixes. Although the three carbonaceous derivatives undergo drastic ECSA drops, likely caused by the collapse of the pristine ZIF-67 microporosity, their CV plots involve new anodic peaks indicating an enhancement of their intrinsic electrochemistry. Apart from the new peaks, the CV of D500 presents elevated current density, probably originated from an effective interaction between its abundant doping N moieties —specially pyridinic groups— and the very small-sized Co-containing

NPs. The D500, D600, and D950 samples preserve in an important extension the "pristine" $PW_{11}Co$@ZIF-67 OER activity, showing intermediate overpotentials —0.53, 0.53, and 0.50 V, correspondingly—. More valuable, D500 and D600 generate significant ORR activity levels (with onset potentials of 0.87 and 0.88 V vs RHE, respectively, and high selectivity levels of 3.6 and 3.7 mol of electrons per mol of reduced oxygen, respectively) exhibiting an incipient bifunctional character.

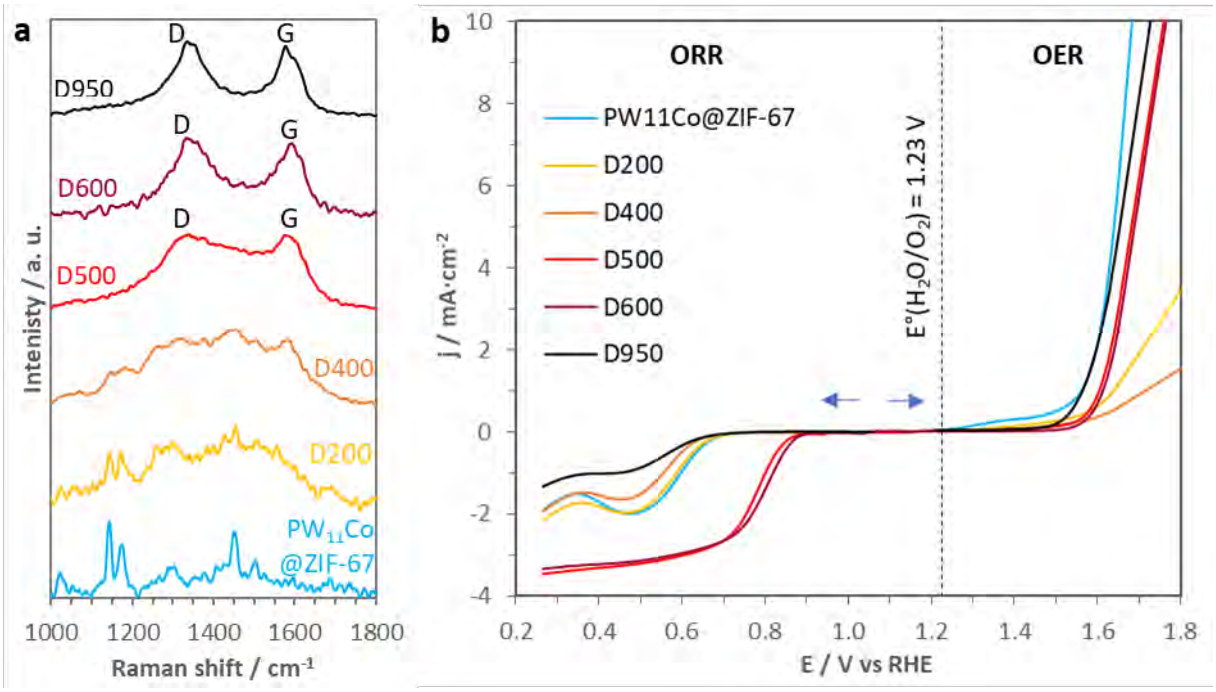


**FIGURE 2**: (a) Raman spectra of $PW_{11}Co$@ZIF-67 and their derivatives, and (b) ORR and OER LSV curves of the same samples.

**Acknowledgements**

This work was partly funded through the strategic project UID/QUI/50006/2019 (for REQUIMTE-LAQV) and the R&D project POCI-01–0145-FEDER-016422 –UniRCell, financed by national funds through the FCT/MCTES (Fundaçao para a Ciência e a Tecnologia/Ministério da Ciência, Tecnologia e Ensino Superior) and when appropriate co-financed by FEDER (Fundo Europeu de Desenvolvimento Regional). VKAF thanks the project UniRCell for his previous work contracts, and the Junta de Andalucía (Spanish regional government) for his current Postdoc contract

**References**

Abdelkader-Fernández, V. K., Fernandes, D. M., Balula, S. S., Cunha-Silva, L. and Freire, C. (2020). Oxygen evolution reaction electrocatalytic improvement in POM@ZIF nanocomposites: A bidirectional synergistic effect. *ACS Applied Energy Materials,* 3, [3], 2925-2934. https://doi.org/10.1021/acsaem.0c00009

Abdelkader-Fernández, V. K., Fernandes, D. M., Balula, S. S., Cunha-Silva, L. and Freire, C. (2020). Advanced framework-modified POM@ZIF-67 nanocomposites as enhanced oxygen evolution reaction electrocatalysts. Journal of Materials Chemistry A, 8, [27], 13509-13521. https://doi.org/10.1039/D0TA03898A

Abdelkader-Fernández, V. K., Fernandes, D. M., Balula, S. S., Cunha-Silva, L., Pérez-Mendoza, M. J., López-Garzón, F. J., Pereira, M. F. and Freire, C. (2019). Noble-metal-free MOF-74-derived nanocarbons: Insights on metal composition and doping effects on the electrocatalytic activity toward oxygen reactions. *ACS Applied Energy Materials,* 2, [3], 1854-1867. https://doi.org/10.1021/acsaem.8b02010

Freire, C., Fernandes, D. M., Nunes, M and Abdelkader, V. K. (2018). POM & MOF-based electrocatalysts for energy-related reactions. *ChemCatChem*, 10, [8], 1703-1730. https://doi.org/10.1002/cctc.201701926

Carbon 2022

# Exploring the synergistic effect of Pd nanoparticles and highly dispersed transition metals on $C_3N_4$/activated carbon composites for boosting ORR electroactivity

**G. Alemany-Molina[1], M. Navlani-García[1], E. Morallón[2], D. Cazorla-Amorós[1]**

[1]Department of Inorganic Chemistry and Materials Institute, University of Alicante, Ap. 99, Alicante, E-03080, Spain.

Email: gabriel.alemany@ua.es

[2]Department of Physical Chemistry and Materials Institute, University of Alicante, Ap. 99, Alicante, E-03080, Spain.

**Keywords**

ORR; palladium; carbon nitride.

## INTRODUCTION

The design of efficient electrocatalysts for the oxygen reduction reaction (ORR) with low metal content remains a significant bottleneck to the large-scale commercialisation of devices such as fuel cells or metal-air batteries. Platinum-based materials are normally used as catalysts due to their high catalytic activity, chemical stability, and high exchange current density (Yu, 2007). However, high Pt loadings are required to overcome the kinetic limitations of the ORR, which entails high costs, together with other important drawbacks such as Pt scarcity or poisoning by CO (Saleh, 2014). In the last years, several strategies to optimise noble metal utilisation have been developed, such as alloying with non-noble metal atoms or the reduction of size of the active phase (Liu, 2020). Thereby, not only the efficiency of the metal utilisation is improved but also the catalytic properties are altered because of the modification of the chemical environment.

Following these strategies, it has been recently reported that Fe-N-C sites can act as nucleation and growth centres leading to strong interfacial interactions which are able to modify the electronic properties and the catalytic activity of Pd nanoparticles (Pd NPs) (Zhong, 2021), which are a known active phase for the ORR (Nunes, 2020). On the other hand, carbon nitride ($C_3N_4$) has been widely studied as a transition metal host in heterogeneous catalysis and electrocatalysis due to the presence of surface Lewis basic sites. It has been reported that transition metals can be anchored to $C_3N_4$ basic sites as ultra-small metal clusters or even as single-atoms (Alemany-Molina, 2022; Li, 2017). However, its low surface area (~ 10 $m^2/g$) due to strong layer stacking makes difficult the full utilisation of the active sites.

In this work, highly dispersed Fe or Cu species were anchored on composite supports based on $C_3N_4$ and an activated carbon with exceptional textural properties (BET surface area > 3000 $m^2/g$) (Alemany-Molina, 2022). The carbon support allowed to maximise the Lewis basic groups exposed to the surface by using a single-step and a reproducible synthetic protocol. Then, Pd NPs were prepared over the composite materials and the physical-chemical properties and the catalytic performance of the resulting electrocatalysts were studied.

## EXPERIMENTAL

The activated carbon used as support (KUA) was prepared through chemical activation of an anthracite with KOH. Fe and Cu-C3N4/KUA catalysts were synthesised using the as-prepared KUA and dicyandiamide as the $C_3N_4$ precursor (Alemany-Molina, 2022). For that, KUA was mixed with dicyandiamide to have a 15 wt% of the initial total mass. Then, the required amount of the metal precursor ($Fe(NO_3)_3$ or $Cu(NO_3)_2$) was added to achieve a nominal metal loading of 1 wt. %. The resulting mixture was dispersed in water by sonicating in an ultrasound bath for 15 min. After that,

water was removed by evaporation until dryness. Next, the samples were subjected to a 4 h heat treatment at 520 ºC, with a heating rate of 5 ºC/min and 150 mL/min of $N_2$-atmosphere. After that, Pd NPs were synthesised by standard impregnation method using $Pd(O_2CCH_3)_2$ as precursor and reduction at room temperature using $Na(BH_4)$ as the reducing agent (1:5 molar relation) in 30 mL of acetone. The samples prepared were named Pd/Cu-C3N4/KUA, Pd/Fe-C3N4/KUA. For comparative purposes, a sample without Cu or Fe was also prepared (sample denoted as (Pd/C3N4/KUA)).

**RESULTS**

The samples preserved a very high apparent surface area and micropore volume after the modification with $C_3N_4$ and metals. TEM micrographs showed that KUA has a disordered structure which is not modified after the incorporation of $C_3N_4$ and Fe or Cu, indicating that no metal NPs detectable by TEM were formed. When Pd is prepared in Pd/C3N4/KUA, NPs with sizes ranging from 2 to 10 nm were formed. However, in presence of the highly dispersed Fe or Cu atoms, the Pd NPs were more homogeneously distributed, and the average particle size was smaller than 3 nm. N 1s XPS spectra presented three contributions at binding energies equivalent to those of bare $C_3N_4$, although it was observed an increase in the contribution at 399.5 eV that may be related to the presence of M-N species. Even though the synthesis of Pd/Cu-C3N4/KUA catalyst was performed under reducing conditions, the contribution of oxidised Cu detected in the Cu 2p XPS spectra was more important in Pd/Cu-C3N4/KUA than in Cu-C3N4/KUA sample.

Fe and Cu-C3N4/KUA samples showed better catalytic activity in terms of onset potential ($E_{onset}$) and half-wave potential ($E_{1/2}$) than that of Pd/C3N4/KUA. However, the performance of those samples is limited by the selectivity. The percentage of $H_2O_2$ produced estimated from the number of transferred electrons obtained from the Koutecky-Levich plot is around 20%. For Pd/C3N4/KUA sample, the selectivity increased significantly up to 3.8 electrons but both $E_{onset}$ and $E_{1/2}$ decreased. Interestingly, it was observed that, when Pd NPs were synthesised in presence of highly dispersed Cu or Fe, the catalytic activity is as high as in Cu-C3N4/KUA but the outstanding selectivity towards the 4-electron pathway of the Pd NPs is maintained.

Moreover, the synthesis route can be modified to prepare more active Fe-N-C or Cu-N-C sites by using high-temperature treatments. It has been observed that, when Pd NPs were prepared using these samples as support, the electron transfer improved obtaining Tafel slopes lower than that of commercial Pt/C electrode and $E_{1/2}$ values up to 0.80 V vs. RHE ($E_{1/2}$(Pt/C)=0.82 V vs. RHE).

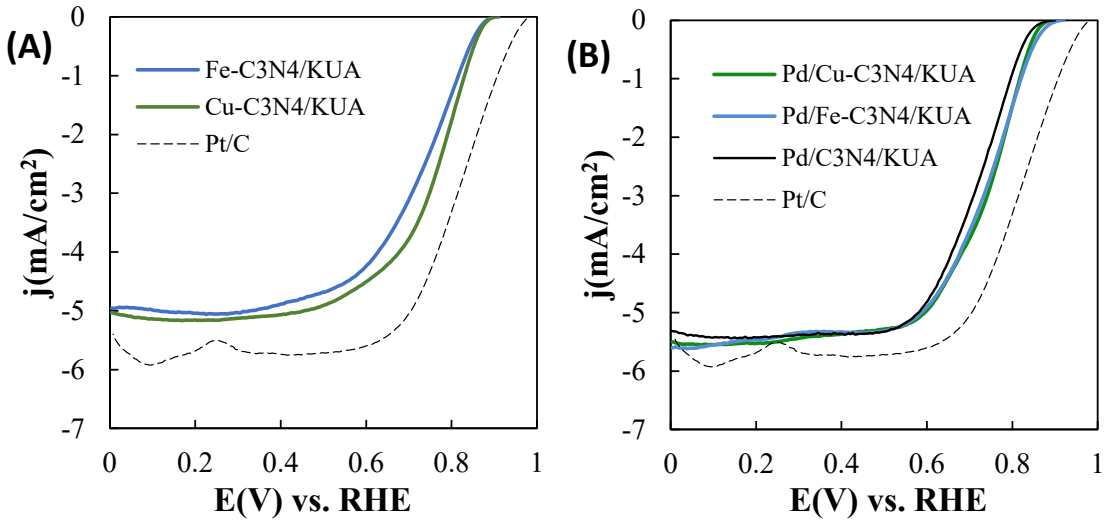


**FIGURE 1**: A) LSV curves of ORR for the supports and B) Pd modified samples compared to Pt/C commercial electrode (KOH 0.1 M, 5 $mV \cdot s^{-1}$, 1600 rpm).

## CONCLUSIONS

Pd NPs are active towards the ORR and show an excellent selectivity to the 4-electron pathway. The presence of highly dispersed Cu or Fe affects the size of the Pd NPs and produces a synergistic effect that enhances the catalytic properties.

**Acknowledgements**

G.A.M. thanks the Ministry of Universities of Spain for the FPU grant (FPU20/03969). M.N.G. thanks Plan GenT of Generalitat Valenciana (CDEIGENT/2018/027) for the financial support. The authors would like to thank MCI/AEI and FEDER, UE (PID2019-105923RB-I00, RTI2018-095291-B-I00 projects) for the financial support.

**References**

Alemany-Molina, G.; Quílez-Bermejo, J.; Navlani-García, M.; Morallón, E.; Cazorla-Amorós, D. Carbon. 2022, 196, 378-390. DOI: 10.1016/j.carbon.2022.05.003.

Li, S. L.; Yin, H.; Kan, X.; Gan, L. Y.; Schwingenschlögl, U.; Zhao, Y. Physical Chemistry Chemical Physics. 2017, 19 (44), 30069–30077. DOI: 10.1039/C7CP05195F.

Liu, L; Corma, A. Trends in Chemistry. 2020, 2(4), 383-400. DOI: 10.1016/j.trechm.2020.02.003.

Nunes, M., Fernandes, D. M., Morales, M. V., Rodríguez-Ramos, I. Guerrero-Ruiz, A., Freire, C. Catalysis Today. 2020, 357, 279-290. DOI: 10.1016/j.cattod.2019.04.043.

F.S. Saleh, E.B. Easton, Journal of Power Sources, 2014; 246:392–401. DOI: 10.1016/j.jpowsour.2013.07.109.

X. Yu, S. Ye, Journal of Power Sources, 2007; 172:133–144. DOI: 10.1016/j.jpowsour.2007.07.048.

Zhong, S., Yang, X., Chen, L., Tsumori, N., Taguchi, N., Xu, Q. ACS Applied Materials & Interfaces 2021 13 (39), 46749-46755. DOI: 10.1021/acsami.1c14009.

# Boron-doped diamond powder as an efficient and highly stable support of iron-containing catalysts for the oxygen reduction reaction

**G. Alemany-Molina[1a], B. Martínez-Sánchez[2a], A. Gabe[3], T. Kondo[4], E. Morallón[2], D. Cazorla-Amorós[1]**

[1]Department of Inorganic Chemistry and Materials Institute, University of Alicante, Ap. 99, Alicante, E-03080, Spain.

Email: gabriel.alemany@ua.es

[2]Department of Physical Chemistry and Materials Institute, University of Alicante, Ap. 99, Alicante, E-03080, Spain.

[3]Department of Biochemistry and Applied Chemistry, National Institute of Technology, Kurume College.

[4]Department of Pure and Applied Chemistry, Faculty of Science and Technology, Tokyo University of Science.

[a]*Authors with equal contribution*

**Keywords**

ORR; boron-doped diamond; iron-based catalysts.

## INTRODUCTION

The interest for the electrodes based on conductive boron-doped diamond powder (BDDP) is increasing in recent years due to their excellent physical and chemical stability, the wide potential window in both aqueous and non-aqueous electrolytes, the relatively large specific surface area, and their great versatility (Kondo, 2021). BDDP is a boron-doped diamond layer deposited on the surface of diamond powder (DP), normally obtained by chemical vapor deposition (CVD) procedure, in which the particle size can be carefully controlled depending on the DP used. In addition, BDDP is a suitable material for the preparation of inks or pastes, which facilitates the subsequent application. Therefore, these materials have been recently studied in numerous electrochemical applications, for example as screen-printed diamond electrodes, preparation of durable Pt-supported catalysts, aqueous electric double layer capacitors, among others (Matsunaga, 2021; Kondo, 2018; Miyashita, 2019).

Regarding their application in electrochemical reactions, the oxygen reduction reaction (ORR) is a well-known cathodic reaction that takes place in many electrochemical devices, such as fuel cells or metal-air batteries, in which platinum (Pt)-based materials are normally used as catalysts due to their high catalytic activity, chemical stability and high exchange current density (Yu, 2007). However, high Pt loadings are required to overcome the kinetic limitations of the ORR, which entails high costs, together with other important drawbacks (Saleh, 2014). Moreover, commercial catalysts for the oxygen reduction reaction (ORR) based on platinum nanoparticles supported on carbon materials, usually carbon blacks, show important corrosion problems of the carbon support that limit the durability of fuel cells.

BDDP-based materials have been proposed as an alternative carbon supports due to their great electrochemical stability and resistance to corrosion when subjected to highly positive potentials, which are usually generated during start-stop operations in fuel cells, for example, in automobiles. Moreover, owing to their wide potential stability range and low double layer current, BDDP substrates can be used for fundamental electrochemical studies to deeply understand the role of specific catalysts on different reactions, such as the ORR, as well as to know the influence of the surface chemistry of BDDP samples in the interaction of catalysts and their electrocatalytic performance. Therefore, we present three BDDP supports with different particle sizes and different surface oxygen contents as supports of different iron species for ORR in alkaline solution.

**EXPERIMENTAL**

BDDP samples were prepared by depositing a BDD layer on commercially available DP substrate. The procedure used was the microwave-assisted plasma chemical vapor deposition (MPCVD) (Kondo et al, 2021). Afterwards, two BDDP supports were subjected to oxidizing conditions (425ºC for 5 hours) to remove $sp^2$ carbon impurities and to obtain an oxidized surface (O-BDDP), whose particle size distribution is centred at 150 nm (O-BDDP-150) and 650 nm (O-BDDP-650). In addition, a third material was obtained by reduction of O-BDDP-150 in hydrogen plasma, obtaining a substrate rich in C-H terminations (H-BDDP-150).

O-BDDP and H-BDDP supports were modified with carbon nitride ($C_3N_4$) or phthalocyanines as anchoring points for iron. For the preparation of the $C_3N_4$-modified materials, Fe precursor ($Fe(NO_3)_3$) was introduced to obtain a nominal metal loading of 1 wt. % and using dicyandiamide as the $C_3N_4$ precursor. The samples were subjected to a heat treatment in $N_2$-atmosphere, resulting in Fe-$C_3N_4$/H-BDDP-150, Fe-$C_3N_4$/O-BDDP-150 and Fe-$C_3N_4$/O-BDDP-650. On the other hand, commercial Fe phthalocyanine (FePc) was supported onto the BDDP substrates by using the incipient wetness impregnation method. An appropriate amount of FePc dissolved in DMF (0.1 mg $mL^{-1}$) was mixed with the BDDP materials to obtain a nominal metal loading of 1 wt. %, resulting in FePc/H-BDDP-150, FePc/O-BDDP-150 and FePc/O-BDDP-650 samples.

**RESULTS**

The surface chemical composition was studied by temperature programmed desorption (TPD) experiments. TPD results evidenced that the surface chemistry of all the substrates was significatively different, in which O-BDDP-150 shows the highest mass loss. The O-BDDP materials show a total oxygen content of 1240 µmol $g^{-1}$ and 520 µmol $g^{-1}$ for O-BDDP-150 and O-BDDP-650, respectively, while H-BDDP-150 presents lower amounts of oxygen functional groups, about 300 µmol $g^{-1}$. Furthermore, the morphological and structural characteristics were studied by TEM and Raman spectroscopy, respectively. From Raman profiles, structural differences are minimal between H-BDDP-150 and O-BDDP-150. O-BDDP-650 shows a clear contribution at 1317 $cm^{-1}$ related to diamond $Csp^3$ contribution, while the contribution at around 1340 $cm^{-1}$ could be associated to disordered $Csp^2$ graphite impurities (Jawhari, 1995).

Fig. 1 shows the electrocatalytic study towards the ORR for the modified samples. The different electrocatalytic performance observed confirmed the strong influence of the surface chemistry of the BDDP supports on the activity of the metallic sites. While Tafel slope values calculated for H-BDDP and O-BDDP supports were similar, the electron transfer was dependent on the surface chemistry for both Fe-$C_3N_4$ and FePc samples (Fig. 1B). The low amount of oxygen functional groups of H-BDDP-150 leads to better electrocatalytic performance, which might be associated to a better conductivity and superior interaction with the Fe species.

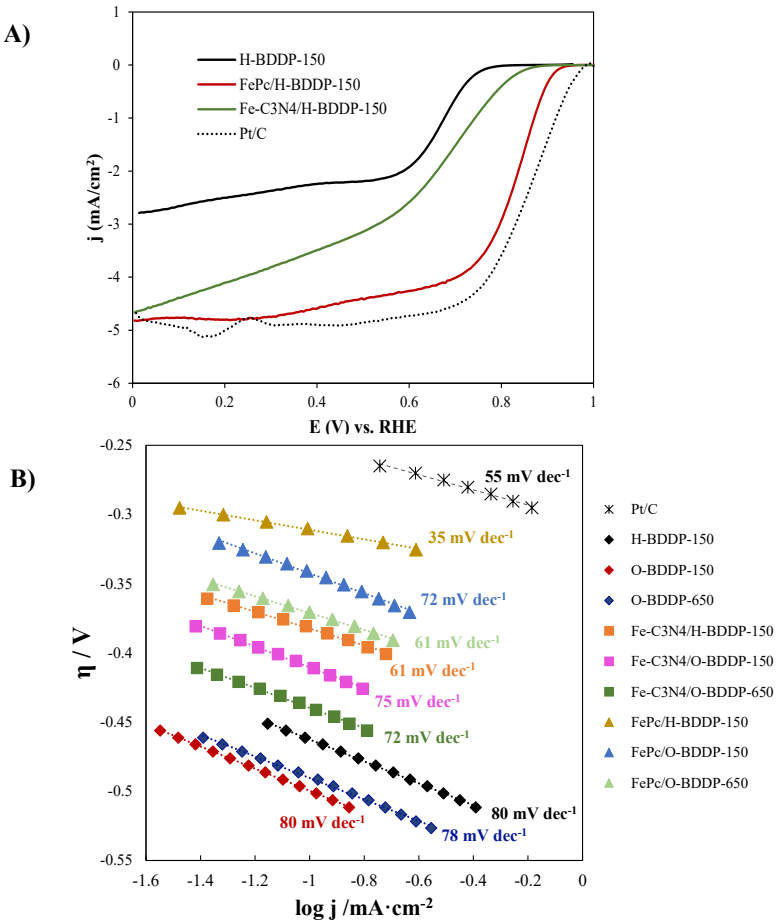


**FIGURE 1**: A) LSV curves of ORR for Fe-C3N4/H-BDDP-150 and FePc/H-BDDP-150 in 0.1M KOH, 5 $mVs^{-1}$ and B) Tafel representations for all the samples compared to Pt/C commercial electrode (20 wt.% Pt).

## CONCLUSIONS

Three BDDP substrates were modified with Fe species. Hydrogen termination in H-BDDP-150 favoured the electron transfer for efficient ORR in alkaline medium. Interestingly, the environment of the iron metal site is also decisive on the electrocatalytic performance towards the ORR.


### Acknowledgements

B.M.S. and G.A.M. thanks the Ministry of Universities of Spain for the FPU grants (FPU18/05127 and FPU20/03969). The authors would like to thank MCI/AEI and FEDER, UE (PID2019-105923RB-I00, RTI2018-095291-B-I00 projects) for the financial support.


### References


T. Jawhari, A. Roid, J. Casado, Carbon 1995, 33, 1561−1565.

T. Kondo, Chemis-try Letters, 2021; 50:733–741. DOI: 10.1246/cl.200870

T. Kondo, M. Kikuchi, H. Masuda, F. Katsumata, T. Aikawa, M. Yuasa, J. Electrochem. Soc., 2018; 165:30-72. DOI: 10.1149/2.0111806jes

T. Matsunaga, T. Kondo, I. Shitanda, Y. Hoshi, M. Itagaki, T. Tojo, M. Yuasa, Carbon, 2021; 173:395. DOI: 10.1016/j.carbon.2020.10.096.

K. Miyashita, T. Kondo, S. Sugai, T. Tei, M. Nishikawa, T. To-jo, M. Yuasa, Sci. Rep., 2019; 9:178-46. DOI: 10.1038/s41598-019-54197-9.

F.S. Saleh, E.B. Easton, Journal of Power Sources, 2014; 246:392–401. DOI: 10.1016/j.jpowsour.2013.07.109.

X. Yu, S. Ye, Journal of Power Sources, 2007; 172:133–144. DOI: 10.1016/j.jpowsour.2007.07.048.

Carbon 2022

# Graphene-based materials as dopant of isotropic carbon fibers

**P. Alvarez, M. Granda, C. Blanco, R. Santamaria, V.G. Rocha, Z. Gonzalez.**
[1] Instituto de Ciencia y Tecnología del Carbono (INCAR-CSIC), C/ Francisco Pintado Fe 26, 33011-Oviedo, Spain
Email: par@incar.csic.es

**Keywords**
Pitch-based general purpose carbon fibers, graphene, electrical conductivity

## INTRODUCTION

Properties of general purpose carbon fibers (GPCF), especially thermal and electrical conductivities, could be substantially improved by the incorporation graphene into their structure. In this preliminary work, a coal-tar pitch, free of any solid particle (especially primary quinoline insoluble particles, QI), was used as the fiber precursor and three thermal reduced graphene oxides, differing in synthesis process, chemical composition and crystalline structure, as dopant. Both, components were mixed by mechanical procedures in several proportions, and the resultant graphene doped precursors were transformed into fibers by a multistage process that involved melt-spinning, stabilization and carbonization. Different behaviors of the graphene-based materials were observed depending on their characteristics, allowing a guideline of selection of graphene-based materials to be stablished.

## EXPERIMENTAL

A semisynthetic carbochemical coal tar pitch (CTPF), prepared in our laboratories, was used as raw material. The primary QI particles were removed from the pitch by filtration. The softening point of this pitch is 215ºC. The elemental composition includes a 93 wt.% C, 1.4wt.%O and 0.5wt.%N.

The graphene materials (thermally reduced graphene oxides) used in this work were prepared via the chemical route from the same graphite oxide and by subsequent thermal treatment under different experimental conditions. In one of the treatments, the graphene oxide and subjected to a flash thermal heating to 300ºC followed by their ramp thermal heating up to 1000ºC (named FlashTRGO-1000). In other experiments, that graphite oxide was initially sonicated to produce a graphene oxide, which was then thermally heated to 1000ºC and 2700 ºC, at a heating rate of 5 ºC /min (named RampTRGO-1000 and TRGO-2700, with respect to the final temperature of treatment). Before utilization, the graphene materials were dispersed in NMP and ultracentrifugated, discarding the solid fraction recovered.

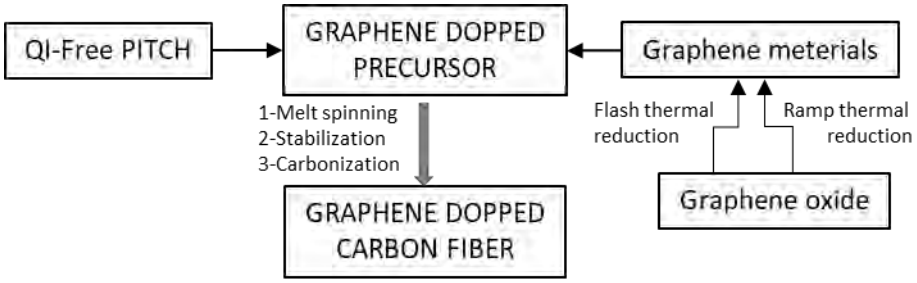


Figure 1: schematic diagram of the process for pitch dopping and the preparation of graphene dopped general purpose carbon fiber.

The graphene doped precursors were prepared by ball milling the mixture graphene/CTPF in different ration (ranging from 0.025 to 0.5 wt.%) for 2h at room temperature. As comparative purposes, the non doped precursor was also processed at the same experimental conditions (Blank).
GPCF were prepared by a typical three-stage process that involved melt-spinning, oxidative stabilization with air and subsequent carbonization. A schematic illustration of the integral process is shown in Figure 1.
Carbon fibers and precursors were characterized in terms of elemental composition and structure (SEM). Their electrical conductivity was measured in monofilament by four-point probe method and current–voltage measurements were done by using Biologic vpm multichanes Potentiostat under atmospheric conditions.

**RESULTS AND DISCUSSION**

The characterization of the graphene materials used in this work reveals structural differences among them, which is a consequence of their different processing conditions during the thermal reduction. Thus, the grapehenes prepared from the graphite oxide by means of a flash procedure (comprising their thermal exfoliations and reduction in the same step) exhibit more corrugated graphene sheets (Figure 2,a). In contrast, the previous separation of the graphene oxide sheets by sonication and subsequent ramp-based thermal heating allows obtaining more planar graphene sheets (Figure 2, b).

The doped precursors (containing from 0.025 to 0.5 wt.% of graphene material) were melt-spun and the green fibers so obtained analysed by SEM. It was determined that, in comparison with the smooth surface showed by doped fibers containing ramp-based grapehenes (Figure 2d), the utilization of graphene materials from Flash treatments led, in all cases, to defects in the surface of the fiber (Figure 2, c), thus discarding their utilization as dopant in carbon fiber precursors. Additionally, it was determined that precursors containing above 0.5 wt.% of ramp-based graphene materials led also to defects in the surface of the fibers.

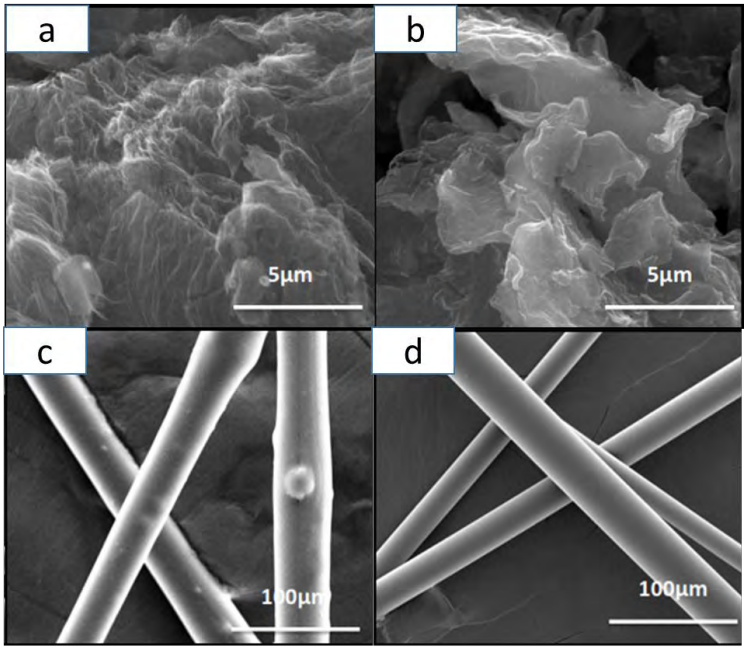


Figure 2: SEM images of grapehene material (a) FlashTRGO-1000 (b) and RampTRGO-1000 and doped GPCF with flash-based graphene (c, GPCF-RampTRGO-1000) and ramp-based graphene (d, GPCF-RampTRGO-1000ºC)

The green fibers with adequate surface properties were stabilized and carbonized and their electrical resistivity calculated. It was determined that doping fibers with graphenes obtained at 1000ºC do not produce any substantial increment in the electrical conductivity of the fibers. In contrast, the utilization of graphene material obtained at 2700ºC in the range studied led to a decrease of the electrical resistivity of the fibers of almost a 50% of the parent resistivity of no doped fibers (figure 3).

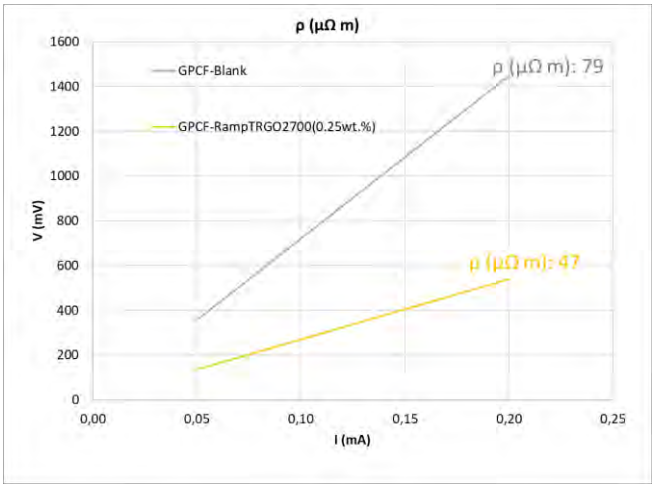


Figure 3: I/V curve from which electrical resistivity was calculated in fibers without doping (grey color, GPCF-Blank) and doped with a 0.25 wt.% pitch/ramp-based graphene ratio (yellow line, GPCF-RampTRGO2700(0.25wt.%)

**CONCLUSIONS**

Graphene-doped general purpose carbon fibers can be successfully prepared from a doped pitch precursors and subsequent melt-spinning, stabilization and carbonization processed. The morphology of the graphene sheets determined by their experimental preparation procedure crucially determined their utilization as dopant of spinnable pitches. The inherent corrugation of the graphene sheets prepared by flash procedures (thermal exfoliation and reduction of graphene oxides) discard their utilization as pitch dopant. In contrast, graphenes prepared by thermal reduction of graphene oxides (US exfoliated) allows to obtain carbon fibers with smooth surface even in rations up to 0.5 wt.%. It was also determined that only the presence of highly reduced grapheme materials (>2700ºC) in the fibers enhances their conductivity, leading to resistivity which decreases up to 50% of that of undoped GPCF.

**References**

Álvarez, P.; Granda, M.; Sutil, J.; Santamaría, R.; Blanco, C.; Menéndez, R. (2011). A unified process for preparing mesophase and isotropic material from anthracene oil-based pitch. Fuel Processing Technology, 92, 421-427. https://doi.org/10.1016/j.fuproc.2010.10.004

Díez, N.; Álvarez, P.; Santamaría, R.; Blanco, C.; Menéndez, R.; Granda, M. Optimisation of the melt-spinning of anthracene oil-based pitch for isotropic carbon fibre preparation. (2012). Fuel Processing Technology, 93, 99-104. DOI:10.1016/j.fuproc.2011.09.016

Diez, N.; Díaz, P.; Álvarez, P.; González, Z.; Granda, M.; Blanco, C.; Santamaría, R.; Menéndez, R. Activated carbon fibers prepared directly from stabilized fibers for use as electrodes in supercapacitors (2014). Materials Letters, 136, 214-217. https://doi.org/10.1016/j.matlet.2014.08.017

Diez, N.; Alvarez, P.; Granda, M.; Blanco, C.; Gryglewicz, G.; Wróbel-Iwaniec, I.; Sliwak, A.; Machnikowski, J.; Menendez, R. (2014). Tailoring micro-mesoporosity in activated carbon fibers to enhance SO2 catalytic oxidation. Journal of Colloid and Interface Science, 428, 36-40. http://dx.doi.org/10.1016/j.jcis.2014.04.027

E. Mora, C. Blanco, V. Prada, R. Santamaría, M. Granda, R. Menéndez. (2002) A study of pitch-based precursors for general purpose carbon fibres. Carbon, 40, 2719-2725. DOI:10.1016/S0008-6223(02)00185-9

Carbon 2022

# Nitrogen doping of carbon xerogels as non-precious metal catalysts for the oxygen reduction reaction

**L. Álvarez-Manuel*, C. Alegre, D. Sebastián, M.J. Lázaro**
Instituto de Carboquímica, CSIC. C/. Miguel Luesma Castán, 4. 50018 Zaragoza
Email: (*)lalvarez@icb.csic.es, mlazaro@icb.csic.es

**Keywords**
Nitrogen-doped carbon xerogel, iron catalysts, fuel cells.

## INTRODUCTION

The development of active and inexpensive non-precious metal catalysts is a necessary and essential requirement to replace currently used Pt-based catalysts, in order to reduce the cost of polymer electrolyte fuel cells (PEFC). [1] Catalysts based on the Fe-N-C structure develop high electroactivity towards the oxygen reduction reaction (ORR), the limiting reaction in fuel cells. To increase the catalysts' activity, Fe must be atomically dispersed in a carbon material with a high surface area. In this context, carbon xerogels are excellent candidates, as their main properties can be easily tailored: porosity, electrical conductivity and surface chemistry. [2] The meso/macroporosity of carbon xerogels can be designed by modifying the conditions of the synthesis process, while microporosity can be generated by subsequent carbonization/activation treatments.

In the present work, on the basis of carbon xerogels with an optimal ratio of micro/meso/ macroporosity, we investigate the effect of two different methods of nitrogen-doping in the catalytic activity of Fe-N-C catalysts. Catalysts are evaluated both in half-cell and single-cell configurations and their activity is correlated to their physical-chemical features.

## EXPERIMENTAL

Organic xerogels (OXG) were synthesized by a sol-gel synthesis method from resorcinol and formaldehyde. The first doping method consisted of mixing the OXG with urea followed by pyrolysis at 800ºC (N-CXG-1). The second doping method consisted of a first pyrolysis of the OXG into carbon xerogel (CXG) at 800°C and then mixing the so-obtained CXG with urea, followed by a second thermal treatment at 800ºC (N-CXG-2). All thermal treatments were carried out in inert atmosphere for 1h duration. The Fe doping was made by mixing either the N-CXG-1 or the N-CXG-2 in a planetary ball mill with iron acetate. The obtained powder was pyrolyzed in $N_2$ atmosphere at 1050°C for 1h, obtaining Fe-N-CXG-1 and Fe-N-CXG-2. [3,4] Subsequently, these materials were treated by a series of acid treatments in $HClO_4$ in order to eliminate inactive iron particles, followed by a thermal treatment at 950°C in $N_2$ flow.

The textural features of the carbon xerogels were determined by means of $N_2$ and $CO_2$ physisorption. The physical-chemical characteristics of the catalysts were determined by X-ray photoelectron spectroscopy (XPS), optical emission spectroscopy with inductive coupled plasma (ICP-OES), and elemental analysis (EA). The activity of the catalysts towards the ORR was determined in a three electrode cell with a rotating disk electrode (RDE) and $O_2$-saturated 0.5 M $H_2SO_4$ electrolyte. Membrane-electrode assemblies (MEAs) were prepared by hot-pressing of cathode (Fe-N-C catalyst, 4 mg $cm^{-2}$) and anode (commercial Pt/C, 0.2 $mg_{Pt}$ $cm^{-2}$) with Nafion®212R membrane. The electrodes were prepared by spraying the catalyst on a GDL-39BC (Sigracet) gas diffusion layer. A Fuel Cell Technologies Inc. test station was used to evaluate the MEA performance at a cell temperature of 80°C and 100%RH.

## RESULTS AND DISCUSSION

Table 1 shows the N/C atomic ratio determined by EA and XPS. Figure 1 presents the high-resolution N1s spectra with the N speciation. The Fe-N-CXG-2 catalyst presents a higher N/C and a higher contribution of N-Fe bond compared to Fe-N-CXG-1.

**TABLE 1:** N/C atomic ratios calculated by EA and XPS.

| | EA | XPS |
|---|---|---|
| | N/C | N/C |
| **N-CXG-1** | 0.07 | 0.12 |
| **N-CXG-2** | 0.07 | 0.09 |
| **Fe-N-CXG-1** | 0.02 | 0.03 |
| **Fe-N-CXG-2** | 0.05 | 0.06 |

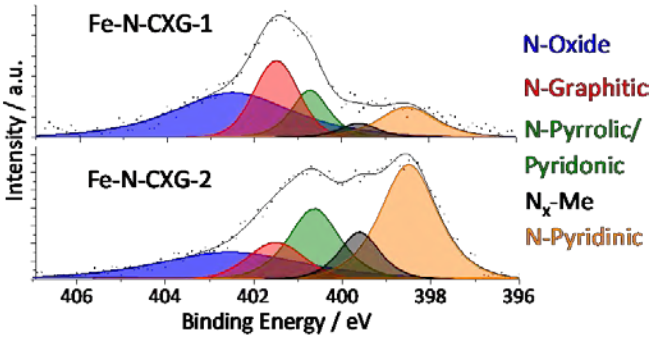


**FIGURE 1:** High-resolution N1s spectra fitted with individual peaks.

Figure 2 (a) shows the catalysts' activity towards the ORR measured in a three-electrode cell system. Fe-N-CXG-2 presents a significantly higher activity compared to Fe-N-CXG-1, what correlates with its higher N/C and N-Fe content. The half-wave potential for Fe-N-CXG-2 is 110 mV lower that the one for the commercial benchmark catalyst, Pt/C (40 wt. % Pt, Johnson Matthey). RDE measurements at different rotation speeds (400 to 2500 rpm) were adjusted to the Koutecky–Levich (KL) equation in order to determine the number of electrons transferred during the ORR (Figure 2 (b)). As expected, the ORR on Pt/C goes through 4e$^-$. Fe-N-CXG-2 catalyst presents a similar slope to Pt/C, meaning that the ORR in this catalyst also goes through a four-electron pathway, whereas Fe-N-CXG-1 follows 2e$^-$ mechanism. [5]

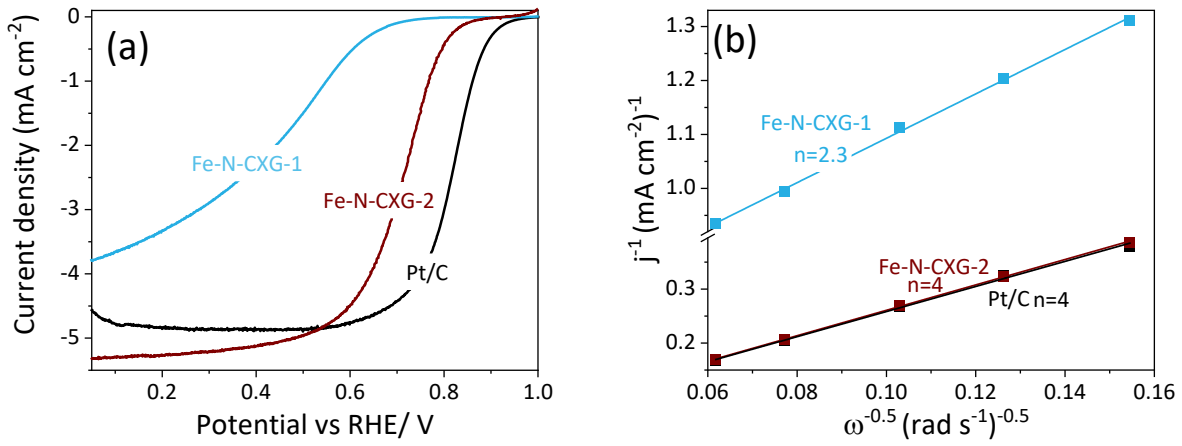


**FIGURE 2:** (a) Polarization curves for the ORR, in RDE at 1600 rpm in $O_2$-saturated 0.5M $H_2SO_4$. (b) Koutecky-Levich plot $j^{-1}$ vs. $\omega^{-0.5}$ at 0.6V vs. RHE.

The Fe-N-CXG catalysts' activity and durability were also studied in a PEFC single cell. Fig. 3 (a) shows the polarization curves and the power density curves. The Fe-N-CXG-2 catalyst exhibits a polarization curve *ca.* 100 mV better than Fe-N-CXG-1, in line with the 3-electrode cell results. Therefore, the maximum power density is about 80% higher for Fe-N-CXG-2. The catalyst's durability is represented in Figure 3(b). After 20h of operation at 0.5 V, both catalysts have a loss of activity of around 20%.

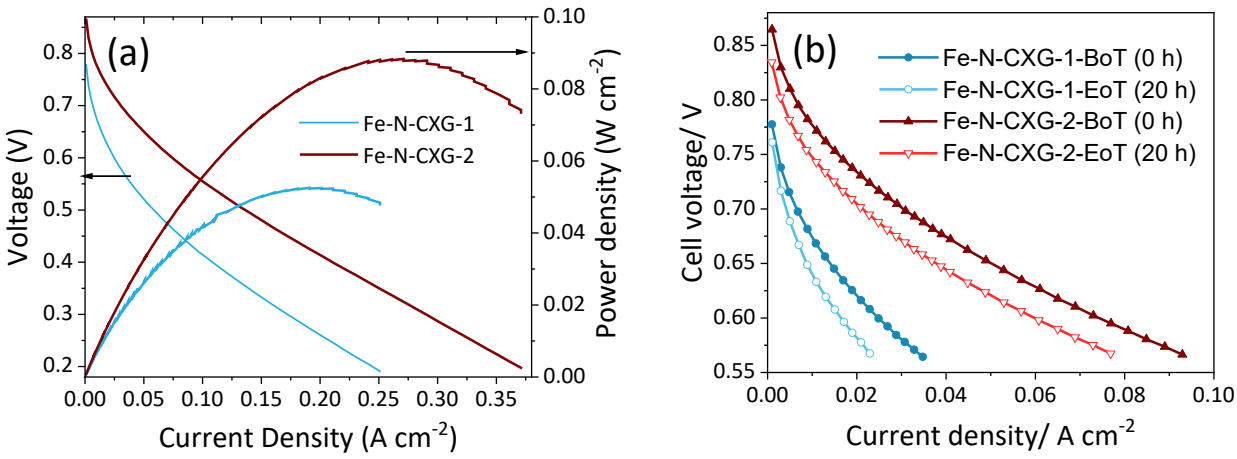


**FIGURE 3:** (a) Power density curves. Cell temperature 80ºC, 100% RH, hydrogen/oxygen (150/130 kPa-g backpressure). (b) Polarization curves for MEAs comprising a cathode made with Fe-N-CXG after and before of 20 h operation test.

## CONCLUSIONS

From these results, the two-step nitrogen-doping method appears more effective for the preparation of Fe-N-C catalysts based on carbon xerogel substrate since a larger amount of Fe-N species is favoured according to XPS results.

**Acknowledgments**

The authors wish to thank the Ministry of Science and Innovation and the AEI (MCIN/ AEI/ 10.13039/ 501100011033) for the funding received with the reference project PID2020-115848RB-C21 and the Government of Aragon for funding the T06-20R group. L. Álvarez-Manuel wishes to thank the Government of Aragon for her pre-doctoral contract.

**References**

[1] Chen, Z., Higgins, D., Yu, A., Zhang, L., Zhang, J. J., Heller, A., Hui, S. Q., Zhang, J. J., Ota, K., Campbell, S. A., Dahn, J. R., Olson, T., Pylypenko, S., Atanassov, P., Ustinov, E. A., & Al., E. (2011). A review on non-precious metal electrocatalysts for PEM fuel cells. *Energy & Environmental Science*, 4, [9], 3167-3177. https://doi.org/10.1039/c0ee00558d

[2] Canal-Rodríguez, M., Rey-Raap, N., Menéndez, J. Á., Montes-Morán, M. A., Figueiredo, J. L., Pereira, M. F. R., & Arenillas, A. (2020). Effect of porous structure on doping and the catalytic performance of carbon xerogels towards the oxygen reduction reaction. *Microporous and Mesoporous Materials*, 293, 109811-109820. https://doi.org/10.1016/j.micromeso.2019.109811

[3] Gokhale, R., Thapa, S., Artyushkova, K., Giri, R., & Atanassov, P. (2018). Fully Synthetic Approach toward Transition Metal-Nitrogen-Carbon Oxygen Reduction Electrocatalysts. *ACS Applied Energy Materials*, 1, [8], 3802–3806. https://doi.org/10.1021/acsaem.8b00537

[4] Proietti, E., Jaouen, F., Lefèvre, M., Larouche, N., Tian, J., Herranz, J., & Dodelet, J. P. (2011). Iron-based cathode catalyst with enhanced power density in polymer electrolyte membrane fuel cells. *Nature Communications*, 2, [1], 416-428. https://doi.org/10.1038/ncomms1427

[5] Vinayan, B. P., Diemant, T., Behm, R. J., & Ramaprabhu, S. (2015). Iron encapsulated nitrogen and sulfur co-doped few layer graphene as a non-precious ORR catalyst for PEMFC application. *RSC Advances*, 5, [81], 66494–66501. https://doi.org/10.1039/c5ra09030j

Carbon 2022

# Role of Surface Defects of Nanoporous Carbons on the Electrochemical Reduction of $CO_2$

**Elhassan Amaterz[1], Jesus Iniesta[2] and Conchi Ania[1]**
[1]CEMHTI, CNRS (UPR 3079), Université d'Orléans, 45071 Orléans, France
[2]Instituto Universitario de Electroquímica, Universidad de Alicante, 03080 Alicante, Spain
Email: elhassan.amaterz@cnrs-orleans.fr

**Keywords**
Nanoporpous carbons; surface defects, $CO_2$ reduction.

## INTRODUCTION

The current extensive consumption of fossil fuels releases huge and unsustainable amounts of carbon dioxide ($CO_2$) into the environment, which leads to global warming. Thus, there is a need to develop strategies to mitigate the $CO_2$ levels in the atmosphere. In addition to $CO_2$ capture and storage, direct conversion of $CO_2$ into value-added chemicals and fuels should be more attractive. Among these products from $CO_2$ reduction, CO is more accessible because selective production CO only needs two electron/proton transfers. More importantly, CO is a very useful intermediate in chemical synthesis of syngas, phosgene, and other fuels (Li, 2016; Lu, 2016). Great efforts has been made over the past years in which researchers have explored a variety of catalysts (including metals, metal oxides and metal complexes) for the $CO_2$RR. The metal-based catalysts such as Au, Ag, Pd and their alloys or oxides are known to exhibit excellent selectivity and activity for CO formation. However, exploring earth-abundant and low-cost alternatives for $CO_2$RR is preferable (Li, 2017). The objective of this study is to investigate the electrochemical $CO_2$ reduction using nanoporous carbon as metal-free electrocatalysts. A series of carbons was selected owing to their different physicochemical features. A detailed physico-chemical characterization has allowed us to clarify the importance of the surface chemistry and the size of the nanopores for an efficient electroreduction of $CO_2$.

## EXPERIMENTAL

Various nanoporous carbons with different characteristics were selected as electrocatalysts: carbons FY (biomass, steam activation), Q (bituminous coal, steam activation), CV (biomass, $H_3PO_4$ activation), and CVH8 (annealing of carbon CV at 850 °C, 30 min, $N_2$ flow 50 ml/min). The carbons were thoroughly characterized (surface chemistry, porosity, composition). The materials were used for the electrocatalytic reduction of $CO_2$ using a single compartment 3-electrode configuration cell and an electrochemical workstation. The working electrode was prepared mixing the active carbon materials with polyvinylidene fluoride (ratio 9:1) in a small volume of N-methyl-2-pyrrolidone. The slurry was coated one side onto a Ti foil (1 $cm^2$) and dried at 60 °C for 4 hours in an oven. A carbon graphite rod was used as counter electrode, and a saturated calomel electrode (SCE) as reference. Linear sweep voltammetry (LSV) was used to evaluate the electrocatalytic activity towards the $CO_2$ reduction. Before experiments, the electrolytes were bubbled with $CO_2$ or He for 30 min. LSV measurements in the gas-saturated electrolyte were carried out in the potential range of 0 V to -1.8 V versus SCE at a sweep rate of 10 mV $s^{-1}$.

## RESULTS AND SICUSSION

The performance of the selected carbons for the electrochemical reduction of $CO_2$ was examined by LSV measurements in $CO_2$ and He-saturated 0.5 M $Na_2SO_4$ electrolyte (Figure 1). As seen, significant

differences in both the onset potentials and the intensities of the current densities are obtained for the series of investigated carbons.

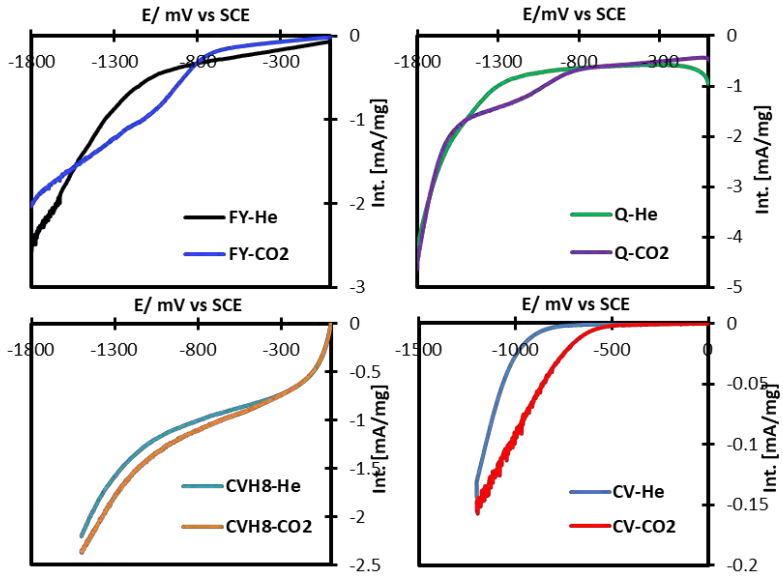


**FIGURE 1**: Linear Sweep Voltammetries of the investigated nanoporous carbons in He and $CO_2$-saturated electrolyte (0.5 M aqueous $Na_2SO_4$ solution). Scan rate 10 mV $s^{-1}$.

For all the carbons with the exception of sample CVH8, the LSV curves show a more positive onset potential compared to the response obtained in the He-saturated electrolyte. This indicates that the $CO_2$ reduction occurs at potential less negative than that of the competing hydrogen evolution reaction. In the case of carbon CVH8, the difference is less noticeable; the profile is rather similar than that in helium atmosphere with a slightly difference in the overall current density from ca. -500 mV due to the contribution of the $CO_2$ reduction. This suggests that the activity of this carbon is lower than that of the other carbons of the series. It can also be observed that hydrophobic carbons Q and FY show larger current densities for the reduction of $CO_2$ than hydrophilic carbon CV (also for CVH8 compared to CV). This is attributed to the high functionalization degree of carbon CV that decreases its conductivity. Regarding the nature of the carbons, data showed that the carbons with high micropore volume exhibited larger current density and similar onset potentials. On the other hand, presence of oxygen-containing functionalities seems to have a negative effect on the performance for $CO_2$ reduction in terms of overall current density (sample CV vs CVH8) due to the lower electron density in the electrode. However, it should be noted that the onset potential of carbon CV is lower than that of the hydrophobic carbons.

## CONCLUSIONS

We have investigated the electrocatalytic activity of a series of nanoporous carbons with different characteristics for the electrochemical reduction of $CO_2$. A preliminary screening by LSV has revealed that hydrophobic carbons with large micropore volumes display large current densities at similar onset potentials. On the other hand, hydrophilic carbons displayed lower onset potentials but lower current densities, due to the large surface functionalization. Based on these results, the electrocatalytic activity will be tested upon long-term catalytic assays, and evaluated the impact on the intermediates generated.

**Acknowledgements**

The financial support of the European Research Council through a Consolidator Grant (684161) is acknowledged.

**References**

Li F. Li, M. Xue, G. P. Knowles, L. Chen, D. R. MacFarlane, and J. Zhang (2017). “Porous nitrogen–doped carbon derived from biomass for electrocatalytic reduction of CO2 to CO,” Electrochim. Acta, 245, pp. 561–568, doi: 10.1016/j.electacta.2017.05.174.

Li W. Li, M. Seredych, E. Rodríguez-Castellón, and T. J. Bandosz, (2016).. Metal-free Nanoporous Carbon as a Catalyst for Electrochemical Reduction of CO2 to CO and CH4 ChemSusChem, 9, 606–616, 10.1002/cssc.201501575.

Lu X. Lu, T. H. Tan, Y. H. Ng, and R. Amal, “Back Cover: Highly Selective and Stable Reduction of CO2 to CO by a Graphitic Carbon Nitride/Carbon Nanotube Composite Electrocatalyst (2016),” Chem. - A Eur. J., 22, 12200, 2016, doi: 10.1002/chem.201602994.

Carbon 2022

# Kinetics and equilibrium studies in the effective removal of atrazine on sustainable nanoporous carbons

**C.P. Amézquita-Marroquín[1], P. Torres-Lozada[1], L. Giraldo[2], P.D. Húmpola[3], P.S. Poon[4], J. Matos[5,*], J.C. Moreno-Piraján[6,*]**

[1] Escuela de Ingeniería de los Recursos naturales y del Ambiente, Facultad de Ingeniería, Universidad del Valle. Calle 13 100-00, Cali, Colombia.

[2] Departamento de Química, Facultad de Ciencias, Universidad Nacional de Colombia, Carrera 45, Bogotá, Colombia.

[3] Facultad de Bioquímica y Ciencias Biológicas, Universidad Nacional del Litoral. Ruta Nacional Nº 168, km 472, Santa Fe, Argentina.

[4] Unidad de Desarrollo Tecnológico (UDT), Universidad de Concepción, Concepción, Chile.

[5] Instituto de Ciencias Químicas Aplicadas, Facultad de Ingeniería, Universidad Autónoma de Chile, 8900000 Santiago, Chile.

[6] Departamento de Química, Facultad de Ciencias, Universidad de los Andes, Carrera Primera 18A-12, Bogotá, Colombia.

*Corresponding authors.

Emails: juan.matos@uautonoma.cl (J. Matos); jumoreno@uniandes.edu.co (J.C. Moreno-Piraján).

**Keywords**

Nanoporous carbon; Atrazine removal; Kinetics/equilibrium studies.

## INTRODUCTION

The industrial revolution has improved the global economy and the quality of life. However, many industries have caused a remarkable environmental damage due to the toxic organic and inorganic compounds released to effluents. For instance, the agroindustry has focused on the development and application of pesticides for the control of crops. Despite the high toxicity, atrazine (AZT) is one of the most widely pesticides used worldwide due to the low cost and high efficiency. In Latin American countries, regulations, or policies for the use of ATZ have not been stablished. Thus, an increasingly common sustainable strategy to remove ATZ is to use agro-industrial wastes to prepare low-cost activated carbon (ACs). As an example of circular bioeconomy, sustainable nanoporous carbons were prepared from mangosteen peels-derived chars by physical activation under $CO_2$ flow and used to remove ATZ (Amézquita-Marroquín et al., 2020).

## EXPERIMENTAL

Mangosteen peels denoted PM were used as agricultural waste. In a first-step, the PM was pyrolized under $N_2$ flow at 800 °C by 3h (1 atm, 100 mL $min^{-1}$). In a second step, this char was activated at 700 °C, 800 °C, and 900 °C, under $CO_2$ flow by 3 h (1 atm, 100 mL $min^{-1}$). The so prepared carbons were denoted APM-7, APM-8 and APM-9 for 700°C, 800°C, and 900°C, respectively. Kinetic and equilibrium studies of atrazine adsorption were carried out varying the temperature, the mean particle size of the adsorbent, and the initial concentration of pollutant. The kinetic data was analysed using different kinetic models (pseudo-first, pseudo-second order and Avrami´s) and different equilibrium models for the adsorption isotherms (Langmuir, Sips and Redlich-Peterson). The carbons were characterized by gas adsorption, scanning and transmission electron microscopy (SEM/TEM), chemical composition by energy dispersed X-ray analysis (EDX), acidic and basic groups on the surface of the ACs by the Boehm acid-base titration method, surface pH of carbons in terms of the point zero charge ($pH_{PZC}$), and Fourier transformed infrared spectroscopy (FTIR).

## RESULTS AND DISCUSSION

Several adsorption models such as Langmuir (two parameter), Sips and Redlich-Peterson (three parameters) were applied to verify the influence of carbon´s properties on the uptake of atrazine. Additional kinetic models (pseudo-first order, pseudo-second order and Avrami´s) allowed to establish that a mixture of physi-/chemisorption describes the interaction between the nanoporous carbons and atrazine. An important diffusion of atrazine from the bulk of solution to the surface of carbons was observed. Several correlations between the kinetic and equilibrium parameters for the atrazine adsorption were found as a function of the textural properties and surface chemistry. Based on the kinetics and equilibrium parameters, the present work proposes a mechanism (Figure 1) for the atrazine adsorption on nanoporous carbons contributing to the understanding of the interactions between pollutant molecules and the surface functional groups on nanoporous carbons in the liquid-solid interface. The mechanism proposed for ATZ adsorption involves that the hydrogen atom from the secondary amine group in atrazine interact through an H-bridge (structure A) with a basic oxygen group such as pyrone. The electronic vacancy formed in the atrazine after adsorption is solvated by a proton of a second adsorbed atrazine molecule (structure B) promoting a polymerization-type process (structure C) yielding by successive steps to the formation of molecular aggregates (structure D and E).

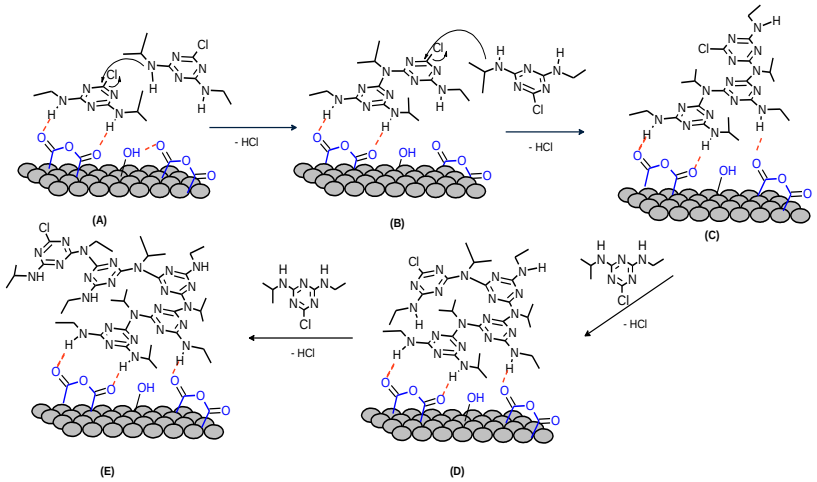


**Figure 1.** Mechanism for the atrazine adsorption on the mangosteen-derived nanoporous carbons.

## CONCLUSIONS

The present work has demonstrated that mangosteen peels can be used as precursor to prepare nanoporous activated carbons for the efficient removal of a common pesticide such as atrazine. The kinetics and the equilibrium parameters for the atrazine adsorption were correlated with the textural properties and surface chemistry of the nanoporous carbons. We do believe the correlations presented in this work open a door for the understanding of the interfacial interaction between molecular clusters of pesticides such as ATZ and the functional groups in carbon-based adsorbents. Accordingly, a mechanism of adsorption has been proposed based on the kinetic and equilibrium studies

**Acknowledgements**

C.P. Amézquita-Marroquín thanks COLCIENCIAS 567 fellow. J.C. Moreno-Piraján thanks the Faculty of Sciences, University of the Andes, 11-28-2017-2019. P.S. Poon thanks the financial support of ANID-PIA/APOYO CCTE AFB170007. J. Matos ANID-FONDECYT 1190591; ANID-FONDEF ID19I10003; ANID-FONDEF ID15I20321.

**References**

Amézquita-Marroquín, C. P., Torres-Lozada, P., Giraldo, L., Húmpola, P. D., Rivero, E., Poon, P. S., Matos, J., Moreno-Piraján, J. C. (2020). Sustainable production of nanoporous carbons: Kinetics and equilibrium studies in the removal of atrazine. J. Coll. Inter. Science. 562, 252-267.

# Solid matter collected from cigarette smoke and heated tobacco product aerosol using a laboratory designed puffing setup.

**A. Amorós-Pérez, L. Cano-Casanova, M.C. Román-Martínez, M.A. Lillo-Ródenas**
MCMA research group, Department of Inorganic Chemistry, Faculty of Sciences and Materials Institute (IUMA). University of Alicante, Alicante, E-03080, Spain.
Email: mlillo@ua.es

**Keywords**
cigarettes, heated tobacco products, aerosol.

## INTRODUCTION

The presence of harmful and potentially harmful constituents in the smoke resulting from burning tobacco is well known. Recently, new nicotine delivery gadgets, such as heated tobacco products (HTPs), have been developed as alternatives to tobacco smoking in order to avoid the intake of compounds generated in the combustion of traditional cigarettes. Since combustion does not occur in HTPs, this system can be considered less harmful than regular cigarettes. However, there are still few studies aiming to characterize the aerosol generated by the use of HTPS and its comparison with the cigarettes smoke.

## EXPERIMENTAL

A laboratory setup recently designed and optimized in our laboratory (Amorós-Pérez *et al.,* 2021; 2022) (Figure 1A) has been used to perform puffing experiments with cigarettes and HTPs (5 and 15 units of each) in the following conditions: inhalation of 55 mL aerosol volume in 2 s every 30 s (similar to the Health Canada Intense regime). The HTPs used, also called Heets, were produced by Phillip Morris. Any generated particulate and/or soluble matter (deposited in different parts of the setup or dissolved in water, resembling what would be deposited in different parts of the body) has been collected and analysed. Deposited matter on glass surfaces has been extracted with 40 ml isopropanol. and the solution (or suspension) has been analysed by: i) High resolution transmission electron microscopy (HR-TEM) in a Thermo Scientific TALOS F200x model with energy dispersive X-ray (EDX) spectroscopy signal detection. The copper grid (Lacey Carbon Supported Copper Grids 200 mesh) was immersed in the solutions and then, the solvent was evaporated and ii) UV-Vis spectrophotometry (UV-vis V-670 JASCO) after filtration of the resulting liquid using a 0.2 µm filter (Chromafil®PET-20/25).

## RESULTS

Puffing experiments with cigarettes (either 5 or 15 ones) leave significant amount of solid matter deposited on several parts of the setup and coloured water in the gas washing flask, while analogous experiments with HTPs leave much cleaner surfaces and colourless water in the gas washing flask. The isopropanol solution resulting from collecting deposited matter is dark yellow after experiments with cigarettes (Fig. 1B) and almost colourless after experiments with HTPs (Fig. 1C). The solutions from cigarettes' tests were too concentrated to be analysed by UV-vis absorption spectrophotometry, leading to saturated signals, and they had to be diluted (DF, dilution factor, of 31). UV-Vis adsorption results (Figure D) clearly show that the filtered solutions from cigarettes' tests are much more concentrated than those from HTPs' ones. TEM and EDX analysis of the solution/suspension from cigarettes tests reveal the presence of some insoluble particles, mainly composed of C and O, but also by traces of S, K, Ca, Fe, As, Na, Al, Si, and Ba. In contrast, the analogous liquid from HTPs tests contains

a much lower proportion of organic compounds soluble in isopropanol and a significantly much lower amount of particulate matter (mainly composed of C and O).

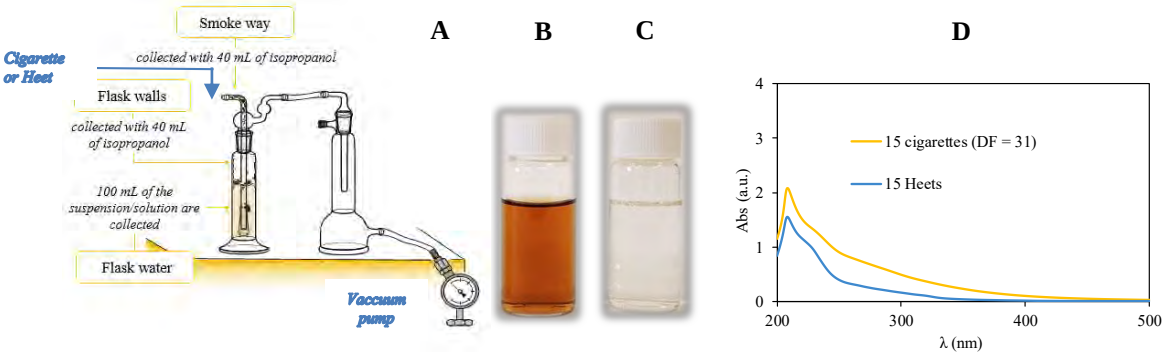


**FIGURE 1**: A) Experimental setup to simulate cigarettes smoking (or Heets use); collected samples from the flask walls of the setup in experiments with puffs: B) from 15 cigarettes and C) from 15 Heets. D) UV-vis absorption spectra of samples collected in isopropanol from flask walls and glass tube after tests with 15 cigarettes or 15 Heets. Sample from cigarettes' tests was diluted (DF=31). (Redrawn from Amorós-Pérez *et al.,* 2021; 2022)

## CONCLUSIONS

The experiments performed, which simulate puffing cigarettes and HTPs, have shown notorious differences between them. Cigarettes puffing leaves a much higher amount of solid matter deposited in different parts of the setup and compounds dissolved in water that HTPs puffing. Besides those substances from cigarettes or Heets experiments have different composition. This study allows to conclude that smoking cigarettes will leave more residues on the human body than the use of HTPs.


### Acknowledgements

The authors would like to acknowledge Philip Morris Products S.A., Switzerland (part of Philip Morris International group of companies) for the financial support. The SSTTI in the University of Alicante and SC-ICYT in the University of Cádiz are also acknowledged.


### References


Amorós-Pérez, A., Cano-Casanova, L., Román-Martínez, M.C. and Lillo-Ródenas, M.A. (2021). Comparison of particulate matter emission and soluble matter collected from combustion cigarettes and heated tobacco products using a setup designed to simulate puffing regimes, Chemical Engineering Journal Advances, 8, 100144. doi: 10.1016/j.ceja.2021.100144.

Amorós-Pérez, A., Cano-Casanova, L., Román-Martínez, M.C. and Lillo-Ródenas, M.A. (2022). Solid matter and soluble compounds collected from cigarette smoke and heated tobacco product aerosol using a laboratory designed puffing setup, Environmental Research, 206, 112619. doi: 10.1016/j.envres.2021.112619.

Carbon 2022

# Photochemistry of Nanoporous Carbons: opportunities in the race towards metal-free catalysis

**Conchi O. Ania**[1,2]
[1] CEMHTI, CNRS (UPR 3079), Université d'Orléans, Orléans, France
[2] Instituto de Ciencia y Tecnología del Carbono, INCAR, CSIC, Oviedo, Spain

Email: conchi.ania@cnrs-orleans.fr

**Keywords**
Photoelectrochemistry, photocatalysis, electrochemistry, nanopores, nanoconfinement.

## INTRODUCTION

Metal-based catalysis is ruling the world's most important industrial processes, including energy generation, conversion and storage. However, it faces multiple disadvantages related to the high cost of precious metals (often most active ones), the uneven geographical distribution of their reserves, and the limited durability due to poisoning during operation. Replacing costly metallic catalysts with abundant materials has become a priority of most research programs to boost sustainable and renewable solutions towards current energetic and environmental challenges.
The proof-of-concept of the potentialities of carbon materials as alternatives to metallic catalysts has been demonstrated (Dai, 2018). Among them, high catalytic activities have been reported for nanoporous carbons, surpassing certain state-of-the-art non-precious metal catalysts for energy conversion and environmental protection (with better performance and durability for certain carbons), complying sustainability, and bringing down costs to competitive levels.
In the field of photocatalysis, our pioneering studies have demonstrated that nanoporous carbons are capable of efficiently absorbing photons, which can be converted into photochemical reactions at the nanopore level (Velasco 2010, 2012). Exploiting the photochemical activity of carbon materials is not straightforward and yet much work needs to be done in the appropriate direction. Building a deeper understanding of the nature of the light/carbon interactions will lead to lay the foundations for boosting their integration in a plethora of novel applications.

## DISCUSSION

In 2010, our group demonstrated the photochemical activity of a semiconductor-free nanoporous carbon (Velasco 2010). Since then and aiming at understanding this behaviour and the mechanisms governing the photochemical activity of carbons, several research directions are being explored:
**Self-photocatalysts**. We have demonstrated the correlation of the photochemical activity of carbons with the formation of radical species and upon irradiation in the full UV-VIS spectrum, the photogeneration of charge carriers and their stabilization through chemical reactions (Velasco, 2013). An adequate choice of the carbon features through appropriate modifications (doping, chromophore sites, porosity) offers the possibility to couple high adsorption capacity to photoactivity, leading to tuneable light harvesting properties. The challenge is in controlling the selectivity by balancing surface composition, nanoporosity and charge-carrier mobility (Gomis-Berenguer 2017). Such systems allow achieving photoinduced reactivation of the exhausted carbons, enabling on-site regeneration.
**Solar energy conversion.** As photoanodes for the photoreforming of water, remarkable photocurrents have been recorded for carbons with varied composition, at overpotentials lower than those reported for benchmark metal-catalysts. The surface functionalization of the carbon has

revealed to be an important factor for its performance as photoanode, if the conductivity is not compromised (Ania, 2014; Gomis-Berenguer, 2016). A balance of both aspects is essential to prevent photocorrosion of the anodes upon long-term operation. In the photorreduction of $CO_2$, promising results combining functionality and porosity of carbons towards the conversion into carbon monoxide in dry conditions (Gesesse, 2021).

**Additives to semiconductors**. Photoactive carbons as additives enhance the visible light harvesting ability of the semiconductor, and favour the charge transfer at the carbon/semiconductor interface and inside the nanopores. The role of the nanoconfinement and their interfacial interactions with the pore walls of the carbon additives are important seem to be important factors that control the overall photoconversion yields. The carbon additive creates a percolation path for the majority carriers, favouring delocalization through the graphitic layers. These hybrid semiconductor/carbon materials have shown good cyclic performance and stability during long-term illumination cycles for the degradation of pollutants and the photoelectrochemical water oxidation (Gomis-Berenguer, 2018.

**Photoassisted synthesis of carbons**. We are investigating the use of light activation to promote the cross-linking of polymer precursors (Cocina, 2021) in the synthesis of porous carbons with controlled features. By changing the chemistry of the organic precursor it is possible to control the porosity of the obtained carbons, as it is defined by the structure of the precursor and the number of reactive positions (Balan 2017). Light irradiation can also control the nature of the surface defects in rGO and GO derivatives (Quezada 2020).

**Photoluminescence of porous carbons**. The phenomenon of photoluminescence has only been demonstrated for certain members of the carbon family with high electron mobility and a high degree of transparency (e.g., graphene-derivatives, carbon dots). We have recently been able to measure light emission features in some porous carbons, by controlling the dispersion conditions in solvents of different polarity. Different emission features have been observed in porous carbons, correlated to the surface functionalization.

**Acknowledgements**

The financial support of the European Research Council through a Consolidator Grant (684161) is acknowledged.

**References**

Ania et al. (2014). Visible light driven photoelectrochemical water splitting on metal free nanoporous carbon promoted by chromophoric functional groups, Carbon 79, 432.

Balan et al (2017). A green and fast approach to nanoporous carbons with tuned porosity: UV-assisted condensation of organic compounds at room temperature, Carbon 116, 264.

Cocina M. (2021). PhD thesis. Photoassisted synthesis of nanoporous carbons. https://tel.archives-ouvertes.fr/tel-03654071

Dai L (Ed). 2018. Carbon-Based Metal-Free Catalysts. Design & Applications, 2 vol. Wiley-VHC.

Gesesse GD, (2021). PhD thesis. Photoelectocatlaytic activity of SC/carbon: application of the degradation of environmental pollutants. https://tel.archives-ouvertes.fr/tel-03654066

Gomis-Berenguer et al. (2019). Insights on the use of carbon additives as promoters of the visible-light photocatalytic activity of Bi2WO6. Molecules 12, 385.

Gomis-Berenguer et al (2017). Photochemistry based on nanoporous carbons: perspectives in energy conversion and environmental remediation, J. Colloid Interf. Sci. 490, 879.

Gomis-Berenguer et al (2016). Surface Modification of a Nanoporous Carbon Photoanode upon Irradiation, Molecules 21, 1611.

Quezada et al (2020). Photochemical and electrochemical reduction of GO thin films: tuning the nature of surface defects, Phys. Chem. Chem. Phys. 22, 20732.

Velasco et al (2010). Role of activated carbon features on photodegradation of phenol, Appl. Surf. Sci. 256, 5254.

Velasco et al (2013). Spectroscopic evidence of light-induced generation of radicals on carbon materials, Appl. Catal A General 453, 310.

Velasco et al (2012). Photochemical response of activated carbons under UV irradiation, Carbon 50, 249.

Carbon 2022

# Enhancing the Stability of Anion-intercalated Graphite Compounds in Dual-ion Batteries

**Habtom D. Asfaw[1], Ismail Yussuf Hassan[1], Wessel van Ekeren[1] and Antonia Kotronia[1,2]**
[1]Department of Chemistry-Ångström Laboratory, Uppsala University, Lägerhyddsvägen 1, Box 538, Uppsala 75121, Sweden
Email: habtom.desta.asfaw@kemi.uu.se

[2]Current address: Department of Chemistry, University of Southampton, Southampton, SO17 1BJ, United Kingdom

**Keywords**
energy storage, dual-ion battery, anion-intercalated graphite

## INTRODUCTION

Interest in the use of anion-intercalated graphite compounds (GICs) as positive electrodes in dual-ion batteries (DIBs) has been increasing over recent years.(Placke *et al.*, 2018; Zhang *et al.*, 2021) The DIB concept relies on the intercalation of both anions and cations in graphite electrodes.(Seel, 2000) In this mechanism, the electrolyte acts as a medium for ion conduction and a source of ions for charge storage in the electrodes. A typical dual-ion battery features anion intercalation in graphite-based electrodes above 4.3 V vs $Li^+/Li$. The following equations summarize the working principle of a DIB with two graphite hosts for lithium and anion intercalation:

$$C + xLi^+ + xe^- \rightleftarrows Li_xC \qquad (-)\ electrode \qquad [1]$$

$$yC + xA^- - xe^- \rightleftarrows A_xC_y \qquad (+)\ electrode \qquad [2]$$

$$xLi^+ + xA^- + (1+y)C \rightleftarrows Li_xC + A_xC_y \qquad overall\ cell\ reaction \qquad [3]$$

Various anions including halides, $AlCl_4^-$, $ClO_4^-$, $BF_4^-$, $PF_6^-$, FSI, and TFSI can be stored in graphitic carbon electrodes.(Guo *et al.*, 2021b; Kotronia *et al.*, 2021a; Guo *et al.*, 2021a; Kravchyk and Kovalenko, 2020) DIBs can reportedly deliver capacities ranging from 60-120 mAh $g^{-1}$ with discharge voltages averaging 4.5-4.7 V, and energy density and specific energy reaching 200 Wh $L^{-1}$ and 100 Wh $kg^{-1}$. Thus, the DIB technology opens up the opportunity for replacing transition metal-containing cathodes with graphite to design more sustainable batteries, especially in combination with a broad selection of abundant electrolytes salts. The most common electrolytes for DIBs are based on organic solvents and ionic liquids (n-butyl pyridinium FSI) with fluorinated inorganic salts. However, organic solvents such as carbonates and phosphates degrade severely on graphite positive and negative electrodes leading to poor coulombic efficiency (CE) and limited cycling life of the DIBs.(Kotronia *et al.*, 2021a) Apart from electrolyte decomposition, Al current collector corrosion, binder degradation, decomposition of intercalated anions and ultimately graphite exfoliation due to solvent co-intercalation contribute to irreversible reactions. Such limitations are inherently aggravated since most electrolytes cannot form a stable cathode-electrolyte interface (CEI) layer unless appropriate salt (e.g. LiBOB, and LiDFOB) and solvent additives (e.g. FEC and VC) are used. (Kotronia et al. submitted manuscript)

In this talk, I will explore the stability of anion-intercalated graphite electrodes prepared in concentrated carbonate-based electrolytes with the help of Raman spectroscopy and *operando* gas pressure measurements. Ongoing efforts aimed at mitigating these limitations through the design of

a stable cathode-electrolyte interface (CEI) layer using additives will be highlighted. Various techniques including electron microscopy, XPS, Raman spectroscopy and operando gas pressure measurements are combined in an attempt to reveal the nature of the CEI layer in different electrolyte systems containing salt additives and co-solvents.

## ELECTROCHEMICAL SYNTHESIS OF ANION-INTERCALATED GRAPHITE COMPOUNDS

Electrochemical intercalation of anions in graphite is defined by a series of peaks in cyclic voltammograms (see **Figure 1 (a)**) attributed to the formation of different p-doped GICs, with different anion content(Kotronia *et al.*, 2021a). The reversibility and efficiency of these processes is dependent on the type of anion and electrolyte solvent used as in can be seen in the cyclic voltammograms. In general, DIBs perform reasonably well at high rates since they make use of both cations and anions in the electrolyte for charge storage. The rate capability of FSI intercalation/de-intercalation in graphite is given in Figure 1 (b)-(d) for currents ranging from 50 to 2000 mA $g^{-1}$. Accordingly, the capacity at 50 mA $g^{-1}$ is typically ~90 mAh $g^{-1}$, and decreases to ~57 mAh $g^{-1}$ at 2 A $g^{-1}$ corresponding to a ~62 % capacity retention. It should be noted, however, that the coulombic efficiency remains fairly low, particularly at lower currents.

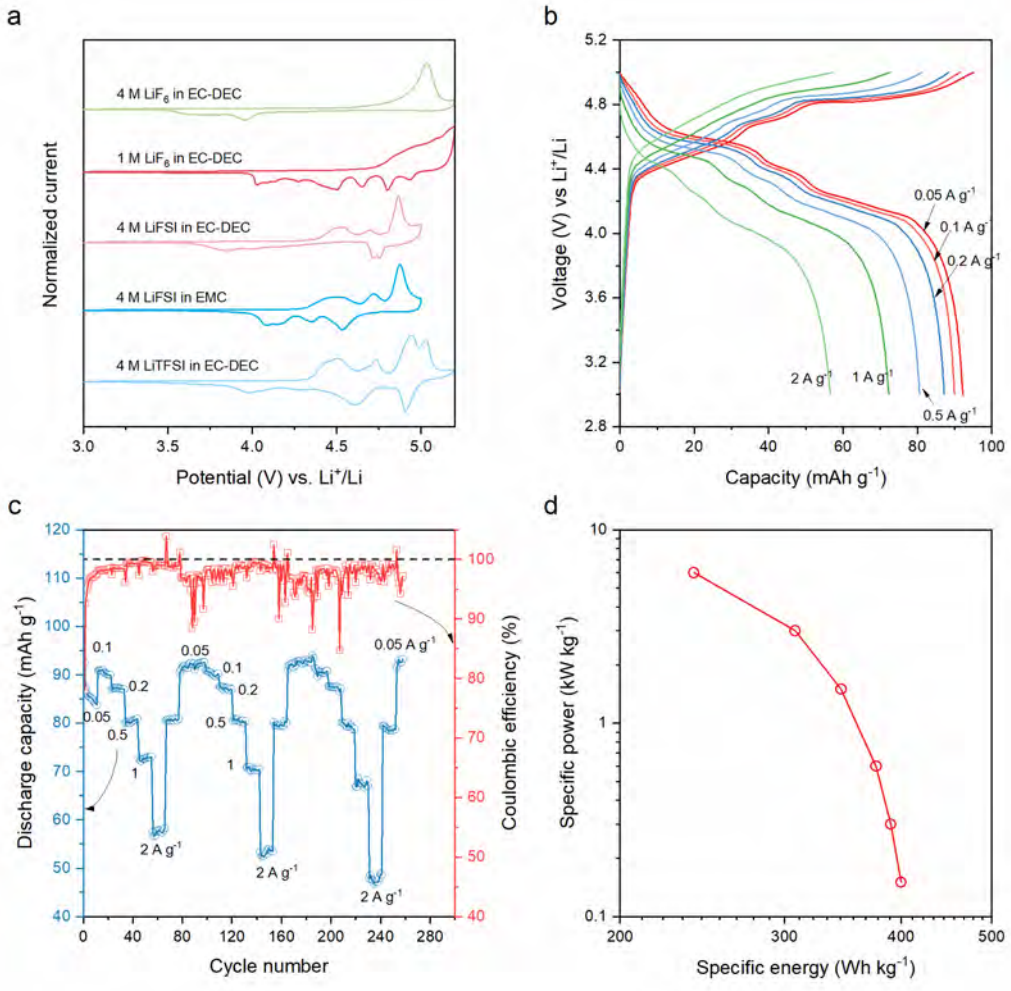


**FIGURE 1**: Electrochemistry of anion-intercalated graphite (a) cyclic voltammograms showing electrochemical intercalation and extraction of various anions in graphite from carbonate-based electrolytes (CV), (b) galvanostatic curves for FSI anion intercalation and extraction in graphite electrode in 4M LiFSI-EMC

electrolyte, (c) the rate performance of FSI anion cycling in graphite at currents ranging from 50 to 2000 mA $g^{-1}$, (d) the Ragone plot showing the specific energy and specific power normalized to the mass of graphite cathode corresponding to data in (c).

## PROBING INTERFACIAL STABILITY OF ANION-INTERCALATED GRAPHITE USING XPS

In our previous study using X-ray photoelectron spectroscopy (see **Figure 2**), we have shown that no stable CEI layer forms in the concentrated electrolytes containing LiFSI, LiTFSI, and KTFSI salts in carbonate solvents (Kotronia *et al.*, 2021a; Kotronia *et al.*, 2021b), unless polymerizing additives such as triallyl phosphate (Asfaw and Kotronia, 2022) are included. Interface characterization using XPS and electron microscopy only help characterize insoluble products forming as a result of electrolyte decomposition. It is likely that most of the parasitic reactions generate gaseous products which are not probed during XPS measurement.

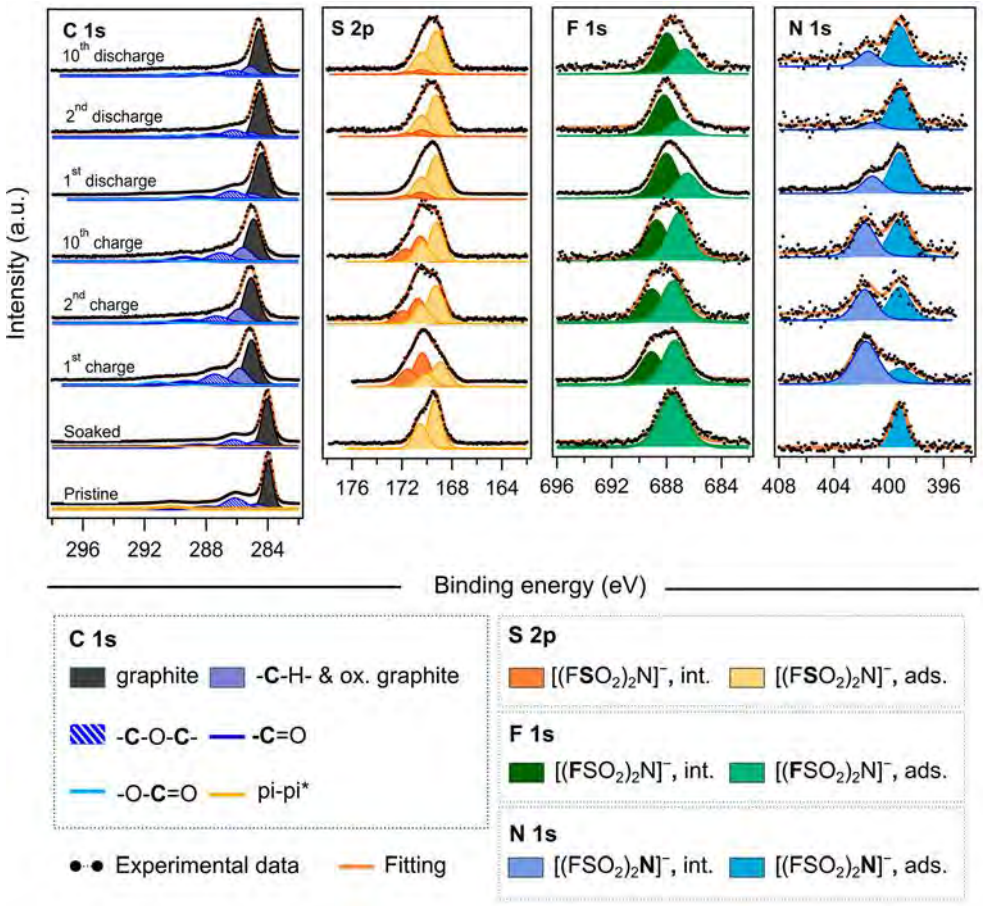


**FIGURE 2**: XPS spectra showing the surface composition of graphite electrodes before and after galvanostatic charge-discharge cycles in 4 M LiFSI EC-DEC electrolyte, reproduced from reference (Kotronia *et al.*, 2021a) licensed under CC-BY

## TRACKING STABILITY OF FSI-INTERCALATED GRAPHITE USING RAMAN SPECTROSCOPY

The galvanostatic curve in **Figure 3 (a)** display a reversible discharge capacity of ~92 mAh $g^{-1}$ at 50 mA $g^{-1}$ and ~97 % coulombic efficiency. Corresponding to the stage plateaus in the galvanostatic curves, multiple peaks are observed in the differential capacity plots characteristic of phase transitions among the different staged GICs. On charge, the peaks centre around 4.4 V, 4.5 V, 4.7 V,

and 4.82 V and the corresponding de-intercalation processes appear on discharge appearing at 4.6 V, 4.4 V, 4.23 V, and 4.13 V. I*n situ* Raman spectroscopy (see **Figure 3 (b)**) was able to support the intricate structural changes accompanying the formation of various FSI-intercalated graphite compounds. The Raman spectra of the electrodes prior to and after charge and discharge to different voltages are shown in **Figure 3 (c)**. Initially, the characteristic bands appear at ~1347 $cm^{-1}$ (D band) and ~1575 $cm^{-1}$ (G band) as expected for pure graphite. Additional bands emerge in the course of FSI intercalation at higher frequencies. At its fully charged state at 4.9-5 V, a new, intense band appears at ~1636 $cm^{-1}$. This can be attributed to resonance enhancements as the blue-coloured stage-II GIC has formed. On discharge, FSI extraction causes a series of phase transformations among the different stage-GICs as verified by the different bands in the Raman spectra. After fully discharged to 3 V, mainly the D, G, and 2D bands are observed similar to the pristine graphite (but at a slightly higher frequency), thereby hinting at the highly reversible nature of FSI intercalation in the electrolyte under consideration.

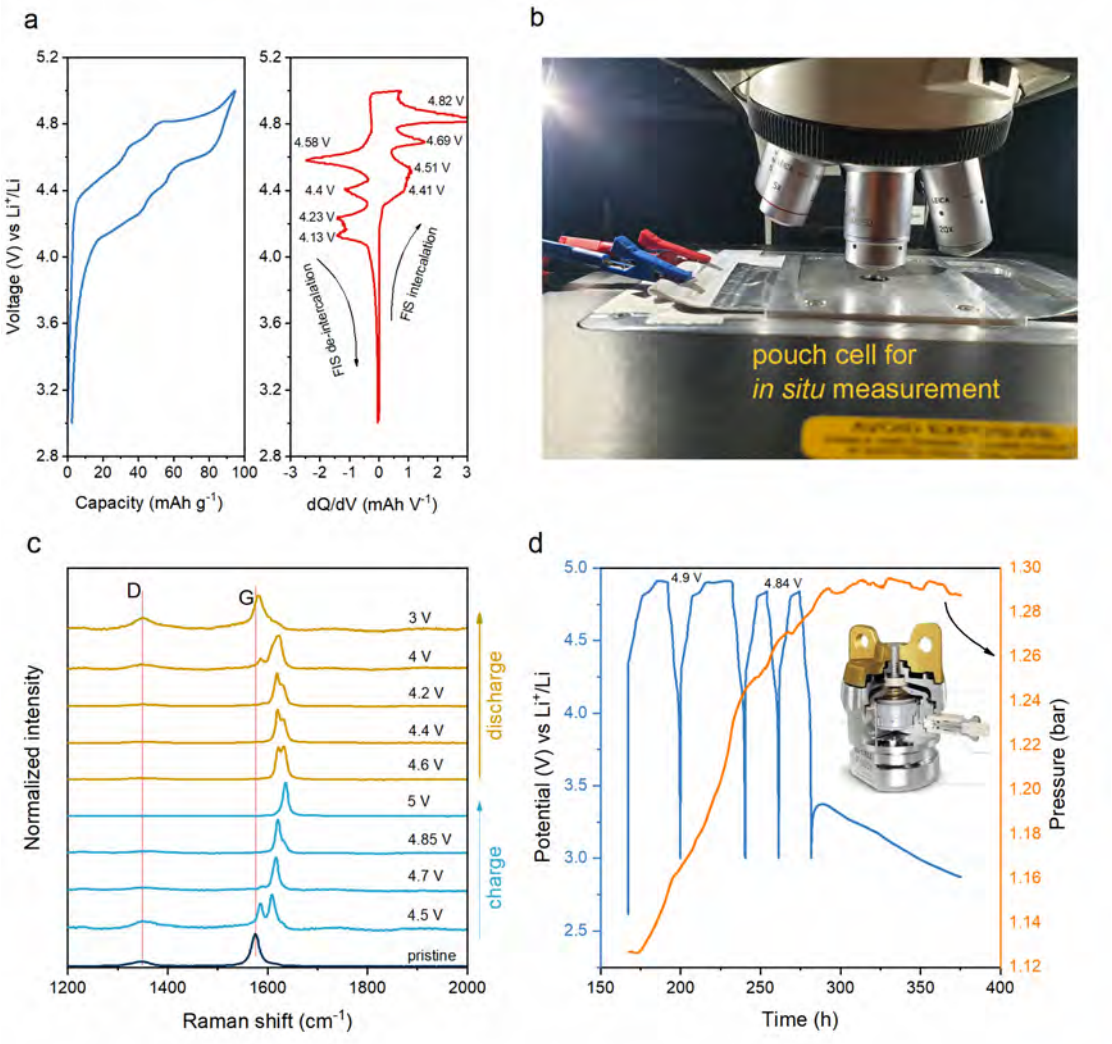


**FIGURE 3**: Reversibility of electrochemical anion intercalation in graphite (a) A galvanostatic curve and the differential capacity plot thereof for FSI anion reaction with graphite positive electrode measured versus lithium reference, (b) a picture of the in situ Raman spectroscopy measurement on a pouch cell, (c) Raman spectra from in situ measurements conducted on graphite electrode charged and discharged to different potentials, (c) operando measurement of gas pressure inside a 3-electrode LTO-graphite vs Li cell in the course of charge and discharge processes. Inset is a picture of the electrochemical cell with a pressure sensor.

## OPERANDO GAS PRESSURE MEASUREMENT

Furthermore, the short- and long-term stability of FSI-intercalated graphite electrodes is assessed using self-discharge tests followed by *ex situ* and *in situ* Raman spectroscopy, and *operando* gas pressure measurements (**Figure 3 (d)**). However, increasing the upper voltage cut-off tends to increase the parasitic current suggesting electrolyte decomposition is aggravated. In a graphite-LTO vs Li three-electrode, it is observed that an extended voltage plateau emerges when the voltage increases to 4.9 V vs. $Li^+$/Li and beyond. This phenomenon is accompanied by a drastic pressure increase inside the cell, indicative of the decomposition of the electrolyte to generate gaseous products.

## CONCLUSIONS

Similar alkali metal GICs, anion intercalation in graphite exhibits staging behaviour in which a series of intercalation compounds are formed (as verified using *in situ* Raman spectroscopy) in the voltage range 4.3 and 5.2 V vs. $Li^+$/Li. These materials are considered attractive for use in dual-ion batteries (DIBs) The unusually high potentials required for anion intercalation trigger electrolyte decomposition leading to poor charge efficiency and short cycling lifetime in DIBs. Based on operando gas pressure measurements, the parasitic reactions result in the formation of gaseous products, which are aggravated as the upper cut-off potential is increased. X-ray photoelectron spectroscopy studies indicate that the concentrated electrolytes fail to form stable interface layer which could have passivated the graphite electrodes and prevented electrolyte decomposition. Thus, there is a need for further studies to find better electrolytes and additives to improve the performance of DIBs.

**Acknowledgements**
The authors acknowledge financial support from The ÅForsk Foundation, Energimyndigheten, and Vinnova.

**References**

Asfaw, H. D. and Kotronia, A. (2022) 'A polymeric cathode-electrolyte interface enhances the performance of MoS2-graphite potassium dual-ion intercalation battery', *Cell Reports Physical Science*, 3(1), pp. 100693.
Guo, Q., Kim, K.-I., Li, S., Scida, A. M., Yu, P., Sandstrom, S. K., Zhang, L., Sun, S., Jiang, H., Ni, Q., Yu, D., Lerner, M. M., Xia, H. and Ji, X. (2021a) 'Reversible Insertion of I–Cl Interhalogen in a Graphite Cathode for Aqueous Dual-Ion Batteries', *ACS Energy Letters*, 6(2), pp. 459-467.
Guo, Z., Xu, Z., Xie, F., Feng, J. and Titirici, M. (2021b) 'Strategies for High Energy Density Dual-Ion Batteries Using Carbon-Based Cathodes', *Advanced Energy and Sustainability Research*, 2(11), pp. 2100074.
Kotronia, A., Asfaw, H. D., Tai, C.-W., Hahlin, M., Brandell, D. and Edström, K. (2021a) 'Nature of the Cathode–Electrolyte Interface in Highly Concentrated Electrolytes Used in Graphite Dual-Ion Batteries', *ACS Applied Materials & Interfaces*, 13(3), pp. 3867-3880.
Kotronia, A., Edström, K., Brandell, D. and Asfaw, H. D. (2021b) 'Ternary Ionogel Electrolytes Enable Quasi-Solid-State Potassium Dual-Ion Intercalation Batteries', *Advanced Energy and Sustainability Research*, n/a(n/a), pp. 2100122.
Kravchyk, K. V. and Kovalenko, M. V. (2020) 'Aluminum electrolytes for Al dual-ion batteries', *Communications Chemistry*, 3(1), pp. 120.
Placke, T., Heckmann, A., Schmuch, R., Meister, P., Beltrop, K. and Winter, M. (2018) 'Perspective on Performance, Cost, and Technical Challenges for Practical Dual-Ion Batteries', *Joule*, 2(12), pp. 2528-2550.
Seel, J. A. a. D. J. R. (2000) '"Electrochemical Intercalation of PF6 Into Graphite"', *J. Electrochem. Soc.*, 147, pp. 892.
Zhang, L., Wang, H., Zhang, X. and Tang, Y. (2021) 'A Review of Emerging Dual-Ion Batteries: Fundamentals and Recent Advances', *Advanced Functional Materials*, 31(20), pp. 2010958.

Carbon 2022

# Development of Non-polymer Electrochemical Electrodes Based on Activated carbons and Few-wall Carbon Nanotubes

**M.K. Atamanov[1,2], A.T.Taurbekov[1,2], Z.A. Mansurov[1,2], T. S. Atamanova[1]**

[1] Institute of Combustion Problems, Almaty, Kazakhstan

[2] Al-Farabi Kazakh National University, Almaty, Kazakhstan

Email: mk.atamanov@gmail.com

**Keywords**

Activated carbons, few-wall carbon nanotubes, electrodes

## INTRODUCTION

The development of new methods of manufacturing electric energy storage devices, such as batteries and electrochemical capacitors, is important for the widespread introduction of electric vehicles and for increased mobility of portable electronics (Kotz and Carlen 2000, Zhang et al. 2009). Therefore, this study uses a unique approach to improve the devices of electrochemical energy storage devices by examining a new nanocomposite system to improve the performance of electrodes based on carbon nanomaterials. In order to fabricate the hybrid electrodes were used activated carbons (AC) obtained from the different source and sub-millimeter long few wall carbon nanotubes (FWCNT). Electrochemical properties of the obtained electrodes were investigated by the cyclic voltammetry method (CV). Electrochemical characteristics were measured using the three-electrode cell contained of AC-FWCNT as a working electrode, a YP-80F-FWCNT counter electrode and a Ag/AgCl reference electrode with an electrolyte of $Na_2SO_4$ (1 M) aqueous solution. Also, the morphological properties of obtained electrodes were studied using scanning electron microscope (SEM), the SSA was investigated by the Brunauer-Emmett-Teller analysis. SSA, conductivity, and resistivity of WS-FWCNT electrodes were summarized. The specific capacitance of AC-FWCNT electrodes made from different size of ACs was about 140 F/g. The volumetric capacitance at scan rate 1 to 100 mV/s lies in the limit 27-18 F/cm$^3$, the areal capacitance at scan rate 1 to 100 mV/s shows 0,39 to 0,27 F/cm$^2$.

## MATERIALS AND METHODS

To achieve the necessary goals and solve the set tasks, the following research methods were used: Electron scanning microscopy, energy dispersive analysis, cyclic voltammetry.

## RESULTS AND DISCUSSION

At the traditional electrode fabrication method is to mix the active material with a binder, conductive fillers to form a sheet or film. At work networks of carbon nanotubes are investigated to replace the polymer binder in the fabrication of hybrid electrodes based on activated carbons obtained from biomass-derived materials. Preparation of electrodes from CNTs with AC in hybrid electrodes has been developed to improve the electrical conductivity of common electrodes, and to replace ordinary additives, as polymeric binder, fillers. From the point of view of practical applications, it is important to take into account the dispersibility and cost of CNTs. In the manufacturing of AC-CNT electrodes, the type of CNTs will affect the characteristics of the final electrode mainly in terms of electrical conductivity due to the different ease of manipulation between them. In this work, FWCNT with a sub-millimeter length, synthesized by the fluidized bed method, were dispersed in ethanol to obtain their electrodes after vacuum filtration

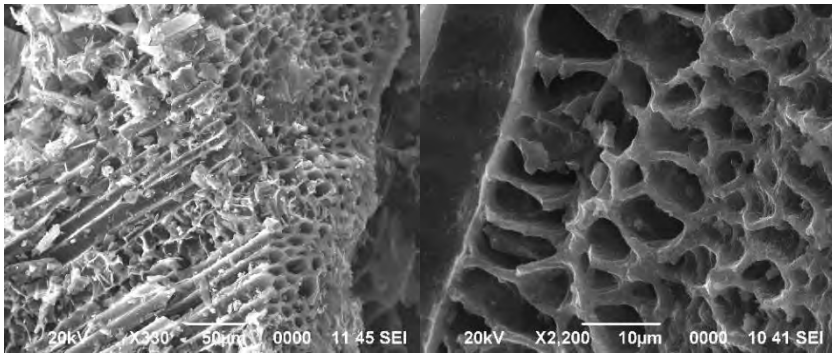


**FIGURE 2:** Example of SEM images of obtained ACs from WS

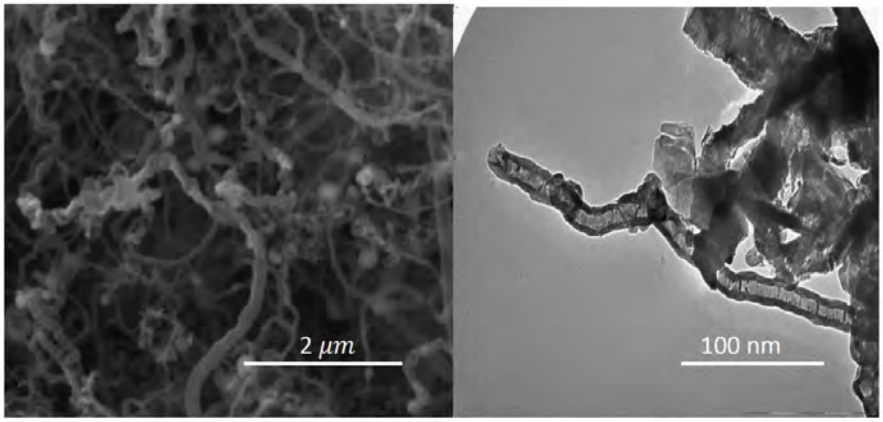


**FIGURE 4:** Example of SEM images of CNTs

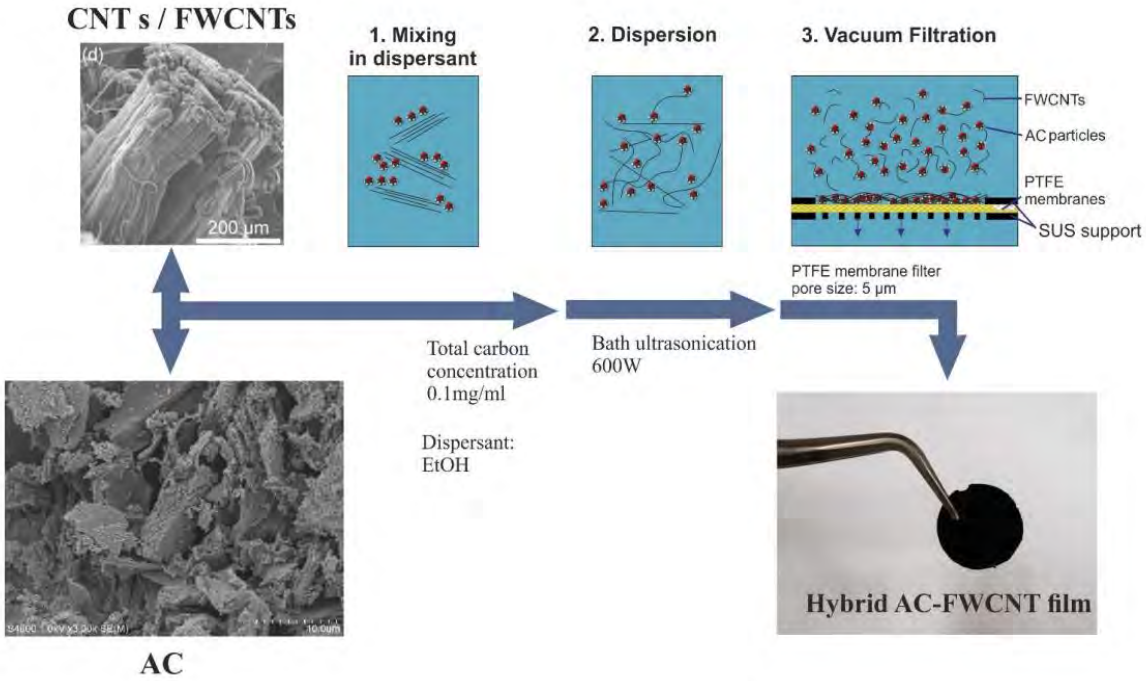


**FIGURE 5:** Scheme of electrode preparation method from FWCNT and AC particles in EtOH by vacuum filtration and image of the final self-supporting hybrid electrode

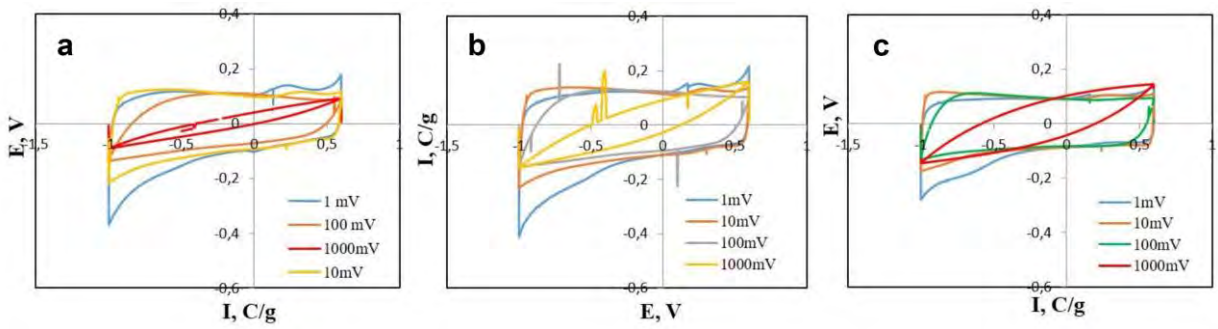


**FIGURE 6:** CV curves of AC-FWCNT electrodes

## CONCLUSIONS

Self-supporting, flexible hybrid EDLC electrodes were obtained by combination of high capacitive biomass derived ACs with an electrically conductive matrix of few-wall carbon nanotubes (FWCNTs). The optimal weight ratio of AC:FWCNT, 90:10 in weight to obtain physically robust, high capacitive electrodes was find. AS-FWCNT, WS-FWCNT hybrid electrodes exhibited higher specific capacitance equal to 140-150 F/g with comparison to the YP80F-FWCNT standard electrode.


## Acknowledgements

This research is funded by the Science Committee of the Ministry of Education and Science of the Republic of Kazakhstan (Grant No. AP09057909).


## References


Kotz R., Carlen M. Principles and applications of electrochemical capacitors //Electrochim Acta. – 2000. – Vol. 45. – P. 2483-2498.

Zhang Y., Feng H., Wu X., Wang L., Zhang A., Xia T. Progress of electrochemical capacitor electrode materials: A review // International Journal Hydrogen Energy. – 2009. – Vol. 34, Iss. 11. – P. 4889-4899.

20 C 22 arbon 2022

# Study of the structure-properties relations of high-SSA activated carbons on electrochemical performances of hybrid electrodes

**T.S. Atamanova[1,2], M. Yeleuov[1], Z.A. Mansurov[1,2]**

[1] Institute of Combustion Problems, Almaty, Kazakhstan

[2] Al-Farabi Kazakh National University, Almaty, Kazakhstan

Email: tolganay.temirgaliyeva@gmail.com

**Keywords**

Activated carbon, Hybrid electrodes, Energy storage

## INTRODUCTION

The granulometric composition of activated carbons (AC) is one of the key parameters affecting the specific capacitance of particle-based electrodes, is the particle size. As is known, hybrid electrodes with smaller particles show higher specific capacitance and operating speed than electrodes with larger ones. In addition, AC with a large specific area and finer particle sizes is effective for improving electrode speed performance (Cao and Zheng 2013). In the case of AC particles, the influence of their size was carefully evaluated. It has been found that hybrid electrodes with smaller particles show higher specific capacitance and speed than electrodes with larger particles. This is due to the low resistivity between the particles and the rapid diffusion of ions in the pores of AC particles. AC dispersed in ethanol were applied by centrifugation to silicon plates, and then observed using microscopes. It has been found that sonication, due to the energy of cavitation, can destroy the particles. To determine the effect of sonication of AC particles, the samples were dispersed in ethanol and sonicated for 10, 30, 60, and 30 + 30 min (sonicated for 30 min, then the vial was shaken and sonicated for 30 min). Based on the results of the scanning microscope, it was shown that the diameter of AC particles after sonication in the bath decreased, the volume ratio of particles with a diameter of less than 10 μm exceeds the number of particles with a diameter of more than 100 mm. This means that the shaking process during processing is necessary to obtain well-distributed smaller diameter particles. Additionally, to separate the exact size fractions, all AC samples were sifted through a sieve (brand: ONE MVS-1). The sieve has 3 parts with different size: 75 μm, 53 μm, 25 μm and has an adjustable automatic shaking mode. After sieving, all AC samples were divided into different sizes in the range: more than 100 μm, 100-75 μm, 75-53 μm, 53-25 μm, less than 25 μm.

## MATERIALS AND METHODS

To achieve the necessary goals and solve the set tasks, the following research methods were used: Raman spectroscopy, thermogravimetric analysis, Brunauer–Emmett–Teller (BET) analysis (low-temperature nitrogen adsorption), energy dispersive analysis, X-ray diffraction analysis.

To obtain (AC) with a high specific surface area and a developed morphological structure, the original cheese of various origins (Apricot stones (AS), walnut shell (WS), rice husk (RH), sunflower seeds (SS) and beet pulp (BP) was thoroughly washed with water and detergents to remove mechanical contaminants and then dried to complete dehydration. After purification, it was subjected to carbonization during multi-stage high-temperature pyrolysis in an inert argon atmosphere at a temperature of 550 °C. The installation diagram is shown in the figure1

## RESULTS AND DISCUSSION

It has been found that hybrid electrodes with smaller particles show higher specific capacitance and speed than electrodes with larger particles. Therefore, all AC samples were sifted through a sieve (brand: ONE MVS-1) for separation into accurate size fractions.

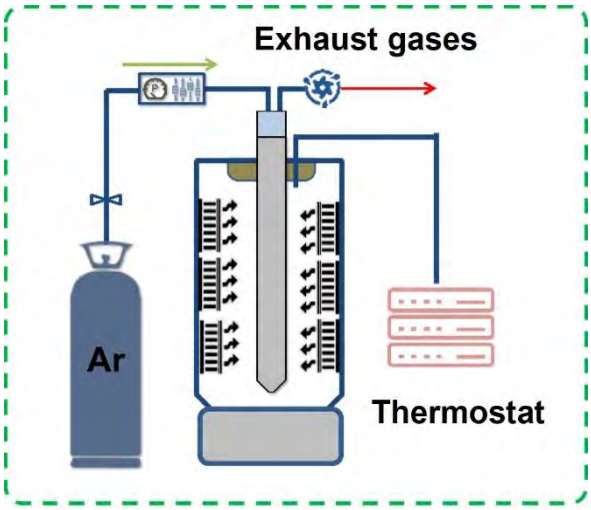


**FIGURE 1:** General view and schematic diagram of a furnace for carbonization and chemical activation of raw materials of plant origin

The sieve has 3 parts with different size: 75 µm, 53 µm, 25 µm and has an adjustable automatic shaking mode. After sieving, all AC samples were divided into different sizes in the range: ⍰ 100 µm, 100-75 µm, 75-53 µm, 53-25 µm, ⍰ 25 µm. Information on the granulometric composition of all obtained ACs was presented. It has been established that AK samples contain particles with a diameter of 55 µm or less. The number of particles with a diameter of 55 µm is more than particles of a smaller diameter. The size distribution of particles at three different points of the RS sample was similar. The volume ratio of SGO and SS particles at different points of the powder is the same, which means that particles of larger and smaller sizes are evenly distributed throughout the volume of the powder. The highest volume content in the AC sample based on SF was shown by particles with a diameter of more than 55 µm. It has been found that sonication, due to the cavitation energy, can destroy and break up the AC particles. To determine the effect of sonication, AC samples were dispersed in ethanol and sonicated for 10, 30, 60, and 30 + 30 min (sonicated for 30 min, then the vial was shaken and sonicated for 30 min). It was established that the diameter of the AC particles after sonication in the bath decreased, the volume ratio of particles with a diameter of less than 10 µm exceeds the number of particles with a diameter of more than 100 µm. This means that the shaking process during processing is necessary to obtain well-distributed smaller diameter particles.
It has been established that all AC samples have two diffraction peaks located in the range 2 theta = 15-30 and 40-60, which indicates the presence of both amorphous and graphitized carbon, which is most likely arbitrarily stacked with carbon masses. Peaks were found in all samples, indicating impurities for iron ions and FeN0.0324. Peaks of divalent iron oxide (Fe3O4) were also found in samples of walnut shell (WHO) and apricot kernel (AK). It has been established that in the diffraction spectrum of the obtained AC, the face of a microcrystalline crystal (002) appears at 2 theta = 22.6, with respect to all samples with different intensities, the diffraction angle of the crystal face for all AC has unique characteristics for each raw material. Raman spectroscopy of the surface of AC samples showed the presence of graphene-like structures. As a result of comparing the ratio of the IG / I2D and ID / IG peaks for all samples, an increase in the number of graphene layers in the sample based on SF up to 5-7 layers was found. In the case of a sample based on CGO (ID / IG ≈ 0.66), the number of graphene layers is similar to other samples, but the defectiveness of the carbon structure has become twice as high. The highest value of defectiveness of the carbon structure was shown by a sample based on rice husk (RH) ID / IG = 0.87, which may indicate disorder and deformed

morphological structure of the graphene layers contained in AC. The presence of a large number of graphene layers and their defectiveness can be due to the parameters of the feedstock, given by nature.

**RESULTS AND DISCUSSION**

**TABLE 1**: Activation methods and specific surface area of AC samples

| AC | Type of source | Activation agent | Specific area, $m^2/g$ |
|---|---|---|---|
| AS | Apricot stones | KOH (70%) | 2464 |
| WS | walnut shell | KOH (70%) | 2584 |
| RH | rice husk | KOH (70%) | 1788 |
| BP | beet pulp | KOH (70%) | 1474 |
| SS | sunflower seeds | KOH (70%) | 1740 |

According to the results of calculation of low-temperature nitrogen adsorption by the BET method, AC samples have a specific area from 1474 m2/g to 2584 m2/g and a mesopore volume of 50–60 cm3/g. AC based on AA - 2464 m2/g, AC based on RSH - 1788 m2/g, AC based on SGO - 2584 m2/g, AC based on SO - 1474 m2/g, AC based on SH - 1740 m2/g.

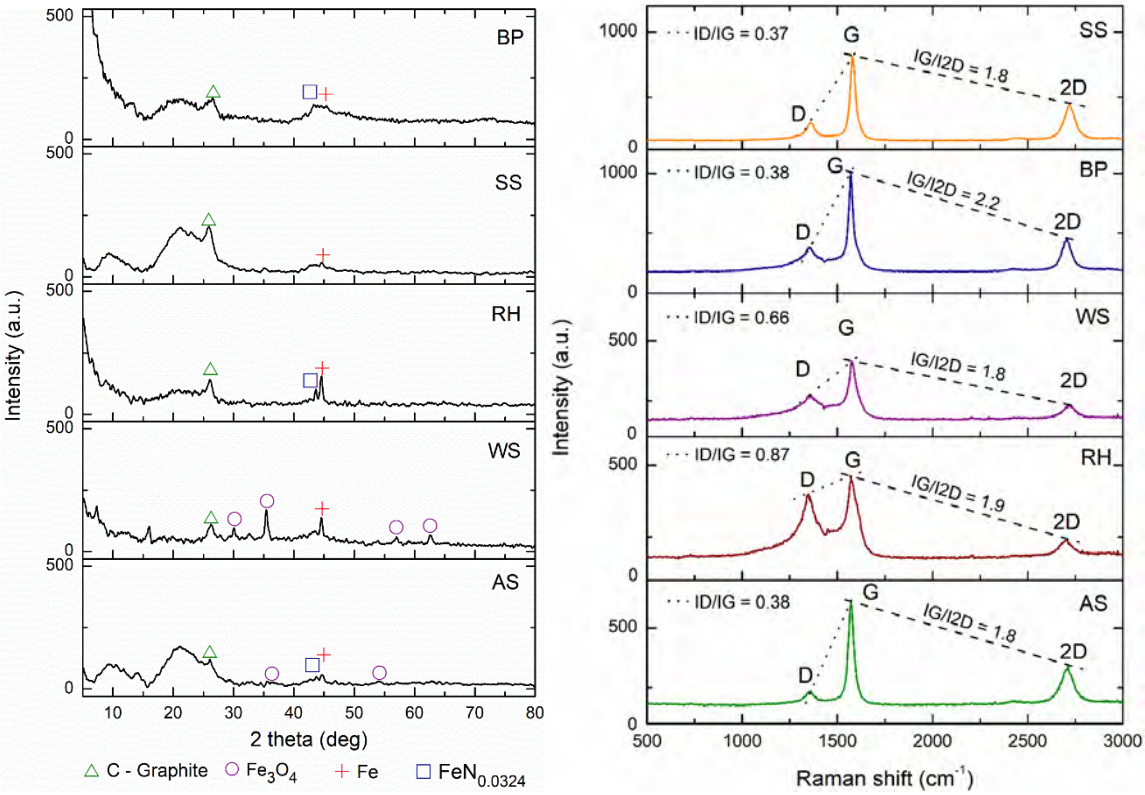


**FIGURE 2:** Raman and XRD spectra of prepared activated carbons from various biomass.

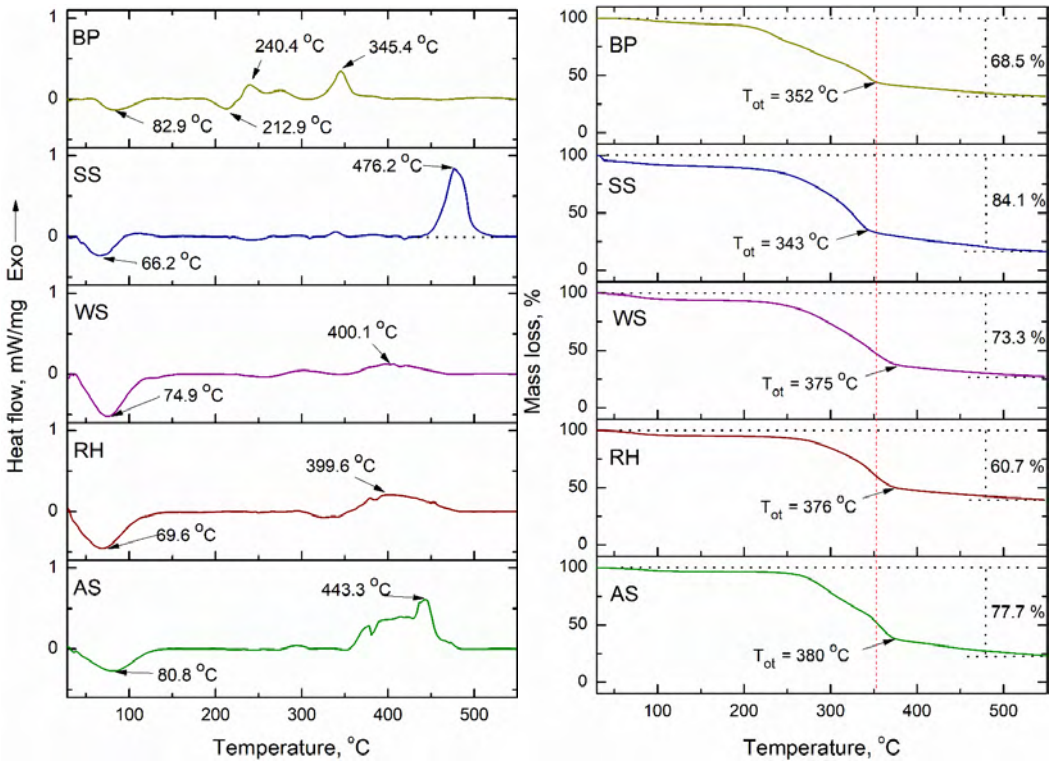


**FIGURE 3:** Thermal analysis of various AC precursors at a heating rate of 5 °C min by DSC-TG.

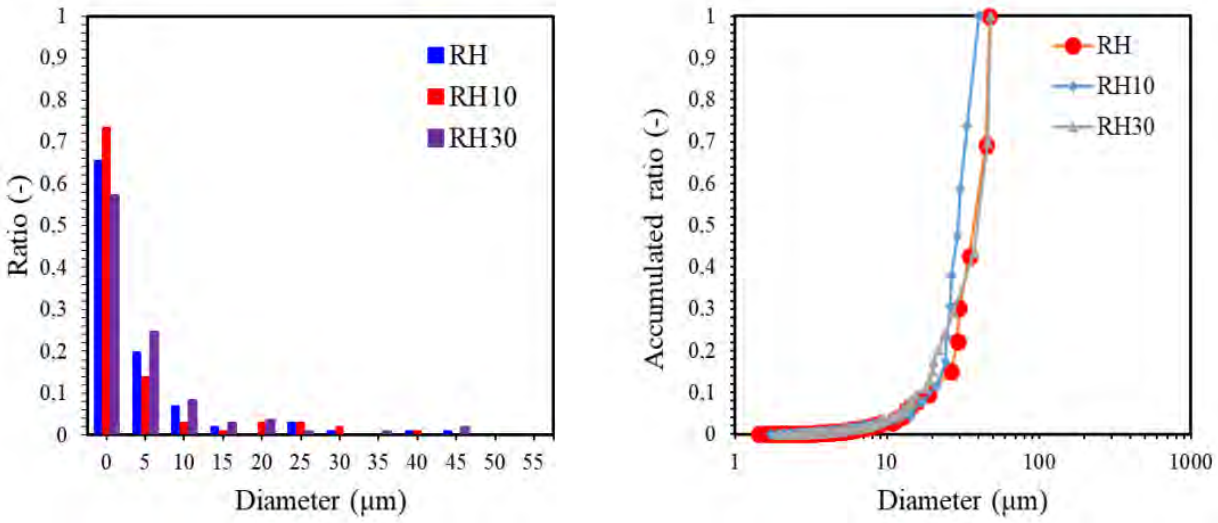


**FIGURE 4:** Example of particle size distribution of RH activated carbons after bath-sonication treatment

**CONCLUSIONS**

All samples were subjected to thermogravimetric (TG) analysis. It was found that for all initial TG samples, the curves were characterized by a bend in the temperature range of ~30–100°C, associated with the removal of moisture. The values of the start of loss (Ti), the maximum rate of weight loss (Tmax) and the end of thermal degradation (Tot) for all sources of feedstock were set to 79.9–202.6, 203.5–352.6 and 353.1–507.1 °C for SJ; 65.7-225.3, 226.4-343.4 and 344.5-517.3°C for SS; 75.4–224.8, 225.1–375.8 and 376.1–524.4 °C for SHO; 68.7–257.3, 258.7–376.7 and 377.8–506.7 °C for RSH; 70.7–260.1, 261.3–380.4 and 381.6–528.6 °C for AK, respectively. The order of thermal

stability is established: SZh> SGO> ShS> RSH> SGO. Analysis of samples by DSC indicates the appearance of exothermic peaks in all initial biomasses. Exothermic peaks can be attributed to the complex and varied chemical reactions involved during the thermal decomposition of extractives.

**Acknowledgements**
This research is funded by the Science Committee of the Ministry of Education and Science of the Republic of Kazakhstan (Grant No. AP09057909).

**References**

Cao W., Zheng J.P. Li-ion capacitors using carbon-carbon electrodes // ECS Transactions. – 2013. – Vol. 45, № 29. – P. 165-172.

Carbon 2022

# How does the zeolite crystal size impact the structural quality of Zeolite-Templated Carbons?

**Thibaud Aumond,[1] Martín Esteves,[2] Yannick Pouilloux,[1] Ricardo Faccio,[2] Alexander Sachse.[1]**
[1] IC2MP, UMR 7285 CNRS, 4 rue Michel Brunet, 86073, Poitiers Cedex 9, France
[2] DETEMA, Centro NanoMat & Area Física, Facultad de Química, Universidad de la República, Montevideo, Uruguay
Email: alexander.sachse@univ-poitiers.fr

**Keywords**
Zeolite-Templated Carbons, ZTCs, Zeolite, nanoporous carbons, crystal size.

## INTRODUCTION

Zeolite-Templated Carbons (ZTCs) feature unique textural properties that reveal very promising for a number of applications and majorly for the design of advanced electrocatalysts as described by Kim *et al.* (2021). These nanostructured carbons are achieved using zeolites as sacrificial templates and develop within their microporous system. After the dissolution of the zeolite, the ZTCs feature textures that can be described as the negative copy of the zeolite structure. Various parameters play an important role in the synthesis of ZTCs such as the structure of the zeolite template and the nature of the counterion.
In this communication, we present the impact of the zeolite crystal size on the textural quality of the resulting ZTCs after a thorough characterization of hybrid materials (zeolites/carbon) and final ZTCs by nitrogen physisorption, XRD, and electron microscopy. A computational study is then carried out in order to determine the atomistic structure of the ZTC in accordance with its characteristics, as described by Aumond *et al.* (2022).

## MATERIALS AND METHODS

Two proton-exchanged *BEA structured zeolites with different crystal sizes of 20 nm named as N-BEA (for Nano-sized crystal *BEA zeolite) and 5 µm named as M-BEA (for Micron-sized crystal *BEA zeolite) have been used as a template for the synthesis of ZTC, respectively named N-ZTC and M-ZTC. After activation of the zeolites, ethylene flow (6.7vol% in $N_2$) was passed through at 700 °C for 4 hours followed by a pyrolysis treatment at 900 °C for 2 hours under $N_2$. The hybrid material was treated with a 49wt% aqueous solution of HF in order to dissolve the zeolite template and obtain the pure ZTC. Both hybrid and final ZTC have been characterized.

## CHARACTERIZATION OF PARENT ZEOLITES

In order to study the impact of the crystal size, two zeolites with *BEA structure with comparable properties have been used. Both proton-exchanged, their Si/Al ratio are of similar values and equal to 12.9 and 14 for N-BEA and M-BEA respectively. Their lattice parameters are the same as well as their microporous volume and their pore opening diameter confirming the similarity between their textural properties. Only the morphology of these zeolites is different and can be described as agglomerates of crystals of approximately 10-20 nm for N-BEA and truncated bipyramidal of 5 µm crystals for M-BEA.

**CHARACTERIZATION OF FINAL ZTCS**

The characterization of the hybrid compounds leads to a higher apparent density for N-ZTC than for M-ZTC which strongly suggests the presence of structural defects on this latter related to mass transfer issues of the carbon precursor within the extended micropore system of M-BEA.

These defects are confirmed by characterizing the resulting ZTCs after zeolite dissolution. Using electronic microscopy images, both N-ZTC and M-ZTC present the same morphology as their template zeolite indicating a good replica of the parent zeolite: particles of N-ZTC measure 10-20 nm while M-ZTC particles size is of 5 µm (figure 1). However, flaccid edges compared to the template zeolite are observed for M-ZTC which can be due to the presence of defects as already suggested. Furthermore, important differences can be observed in the pore size distribution of these two ZTCs (figure 2a). N-ZTC presents only one contribution indicating that the entirety of the porosity in the ZTC is due to the templating of the zeolite. Two contributions in the micropore range are observed for M-ZTC. The first is centered at a similar value as for N-ZTC and the second occurs at 2 nm indicating the presence of larger micropores (supermicropores), resulting from defect zones in the ZTC.

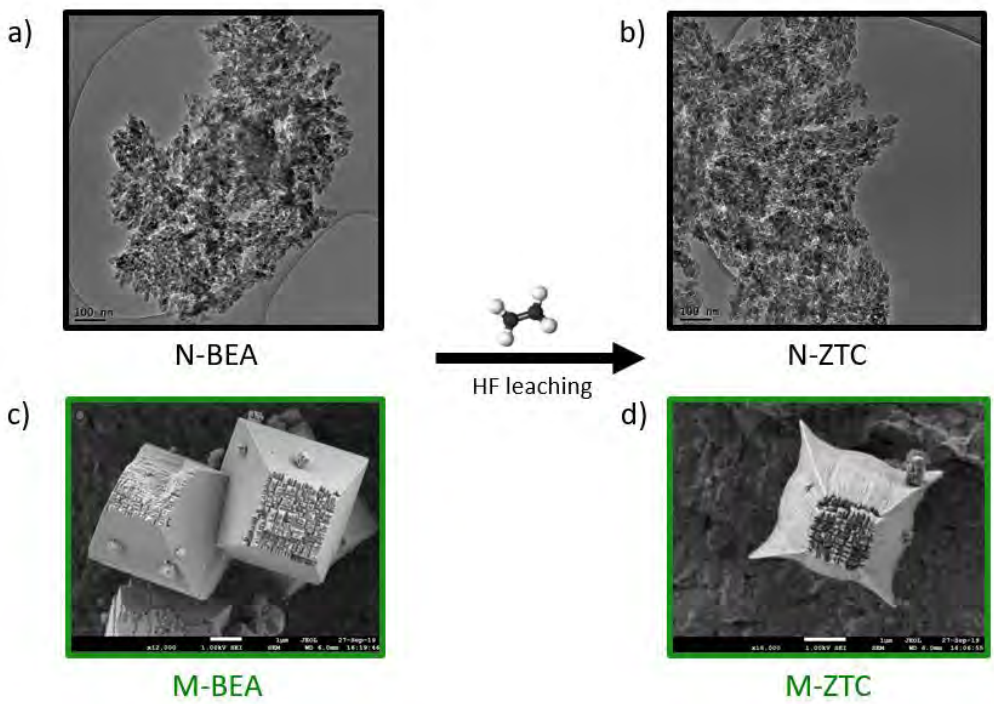


**FIGURE 1**: SEM images of N-BEA (a) and resulting N-ZTC (b) and M-BEA (c) and resulting M-ZTC (d).

These defects are further inferred by a shift to higher binding energy of the $C_{1s}$ photoelectron peak in XPS, suggesting a higher degree of $sp^3$ hybridization for M-BEA than N-BEA. Another method that allows to confirm these defects is the differential temperature analysis which clearly shows a second contribution at higher temperatures during the carbon oxidation for M-ZTC due to the presence of ill-templated carbon that results from the defects in the structure.

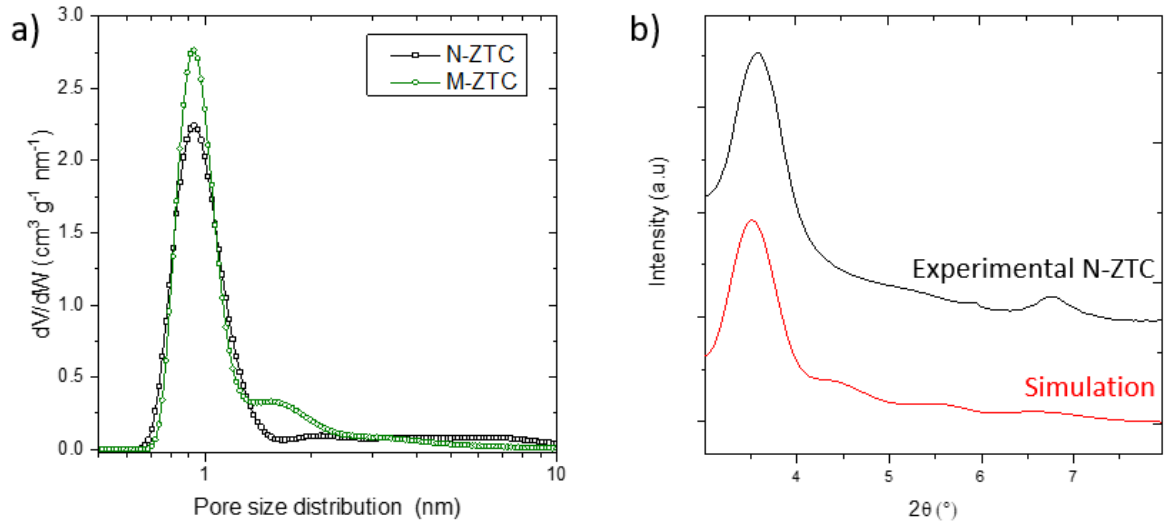


**FIGURE 1**: (a) PSD of N-ZTC and M-ZTC,
(b) diffractograms of experimental N-ZTC (top) and simulation (bottom).

Surprisingly, the XRD powder patterns present long-range structural order peaks for both N- and M-ZTC. Three reflection peaks can be observed centered at 3.58, 5.95, and 6.73° 2theta. In order to achieve further insights into the long-range pore-to-pore ordering revealed by XRD, powder patterns were simulated considering the ribbons to form a crisscrossed long order structure that matches well with the experimental diffractograms (figure 2b).

## CONCLUSIONS

Both N- and M-BEA zeolites lead to the formation of ZTCs. Nevertheless, using large crystal zeolite leads to structural defects in the carbon structure due to mass transfer issues within the micropore system of the zeolite during the synthesis. These defects can be revealed using $N_2$ physisorption, SEM, and XPS characterization techniques while XRD patterns present long-range structural order no matter the crystal size. Simulated XRD powder patterns allowed to propose a graphene-based nanoribbon structure grown in the zeolite pores as a satisfactory model for ZTCs in *BEA zeolite structure.

**Acknowledgments**

The authors acknowledge financial support from the European Union (ERDF) and “Région Nouvelle Aquitaine”.

**References**

Aumond, T., Esteves, M., Pouilloux, Y., Faccio, R., Sachse, A., (2022). Impact of the crystal size of beta zeolite on the structural quality of zeolite templated carbons. *Microporous and Mesoporous Materials*, 331, 111644. https://doi.org/10.1016/j.micromeso.2021.111644

Kim, N. S., Oh, M., Kim, K., Jo, C., (2021). 3D graphene-like zeolite-templated carbon with hierarchical structures as a high-performance adsorbent for volatile organic compounds. *Chemical Engineering Journal*, 409, 128076. https://doi.org/10.1016/j.cej.2020.128076

# Brønsted acid site concentration: a key parameter for the synthesis of Zeolite-Templated Carbons

**Thibaud Aumond,[1] Alain Moissette,[2] Hervé Vezin,[2] Annaig Le Person,[2] Yannick Pouilloux,[1] Isabelle Batonneau-Gener,[1] Alexander Sachse.[1]**

[1] IC2MP, UMR 7285 CNRS, 4 rue Michel Brunet, 86073, Poitiers Cedex 9, France

[2] LASIR, UMR-CNRS 8516, 59655 Villeneuve d'Ascq Cedex, France

Email: alexander.sachse@univ-poitiers.fr

**Keywords**

Zeolite-Templated Carbons, ZTCs, Zeolite, nanoporous carbons, carbon synthesis

## INTRODUCTION

Zeolite-templated carbons (ZTCs) have been synthesized for the first time by Kyotani (1997) and are today a well-established class of microporous carbons. They feature defined textural proprieties that reveal very interesting in a number of fields including (electro)catalysis and adsorption as shown by Wang (2009), due to their unique electronic properties in combination with very high porous volume and homogeneous micropore size distribution related in Nishihara's review (2018). These ZTCs develop within the microporous system of a template zeolite and are hence a negative copy of their structure.

In this communication, we present the impact of the active site concentration of the template zeolite (FAU structure) and the synthesis temperature on the properties of achieved ZTCs. Despite the known impact of acid site density in many zeolite catalyzed reactions, this parameter has never been taken into consideration for ZTC synthesis. The thorough characterization of hybrid materials (zeolites/carbon) and final ZTCs by nitrogen physisorption, XRD, electron microscopy, conductivity, MAS NMR, Raman, and EPR allowed us to draw sound conclusions on the ZTC formation mechanism as a function of the studied parameters.

## MATERIALS AND METHODS

Five proton-exchanged FAU structured zeolites with acidities varying from 54 to 1004 µmol $g^{-1}$ were used as zeolite templates. After activation of the zeolites, ethylene flow (6.7vol% in $N_2$) was passed through at a target temperature (690, 740, 790, and 840 °C) for 4 h. Additional pyrolysis treatment was carried out at 900 °C for 2 h under $N_2$ flow. The achieved hybrid materials were treated with aqueous HF, which allowed to dissolve the template zeolites and obtain the pure ZTCs.

## RESULTS AND DISCUSSION

In a relatively narrow range of synthesis temperatures very different behaviors of ZTCs formation can be identified. For low synthesis temperatures (*i.e.* 690 and 740 °C), the structural packing density (SPD) of the hybrid materials which refers to the amount of carbon within the zeolite micropores, clearly depends on the acidity (figure 1). By increasing the acidity, an increase in SPD can be noted as well as a decrease of the residual microporous volume of the hybrid material. That informs about carbon filling within the micropores only, where the acid sites are located. For a synthesis temperature of 790 °C, a similar SPD no matter the acidity of the template zeolite is obtained as well as an almost complete filling of micropores. On the contrary, using the highest synthesis temperature (840 °C) involves a decrease of the SPD by increasing the acid site content. This can be explained by the textural properties of the template zeolites: mesoporous volume that is filled using

this temperature decreases linearly by lowering Si/Al ratio. Acid sites no longer govern the synthesis of ZTC but it is the textural properties of the template zeolite.

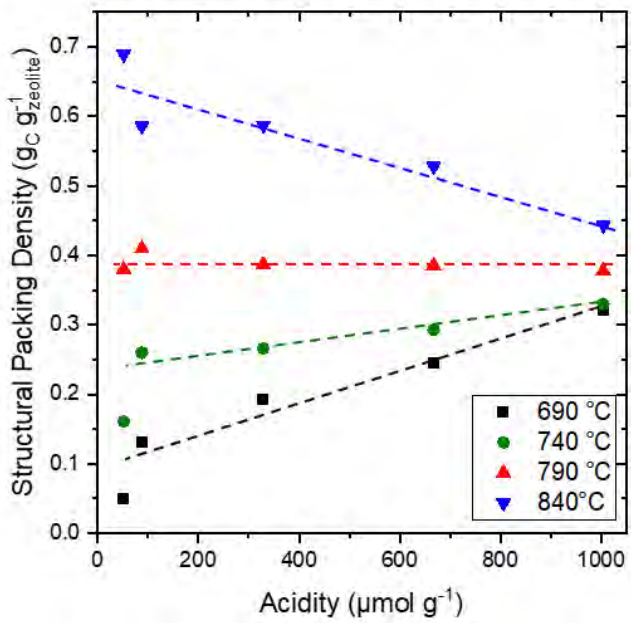


**FIGURE 1**: Structural packing density as a function of acid site concentration for the four synthesis temperatures.

These observations are confirmed by characterizing the final ZTC materials after zeolite dissolution. TEM images show perfect replicas of zeolite for low synthesis temperatures only when the acid site content is high enough. On the contrary, when a zeolite containing low acidity is used as template a mixture of ZTC and unstructured carbon compound is obtained (figure 2). At 790 °C, the morphology of the ZTC is similar to the one of the template zeolite no matter the acidity of the template. Finally, at 840 °C the morphology is also transcribed to the ZTC but external carbon deposition occurs as well as mesopore filling. The composition also depends both on the synthesis temperature and acid sites content: using low synthesis temperature C/H ratios clearly decrease by decreasing the acidity while these ratios are equal no matter the acidity at 790 °C, and increase by decreasing the acidity at 840 °C due to mesopores filling and carbon deposition on the external surface.

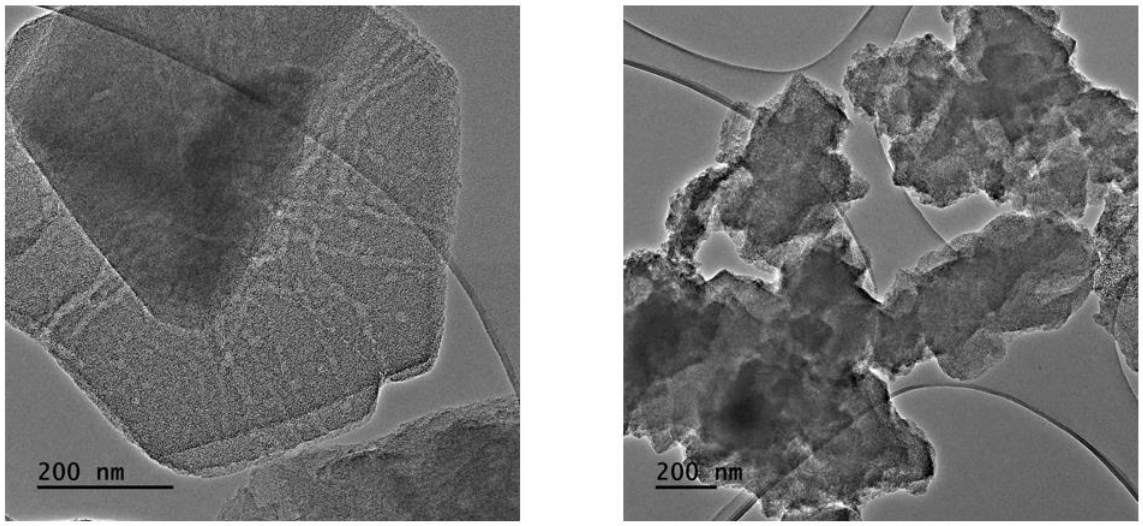


**FIGURE 2**: TEM images of ZTCs obtained for a synthesis temperature of 690 °C from high acid site concentration (*i.e.* 1004 µmol $g^{-1}$, left) and from low acid site concentration (*i.e.* 54 µmol $g^{-1}$, right).

Interestingly, ZTC which seemed to present similar properties for a synthesis temperature of 790 °C show important differences as far as their electronical conductivity, as well as their structuring order are concerned. This can be explained by a higher amount of acid sites that favor condensation of carbon compounds

## CONCLUSIONS

These observations together with nitrogen physisorption, electron microscopy images, Raman, and EPR spectroscopy allow to conclude that as a function of the acid site concentration and synthesis temperature different ZTC formation mechanisms are involved: the synthesis of ZTCs *i*) using low and medium synthesis temperatures (*i.e.* 690, 740 and 790 °C) the synthesis is importantly impacted by the acid site concentration. and, *ii*) using high synthesis temperature (*i.e.* 840 °C) the textural properties of the zeolite sole seem to direct the synthesis of carbons.

**Acknowledgments**

The authors acknowledge financial support from the European Union (ERDF) and "Région Nouvelle Aquitaine".

**References**

Kyotani, T., Nagai, T., Inoue, S., Tomita, A. (1997). Formation of New Type of Porous Carbon by Carbonization in Zeolite Nanochannels. *Chem. Mater.*, 9, 609-615. https://doi.org/10.1021/cm960430h

Nishihara, H., Kyotani, T. (2018). Zeolite-templated carbons – three-dimensional microporous graphene frameworks. *Chem. Commun.*, 54, 5648-5673. https://doi.org/10.1039/C8CC01932K

Wang, H. L., Gao, Q. M., Hu, J., Chen, Z. (2009). High performance of nanoporous carbon in cryogenic hydrogen storage and electrochemical capacitance. *Carbon*, 47, 2259-2268. https://doi.org/10.1016/j.carbon.2009.04.021

Carbon 2022

# The role of functional groups in governing photoactivity and selectivity on S-doped nanoporous carbons

**Teresa J. Bandosz[1,*], Alfonso Policicchio[1], Marc Florent[1], Wanlu Li[1,2], Po S. Poon[3], Juan Matos[4,*]**

[1] Department of Chemistry and Biochemistry, The City College of New York, NY, 10031, USA.

[2] Department of Chemistry, Saint Peter's University. Jersey City, NJ 07306, USA.

[3] Unidad de Desarrollo Tecnológico (UDT), Universidad de Concepción, Chile.

[4] Instituto de Ciencias Químicas Aplicadas, Facultad de Ingeniería, Universidad Autónoma de Chile, 8900000 Santiago, Chile.

*Corresponding authors.

Emails: juan.matos@uautonoma.cl (J. Matos); tbandosz@ccny.cuny.edu (T.J. Bandosz).

**Keywords**

S-doped carbon; Photoactivity/Selectivity; Photocatalysis.

## INTRODUCTION

Treatment of polluted water is still one of the main challenges for scientists and engineers. Water pollution by so-called emerging pollutants becomes a major environmental issue with the potential to cause adverse ecological and human health effects. This problem is related not only to residual industrial liquids (RILs) but also to residual domestic waters (RDWs). However, RILs include toxic cancerogenic molecules such as phenol from pharmaceutical industry. The removal of this class of pollutants can be addressed by advanced oxidation processes (AOPs) based on Fenton, Photo-Fenton, hydrogen peroxide, ozonolysis and heterogeneous photocatalysis. Therefore, important efforts have been devoted in the search of alternative photoactive materials for the treatment of polluted waters. In the present work, metal-free nanoporous carbons, either as received or sulphur doped, have been studied as photocatalysts for the degradation of phenol under solar light irradiation (Bandosz et al., 2020).

## EXPERIMENTAL

Commercial wood-based carbon, BAX 1500 (Mead Westvaco) and two synthetic carbons, C1 and C2, were used in this study. The latter two were obtained from Poly(4-styrenesulfonic acid-co-maleic acid) sodium salt (Aldrich) and poly(4-styrene sulfonic acid) sodium salt (Aldrich), respectively, by heating at 800 °C for 40 min with a nitrogen flow of 300 mL $min^{-1}$ and heating rate 50 °C $min^{-1}$. To introduce sulfur species, all carbons were heated in $H_2S$ atmosphere (1000 ppm in $N_2$) from a room temperature to 800 °C with 3 hours holding time at 800 °C (flow rate 150 mL $min^{-1}$ and heating rate 10 °C $min^{-1}$). The modified carbons were denoted as BAX-S, C1-S and C2-S. An open-to-air batch photoreactor was employed (Bandosz et al., 2020). Irradiation was performed by using a solar simulator with a Xe-lamp (450 W $m^{-2}$). The catalysts were evaluated using the adsorption of nitrogen, thermal analysis, potentiometric titration and XPS. Various parameters related to phenol adsorption and photodegradation were investigated. They include the kinetics of adsorption and the intraparticle diffusion coefficient. The effect of the surface density of the molecules adsorbed in the dark on the efficiency of photodegradation was also evaluated.

## RESULTS AND DISCUSSION

As listed in Table 1, the photocatalytic activity in terms of the surface-catalysed reaction-rate ($\phi_{rel\text{-}vsur}$) is ca. 25, 2 and 3 times higher after sulfidation for the BAX, C1 and C2 series, respectively. As XPS analysis indicated, sulfidation introduced more sulfur, and mainly that in thiophenic configurations, especially in the case of BAX where 100 % sulfur is in thiophenes. Even though some sulfur is present in C1 and C2, it is evenly distributed between reduced and oxidized species. After sulfidation, both sulfur content and the contributions of reduced sulfur increased, and both these features are responsible for an increase in the photoactivity for C1-S and C2-S. Nevertheless, the deactivation of the C2 series during the experiments deserves further attention, and the reason for this is likely related in a specific surface chemistry. For this series, an increase in the density of adsorbed phenol after sulfidation was the least pronounced and only about 10 %. That series of samples, and especially C2-S, was also the most hydrophobic based on the potentiometric titration results. It was found that thiophenic groups in small pores enhance phenol adsorption via providing basicity and hydrophobicity and contribute to photoactivity by inducing defects altering the energy band gap. Sulfoxides and sulfones, on the other hand, increase the selectivity of phenol oxidation to catechol and participate in oxidation through increasing the population of holes, which might promote the formation of reactive sulfur and oxygen species.

**Table 1.** Kinetic parameters of the PhOH photodegradation.

| Sample | $k_{app} \times 10^{-3}$ ($min^{-1}$) [a] | $R^2$ [b] | $\phi_{rel\text{-}kapp}$ [c] | $C_{5h}$ [d] (%) | $v_{sur} \times 10^{-3}$ ($molec.nm^{-2}.min^{-1}$) [e] | $\phi_{rel\text{-}vsur}$ [f] |
|---|---|---|---|---|---|---|
| Photolysis | 0.06 | 0.777 | --- | 4 | -0- [g] | --- |
| BAX | 4.10 | 0.888 | 1.0 | 31 | 0.271 | 1.0 |
| BAX-S | 40.5 | 0.949 | 9.9 | 100 | 6.880 | 25 |
| C1 | 1.90 | 0.941 | 1.0 | 87 | 2.401 | 1.0 |
| C1-S | 2.60 | 0.904 | 1.4 | 100 | 4.710 | 2.0 |
| C2 | 6.10 | 0.946 | 1.0 | 44 | 2.195 | 1.0 |
| C2-S | 17.5 | 0.894 | 2.9 | 59 | 6.894 | 3.1 |

[a] Obtained from the linear regression of the kinetic data according to a first-order kinetic model. [b] First-order quadratic linear factor ($R^2$). [c] Photoactivity relative to the analogous non-sulfur treated sample in terms of $k_{app}$. [d] PhOH conversion after 5h irradiation. [e] Surface-catalysed reaction-rate defined by $v_{sur} = k_{app}.\rho_{sur}$, where $\rho_{sur}$ is the surface density of phenol molecules adsorbed in the dark. [f] Photoactivity relative to the analogous non-sulfur treated sample in terms of $v_{sur}$. [g] Photolysis is a homogenous phase reaction.

## CONCLUSIONS

The results collected show the high activity of sulfur doped hydrophobic carbons not only for phenol adsorption in the dark but also for its photochemical degradation under solar light. That degradation ability is linked to the visible light photoactivity of the S-doped carbons and to their favourable porosity (a high contribution of ultramicropores similar in sizes to phenol molecule).

**Acknowledgements**

P.S. Poon thanks the financial support of ANID-PIA/APOYO CCTE AFB170007. J. Matos thanks the funds from ANID-FONDECYT 1190591; ANID-FONDEF ID19I10003; and ANID-FONDEF ID15I20321.

**References**

Bandosz, T. J.; Policicchio, A.; Florent, M.; Li, W.; Poon, P. S.; Matos J. (2020). Solar light-driven photocatalytic degradation of phenol on S-doped nanoporous carbons: The Role of functional groups in governing activity and selectivity. Carbon 156, 10-23.

Carbon 2022

# Cellulose And Biomass Photoreforming For The Generation Of Hydrogen

**S. Belda-Marco, M. Bouchabou, M.A. Lillo-Ródenas, M.C. Román-Martínez***

MCMA research group, Department of Inorganic Chemistry and Materials Institute. Faculty of Sciences. University of Alicante, Alicante, E-03080, Spain
*E-mail: mcroman@ua.es

**Keywords**
Cellulose, Photoreforming, Hydrogen.

## INTRODUCTION

The current energy model involves significant negative environmental effects, many of them related with the growing concentration of $CO_2$ in the atmosphere. To reduce $CO_2$ emissions, it is necessary to replace fossil fuels and, for that purpose, green $H_2$, i.e. generated using renewable energy sources, is one of the best options. Thus, this study focuses on the photo-reforming of cellulose and lignocellulosic biomass (almond shell wastes) in aqueous medium with the aim of obtaining hydrogen (Caravaca, 2016; Zhang, 2016; Granone, 2018). For this purpose, $TiO_2$-M (Cu and Ni) (1 wt. % M) catalysts have been prepared using different synthesis methods with commercial and synthesised titania (in this latter case also including carbon doping). The aim is to achieve high hydrogen production, with a high $H_2/CO_2$ ratio, and to obtain value-added products in solution.

## EXPERIMENTAL SECTION

A series of photocatalysts has been prepared using the commercial titania P25 (Degussa) by the following procedures (i) impregnation with aqueous copper or nickel nitrate solution (P25-Cu-i and P25-Ni-i), (ii) calcination at 500 °C of P25-Cu-i (P25-Cu-ic), (iii) reduction in $H_2$ flow at 500 °C of P25-Cu-i and P25-Cu-ic (P25-Cu-ih and P25-Cu-ich, respectively), (iv) impregnation and reduction with $NaBH_4$ (P25-Cu-ib). Other photocatalysts have been prepared from $TiO_2$ synthesised by a hydrothermal process (12 h, 180 °C) using titanium tetraisopropoxide or from an additional $TiO_2$-C sample prepared adding sucrose (C precursor) to the synthesis medium. After drying (100 °C, 12 h) these samples were calcined (350 °C, 2h). $TiO_2$ and $TiO_2$-C were impregnated with aqueous copper nitrate solution, leading to $TiO_2$-Cu-i and $TiO_2$-C-Cu-i, respectively. The catalysts were characterised by ICP-OES atomic spectroscopy, X-ray diffraction, X-ray photoelectron spectroscopy and transmission electron microscopy. The catalytic activity tests were performed in a Heraeus UV-RS-2 glass reactor with a 150 W mercury lamp (365 nm). In each experiment, 1 g cellulose or biomass (both milled), 20 mg photocatalyst and 500 mL distilled water were used. The generated gas is swept by He flow (60 mL/min) and continuously analysed by mass spectrometry (Omnistar GSD 301 O1, Balzers). At the end of the experiment (5 h), the solution is collected and analysed for total organic carbon.

## RESULTS AND DISCUSSION

According to ICP-OES, the M content (wt. %) is very close 1 wt.% in all catalysts, excepting P25-Cu-ib, in which the Cu content is 0.5 wt. %.

XRD data for the catalysts show the characteristic peaks of $TiO_2$ and very low intensity peaks that could correspond to Cu species. A mixture of copper species, such as CuO, $Cu_2O$, and Cu in different proportions, seems to be present in the catalysts.

Table 1 shows the main results regarding the oxidation state of the supported Cu species. The P25-Ni-i catalyst exhibits BE at 855.6 and 856.85 eV corresponding to Ni (II) and Ni (III), respectively.

Fig. 1 shows TEM images of the P25-Cu photocatalysts, including the determined average particle size, which is lower than 3 nm in all catalysts.

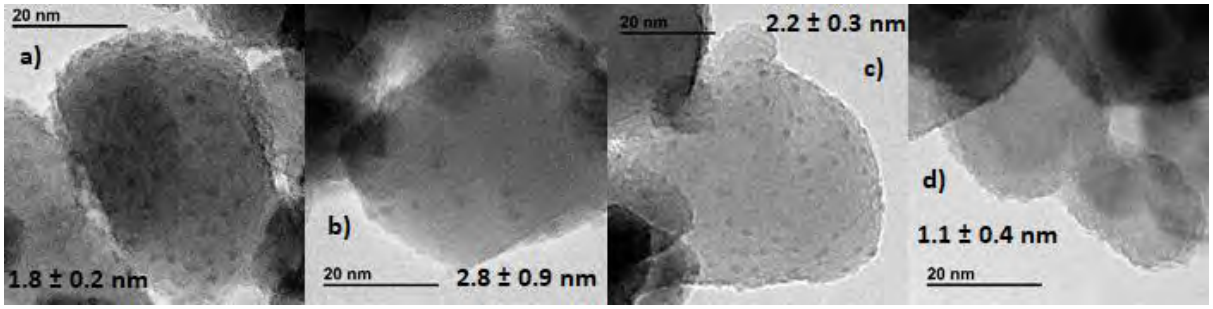


**FIGURE 1:** TEM images a) P25-Cu-i, b) P25-Cu-ic, c) P25-Cu-ich and d) P25-Cu-ib

Table 1 shows the amount of $H_2$ and $CO_2$ generated (in $\mu mol \cdot h^{-1} \cdot gcat^{-1}$) using all the tested photocatalysts, revealing that the Cu catalysts are more active than pure P25 and thus, the positive effect of copper species as co-catalysts. On the other hand, Ni seems to be no effective as co-catalyst. Using the synthesized titania the results are similar or better than using P25, and it is outstanding that the incorporation of carbon during the synthesis of $TiO_2$ (and subsequent Cu impregnation) leads to an increased $H_2$ generation. Using biomass as substrate the hydrogen generation is very limited, probably because other reduction reactions compete and are more favoured.

**Table 1.** XPS data of the supported copper species; and hydrogen and carbon dioxide generated in photocatalytic tests.

| | **XPS data** | | **Catalytic activity results** | | |
|---|---|---|---|---|---|
| **Catalyst** | **B.E. (eV)** | | **$H_2$** ($\mu mol \cdot h^{-1} \cdot gcat^{-1}$) | **$CO_2$** ($\mu mol \cdot h^{-1} \cdot gcat^{-1}$) | **$H_2/CO_2$** |
| | Cu(I) or Cu(0) | Cu(II) | | | |
| P25 | | | 297 | 211 | 1.4 |
| P25-Ni-i | | | 265 | 224 | 1.2 |
| P25-Cu-i | 932.1 (76%) | 934.2 (24%) | 731 | 407 | 1.8 |
| P25-Cu-i[*B] | - | - | 38 | 357 | 0.1 |
| P25-Cu-ic | 932.38 (87%) | 933.99(13%) | 437 | 277 | 1.6 |
| P25-Cu-ih | - | - | 510 | 313 | 1.6 |
| P25-Cu-ich | 932.34 (91%) | 933.63 (9%) | | 275 | 1.7 |
| P25-Cu-ib | 932.34 (91%) | 933.63 (9%) | 653 | 341 | 1.9 |
| $TiO_2$-Cu-i | 932.11 (88%) | 933.12 (12%) | 733 | 488 | 1.5 |
| $TiO_2$-C-Cu-i | 932.18 (89%) | 933.89 (11%) | 954 | 610 | 1.6 |
| Blank[**] | - | - | 69 | 19 | 3.6 |

[*B] Using almond shell as substrate. [**]With P25 and without cellulose or biomass

## CONCLUSIONS

The Cu containing photocatalysts are more active than the pristine P25 and that the P25-Ni catalyst. The P25-Cu-i sample stands out for its very good catalytic activity results and for its simple and cheap preparation procedure. It is observed that Cu-based catalysts prepared with the synthesised titania

are very active and that the incorporation of carbon during titania synthesis provides higher $H_2$ evolution values. The test carried out with biomass has led to a small $H_2$ evolution which is related with the much more complex structure of this substrate.

**Acknowledgements**

The authors would like to thank the PROMETEO/2018/076 (GV/Feder), RTI2018-095291-B-I00 (Spanish Ministry of Science and Innovation) and VIGROB-136 (University of Alicante) for financial support

**References**

Caravaca, A., Jones W., Hardacre C. and Bowker M. (2016) '$H_2$ production by the photocatalytic reforming of cellulose and raw biomass using Ni, Pd, Pt and Au on titania', *Proceedings of the Royal Society A: Mathematical, Physical and Engineering Sciences*, 472(2191), pp. 1–21. doi: 10.1098/rspa.2016.0054.

Granone, L. I., Sieland F., Zheng N., Dillert R. and Bahnemann D. W. (2018) 'Photocatalytic conversion of biomass into valuable products: A meaningful approach?', *Green Chemistry*, 20(6), pp. 1169–1192. doi: 10.1039/c7gc03522e.

Zhang, G. *et al.* (2016) 'Simultaneous cellulose conversion and hydrogen production assisted by cellulose decomposition under UV-light photocatalysis', *Chemical Communications*, 52(8), pp. 1673–1676. doi: 10.1039/c5cc09075j.

20 C 22 arbon 2022

# Competitive Adsorption of $CO_2$, $H_2O$ Vapor, $N_2$, and $SO_2$ on Activated Carbon for $CO_2$ Capture from Flue Gases

**Jon G. Bell[1], Michael J. Benham[2], Mark G. Roper[2] and K. Mark Thomas[1]**

[1]School of Engineering, Newcastle University, Newcastle upon Tyne, UK, NE1 7RU

Email: mark.thomas@ncl.ac.uk

[2]Hiden Isochema Ltd, 422 Europa Blvd, Warrington, WA5 7TS, UK

**Keywords**

Carbon Dioxide Capture, Competitive Adsorption, Selectivity

## INTRODUCTION

Combustion of fossil fuels for power generation has a major environmental impact through emissions of $CO_2$, SOx, NOx, and other trace species. Post combustion capture of $CO_2$ from flue gases at source has the potential for mitigating global warming and climate change. However, existing $CO_2$ capture technology is currently not economically viable (Sholl, 2016). $CO_2$ (10−15%), $H_2O$ vapor (8−12%), and residual $O_2$ (2−3%) and $N_2$ (67−78%) are the main components of flue gas from natural gas combustion with NOx (150−500 66 ppm) as a minor component (Chaffee, 2007). Natural gas combined cycle power plants have flue gases with lower concentrations of $CO_2$ with typical compositions of $CO_2$ (3.9%) with a balance of $N_2$ (74.4%), $O_2$ (12.4%), $H_2O$ (8.4%), and Ar (0.9%) (Siegelmann, 2019). Flue gases produced by coal combustion also contain SOx (500−3000 ppm) as well as other trace inorganic species. The use of porous adsorbent materials for carbon capture and storage (CCS) from flue gases is being considered as a low-energy economic method (Webley, 2014). $CO_2$ cyclic separation processes proposed include pressure swing adsorption/vacuum swing adsorption (PSA/VSA) (Vos, 2014) and temperature swing adsorption (TSA) (Merel, 2008).

Adsorption of flue gas on porous materials is a complex process due to competitive adsorption of species with different mechanisms and potential reactions of species in the pores. A comparison of multicomponent ($CO_2$, $H_2O$, and $N_2$) and pure $CO_2$ adsorption showed that multicomponent studies were essential for the assessment of adsorbents for $CO_2$ capture (Mason, 2015).

In this work, the adsorption/desorption characteristics of pure $N_2$, $CO_2$, and $SO_2$ gases, and $H_2O$ vapor on an activated carbon, including both thermodynamics and adsorption dynamics, were systematically investigated to give a comprehensive representation of the adsorption processes. The $CO_2/N_2$ competitive adsorption was determined by the integral mass balance (IMB) experimental method (Bell, 2021) and the isotherm and selectivity results were compared with Ideal Adsorbed Solution Theory (IAST) (Myers,1965).

## RESULTS AND DISCUSSION

Carbon F400 was used in a previous European interlaboratory study of $CO_2$ adsorption with temperatures in the range 318-318.8 K. Comparison of the high-pressure carbon dioxide adsorption up to 50 bar at 318.5 K for the F400 sample used in this study showed that it was not significantly different from the sample used in the interlaboratory study (Bell, 2021). $CO_2$ adsorption studies showed that the Dubinin-Radushkevich micropore volume was 0.363 $cm^3\ g^{-1}$ and the total pore volume was 0.55 $cm^3\ g^{-1}$. The adsorption isotherms for the main components of flue gas show that there are major differences in adsorption characteristics. The isotherms for adsorption of $H_2O$ vapor, $SO_2$, $CO_2$ and $N_2$ at 298.15 K are shown in Figures 1a and b. The adsorption isotherm for $H_2O$ vapor is Type V in the IUPAC classification whereas the $SO_2$ isotherm is Type I/II. The isotherms intersect each other at low pressure (~13 mbar) because of the different adsorption mechanisms, which give different isotherm shapes. It is apparent from the isotherms that the spreading pressure for the flue gas components was in the order: $H_2O > SO_2 > CO_2 > N_2$ for surface excess values > 1 mmol $g^{-1}$. The

isosteric enthalpies of adsorption for $H_2O$ vapor (193.15-303.15 K), $SO_2$ (290.65-303.15 K), $CO_2$ (283.15-318.49 K) and $N_2$ (298.15-313.15 K) were determined as a function of surface excess using the Clausius-Clapeyron equation. Virial methods were used to determine the isosteric enthalpies at zero surface coverage using virial methods for $SO_2$, $CO_2$ and $N_2$ adsorption. The isosteric enthalpies of adsorption for the flue gas components was in the order: $H_2O > SO_2 > CO_2 > N_2$ for surface excess values > 1 mmol $g^{-1}$.

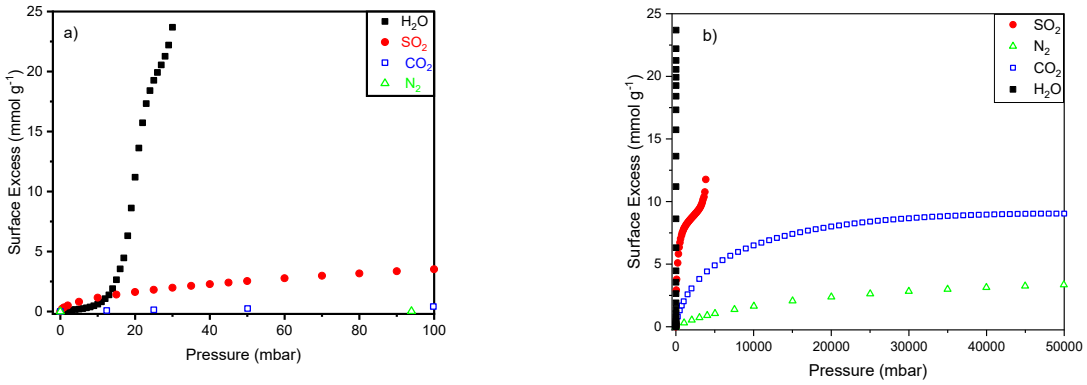


**FIGURE 1.** Adsorption isotherms for $H_2O$ vapor, $SO_2$, $CO_2$ and $N_2$ on carbon F400 at 298.15 K a) 0-100 mbar and b) 0-50000 mbar.

$H_2O$ vapor and $SO_2$ adsorption studies showed that these components had much slower adsorption kinetics that either $CO_2$ or $N_2$ (Bell, 2021). The kinetics for both $H_2O$ and $SO_2$ adsorption obey the Linear Driving Force (LDF) model and this is consistent with the presence of a surface barrier. The adsorption and desorption kinetic minima with surface excess for $H_2O$ vapor are attributed to the formation of $H_2O$ clusters. The $SO_2$ adsorption/desorption are attributed to dipole−dipole interactions on the surface. The adsorption of water vapor has potentially a large effect on the capture of $CO_2$ because of the large amounts present in flue gas and the low rates of adsorption of water vapor in the steep uptake region of the Type V isotherm due to the effect of clustering of water molecules in pores. These water vapor adsorption rates were much slower than $SO_2$ and this is a result of the different adsorption mechanisms. Both the $SO_2$ adsorption and desorption kinetics are also very similar for specific surface excess values, and there is a minimum in the kinetics.

Figure 2 shows a comparison of experimental isotherm measurements and selectivities for $CO_2/N_2$ mixtures using the IMB method as a function of mole fraction and corresponding IAST calculations, which are based on the pure gas isotherms (see Figure 1b). Results for $CO_2/N_2$ mixtures show how spreading pressure controls competitive adsorption and the $CO_2/N_2$ selectivity decreases with increasing $CO_2$ mole fraction. The experimental and IAST isotherms were comparable, but the experimental $CO_2/N_2$ selectivities were significantly different from IAST calculations. Small differences in the isotherms are significant in determining selectivity, in particular, at the extremes of $CO_2/N_2$ gas phase ratios. The $N_2$ IAST isotherm values are significantly higher than the experimental values. Comparison of the predictions of the IAST model for $CO_2/N_2$ selectivity with experimental selectivity measurements showed that experimental selectivity determinations were needed for process development. $CO_2/N_2$ is a straightforward binary mixture compared with flue gas. IAST calculations are appropriate for $CO_2/H_2O$ mixtures because of the different adsorption mechanisms and therefore $CO_2/H_2O$ selectivity has to be determined experimentally. This research shows the need for experimental determinations of amounts of adsorbed species from complex flue gas mixtures to determine selectivity as a function of relevant conditions for process development. The capture of $CO_2$ from flue gases on porous materials is strongly influenced by other components with a higher spreading pressure as well as kinetic effects for diffusion of $SO_2$ and $H_2O$ in pores and possible reactions of species such as $CO_2$ and $SO_2$ with $H_2O$ in pores.

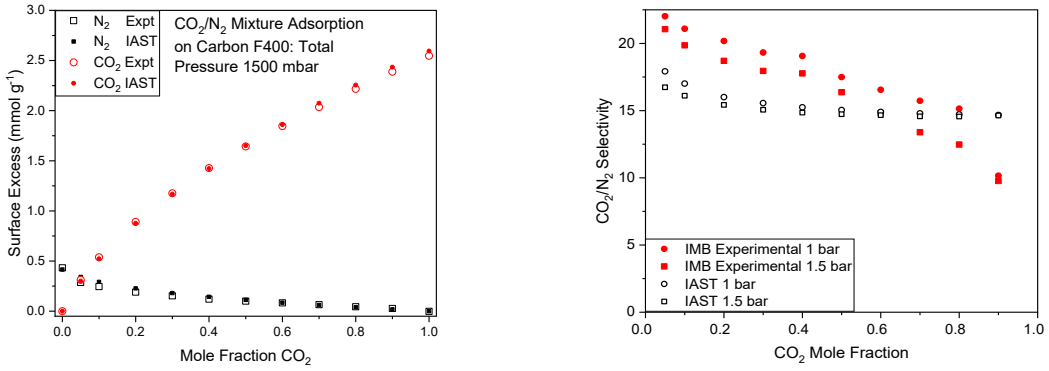


**FIGURE 2.** Adsorption of $CO_2/N_2$ mixtures on F400 at 298.15 K a) The variation of experimental surface excess adsorbed for $N_2$ and $CO_2$ with IAST predictions for total gas phase pressure of 1.5 bar, b) The variation of $CO_2/N_2$ selectivity calculated using IAST and experimental values obtained using the IMB method with $CO_2$ mole fraction for total pressures of 1 and 1.5 bar.

## CONCLUSIONS

Measurements of competitive adsorption are challenging for flue gas. Spreading pressure is a key factor in controlling the capture of $CO_2$ from flue gas mixtures with the main components in the order: $H_2O > SO_2 > CO_2 > N_2$ for surface excess values > 1 mmol $g^{-1}$. The order for isosteric enthalpies of adsorption is the same as for the spreading pressures over an identical surface excess range. Adsorption and desorption kinetics of $H_2O$ are also a critical aspect in the capture of $CO_2$ from flue gases since kinetics are slow and could lead to loss of capacity with increasing adsorption/desorption cycles and more frequent adsorbent regeneration.

Selectivity is a key parameter in the design of separation processes. Comparison $CO_2/N_2$ selectivity measured by the integral mass balance method and IAST calculations based on high resolution pure component measurements showed significant differences indicating that experimental measurements of selectivity were necessary for process design calculations. Even in the case of $CO_2/N_2$ where the adsorption mechanisms are similar, Ideal Adsorbed Solution Theory (IAST), which uses isotherms for pure gases as the starting point for the calculation, does not give a sufficiently accurate prediction of selectivity for use in process design. $H_2O/CO_2$ selectivity have different adsorption mechanisms and therefore selectivity must be determined experimentally in this case.

## REFERENCES


Bell, J. G., Benham, M.J. and Thomas, K. M. (2021) Adsorption of carbon dioxide, water vapor, nitrogen, and sulfur dioxide on activated carbon for capture from flue gases: Competitive adsorption and selectivity aspects *Energy Fuels* 35, 8102−8116

Chaffee, A. L., Knowles, G. P., Liang, Z., Zhang, J., Xiao, P. and Webley, P. A. (2007) $CO_2$ capture by adsorption: Materials and process development. *Int. J. Greenhouse Gas Control* 1 (1), 11−18.

Mason, J. A., McDonald, T. M., Bae, T. H., Bachman, J. E., Sumida, K., Dutton, J. J., Kaye, S. S., Long, J. R. (2015) Application of a High-Throughput Analyzer in Evaluating Solid Adsorbents for Post-Combustion Carbon Capture via Multicomponent Adsorption of $CO_2$, $N_2$, and $H_2O$. *J. Am. Chem. Soc.* 137 (14), 4787−4803.

Merel, J., Clausse, M. Meunier, F. Experimental investigation on $CO_2$ post-combustion capture by indirect thermal swing adsorption using 13X and 5A zeolites. *Ind. Eng. Chem. Res.* 2008, 47 (1), 209−215.

Myers, A. L. and Prausnitz, J. M. (1965) Thermodynamics of Mixed-Gas Adsorption. *AIChE J* 11, 121−127.

Sholl, D.S. and Lively, R.P. (2016) Seven chemical separations to change the world *Nature* 532,435

Siegelman, R. L., Milner, P. J., Kim, E. J., Weston, S. C. and Long, J.R. (2019) Challenges and opportunities for adsorption-based $CO_2$ capture from natural gas combined cycle emissions. *Energy Environ. Sci.* 12 (7), 2161−2173.

Voss, C. (2014) $CO_2$ removal by PSA: an industrial view on opportunities and challenges. *Adsorption* 20 (2−3), 295−299.

Webley, P. A. (2014) Adsorption technology for $CO_2$ separation and capture: a perspective. *Adsorption* 20 (2−3), 225−231.

# Electroactive Biochar: a new concept of carbon electrode with unique properties to promote microbial extracellular electron transfer for biodegrading pollutants

**Raúl Berenguer[1,*], Amanda Prado[2,3] and Abraham Esteve-Núñez[2,3]**

[1] Instituto Universitario de Materiales, Departamento de Química Física, Universidad de Alicante UA, Apartado 99, 03080-Alicante, Spain

[2] Chemical Engineering Department, Universidad de Alcalá, Alcalá de Henares, Spain

[3] IMDEA Agua, Parque Tecnológico de la Universidad de Alcalá, 28805, Alcalá de Henares, Spain

*Email: raul.berenguer@ua.es

**Keywords**

electroactive biochar, microbial electrochemical systems, wastewater treatment

## INTRODUCTION

In a recent study of a biochar showing certain electroconductivity (Prado, 2019), we proposed that carbon properties other than conductivity greatly promote the response of the material towards electron transfer with electroactive bacteria for pollutants degradation in a bioelectrochemically-assisted constructed wetland (METland®). This material, the so-called electroactive biochar, is the most promising candidate for large-scale environmental applications of microbial electrochemical systems (Schievano, 2019). Despite this interest, the role of conductivity and other carbon properties determining these bioelectrogenic processes, i.e. the concept of electroactive biochar, needs to be explored. This work compares for the first time the response of an electroconductive biochar (ecB) with a non-conductive one (ncB), together with other reference conductive or isolating materials (graphite, coke (C), and gravel (G)), for the treatment of a real urban wastewater.

## EXPERIMENTAL

Different laboratory-scale upflowed biofilters (METland®-type), in the absence or presence of plants, were built with the 5 different materials (beds) (Fig. 1A). The materials were thoroughly analysed by different techniques (SEM, Raman, XRD, $N_2$ and $CO_2$ adsorption, Hg porosimetry, TPD, XPS, and four-probe conductivity measurements) to establish properties-performance correlations. The impact of the different physicochemical properties on the wastewater treatment efficiency (COD and N removal), bioelectrochemical response, and diversity of microbial communities was studied. The bioelectrochemical activity was evaluated from cyclic voltammetry and in-depth electric potentials (EP) profiles. These EP profiles were measured as potential differences between two Ag/AgCl/Cl-(sat.) reference electrodes connected to a digital voltmeter, one fixed in the upper layer (surface) of the biofilter immersed in water (reference potential), and the other one moving every 3 cm along depth, at time 0 (abiotic conditions) and during the start-up (10 days) and the steady state (20 days) periods. The microbial diversity was analysed by 16S rRNA metagenomic sequencing.

## RESULTS

Materials analysis (Table 1) evidences a negligible conductivity and porosity in the gravel, while the coke exhibits high conductivity and porosity (Hg), but lacks surface oxygen groups (SOGs) and microporosity. Contrarily, SOGs abound in both biochars, mainly in the non-conductive (ncB), and both present a developed and hierarchical porosity, but the conductive biochar (ecB) presents a conductivity 5 orders of magnitude higher and a higher microporosity. The biodegradation results show that the electroconductive materials outperformed the non-conductive ones, being the

electroconductive biochar the one with the best overall response (Table 1), allowing removal rates as high as 175-180 gCOD/bed*$m^3$ day and capable to support a land footprint as low as 0.4 $m^2$/pe.

**TABLE 1**: Main physicochemical properties, biodegradation efficiency at 20 days (influent: 862.0 mg/L COD and 64.7 mg/L $NH_4^+$) and key functional microbes found for the materials (results of planted reactors).

| | | Textural properties | | | Surface Chemistry (TPD) | | Removal Efficiency | | Bacteria (reads) | |
|---|---|---|---|---|---|---|---|---|---|---|
| Material | Cond. (S/cm) | $S_{BET}$ ($m^2$/g) | $A_{CO_2}$ ($m^2$/g) | Porosity (Hg) (%) | CO (µmol/g) | $CO_2$ (µmol/g) | COD (%) | $NH_4^+$ (%) | EAB | Annamox |
| gravel | <1E-12 | < 1 | --- | 2 | --- | --- | 63.0 | 49.1 | 1447 | 5186 |
| nc-biochar | 2.6E-9 | 1.3 | 395 | 53 | 2725 | 1953 | 82.2 | 82.3 | 6184 | 4224 |
| ec-biochar | 5.8E-4 | 305 | 630 | 37 | 994 | 605 | 90.8 | 83.4 | 21898 | 4411 |
| coke | 10.4 | 1.2 | 5 | 46 | 42 | 68 | 89.8 | 56.2 | 2391 | 825 |

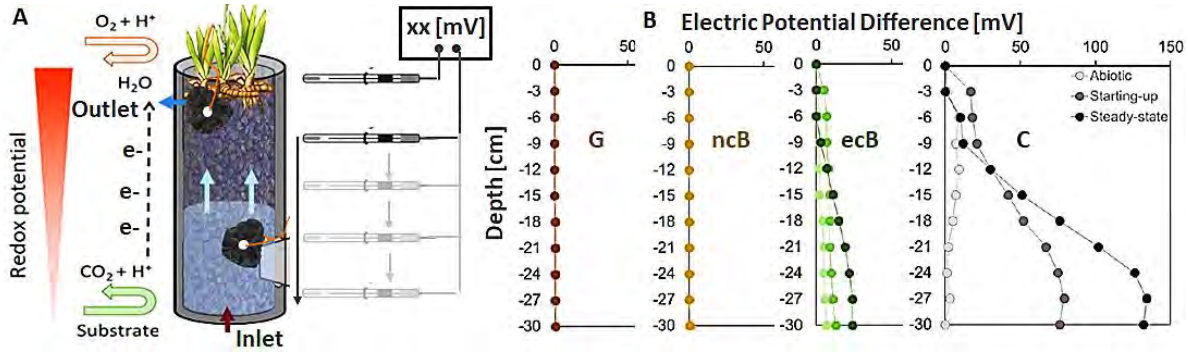


**FIGURE 1**: (A) Scheme of the METland®-type reactor; and (B) in-depth electric potential profiles of the biofilters with the different materials at different operation conditions.

Microbial biodiversity analysis (Table 1) revealed that the properties of this material favour the presence of Geobacter and annamox bacteria, the most efficient for electrogenic degradation of organics and nitrogen removal, respectively. Furthermore, the presence of a marked electric potential profile along the bed height in electroconductive materials (Fig. 1B) demonstrated that electroconductivity is necessary for an effective electron flow from bottom to uppermost layers of the bed and, consequently, an unlimited metabolism.

## CONCLUSIONS

The electroconductive biochar has been found the most effective material for urban wastewater treatment in METlands. Its superior response is attributed to the combination of a rich surface chemistry with electroactive SOGs and adequate microporosity, favouring the “geobattery” mechanism of e-transfer with bacteria; together with a sufficient conductivity to promote the "geoconductive" mechanism and support the electron flow through the bed.

**Acknowledgements**

MINECO and FEDER funds (Ramon y Cajal contract, RYC-2017-23618) and European Union's Horizon 2020 programme (ELECTRA project, grant No. 826244) are gratefully acknowledged.

**References**

Prado, A., Berenguer, R. and Esteve-Núñez, A. (2019). Electroactive biochar outperforms highly conductive carbon materials for biodegrading pollutants by enhancing microbial extracellular electron transfer. Carbon, 146, 597-609. https://doi.org/10.1016/j.carbon.2019.02.038

Schievano, A., Berenguer, R., Goglio, A., Bocchi, S., Marzorati, S., Rago, L., Louro, R.O., Paquete, C. M., Esteve-Núñez, A. (2019). Electroactive biochar for large-scale environmental applications of microbial electrochemistry. ACS Sust. Chem. Eng. 7, 18198-18212. https://doi.org/10.1021/acssuschemeng.9b04229

Carbon 2022

# The multifacets of functional graphene oxide in cancer therapy

**Alberto Bianco**
CNRS, Immunology, Immunopathology and Therapeutic Chemistry, UPR 3572, University of Strasbourg, ISIS, 67000 Strasbourg, France
Email: a.bianco@ibmc-cnrs.unistra.fr

**Keywords**
Carbon nanomaterials, 2D materials, organic functionalization, glioblastoma, therapy, imaging, cytotoxicity.

## INTRODUCTION

Graphene oxide (GO), the oxidized form of graphene, is a versatile platform to prepare multifunctional systems as it is full of oxygenated groups that can be chemically modified using controlled reactions (Guo, 2022). In this context, GO has been extensively explored for biomedical applications and its biocompatibility and biodegradability have been proved (Ma, 2020). The possibility to modulate the number of defects and functions, the insertion of new functional groups and the control of the size distribution allow to render this material safe in the biomedical field. We have recently exploited GO for different applications in combined cancer therapies, focusing on solid tumours and glioblastoma.

## RESULTS AND DISCUSSION

One of the mechanisms of killing cancer cells is based on depletion of glutathione (GSH) and generation of reactive oxygen species (ROS) (Ma, 2021a). Starting from GO, we have first reduced it to so-called reduced graphene oxide (rGO). rGO was combined with manganese dioxide nanoparticles ($MnO_2$ NPs) to design a multifunctional platform (rGO@$MnO_2$) for efficient photothermal/chemodynamic combined therapies (PTT/CDT) (Figure 1) (Ma, 2021b). Manganese-based NPs were complexed to the surface of rGO nanosheets (rGO NSs). We found that these NPs are able to oxidize intracellular GSH, generating manganese ions that convert hydrogen peroxide into hydroxyl radicals by Fenton reaction. As graphene materials have the capacity to adsorb light in the near infrared region and generate heat, we also applied rGO NSs-mediated PTT to enhance the mortality of cancer cells. The high temperature caused by the photothermal conversion increases the Fenton reaction rate, ameliorating the efficacy of $MnO_2$ NPs-induced chemodynamic effect. These hybrid materials have great potential in cancer therapy by exploiting the synergistic effect of photothermal and chemodynamic combined therapeutic modalities.


**FIGURE 1**: rGO@$MnO_2$-mediated photothermal therapy (PTT) and photothermal/delivery effect enhanced chemodynamic therapy (CDT) for synergistic elimination of cancer cells.

Glioblastoma is the most common and malignant primary brain tumor in adults associated with a high mortality rate and survival between twelve and fifteen months after diagnosis. Unfortunately, glioblastoma poorly benefits from modern molecular therapies. Peritumoral brain invasion is one of the main targets to cure glioblastoma. Chemo/radiotherapy and targeted therapies failed to combat peritumoral relapse. Brain inaccessibility and tumour heterogeneity explain this failure. We have found that rGO can provide a unique opportunity to modulate the local brain microenvironment (Chin, 2022). Multimodal graphene impacts have been reported on glioblastoma cells in vitro but failed when translated in vivo because of low diffusion. To solve this issue, we have developed a protocol to prepare a functional rGO, involving rapid ultra-mixing during the functionalization with polyethyleneimine (PEI), leading to the formation of highly water stable rGO-PEI. Wide mice brain diffusion and biocompatibility were demonstrated. Using an invasive GL261 model, we observed a strong anti-invasive effect. These results open the way to a new microenvironment anti-invasive therapy using graphene-based nanomaterials that have been optimized for in vivo brain delivery.

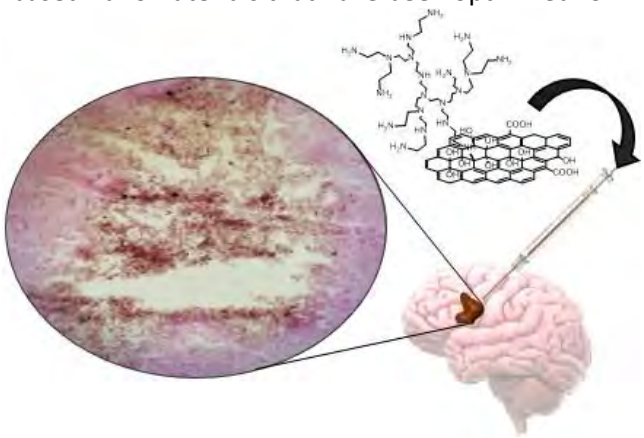

**FIGURE 1**: PEI-functionalized rGO distribution in a mouse brain affected by a glioblastoma.

## CONCLUSIONS

Graphene oxide is a versatile carbon material that allows designing multifunctional systems following a controlled chemical modification of its surface, leading to complex conjugates with specific biological properties that can be exploited to treat different types of cancer.

**Acknowledgements**

The authors gratefully acknowledge the financial support from the EU Graphene Flagship project (no. 785219). This work was partly supported the Agence Nationale de la Recherche (ANR) through the LabEx project Chemistry of Complex Systems (ANR-10-LABX-0026_CSC). We wish to acknowledge the CNRS through the International Research Project MULTIDIM between UPR3572 Unit and Okayama University and the International Center for Frontier Research in Chemistry.

**References**

Chin, S. M., Reina, G., Chau, N. D. Q., Chabrol, T., Wion, D., Bouamrani, A., Gay, E., Nishina, Y., Bianco, A. and Berger, F. (2022). Functional graphene for peritumoral brain microenvironment modulation therapy in glioblastoma. Under revision.

Guo, S., Garaj, S., Bianco, A. and Ménard-Moyon, C. (2022) Controlling covalent chemistry on graphene oxide. *Nature Reviews Physics*, 4, 247-262. https://doi.org/10.1038/s42254-022-00422-w

Ma, B., Martìn, C., Kurapati, R. and Bianco, A. (202) Degradation-by-design: how chemical functionalisation enhances the biodegradability and safety of 2D materials. *Chemical Society Review*, 49, 6224-6247. https://doi.org/10.1039/c9cs00822e

Ma, B., Guo, S., Nishina, Y. and Bianco, A. (2021a). Reaction between Graphene Oxide and Intracellular Glutathione Affects Cell Viability and Proliferation. *ACS Applied Materials and Interfaces*, 13, 3528-3535. https://doi.org/10.1021/acsami.0c17523

Ma, B., Nishina, Y. and Bianco, A. (2021b). A glutathione responsive nanoplatform made of reduced graphene oxide and MnO2 nanoparticles for photothermal and chemodynamic combined therapy. *Carbon*, 178, 783-791. https://doi.org/10.1016/j.carbon.2021.03.065

Carbon 2022

# ALMOND SHELL WASTE AS SUBSTRATE FOR PHOTOREFORMING: INFLUENCE OF DIFFERENT PRETREATMENTS OVER THE LIGNOCELLULOSIC WASTE.

**M. Bouchabou, S. Belda-Marco, M.C. Román-Martínez, M.A. Lillo-Ródenas.**

*MCMA research group, Department of Inorganic Chemistry and Materials Institute (IUMA). Faculty of Sciences. University of Alicante, Alicante, E-03080, Spain.*

Email: mlillo@ua.es

**Keywords**

Biomass photoreforming, valuable products, pretreatment.

## INTRODUCTION

Lignocellulosic biomass residues (LBR) are attractive and promising starting materials for the sustainable production of fuels and chemicals. Different avenues can be used for such revalorization (Taylor *et al.*, 2019). Photocatalysis is among the most appropriate ones because it is efficient, simple, and less expensive than others (Liu *et al.*, 2019). In this context, the present study focuses on the photocatalytic reforming of almond shell, a local lignocellulosic biomass waste used as a model, to produce hydrogen. For that purpose, Metal/$TiO_2$ photocatalysts have been prepared, and different pretreatments (physical, thermochemical, etc.) have been assayed over the lignocellulosic biomass to increase its reactivity and, thus, the photo-reforming efficiency.

## EXPERIMENTAL

The almond shell sample (**AS**, local origin, with a 35 wt. % cellulose content) was submitted to the following treatments: i) Grinding (electric grinder), sieving to get the 1 mm fraction and milling in a planetary ball mill (PM 200 Retsch ball mill, 3:1 steel balls/solid weight ratio, 500 rpm, 7 h), resulting in sample named **MAS**, ii) Pyrolysis of MAS at 450 °C for 1 h in $N_2$ flow (sample **PMAS**) and iii) Hydrothermal carbonization (HTC) of MAS at 200 °C for 6 h. From this HTC treatment, the generated solid sample (**HMAS-S**) and the solution (**HMAS-L**) were separated. For comparison purposes, α-cellulose (Sigma-Aldrich) was also ball milled in conditions previously described (leading to sample **MC**). Catalysts with 5 wt.% metal were prepared by impregnation of titania P25 (Degussa) with aqueous solutions of $Ni(NO_3)_2{\cdot}6H_2O$ and $Cu(NO_3)_2{\cdot}3H_2O$ (both Panreac), as follows: 5 mL of the metallic salt solution were mixed with 2 g of P25, stirred for 2h, followed by 30 min sonication. Water was removed at 80 °C for 24 h, resulting in **Ni/$TiO_2$** and **Cu/$TiO_2$** catalysts. These catalysts were tested as prepared or after reduction treatment ($H_2$, 60 mL/min flow, 5 °C/min up to 500 ◦C, 2 h, then named **Ni/$TiO_2$-r** and **Cu/$TiO_2$-r**). The techniques used for the characterization of substrates and/or catalysts include physical adsorption of $N_2$ and $CO_2$ (Autosorb-6, Quantachrome Instruments), X-ray diffraction (Bruker D8-Advance), scanning electron microscopy (Jeol, model IT500HR), transmission electron microscopy (FEI Talos F200X) and ICP-OES (Perkin Elmer, 7300 DV). The photocatalytic tests were conducted in a cylindrical glass reactor (Heraeus UV-RS-2) with a UV lamp (Heraeus TQ-150, 150 W, λmax=365 nm) in the following conditions: 20 mg catalyst, 500 mL water, stirring, 30 mL/min He, 5 h, and variable amounts of the substrate (pretreated samples): 5 g of MAS, the amounts of PMAS and HMAS-S obtained by treating 5 g of MAS, or the amount of MC equivalent

to the cellulose contained in 5 g of MAS. Water splitting tests with Cu/P25 and photolysis assays were also conducted. The gaseous products were analyzed by mass spectrometry (Omnistar GSD301 01, Pfeiffer), whereas the solution at the end of the reaction was analyzed for total organic carbon determination (TOC-V CSN Shimadzu analyzer).

## RESULTS AND DISCUTION

The SEM analysis has shown that the average particle size of the MAS, PMAS and HMAS-S sample is 12, 18 and 22 µm, respectively. The textural characterization has confirmed some porosity creation in PMAS and HMAS-S. TEM images of the catalysts show a very good dispersion of Cu or Ni over $TiO_2$. Photocatalytic tests with Cu-$TiO_2$ or Ni-$TiO_2$ using MAS as substrate lead to similar productions of $H_2$ (32 $\mu molh^{-1}gcat^{-1}$), well above the water splitting (7 $\mu molh^{-1}gcat^{-1}$), or photolysis test (1 $\mu molh^{-1}$). Considering the lower cost and greater availability of Cu, most of the study has focused on Cu-$TiO_2$. Regarding the influence of the catalysts reduction treatment, it has been concluded that it does not improve the activity and it can be skipped with the important advantage or reducing costs and energy consumption. Similar amount of $H_2$ is obtained using PMAS or HMAS-S (around 15 and 16 $\mu molh^{-1}gcat^{-1}$, respectively), highlighting that despite their slightly higher porosity compared to MAS pyrolysis and hydrothermal carbonization are not suitable treatments. Using the liquid from hydrothermal carbonization (HMAS-L) a high amount of $H_2$ (73 $\mu molh^{-1}gcat^{-1}$) is obtained, opening the possibility of using this residue as an efficient substrate. As expected, the highest production of $H_2$ was achieved using the milled cellulose simpler substrate, 930 $\mu molh^{-1}gcat^{-1}$. The TOC values of the resulting solutions depend on the substrate used and, in general, they are higher in those tests in which the generation of hydrogen is also higher.

## CONCLUSIONS

Biomass photorreforming largely depends on the substrate and the applied pre-treatments. Good results have been obtained using Cu-$TiO_2$ photocatalysts prepared by a simple and economical procedure (avoiding high-temperature treatments). The liquid from the hydrothermal carbonization of almond shell has shown particularly attractive results, which opens the way to revalorize this residue.

**Acknowledgements**

The authors thank PROMETEO/2018/076 (GV/Feder), RTI2018-095291-B-I00 and VIGROB-136 (University of Alicante) for financial support. Meryem Bouchabou acknowledges the Algerian government for the predoctoral scholarship.

**References**

Liu, X., Duan, X., Wei, W., Wang, S. et al. (2019). Photocatalytic conversion of lignocellulosic biomass to valuable products, *Green Chemistry*, 21(16), 4266–4289. doi: 10.1039/c9gc01728c.

Taylor, M. J., Alabdrabalameer, H. A. and Skoulou, V. (2019). Choosing physical, physicochemical and chemical methods of pre-treating lignocellulosic wastes to repurpose into solid fuels, *Sustainability*, 11(13). 3604. doi: 10.3390/su11133604.

Carbon 2022

# Removal of Malachite Green in Aqueous Solution: Adsorption in a Biomass-Derived Activated Carbon Versus Combined Photocatalytic Degradation Under Sunlight in $TiO_2$/AC Composites

**S. Boumad [1,2], L. Cano-Casanova [1], M.C. Román-Martínez [1], N. Bouchenafa-Saib [2], M.A. Lillo-Ródenas [1].**

[1] Grupo MCMA, Dept. of Inorganic Chemistry and University Institute of Materials (IUMA). Faculty of Sciences. University of Alicante, Alicante, E-03080, Spain.

[2] Blida University 1, Lab. Physical Chemistry of Materials Interfaces Applied to the Environment, Fac. of Technology, B.P. 270 Route de Soumaa 09000 Blida. Algeria.

Email: mlillo@ua.es

**Keywords**

Adsorption, photocatalysis, organic dye

## INTRODUCTION

Heterogeneous photocatalysis using $TiO_2$ is effective for the treatment of wastewater containing recalcitrant contaminants. Reported studies have highlighted that the addition of activated carbon (AC) to $TiO_2$ improves its dispersion and increases the concentration of contaminants on its surface (Che Ramli, 2014), which can favour or enhance the photocatalytic process. Thus, this study compares the removal of an organic contaminant by a $TiO_2$/AC photocatalyst with its adsorption on the AC, both analyzing results at equilibrium and the process kinetics.

## EXPERIMENTAL

An activated carbon (named **AC**) was prepared from *Luffa cylindrica* by impregnation at reflux with an 85 wt.% $H_3PO_4$ solution, at a weight ratio $H_3PO_4$/luffa equal to 3/1 , followed by heat treatment at 500°C in $N_2$ flow of 60 ml/min (Boumad, 2021). Commercial titania **P25** (Degussa) was used as photocatalyst, and also for the preparation, by a simple mechanical mixing method, of the composite named **P25-AC** (containing 70% P25 and 30% AC). The materials were characterized by physical gas adsorption (QuantaChrome Autosorb-6B) and X-ray diffraction (Miniflex II Rigaku (30 kV/15 mA), and were used in the removal of malachite green dye (MG) in solution via: a) adsorption (under dark) or b) photocatalytic degradation under simulated sunlight (ATLAS SUNTEST CPS+ instrument with a xenon arc lamp (NXE 1500B) for 2 hours, noting that the UV-lamp was switched on for the photodegradation tests at t= 0 min, without establishing the adsorption equilibrium. In both cases, 250 ml of 10 mg/L MG solution and 0.125 g of adsorbent or photocatalyst were used. Before irradiation, the suspension was sonicated for 2 min to well disperse the photocatalysts. At specified time intervals, 4 ml of the solution were taken, filtered, and analyzed by UV-vis spectrophotometry (Shimadzu PC1201) to follow the evolution of the MG concentration with time.

To study the mechanism of photocatalytic degradation, tests were carried out using 2 ml solution with 2 mol/L concentration of: i) absolute methanol (99.8%), ii) benzoquinone (99%), or iii) 2-propanol (>99.5%) solutions (from Sigma Aldrich), as inhibitors of superoxide radical anions ($O_2^-$•), hydroxyl radicals (OH•) or positive holes ($h^+$), respectively.

## RESULTS AND DISCUSSION

The study of the textural properties revealed that the specific surface areas of the AC, P25 and P25-AC samples are, respectively, 1139 $m^2/g$, 60 $m^2/g$ and 383 $m^2/g$. P25 contains 73% anatase and 13% rutile and P25-AC sample maintains its crystallinity and phase contributions.

Fig. 1a presents the MG removal from solution by AC adsorption, showing that MG is completely adsorbed in less than 30 minutes on the AC and P25-AC samples, whereas there is practically no MG adsorption for P25. Fig. 1b presents the removal of MG from solution under simulated sunlight, showing that P25 is a good photocatalyst for this reaction, with a fast degradation of MG. Using the composite, the MG removal is much more efficient, but comparison with MG removal by adsorption in AC shows that using the P25-AC composite is hardly an advantage (over the AC). It must be considered that MG removal by P25-AC is the result of the combination of MG photodegradation and adsorption, meaning that the reaction products from MG photodegradation should be identified (to evaluate if total mineralization occurs), whereas MG removal by AC adsorption should imply a subsequent desorption step, both for the regeneration of the adsorbent and/or for MG recovery.

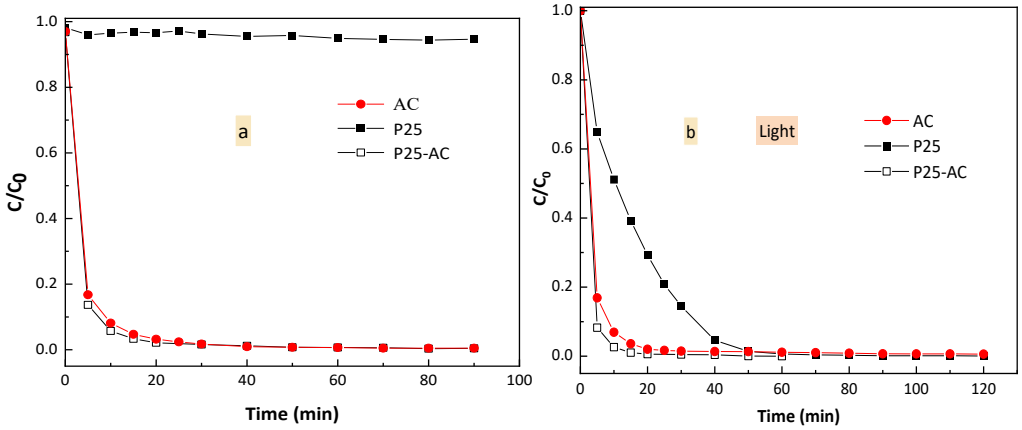


**FIGURE 1**: MG removal: by adsorption (a) and under simulated sunlight (b).

Regarding the photodegradation mechanism, different scavengers for the reactive oxidative species (ROS) have been added to the solution tests, in separated experiments, to analyze which one is the dominant in the photooxidation mechanism. Obviously, the presence in solution of the scavengers significantly decreases the photodegradation efficiency. It can be concluded that, using P25, superoxide anion radicals are the most contributing ROS, followed by a moderate contribution of positive holes, while hydroxyl radicals contribute the least. Using the P25-AC composite, superoxide radicals are also the most determining ROS, although the relative influence of positive holes and hydroxyl radicals is greater than for P25.

## CONCLUSIONS

Under the studied conditions the removal of MG in aqueous solution is more efficient by adsorption (in activated carbon) than by photocatalytic degradation with titania using simulated sunlight. The incorporation of AC to the catalyst implies no clear advantage from the point of view of MG removal efficiency and kinetics**.** The study of the photocatalytic degradation mechanism by scavengers highlights that superoxide radicals are the most influencing ROS in the photodegradation.


### ACKNOWLEDGEMENTS

The authors thank the projects PROMETEO/2018/076 (Generalitat Valenciana/Feder), VIGROB-136 (University of Alicante), and the MESRS (Algeria) for the PNE grant.


### REFERENCES


Boumad, S., Infantes-Molina, A., Barroso-Martín, I., Moretti, E., et al. (2021), Advantages of the Incorporation of Luffa-Based Activated Carbon to Titania for Improving the Removal of Methylene Blue from Aqueous Solution, *Applied Science*, 11(16), 7607. https://doi.org/10.3390/app11167607.

Che Ramli, Z.A., Asim, N., Isahak, W.N.R.W., Emdadi, Z. et. al. (2014), Photocatalytic degradation of methylene blue under UV light irradiation on prepared carbonaceous $TiO_2$, *The Scientific World Journal*, 415136. https://doi.org/10.1155/2014/415136.

20 C 22 arbon 2022

# Pushing the Limits of Tyre-derived Activated Carbon: Novel Ultra-microporous Adsorbents for $CO_2$ Capture

**Alex J Bowles and Geoffrey D Fowler**
Department of Civil and Environmental Engineering, Imperial College London
Email: alex.bowles15@imperial.ac.uk

**Keywords**
Waste tyre, ultramicropore, $CO_2$ capture.

## INTRODUCTION

Waste tyres are problematic: over one billion are produced per year and the majority of them are not recycled (Bowles and Fowler, 2022). Despite these drawbacks, tyres have a high carbon content due to the addition of carbon black (Cb) as a filler in rubber formulations during the tyre manufacturing process. Cb contains unique spheroidal carbon lattice assemblages which are potentially excellent sites for activation due to the high density of aromatic structures in their conducting phase (Doja et al., 2022). The potassium hydroxide (KOH) activation process has been thoroughly researched for producing highly microporous biomass-derived activated carbons (Blankenship and Mokaya, 2022), yet has been neglected for tyre char porosity enhancement, especially in $CO_2$-capture applications. This study has rigorously investigated the effectiveness of KOH activation for producing microporous $CO_2$ adsorbents from tyre char.

## METHODS

Waste car and truck tyre granules (100 g) were pyrolysed at a 20 °C/minute ramp rate to 550 °C under flowing $N_2$ in a batch rotary kiln, which has been previously described elsewhere (Fan et al., 2017). The tyre char produced was then chemically impregnated with KOH at KOH:C mass ratios of 1, 3, 6, and 9. The KOH-impregnated chars were then heated in a Carbolite TF 12/65/550 horizontal tube furnace, fitted with a bespoke quartz reactor system, at 800 °C for 2 h under $N_2$ flow (see Figure 1). The resulting activated carbon was then washed with 5 M HCl for 1 h and then deionised water, and finally dried at 105 °C for 24 h.

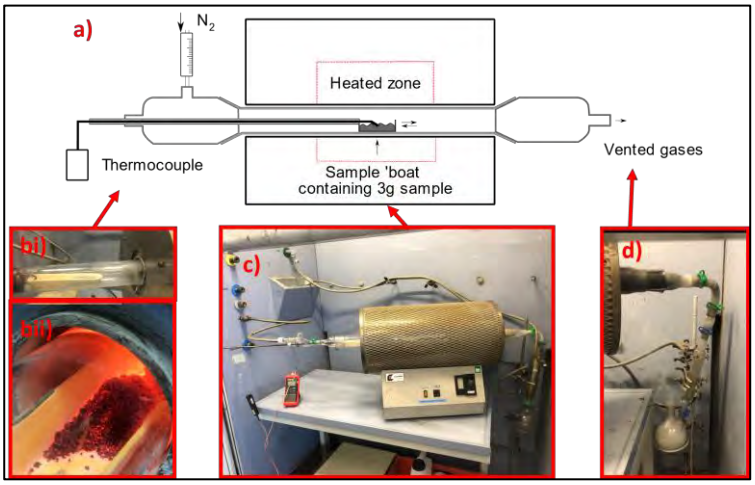


**FIGURE 1**: a) Diagram of the tube furnace. bi) Sample boat pre- and bii) post-activation. c) Photograph of the reactor setup. d) Photograph of the condensation system used.

The carbons were then analysed for ash content (ASTM D36.10), surface area (ASTM D6556-19a), pore size distribution (by applying the NLDFT model to $N_2$ and $CO_2$ isotherms measured at 77 K and 273 K respectively), and $CO_2$ adsorption capacity on an Autosorb iQ 3 (Quantachrome Corp).

## RESULTS AND DISCUSSION

Table 1 shows that increasing the KOH:C mass ratio caused a linear increase in the activated carbons BET surface area (by ~80 $m^2$/g/KOH:C) and pore volume (by 0.08 $cm^3$/g/KOH:C), yet a linear decrease in its yield (by ~7%/KOH:C). Ash content increased, especially at higher KOH:C ratios, as the carbon framework was selectively removed. The average pore width reduced, due to the opening of new micropores and ultramicropores within the non-porous part of the carbon black structure that was present in the blank sample. Despite the large average pore widths (see AvPW of Table 1), Figure 2 shows that ultramicropores contributed to most of the surface area, accounting for approximately 72% of BET surface area in AC-KOHC-1, reducing to 53% in AC-KOHC-9.

**Table 1**: Showing the yield (Y), Ash content, BET surface area (BET-SA), total pore volume (tPV), and average pore width (AvPW) of the activated carbons.

| Sample | KOH:C | Y [%] | Ash [%] | BET-SA [$m^2$/g] | tPV [$cm^3$/g] | AvPW [nm] |
|---|---|---|---|---|---|---|
| Blank | 0 | 86.7 | 2.8 | 80.1 | 0.71 | 3520 |
| AC-KOHC-1 | 1 | 65.6 | 6.5 | 179.9 | 0.90 | 1657 |
| AC-KOHC-3 | 3 | 57.5 | 6.6 | 333.3 | 1.01 | 1196 |
| AC-KOHC-6 | 6 | 35.2 | 10.7 | 651.3 | 1.31 | 988 |
| AC-KOHC-9 | 9 | 18.2 | 23.65 | 812.5 | 1.45 | 662 |

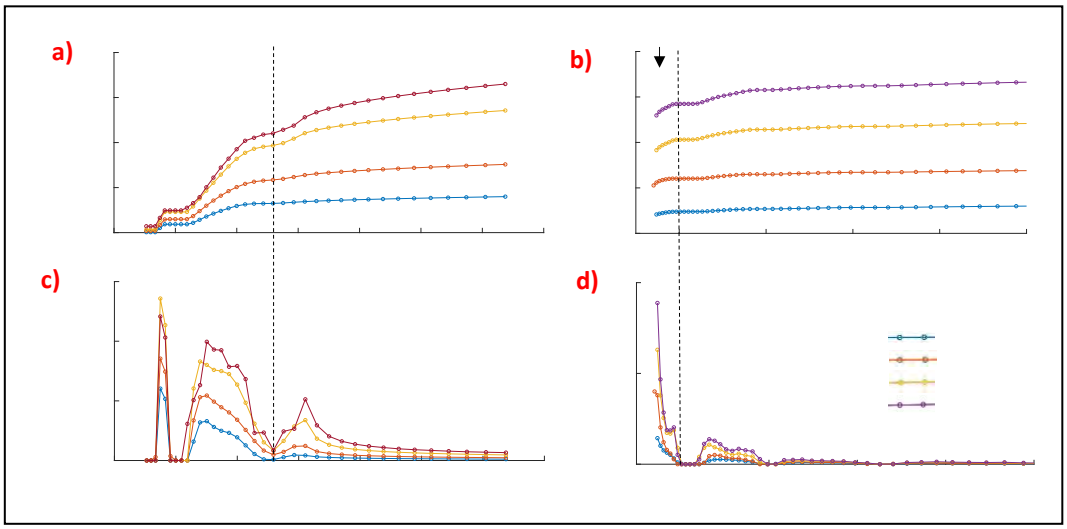


**FIGURE 2**: a-b: Cumulative pore surface areas as a function of pore width attained from a) $CO_2$ and b) $N_2$ isotherms. c-d Change in pore surface area as a function of pore width for c) $CO_2$ and d) $N_2$ isotherms. P-W = pore width.

These high ultramicropore surface areas are unique to KOH activation (Blankenship and Mokaya, 2022), and suggest that $K^+$ intercalates at the interstices of the lamellae (Chen et al., 2020), causing plane distortion as illustrated in Figure 3. The increase in ultramicropore surface area with greater KOH:C ratio (around 51 $m^2$/g/KOH:C) is maintained between KOH:C ratios of 1-6, suggesting that the mass of KOH is the primary a limiting factor in the reaction. Between AC-KOHC-6 and AC-KOHC9, the increase in ultramicropore surface area reduced in magnitude (18 $m^2$/g/KOH:C) (see Figure 2c). This may be due to limited conducting phase availability for the $K^+$ intercalation reaction, as the carbon framework started to become saturated with KOH. Alternatively, ultramicropore destruction may have increased relative to formation, minimising additional ultramicropore surface area.

The surface area of the tyre char feedstock (~76 $m^2/g$) provided sufficient accessibility for the KOH to enter the conducting phase of conjugated aromatic compounds, enhancing the activation process. After contact with the conducting phase, KOH may cause oxidation of carbon to the carbonate ion to form $K_2CO_3$ (Wang et al., 2009). Liquid-solid reactions between $K_2O$ and the carbon would similarly chemically oxidise its surface. Oxidising gasification reactions would then occur from the resulting $CO_2$ and $H_2O$ produced as by-products, further degrading the carbon structure (see Figure 3).

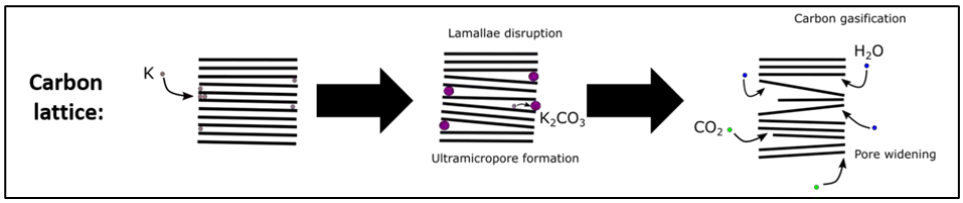


**FIGURE 3**: Illustration of the $K^+$ intercalation process.

The high contribution of ultramicropores to the overall surface area suggests significant potential for these tyre-char derived activated carbons as adsorbents for $CO_2$ capture, because ultramicropores exhibit an adsorptive force onto the quadrupole moment of $CO_2$ (Blankenship and Mokaya, 2022). Ongoing experiments investigating $CO_2$ capture via gas sorption show that these carbons have high $CO_2$ adsorption capacities of over 80 mg $CO_2/g$ at 25 °C and 1 bar pressure. This shows that tyre-derived chemically activated carbons have promising potential for use in high performance applications such as carbon-capture and storage. This finding is important in several sectors because it not only supports zero-pollution initiatives, but also circular economy principles and in the ongoing work to mitigate climate change.

## CONCLUSIONS

- KOH activation is an effective process to increase the surface area, porosity, and $CO_2$ adsorption capacity of tyre char. Ultramicropore surface areas of between 130 and 420$m^2/g$ were produced.
- Further work regarding understanding the KOH-carbon reaction mechanism during activation is required to optimise these adsorbents.
- Waste tyres offer an abundant supply of feedstock that can be recycled into a product which could benefit the mitigation of climate change.

**Acknowledgements**

The authors would like to acknowledge the Engineering and Physical Sciences Research Council (EPSRC, grant number EP/R513052/1) and Pyrenergy Ltd. for funding this work.

**References**

Blankenship, L.S., Mokaya, R., 2022. Modulating the porosity of carbons for improved adsorption of hydrogen, carbon dioxide, and methane: a review. Mater. Adv.

Bowles, A.J., Fowler, G.D., 2022. Assessing the impacts of feedstock and process control on pyrolysis outputs for tyre recycling. Resour. Conserv. Recycl. 182, 106277.

Chen, W., Gong, M., Li, K., Xia, M., Chen, Z., Xiao, H., Fang, Y., Chen, Y., Yang, H., Chen, H., 2020. Insight into KOH activation mechanism during biomass pyrolysis: Chemical reactions between O-containing groups and KOH. Appl. Energy 278, 115730.

Doja, S., Pillari, L.K., Bichler, L., 2022. Processing and activation of tire-derived char: A review. Renew. Sustain. Energy Rev. 155, 111860.

Fan, Y., Fowler, G.D., Norris, C., 2017. Potential of a pyrolytic coconut shell as a sustainable biofiller for styrene–butadiene rubber. Ind. Eng. Chem. Res. 56, 4779–4791.

Wang, H., Gao, Q., Hu, J., 2009. High hydrogen storage capacity of porous carbons prepared by using activated carbon. J. Am. Chem. Soc. 131, 7016–7022.

20 C 22 arbon 2022

# Catalytic activation of carbon fibers, nonwoven, and woven materials with various sulfate salts for the use as gas filter materials

**Stefan Breitenbach[1], Christoph Unterweger[1], and Thomas Stifft[2]**
[1]Wood K plus – Kompetenzzentrum Holz GmbH, Altenberger Strasse 69, 4040 Linz, AT
Email: s.breitenbach@wood-kplus.at
[2]AdFiS products GmbH, Am Kellerholz 14, 17166 Teterow, DE

**Keywords: Gas Filter, Activated Carbon, Sulfate Salts**

## INTRODUCTION

Activated carbon, which can be produced by carbonization and activation of plant, animal, mineral or petrochemical substances, is characterized by its high specific surface area of over 1000 $m^2 g^{-1}$. Due to this high surface area, it can be used as an adsorbent for unwanted substances in gas phase, i.e. as a gas filter. Thus, activated carbon filters are already finding applications in respiratory protection masks, as cabin air filters, or for cleaning exhaust gases from production plants. During the activation of the carbon material, i.e. the formation of the pore structure responsible for the high surface area, temperatures of 700 – 1000 °C are typically used. In this process, coal is usually partially gasified with steam or $CO_2$. With the use of catalytically acting chemicals such as KOH or KCl, the gasification of coal can be accelerated, which significantly improves the activation process and can save a considerable amount of energy. In this study, different sulfate salts will be used to accelerate the activation of bio-based carbon fibers and fabrics to form a pore structure that is well suited for adsorption from gas phase.

## EXPERIMENTAL

Commercially available viscose fibers (1.7 dtex; 36 mm) were impregnated with a 5 wt.% diammonium hydrogen phosphate (DAHP) solution and carbonized at 850 °C under nitrogen atmosphere at 10 °C $min^{-1}$. The carbonized fibers were treated with different salt solutions (Table 1). After drying, 20 g of each sample was activated for 105 min at 870 °C with a $CO_2$ flow rate of 80 L $h^{-1}$. The obtained activated carbon fibers (ACFs) were analyzed by $N_2$ isothermal adsorption (77 K) using the Brunauer–Emmett–Teller (BET) method and non-local density functional theory (NLDFT) to calculate the specific surface area $S_{BET}$ and derive the pore size distribution (PSD), respectively.

## RESULTS AND DISCUSSION

The sample that was not treated with DAHP prior to carbonization shows a low total yield of only 2.4 % with an $S_{BET}$ of 1791 $m^2 g^{-1}$ (Table 1). By using the DAHP solution, the total yield increases to 15.9 %, while the $S_{BET}$ also increases to 2024 $m^2 g^{-1}$. This behavior could already be demonstrated by us in more detail (Breitenbach, 2020). The treatment with 0.1 N ammonium, sodium, magnesium, iron, copper, and zinc sulfate solution before activation results in a partly significantly higher activation yield, while the specific surface area is lower than without the treatment. These chemicals, therefore, do not seem to accelerate the activation process with $CO_2$. With the use of 0.1 N $K_2SO_4$ or KOH solution, the activation yields decrease to 13.9 % and 12.4 %, respectively. At the same time, the $S_{BET}$ increases to 2442 $m^2g^{-1}$ and 2208 $m^2g^{-1}$, respectively. Both potassium-containing solutions catalyze the gasification of coal and thus the formation of porosity (Arnold, 2019). According to previous results, $K_2SO_4$ seems to be more effective than KOH (Hüttinger, 1986). However, an interaction of $K_2SO_4$ with phosphate-containing compounds resulting from impregnation of the fiber prior to carbonization cannot be excluded. This interaction could enhance catalytic activity during activation (Laine, 1991). For a more detailed investigation, the concentration of the $K_2SO_4$ solution was varied. Here, the result is shown

with a 0.05 N $K_2SO_4$ solution, where the activation yield of 35.0 % is lower than with the 0.1 N $K_2SO_4$. However, the $S_{BET}$ is significantly higher at 3419 $m^2 g^{-1}$. Thus, the use of small amounts of $K_2SO_4$ seems to catalyze the activation and favor the formation of the pore structure. The potassium-containing solutions also shift the PSD towards larger radii (Figure 1), whereby pore radii of 0.8 – 4.0 nm are achieved. Interestingly, Zn also has a similar effect.

**TABLE 1**: Overview of activated carbon fibers produced.

| Sample | DAHP / wt.% | Salt solution | Activation yield / % | Total yield / % | $S_{BET}$ / $m^2 g^{-1}$ |
|---|---|---|---|---|---|
| AC-b | 0 | - | 15.0 | 2.4 | 1791 |
| AC-D | 5 | - | 46.9 | 15.9 | 2024 |
| AC-D-NH4 | 5 | 0.1 N $(NH_4)_2SO_4$ | 84.8 | 28.8 | 1007 |
| AC-D-Na | 5 | 0.1 N $Na_2SO_4$ | 54.1 | 18.4 | 1715 |
| AC-D-K | 5 | 0.1 N $K_2SO_4$ | 39.8 | 13.9 | 2442 |
| AC-D-K_0.05 | | 0.05 N $K_2SO_4$ | 35.0 | 11.9 | 3419 |
| AC-D-Mg | 5 | 0.1 N $MgSO_4$ | 55.9 | 19.0 | 1382 |
| AC-D-Fe | 5 | 0.1 N $FeSO_4$ | 50.3 | 17.1 | 1514 |
| AC-D-Cu | 5 | 0.1 N $CuSO_4$ | 38.1 | 12.9 | 1708 |
| AC-D-Zn | 5 | 0.1 N $ZnSO_4$ | 47.8 | 16.3 | 1952 |
| AC-D-KOH | 5 | 0.1 N KOH | 36.6 | 12.4 | 2208 |

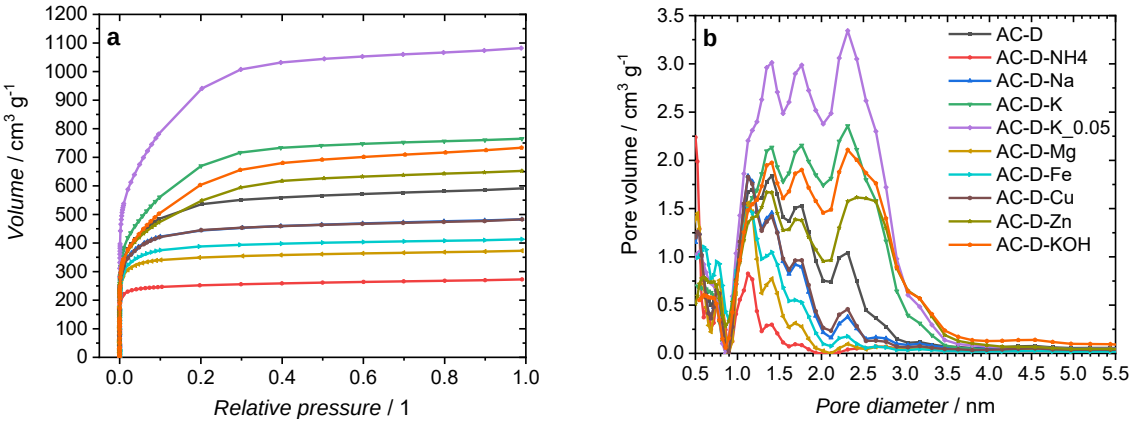


**FIGURE 1**: (a) Nitrogen adsorption isotherms and (b) PSD of the produced ACFs.

## CONCLUSIONS

The use of potassium-containing solutions made it possible to catalyze the activation with $CO_2$ of viscose-based carbon fibers. Despite the short activation time of 105 min, ACFs with a $S_{BET}$ of more than 3400 $m^2g^{-1}$ and pores between 0.8 – 4.0 nm were produced. In combination with SEM, XPS, and pH analyses we conclude that the produced ACFs are well suited for use as gas filter materials.

**Acknowledgment:** The authors gratefully acknowledge the financial support of the Austrian Research Promotion Agency FFG within the COMET program.

### References

Arnold, R. A., Hill, J.M. Catalysts for gasification: a review (2019). *Sustainable Energy & Fuels*, 3, 656-672. https://doi.org/10.1039/C8SE00614H

Breitenbach, S., Lumetzberger, A., Hobisch, M. A., Unterweger, C. , Spirk, S., Stifter, D., Fürst, C. and Hassel, A. W. (2020). Supercapacitor Electrodes from Viscose-Based Activated Carbon Fibers: Significant Yield and Performance Improvement Using Diammonium Hydrogen Phosphate as Impregnating Agent. *C*, 6, [2]. https://doi.org/10.3390/c6020017

Hüttinger, K. J., Minges, R. (1986). The influence of the catalyst precursor anion in catalysis of water vapour gasification of carbon by potassium: 2. Catalytic activity as influenced by activation and deactivation reactions. *Fuel*, 65, [8], 1122-1128. https://doi.org/10.1016/0016-2361(86)90180-8

Laine, J., Calafat, A. (1991). Factors affecting the preparation of activated carbons from coconut shell catalized by potassium. *Carbon*, 29, [7], 949-953. https://doi.org/10.1016/0008-6223(91)90173-G

Carbon 2022

# Comparative behavior of cellulose-based supercapacitor electrodes activated by KOH, $H_2O$, and $CO_2$

**Stefan Breitenbach[1,2,*], Christoph Unterweger[1], Achim Walter Hassel[2], and Christian Fürst[1]**
[1]Wood K plus - Kompetenzzentrum Holz GmbH, 4040 Linz, Austria
[2]Institute of Chemical Technology of Inorganic Materials (TIM), Johannes Kepler University Linz, 4040 Linz, Austria
Email: s.breitenbach@wood-kplus.at

**Keywords**
Activated Carbon, Electrode Materials, Supercapacitor

## INTRODUCTION

Global energy consumption has accelerated alarmingly due to the rapid development of the global economy and the growing world population. To meet the growing energy demand needed to maintain today's standard of living while avoiding resource depletion and pollution, it is necessary to develop efficient, cost-effective, and environmentally friendly energy sources. Research efforts are currently focused on improving the performance of energy storage devices, e.g. supercapacitors. Carbon-based materials have attracted great interest in the application as supercapacitor electrodes due to their frequency, chemical and thermal stability, processability, and the ability to adapt their structural properties. Activated carbon materials in particular are characterized by their large surface area (>1000 $m^2\ g^{-1}$) and their pore volume (>0.5 $cm^3\ g^{-1}$) at relatively low costs.
In the current work, cellulose-based viscose fibers were chosen as precursor material. These are man-made fibers from bio-based resources, thus combining sustainability and availability in good and constant quality, while also offering the full advantage of fibrous materials. Three different activation methods are applied and their effects on the porosity of the activated carbon fibers (ACFs) and their properties on the electrochemical performance of the supercapacitor are investigated. The physical activation after carbonization by means of carbon dioxide and water vapor is considered. In addition, the chemical activation by means of potassium hydroxide, which takes place during the carbonization step, is examined

## EXPERIMENTAL

Cellulose-based viscose fibers were treated with a 37.9 mmol $L^{-1}$ diammonium hydrogen phosphate (DAHP) solution, dried, and carbonized in nitrogen atmosphere in a chamber furnace with a heating ramp of 10 °C $min^{-1}$ up to 850 °C. The activation with $H_2O$ and/or $CO_2$ was done after carbonization in a rotary kiln. The furnace was heated to 870 °C under nitrogen and kept isothermal for 30 min prior to the actual activation. A gas flow of 80 L $h^{-1}$ for 180 min was used for the $CO_2$ activation. For the activation with $H_2O$, 1.0 mL $min^{-1}$ of water was injected with a peristaltic pump for 180 min. Activation using KOH took place during the carbonization step. The DAHP-impregnated and dried viscose fiber was impregnated again with a 50 wt.% KOH solution. The ACF made like this was washed several times with a 10 % HCl solution and with distilled $H_2O$ until a neutral pH was achieved. The ACFs were ground in a mortar mill. After adding 10 wt.% graphite and 10 wt.% PTFE, the ACFs were ground again until a kneadable dough was obtained. This dough was rolled out to a thickness of 90 – 100 µm using a sheet metal roller and electrodes were punched out. The electrodes were dried in vacuo overnight at 110 °C. Two symmetrical electrodes soaked with a 1 M TEMA $BF_4$ solution in PC were used in a 2-electrode test cell. All cells were built under argon atmosphere. A potentiostat was used for cyclic voltammetry (CV), and galvanostatic discharge curves (GDC).

**RESULTS AND DISCUSSION**

The CVs of the supercapacitors are recorded at a scan rate of 10 mV $s^{-1}$ with a potential window of -2.7 – 2.7 V (Figure 1a). The test cell prepared from the $CO_2$- and the $H_2O$-activated fibers have a quasi-rectangular shape, which is typical for EDLCs. The KOH-activated sample shows a parallelogram, indicating a higher internal resistance. A similar trend can be seen in the GDCs measured at 1.0 A $g^{-1}$ (Figure 1b). While the EDLC made from $CO_2$-activated ACFs shows a relatively small internal resistance (IR) drop, the other two samples have a much stronger decline. The calculated equivalent series resistance (ESR) is 584 Ω for the KOH-activated sample, 430 Ω for the $H_2O$-activated sample, and only 254 Ω for the $CO_2$-activated EDLC. The specific capacitance $C_{S,CV}$, derived from the CVs at various scan rates $v$, is shown in Figure 1c. At the smallest scan rate studied (1 mV $s^{-1}$), the highest specific capacitance is achieved. The $H_2O$-activated sample shows the largest specific capacitance at 180 F $g^{-1}$, the electrode made of $CO_2$-activated fibers 171 F $g^{-1}$, and the KOH-activated sample 166 F $g^{-1}$. This trend persists at more rapid scan rates. Even at very fast scan rates of 300 mV $s^{-1}$, the investigated EDLCs still reach values of 45 F $g^{-1}$ ($H_2O$), 34 F $g^{-1}$ ($CO_2$), and 24 F $g^{-1}$ (KOH). Evaluation of specific capacitance by GDC is recommended over that by CV because side reactions can occur, especially at the edges of the potential window, which can enlarge the specific capacitance calculated by CV. The calculated specific capacitance $C_{S,GDC}$ of the samples Figure 1d) behave slightly different than $C_{S,CV}$. Here, the KOH-activated sample shows the maximum specific capacitance of 140 F $g^{-1}$ at the lowest specific current $I_S$ of 0.1 A $g^{-1}$. For the electrodes produced from $CO_2$-activated ACFs, $C_{S,GDC}$ is 121 F $g^{-1}$, and for the $H_2O$-activated fibers 112 F $g^{-1}$. With the increase of $I_S$, a larger voltage drop occurs, probably caused by a high internal resistance of the KOH sample, causing $C_{S,GDC}$ to drop sharply. At currents of 2.0 A $g^{-1}$ and higher, the IR drop was so large that no specific capacitance could be determined. The best performance at discharge currents above 0.6 A $g^{-1}$ is shown by the $CO_2$-activated sample. From the GDCs, the specific energy $E_S$ and the specific power $P_S$ of the complete EDLC (not per electrode) are calculated and are shown in a Ragone plot (Figure 1e). The highest power of 1360 W $kg^{-1}$ is obtained with the $CO_2$ activated electrodes, followed by the $H_2O$ activated (626 W $kg^{-1}$) and the KOH activated electrodes (410 W $kg^{-1}$). Also, the highest specific energy of 25.9 W h $kg^{-1}$ is achieved by the $CO_2$-activated fibers. The other two samples reach specific energies of 20.8 W h $kg^{-1}$ ($H_2O$) and 18.9 W h $kg^{-1}$ (KOH) per device, respectively.

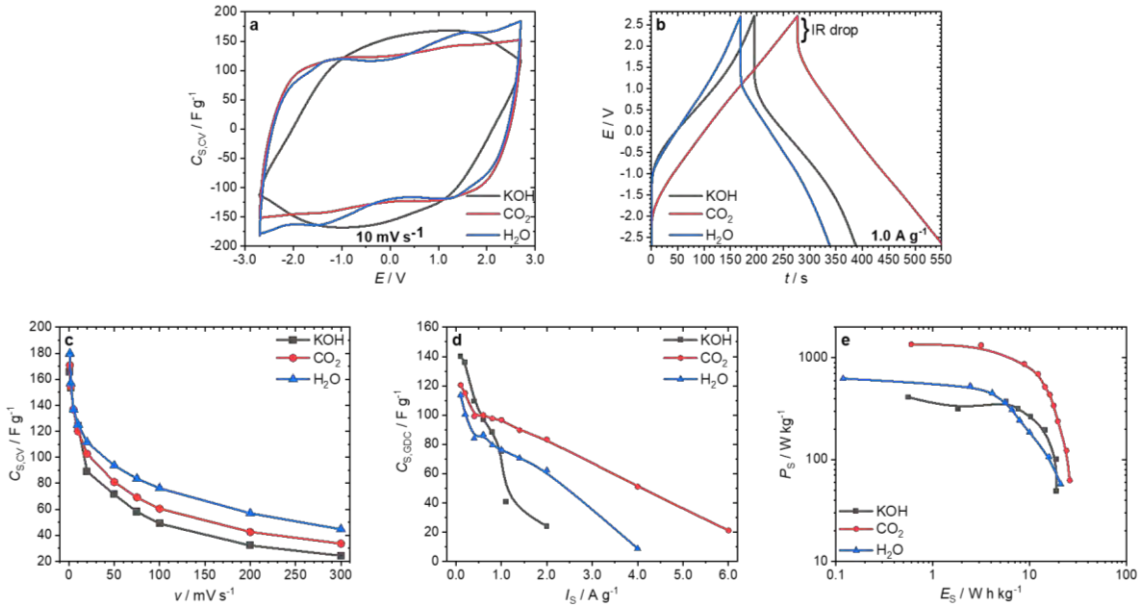


**FIGURE 1**: Electrochemical measurements of the EDLCs: CVs at a scan rate v of 10 mV $s^{-1}$ (a), GDC at a specific current $I_S$ of 1.0 A $g^{-1}$ (b), $C_{S,CV}$ at different scan rates $v$ (c), $C_{S,GDC}$ at different current densities $I_S$ (d), and Ragone plot calculated from GDC per device (e).

## CONCLUSIONS

Three different ways of obtaining activated carbon from DAHP-impregnated viscose fiber and using it as electrode material for supercapacitors were investigated. It was shown that activation by $CO_2$ or $H_2O$ yields ACFs with a high specific surface area and a PSD that is very suitable for use as an electrode material for supercapacitors. Unlike activation with KOH, which requires immense amounts of chemicals and additional washing steps, here the fiber structure was preserved, resulting in cells with remarkably low internal resistance. The $H_2O$ activation also allowed the removal of the majority of heteroatoms without the need for a subsequent washing step as can be shown by EDX analysis. By combining the two activation methods involving $CO_2$ and $H_2O$, ACFs can be produced, which due to their porosity with pores between 0.5 – 5.5 nm and a specific surface area of 2850 $m^2 g^{-1}$, morphology, and purity are ideally suited for use in EDLCs. Thus, supercapacitors could be produced that exceeded a specific capacitance of 178 F $g^{-1}$ per electrode (calculated from GDC) and an energy density of 42 W h $kg^{-1}$ for the device.

**Acknowledgments**

This work was funded by the European Regional Development Fund (EFRE) and the province of Upper Austria through the program IWB 2014-2020 (project BioCarb-K).

Carbon 2022

# Steam Reforming of Model compounds of Pyrolysis Liquids Using P-containing Activated Carbon as Ni Catalyst Support

**Paula Cabrera-Reyes, José Palomo, Behnam Hosseinzaei, Francisco José García-Mateos, Ramiro Ruiz-Rosas, Juana María Rosas, José Rodríguez-Mirasol, Tomás Cordero**
Universidad de Málaga, Andalucía Tech, Departamento de Ingeniería Química, Escuela de Ingenierías Industriales, Campus de Teatinos s/n, 29071 Málaga, España
Email: mirasol@uma.es

**Keywords**
Steam reforming, phosphorus, pyrolysis liquids.

## INTRODUCTION

Fossil fuels still represent the main source for obtaining primary energy and plenty of chemical products, despite all the greenhouse gases emission problems related to these uses. New directives and plans for decarbonization of energy propose the use of green hydrogen, obtained in a sustainable way from renewable sources, as an energetic vector and an industrial raw material. One alternative to produce green hydrogen lies in steam reforming (SR) of the liquids resulting from biomass waste pyrolysis. Nickel based catalysts were regarded as the most active for SR. However, their low stability and sustainability needed to be addressed (Li and Gong, 2014). The latter could be increased by using activated carbons (ACs) as catalytic support, prepared from the same biomass waste used as pyrolysis feedstock. However, they might suffer from gasification, when operating at high temperatures or high steam content. In this sense, chemical activation with $H_3PO_4$ of lignocellulosic waste generated surface phosphorus functionalities with acid character (Rosas *et al.*, 2009). These P groups also governed the carbon reactivity with oxygen, conferring strong oxidation resistance to ACs (Rosas *et al.*, 2012; Valero-Romero *et al.*, 2017). In this work, the effect of P surface groups on the activity and stability of Ni-AC catalysts for steam reforming of model compounds of pyrolysis liquids was studied.

## MATERIALS AND METHODS

Pistachio shell was chosen as the activated carbon precursor since it represents a non-edible and abundant agroforestry waste. A P-containing activated carbon, named PS3P, was obtained by chemical activation with $H_3PO_4$ of the raw material using a 3:1 acid-to-precursor mass ratio and an activation temperature of 500 °C, followed by a washing stage. P surface groups in PS3P were reduced by applying a hydrogen treatment at 600 °C for 4 h, obtaining the corresponding PS3LP sample. Finally, a P-free AC was also prepared by partial gasification of pistachio shell char with $CO_2$ at 800 °C for 2 h (PSG sample). 10 % wt. Ni nominal loading was supported onto the ACs by incipient wetness impregnation method, with $Ni(NO_3)_2{\cdot}6\ H_2O$ and thermal annealing in $N_2$ atmosphere at 700 °C for 2 h.

Resulting catalysts have been evaluated for steam reforming of an equimolar mix of ethanol, acetone and acetic acid, as model compounds of pyrolysis liquids, at 700 °C, using a space time of 50 $mg_{cat}{\cdot}s{\cdot}\mu mol^{-1}$ and a concentration of 0.75 % for each model compound. Steam to Carbon (S/C) molar ratio was set to the stochiometric value.

Bulk and surface chemical composition and oxidation state were determined by XRF and XPS. In addition, the porosity and the crystalline composition of the catalysts were analysed by $N_2$ adsorption-desorption and X-ray diffraction (XRD) analyses, respectively.

## RESULTS AND DISCUSSION

The three obtained catalysts showed a very similar specific surface area with values around 950 $m^2/g$, although PSG sample presented mainly a microporous structure ($V_{micro}$=0.36 $cm^3/g$ and $V_{meso}$=0.07 $cm^3/g$), whereas PS3P and PS3LP were mostly mesoporous catalysts ($V_{micro}$=0.32 and 0.37 $cm^3/g$ and $V_{meso}$=0.82 and 0.88 $cm^3/g$, respectively). Bulk phosphorus content varied from 0.5 down to 0.25 and 0.00 wt.% for PS3P, PS3LP and PSG support, respectively. After nickel loading, the Ni2p XPS region of P-free PSG catalyst showed the highest peak intensity at 852.5 eV, indicative of the presence of metallic nickel content. Differently, the PS3LP and PS3P catalysts showed a lower peak intensity of this band. Both catalysts also showed a small band at 128 eV in P2p XPS spectra, related to the presence of phosphide. The XRD patterns of the catalysts are shown in Figure 1. According to these results, nickel in PSG sample appears as metallic nickel, meanwhile, in PS3P catalysts, nickel phosphides are the main species formed, probably as a consequence of the interaction of surface phosphorus with nickel. PS3LP, which shows a lower P content, presents an intermediate behaviour, showing an incipient contribution of nickel phosphides, being the metallic nickel the most abundant compound.

The results of steam reforming of model compounds at stoichiometric S/C ratio (Figure 2) revealed that PSG catalyst needs a 3-hours induction period during which nickel was *in situ* reduced before starting to produce $H_2$. This period was not necessary when using PS3P, which was probably related to the presence of nickel phosphides as active phase. When a previous reduction was carried on, PSG provided a greater initial $H_2$ yield, followed by PS3LP. However, PSG catalyst, with and without previous reduction, suffered from a strong deactivation with time on stream, whereas PS3P showed a very stable $H_2$ yield at the operation conditions studied. A fast initial deactivation was also observed for PS3LP, from which a stable yield value was observed. This value was similar to that observed for PS3P.

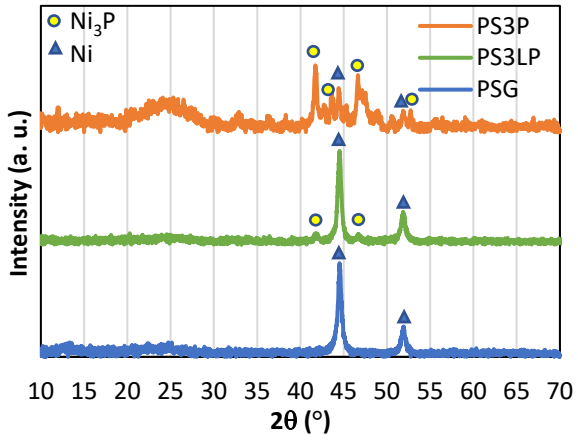


**FIGURE 1**: XRD profiles of Ni-AC catalysts

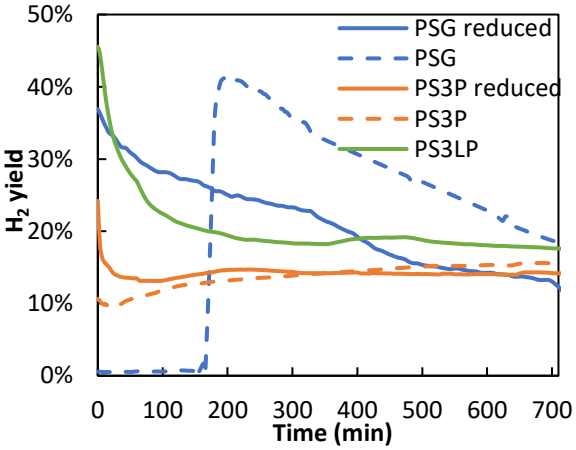


**FIGURE 2**:. $H_2$ yield during reaction at 700 °C

## CONCLUSIONS

The presence of phosphorus in ACs support for nickel catalysts promoted the formation of nickel phosphides. As a result, the reduction of the active phase before steam reforming reaction of pyrolysis liquids became unnecessary. Despite pre-reduced, P-free carbon support initially showed a larger hydrogen yield. However, a more stable activity was observed for P-containing catalysts. These results suggested that nickel phosphides as active phases provided a better long-term stability of the catalysts.

**Acknowledgements**
The authors gratefully thank MICCIN (RTI2018-097555-B-100) and Junta de Andalucía (P18-RT-4592) for financial support.

**References**
Li, S. and Gong, J. (2014) 'Strategies for improving the performance and stability of Ni-based catalysts for reforming reactions', *Chemical Society Reviews*, 43(21), pp. 7245–7256. doi: 10.1039/c4cs00223g.
Rosas, J. M. *et al.* (2009) 'HEMP-derived activated carbon fibers by chemical activation with phosphoric acid', *Fuel*, 88(1), pp. 19–26. doi: 10.1016/j.fuel.2008.08.004.
Rosas, J. M. *et al.* (2012) 'Kinetic study of the oxidation resistance of phosphorus-containing activated carbons', *Carbon*, 50(4), pp. 1523–1537. doi: 10.1016/j.carbon.2011.11.030.
Valero-Romero, M. J. *et al.* (2017) 'Role of surface phosphorus complexes on the oxidation of porous carbons', *Fuel Processing Technology*, 157, pp. 116–126. doi: 10.1016/j.fuproc.2016.11.014.

Carbon 2022

# A carbon xerogel-based cathode for sodium dual-ion batteries

**Ignacio Cameán, Belén Lobato, Natalia Rey-Raap[2], Lucía dos Santos-Gómez[2], Samantha L. Flores-López, Ana Arenillas and Ana B. García**
Instituto de Ciencia y Tecnología del Carbono (INCAR), CSIC, Francisco Pintado Fe 26, 33011, Oviedo, Spain
Email: icamean@incar.csic.es

[2]Departamento de Química Física y Analítica, Universidad de Oviedo-CINN-CSIC, 33006, Oviedo, Spain

**Keywords**
Carbon xerogel, cathode, sodium dual-ion battery

## INTRODUCTION

Carbon xerogels (CXs) are polymeric materials that can be produced with controlled chemistry and porosity. They can be treated at high temperatures to produce graphitic materials while preserving porosity. These characteristics are significant for electrochemical applications. On the other hand, sodium dual-ion batteries (Na-DIBs) operation, which can used carbon materials in both electrodes, is based on the reversible intercalation/insertion of anion and cation from the electrolyte sodium salt in the cathode (graphitic) and in the anode (no graphitic). Herein, the intercalation of $PF_6^-$ anions in a graphitized xerogel doped with graphene oxide (GXGO) was studied by galvanostatic cycling.

## EXPERIMENTAL

GXGO was prepared from a carbon xerogel doped with graphene oxide by heat treatment at 2800 °C in Ar flow (Canal-Rodríguez, 2019). Two-electrode (working, WE, and counter, CE) Swagelok-type cells were used. WE composition was 80 wt.% of GXGO, 10 wt.% of NaCMC binder and 10 wt.% of carbon black. WEs were prepared by tape-casting with a doctor blade of 350 µm. A metallic sodium disc was used as CE. WE and CE were separated by two microfiber glass discs of 12 mm diameter soaked by 165 µL of the electrolyte: solutions of $NaPF_6$ at concentrations of 1.2, 1.5 and 2.0 M in 1:1 mixtures (w:w) of ethylene carbonate (EC) and dimethyl carbonate (DMC), diethyl carbonate (DEC) or ethyl methyl carbonate (EMC) with and without the addition of 20 wt.% of fluoroethylene carbonate (FEC), henceforth denoted as for example 1.2M$NaPF_6$/EC:EMC(FEC). The cells were assembled in a glove box. Because the potential refers to the redox pair $Na/Na^+$, the term voltage is used instead of potential. Galvanostatic cycling of the cells (GXGO/Na) were conducted in a Biologic battery tester in 2.9-5.0 V or 2.9-5.1 V ranges, at 372.0 mA $g^{-1}$ during 2500 charge-discharge cycles.

## RESULTS AND DISCUSSION

Fig. 1 shows the specific capacity (SC) and the coulombic efficiency (Ef) vs. cycle number plots of GXGO cathode (versus metallic sodium) in the 2.9-5.0 V and 2.9-5.1 V ranges, using free-FEC 1.2M$NaPF_6$/EC:EMC and added-FEC (20 wt%) 1.2M$NaPF_6$/EC:EMC(FEC) electrolytes. The presence of FEC improves the performance of GXGO as regards (i) irreversible capacity during the first cycle with a decrease from 70% to 53%, (ii) Ef, and (iii) cycling stability with capacity retention values of 100% after the initial cycles in which electrolyte decomposition on the electrode surface occurs. An increase of the upper cut-off voltage (UCOV) from 5.0 to 5.1 V initially leads to higher capacity. However, despite FEC, also cause larger electrolyte decomposition as indicated by the decrease of the Ef and the continuous capacity fading, which implies GXGO cathode material degradation.

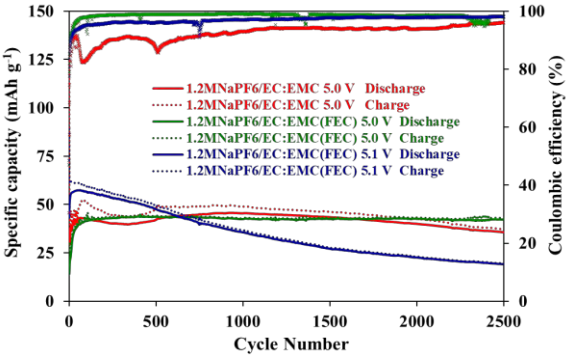


**FIGURE 1:** Effect of FEC and voltage range.

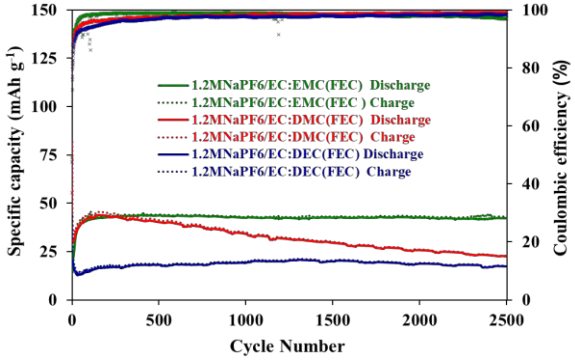


**FIGURE 2:** Effect of electrolyte solvent mixture.

Fig. 2 exhibits the SC and the Ef vs. cycle number plots of GXGO cathode in the three electrolyte solvent mixtures at UCOV of 5 V. The best results were reached in EC:EMC(FEC). To explain this, the differential capacity vs. voltage plots for the intercalation/de-intercalation of $PF_6^-$ anions for cycle 1500 appears in Fig. 3. In EC:EMC(FEC), GXGO cathode presents more and sharper anion intercalation peaks and the onset voltage ($PF_6^-$anions intercalation starts) is lower, which implies that less work is needed for this intercalation, thus accounting for the larger specific capacity achieved.

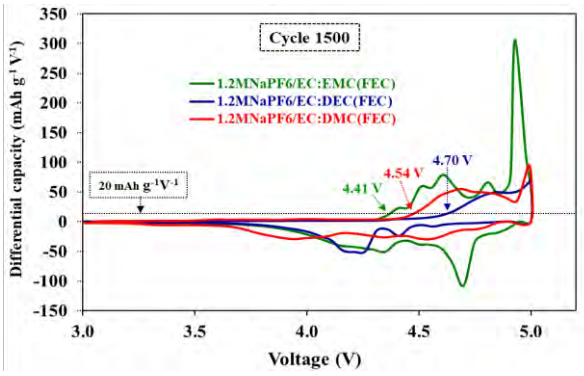


**FIGURE 3:** Differential capacity vs. voltage.

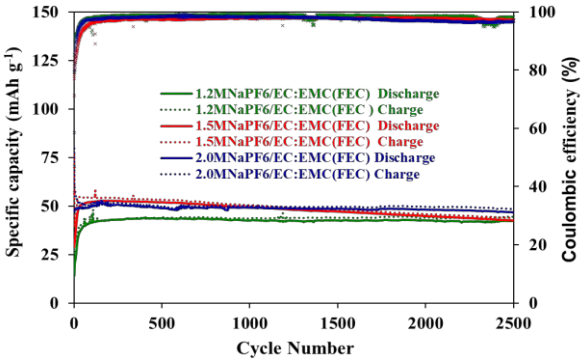


**FIGURE 4:** Effect of electrolyte salt concentration.

The SC of GXGO cathode increases by increasing the electrolyte salt concentration (Fig. 4). Specifically, this increase is particularly remarkable during the first cycles in which the electrode activation occurs, i.e. the electrode activation is accelerated.

## CONCLUSIONS

The best performance of GXGO material as cathode for Na-DIBs was achieved in 2.0M $NaPF_6$/EC:EMC(FEC) electrolyte for the 2.9-5.0 V range.

**Acknowledgements**

Projects: PID2020-113001RB-100 funded by MCIN/AEI and the European Union NextGenerationEU/PRTR; and IDI/2021/50921 from Principado de Asturias. NRR and LdSG acknowledge the Ministerio de Ciencia e Innovación for their Juan de la Cierva grants (IJC2019-040875-I and IJC2020-044746-I).

**References**

Canal-Rodríguez, Ramírez-Montoya, L. A., Villanueva, S. F., Flores-López, S., Menéndez, J. A., Arenillas, A., Montes-Morán, M.A. (2019). Multiphase graphitisation of carbon xerogels and its dependence on pore size. *Carbon*, 152, 704-714.

Carbon 2022

# Customized Carbon Aerogels as positive electrode materials in Li-ion capacitors

**Canal-Rodríguez M.[1], Arnaiz M.[1], Rey-Raap N.[2], Arenillas A.[2], Ajuria J.[1]**
Email: mcanal@cicenergigune.com

[1]Centre for Cooperative Research on Alternative Energies (CIC energiGUNE), Basque Research and Technology Alliance
[2] INCAR-CSIC, Francisco Pintado Fe 26, 33011 Oviedo, Spain

**Keywords**
Carbon aerogels, tailored porosity, Li-ion capacitors

## INTRODUCTION

Carbon Aerogels (CAs) are materials which structural and chemical properties can be easily tailored according with the required application. Between all the possibilities, these carbons have been widely used in different energy storage systems such as fuel cells[1] and mainly in supercapacitors[2] and Li-ion batteries[3], showing competitive results with respect to those obtained with the already available commercial carbons. However, their performance in new emerging energy devises such us Li-ion capacitors (LICs) is still poorly known.

Li-ion capacitors are nowadays raising interest due to its ability to gather Li-ion batteries and supercapacitors advantages in a single device. This is achieved combining a capacitor-like positive electrode with a battery-like negative one.

In the present study, CAs with *ad-hoc* designed porous characteristics have been synthesized by an easy and straightforward methodology to be used as positive electrode in LICs. The way the porosity affects electrode performance has been evaluated. Moreover, a full-LIC was assembled with the best CA employing a commercial hard carbon as anode. The results have been compared with those of an analogous LIC but with a commercial activated carbon as the EDLC like electrode.

## MATERIALS AND METHODS

Both pristine and hybrid organic aerogels were synthesized by a sol-gel process using resorcinol (R) and a solution of formaldehyde (F) as main reagents, water as solvent and a solution of NaOH 0.1 M as catalyst. The hybrid gel was easily obtained by the substitution of 100% of the water used as solvent by a GO suspension. The initial conditions of the precursor solution were a R/F ratio of 0.5, a dilution of 5.7 and a pH of 6.5. The precursor mixtures were then placed in a microwave oven at 85°C for 5h to undergo gelation, ageing and drying.

To obtain the respective activated carbons, the organic precursors were subjected to two one-step carbonization/activation process in a horizontal tubular reactor under a $CO_2$ flow of 50 ml $min^{-1}$ and a heating rate of 50 °C $min^{-1}$ up to 1000° C. The residence times were adjusted to obtain two different surface areas of ca. 1700 and 2300 $m^2$ $g^{-1}$. The nomenclature employed for the materials was: *"$CAS_{BET}$"* in the case of the pristine xerogels and *"$CAGOS_{BET}$"* for the hybrid one.

The textural properties of the carbons were estimated from $N_2$ adsorption-desorption isotherms at 77K (Micromeritics Tristar 3020). The electrochemical measurements were performed in a VMP3

potentiostat from Biologic using both two and three-electrode Swagelok testing cells and 1 M $LiPF_6$ (EC:DMC)(50:50 wt%) as electrolyte.

For the electrochemical characterization of the materials, self-standing electrodes were prepared by a 90 wt% of active material and 10 wt% of PVdF as binder. Electrodes made by 90/5/5 wt% of active material/C65/NMP and Al foil as current collector were employed for the Full-LIC evaluation.

**RESULTS AND DISCUSSION**

The rate capability of the carbon aerogels and YP80F (Figure 1), was firstly analysed in a half Swagelok cell configuration, employing metallic lithium as the counter electrode and self-standing electrodes as the working ones. Clear variations were observed, attributed mainly to the different porous characteristics of the materials under study (Table 1).

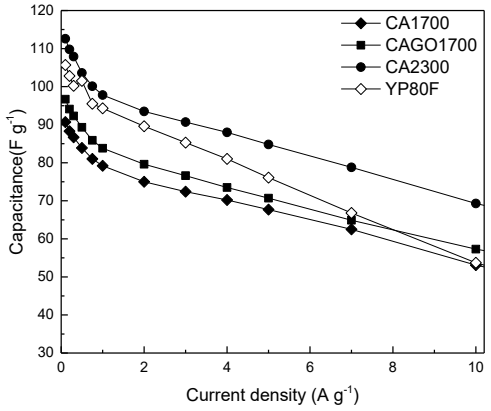


**FIGURE 1**. Specific capacitance of the carbons under a voltage window between 2,0-4,0 V vs $Li^+/Li$.

**TABLE 1**. Porous characteristics of the carbons studied.

| | $V_p$ ($cm^3g^{-1}$) | $V_{meso}$ ($cm^3g^{-1}$) | $D_{meso}$ (nm) | $S_{BET}$ ($m^2g^{-1}$) |
|---|---|---|---|---|
| **CA1700** | 1,1 | 0,5 | 7,0 | 1796 |
| **CAGO1700** | 1,2 | 0,6 | 14,2 | 1652 |
| **CA2300** | 1,7 | 0,9 | 6,6 | 2248 |
| **YP80F** | 1,2 | 0,4 | 2,5 | 2312 |

At the range of low current densities, a relation between microporosity and charge storage was detected as micropores are the pores where the ions are stored[2]. Hence, at 0.1 A $g^{-1}$, those materials with higher $S_{BET}$ (AX2300 and YP80F) registered capacitances of 113 and 105 F $g^{-1}$, while the capacitances of CA1700 and CAGO1700 were 91 and 97 F $g^{-1}$, respectively.

As the current density increased, the capacitance decreased, however, a noticeable difference was observed in the curve slope between YP80F and all CAs, being the former more pronounced due to the narrow diameter of mesopores. Mesopores act as transport pores that enable a suitable movement of ions though the carbonaceous framework until they rich the micropores[2]. Nevertheless, comparing the performances of CA1700 and CAGO1700 it can be concluded that there is a maximum mesopore diameter above which no improvements are attained, as even though the last one, has a $D_{meso}$ double that of CA1700, the capacitance decay of both materials was of ca. 50%. CA2300 was the most stable carbon at all range of current densities applied, due to its high content of micropores and a suitable volume and diameter of mesopores.

Consequently, CA2300 was the one used as positive electrode to assemble a full LIC with a commercial HC as anode and a disc of Li metal as reference. The full device was analysed by a rate capability study under a cell voltage window between 2.2-3.8 V vs $Li^+/Li$. As it is observed in Figure 2, the device registered a really stable performance even at a high current density of 5 A $g^{-1}$, that corresponds to 9 s of discharge time.

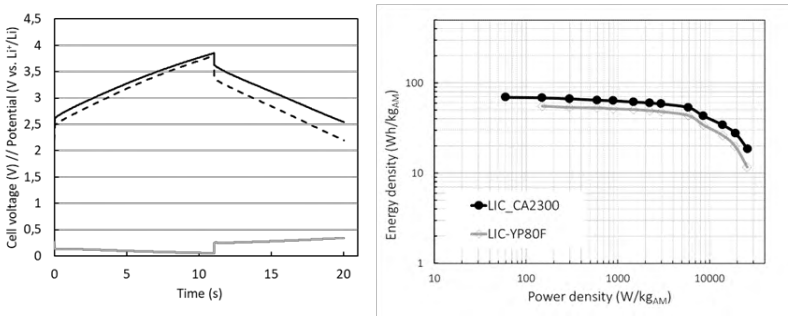


**FIGURE 2.**GA charge/discharge profiles of LIC-CA2300 at 5 A $g^{-1}$ and Ragone plot of both LICs.

At these demanding conditions, the CA potential swings from 2,5 to 4,0 vs $Li^+$/Li, coupling perfectly with the cell voltage swing. That, allows to exploit the maximum capacitance the HC is able to provide, avoiding Li-plating as it swings above 0 V, specifically between 200-50 mV vs $Li^+$/Li.

This suitable performance was also reflected in the Ragone plot (Figure 2), where it is evidenced that the LIC made by CA2300 is able to store high energy densities even when high power densities are required. What is more, the values obtain are competitive to those of the LIC made with the already available commercial carbon YP80F.

## CONCLUSIONS

Carbon aerogels are potential candidates to be used in energy storage devices due to the possibility to tailor their porous characteristics. So far, they have been mainly employed in Li-ion batteries and supercapacitors, however an in-depth study is required for their used in novel energy devices such as Li-ion capacitors. In the present study, it was found that the presence of micropores plays an important role for the positive electrode to reach high capacitances mainly at low current densities. Nevertheless, a suitable diameter of mesopores is the clue to obtain a stable device able to retain these high values at more demanding conditions without penalizing power delivery. By synthesizing CAs with the same volume of micropores but different diameter of mesopores, it could be concluded that it is a maximum diameter of mesopore above which the capacity retention does not improve anymore. The CA with a $S_{BET}$ of 2248 $m^2$ $g^{-1}$ and $V_{meso}$ of 0,9 $cm^3$ $g^{-1}$ with a diameter of 6,6 nm, was the material that delivered the best performance at all range of current densities studied. When this carbon was used in a full LIC as positive electrode versus a HC as anode, the device showed really stable performance with energy and power density values similar to those of a LIC made by commercial carbons.

**Acknowledgements**

This research was possible thanks to the grants PID2020-113001RB-I00 and PCI2020-112039 funded by MCIN/AEI/ 10.13039/501100011033 and by the European Union NextGenerationEU/PRTR. NRR also thanks to MICIN IJC2019-040875-I.

**References**

[1] María Canal-Rodríguez, Natalia Rey-Raap, J. Ángel Menéndez, Miguel A. Montes-Morán, José Luis Figueiredo, Manuel Fernando R. Pereira, Ana Arenillas, (2020), Effect of porous structure on doping and the catalytic performance of carbon xerogels towards the oxygen reduction reaction, Microporous and Mesoporous materials, 293, 09811. https://doi.org/10.1016/j.micromeso.2019.109811.

[2] María Canal-Rodríguez, Ana Arenillas, Natalia Rey-Raap, Gloria Ramos-Fernández, Ignacio Martín-Gullón, J. Angel Menéndez (2017), Graphene-doped carbon xerogel combining high electrical conductivity and surface area for optimized aqueous supercapacitors, Carbon, 118, 291-298. https://doi.org/10.1016/j.carbon.2017.03.059.

[3] María Canal-Rodríguez, Ana Arenillas, J. Angel Menéndez, Daniel Beneroso, Natalia Rey-Raap (2018), Carbon xerogels graphitized by microwave heating as anode materials in lithium-ion batteries, Carbon, 137, 384-394. https://doi.org/10.1016/j.carbon.2018.05.045.

Carbon 2022

# Solar light-induced methylene blue removal by spent coffee grains derived activated carbons and $TiO_2$ composites and their photoregeneration

**Ana P. Carvalho[1], Fernanda Dalto[2], Iwona Kuźniarska-Biernacka[2], Clara Pereira[2], Elsa Mesquita[3], Olívia Salomé G.P. Soares[4], Fernando R. Pereira[4], Maria João Rosa[3], Ana S. Mestre[1], Cristina Freire[2]**

[1] Centro de Química Estrutural, Institute of Molecular Sciences, Departamento de Química e Bioquímica, Faculdade de Ciências, Universidade de Lisboa, 1749-016 Lisboa, Portugal

[2] *REQUIMTE/LAQV, Departamento de Química e Bioquímica, Faculdade de Ciências, Universidade do Porto, Rua do Campo Alegre s/n, 4169-007 Porto, Portugal*

[3] *Water Quality and Treatment Laboratory, Urban Water Unit, Hydraulics and Environment Department, LNEC—National Laboratory for Civil Engineering, Av. Brasil 101, 1700-066 Lisboa, Portugal*

[4] *LSRE-LCM, Departamento de Engenharia Química, Faculdade de Engenharia, Universidade do Porto, Rua Dr. Roberto Frias s/n, 4200-465 Porto, Portugal*

Email: ana.carvalho@fc.ul.pt

**Keywords**
$TiO_2$/AC composites; UV regeneration; water treatment

## INTRODUCTION

Advanced technologies have the potential to ensure safe and sustainable water supply, a major global challenge of the nearest future. Among, these technologies those harnessing solar light emerged as promising processes for mineralization of non-biodegradable pollutants under mild and environmentally benign conditions. $TiO_2$-containing photocatalysts, which combine $TiO_2$ with carbon-based materials, are promising materials for wastewater treatment due to synergistic photodegradation and adsorption phenomena (Mestre & Carvalho 2019). In an even more sustainable perspective, there are some literature studies reporting the self-photo-activity of activated carbon materials.

Moreover, the $TiO_2$/AC composites (and other semiconductor/AC materials) can also promote the regeneration of the system through an oxidative process, instead of the ex-situ and high energy consuming conventional thermal regeneration. The oxidative regeneration by a photocatalytic process is a convenient but scarcely explored approach with potential to enhance both the removal and/or mineralization of the target pollutants and the number of reuse cycles without extra reagents consumption (Salvador et al. 2015).

The purpose of this study was to develop $TiO_2$/AC composites and test fresh and photo-regenerated materials for the removal of methylene blue in aqueous solution prepared in ultrapure water or in wastewater effluent.

## EXPERIMENTAL

$TiO_2$/AC composites were produced by the *in situ* immobilization of $TiO_2$ over activated carbon (AC) obtained by steam activation of spent coffee grains, using two different $TiO_2$/AC proportions. The $TiO_2$/AC composites and the AC material were tested as adsorbents (dark) and as photocatalysts in a combined adsorption+photocatalytic process (solar irradiation) for methylene blue (MB) removal from ultrapure water, and from a secondary effluent (SecEf) of an urban wastewater treatment plant. All the materials were characterized by X-ray diffraction, $N_2$ adsorption isotherms at −196 °C, scanning

electron microscopy, UV-Vis diffuse reflectance, Fourier-transform infrared spectroscopy, temperature programmed desorption, X-ray photoelectron spectroscopy, and thermogravimetric analysis.

## RESULTS AND DISCUSSION

The TiAC60 (60% C) composite presented the lowest band gap (1.84 eV), while, for TiAC29 (29% C), the value was close to that of bare $TiO_2$ (3.18 vs. 3.17 eV).

Regardless of the material, the solar irradiation improved the percentage of MB discolouration when compared to adsorption in dark conditions. In the case of simultaneous adsorption+photocatalytic assays performed in ultrapure water, TiAC29 presented the fastest MB removal. Nevertheless, both TiAC29 and TiAC60 led to excellent MB discolouration percentages (96–98%).

UV-induced photoregeneration was a promising strategy to recover the adsorption and photocatalytic capacity of the materials, especially for TiAC60 and AC which attained colour removals of 96-98% (Figure 1). When the assays were performed in SecEf, all the materials promoted discolouration percentages close to those obtained in ultrapure water. The bulk water parameters revealed that TiAC60 allowed the removal of a higher amount of MB, associated with the overall improvement of the SecEf quality.

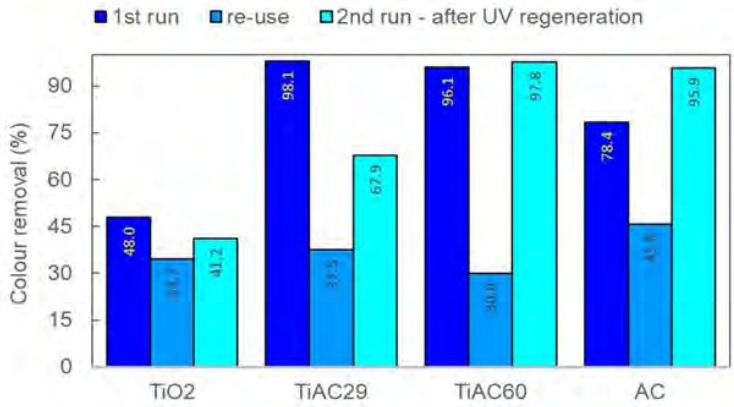


**FIGURE 1.** Comparison of methylene blue removal percentage during combined adsorption + photocatalytic removal of MB, between the original (first run), re-used without regeneration (reuse) and UV regenerated catalysts (second run after UV regeneration for 90 min).

## CONCLUSIONS

The advantage of the combination of the $TiO_2$ with the AC material for the effective removal of MB and of the background organic matter was clearly demonstrated by the improved performance of the $TiO_2$/AC compared to the bare $TiO_2$.


### Acknowledgements

This research was funded by Fundação para a Ciência e a Tecnologia (FCT)/MCTES through: projects UIDB/50006/2020 (LAQV/REQUIMTE), UIDB/00100/2020 and UIDP/00100/2020 (CQE), UIDB/50020/2020 and UIDP/50020/2020 (LSRE-LCM); employment contracts DL 57/2016—Norma transitória REQUIMTE/ EEC2018/14 (I.K.B.), FCT Investigator contract IF/01080/2015 (C.P.), Scientific Employment Stimulus Institutional Call CEECINST/00049/2018 (O.S.G.P.S.), and Scientific Employment Stimulus-Individual Call CEECIND/01371/2017 (Embrace Project, A.S.M.); and national funds.


### References


Mestre, A. S. & Carvalho, A. P. (2019) Photocatalytic degradation of pharmaceuticals carbamazepine, diclofenac, and sulfamethoxazole by semiconductor and carbon materials: A review. Molecules 24, 3702-3742 https://doi.org/10.3390/molecules24203702

Salvador, F.; Martin-Sanchez, N.; Sanchez-Hernandez, R.; Sanchez-Montero & M. J.; Izquierdo, C. (2015) Regeneration of carbonaceous adsorbents. Part II: Chemical, Microbiological and Vacuum Regeneration. Microporous and Mesoporous Materials 202, 277-296 https://doi.org/10.1016/j.micromeso.2014.08.019

Carbon 2022

# Electrochemical characterization of 2D and 3D printed electrodes based on carbon materials towards sensing of halogenated nucleobases

**Ana Casanova[1], Alicia Gomis-Berenguer[1] and Jesus Iniesta[1,2]**
Institute of Electrochemistry, University of Alicante, Alicante, Spain
Email: alicia.gomis@ua.es

[2]Physical Chemistry Department, University of Alicante, Alicante, Spain

**Keywords**
Carbon-based screen printed electrodes, electrochemical sensing, halogenated nucleobases.

## INTRODUCTION

Nucleobases are biological compounds that form nucleosides, which are components of nucleotides, with all of these monomers constituting the basic building blocks of nucleic acids. The nucleobases are fundamental units of the genetic code; adenine (A), guanine (G), cytosine (C) and thymine (T) are found in DNA, while (A), guanine (G), cytosine (C) and uracil (U) are present in RNA. DNA modification plays an important role in several biological processes and diseases, including development, aging, cancer, etc. Similarly, cellular RNA is also decorated with diverse chemical modifications which affect the RNA metabolism. Different type of bases modifications can occur such as, methylation, oxidation, and also nucleic base halogenation (Sanjuán, 2018). For this reason, the interest in the fast and simple detection of the DNA and RNA bases modifications has been growing during the last decades with the aim to achieve a useful tool for an early detection of diseases.

In this regard, electrochemical techniques show great potentialities to meet this need in the fields of "point-of-care" techniques using electrochemical devices capable of detecting the above-mentioned modifications. Furthermore, miniaturization of these electrochemical devices takes on a fundamental role in the evolution of electrochemical techniques which can be achieved thanks to the development of two- and three-dimensional printing technologies.

This work will deal with the use of some additive manufacturing techniques for the fabrication of miniaturized electrochemical sensors and their applications towards the detection of epigenetic modifications in nucleobases. To do that, the electrochemical characterization of two- and three-dimensional printed platforms has been addressed i.e., - graphite and graphene films when using two-dimensional screen-printed electrodes. All carbon-based films have been used for the qualitative determination of various halocytosines, haloguanines and halouraciles.

## EXPERIMENTAL

Solutions of different nucleic bases were prepared in 0.1 M phosphate buffer solution (PBS) of pH 7.0 (close to physiologic pH) in the concentration range between 0.3 and 2.5 mM. All the electrochemical experiments were carried out under atmospheric conditions. Cyclic voltammetry and square wave voltammetry (SWV) have been used for the qualitative detection of the selected bases upon two and three dimensions-based screen-printed electrodes. Glassy carbon electrode was also employed with comparison purposes.

## RESULTS

Figure 1 shows the SWV response of the explored nucleobases on graphite-based screen-printed electrode. The results reveal an oxidation peak for each compound between 0.4 and 1.5 V *vs.* Ag.

Well-differentiated oxidation peaks for the bromided bases (Figure 1 left) with values of +0.6, +1.0 and +1.1 V *vs.* Ag for BrG, BrU and BrC, respectively, were observed. With regard to the current intensity, BrG showed ca. two times current intensity peak compared with BrU and BrC, despite the same concentration is employed. Differences obtained in terms of peak potential and current intensity is mainly associated to the interaction between the compound and the carbonaceous electrode.

On the other hand, the series of halocytosines (Figure 1 right) shows an overlapped oxidation peaks for all the halogenated compounds, with a slight trend for the oxidation potential following FC < ClC < BrC. The observed trend is in agreement with electron-withdrawing effect due to the electronegativity of the halogen atoms. The higher electronegativity makes the compound less hydrophilic, enhancing their interaction on hydrophobic carbonaceous electrodes.

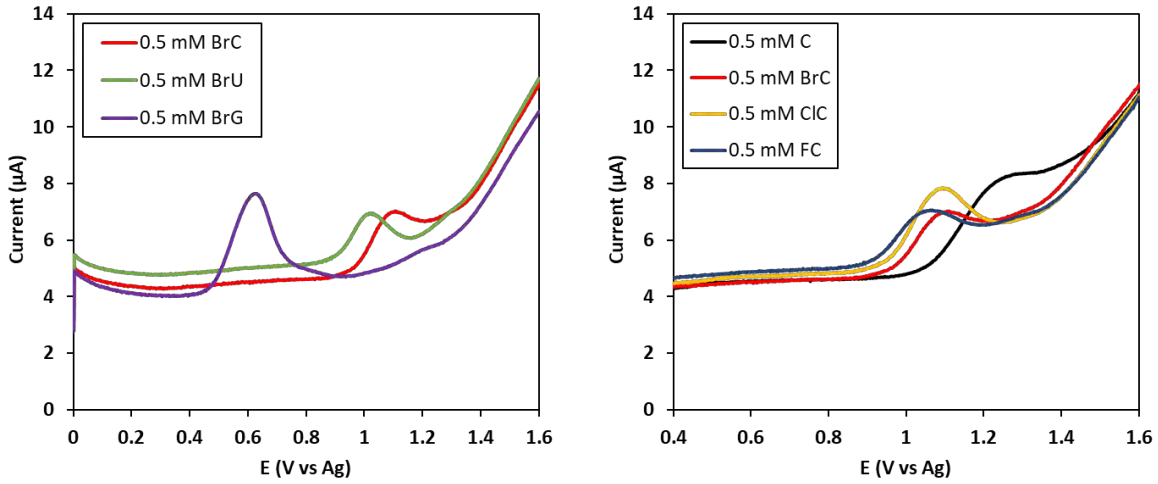


**FIGURE 1**: Square wave voltammetry of 0.5 mM of BrC, BrU and BrG (left), and C, BrC, ClC and FC (right) in 0.1 M PBS pH 7.0 using a graphite screen printed electrode. SWV parameters: modulation amplitude 25 mV; frequency, 8 Hz; modulation step, 2 mV.

## CONCLUSIONS

In this work, we have been studied the electrochemical behaviour of various halogenated nucleobases on carbon-based screen-printed electrodes with the aim to show the qualitative detection of different modifications on the bases. Results reveal the appearance of well-defined peaks associated to the electrooxidation of the compounds at physiologic pH. The different electrochemical response, in terms of position, shape and intensity of the oxidation peaks, could be attributed to changes in the electronic density within the molecule through the effect of the halogen atom, which have a considerable influence on the interaction between the molecule and the carbon-based electrode surface.

**Acknowledgements**

The financial support of the Spanish MINICINN (project PID2019-108136RB-C32) is acknowledged. A.G-B. thanks European Union NextGenerationEU (ZAMBRANO21-10) for the funding.

**References**

Sanjúan, I, Martín-Gómez, A.N., Graham, J., Hernández-Ibáñez, N., Banks, C., Thiemann, T. and Iniesta, J. (2018). The electrochemistry of 5-halocytosines at carbon based electrodes towards epigenetic sensing. *Electrochimica Acta*, 282, 459. https://doi.org/10.1016/j.electacta.2018.06.050.

Carbon 2022

# Molecular Sieving of Linear and Branched $C_6$ Alkanes by Tannin-Derived Mesoporous Carbons

**Jimena Castro-Gutiérrez, Erika De Oliveira Jardim[2], Rafael L. S. Canevesi, Joaquin Silvestre-Albero[2], Martin Kriesten[3], Matthias Thommes[3], Alain Celzard and Vanessa Fierro**
Université de Lorraine, CNRS, Institut Jean Lamour, Epinal, France, 88051
Email: jimena.castro-gutierrez@univ-lorraine.fr

[2] Laboratorio de Materiales Avanzados, Departamento de Química Inorgánica-IUMA, Universidad de Alicante, San Vicente del Raspeig, Spain, 03690
[3] Institute of Separation Science and Technology, Friedrich-Alexander-Universität Erlangen-Nürnberg, Erlangen, Germany, 91058

**Keywords**
Alkane separation, Micro-mesoporous carbons, Molecular sieves

## INTRODUCTION

Higher-quality gasoline is obtained when high-octane number $C_5$ – $C_7$ di-branched alkanes are present in the blend. Therefore, molecular sieves are of great industrial interest as they are able to separate di-branched alkanes from mono-branched and linear ones (Laredo *et al.*, 2013). Herein, two micro-mesoporous carbons: a disordered mesoporous carbon and an ordered mesoporous carbon (DMC and OMC, respectively), are proposed as molecular sieves for the separation of $C_6$ isomers, namely n-hexane (nHEX), 2-methylpenthane (2MP) and 2,2-dimethylbutane (22DMB).

## MATERIALS AND METHODS

Mimosa tannin extract was used as a carbon precursor to synthesize the materials by an easy, low-cost, and green mechanosynthesis method, as detailed by Castro-Gutiérrez *et al.* (2018). The characterization of the materials was carried out using different techniques such as: TEM imaging; physisorption of Ar at 87K, $N_2$ at 77K and $CO_2$ at 273K; immersion calorimetry; and vapor adsorption of the alkanes at 318K. The pore size distributions (PSDs) were obtained by applying the QSDFT model to either Ar or $N_2$ isotherms and the NLDFT model to $CO_2$ isotherms. Using the ideal adsorbed solution theory (IAST), multi-component adsorption isotherms for binary and ternary mixtures of the $C_6$ alkanes were obtained from the single-component isotherms.

## RESULTS AND DISCUSSION

### Textural properties and mesoporous network

The Ar and $N_2$ isotherms of DMC and OMC are a combination of type Ia and type IVa isotherms, which are characteristic of micro-mesoporous materials (Thommes *et al.*, 2015). The PSDs clearly demonstrate that both materials have similar microporous textures due to the use of the same carbon precursor for their synthesis. The differences are essentially in the mesopore range, where the OMC exhibits a narrow PSD centered at ~6 nm while the DMC contains pores over a wider range of mesopores, from 3 to 30 nm.

Information on the pore network connectivity was obtained by a thorough comparison of the PSDs obtained from both adsorption and desorption branches using different probe molecules, here Ar and $N_2$. By identifying the mechanisms of desorption from the mesopores, it is possible to distinguish freely accessible mesopores from constricted mesopores (Cychosz *et al.*, 2017). For the DMC, Figure 1a demonstrates very good agreement between the PSDs obtained from the corresponding Ar and $N_2$

adsorption branches. The PSDs obtained from the desorption branches, Figure 1b, show differences in the lower mesopore range that are due to cavitation-induced evaporation from a small fraction of the mesopores, which can only be accessed through narrow pore necks. For the OMC material, the strong disagreement of the PSDs obtained from the Ar and $N_2$ desorption isotherms (Figure 1d) suggests that evaporation from the entire mesoporosity of the OMC occurs primarily by cavitation. In addition to its mesoporous network, the OMC exhibits mainly ultramicropores; hence, these micropores must be the narrow constrictions connecting the mesopores that lead to cavitation-induced evaporation. As OMC and DMC samples have similar microporosity, the micropores must also be responsible for the fraction of the mesopores that is emptied by cavitation in the DMC.

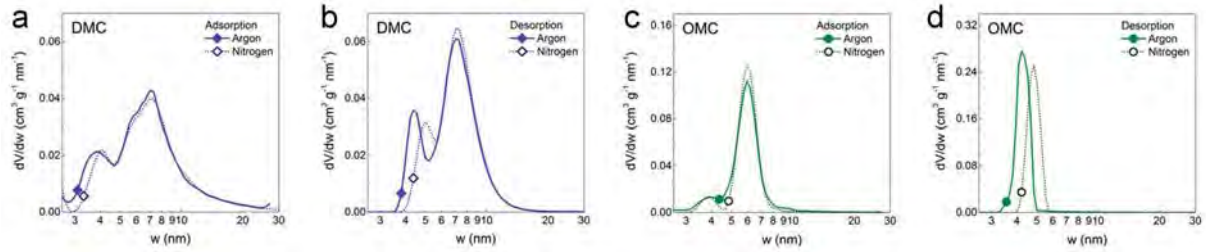


**FIGURE 1**: Pore size distributions (PSDs) in the mesopore range obtained from Ar and $N_2$ isotherms using their (a, c) adsorption branches, and (b, d) desorption branches. [Adapted from (Castro-Gutiérrez *et al.*, 2021)]

To further assess the accessibility of the $C_6$ isomers to the inner pores of OMC and DMC materials, immersion calorimetry measurements were performed using all three iso-alkanes in the liquid phase. The enthalpy of immersion was used to calculate the surface area accessible to each $C_6$ isomer, *S*. Values of *S* decrease as the kinetic diameter of the probe molecule increases ($S_{nHEX} > S_{2MP} > S_{22DMB}$). However, for the OMC, *S* decreases more rapidly than for the DMC. The poor accessibility of 22DMB in the OMC sample indicates that the constrictions connecting its mesoporous network are slightly wider than 0.5 nm, allowing partial access to 2MP and almost excluding 22DMB. On the contrary, the higher values of *S* observed for the three $C_6$ isomers in the DMC corroborate that its porous network is connected by pores of various sizes, improving the accessibility of the surface even to the largest probe molecule.

**Vapor adsorption and selectivity of $C_6$ isomers**

Again, vapor adsorption at 318K of the $C_6$ isomers indicates significant differences between the DMC and OMC samples. In the DMC, nHEX has full access to the entire inner structure, and increasing the size of the molecule reduces the accessible pore volume while maintaining the hysteresis loop practically unchanged. This indicates that accessibility to the mesoporous network is not completely limited, even for the bulkier 22DMB. For the OMC, nHEX can access the inner porous structure, while 2MP has limited access to the micro-mesopore network, and 22DMB is almost completely excluded. The schemes in Figure 2a and 2c illustrate the connectivity of the porous structure of the materials based on the characterization results.

The adsorbed amounts of each component from binary and ternary gas mixtures of nHEX, 2MP, and 22DMB (at 318K) were obtained by using the single-component adsorption isotherms as input data for the IAST. These data were then used to calculate the selectivity of nHEX (in binary mixtures) and nHEX+2MP (in ternary mixtures). For the ternary mixtures, Figure 2b shows the adsorption selectivity of nHEX+2MP over 22DMB when increasing the pressure from 5 to 55 kPa for the DMC. The selectivity decreases with increasing pressure until reaching minimum values, between 2 and 3.7, at 55 kPa. Remarkably, for the OMC, the minimum values of selectivity of nHEX+2MP over 22DMB at the lowest pressure (5 kPa) are already around 40 and increase significantly with pressure, as shown in Figure 2d. For binary mixtures, regardless of the amount of nHEX in the mixture, the values of selectivity are higher at pressures < 20 kPa, where the effect of the larger kinetic diameter is more obvious. For higher pressures, the selectivity decreases considerably and remains almost constant at ~2 and ~4 for

the nHEX+2MP and nHEX+22DMB mixtures, respectively. On the other hand, the OMC exhibits a relatively low selectivity, between 1.5 and 3.8, in nHEX+2MP mixtures. However, for binary mixtures of nHEX+22DMB and ternary mixtures, a higher selectivity towards linear hydrocarbons is achieved. In this case, selectivity increases with pressure and with the % of nHEX in the mixture up to values of the order of ~$10^6$. The high selectivity of the OMC in binary and ternary mixtures, especially those containing 22DMB, is a clear consequence of the narrow size of the constrictions connecting the mesoporous structure, very close to the kinetic diameter of 22DMB, resulting in the exclusion of the di-branched isomer from the material.

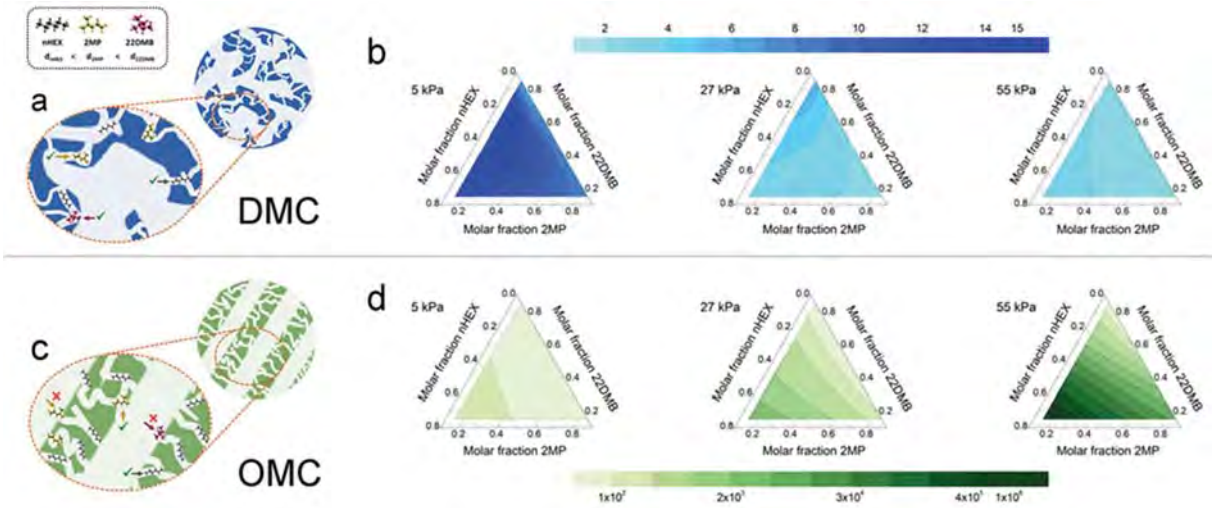


**FIGURE 2**: Schematic representation of the porous structure of (a) DMC and (c) OMC. Selectivity of nHEX+2MP over 22DMB from ternary mixtures at 318K and different pressures for (b) DMC and (d) OMC. [Adapted from (Castro-Gutiérrez *et al.*, 2021)]

## CONCLUSION

The results of this study clearly demonstrate that the unique pore structure of the OMC, where the entire mesoporous network is exclusively accessible through ultramicropores, is ideal for the separation of $C_6$ isomers, with the advantage of being produced by an easy, low-cost, and green synthesis method.


### Acknowledgements

Financial support from: CONACYT-SENER scholarship (601021/438978); French PIA project "Lorraine Université d'Excellence" (ANR-15-IDEX-04-LUE); TALiSMAN project (FEDER 2019-000214); MINECO (PID2019-108453GB-C21); H2020 (MSCA-RISE-2016/NanoMed Project).


### References


Castro-Gutiérrez, J. et al. (2018) 'Synthesis of perfectly ordered mesoporous carbons by water-assisted mechanochemical self-assembly of tannin', Green Chemistry, 20(22), pp. 5123–5132. doi:10.1039/c8gc02295j.

Castro-Gutiérrez, J. et al. (2021) 'Molecular sieving of linear and branched $C_6$ alkanes by tannin-derived carbons', Carbon, 174, pp. 413–422. doi:10.1016/j.carbon.2020.12.061.

Cychosz, K.A. et al. (2017) 'Recent advances in the textural characterization of hierarchically structured nanoporous materials', Chemical Society Reviews, 46(2), pp. 389–414. doi:10.1039/C6CS00391E.

Laredo, G. et al. (2013) 'Separation of Linear and Branched Paraffins by Adsorption Processes for Gasoline Octane Number Improvement', Recent Patents on Chemical Engineering, 5(3), pp. 153–173. doi:10.2174/2211334711205030001.

Thommes, M. et al. (2015) 'Physisorption of gases, with special reference to the evaluation of surface area and pore size distribution (IUPAC Technical Report)', Pure and Applied Chemistry, 87(9–10). doi:10.1515/pac-2014-1117.

Carbon 2022

# Periodic carbon structures for electromagnetic applications

**Alain Celzard[1], Alexander Zharov[1], Pauline Blyweert[1], Vincent Nicolas[1], Dzmitry Bychanok[2], Jan Macutkevic[3], Vanessa Fierro[1], Gleb Gorokhov[2] and Polina Kuzhir[4]**

[1]Institut Jean Lamour, UMR 7198 CNRS and Université de Lorraine, Épinal, France
Email: alain.celzard@univ-lofraine.fr

[2]Institute for Nuclear Problems, Belarusian State University, Minsk, Belarus

[3]Faculty of Physics, Radiophysics Department, Vilnius University, Vilnius, Lithuania

[4]Institute of Photonics, Department of Physics and mathematics, University of Eastern Finland, Joensuu, Finland

**Keywords**
3D-printing; GHz – THz applications; metamaterials; photonic crystals; periodic architectures.

## INTRODUCTION

This work fits into the context of carbon and electromagnetic (EM) waves. To be exact, the frequency domain concerned is that of radio frequencies, and in particular that of the Ka band, between 26.5 and 40 GHz. This domain, corresponding to wavelengths between 0.75 and 1.13 cm, has indeed many advantages: (i) non-ionizing radiation (*i.e.*, not able to alter the DNA); (ii) very small parabolas required (20 cm diameter); (iii) very directional generated beams for a concentration of energy and better exploitation of the spectrum; (iv) many frequencies available vs. other bands. Therefore, it is commonly accepted that the Ka band represents the future of space communications, including the Internet by satellite. Thus, there is an urgent need to develop appropriate materials for handling EM waves in the GHz range, whether as focusing devices (EM lenses for centimetre waves) or as shielding devices. In this very particular context, carbons are a material of choice because they are electrical conductors with Ohmic losses *i.e.*, with a conductivity much lower than that of a perfect metal, resulting in a greater skin depth and absorption, and therefore not only reflection of EM waves. It is also easy to produce porous carbon structures, from where a favoured attenuation and/or possible resonance phenomena depending on the pore size. Finally, multiple geometries are possible for the realisation of a large number of systems, which leads to the concept of metamaterials and carbon photonic crystals, the objects of this work.

## MATERIALS AND METHODS

In electromagnetics, a metamaterial is an artificial composite that has EM properties not found in a natural material. It is most often a periodic structure, dielectric or metallic, which behaves like a homogeneous material that does not exist in its natural state. Whereas a photonic crystal is a special case of a metamaterial that modifies the propagation of EM waves. To realise carbon materials having such special properties, two cases were considered and treated separately: 3D periodic lattices on the one hand, and 2D arrays of hollow spheres on the other.

The EM response of the different materials was measured in a waveguide as signal ratios: reflected/incident ($S_{11}$) and transmitted/incident ($S_{21}$) in the 26-37 GHz range. Fig. 1 shows how the reflectance (R), absorbance (A) and transmittance (T) are then calculated. The results were next compared with models made with the help of CST Studio® 3D electromagnetic simulation software.

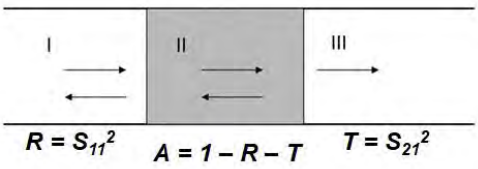


**FIGURE 1:** Measurement of reflectance (R), absorbance (A) and transmittance (T) in waveguide. The incident wave arrives from the left and the material is represented by the grey area.

## RESULTS AND DISCUSSION

### 3D periodic carbon lattices

3D periodic architectures, see Fig. 2, have been prepared in two different ways: (i) by laser stereolithography (SLA) and phenolic resin (Szczurek *et al.*, 2015); or (ii) by fused deposition modeling (FDM) of ABS filled with short carbon fibers (Kuzhir *et al.*, 2021). Methods (i) and (ii) thus produced materials with a bulk electrical conductivity of about 1200 to 2000 S/m and 0.5 to 10 S/m, respectively.

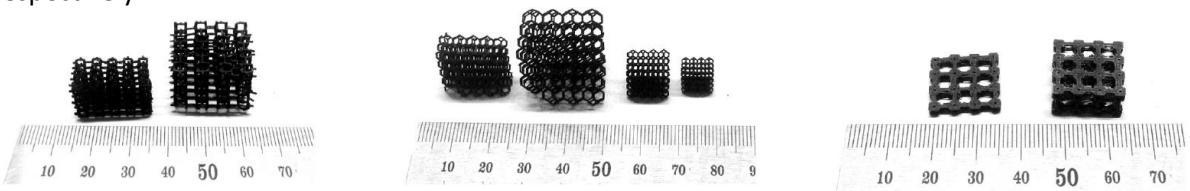

**FIGURE 2:** Periodic 3D carbon architectures produced by SLA (left and centre) or FDM (right), based on Gibson-Ashby (left and right) or Kelvin (centre) cells.

Experiments and modelling demonstrated that these 3D cellular structures give: (i) high (not perfect, but over 85% if their conductivity is 10 - 30 S/m with this geometry) broadband absorption if made with low-conducting carbon (Kuzhir *et al.*, 2021); or (ii) perfectly tunable resonant absorption if made with high-conducting carbon (Bychanok *et al.*, 2016a). The use of either approach, SLA or FDM, to achieve the required EM performance therefore depends on the intended application.
Modelling can help to find the most suitable geometry to achieve broadband or perfect resonance from a given conductivity carbon, which is difficult to scale. In cubic geometry, substantial changes in conductivity (e.g. from 5 to 40 S/m) do not significantly change the EM response, so it is not strictly necessary to control the conductivity of the carbon (Kuzhir *et al.*, 2021).

### Hollow carbon spheres

Two types of hollow spheres were prepared: (i) by impregnation under hydrothermal conditions of polymer beads with sucrose (Celzard *et al.*, 2019), followed by pyrolysis at different temperatures between 700 and 1500°C; and (ii) by 3D printing (by SLA) of a silica-filled photoresin, followed by pyrolysis at 900°C. Methods (i) and (ii) thus produced hollow spheres of the same diameter (0. 8 - 1 mm) but with different conductivities (from $3.5 \times 10^{-6}$ to $15 \times 10^{3}$ S/m), and of different diameters (5, 4, 3, 2, 1 and 0.8 mm) but of the same conductivity (125 S/m), respectively, see Fig. 3.

**FIGURE 3:** Hollow carbon spheres: of the same diameter (0.8 - 1 mm) and different conductivities (from $3.5 \times 10^{-6}$ to $15 \times 10^{3}$ S/m) on the one hand (left), and of different diameters (5, 4, 3, 2, 1 and 0.8 mm) but the same conductivity (125 S/m) on the other hand (right).

Modelling showed the existence of an optimum shell diameter and thickness for a given carbon skeleton conductivity, leading to excellent microwave absorption (almost 100%) (Bychanok *et al.*, 2016b). Conversely, for a given size of hollow sphere, there is an optimal conductivity, neither too low nor too high, to have a good absorption (Bychanok *et al.*, 2021). It is therefore possible to predict the best structure for a given application, in particular for the realization of anti-reflection systems in the microwave domain, as are the eyes of moths in the visible domain, which is a typical example of bioinspired material (Bychanok *et al.*, 2016b).
Producing a 2D array of hollow carbon spheres therefore allows for a very compact and lightweight GHz absorber. Depending on whether this 2D packing is in contact with a conductive plate or separated from it by an air gap, one can have a broadband absorber or a resonant absorber. Finally, the value of the air gap allowing obtaining an asymmetric absorption peak, another possible application of these materials are microwave filters (Bychanok *et al.*, 2017).

## CONCLUSIONS

The data obtained in this work, combined with those from our previous research on the same subject, are necessary for the construction of ordered networks and metasurfaces, for example (but not only) using conductive hollow spheres as building blocks. The next step will be, among others, the development of gradient metamaterials by varying the dimensions of the building blocks and the lattice constant, with an expected partial focusing effect for the transmitted EM waves. Possible applications are tunable electromagnetic lenses and filters, wave absorbers, surface and bulk waveguiding systems, stealth devices, negative refractive index optical systems, etc., for radio/telecommunication technologies.

**Acknowledgements**

This study was partially funded by ERDF [TALiSMAN project (2019-000214)]. It received funding from Campus France and Lithuanian Science Council through the joint program PHC Gilibert #46414VC "Hybrid gels for electromagnetic applications". It was also sponsored by the NATO Science for Peace and Security Program [Grant G5697 CERTAIN "Globular carbon-based structures and metamaterials for enhanced electromagnetic protection"] and by Horizon 2020 EC [grant H2020 RISE 734164 Graphene 3D].

**References**

Bychanok, D., et al. (2016a). Carbon photonic crystals for electromagnetic applications. *Proceedings of the International Conference Carbon 2016 Conference, State College (PA, USA*) 10 – 15 July. ISBN: 978-1-5108-7519-7

Bychanok, D., et al. (2016b). Hollow carbon spheres in microwaves: a bioinspired absorbing coating. *Applied Physics Letters* 108, 013701-1 – 013701-5. https://doi.org/10.1063/1.4938537

Bychanok, D., et al. (2017). Fully carbon metasurface: absorbing coating in microwaves. *Journal of Applied Physics* 121, 165103-1 – 165103-9. https://doi.org/10.1063/1.4982232

Bychanok, D., et al. (2021). Characterization of Individual Hollow Spheres Metaatoms in Microwaves. *Proceedings of the International Conference On Microwaves, Communications, Antennas, Biomedical Engineering & Electronic Systems (IEEE COMCAS 2021), Tel Aviv (Israel), pp. 461-464*. DOI: 10.1109/COMCAS52219.2021.9629019

Celzard, A., et al. (2019). Floating hollow carbon spheres for improved solar evaporation. *Carbon* 146, 232 – 247. https://doi.org/10.1016/j.carbon.2019.01.101

Kuzhir, P., et al. (2021). 3D-printed, carbon-based, lossy photonic crystals: is high electrical conductivity the must? *Carbon* 171, 484 – 492. https://doi.org/10.1016/j.carbon.2020.09.020

Szczurek, A., et al. (2015). Carbon periodic cellular architectures. *Carbon* 88, 70-85. https://doi.org/10.1016/j.carbon.2015.02.069

20 C 22 arbon 2022

# Synthesis of Low Ash Coal-based Carbon Foam

**Vimal Kumar Chandaliya, Chandrachur Banerjee, Pratik Swarup Dash**
R&D, Tata Steel, Jamshedpur-831001, India
Email: vkchandaliya@tatasteel.com

**Keywords**
Carbon foam; Clean coal; Solvent extraction

## INTRODUCTION

Indian high ash coal was converted to value added products such as carbon foam by solvent extraction followed by carbonization. The Indian metallurgical coal having 17% ash content was taken for the solvent extraction. The coal was mixed with N-methyl-2-pyrollidone (NMP) and ethylene diamine (EDA) and heated to about 180 °C for 1 h. The solution was filtered twice to get the two different clean coals. The clean coal thus obtained, was placed inside a tube furnace in alumina boat. The coal is heated to 600 ˚C with a heating rate of 3-5˚C/min under nitrogen flow of 2 LPM to get the green foam. It is kept at that temperature for 1-5 h and then cooled to room temperature. The green foam was carbonized at 1000˚C for 1 h to get the carbon foam. The foam is characterized with TGA, SEM, BET, density, proximate and ultimate analysis. The produced carbon foam had 6.9-8.3 MPa compressive strength and 0.21-0.22 g/cc density. The produced carbon foam can be used in various fields like structural materials, carbon-carbon composites, and insulating material for furnace.

## EXPERIMENTS

Low ash clean coal prepared by solvent extraction of coal A is used as precursor for atmospheric pressure foaming. Two grades of clean coal, one containing 5% ash (SCC-I) and another containing 0.72% ash (SCC-II) is used (Chen, 2006).100 g Coal A of less than or equal to 250-micron particle size (-60 mesh) is taken in a round bottom flask. N-methyl pyrrolidone (NMP) is taken as solvent and ethylene diamine (EDA) is taken as co-solvent for the extraction of clean coal. 1:10 ratio of coal to solvent is taken. Therefore, 1000 ml of solvent is taken for extraction. Solvent to co-solvent ratio is maintained at 17:1. So, 945 ml of NMP & 55 ml of EDA is added to the coal, then the mixture is heated in a rotary vacuum evaporator under normal atmospheric pressure, at 180 ˚C for 1 hour. After extraction is completed, solution is filtered in 500 SS wire mesh. The filtrate obtained, is termed as super clean coal (SCC ). This filtrate is then filtered for the second time to further reduce the ash percentage of the coal. The residue part that is obtained as the cake from the filter mesh is called residue coal. We get two different grades of super clean coal from the two-step filtration. The super clean coal along with solvent is then again sent back to the vacuum evaporator to separate the solvent. This is done under vacuum. Pressure inside the system is maintained at 700 mm Hg by a vacuum pump. Temperature is kept at 120 ˚C. This process is carried out until a dry cake of clean coal is obtained in the flask. Separated solvent is collected in a receiver flask, placed after the condenser. The super clean coal is then removed from the flask and washed with distilled water to remove the residual solvent. Then it is dried at 110 ˚C for 3 hours to get the dry super clean coal of very low ash content. Precursor in the powder form in an alumina boat is placed inside a tube furnace. Then it is heated to 600 ˚C with a heating rate of 3-5˚C/min under nitrogen flow of 2 LPM. It is kept at that temperature for 1-5 hours and then cooled to room temperature. Carbonization is

done at 1000˚C at the rate of 3˚C/min with holding time of 1 hour. Nitrogen flow is maintained at 2 LPM for all the time (Lewis, 1980).

**RESULTS**

As the pore gets larger, NMP diffuses inside the particles and as a result, a better extraction is achieved. NMP dissolves the organic parts and bring them in the extracted phase. So, when the extraction is carried out for a sufficient time, residue coal only contains high amount of ash in it. Yield of SCC-I by this process is around 36% and SCC-II is 12%. Here, SCC-I refers to the coal that is obtained on top of the filter paper of 2$^{nd}$ filtration & SCC-II is the clean coal obtained after solvent separation of 2$^{nd}$ filtrate. It is interesting to note that fixed carbon is decreasing to a smaller extent and volatile matter is increased largely. This means that the short chain components present in the parent coal is getting extracted selectively by the organic solvent (Inagaki, 2015).

**Table 1: Proximate analysis result of Coal A & SCC**

| Coal | Ash | VM | IM | FC |
|---|---|---|---|---|
| **Coal A** | 17.00 | 24.77 | 1.52 | 56.71 |
| **SCC-I** | 5.08 | 38.64 | 3.47 | 52.81 |
| **SCC-II** | 0.72 | 44.71 | 3.63 | 50.94 |

TGA-DTA curves for the SCC is presented in figure 1. This is important to determine the self-foaming temperature. It also indicates the temperature at which the volatiles start evolving rapidly. The temperature at which rate of mass loss i.e., the rate of volatile evolvement drops again, is the temperature about which, self-foaming is required to be done. For the coals, 600 ˚C is chosen as the self-foaming temperature.

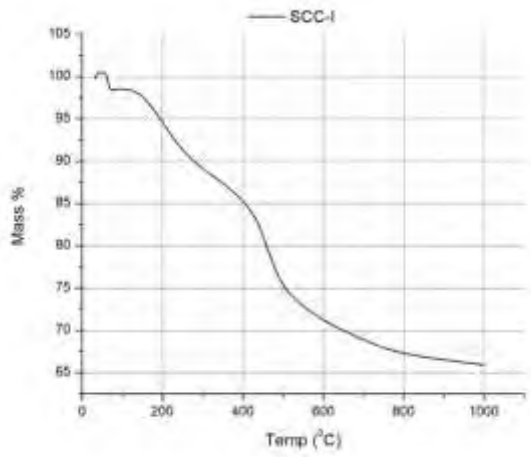


Figure 1: TGA-DTA curve of SCC-I

In case of super clean coal, mass loss is consistent with temperature. This again signifies that short chain hydrocarbons are present in the precursor because of selective extraction of such compounds.

Self-foaming of SCC-I & SCC-II is done following the same foaming & carbonization conditions. SCC-I has ash content of 5.08% and SCC-II has ash content of 0.72%. Though the temperature for foaming

should be different for treated coal tar pitches and clean coals depending on the TG-DTA data, still to compare the foam samples, all are treated with the same conditions. Ash content plays a significant role in self-foaming. Lower the ash content of the precursor, better is the swelling and development of porosity. This is because ash constituents are heavy inert particles which try to settle down and resist the swelling. Foam prepared from SCC-I & SCC-II gave good results.

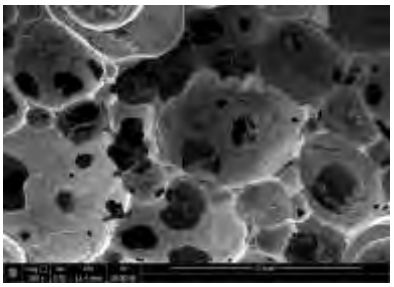

Figure 2: SEM image of SCC-I self-foam

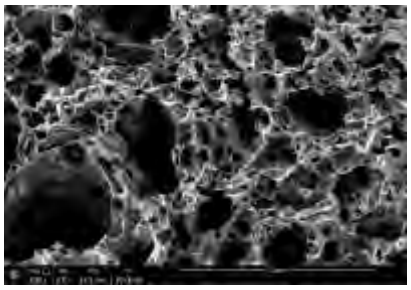

Figure 3: SEM image of SCC-II self-foam

Figure 2 shows that SCC-I self-foam exhibits pores of 350–500-micron diameters i.e., macrpores with window of 15-25-micron diameter. Pore distribution is uniform, and pores are not circular. Structure is interconnected throughout with carbon walls of 40-45-micron thickness. Figure 3 shows that SCC-II self-foam of well interconnected structure. Pore distribution is uniform but there is wide range of pore sizes. Pores of 215-micron diameter are observed and also pores of 50-micron diameter are also seen.

## CONCLUSIONS

Self-foaming process is better as compare to template foaming because of high yield with more compressive strength. Super clean coal obtained using solvent extraction method gave good results in terms of different carbon foam properties. In case of self-foaming, heating rate should be controlled depending on the volatile matter present in the precursor.

**Acknowledgements**

Authors thank Tata Steel management for providing necessary support during the execution of this project.

**References**

Chen, C., Kennel, E., Stiller, A., Stansberry, P., and Zondlo, J (2006). Carbon foam derived from various precursors. Carbon, 44, 1535–1543.

Lewis, I. (1980). Thermal polymerization of hydrocarbons, Carbon, 18, 191-196.

Inagaki, M., Qiu, J., and Guo, Q (2015). Carbon foam: preparation & application, Carbon, 53, 283-287.

Carbon 2022

# $H_2$ production from formic acid using highly stable carbon-supported Pd-based catalysts derived from soft-biomass residues: Effect of heat treatment and functionalisation of the carbon support

**Jessica Chaparro-Garnica[1,*], Miriam Navlani-García[1], David Salinas-Torres[2,3], Emilia Morallón[2], Diego Cazorla-Amorós[1]**

[1] Departamento de Química Inorgánica e Instituto de Materiales, Universidad de Alicante, Ap. 99, 03080, Alicante, España

Email: jessica.chaparro@ua.es

[2] Departamento de Química Física e Instituto de Materiales, Universidad de Alicante, Ap. 99, 03080, Alicante, España

[3] Departamento de Ingeniería Química y Ambiental, Universidad Politécnica de Cartagena, E-30202, Cartagena, España

**Keywords**
Soft-biomass, Pd-based catalyst, formic acid dehydrogenation.

## INTRODUCTION

The concern about environmental problems derived from the use of fossil fuels has brought the search for alternative energy sources to the forefront of research. Among the explored alternatives, the use of hydrogen is very promising yet challenging. One of the main drawbacks that might overshadow the potential of hydrogen in the energy supply is its difficult storage. The production of hydrogen from liquid organic hydrogen carrier (LOHC) molecules stands up as a promising option over the conventional hydrogen storage methods. Formic acid (HCOOH, FA) has received great attention during the last decade (Eppinger, 2017; Wang, 2018). The production of hydrogen from FA proceeds *via* a dehydrogenation reaction ($HCOOH \leftrightarrow H_2 + CO_2$) (Iglesias, 2018). The heterogeneous catalysts used in this reaction are frequently based on Pd nanoparticles supported on materials of diverse compositions, with carbon materials being some of the most common supports (Navlani-García, 2018). Despite the vast literature reporting on Pd-carbon-based catalysts for the dehydrogenation of FA, most of the studies are aimed at optimising the properties of the catalytic active phase, while the potential of tailoring the properties of the carbon support is frequently disregarded. In this study, we explore the potential of FA as a convenient hydrogen carrier. For that, soft-biomass-derived carbon-supported Pd catalysts were synthesised by a $H_3PO_4$-assisted hydrothermal carbonisation method and further heat treatment. To assess the impact of the properties of the support in the catalytic performance towards the dehydrogenation of formic acid, three different strategies were employed: (i) incorporation of nitrogen functional groups; (ii) modification of the surface chemistry by performing a thermal treatment at high temperatures (i.e., 900 ºC); and (iii) combination of both thermal treatment and nitrogen functionalisation.

## MATERIALS AND METHODS

The activated carbon (denoted as BC) was prepared by hydrothermal carbonisation (HTC) assisted by phosphoric acid at low concentrations and using a soft biomass residue as a precursor (Quesada-Plata, 2016). From this activated carbon, N-BC and BC_TT samples were synthesised by modification of the starting activated carbon. N-BC was prepared through N doping of BC using an organic reaction under mild temperature conditions (Chaparro-Garnica, 2020), while BC_TT was obtained by

heat treatment at 900 ºC. Finally, BC_TT was modified with nitrogen following the same strategy. The resulting sample was denoted as N-BC_TT. Pd catalysts were synthesised by impregnation of the precursor salt and without adding any reducing agent (Chaparro-Garnica, 2020). The performance of the catalysts for the dehydrogenation of formic acid in the liquid phase was evaluated using a volumetric system. The catalyst was mixed with an aqueous solution of formic acid and sodium formate with a molar ratio of 9 to 1, and a final concentration of 1 M.

**RESULTS AND DISCUSSION**

Mainly microporous activated carbons were obtained, although the presence of mesopores was also observed. Nitrogen content ranges from 1.3 to 1.7 wt %. Regarding the surface chemistry, the nitrogen groups present in the samples contribute to the basicity of the support, which was confirmed by measuring the pH at the point of zero charge. The Pd content was close to 1 wt % for all the catalysts. Pd present in the fresh catalysts mainly corresponds to $Pd^{2+}$ species, which are reduced in the reaction medium giving rise to the formation of nanoparticles with an average size between 2.6 and 3.7 nm (observed in the used catalysts after 6 reaction cycles). Figure 1 shows the gas evolution profiles for all the catalysts in the first reaction cycle. It can be observed that the catalytic performance depended on the support. Catalysts prepared with heat-treated supports showed a better activity compared to non-heat-treated counterparts. Among the heat-treated catalysts, Pd/BC_TT presented a higher volume of gas generated than that of Pd/N-BC_TT in the first reaction cycle. However, the evolution of the catalytic activity with the cycles showed that Pd/N-BC_TT was the most stable catalyst. This might be indicating the stabilising effect of nitrogen groups on Pd nanoparticles. ICP results confirmed that no leaching of metal nanoparticles occurred during the reaction.

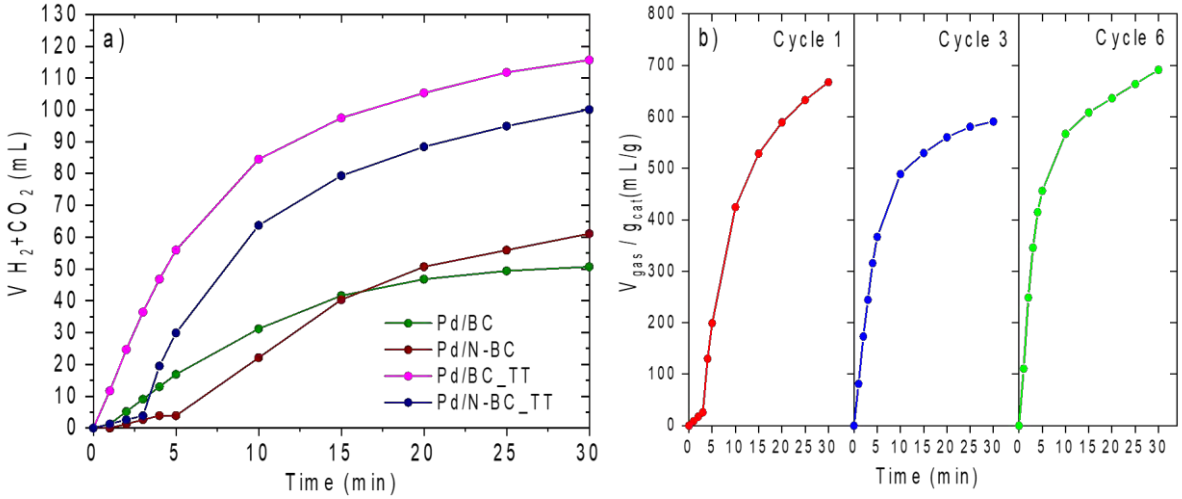


**FIGURE 1**: a) Gas evolution profiles ($H_2$ + $CO_2$) attained in the first reaction cycle for all the catalysts studied in the dehydrogenation of formic acid, b) Gas evolution profiles achieved in cycles 1$^{st}$, 3$^{rd}$, and 6$^{th}$ for Pd/N-BC_TT.

**CONCLUSIONS**

Pd catalysts supported on activated carbon derived from biomass residues showed promising catalytic activity and excellent stability even after several consecutive cycles of reaction. It was observed that a suitable modification of the support by both heat treatment and nitrogen functionalisation resulted in catalysts with a better catalytic performance compared to that of the catalyst with unmodified support. This effect was related to the decrease in the acidity of the support due to the loss of oxygen groups and the incorporation of nitrogen groups.

**Acknowledgements**
Work financed by the MICINN, FEDER (RTI2018-095291-B-I00). JCG thanks for her predoctoral scholarship (GRISOLIA/2018/105) funded by the Generalitat Valenciana. MNG thanks Plan GenT (CDEIGENT/2018/027) for the financial support. MNG thanks Vicerrectorado de Investigación y Transferencia de Conocimiento of the University of Alicante for financial support (GRE20-19-A).

**References**

Chaparro-Garnica, J., Navlani-García, M., Salinas-Torres, D., Morallón, E. and Cazorla-Amorós, D. (2020). Highly Stable N-Doped Carbon-Supported Pd-Based Catalysts Prepared from Biomass Waste for $H_2$ Production from Formic Acid. *ACS Sustain. Chem. Eng.*, 8, 15030-15043. https://doi.org/10.1021/acssuschemeng.0c05906

Eppinger, J. and Huang, K.W. (2017). Formic acid as a hydrogen energy carrier. ACS Energy Lett., 2, 188–195. https://doi.org/10.1021/acsenergylett.6b00574

Iglesias, M. and Oro, L.A. (2018). Mechanistic considerations on homogeneously catalyzed formic acid dehydrogenation. Eur. J. Inorg. Chem., 2125–2138. https://doi.org/10.1002/ejic.201800159

Navlani-García, M., Mori, K., Kuwahara, Y. and Yamashita, H. (2018). Recent strategies targeting efficient hydrogen production from chemical hydrogen storage materials over carbon-supported catalysts. NPG Asia Mater., 10, 277–292. https://doi.org/10.1038/s41427-018-0025-6

Quesada-Plata, F., Ruiz-Rosas, R., Morallón, E. and Cazorla-Amorós, D. (2016). Activated carbons prepared through $H_3PO_4$-assisted hydrothermal carbonisation from biomass wastes: porous texture and electrochemical performance. *Chempluschem*, 81, 1349-1359. https://doi.org/10.1002/cplu.201600412

Wang, X., Meng, Q., Gao, L., Jin, Z., Ge, J., Liu, C. and Xing, W. (2018). Recent progress in hydrogen production from formic acid decomposition. Int. J. Hydrogen Energy, 43, 7055–7071. https://doi.org/10.1016/j.ijhydene.2018.02.146

20 C 22 arbon 2022

# Decomposition of formic acid catalyzed by Pd and PdAg nanoparticles supported on activated carbons derived from biomass residues

**Jessica Chaparro-Garnica[1,*], Miriam Navlani-García[1], David Salinas-Torres[2,3], Ángel Berenguer-Murcia[1], Emilia Morallón[2], Diego Cazorla-Amorós[1]**

[1] Departamento de Química Inorgánica e Instituto de Materiales, Universidad de Alicante, Ap. 99, 03080, Alicante, España

Email: jessica.chaparro@ua.es

[2] Departamento de Química Física e Instituto de Materiales, Universidad de Alicante, Ap. 99, 03080, Alicante, España

[3] Departamento de Ingeniería Química y Ambiental, Universidad Politécnica de Cartagena, E-30202, Cartagena, España

**Keywords**

N-doped activated carbon, bimetallic nanoparticles, formic acid decomposition.

## INTRODUCTION

Hydrogen is one of the most promising alternatives to replace conventional fossil fuel-based energy. However, its use is limited by problems related to its storage and transport. In this sense, the chemical storage of hydrogen offers advantages over physical methods. There are numerous molecules used for the chemical storage of hydrogen and, among them, formic acid (HCOOH) has been postulated as one of the most promising liquid organic hydrogen carriers, due to its properties and its high hydrogen content (43.8 g $H_2$ $kg^{-1}$ and 52 g $H_2$ $L^{-1}$) (Wen, 2019; Chen, 2020). Numerous studies dealing with the development of efficient catalysts able to boost the dehydrogenation of formic acid can be found in recent literature. However, most of them show a lack of long-term stability, so that finding stable catalysts is highly desirable but challenging (Bulushev, 2015; Wu, 2017; Navlani-García, 2019). In the present study, catalysts based on Pd and PdAg nanoparticles supported on activated carbon derived from biomass residues were prepared following a simple synthesis protocol. The effect of the modification of both the metal phase and the support has been evaluated by incorporating Ag in the form of bimetallic nanoparticles and functional nitrogen groups, respectively. The effect of the method followed for the preparation of the catalysts was also checked. The incorporation of Ag in the metal phase and nitrogen functional groups significantly improved the catalytic behaviour compared to the reference materials. The selection of a suitable protocol for the synthesis of PdAg/N-C catalysts gave rise to materials that showed very promising catalytic activities and great stability under the reaction conditions used in the decomposition of formic acid in the liquid phase. In conclusion, the present study highlights the potential of modulating the features of the catalysts, not only in terms of the composition of the metal phase and the incorporation of heteroatoms in the support but also in terms of the synthetic protocol used.

## MATERIALS AND METHODS

Activated carbons were prepared from almond shell residues by hydrothermal carbonisation assisted with phosphoric acid at low concentrations, followed by activation treatment in an inert atmosphere (Chaparro-Garnica, 2020). The activated carbon obtained (AS) was functionalised with nitrogen through an organic reaction (Chaparro-Garnica, 2021), and the resulting material was

named as N-AS. Both AS and N-AS were used as support for the Pd and PdAg nanoparticles, with the total amount of Pd being 1 wt % for all catalysts and with a molar ratio Pd/Ag=0.5 in the case of bimetallic nanoparticles. The catalysts were prepared by impregnation with the precursor salts, using two reduction strategies: (i) addition of sodium borohydride, (ii) *in situ* reduction step under reaction conditions. The catalysts that were reduced prior to the reaction were named X/AS and X/N-AS (X = Pd or Pd/Ag), while the nomenclature of the *in situ* reduced catalysts was X/AS (n.r.) and X/N-AS (n.r.). The catalytic activity towards the decomposition of formic acid, as well as the stability of the prepared catalysts, was monitored by measuring the evolution of the gases generated at 75 ºC.

## RESULTS AND DISCUSSION

Both monometallic and bimetallic catalysts presented a Pd content close to 1 wt %, while the percentage of Ag was around 0.35 wt %. As shown in Figure 1 (a), the incorporation of Ag in the nanoparticles and N functionalities in the support improved the catalytic activity compared to the reference sample (Pd/AS). Likewise, the preparation method also plays a significant role in the final behaviour of the catalysts (Figure 1(b)). This difference in the catalytic activity may be related to the formation of PdAg alloy in the case of the pre-reduced catalysts, while the *in-situ* method could lead to segregated Pd and Ag species and/or particles with non-optimal size or non-adequate electronic properties for the studied reaction. All catalysts showed great stability under reaction conditions, even during 6 consecutive cycles. Among the samples studied, PdAg/N-AS catalyst displayed the best catalytic behaviour, reaching a TOF of 1577 $h^{-1}$.

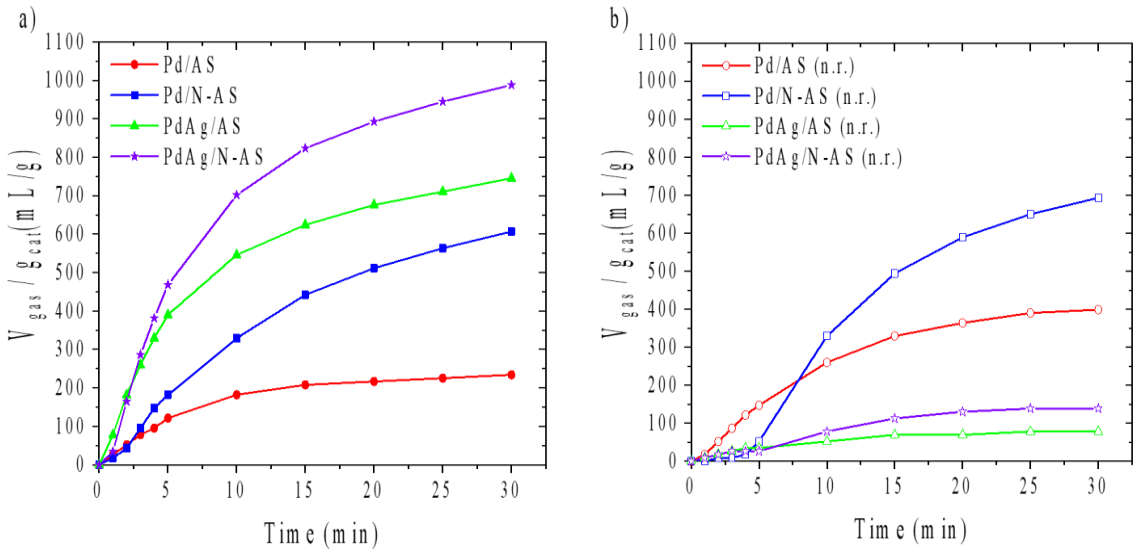


**FIGURE 1**: Gas evolution profiles ($H_2$ + $CO_2$) for the catalysts with: (a) pre-reduced nanoparticles; (b) *in situ* reduced nanoparticles.

## CONCLUSIONS

The selection of a suitable catalyst synthesis protocol directly influenced on the catalytic activity for the decomposition of formic acid. The combination of the nitrogen functional groups together with the incorporation of Ag in the metallic nanoparticles gave rise to the preparation of outstanding catalysts for the studied reaction. Among the catalysts studied, PdAg/N-AS exhibited the best catalytic behaviour, which was attributed to the small size and good distribution of the nanoparticles, as well as to the modification of the electronic properties of Pd by an effective formation of PdAg alloy. In addition, the presence of nitrogen contributed to the basicity of the catalyst, which favours the interaction between the support and formic acid molecules.

**Acknowledgements**
Work financed by the MICINN, FEDER (RTI2018-095291-B-I00). JCG thanks for her predoctoral scholarship (GRISOLIA/2018/105) funded by the Generalitat Valenciana. MNG thanks Plan GenT funded by the Generalitat Valenciana (CDEIGENT/2018/027) for the financial support. MNG thanks Vicerrectorado de Investigación y Transferencia de Conocimiento of the University of Alicante for financial support (GRE20-19-A).

**References**

Bulushev, D.A., Bulusheva, L.G., Beloshapkin, S., O'Connor, T., Okotrub, A.V. and Ryan, K.M. (2015). Pd Clusters Supported on Amorphous, Low-Porosity Carbon Spheres for Hydrogen Production from Formic Acid. ACS Appl. Mater. Interfaces, 7, 8719– 8726. https://doi.org/10.1021/acsami.5b00983

Chaparro-Garnica, J., Navlani-García, M., Salinas-Torres, D., Morallón, E. and Cazorla-Amorós, D. (2020). Highly Stable N-Doped Carbon-Supported Pd-Based Catalysts Prepared from Biomass Waste for $H_2$ Production from Formic Acid. *ACS Sustain. Chem. Eng.*, 8, 15030-15043. https://doi.org/10.1021/acssuschemeng.0c05906

Chaparro-Garnica, J., Salinas-Torres, D., Mostazo-López, M.J., Morallón, E. and Cazorla-Amorós, D. (2021). Biomass waste conversion into low-cost carbon-based materials for supercapacitors: A sustainable approach for the energy scenario. *J. Electroanal. Chem.*, 880, 114899. https://doi.org/10.1016/j.jelechem.2020.114899

Chen, X., Liu, Y. and Wu, J. (2020). Sustainable Production of Formic Acid from Biomass and Carbon Dioxide. Mol. Catal., 483, 110716. https://doi.org/10.1016/j.mcat.2019.110716

Navlani-García, M., Mori, K., Salinas-Torres, D., Kuwahara, Y. and Yamashita, H. (2019). New Approaches Toward the Hydrogen Production from Formic Acid Dehydrogenation Over Pd-Based Heterogeneous Catalysts. Front. Mater., 6, 44. https://doi.org/10.3389/fmats.2019.00044

Wen, M., Mori, K., Futamura, Y., Kuwahara, Y., Navlani-García, M., An, T. and Yamashita, H. (2019). PdAg Nanoparticles within Core-Shell Structured Zeolitic Imidazolate Framework as a Dual Catalyst for Formic Acid-Based Hydrogen Storage/Production. Sci. Rep., 9, 15675. https://doi.org/10.1038/s41598-019-52133-5

Wu, Y., Wen, M., Navlani-García, M., Kuwahara, Y., Mori, K. and Yamashita, H. (2017). Palladium Nanoparticles Supported on Titanium Doped Graphitic Carbon Nitride for Formic Acid Dehydrogenation. Chem. - Asian J., 12, 860– 867. https://doi.org/10.1002/asia.201700041

Carbon 2022

# Engineering of assembly behavior of CNT bundles for high strength carbon nanotube yarns

**Young Shik Cho[1], Seung Jae Yang[2] and Chong Rae Park[1*]**
[1]Department of Materials Science & Engineering and Research Institute of Advanced Materials, Seoul National University, Seoul, 08826, Republic of Korea
Email: choyoungshik@snu.ac.kr / crpark@snu.ac.kr

[2]Department of Chemistry and Chemical Engineering, Education and Research Center for Smart Energy and Materials, Inha University, Incheon, 22212, Republic of Korea

**Keywords**
Carbon nanotube yarn, Bundle model, Direct spinning.

## INTRODUCTION

A carbon nanotube yarn (CNTY) (Li et al. 2004), a one-dimensional assembly of CNTs, is known to have strength equivalent to a few percent of individual CNTs. A fiber implementing the mechanical properties of CNT have not yet been reported due to yarn failure mechanism based on slippage between CNTs (Bai et al. 2018). Accordingly, recent advances in CNTYs have been directed toward strengthening the interaction between CNTs, which determines the performance of CNTY. The tensile strength of CNTY scales with the aspect ratio of constituent CNTs as long as the intertube friction dominantly determines the strength of CNTY. The theoretical calculation has predicted that the achievable strength of CNTY could be comparable to that of CNT if the constituent CNTs are longer than a certain length and perfectly dense along the yarn axis (Yakobson et al. 2000).
Herein, we report a possible route to enhancing the specific tensile strength of CNTY closely to its theoretical maximum strength through the direct spinning method, which is fast, simple, and ecologically friendly. The specific strength of CNTYs with various bundle structures was analyzed according to the theory and the maximum strength possible through the direct spinning technique was predicted to be 5.6 N/tex with our CNTs. Furthermore, we successfully fabricated as-spun CNTY with an average specific strength of 4.5 N/tex, which is 80% of the estimated maximum strength achievable, exceeding that of previously ever-reported as-spun CNTY. The self-assembly behavior control was suggested to be one of the most influential factors determining the specific strength of the resultant as-directly-spun CNTY.

## METHODOLOGY

Double-walled CNTs are synthesized at 1200 °C by a floating catalyst chemical vapor deposition method in a vertical alumina tube reactor. The carbon source, methane of 60 sccm, was flowed into a furnace together with hydrogen at 1200 sccm and argon at 500 sccm. Ferrocene, a catalyst precursor kept at 80 °C and thiophene, a promoter kept at -20 °C were carried by a hydrogen flow into the furnace at corresponding rates of 0.5 mg/min and 3.6 mg/min while keeping the total hydrogen flow rate at 1200 sccm. The DWCNTs were directly spun into CNTYs by passing through a water-bath and two guide rollers, whereby guide-roller A is immersed in water and guide-roller B is located directly above the water-bath, followed by a take-up roller of which the winding speed was varied in the range of 5 m/min to 9 m/min. The sample of CNTYs taken up directly after running through guide-roller A only is denoted as CNTY-AX, while that obtained after running through both guide-rollers A and B is denoted as CNTY-BX, where X states the winding speed.

## RESULTS AND DISCUSSIONS

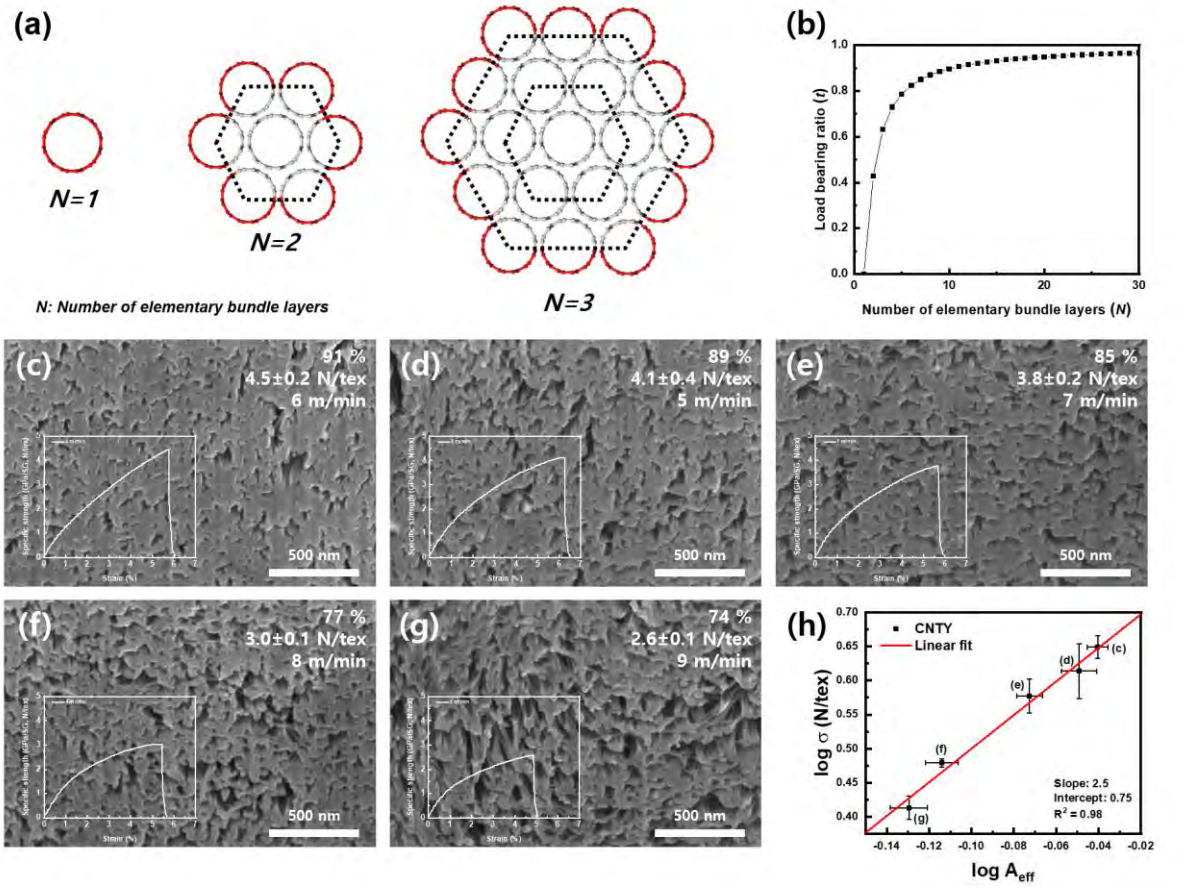


**FIGURE 1**: (a) Schematic of a hexagonally packed CNT elementary bundle and (b) the plot of a load-bearing ratio (*t*) with the number of elementary bundle layers (*N*). (c-g) SEM micrographs of radial cross sections of FIB cuts of CNTY-B series with effective area ratios, specific strengths and winding rates in the upper right of the image. (inset: stress-strain curve of corresponding CNTY) (h) The log-log plot of specific strength ($\sigma$) and effective area ratio ($A_{eff}$) are based on FIB data (c-g).

Before fabrication of CNTY, we tried to develop a theoretical model and equation that enables us to predict the ultimate strength of CNTY within the model system. As we already know that the load-bearing mechanism of CNTY is based on the slippage between the load-bearing elements, the elementary bundles in a secondary bundle, the strength of CNTY would be proportional to the area where the elements are in contact with each other. To estimate the strength of CNTY, we considered a hexagonal array of load-bearing element as shown in Figure 1a (Vilatela et al. 2011). In the model, the gray area excludes the area in the perimeter of the array and contributes to the strength of CNTY. The specific strength will be proportional to the ratio of the aforementioned region to the entire region of the array. This is expressed as the load-bearing ratio (*t*), which can be expressed as the number of elementary bundle layers in the secondary bundle (*N*) (Equation 1, Figure 1b).

$$\mathrm{t} = 1 - \frac{3N - 2}{3N^2 - 3N + 1} \qquad [1]$$

Among as-directly-spun CNTYs, we experimentally achieved specific strength of 4.5±0.2 N/tex through CNTY-B6, an increase of 48% from 3.0±0.1 N/tex of CNTY-A6. The FIB analysis for CNTY-B5~9 was performed to confirm the correlation between bundling behavior and strength (Figures 1c-g). When the spinning rate was 6 m/min, the specific strength ($\sigma$) reached the optimal point. As the rate increased, the specific strength decreased, which matches the bundling behavior. As shown in Figures 1c-g, it becomes impossible to measure the diameter of the secondary bundle as CNT aggregation takes place. Thus, we propose a new parameter, the effective area ratio ($A_{eff}$), which indicates the ratio of the area occupied by CNTs in the entire cross section.

$$\sigma \propto t \propto \left(A_{eff}\right)^{k};\ \ \log\sigma = k\log A_{eff} + C \qquad [2]$$

The relationship between $t$, $\sigma$, and $A_{eff}$ is shown in Equation 2. The specific strength is expressed as an exponential function for $A_{eff}$. Since $k$, the index of $A_{eff}$, is an empirical factor, $A_{eff}$ and $\sigma$ of Figures 1c-g were plotted on a logarithmic scale to confirm the equation (Figure 1h). The graph clearly shows that the equation linearly fits well to experimental data, resulting in a slope of 2.5 and intercept of 0.75. This supports the assumption that the load-bearing element of the CNT yarn proposed previously was correct. The intercept indicates the logarithm of maximum specific strength is achievable through CNT bundling when the intrinsic property of CNT is determined. The maximum specific strength of the CNTY that can be achieved with CNT synthesized under the same conditions was 5.6 N/tex. Our results reached 80% of the theoretically predicted maximum specific strength, which surpassed the carbon fiber T1100 (~3.9 N/tex), known as one of the strongest fibers in recent times through engineering of assembly behavior of CNT elementary bundles.

## CONCLUSIONS

We modified a direct spinning technique to fabricate CNTYs with comparable or even superior properties to commercialized superfibers and engineering metals. Our findings showed that the theoretical maximum strength of the as-directly-spun CNTY is clarified by the suggested model system, followed by the best ever reported specific strength of the as-directly-spun experimental CNTY. These results highlighted the suitability of appropriate self-assembly engineering with a simple modified direct spinning technique for achieving ultra-strong CNTYs.

**Acknowledgements**

This research was supported by the Material/Parts Technology Development Program (20017548) funded by the Ministry of Trade, Industry & Energy (MOTIE, Korea).

**References**

Bai, Y., Zhang, R., Ye, X., Zhu, Z., Xie, H., Shen, B., Cai, D., Liu, B., Zhang, C., Jia, Z., Zhang, S., Li, X. and Wei, F. (2018) 'Carbon nanotube bundles with tensile strength over 80 GPa', *Nat Nanotechnol,* 13(7), 589-595. https://doi.org/10.1038/s41565-018-0141-z

Li, Y.-L., Kinloch, I. A. and Windle, A. H. (2004) 'Direct Spinning of Carbon Nanotube Fibers from Chemical Vapor Deposition Synthesis', *Science,* 304(5668), 276-278. https://doi.org/10.1126/science.1094982

Vilatela, J. J., Elliott, J. A. and Windle, A. H. (2011) 'A Model for the Strength of Yarn-like Carbon Nanotube Fibers', *ACS Nano,* 5(3), 1921-1927. https://doi.org/10.1021/nn102925a

Yakobson, B. I., Samsonidze, G. and Samsonidze, G. G. (2000) 'Atomistic theory of mechanical relaxation in fullerene nanotubes', *Carbon,* 38(11–12), 1675-1680. https://doi.org/10.1016/S0008-6223(00)00093-2

# Calorimetric study of the competitive adsorption the caffeine and diclofenac sodium on biochar from fique residues

Yaned Milena Correa-Navarro[1,2], Juan Carlos Moreno-Piraján[2,*], Liliana Giraldo[3]

[1]Departamento de Química, Facultad de Ciencias Exactas y Naturales, Universidad de Caldas, Calle 65 No. 26 - 10, Manizales 170004, Caldas, Colombia. https://orcid.org/0000-0001-9236-209X

[2]Departamento de Química, Facultad de Ciencias, Grupo de investigación en Sólidos Poroso y Calorimetría, Universidad de los Andes, Carrera 1 No. 18 A-12, Bogotá 111711, Colombia.

[3]Departamento de Química, Facultad de Ciencias, Universidad Nacional de Colombia, Sede Bogotá. Avenida Carrera 30 No. 45-03, Bogotá 11001, Colombia.

*E-mail corresponding author: jumoreno@uniandes.edu.co

**Keywords:** Immersion Calorimetry; Adsorption isotherms; Caffeine**;** Sodic Diclofenac**;** Competitive adsorption.

## 1. Introduction

In Colombia, fique bagasse is an agro-industrial waste derived from the fique fiber extraction process, generates a by-product that is almost 25% - by weight- with respect to the fique leaf. Unfortunately, it is normal for this waste to be left to decompose in the crop or discarded in aquifers, which generates a problem of environmental contamination [1]. Therefore, it is important to look for alternatives for the use of this biomass and to be able to socialize these alternatives with the communities. Nevertheless, the study of each adsorbent, as well as adsorbate-adsorbent interactions have become a new challenge when researching new adsorbents and their application in the retention of certain contaminants. Using calorimetry to analyze this process is very interesting. There is still a lack of information in the scientific literature that clearly establishes the type of interactions between adsorbate-adsorbent from thermodynamics, using a material as novel as fique and correlating it with simple and competitive adsorption isotherms in emerging-type pollutant molecules. That is why this research was approached, with the aim of studying the type of interactions that occur between five biochar materials prepared from fique waste in different probe molecules, using immersion calorimetry. Finally, the competitive adsorption capacity of caffeine and diclofenac sodium in the five-fique bagasse biochar was determined.

## 2. Materials and Methods

### *2.1 Biochar Preparation*

The procedure followed to prepare and modify the different biochars in this research is detailed in a recent publication by Correa et.al., [2].

### *2.2 Immersion Calorimetry Measurements*

In order to acquire information that allows obtaining an adequate understanding of the interactions between the adsorbate-adsorbent, various analytical techniques have been used. However, immersion calorimetry is a little-explored technique that allows characterizing adsorption-adsorbent systems. Of the different types of calorimetry, the one that is adequate to address this type of study is immersion calorimetry. By means of immersion calorimetry it is possible to measure immersion enthalpy ($\Delta H_{imm}$), which is defined as the change in enthalpy, at constant temperature and pressure, that occurs when a solid is immersed in a liquid in which it does not dissolve or react [1].

### *2.3 Competitive adsorption procedure*

To start with, stock solutions of caffeine (CFN) and diclofenac sodium (DCF) were prepared in ultrapure water. Afterwards, different volumes of each compound solution were taken to prepare mixtures of these two substances at different concentrations. Thereafter, 5.0 mL of each mixture were placed in a glass vial and were put in contact with 20.0 mg of each of the biochar evaluated, after that, the vessels were placed in an orbital shaker and shaken for 48 h at 20.0 °C. Finally, a sample of each solution was taken, filtered, and analyzed by High Performance Liquid Chromatography (HPLC) to obtain the amount of caffeine and diclofenac adsorbed at equilibrium $Q_e$ (mg $g^{-1}$) using equation 1.

$$Q_e = \frac{V(Co - Ce)}{m} \quad (1)$$

Where $C_o$ and $C_e$ correspond to the initial and equilibrium concentrations of CFN or DCF, respectively (mg $L^{-1}$); V is the volume of solution (L) and m is the mass of the biochar used in each determination (g).

## *3.* Results and discussion

### *3.1 Calorimetric Experiments*

Figure 1 shows the results obtained for each of the biochars samples based on their adsorption capacity for the DCF and CFN molecules and the hydrophobic factor. These results show that for DCF the adsorption capacity increases as the hydrophobic factor increases, showing that a direct relationship between the hydrophobicity factor was evaluated. Here again a clearly linear correlation can be seen. For the CFN molecule, its adsorption capacity also increases as a function of the hydrophobic factor, but the results are more dispersed. According to Figure 1, the highest adsorption capacities are reached for samples F850-3N and F850-3Na. These results agree with what was previously discussed with those obtained with immersion calorimetry, since it is observed that the adsorption capacity of the biochars prepared in this research is directly related to the surface chemistry and the porosity of the prepared adsorbent.

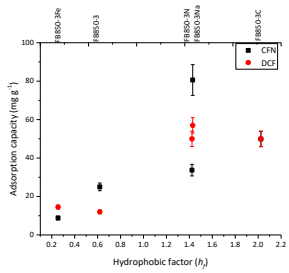


Figure 1. Relationship between the hydrophobic factor and the maximum adsorption capacity of the fique bagasse biochars evaluated.

Figure 2 shows in the form of a histogram, the enthalpies of the interactions ($\Delta H_{int}$) between the different FBB samples and the caffeine molecules, diclofenac, in water; It can be seen that the enthalpies corresponding to the interactions with these molecules were lower than $\Delta H_{int}$ of these same biochars when they were placed in contact with water, except for the sample FB850-3C.

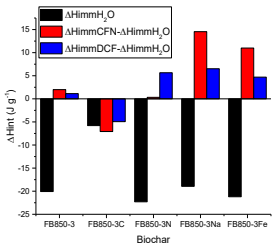


Figure 2**.** Enthalpy of interaction of caffeine and diclofenac at 50 mg $L^{-1}$ and immersion enthalpy of water into fique bagasse biochar evaluated.

Thanks to this it is possible to infer that the values of the immersion enthalpies measured (by immersion calorimetry) are associated with the $H_2O$-adsorbent interactions, they decreased with the presence of CFN and DCF. These results suggest that to overcome the attractive forces of the adsorbent $H_2O$, it was necessary to obtain energy from the environment to displace the water from the surface of the FBB and achieve the desolvation of CFN and DCF. On the other hand, for the FB850-3C sample, negative $\Delta H_{int}$ values were obtained in this study, which supports the idea that the adsorbate-adsorbent interactions were mainly influenced by the hydrophobic character of this biochar, and it is feasible to assume that the interactions happened due to factors such as: (a) decreased competitive adsorption with water because in this case additional hydrogen bonds were formed; (b) greater availability of electrons from the graphene layers in the tested FBB and the aromatic rings of CFN and DCF, which favored the formation of the $\pi$-$\pi$ donor-adsorbate complex [3].

In summary, up to this point it can be stated that using wave molecules of different molecular size, it is possible to obtain the "Calorimetric PSDs" that reasonably coincide with those obtained with the classical models calculated from the isotherms of $N_2$ at 77 K. Additionally, when performing adsorbate-adsorbent studies using this technique can make correlations with parameters such as the hydrophobic factor evaluated from immersion calorimetry in benzene and water.

## 3. Conclusions

For the fique bagasse biochar evaluated, the pore size distribution (PSD) was determined through density functional theory correlated with the PSD obtained by immersion calorimetry in liquids of different molecular dimensions. Furthermore, through the pore size it was evidenced that the microporosity of the FBB allowed the adsorption of CFN and DCF molecules. However, the increase of the molecule size, either by a solvation or by the formation of dimers, limited the access of these analytes to the inner porous structure of the FBB analyzed, particularly in the competitive adsorption.

**Acknowledgements**

The authors thank the Faculty of Sciences of Universidad de los Andes for the partial funding through the project INV-2019-86-1819 and the Universidad de Caldas for their support for doctoral studies. The another hand, the authors thank the framework agreement between Universidad Nacional de Colombia and Universidad de los Andes (Bogotá, Colombia) under which this work was carried out. The Professor doctor Juan Carlos Moreno-Piraján also thanks for an award the Facultad de Ciencias of Universidad de los Andes (Bogotá, Colombia) by the grant number INV-2021-128-2257.

**References**

[1] J. Silvestre-Albero, A. Gómes de Salazar, C. Sepúlveda-Escribano, F. Rodriguez-Reinoso, Characterization of microporous solids by immersion calorimetry, Colloids Surfaces A Physicochem. Eng. Asp. 187–188 (2001) 151–165. doi:10.1016/S0927-7757(01)00620-3.

[2] Y.M. Correa-Navarro, J.C. Moreno-Piraján, L. Giraldo, Processing of fique bagasse waste into modified biochars for adsorption of caffeine and sodium diclofenac, Brazilian J. Chem. Eng. (2021). doi:10.1007/s43153-021-00191-6.

[3] V. Bernal, A. Erto, L. Giraldo, J. Moreno-Piraján, Effect of Solution pH on the Adsorption of Paracetamol on Chemically Modified Activated Carbons, Molecules. 22 (2017) 1032. doi:10.3390/molecules22071032.

Carbon 2022

# Nanocatalysts Supported on Carbon Nanotubes for Bromate Reduction in Natural Drinking Water

**João M. C. B. Costa[1,2], José R. M. Barbosa[1,2], João Restivo[1,2], Carla A. Orge[1,2], Anabela Nogueira[3], Sérgio Castro-Silva[3], Manuel F.R. Pereira[1,2], Olívia S.G.P. Soares[1,2*]**

[1]Laboratory of Separation and Reaction Engineering – Laboratory of Catalysis and Materials (LSRE-LCM), Faculty of Engineering, University of Porto, Rua Dr. Roberto Frias, 4200-465 Porto, Portugal

[2]ALiCE - Associate Laboratory in Chemical Engineering, Faculty of Engineering, University of Porto, Rua Dr. Roberto Frias, 4200-465 Porto, Portugal

[3]Adventech – Advanced Environmental Technologies, Centro Empresarial e Tecnológico, Rua dos Fundões, 151, 3700-121 – São João da Madeira, Portugal

*Email: salome.soares@fe.up.pt

**Keywords**
Catalytic reduction with hydrogen; bromate reduction; nanostructured catalysts.

## INTRODUCTION

Bromate in drinking water is classified as possibly carcinogenic to humans and the World Health Organization (WHO) has established a maximum value of 0.01 mg/L as a guideline value for bromate in drinking water (WHO, 2017). Once formed, bromate removal from drinking water presents several challenges and it is not readily achieved in conventional water treatment plants. Catalytic reduction with hydrogen is one of the most promising alternatives for the reduction of bromate, presenting several advantages, particularly its high removal efficiency and no production of unwanted sludges and secondary streams (Restivo, 2015). It has been demonstrated that various noble metal monometallic catalysts are highly active and efficient in bromate reduction, and their performance is highly dependent on the support used for the metal phase (Soares, 2019, Restivo, 2015). Carbon materials, in particular, carbon nanotubes, have already proved to be good candidates for metal catalysts supports; moreover, the catalytic performance can be enhanced by tuning their surface with functional surface groups (Soares, 2019).

In the present work, we aim to evaluate and improve the efficiency of the catalytic reduction of bromate at environmentally relevant levels (i.e., micrograms per litre) and provide insights on the transition from batch stirred tank reactors to a continuous system. For this end, using palladium-based catalysts, a systematic comparison between supports with different chemical and textural properties for the metal phase was carried out using a stirred tank reactor. The best performing catalysts were then selected for testing in real water matrices in a lab-scale fixed-bed continuous reactor pilot unit, evaluating the capability of the catalysts to achieve contamination levels below those in the relevant legislations or recommended by the authorities when used in practical conditions.

## MATERIALS AND METHODS

Multi-walled carbon nanotubes of 90% purity (MWCNT-O, from Nanocyl, Sambreville, Belgium, NC7000) were used as-received and after modification of their surface chemical and textural properties. A commercial activated carbon support was also used for comparison purposes as an example of a traditional catalyst support (AC). The nanostructured 1 wt.% palladium metallic catalysts were prepared by incipient wetness impregnation using an aqueous solution from the corresponding metal salt ($PdCl_2$), using the modified supports. After impregnation, the catalysts were heat-treated under nitrogen flow and later reduced under hydrogen flow, at 200 $^0$C.

The catalysts were tested in semi-batch and continuous mode. The semi-batch experiments were carried out in a semi-batch tank reactor equipped with a magnetic stirrer for a total reaction time of 3 h, using hydrogen as a reducing agent. Hydrogen flow rate was kept at 50 $cm^3$ $min^{-1}$, and the catalyst suspension was maintained under constant stirring at 400 rpm. A pre-reduction/saturation step was used where the 100 mg of catalyst were added to 790 mL of distilled water and stirred under flowing hydrogen for 15 min. After this period, 10 mL of a concentrated bromate solution was added to the reactor to achieve an initial concentration of 200 ppb.

The continuous reactions were carried out with a 5 mL $min^{-1}$ feed flow rate of water containing a concentration of 200 ppb of bromate in a fixed bed reactor. The system used consisted of two columns; one was used to saturate the bromate solution with hydrogen, where a flow rate of 50 $cm^3$ $min^{-1}$ was maintained throughout the reaction. The bromate solution was subsequently circulated with a peristaltic pump to the other column, in which 200 mg of the selected catalyst was located. Later, experiments were carried out varying operation conditions, towards the optimization of the continuous catalytic system, where the removal of bromate in a real water collected in a water treatment plant (WTP) using the most promising conditions was assessed. The bromate reduction progress was followed using a Shimadzu Bromate Analysis liquid chromatography system.

**DISCUSSION**

Figure 1 presents the performance of the 1 wt.% Pd catalysts during bromate reduction under hydrogen, supported on as-received and modified nanostructured carbon supports.

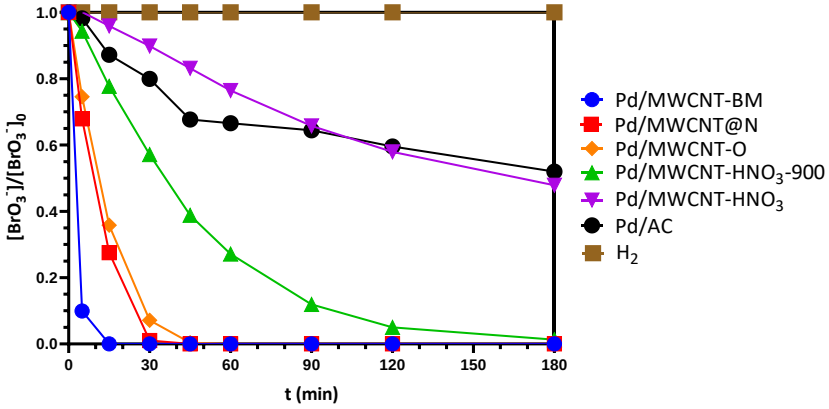


**FIGURE 1:** Dimensionless bromate concentration during semi-batch hydrogen reduction over 1 wt.% Pd catalysts on different carbon supports. ($H_2$ = 50 $cm^3$ $min^{-1}$, $C_0$ ($BrO_3^-$) = 200 ppb, 0.125 $g_{CAT}$ $L^{-1}$).

It is clear from Figure 1 that the nature of the support used for the metallic phase has a substantial impact on the performance of the catalyst, being highly influenced by the textural and surface chemical properties. Palladium supported on the ball milled multi-walled carbon nanotubes (MWCNT-BM) showed a complete removal after 15 min, thus being the most efficient. It is noteworthy that palladium supported on MWCNT doped with nitrogen (MWCNT@N) and on the original MWCNT (MWCNT-O) and also showed great efficiency. Figure 2a) presents the performance of the three best performing 1 wt.% Pd catalysts during the continuous bromate reduction in the fixed bed reactor. Here, the Pd catalyst supported on the original multi-walled carbon nanotubes (MWCNT-O) showed to be the most promising, resulting in outlet bromate concentrations significantly below the legal limit of 10 µg $L^{-1}$ throughout the entire duration of the reaction. Figure 2b) shows bromate concentrations using the MWCNT-O sample in the fixed bed reactor for a continuous operation reaction, where a constant decrease in the performance of the catalyst was observed when using real water, suggesting a constant mechanism of deactivation. This catalyst deactivation is mainly related to the competitive adsorption of co-existing ions or the formation of mineral deposits on the catalyst active centers, with only small compromises related to the presence of organic matter and the dissolution of Pd.

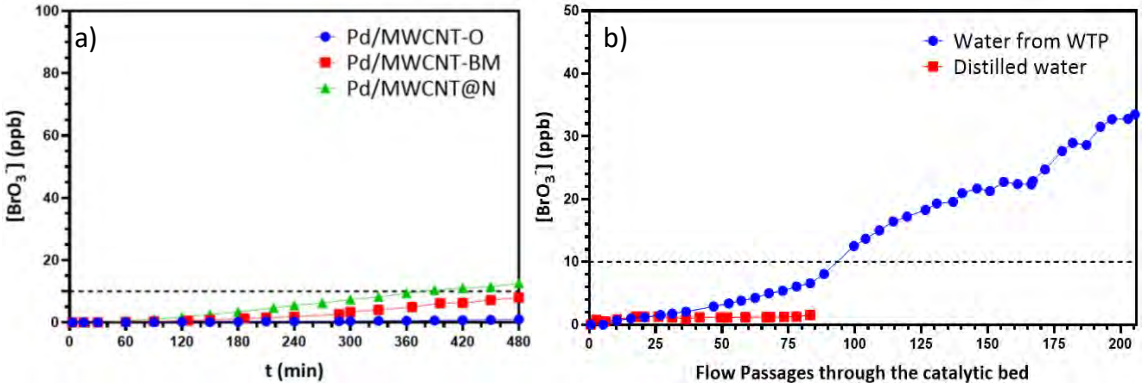


**FIGURE 2:** Bromate concentration (ppb) during continuous hydrogen reduction using 1 wt.% Pd catalysts on different supports (a) (Q = 5 mL $min^{-1}$, 200 $mg_{CAT}$, $H_2$ = 50 $cm^3$ $min^{-1}$) and the 1 wt.% Pd/MWCNT-O catalyst using the optimized conditions with distilled water and water from a water treatment plant (b) (Q = 7.8 mL $min^{-1}$, 200 $mg_{CAT}$, $H_2$ = 12.5 $cm^3$ $min^{-1}$).

Further studies are required with this catalytic system to design an efficient regeneration system, provided the deactivation mechanism can be further understood.

## CONCLUSIONS

A systematic study was carried out to assess the role of the properties of nanostructured carbon supports in the performance of a catalytic system for the reduction of bromate over palladium. It has been observed that it is possible to reduce bromate in water with hydrogen using both semi-batch and continuous operation modes. The chemical and textural properties of the supports have been shown to significantly affect the performance of the catalysts. In semi-batch experiments, the following trend for the catalyst supports was found: oxidative treatment < original < nitrogen-doped < milling process. In the continuous fixed bed reactor, the Pd catalyst supported on the original multi-walled carbon nanotubes (MWCNT-O) showed to be the most promising.

A decrease in the catalytic performance for the real waters tested was observed where a tendency for a deactivation of the catalyst over time was also apparent, likely related to the competitive adsorption of inorganic matter on the catalyst active centers or formation of mineral deposits on the catalyst active centers.

**Acknowledgements**

NanoCatRed (NORTE-01-0247-FEDER-045925) (ERDF –– COMPETE 2020, – NORTE 2020 and– FCT under UT Austin Portugal) and by InTreat-PTDC/EAM-AMB/31337/2017 - POCI-01-0145-FEDER-031337- (ERDF, COMPETE2020- FCT/MCTES); This work was financially supported by: LA/P/0045/2020 (ALiCE), Base-UIDB/50020/2020 and Programmatic-UIDP/50020/2020 Funding of LSRE-LCM, funded by national funds through FCT/MCTES (PIDDAC). CAO acknowledges FCT funding under DL57/2016 Transitory Norm Programme. OSGPS acknowledges FCT funding under the Scientific Employment Stimulus - Institutional Call CEECINST/00049/2018. JRMB acknowledges funding under the 2SMART NORTE-01-0145-FEDER-000054 funded by CCDR-N (Norte2020)

**References**

Restivo, J., Soares, O. S. G. P., Órfão, J. J. M. & Pereira, M. F. R. (2015). Metal assessment for the catalytic reduction of bromate in water under hydrogen. *Chemical Engineering Journal,* 263**,** 119-126. https://doi.org/10.1016/j.cej.2014.11.052

Soares, O. S. G. P., Ramalho, P. S. F., Fernandes, A., Órfão, J. J. M. & Pereira, M. F. R. (2019). Catalytic bromate reduction in water: Influence of carbon support. *Journal of Environmental Chemical Engineering,* 7**,** 103015. https://doi.org/10.1016/j.jece.2019.103015

World Health Organization (2017). *Guidelines for drinking-water quality: fourth edition incorporating first addendum,* Geneva, World Health Organization.

Carbon 2022

# Impact of salinity and natural organic matters on the adsorption of organic micropollutants: a dynamic adsorption study with RSSCT for industrial applications in mollusc hatcheries.

**Julie COULEAUD[1], Sylvain GIRAUDET[1], Nicolas CIMETIERE[1], Dominique WOLBERT[1], Pierre LE CLOIREC[1]**

[1]Université de Rennes, ENSCR, CNRS, UMR 6226, Rennes, France

Email: julie.couleaud@ensc-rennes.fr

**Keywords**

RSSCT, seawater, organic micropollutants, influence of salinity

## INTRODUCTION

The oyster French production represents 85% of total European production (Agri d'Agreste, 2021) so the production of marine molluscs is an important economic activity. In shellfish hatcheries, a good water quality is required for the different stages of rearing. Different processes such as sand filtration, activated carbon adsorption and ultraviolet radiation disinfection, are used to deal with emerging contaminations, either biological or chemical in nature. The optimisation of these water treatment processes is necessary due to the presence of organic micropollutants in coastal waters, at trace concentrations, from a few tens of $ng.L^{-1}$ to a few $\mu g.L^{-1}$ (ADAQUA Ifremer, 2017).

Therefore, the adsorption of 22 organics micropollutants at trace concentrations such as pesticides and pharmaceutical residues were studied at lab scale with various granular activated carbons (GAC) from different origins (wood, bituminous coal and coconut shell) and several types of water: ultrapure water (UPW), synthetic seawater (SSW) without organic matter (ASTM D1141- 98, 1998), and coastal seawater (CSW) directly taken in shellfish hatcheries.

According to the scientific literature, salts can have a neutral or negative impact depending on the surface properties of the adsorbent and the adsorbed molecules. A phenomenon of charge neutralization was observed blocking the adsorption of molecules, either when the cations neutralize the negative charges on the surface of the material (Wibowo, 2016), or by interactions of cations with the molecules to be adsorbed (Arafat, 1999). However, increasing salinity may have no effect on adsorption on powdered carbon (Younker, 2015) or on carbon nanotubes (Joseph, 2011). However, too few studies have been carried out on the impact of marine natural organic matters (MNOM) on adsorption and its competition with organic micropollutants at environmental concentrations. Therefore, it is not advisable to make assumptions about MNOM impact on the adsorption of organic micropollutant.

Thus, the mass transfer was studied by plotting isotherm curves of adsorption in batch reactors and breakthrough curves obtained thanks Rapid Small-Scale Column Tests (RSSCT). Breakthrough curves modelling lead to a deeper understanding of the limiting mass transfers and the influence of operating conditions. To model the breakthrough curves over a longer period of time, the equilibrium

parameters from the Freundlich model were used in combination to the Homogeneous Surface Diffusion Model (HSDM) for the external/internal mass transfers.
The objectives were, firstly, to optimize the removal efficiencies during seawater treatment processes in order to secure the production of marine mollusc, and secondly, to approach the mechanisms and the impact of salinity and MNOM on adsorption capacities and kinetics of trace contaminants.

## MATERIALS AND METHODS

The GAC studied are produced from different precursors but are all steam activated. Various characterisations were carried out to understand their differences: point of zero charge (PZC), ash content, specific surface area and pore size distribution using nitrogen adsorption at 77 K, mercury porosimetry and surface chemistry. Some characteristics are shown in Table 1. The specific surface area and the surface chemistry are relatively similar for all carbons and their PZC is higher than the pH of seawater, which is on average 8.2, so the surfaces of the three carbon are positively charged.

| **Structure** | | | |
|---|---|---|---|
| **Origin** | Wood | Coconut shell | Bituminous coal |
| **BET - Specific surface area ($m^2.g^{-1}$)** | 1196 | 1036 | 1005 |
| **Total pore volume ($cm^3.g^{-1}$)** | 0,634 | 0,511 | 0,784 |
| **Relative number of macropores and mesopores (>2nm)** | 29% | 26% | 56% |
| **Relative number of micropores (<2nm)** | 71% | 74% | 44% |
| **Surface chemistry** | | | |
| **PZC** | 11,2 | 9,3 | 9,4 |
| **Carboxylic ($\mu eq.g^{-1}$)** | 58 | 82 | 65 |
| **Lactone ($\mu eq.g^{-1}$)** | 106 | 98 | 87 |
| **Phenolic ($\mu eq.g^{-1}$)** | 6 | 7 | 15 |
| **Acidic surface ($\mu eq.g^{-1}$)** | 170 | 188 | 167 |
| **Basic surface ($\mu eq.g^{-1}$)** | 72 | 76 | 76 |

**TABLE 1**: Physico-chemical characteristics of wood, coconut shell and bituminous coal carbon.

The organic molecules studied were chosen to represent a wide range of molecular weights, hydrophobicity values and industrial applications. The molecules ranked in order of increasing hydrophobicity from $LogD_{(pH7,4)}$ =-3.34 to $LogD_{(pH7,4)}$ =5.62 are: metolachlor-ESA, nicosulfuron, ofloxacin, metolachlor-OA, atrazine-2-hydroxy, lincomycin, ketoprofen, diuron, caffeine, carbamazepine, naproxen, diclofenac, benzotriazole, atrazine-desethyl, isoproturon, atrazine, metolachlor, propyzamide, tributyltin, oxybenzone, difenoconazole, quinoxyfen. All the analysis was performed using an online solid-phase extraction coupled with an ultra-performance liquid chromatography-tandem mass spectrometer (online-SPE-UPLC-MS/MS).

RSSCT were chosen to predict the breakthrough curves of an industrial GAC filter, used in hatcheries and fed with seawater. The experimental setup was designed for a flow velocity and a GAC particle size in order to respect the hydraulic conditions of the industrial filter. Therefore, the hydraulic Reynolds is similar at both scales (Reynolds numbers = 4.2). The Empty Bed Contact Time (EBCT) is 5 seconds for the RSSCT corresponding to 339 seconds for the industrial scale while a particle diameter ratio of 4 between two scales was determined. The inlet concentration ($C_0$) of organic micropollutant was at about 1 $\mu g.L^{-1}$ and the outlet concentrations (C), ranged from 10 $ng.L^{-1}$ to 1 $\mu g.L^{-1}$. All curves are expressed as $C/C_0$ ratio versus treated bed volume (TBV) which represents the volume treated at a given flow rate and through a defined volume of carbon fixed bed.

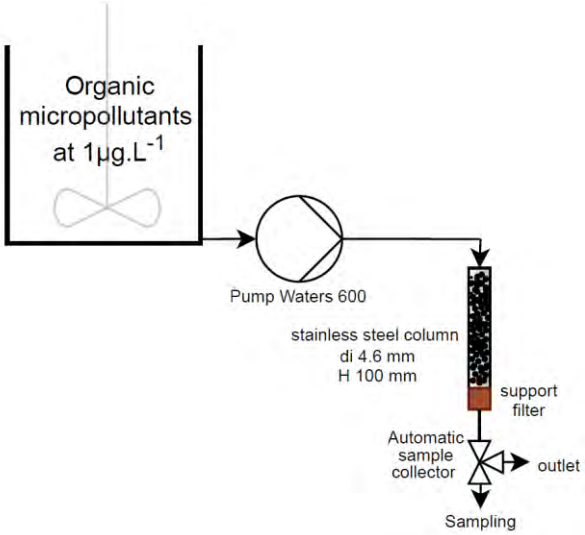


**SCHEMA 1**: RSSCT laboratory set-up

## RESULTS AND DISCUSSION

Similar behaviors were observed for all the molecules and the adsorption of diuron (Graphic 1) is used for illustration. In UPW, (Graphic 1, a), the breakthrough curves highly depend on the nature of the adsorbent. The carbon produced from coconut shells seems to have a better adsorption capacity, followed by adsorbents from other precursors, bituminous coal and finally wood. The wood GAC has a low adsorption capacity because the breakthrough curves show rapid saturation of the carbon. Contrary, coconut and bituminous coal carbon seem to have better adsorption capacities. They differ from each other in their adsorption kinetics: at the beginning of the breakthrough curve, adsorption is fast in the case of coconut coal and adsorption is slower in the case of bituminous coal carbon.

On the other hand, in SSW, i.e. seawater without MNOM, (Graphic 1, b), differences between the adsorbents are less pronounced and activated derived from bituminous coal exhibited the largest adsorption capacity. Thus, the type of carbons has a much greater impact in the absence of salts. The lower adsorption capacity of wood-based activated carbon could be explained by its higher PZC. On the contrary, the higher total pore volume of bituminous coal carbon may be an advantage and could explain the higher adsorption capacity of this adsorption in SSW.

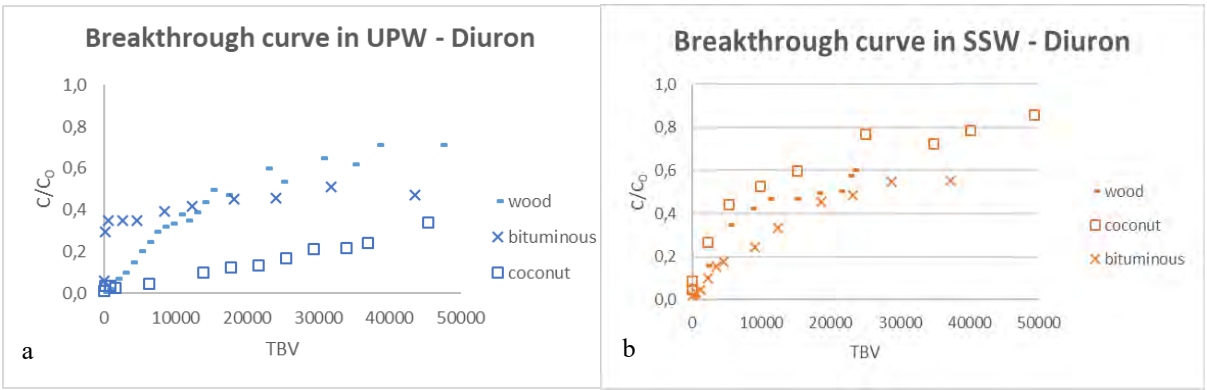


**Graphic 1:** Breakthrough curve of diuron onto activated carbons made from bituminous coal, wood, and coconut shells in UPW [a] and SSW [b].

Regarding the impact of salinity, regardless of the type of activated carbon, the increase in salinity considerably modified the shape of the breakthrough curves (Graphic 2 shows the breakthrough curves obtained with nicosulfuron). For all molecules, the total breakthrough, expressed as $C/C_0=1$, was reached more quickly in SSW than in UPW.

The surface of the carbon is positively charged at pH = 8.2, so, according to the literature, two hypotheses can be made: Firstly, the anions present in the seawater interact on the surface of the

carbon, thus blocking the adsorption sites for the organic molecules. Secondly, the ions interact with the chemical groups of the molecules and slow down their transfer to the adsorption sites.

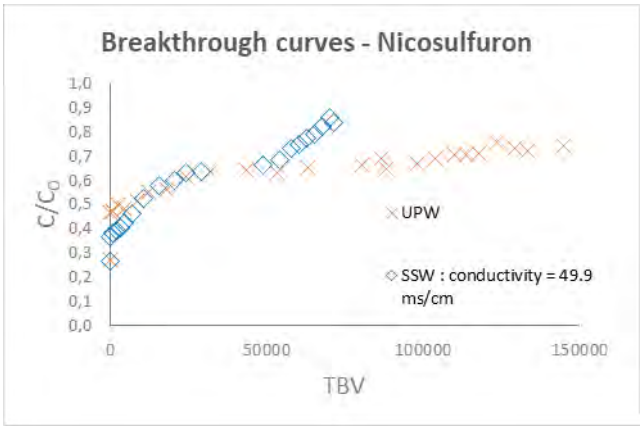


**Graphic 2:** Breakthrough curve of nicosulfuron onto bituminous coal-based activated carbon in two different matrices: UPW and SSW.

Regarding the impact of the MNOM, there is a slight difference in adsorption capacities between CSW and SSW. The RSSCT experiments compared two matrices (Graphic 3): real CSW and real CSW diluted with SSW in order to lower the concentration of MNOM. The CSW used by the hatcheries had quite low contents of organic matter as the total organic carbon (TOC) is 2.6 $mg.L^{-1}$. After dilution, the MNOM content was lowered to 1.2 $mg.L^{-1}$.

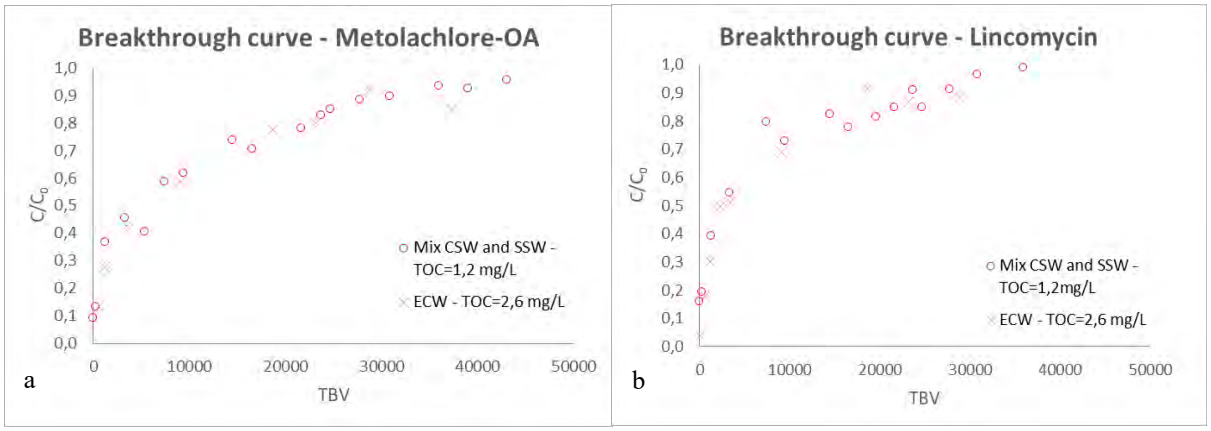


**Graphic 3:** Breakthrough curve of Metolachlor-OA [a] and Lincomycin [b] with bituminous coal carbon in two different amounts of TOC.

There was no significant impact of the content of MNOM on the breakthrough curves for metolachlor-OA (Graphic 3, [a]), and lincomycin (Graphic 3, [b]) and this conclusion was drawn for the majority of micropollutants in the study. Experiments in seawater with a higher concentration of MNOM should be carried out in order to define the threshold content of organic matters above which a significant impact could be observed. This last result also showed that a slight variation in seawater quality will not directly impact the adsorption performance.

## CONCLUSIONS

The monitoring of micropollutants in seawater was possible thanks to a sensitive and rapid analytical method based on online solid-phase extraction coupled with UPLC-MS/MS runs. This method permits the accurate and rapid multi-residual determination of 22 organic micropollutants in seawater at low detection and quantification limits, on average 10 $ng.L^{-1}$.

The RSSCT methodology highlighted the differences in kinetics and adsorption capacities between three carbons of different origins and three different water matrices. A granular activated carbon with a large pore volume (0.78 $cm^3.g^{-1}$), produced from bituminous coal, was the most suitable for the adsorption of organic micropollutants in coastal sea water. Salinity has an impact on the breakthrough of organic micropollutants through the adsorbent: the mass transfer is limited and the adsorption capacity is lowered. Therefore, this difference must be considered in the design of industrial-scale filters. Regarding the amount of MNOM in seawater, no impact was observed between a salty matrix with TOC= 1.2 $mg.L^{-1}$ and TOC= 2.6 $mg.L^{-1}$, so it can be assumed that small variations in water quality in terms of marine organic matter will not impact adsorption on activated carbon. Nevertheless, these are relatively low TOC values from a specific hatchery and are not necessarily representative of other coastal water sources. The differences observed between the UPW, SSW and CSW show the importance of performing experiments in the target matrix in order to obtain the best predictions of the breakthrough curves. In addition to these conclusions from RSSCT, a larger experimental unit should validate the conclusions in seawater and confirm the scale-up procedure.

**Acknowledgements**

The authors acknowledge the financial support of the *Fédération Européenne des Affaires Maritimes et de la Pêche* (FEAMP), hatcheries company Novostrea Bretagne and France Naissain. We would like to thank the various partners of the SOAP project: Philippe Moulin, Mathias Monnot and Clémence Cordier from the Université Aix-Marseille, Christophe Stavrakakis, Virginie Le Razavet and Frédéric Girardin from Ifremer, and Valérie Héquet from IMT-Atlantique. A special thank you to the CIP team at the ENSCR, which made a significant technical contribution to this study.

**References**

Arafat H.A., Franz M., Pinto N.G. (1999) Effect of Salt on the Mechanism of Adsorption of Aromatics on Activated Carbon. *Langmuir 1999*, 15, 5997-6003. https://doi.org/10.1021/la9813331

ASTM International. (1998) Standard Practice for Substitute Ocean Water. ASTM D1141- 98

Crittenden, J. C., Berrigan, J. K. and Hand, D.W. (1986) Design of rapid small-scale adsorption tests for a constant diffusivity. *Journal Water Pollution Control Federation,* 58 (4), 312–319. DOI: 10.2307/25042907

Graph'Agri d'Agreste. (2021), L'agriculture, la forêt, la pêche et les industries agroalimentaires. GraFra2021_integral.pdf

Joseph L., Heo J., Yong-Gyun Park Y-G., Flora J.R-V., Yoon Y. (2011) Adsorption of bisphenol A and 17α-ethinyl estradiol on single walled carbon nanotubes from seawater and brackish water. *Desalination 281 (2011)* 68–74. DOI:10.1016/j.desal.2011.07.044

Ifremer. (2017) ADAQUA, Analyse par capteurs passifs avec et sans système de traitement. https://archimer.ifremer.fr/doc/00416/52765/

Wibowo E., Rokhmat M., Sutisna, Khairurrijal, Abdullah M. (2016) Reduction of seawater salinity by natural zeolite (Clinoptilolite): Adsorption isotherms, thermodynamics and kinetics. *Desalination 409 (2017)* 146–156. http://dx.doi.org/10.1016/j.desal.2017.01.026

Younker J.M. Walsh M.E. (2015) Impact of salinity and dispersed oil on adsorption of dissolved aromatic hydrocarbons by activated carbon and organoclay. *Journal of Hazardous Materials 299 (2015)* 562–569. http://dx.doi.org/10.1016/j.jhazmat.2015.07.063

Carbon 2022

# Comparison of ex-situ and online Raman spectroscopies in studying soot materials

**Kim Cuong Le[1], Saga Bergqvist[1], Jonatan Henriksson[1], Thomas Pino[2], Per-Erik Bengtsson[1]**

[1] Division of Combustion Physics, Department of Physics, Lund University, Sweden

[2] Institut des Sciences Moléculaires d'Orsay, CNRS, Univ Paris Sud, Université Paris-Saclay, France

Email: thi_kim.cuong_le@forbrf.lth.se

**Keywords**

Raman scattering, soot, oxidation, structural modification

## INTRODUCTION

Raman spectroscopy is a standard nondestructive tool for characterizing structural information of carbonaceous materials. This technique is applied on a large scale of carbonaceous materials varying from order, disorder to amorphous carbon. Nowadays, the application of Raman scattering for ex-situ measurements is largely dominating where the samples are collected before characterization being conducted in laboratory. However, our recent studies demonstrated that the sampling process and oxidization while performing ex-situ Raman measurements under atmospheric conditions may lead to problems from modification of soot structures. In this perspective, development of online Raman scattering for the structural analysis of carbonaceous materials in the aerosol phase without the sampling problem is required. This presentation will provide the delimitations of ex-situ Raman spectroscopy and introduce online Raman spectroscopy to the community.

## MATERIAL AND METHODS

Two sets of experiments were performed. One set was performed to compare the aerosol soot and the deposited soot Raman spectra using online and ex-situ Raman spectroscopy (Le, Lefumeux and Pino, 2022). In this work, we used flame soot produced in low pressure premixed ethylene/oxygen flame (p = 40 mbar, Φ = 3.15) at the height of 18 mm from the burner. The second set was devoted to soot oxidation during ex-situ measurements. Two typical types of soot representing black/mature and brown/immature soot were investigated for comparing their potential different behaviors. A mini-CAST soot generator was used to produce OP1 soot (black soot) and OP6 soot (brown soot). Their distinct optical, structural and chemical properties were presented in our previous works (Török *et al.*, 2018; Le *et al.*, 2019). The samples were oxidized by two methods involving long-term exposure to the laser radiation and heat treatment in the air environment. These results were then compared to the measurements in nitrogen environment where no oxidation was occurred. In both studies, Raman signals were observed by our home-build Raman set-ups whose excitation wavelength was 532 nm. While the laser power in ex-situ measurements were a few kW/cm$^3$, the laser irradiance of about few tens kW/cm$^2$ was procured in the online measurement due to low concentration of soot in the aerosol phase.

## RESULTS AND DICUSSION

### Influence of sampling process on soot structure

Fig. 1a shows raw spectra while in Fig. 1b the spectra are plotted after subtraction of the fluorescence (PL) backgrounds, and normalized to the maximum of the band at about 1600 cm$^{-1}$. In the aerosol phase, the PL is probably dominated by the molecular component (mainly free-flying polycyclic aromatic hydrocarbons (PAHs) (Ciajolo, 2009) and decreases in intensity with Stokes shift. In the deposited phase the PL probably arises from PAHs adsorbed on the soot particles with the maximum appearing shifted to longer wavelength, as is usually observed using an excitation at 532 or 514 nm. It should be noted that the intensities of the bands observed in the spectral region between 1700–2300 cm$^{-1}$ are clearly weaker in the Raman spectra of the deposited soot.

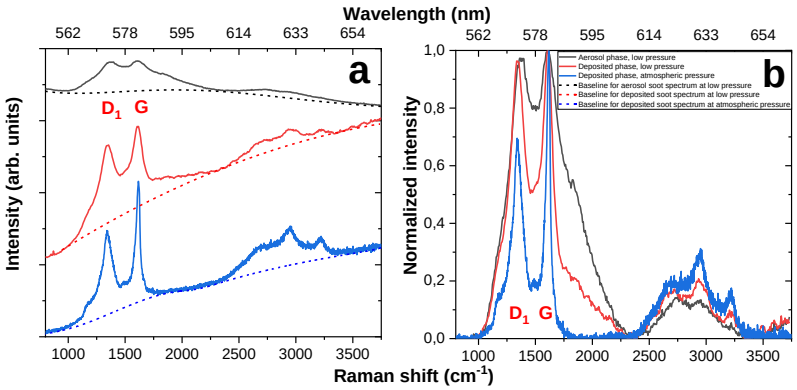


**FIGURE 1:** Raman spectra of soot produced by the same ethylene/oxygen flame conditions (C/ O = 1.05, P = 40 mbar, HAB = 18 mm) in the aerosol phase at low pressure (black curve), deposited phase under vacuum (red curve) and deposited phase at atmospheric pressure (blue curve). (a) Raw data, (b) Raman spectra after subtraction of the fluorescence background, their relative intensity being scaled to the maximum at about 1600 cm −1 Raman shift.

The aerosol phase spectrum is successfully fitted by a combination of nine Gaussian bands as shown in Fig. 2a. For comparison of the spectral variation between aerosol and deposited soot, we use the same fitting procedure. More details on the fitting procedure can be found in subsection 4.2 of our published paper (Le, Lefumeux and Pino, 2022). Indeed, the band's FWHM traces the degree of disorder of the samples. The large FWHMs in our samples trace a high disorder and presence of defects. These contribute to the shortening of the phonon lifetime and, correspondingly, broaden the homogeneous linewidth. In addition, the large variety of local bonding induces a strong inhomogeneous broadening that lead to the mostly Gaussian profile. This indicates that the soot nanostructure is less disordered with mostly polycyclic aromatic content after deposition than that in the aerosol phase. It suggests that exposure to ambient air or atmospheric pressure leads to additional reorganization of the soot sample, especially the rapid disappearance of $C_1$ and $C_2$ peaks. They are representative of carbon chain structures consisting of cumulenic double-bond stretching (=C=C=) and polyynic triple-bond stretching (−C≡C−), respectively. These effects clearly plead for online diagnostics of aerosol soot.

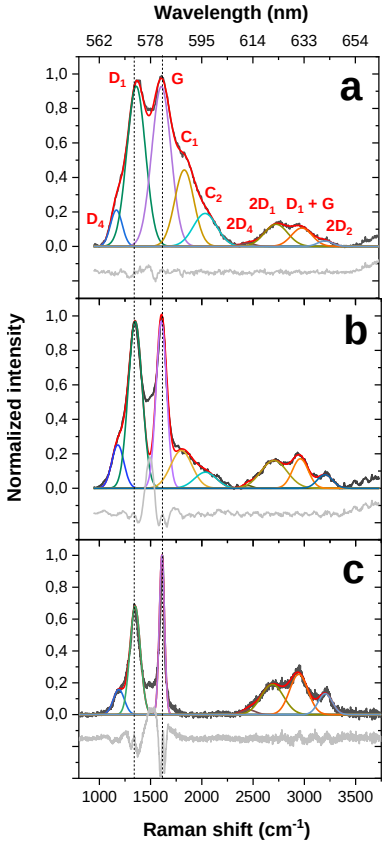


**FIGURE 2**: Decomposition of the Raman spectrum of soot (black line) in the aerosol phase (a) and deposited phases (b, c). The residual gray line (vertically shifted) shows the difference between the spectrum and the result of the fit.

**Soot oxidation in ex-situ Raman measurements**

Figure 3 compares Raman spectra of black soot/mature soot (OP1) and brown/immarure soot (OP6) under laser radiation ($a_1$, $b_1$, $c_1$, $d_1$) and heat treatment ($a_2$, $b_2$, $c_2$, $d_2$) in nitrogen and air environments. Once stored in nitrogen, Raman signals of black soot (Fig. $a_1$) and brown soot (Fig. $c_1$) are stable though the samples were irradiated. However, there was a significant change in the spectra of brown soot in the air (Fig. $d_1$) while this can be negligible in black soot (Fig. $b_1$).

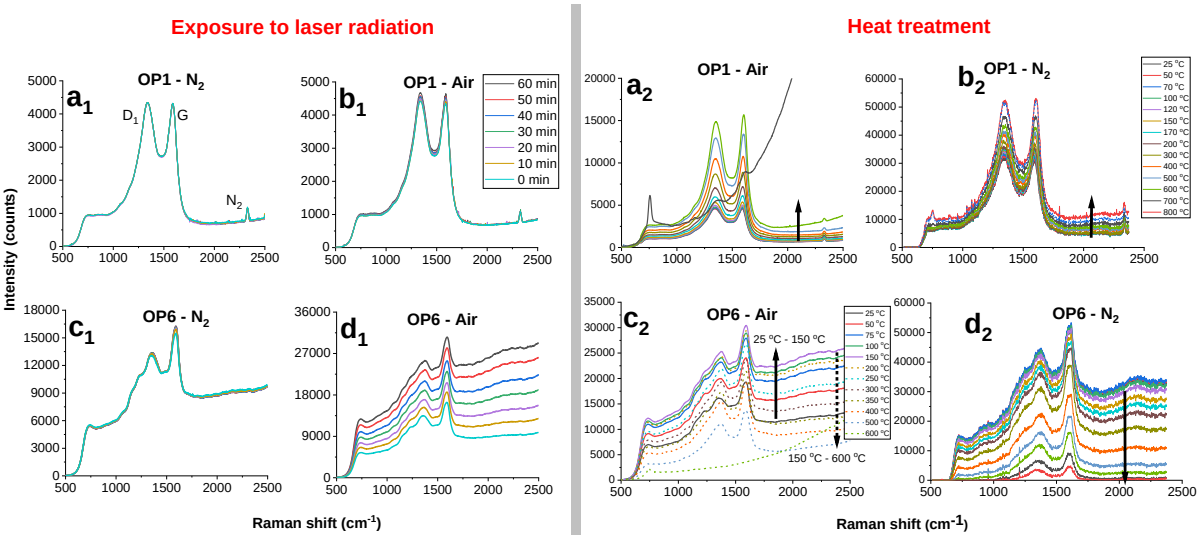


**FIGURE 3:** Raman spectra of OP1 and OP6 soot exposed to the laser radiation (on the left) and during heat treatment (on the right) in air and nitrogen environments.

In Fig. 3 $a_2$, $b_2$, $c_2$, $d_2$, we show spectral evolution when heating soot in nitrogen and in the air. The immature sample was clearly oxidized faster than the mature one as the former was completely oxidized at 600°C while the latter is slightly above 700°C. During heat treated temperature (HTT), while the signals of mature soot always increase no matter the environments, the signals of immature soot in nitrogen steady decrease. The HTT behavior of immature soot becomes even more complicated in air. It rapidly increased between 25°C and 150°C then showed a sharp decline before completely oxidized. The heat treated temperature also changes the color of soot towards more blackish as volatiles/semi-volatiles or organic compounds are vaporized. This means that HTT enhanced their absorption properties. The authors are looking forward to discussing with the audiences about the oxidation phenomenon happening in ex-situ Raman measurements of soot at the conference.

## CONCLUSIONS

For the first time, a comparison between online and ex-situ Raman measurements on the same soot has been carried out. Cumulenic structures have been found to dominate the sp carbon components. Both cumulenic and polyynic structures are less stable in the soot nanostructure after deposition and under atmospheric conditions. Our results reflect the influence of sampling processes on the structure characterization of soot, particularly on the sp hybridized structures and the disordered character of the $sp^2$ polycyclic aromatic components. Additionally, soot oxidation process could happen during ex-situ measurements modifying soot properties and morphology. Notice that soot oxidation is also one of steps in atmospheric soot aging routines. Atmospheric soot properties are interest of reflecting their impacts on climate and human health. They thus attract a great attention from many scientific communities.

**Acknowledgements**

K.C.L acknowledges the Swedish Research Council [project 2021-04064] and Crafoord Foundation [reference number 20210986] supporting this research.

**References**

Ciajolo, A. (2009) “Condensed phases in soot formation process,” in Bockhorn, H. et al. (eds.) *Combustion generated fine carbonaceous particles*. Karlsruhe: KIT scientific publishing, pp. 333–344.

Ferrari, A. C. and Robertson, J. (2001) “Resonant Raman spectroscopy of disordered, amorphous, and diamondlike carbon,” *Physical Review B*, 64(7), p. 075414. doi: 10.1103/PhysRevB.64.075414.

Le, K. C. *et al.* (2019) “Raman spectroscopy of mini-CAST soot with various fractions of organic compounds: Structural characterization during heating treatment from 25 °C to 1000 °C,” *Combustion and Flame*. Elsevier, 209, pp. 291–302. doi: 10.1016/j.combustflame.2019.07.037.

Le, K. C., Lefumeux, C. and Pino, T. (2022) “Watching soot inception via online Raman spectroscopy,” *Combustion and Flame*. Elsevier Inc., 236, p. 111817. doi: 10.1016/j.combustflame.2021.111817.

Török, S. *et al.* (2018) “Investigation of the absorption Ångström exponent and its relation to physicochemical properties for mini-CAST soot,” *Aerosol Science and Technology*, 52(7), pp. 757–767. doi: 10.1080/02786826.2018.1457767.

Carbon 2022

# Selective Separation of $^{165}$Er from Ho target using functionalized mesoporous carbons

**Isidro DA SILVA*, Eder AMAYUELAS, Louis FREALLE, Conchi ANIA[1]**
CEMHTI, CNRS (UPR 3079), Université d'Orléans, 45071 Orléans

Email: isidro.dasilva@cnrs-orleans.fr

**Keywords**
Radiochemical; separation; functionalization; mesoporous carbon.

## INTRODUCTION

Radionuclides emitting Auger electrons with low energy (ca. 0.02-50 keV) are of interest in Targeted Radionuclide Therapy (TRT) (cancer diagnosis, preclinical studies, radiolabeling, imaging) [1]. Among them, $^{165}$Er is a pure Auger Electron (AE) emitter and a useful tool for fundamental studies on the biological effects of AE emitter. Furthermore, $^{165}$Er may be easily produced by irradiation of natural holmium target with proton or deuteron beams. However, separation of adjacent lanthanides is challenging as they have similar oxidation states, coordination chemistry, and unfavorable mass ratio in the target (e.g., 1:$10^4$ for $^{165}$Er:Ho) [2]. Radiochemical separations of lanthanides may be performed by solid−liquid extraction methods using functionalized porous supports. In this regard, recent works have highlighted the potential advantages of other materials (i.e., silica, layered double hydroxides) due to their higher stability under harsh irradiation conditions, easy functionalization, low cost and versatile of forms and pore architectures [3].

The objective of this study was the use of mesoporous carbons of varied origin and physicochemical properties for the selective separation of $^{165}$Er from an irradiated Ho target. The carbons were modified upon impregnation with organophosphorous extractant bis(2-ethylhexyl) phosphoric acid (HDEHP), commonly used to separate lanthanides [4]. Performance was compared to commercially available resins (e.g., LN®, Triskem) manufactured with similar extractants. Extractive performance in static (coefficient of distribution) and dynamic tests have demonstrated similar profiles of $^{165}$Er/Ho separation with certain of the studied modified carbons than those of the commercial resin, using lower concentration of nitric acid. Such improved extraction performance is explained by the tight immobilization of the extractant inside the mesopores. Furthermore, the functionalized materials proved to be stable after at least one year. The obtained results are in line with those of commonly used supports for the $^{165}$Er/Ho radiochemical separation, opening new perspectives for mesoporous carbons in this application.

## EXPERIMENTAL

Various nanoporous carbons with different characteristics were selected as for the immobilization of the linker. Radiotracers of Ho, $^{166}$Ho, and Er, $^{165}$Er, were produced by irradiation of Ho foil with a 17,5 MeV deuteron beam. Quantification of each element was determinated by spectrometry gamma. Each test has been triplicated: for extractive performance in static, concentration of $HNO_3$ (0,01 to 5M) and used Ho quantity (capacity of resin : 20 to 400%) have been modified. Used protocol for production of $^{165}$Er has been applied with 1mg of irradiated Ho target to the best expected nanoporous carbon support. A comparison with LN (50-100µm), LN2 (20-50 and 50-100µm) was been done and only profile of elution of $^{165}$Er was established by measurement with an activimeter.

## RESULTS AND DISCUSSION

Selected carbons have the following properties (Figure 1) :

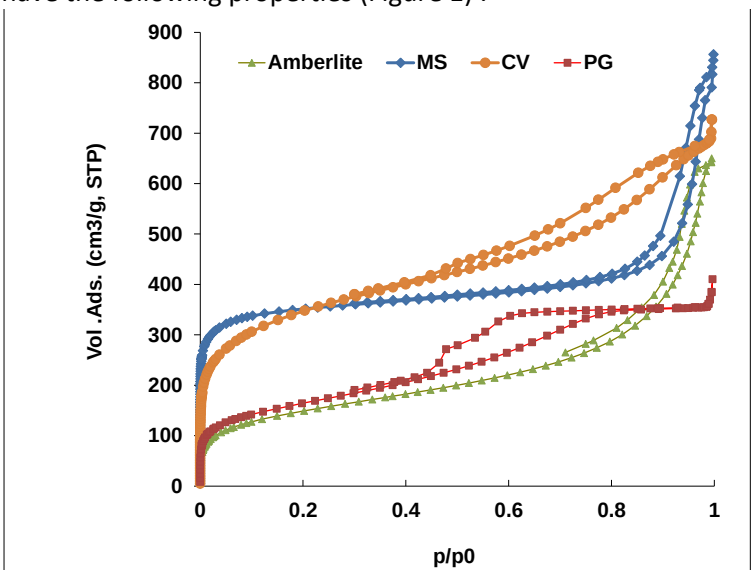


**FIGURE 1**: Adsorption profile of 4 used supports

MS sample (spheres) has a similar semiporosity as Amberlite (support of comercial resins LN). CV sample (powdered porous carbon) has a large mesoporisity whereas PG simple (powdered) is narrower mesoporosity and has a lower volume. For separation of $^{165}$Er from Ho target, impregnated Ms sample demonstrated no effects with variation of nitric concentration. PG sample have given similar results in static tests as Amberlite support but no stability to high concentration of acid (2 - 5M). At least, only CV sample has selective capacity of separation with stability to acid and radiations exposure. On column tests, profiles of CV sample are similar to LN2 resin ever the linker is different. Reproducibility of separation Ho/Er and recycling CV sample have been validated.

## CONCLUSIONS

We have investigated the separation of $^{165}$Er from a Ho target using nanoporous carbon. CV sample, powdered carbon, with a large mesoporosity and 78% of linker impregnation was stable to high concentration of nitric acid (5M) and radiations exposure. Coefficient of distribution (Dw) was drift to lower nitric acid compared to Dw of LN resin. Elution profile of Ho/Er with CV sample was near to LN2 resin (20-50µm) using a different linker. These first results demonstrate potential interests of mesoporous in production of radionuclides for imaging applications.

**Acknowledgements**

The financial support of the European Research Council through a Consolidator Grant (684161) is acknowledged.

**Reference,**

[1] A Ku, V.J. Facca, Z. Cai, R.M. Reilly, EJNMMI Radiopharm Chem 4 (2019)27.

[2] I. Da Silva, T. R. Johnson, J. C. Mixdorf, E. Aluicio-Sarduy, T. E. Barnhart, R. J. Nicklesa, J. W. Engle, P. A. Ellison, Molecules 26 (2021) 7513.

[3] L. Lefrançois Perreault, S. Giret, M. Gagnon, J. Florek, D. Larivière, F. Kleitz, ACS Appl. Mater. Interfaces 9 (2017), 12003.

[4] D. R. McAlister and E. P. Horwitz, Solvent Extr. Ion Exch., 25 (2007) 757.

20 C 22 arbon 2022

# Enteric viruses' passive sampling by adsorption on activated carbon

**Doriane Delafosse[1], Laurent Duclaux[2], Laurence Reinert[2], Philippe Azaïs[3], Yasushi Soneda[4], Dominique Fontvieille[1],**

[2]Université Savoie Mont Blanc, CNRS, EDYTEM, F-73000 Chambéry, France

Email: laurent.duclaux@univ-smb.fr

[1]Laboratoire Abiolab, 38330 Montbonnot-Saint-Martin, France

[3]CEA/DES/DPE, 38054 Grenoble, France

[4]Institute of Advanced Industrial Science and Technology, Energy Process Research Institute, 16-1 Onogawa, Tsukuba, Ibaraki 305-8569, Japan

**Keywords**

Activated carbon, adsorption/retrieval, enteric virus

## INTRODUCTION

Enteric viruses (particles of ~30 nm diameter) are widely spread in water environments, some being harmful for human communities and responsible for gastroenteritis. They are emitted from human feces and driven to Waste Water Treatment Plant (WWTP). Regular epidemics highlight the usefulness of such virus's analysis in wastewaters as a tool for epidemiologists to monitor their dissemination extent among populations. With the aim of developing a passive sampler of the enteric viruses, we studied their adsorption and recovery on various forms of Activated Carbon (AC) in order to allow their quantitative analysis by RT-qPCR (Quantitative Reverse Transcription Polymerase Chain Reaction). In a first approach, Murine Noroviruses (MNV) adsorption/recovery was studied as they are considered as models of human enteric viruses. Then, an automatized sampler was developed for field detection of human enteric virus in wastewater issued from WWTP.

## EXPERIMENTAL

### Activated Carbon materials and characterization

A Norit 1240 microporous AC was milled in powder and compressed with additives (15 wt. % PTFE and 5% carbon black) at 50 MPa in order to obtain a pellet.

The CNovel$^{TM}$ (50 nm) porous carbon (from Toyo Tanso, Japan) is mesoporous and obtained from the dissolution of MgO nanoparticles templates (Soneda et al., 2013). CNovel$^{TM}$-based self-supported films or deposits on a polymer "brush" (Figure 1 (a) and (b)) were prepared by evaporation of an "ink-like" mixture made out from the AC and 14 wt. % of PTFE or PVDF and 6 wt. % of carbon black in N-methyl-2-pyrrolidone. The "brush" comprised of thin Nylon rods was 3D-imprinted.

The activated carbons were characterized by SEM, $N_2$ adsorption-desorption (77 K), $CO_2$ adsorption (273 K), and by zeta potential versus pH measurements of AC suspensions (1g/L) prior and after MNV adsorption (at $C_0$=$10^6$ ug/mL).

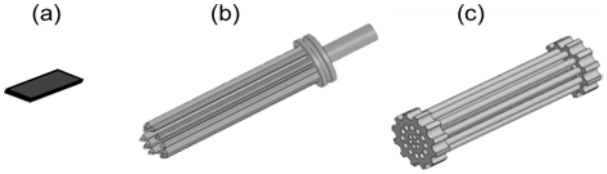


**FIGURE 1**: AC self-supported film (a). Brush-type (b) and Probe (c) designs were coated with AC.

**Batch norovirus adsorption kinetics and adsorption/retrieval experiments**

The viral genetic materials were analysed by RT-qPCR in order to obtain the virus concentrations of the studied solutions expressed in genome unit per mL as reported by Delafosse et al. (2022).

Adsorption kinetic and isotherm at 25°C of Murine Noroviruses (MNV) (at $C_0$=3.8 $10^6$ ug.mL$^{-1}$) were studied in bare saline solutions (0.1 M NaCl) or in phosphate buffer (pH 7.4) on pelletized Norit 1240 (0,1 g/50 mL). MNV ($C_0$=$10^8$ ug.mL$^{-1}$) adsorption kinetics were studied on CNovel™ self-supported films (1,2 g/30 mL) in saline solutions (0.1 M NaCl).

MNV adsorption/retrieval cycles and adsorption assays under polarization (cf. protocol details reported by Delafosse et al. (2022)) were studied on CNovel™ AC in the form of self-supported films and MNV adsorption/recovery tests were performed in saline solutions (0.1 M NaCl) on CNovel™ coated on "brush" polymer rods.

**On field virus adsorption/retrieval sampling by activated carbon probe**

A home-made automatized sampler was designed and tested *in situ* on wastewater at the outlet of the "Grand Chambéry" WWTP) (France), i.e. after it went through both, primary physicochemical and secondary biological processes. The human Norovirus of Genogroup I (NoV-GI) and Adenovirus (AdV) recovery were measured using protocols reported by Delafosse et al. (2022) on Nylon 3D imprinted probe coated with CNovel™ (Figure 1 (c)).

**RESULTS AND INTERPRETATIONS**

**Characterization of activated carbon materials**

The Norit 1240 AC is mainly microporous ($V_{micropore}$=0.20 cm$^3$.g$^{-1}$, $S_{BET}$=1083 m$^2$.g$^{-1}$) while the CNovel™ is mainly mesoporous ($V_{mesopore}$=0.82 cm$^3$.g$^{-1}$, $S_{BET}$=660 m$^2$.g$^{-1}$). The mesoporosity (50 nm mean ∅ given by BJH method) is preserved in films despite a loss of volume ($V_{mesopore}$=0.48 cm$^3$.g$^{-1}$, $S_{BET}$=375 m$^2$.g$^{-1}$).

A decrease in the zeta potential is observed after MNV adsorption (negatively charged viral envelop) in the pH range 4-5 and 5-8 for Norit 1240 AC and CNovel™ AC (Figure 2), respectively, as adsorption is promoted by electrostatic attractions and additional weak interactions. Thus, CNovel™ is more suitable for MNV adsorption in wastewater (pH range 7 to 8).

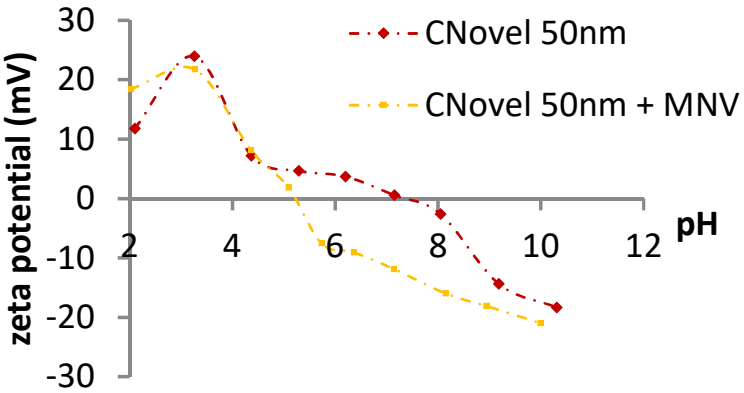


**FIGURE 2**: pH variation of the zeta potential of the CNovel™ 50 nm AC loaded or not with MNV.

**Norovirus batch adsorption and retrieval**

The MNV kinetics of adsorption on Norit 1240 pellets are rapid (2h equilibrium time) compared to the diffusion-limited ones on CNovel™ films (24h equilibrium time). MNV adsorption isotherm on Norit 1240 pellets shows a typical Freundlich profile without any saturation in the concentration range 10-$10^5$ ug.mL$^{-1}$ as previously reported by Gerba et al. (1975) for poliovirus on AC. In saline solution, the CNovel™ films MNV ($C_{initial}$ = 1.8 $10^7$ ug.mL$^{-1}$) adsorption capacity (38 mg/2 mL) reached ~90% of the virus initial amount. No saturation was obtained after four repeated adsorptions on the

same film with fresh virus suspension. CNovel™ film polarization did not increase the adsorption equilibrium compared to the non-polarized experiment.
The MNV retrieval rate on films is higher than 10% and improved after four adsorption/recovery cycles (14±2% at 1st cycle and 36±7% at 4th cycle) suggesting that weaker interactions are needed for its promotion. Moreover, a limitation of the lysis buffer diffusion in the AC porosity and a possible re-adsorption of genetic material after lysis might have occurred.
MNV adsorption/retrieval studies on CNovel™-coated brushes have shown their possible reuse on at least three adsorption/recovery cycles and confirmed that retrieval yield increases (up to 30%) after a 2nd or a 3rd cycle.

**Field virus adsorption/retrieval sampling with activated carbon probe**

A preliminary field assay of a passive sampler in a WWTP yielded to the detection of autochthonous human Norovirus Genogroup I (NoV GI) and Adenovirus (AdV) in wastewaters (Figure 3) where retrieved virus amounts are divided by the total water volume which had passed through the probe.
It suggests a promising application as virus detection tool in such high loaded and complex waters. Despite a low retrieval rate of virus, this study has shown that the optimization of the sampler exposition time is needed as the retrieval rate was higher after 2,5 h exposition than after 5 h. Adenovirus have been detected by the coated-probe type sampler despite their 80 nm diameter, higher than the 50 nm average pore diameter of CNovel™ AC.

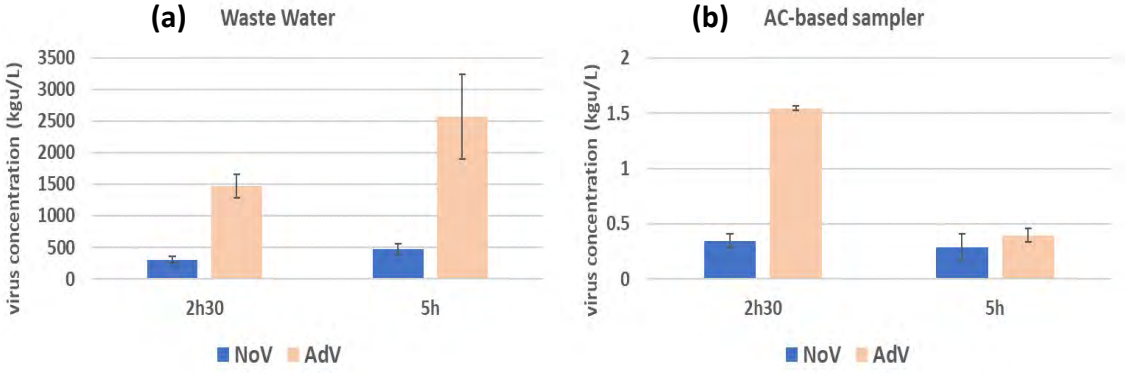


**FIGURE 3**: Wastewater concentration ofHuman Norovirus Genogroup I (NoV GI) and Adenovirus (AdV): (a) from wastewater direct analysis, (b) as assessed from the AC-based probe .

## CONCLUSIONS

The developed "*catch and retrieve*" protocol, using the mesoporous CNovel™ AC -based sampling tools allowed to collect virus samples to proceed downstream RT-qPCR molecular analysis.
As it, the sampler should be considered only as a virus detection tool. In addition, the experiments highlighted the next important tasks that should be addressed: 1/ to evaluate an exposition time balancing efficient adsorption and virus recovery, 2/ to improve the virus recovery, 3/ to develop an AC with appropriate adsorption mesoporous sites allowing desorption, and finally 4/ to convert the virus detection probe into a concentration one.

**Acknowledgements**

This research was supported by the ABIOLAB laboratory (Montbonnot Saint-Martin, France) and by the ASPOSAN association. Fields experiments were possible thanks to the "Grand Chambéry" WWTP authorities.

**References**

Gerba, C. P., Sobsey, M. D., Wallis, C. and Melnick, J. L. (1975). Adsorption of Poliovirus onto Activated Carbon in Wastewater. *Environmental Science & Technology,* 9, [8], 727-731. https://doi.org/10.1021/es60106a009

Soneda, Y. and Kodama, M., (2013). Effect of Mesopore in MgO Templated Mesoporous Carbon Electrode on Capacitor Performance. *Electrochemistry*, 81,[10], 845-848. https://doi.org/10.5796/electrochemistry.81.845

Delafosse, D., Reinert, L., Azaïs, P., Fontvieille, D., Soneda, Y., Morand, P. and Duclaux, L., (2022). Potentialities of a mesoporous activated carbon as virus detection probe in aquatic systems. *J. Virol. Methods,* 303, 114496. https://doi.org/10.1016/j.jviromet.2022.114496

Carbon 2022

# Topographic and electrical characterization of Proton Exchange Membrane fuel cell catalytic layers prepared using carbon black and carbon xerogel supports

**F. Deschamps[1], J.G. Mahy[1], A.F. Léonard[1], A. Dewandre[2], B. Scheid[2], N. Job[1]**
*[1]Dept. Chemical Engineering, Liège Université, B6a, allée du 6 août 11, 4000 Liège, Belgium*
Email : nathalie.Job@uliege.be
*[2] Université libre de Bruxelles, Transferts, Interfaces et Procédés (TIPs), Avenue F.D. Roosevelt 50, 1050 Brussels, Belgium*

**Keywords**
PEM fuel cells, carbon supports, catalytic layers, conductivity, topography.

## INTRODUCTION

Catalytic layers of Proton Exchange Membrane (PEM) fuel cells are usually made of a Pt/C catalyst blended with a proton-conductiong polymer, Nafion®, the role of which is to ensure both the layer cohesion and its ionic conductivity. In order to enhance the properties of this layer regarding mass transport and durability, many carbons have been used in literature to replace the commonly selected carbon blacks (Maillard, 2013). However, modifying the nature of the support leads to many other modifications in the final catalytic layer properties: pore texture, morphology, Pt dispersion and accessibility, contact with Nafion®, ionic and electrical conductivity, *etc.* All these parameters depend on the carbon chosen and have an impact on the cell performance. It is thus important to measure them accurately.

In the present work, the topography of catalytic layers prepared from (i) a classical carbon black and (ii) carbon xerogels was studied. To do so, two inks composed of Nafion® and carbon black or a carbon xerogel with controlled pore texture were deposited on Kapton® sheets by film-casting and spray-coating. The surface topography was characterized by contact profilometry and laser 3D microscopy. Data were processed to obtain accurate 3D images of the layer surfaces, in order to measure the thickness and check for homogeneity. Similar layers containing various amounts of Nafion® were prepared and *ex situ* four-point measurements were developed to determine their ionic and electrical resistivity, using chronopotentiometry techniques. The present work shows that layers prepared using different carbon supports can display different limiting transport phenomena: (i) ionic conductivity in the case of the carbon black and (ii) electrical conductivity in the case of carbon xerogels.

## EXPERIMENTAL

The carbon black selected for the study was the classical XC-72R from Cabot. Three carbon xerogels were prepared using a well-known procedure (Job, 2004) and displayed average mesopore sizes of 45, 85 and 210 nm. The samples are named CX45, CX85 and CX210 hereafter. They were grinded as particles with a size of ~500 nm. A second batch with larger particles (~7 µm) was also prepared.

For topographic characterization, layers containing carbon and Nafion® were prepared either by film casting or by spray coating. In the case of film casting, an Elcometer 4340 bar-coating device was used together with an Elcometer 3580 film applicator. For spray-coating, the device was a home-made robotized spray-coater using a a Nordson EFD 781 nozzle with a 781S-SS tip. In both cases, the Nafion®/Carbon (N/C) mass ratio was fixed at 1, and the solvent/solid mass ratio was adjusted depending on the coating device (film casting: 13; spray-coating: 500), since they require very different ink viscosities. The solvent chosen was isopropanol, and Nafion® was used as a 15 wt.% suspension in

isopropanol/water (LQ-1115 1100 EW from Liquion). 7 cm x 7 cm layers of various thicknesses were prepared using both methods and two different carbons (carbon black and carbon xerogel CX85).

Contact profilometry was performed using a Veeco Dektak 8 contact profilometer; confocal 3D laser scanning microscopy measurements were performed on a Keyence VK-X200 device. Contact profilometry enables performing measurements on the whole sample surface (5 cm × 5 cm). In the case of 3D laser microscopy, only a small fraction is analysed (0.25 $cm^2$) with high definition. The comparison between the two techniques was done *via* simulation of the profilometer tip motion on the microscopy profile, which allowed to determine the error on profilometry measurement.

Specific 4-point measurement displays were set up to determine (i) the electrical and (ii) the ionic conductivity of layers made of carbon and Nafion® by spray-coating. It both consists in applying a voltage between 2 outer points of a layer strip, and measuring the voltage between two inner points; however, in the case of ionic conductivity, small pieces of Nafion® are also placed between the sample and the metallic (Pt) contacts so as to impose an electrochemical reaction at the Pt/Nafion® interface and thus induce proton exchange. Resistivities were measured using chronopotentiometry; the behaviour of the layers was modelled using transmission lines to extract the ionic conductivity from the transient data. The impact of the carbon nature as well as that of the Nafion® content were investigated. In the case of carbon xerogels, measurements were performed using ~5 µm particles.

**RESULTS AND DISCUSSION**

Results show that the layer topography (i) is quite different using the two different carbons and (ii) is much influenced by the deposition technique (Figure 1). Globally, film casting leads to poor homogeneity and thickness control is not easy, while spray-coating allows for better layer homogeneity, reproducibility and thickness tuneability. The use of carbon xerogels often leads to the detection of large particles at the surface, even when grinded at ~0.5 µm, which in turn can lead to internal short-circuits. Since grinding is unavoidable in the case of carbon xerogels, the final powder granulometry remains a source of problems in electrode manufacturing. The elimination of the largest particles should be done prior to any processing.

In general, the catalytic layer ionic resistance is preponderant (*vs.* electrical resistance) when carbon blacks are used; electrical resistance is thus often neglected right away in the analysis of cell performance (Maillard, 2013). However, the latter can be much higher than expected when new carbons with different structural properties are used. The *ex situ* four-point measurement method was first validated with carbon black/Nafion® layers. Transient regimes were modelled by a transmission line representing two distinct conduction lines (ionic and electrical) separated by capacities. The measured transient profiles agree with modelling results. It was also shown that increasing the N/C ratio from 1 to 4.6 leads to both an increase in electrical resistivity and a decrease in ionic resistivity (Table 1). Usually, N/C is close to 1 in practical applications.

The method was then applied to carbon xerogel-based layers, using various xerogels and N/C = 1. In that case, and opposite to what is usually observed, the electrical resistance of the layer is not at all negligible compared to the ionic resistance (Table 1), whatever the carbon pore texture. This impacts the further design of fuel cell Membrane-Electrode Assemblies and their final behaviour in the real device. Indeed, when identifying (and solving) performance issues, one cannot neglect anymore the limitations due to electrical resistance. This difference is attributed to the fact that nanostructured carbons are made of larger particles than carbon blacks, which significantly decreases the number of contact points between the carbon particles, hence decreasing drastically the electrical conductivity of the layers. By contrast, the ionic conductivity is rather constant and close to that observed with the carbon black-based layers prepared with the same N/C ratio (Table 1).

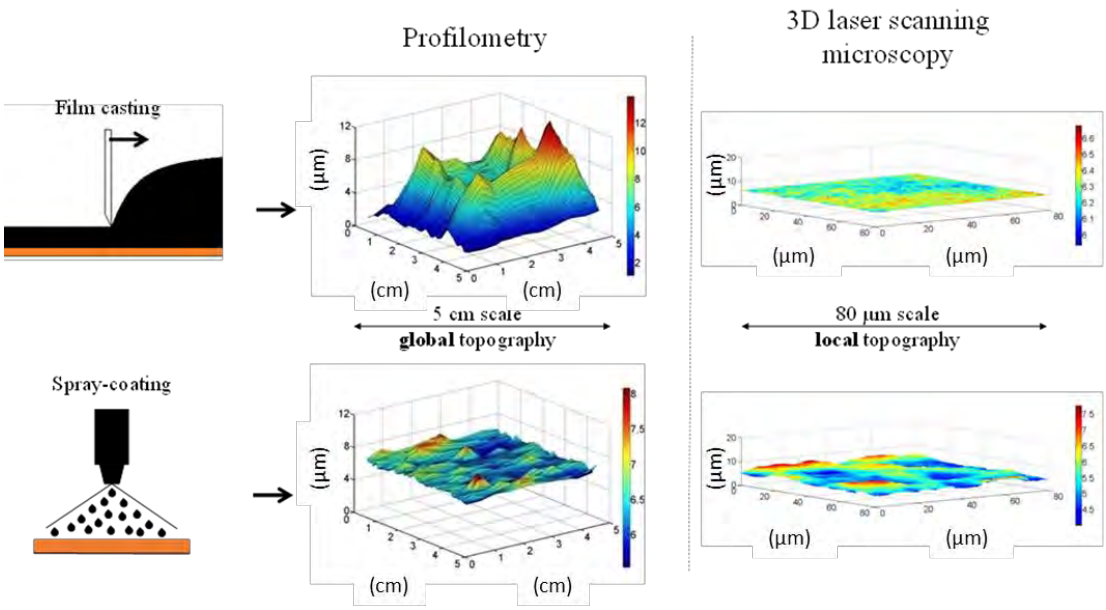


**FIGURE 1**: Topography of layers (XC-72R) prepared by film casting (up) and spray-coating (down) measured by profilometry (left) and 3D microscopy (right) (Deschamps, 2020).

**TABLE 1**: Electrical ($\rho_{el}$)and ionic ($\rho_{ion}$) resistivities for layers made of carbon black or carbon xerogel and Nafion, as a function of the N/C ratio and the carbon xerogel pore texture.

| **Carbon** | **XC72R** | **XC72R** | **XC72R** | **CX45** | **CX85** | **CX210** |
|---|---|---|---|---|---|---|
| N/C | 1 | 2 | 4.6 | 1 | 1 | 1 |
| $\rho_{el}$ (Ω.m) | **0.96** | 2.7 | **24** | **234** | **86** | **186** |
| $\rho_{ion}$ (Ω.m) | **37** | 14 | **6.9** | 52 | 43 | 35 |

## CONCLUSIONS

This work sheds light on features that are quite often overlooked in fuel cell catalytic layer studies, *i.e.* the quality of the layer deposition and its electrical/ionic conductivity, while both have strong impacts on the behaviour of the catalytic layer in the fuel cell, especially at high current densities. In particular, the electrical resistance cannot be neglected if carbon black is replaced by a nanostructured carbon material such as a xerogel with µm-sized particles: on the contrary, it may become the limitating transport phenomenon in the final catalytic layer, which has to be taken into account when designing Membrane-Electrode Assemblies from innovative catalyst structures.

**Acknowledgements**

The authors thank the F.R.S-FNRS and the Walloon Region (project Hylife) for the financial support.

**References**

Deschamps, F., Mahy, J. G., Léonard, A.F., Lambert, S.D., Dewandre, A., Scheid, B. and Job, N. (2020) A practical method to characterize PEMFC catalyst layer topography: application to two coating techniques and two catalyst supports. *Thin Solid Films* 695, 137751. https://doi.org/10.1016/j.tsf.2019.137751

Job, N., Pirard, R., Marien, J. and Pirard, J.-P. (2004). Porous carbon xerogels with texture tailored by pH control during sol-gel process. *Carbon* 42, 619-628. https://doi.org/10.1016/j.carbon.2003.12.072

Maillard, F., Job, N. and Chatenet, M. (2013) *In*: New and Future Developments in Catalysis. Batteries, Hydrogen Storage and Fuel Cells (Ed. S. Suib), 1st edition, Elsevier, pp. 407-428.

20 C 22 arbon 2022

# Monodisperse Porous Carbon Nanospheres with Ultra-High Surface Area for Energy Storage in Electrochemical Capacitors

**Noel Díez, Marta Sevilla, Alba Fombona-Pascual and Antonio B. Fuertes**
Instituto de Ciencia y Tecnología del Carbono (INCAR), CSIC, Francisco Pintado Fe 26, 33011 Oviedo, Spain
Email: noel@incar.csic.es

**Keywords**
carbon nanoparticle, porous carbon, electrochemical capacitor

## INTRODUCTION

Carbon nanomaterials have generated a great interest for electrochemical applications given their good dispersibility and mixing, large external surface area for chemical modification and short diffusional pathways. To be used in supercapacitors, these nanoparticles must also have a large specific surface area and a controlled pore size. However, the production of highly porous carbon nanoparticles (d ≤ 100 nm) by easy and sustainable procedures is still a significant challenge. In this work we present a straightforward synthesis strategy to produce highly porous carbon nanospheres with a monodisperse size distribution (d ~ 100 nm) and ultra-high BET surface areas (>3000 $m^2$ $g^{-1}$) associated to micropores and small mesopores (< 4 nm). Pyrrole has been selected as the carbon precursor as it can be easily polymerized in the form of nanospheres, and polypyrrole has a high carbon yield (> 50%). The polymeric nanospheres were directly activated with benign potassium bicarbonate ($KHCO_3$), yielding highly porous nanoparticles that retained their morphology and remained uncoalesced. These nanoparticles were analysed as the electrode material in symmetric electrical double layer capacitors using aqueous and organic electrolytes, showing a high capacitance and an excellent electrochemical response at high power demand.

## EXPERIMENTAL

Polypyrrole nanospheres were synthesized in aqueous media following the procedure reported by Lee *et al.* (Kwon, 2010). Briefly, PVA was dissolved in distilled water under vigorous stirring and, then, $FeCl_3$ was added and stirred for 1 h. Subsequently, recently distilled pyrrole was slowly added. After 2 h under stirring, the solid black product was collected by centrifugation, washed with water and lyophilised. The nanoparticles were chemically activated by using a solution of $KHCO_3$ ($KHCO_3$/PPy wt. ratio=6). After evaporating the water, the solid mixture was heated up to 750-950 ºC for 1 h in nitrogen flow. The carbonized product was washed using distilled water and dried at 120 ºC (Diez, 2022).

## RESULTS AND DISCUSSION

The polymerization of pyrrole in the presence of PVA as stabilizing agent and $FeCl_3$ as oxidant gives rise to polymer nanoparticles with a mean diameter of 112 nm. After mixing with $KHCO_3$ and a subsequent thermal treatment, the carbonization of the polymer and the generation of internal pores takes place. During this treatment, the bicarbonate decomposes to potassium carbonate at 150-200 ºC (eq. 1). At higher temperatures (>700 ºC), the carbonate oxidizes the carbonaceous matter (eq. 2), which, together with the intercalation of K vapours, leads to the generation of microporosity. At higher temperatures (>850 ºC), the carbonate decomposes to $K_2O$ and $CO_2$ (eq. 3), both of which can further oxidize the carbon, enlarging thus the micropores or generating new microporosity. After activation, the inorganic impurities were removed by simply water washing.

$2\ KHCO_3 \rightarrow K_2CO_3 + CO_2 + H_2O$ [1]

$K_2CO_3 + 2\ C \rightarrow 2\ K + 3\ CO$ [2]

$K_2CO_3 \rightarrow K_2O + CO_2$ [3]

**Morphology and Physicochemical Properties of the Porous Carbon Nanoparticles**

After activation, the size of the porous carbon nanospheres (PCNs) is slightly reduced to 90-97 nm, depending on the activation temperature. Remarkably, the nanospheres did not agglomerate and retained their spherical morphology (Figure 1a). A closer inspection of the activated materials reveals that the porous nanoparticles consist of randomly oriented graphene-like layers enclosing narrow micropores (Figure 1a, inset). The $N_2$ adsorption isotherms of the PCNs are of type Ib, which reveals that their porosity is made up of micropores and small mesopores (Figure 1b). The broadening of the knee at low relative pressures with the increase of the activation temperature indicates a widening of the pore size. In fact, the pore size distributions (Figure 1c) indicate a decrease in the number of pores with a size of ~ 0.8 nm and an enlargement of the second pore system that extends to the mesopore range, likely due to the additional carbon etching produced by the $K_2CO_3$ decomposition products. As shown in Table 1, the PCNs have ultra-high BET surface areas exceeding 3000 $m^2\ g^{-1}$, as well as large pore volumes of 1.4-1.8 $cm^3\ g^{-1}$. Carbonization in the absence of $KHCO_3$ led to carbon nanoparticles with low surface area and pore volume (sample CNP, Table 1). Despite the carbon precursor being a N-rich substance, the activation brings about the complete removal of N-groups (N content < 1.2 wt%). The removal of oxygen with the increase of temperature (from 7.5wt% at 750 ºC to 3.8 wt% at 950 ºC), together with the progressive rearrangement of carbon atoms, leads to the increase of their electrical conductivity to values that compare well with those of commonly used conductive additives.

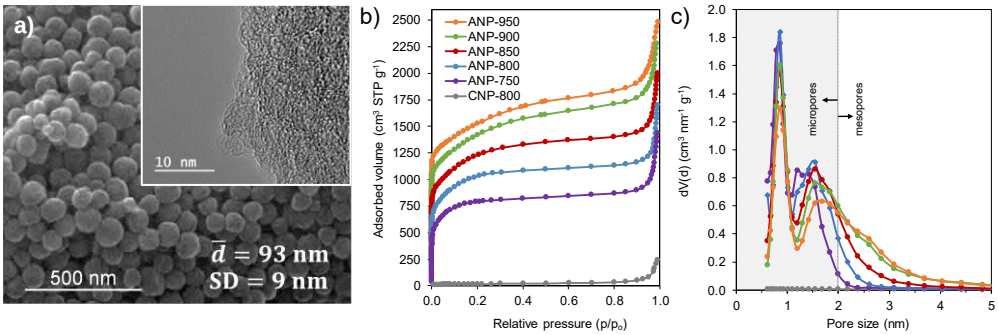


**FIGURE 1**: (a) Scanning electron microscope and (inset) transmission electron microscope images of ANP-750. (b) $N_2$ isotherms and (c) pore size distributions of the PCNs obtained at different temperatures.

**TABLE 1**: Physico-chemical properties of the carbonized (CNP) and activated (ANP) nanospheres.

| Sample code | Carbon yield [%] | Diameter [nm] | $S_{BET}$ [$m^2\ g^{-1}$] | $V_p$ [$cm^3\ g^{-1}$] | $V_{micro}$ [$cm^3\ g^{-1}$] | Electrical conductivity [$S\ cm^{-1}$] | Electrode density [$g\ cm^{-3}$] |
|---|---|---|---|---|---|---|---|
| CNP-800 | 54 | 89 ± 11 | 60 | 0.08 | 0.01 | 3.1 | - |
| ANP-750 | 31 | 93 ± 9 | 3040 | 1.40 | 1.16 | 1.6 | 0.40 |
| ANP-800 | 27 | 90 ± 11 | 3090 | 1.50 | 1.21 | 2.4 | 0.38 |
| ANP-850 | 26 | 93 ± 10 | 3010 | 1.62 | 1.16 | 3.7 | 0.34 |
| ANP-900 | 19 | 96 ± 12 | 2980 | 1.81 | 1.07 | 4.2 | 0.35 |
| ANP-950 | 14 | 97 ± 11 | 2640 | 1.71 | 0.91 | 7.6 | 0.37 |

**Electrochemical Properties of the Porous Carbon Nanoparticles**

Due to their large specific surface area, short ion migration pathways and good electronic conductivity, a large energy storage capacity and fast electrochemical response is expected from the PCNs. Thus, electrodes with a mass loading typical of commercial EDLC (~9-10 mg $cm^{-2}$) were assembled in symmetric cells using 1 M $H_2SO_4$, 1 M $TEABF_4$ in acetonitrile (AN) and EMIMTFSI in AN as the electrolytes. The Nyquist plots obtained for the PCNs show a much shorter Warburg region compared to that of the commercial YP-17D carbon, which indicates an easier diffusion of the electrolyte ions throughout their porosity. As shown in Figure 2b, the relaxation time constant calculated for the PCNs is also much lower than that of YP-17D, especially in the case of the PCNs containing small mesopores. The charge storage capacity and rate capability of the PCNs was evaluated by galvanostatic charge-

discharge experiments. In the aqueous electrolyte, ANP-750 achieves the highest capacitance, of 262 F $g^{-1}$, by virtue of its larger micropore volume. The commercial activated carbon (AC) shows a capacitance of only 135 F $g^{-1}$, and fails at current densities over 40 A $g^{-1}$. On the contrary, the PCNs withstand ultrahigh current densities of up to 80 A $g^{-1}$ in the case of the micro-mesoporous ANP-900. Even in volumetric terms, the electrode made up of the ANP-750 nanospheres surpasses that made out of YP-17D (89 *vs.* 78 F $cm^{-3}$), despite its lower electrode density (0.40 *vs.* 0.68 g $cm^{-3}$). Replacing the aqueous electrolyte by 1 M $TEABF_4$ in AN and EMIMTFSI in AN allowed increasing the cell voltage up to 2.7 and 3 V, respectively. Despite the lower conductivity and higher viscosity of these electrolytes, the PCNs were able to withstand much higher current densities than the commercial AC. Remarkably, the wider pore size distribution of ANP-900 allowed taking full advantage of the high voltage EMIMTFSI/AN electrolyte, and could be charged and discharged up to a high current density of 50 A $g^{-1}$ retaining 70 % of its maximum capacitance. In this electrolyte, ANP-750 and ANP-900 achieved a maximum energy density of 52 and 48 Wh $kg^{-1}$, the latter retaining 31 Wh $kg^{-1}$ at a high-power density of 31 kW $kg^{-1}$. The PCNs could be steady cycled up to 10000 charge-discharge cycles, experiencing a capacitance loss lower than 6 % and 14 % for aqueous and organic electrolytes, respectively.

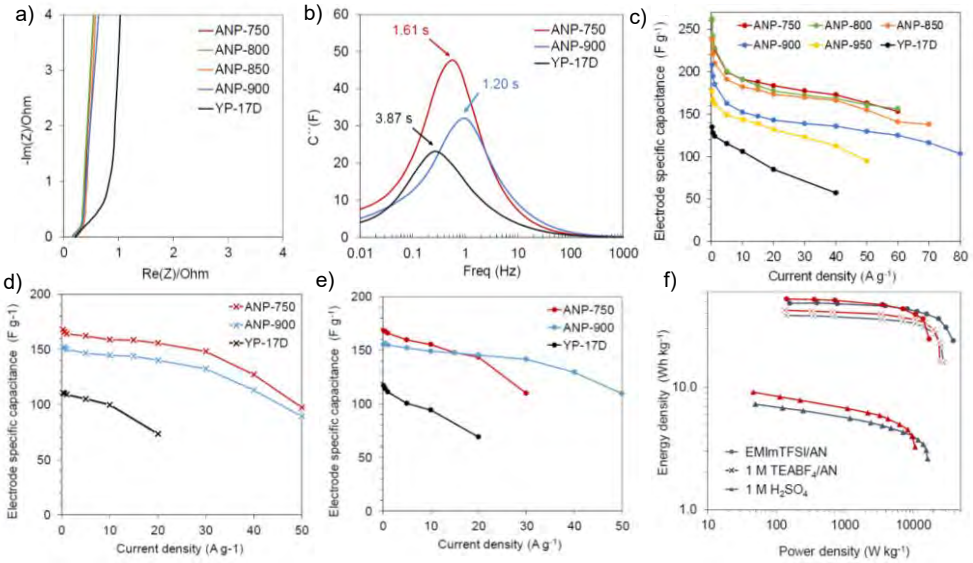


**FIGURE 2**: Electrochemical characterization of the PCNs: (a) Nyquist and (b) Bode plots in 1 M $H_2SO_4$. Rate performance in (c) 1 M $H_2SO_4$, (d) 1 M $TEABF_4$/AN and (e) EMIMTFSI/AN. (f) Ragone plot.

## CONCLUSIONS

Monodisperse, highly porous carbon nanospheres have been successfully obtained by direct activation of polypyrrole nanoparticles with $KHCO_3$. They combine a high electronic conductivity with an ultra-high BET surface area (>3000 $m^2$ $g^{-1}$) and short ion diffusion pathways. Due to the unrestricted access of electrolyte ions to their microporosity, they show high capacitance, good rate capability and excellent cycling stability in aqueous and organic electrolytes.


### Acknowledgements

This research work was supported by projects RTI2018-093712-B-I00 (MCIU/AEI/FEDER, UE) and IDI/2018/000148 (regional GRUPIN2018).


### References


Kwon, O.S., Hong, J.Y., Park, S.J., Jang, Y., Jang, J. (2010). Resistive gas sensors based on precisely size-controlled polypyrrole nanoparticles: effects of particle size and deposition method. *J. Phys. Chem. C*, 114, [44], 18874-18879. https://doi.org/10.1021/jp1083086

Diez, N., Sevilla, M., Fombona-Pascual, A., Fuertes, A.B. (2022). Monodisperse porous carbon nanospheres with ultra-high surface area for energy storage in electrochemical capacitors. *Batteries & Supercaps*, 5, e20210016. https://doi.org/10.1002/batt.202100169

20 C 22 arbon 2022

# Enriched activated carbons from chitosan for indoor air removal of nitrogen dioxide and formaldehyde

**Laurent Duclaux[1], Fabrice Guy[1,2], Michel Ondarts[2], Laurence Reinert[1], Jonathan Outin[2], Yasushi Soneda[3],**

[1]Université Savoie Mont Blanc, CNRS, EDYTEM, F-73000 Chambéry, France
Email: laurent.duclaux@univ-smb.fr

[2]Université Savoie Mont Blanc, CNRS, LOCIE, F-73000 Chambéry, France
[3]Institute of Advanced Industrial Science and Technology, Energy Process Research Institute, 16-1 Onogawa, Tsukuba, Ibaraki 305-8569, Japan

**Keywords**
Activated carbon, indoor air, nanoparticles

## INTRODUCTION

For the past few decades, indoor air quality has been recognized as an important public health concern with a non-negligible economic impact. Indeed, people are commonly exposed to household air pollutants including particulate matter, formaldehyde ($CH_2O$), carbon monoxide (CO), ozone ($O_3$), nitrogen dioxide ($NO_2$) and some volatile organic compounds (VOCs). The indoor air quality can be improved by reduction of pollution sources, and the optimization of ventilation performances (diluting pollutants issued from indoor sources). But an alternative consists in removing pollutants by adsorbent filters based on Activated Carbons (ACs) integrated in heating, ventilation and air-conditioning system. Some investigations are nevertheless needed to overcome process limitations as some pollutants such as formaldehyde are poorly adsorbed due to moisture competitive adsorption and a low affinity that drastically decreases the adsorption capacities (Suresh et al., 2018). In the case of $NO_2$, a chemical reduction to NO occurs on ACs, yielding to the formation of oxygenated surface groups thus its physisorption is rather limited.

Formaldehyde can be removed on ACs by physisorption, by chemisorption on amine surface groups or by catalytic degradation on supported metallic or oxide nanoparticles. Previous studies have shown both the importance of a high ultramicroporous volume (Song et al., 2017) and the presence of nitrogen groups for the removal of formaldehyde by ACs (Suresh et al., 2018). The role of a high microporosity and the presence of appropriated oxygenated groups on ACs was pointed out for increasing the $NO_2$ removal (Ghouma et al., 2018).

Carbon beads were reported to be prepared from biopolymers such as alginate and chitosan (Guy et al., 2021). Chitosan, a random linear copolymer of β-(1–4)-linked D-glucosamine and N-acetyl-D-glucosamine mainly derived from crustacean waste, is a carbon materials precursor of interest because of its abundance and its high content in nitrogen groups. In this study, new nitrogen enriched ACs in form of beads, possibly supported by Cu/CuO nanoparticles, have been prepared by tailored activation of chitosan,to make them suitable for the purification of formaldehyde and nitrogen dioxide from indoor air.

## ACTIVATED CARBONS PREPARATION AND CHARACTERIZATION

### Activated carbons preparation

The AC beads were prepared by thermochemical activation of chitosan hydrogel spheres enriched or not in $CuCl_2$ and impregnated with KOH or $NH_3$ solutions at 63 wt. % impregnation ratio with respect to the chitosan precursor. This activation was performed at 500°C and 700°C for the hydrogels

impregnated with KOH (giving samples referred to KOH500-63, KOH700-63, respectively), and at 900°C for the one impregnated with $NH_3$ (referred to $NH_3$900-63). KOH and $NH_3$ had a dual role of chitosan gelation agent and activating agent generating the microporosity. The $CuCl_2$ addition allows the growth of CuO (and Cu at 500°C) nanoparticles supported on the carbons activated by KOH (referred to KOH500-63Cu and KOH700-63Cu) or activated by $NH_3$ (named $NH_3$900-63Cu).

**Textural and chemical characterization of adsorbents**

The BET specific surface areas ($S_{BET}$) of the synthesized ACs vary from ~ 640 $m^2.g^{-1}$ to 1145 $m^2.g^{-1}$ and from ~ 1260 $m^2.g^{-1}$ to 1340 $m^2.g^{-1}$ for activation by KOH and by $NH_3$, respectively (Table 1). The highest $S_{BET}$ was obtained for after activation by $NH_3$ (Table 1, sample $NH_3$900-63). All ACs samples were found mainly microporous (⌀ pores < 2 nm, determined by $N_2$ adsorption at 77K) with the preponderance of ultramicropores (⌀ pores < 0.8 nm, determined by $CO_2$ adsorption at 273K). The presence of homogeneously dispersed Cu and copper oxide nanoparticles (in the AC beads obtained from Cu-doped chitosan) was evidenced by SEM and XRD (Guy et al., 2021). The prepared samples possess pyridine, pyrrole, amide and amine type nitrogen functional groups observed by X-Ray Photoelectron Spectroscopy (XPS) analyses. Elemental analyses indicate a higher amount of nitrogen groups and a lower content of oxygen groups for the samples activated by $NH_3$. The water sorption isotherms by the ACs measured at 25°C in the $P/P_0$ range [0-0.8] showed that carbons activated by $NH_3$ have a significantly lower affinity with water vapor than those activated by KOH.

**TABLE 1**: Summary of ACs structural and chemical properties.

| | Textural properties | | | | surface groups content from XPS (wt. %) | | | |
|---|---|---|---|---|---|---|---|---|
| | $S_{BET}$ ($m^2.g^{-1}$) | $V_{ultramicropore}$ ($cm^3.g^{-1}$) | $V_{micropore}$ ($cm^3.g^{-1}$) | $V_{mesopore}$ ($cm^3.g^{-1}$) | O=C | O-C | Pyridine | Amide, Amine Pyrrole |
| KOH500-63 | 642 | 0.24 | 0.29 | 0.02 | 34.4 | 4.4 | 1.7 | 3.8 |
| KOH700-63 | 1081 | 0.44 | 0.55 | 0.02 | 21.4 | 11.7 | 0.4 | 2.3 |
| $NH_3$900-63 | 1340 | 0.53 | 0.60 | 0.03 | 2.4 | 12.1 | 5.7 | 3.7 |
| KOH500-63Cu | 608 | 0.23 | 0.25 | 0.09 | 17.5 | 9.7 | 2.7 | 4.2 |
| KOH700-63Cu | 1145 | 0.35 | 0.41 | 0.09 | 4.8 | 19.4 | 2.7 | 4 |
| $NH_3$900-63Cu | 1257 | 0.48 | 0.54 | 0.04 | 1.8 | 10.3 | 6.4 | 13.4 |

## NITROGEN DIOXIDE AND FORMALDEHYDE REMOVAL

**Experimental**

The breakthrough curves were studied on ACs powder (20 mg) obtained from AC beads milling, at 850 ppbv initial concentration of $NO_2$ (or $CH_2O$) in air (total flow: 1,5 $mL.min^{-1}$, gas speed in empty column: 1.98 $m.s^{-1}$) upon given relative humidity (0% RH, 20% RH, and 50 % RH). For the most relevant samples, concentrations in the range 250 to 1500 ppbv were studied. Some breakthrough tests were performed on beads (250 mg) in a cylindrical column (diameter 15 mm, flow: 4.5 $L.min^{-1}$).

**Nitrogen dioxide removal**

For carbons activated by $NH_3$, the maximum $NO_2$ removal amount (~140 $mg.g^{-1}$) is reached in dry air and is quite higher than the average values reported in the literature. The $NO_2$ removal amount decreases as increasing humidity in relation with a competition effect with water.

For carbons from pure chitosan activated by KOH, a maximum $NO_2$ removal uptake of about 80 $mg.g^{-1}$ is reached at RH = 20%. This means that water molecules interfere in the $NO_2$ adsorption mechanism. $NO_2$ can be directly hydrated in nitrous acid ($HNO_2$) and nitric acid ($HNO_3$) mixture or chemisorbed by reaction with oxygenated carbon atom according to -(CO) + $NO_2$→ $C(ONO_2)$ reaction. The $C(ONO_2)$ hydration can also yield to $HNO_2$ and $HNO_3$, thus increasing the AC pH after testing.

The presence of nanoparticles induces a $NO_2$ catalytic degradation into nitrogenous subspecies. The maximum of $NO_2$ degradation is reached at RH = 20% which could be explained by the free radicals' formation in water, thus improving this catalytic effect. The catalytic conversion rate at 20% RH is 1.3 $10^{-8}$ $mol.g^{-1}.s^{-1}$ for samples NH3900-63Cu and KOH700-6Cu.

**Formaldehyde removal**

The maximum formaldehyde adsorption capacity at RH = 50% reaches about 43 $mg.g^{-1}$ for carbon activated by $NH_3$ from pure chitosan (sample $NH_3$900-63). This can be related to the presence of high amounts of ultramicropores (⌀ pores < 0.8 nm) and nitrogen functional groups on its surface (Table 1). The adsorbed uptake varies linearly as the concentration increases from 250 to 1500 ppbv according to the Henry's law. For all the carbons prepared from pure chitosan, the maximum adsorption capacity is achieved in dry air.

Similarly, the ACs including CuO nanoparticles, display their highest adsorption capacity at 0 % RH. The nanoparticles presence induces the $CH_2O$ catalytic degradation into $CO_2$ and $H_2O$ regardless of the tested relative humidity. The $CH_2O$ conversion rate is the highest at 20% RH (2.7 $10^{-8}$ $mol.g^{-1}.s^{-1}$ for sample $NH_3$900-63Cu) suggesting that the water presenceimproves the CuO catalytic activity.

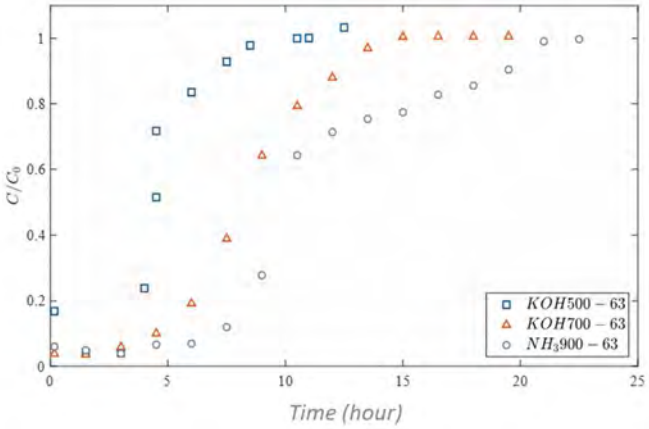


**FIGURE 1**: Formaldehyde breakthrough adsorption curves on ACs from chitosan ($C_0$=850 ppbv and 50 % RH).

**CONCLUSIONS**

The $NH_3$-activated beads were found more efficient for formaldehyde adsorption and less effective for $NO_2$ removal than KOH-activated ones. This is related with a lower number of oxygenated groups and higher amount of nitrogen groups such as pyridinic and pyrrolic ones (evidenced by XPS) in $NH_3$ ACs (~ 10 wt. %) compared to KOH-activated ones. The removal uptake capacities at 50 % RH were found around 140 $mg.g^{-1}$ and 60 $mg.g^{-1}$ for $NO_2$ and formaldehyde, respectively. The $CH_2O$ adsorption competes with water vapor adsorption while $NO_2$ removal is promoted by humidity through chemisorption reactions (Gao et al., 2011). For the AC beads including CuO nanoparticles, both for $NO_2$ and $CH_2O$ removal, a catalysis plateau was observed in the breakthrough curves showing on the one hand the possible catalytic reduction of $NO_2$ (maximum at 20% RH) and on the other hand the $CH_2O$ decomposition in water and $CO_2$ (40% of the total removed formaldehyde).

**References**

Gao, X., Liu, S., Zhang, Y., Luo, Z, Ni, M. and Cen, K. (2011). Adsorption and reduction of $NO_2$ over activated carbon at low temperature. *Fuel Processing Technology,* 92, [1],.139-146. https://doi.org/10.1016/j.fuproc.2010.09.017

Ghouma, I., Jeguirim, M., Limousy, L., Bader, N., Ouederni, A. and Bennici, S. (2018). Factors Influencing $NO_2$ Adsorption/Reduction on Microporous Activated Carbon: Porosity vs. Surface Chemistry. *Materials,* 11, [4], 622. https://doi.org/10.3390/ma11040622

Guy, F., Runtti, H., Duclaux, L., Ondarts, M., Reinert, L., Outin, J., Gonze, E., Bonnamy, S. and Soneda, Y. (2021). Synthesis and characterization of Cu doped activated carbon beads from chitosan. *Microporous and Mesoporous Materials,* 322, 111147. https://doi.org/10.1016/j.micromeso.2021.111147

Song, Y., Qiao, W., Yoon, S.-H., Mochida, I., Guo, Q. and Liu, L. (2007). Removal of formaldehyde at low concentration using various activated carbon fibers. *Journal of Applied Polymer Science,* 106, [4], 2151–2157. https://doi.org/10.1002/app.26368

Suresh, S. and Bandosz, T.J. (2018). Removal of formaldehyde on carbon -based materials: A review of the recent approaches and findings. *Carbon,* 137, 207–221. https://doi.org/10.1016/j.carbon.2018.05.023

20 C 22 arbon 2022

# How chemical defects influence the charging of nano-porous carbon-based supercapacitors?

**Romain Dupuis[1], Katerina Ioannidou[1] and Roland Pellenq[2]**
[1] LMGC, CNRS and Montpellier University, 490 Rue St Priest, 34000 Montpellier, France
[2] EpiDaPo Lab - CNRS and George Washington University
Children's National Medical Center | Children's Research Institute
111 Michigan Ave. NW, Washington, DC 20010, USA

Email: roland.pellenq@cnrs.fr

**Keywords**
Electrical double-layer supercapacitors, molecular simulations, nanoporosity

## INTRODUCTION

Ion desolvation and confinement are key physical processes in porous-carbon-based Electrical Double-Layer supercapacitors (EDL) undergoing charging and discharging cycles. The term of electrical double layer (EDL) capacitor comes from the classical picture of non-porous electrodes that accumulate oppositely charged ions at their vicinity upon voltage polarization in a mean-field dielectric continuum description of the solvent populated with point charged ions at a given concentration. This picture although very popular obviously does not hold for porous electrodes with sub-nanometric pores. In particular, the mean-field Gouy–Chapman–Stern description of a EDL fails in high molar concentrations and for pore sizes smaller than a few nanometers (typically 4 nm for car- 25 bon substrates). EDL predictions usually rely on the Poisson-Boltzmann theory and modified versions such as Debye-Hückel. Presently, there is no theory capable of solving the electrostatics problem for ions confined in the nanopores of a disordered porous carbon material commonly used in electrochemical devices.

## METHODS

In this work, we proposed a modified version of the constant charge CC method guided by experimental and theoretical DFT results showing the key role of chemical defects and subnanopores in the building up of the capacitance (Chiamola, 2006). We call this approach "Chemistry Driven Charge localization (CDCL, Dupuis 2022). The local electrostatic field generated by the matrix defects (in the present work non sp2-carbon atoms and edge hydrogen species) drives ion adsorption on the electrode external surface as well as in the whole porosity including the sub-nanopores. Our electrodes are made of porous carbon texture that is found to be realistic for charcoal, activated carbon as well as for mature kerogen (Pikunic 2003). It was obtained using Hybrid reverse Monte Carlo with a density around 1g/cc. Note that our activated carbon texture mainly contains sub-nanometric pores. We used MD simulations with the COMPASS force field at 300K. The electrodes are separated by 30Å on both sides. The system is periodic in all directions and it is initially prepared with water molecules, sodium and chloride ions in the inter-electrodes regions corresponding to a salt concentration of 0.67 132 mol/L (see Fig. 1).

## RESULTS

Under polarization this drives ionic and water adsorption in sub-nanometric pores. We provide insights at the molecular level looking into the free distribution in the carbon nanopores. First we observe an asymmetrical desolvation process of sodium and chloride ions at the external surface of the electrodes. We found that the ionic distribution at the external surface of the electrodes is

consistent with the Debye-Hückel electric potential equation. In a second stage, we demonstrate that the nano-porosity of the electrodes is filled with ions and scarce water molecules and contributes to a significant part of the overall capacitance (See Fig. 1) that is in quantitative agreement with experiment with capacitance values at around 100 F/g for carbon-based supercapacitors (Simon 2008). We also found that a non-negligible fraction of desolvated ions are irreversibly trapped in the core of electrodes during discharge. While maintaining the overall electroneutrality of the simulation cell, we found that anodes and cathodes do not carry the same amount of ions at all time steps leading to charge unbalance.

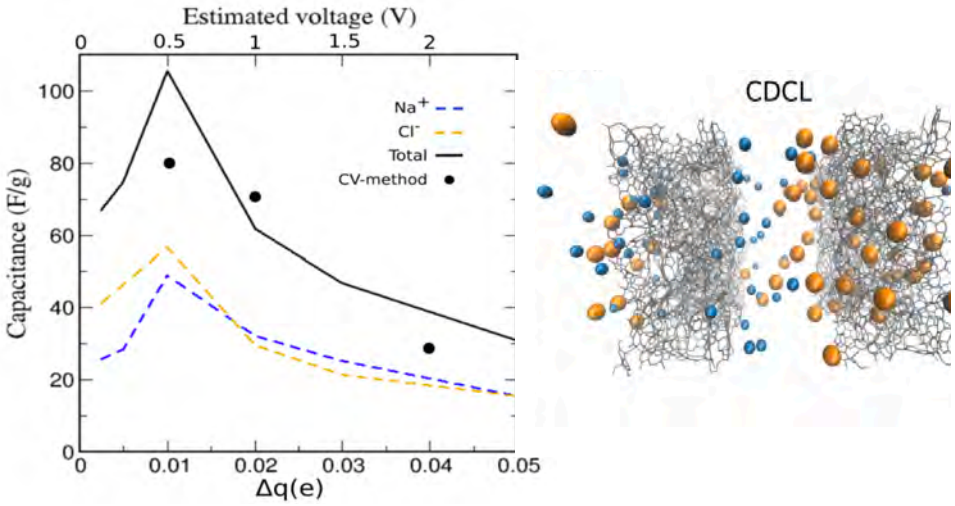


**FIGURE 1**: left: capacitance as a function of voltage showing the different contributions of cations and anions, right: atomistic configuration of sodium (blue) and chlorine (orange) ions in the 2 electrodes under 1 V polarization (water molecules not shown)

**CONCLUSIONS**

We propose a new approach to describe the charge and discharge process in sub-nanoporous carbon made electrodes, in a supercapacitor setting, that we call chemically driven charge localization model (CDCL). Despite its mean-field character, the CDCL approach is an improvement of the current standard methods to simulate charged devices at the atomic scale, namely the constant charge and the constant voltage methods that are ineffective to correctly describe ionic docking in sub-nanopores. Informed from DFT calculations, the CDCL method consists in localizing charges on defective non-sp2 carbon sites, including chemical or topological defects. By contrast to the standard methods, this allows simulating both adsorption on the electrodes external surfaces and in-sub-nanopore docking. Applied to a realistic texture of nanoporous carbon, we could unravel the fundamental processes underlying the capacitive effect of a sub-nanoporous carbon-based supercapacitor device in operation. We show in particular that subnanometric pores constitute about 20% of the capacitance of such a device using a standard aqueous electrolyte. In more details, we show that the docking of ions in pores is preceded by an assymetrical desolvation at the vicinity of the external pore surface. The desolvation process is actually different for sodium and for chloride ions as the hydration shell of sodium is tighter than that of chloride. Once ions are desolvated, they can access nanopores; sub-nanopores being mostly populated with bare ions in agreement with in-situ X-rays experiments (Prehal 2017).

**References**

Chamiola J, et al, Anomalous increase in carbon capacitance at pore sizes less than 1 466 nanometer. *Science* 313, 1760–1763 (2006).

Dupuis R, et al, How chemical defects influence the charging of nanoporous carbon-based supercapacitors? PNAS, 2022, https://doi.org/10.1073/pnas.2121945119Pikunic J, et al, Structural modeling of porous carbons: Constrained reverse monte carlo method. *Langmuir* 19, 8565–8582 (2003).

Prehal C, et al., Quantification of ion confinement and desolvation in nanoporous carbon 460 supercapacitors with modelling and in situ x-ray scattering. *Nat. Energy* **2**, 16215 (2017).

Simon P et al, Materials for electrochemical capacitors. *Nat. Mater*. **7**, 845–854 (2008).

20 C 22 arbon 2022

# Operando electrochemical dilatometry – thickness change measurements of carbon electrodes in sodium-ion batteries

**Ines Escher, Guillermo A. Ferrero, Mustafa Goktas, Yuliia Kravets, Philipp Adelhelm**
Humboldt Universität zu Berlin, Brook-Taylor-Str. 2, 12489 Berlin, Germany
Email: ines.escher@hu-berlin.de

**Keywords**
electrochemical dilatometry, sodium-ion batteries, anode material

**EXTENDED ABSTRACT**

In situ and operando techniques become more and more important tools to study electrode and cell reactions during charging and discharging. Operando electrochemical dilatometry (ECD) is a powerful method to investigate the thickness change of an electrode during electrochemical cycling. In contrast to X-ray diffraction or spectroscopic methods, that provide information on the chemical/structural changes during the electrode reaction, ECD gives information on the overall expansion of the electrode, including also influences from inactive electrode components, e.g. the binder. ECD has been used to investigate different electrode materials for lithium- and sodium-ion batteries (LIBs, SIBs) (see also Figure 1). (Escher et al., 2022) The focus for this abstract should be on carbon materials as negative electrodes in sodium-ion batteries.

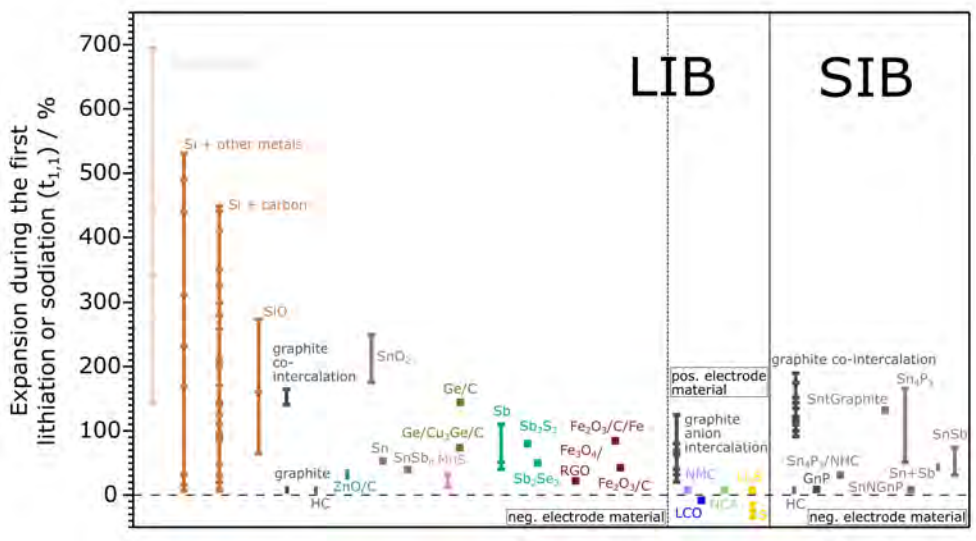


**FIGURE 1**: Thickness change of several electrode materials for LIBs and SIBs in the first cycle, measured with electrochemical dilatometry. Reproduced under terms of the CC-BY license. (Escher et al., 2022) Copyright 2022, Wiley-VCH GmbH.

Graphite is the most common anode material for lithium-ion batteries. In this case, binary graphite intercalation compounds (b-GICs) are formed during the charging process. (Nayak et al., 2018) Similar reactions are found for other alkali metals except sodium for which the formation of sodium rich b-GICs is thermodynamically not favorable. (Moriwake et al., 2017) The problem can be

overcome by the intercalation of solvated sodium ions, resulting in the formation of a ternary graphite intercalation compound (t-GIC). (Jache and Adelhelm, 2014) This co-intercalation reaction results in a quite high electrode expansion, which can be easily followed using ECD. Even though, the reaction is highly reversible (Goktas et al., 2018) a reduction of the expansion is favorable, especially for the use in a full cell application. The comparison of the electrode expansion using different binder materials and the addition of a co-solvent showed promising outcomes using CMC (sodium salt of carboxy methylcellulose) as binder and the addition of 10 vol% ethylenediamine. (Escher et al., 2021b)

Hard carbons have also become promising anode materials in SIBs due their redox potential close to $Na^+/Na$, a storage capacity which is typically between 150 – 350 mAh $g^{-1}$ and especially low cost. (Dou et al., 2019) Even though, a lot of research has been done on this field the storage mechanism is not totally clarified yet. Operando ECD helps to get further insights into the storage mechanism of a commercial hard carbon electrode. The storage mechanism of the intercalation of sodium- and lithium-ions has been compared and differences, especially in the low voltage region, were detected. In this way, an intercalation – pore filling – plating process was proposed for the storage of sodium ions whereas an intercalation – pore filling mechanism was found in the case of lithium ions (see Figure 2). (Escher et al., 2021a)

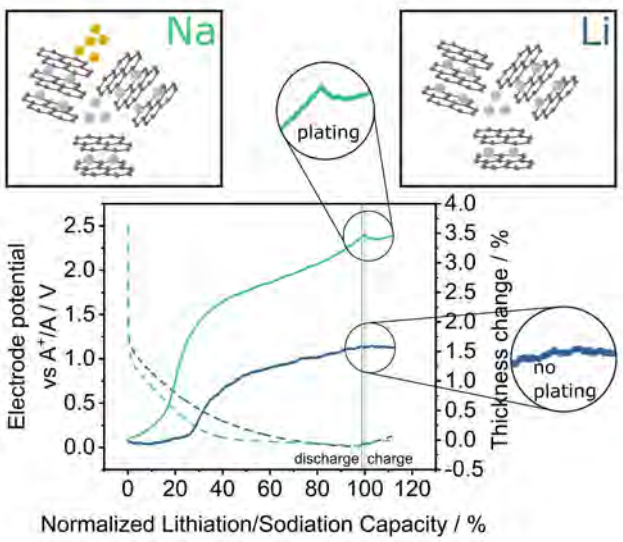


**FIGURE 2**: Electrochemical dilatometry results for the storage of sodium and lithium ions in hard carbon electrodes. Differences in the low voltage region can be clearly seen. Dashed lines indicate the electrode potentials, full lined the dilatation. Reproduced under terms of the CC-BY license. (Escher et al., 2021a) Copyright 2021, Wiley-VCH GmbH.

In conclusion, electrochemical dilatometry was found to be a powerful tool to get further insights into the influence of different components (binder, co-solvent) on the co-intercalation of sodium ions in graphite as well the charge storage mechanism in hard carbon electrodes.

**Acknowledgements**

The projects have received funding from the Deutsche Forschungsgemeinschaft (DFG, German Research Foundation, Grant Nos. 298787956 and 325774457), the European Research Council (ERC) under the European Union's Horizon 2020 research and innovation programme (Grant Agreement No. 864698, SEED) and from the EIG Concert Japan program (LIBRA, BMBF 01DR18003). The authors thank BASF for providing high purity sodium and Kureha Corp. for providing the hard carbon. The authors thank Dongjiu Xie (Group of Prof. Yan Lu)

from the Helmholtz-Zentrum Berlin for the BET measurements. The authors thank Stefanie Markstein from the Humboldt Universität zu Berlin for the elemental analysis. Open access funding enabled and organized by Projekt DEAL.

**References**

Dou, X., Hasa, I., Saurel, D., Vaalma, C., Wu, L., Buchholz, D., Bresser, D., Komaba, S. & Passerini, S. (2019). Hard carbons for sodium-ion batteries: Structure, analysis, sustainability, and electrochemistry. *Materials Today,* 23, 87-104. https://doi.org/10.1016/j.mattod.2018.12.040

Escher, I., A. Ferrero, G., Goktas, M. & Adelhelm, P. (2021a). In Situ (Operando) Electrochemical Dilatometry as a Method to Distinguish Charge Storage Mechanisms and Metal Plating Processes for Sodium and Lithium Ions in Hard Carbon Battery Electrodes. *Advanced Materials Interfaces,* 9, [8], 2100596. https://doi.org/10.1002/admi.202100596

Escher, I., Hahn, M., A. Ferrero, G. & Adelhelm, P. (2022). A practical guide for using electrochemical dilatometry as operando tool in battery and supercapacitor research. *Energy Technology,* 10, [5], 2101120. https://doi.org/10.1002/ente.202101120

Escher, I., Kravets, Y., Ferrero, G. A., Goktas, M. & Adelhelm, P. (2021b). Strategies for Alleviating Electrode Expansion of Graphite Electrodes in Sodium-ion Batteries Followed by In Situ Electrochemical Dilatometry. *Energy Technology,* 9, [3], 2000880. https://doi.org/10.1002/ente.202000880

Goktas, M., Bolli, C., Berg, E. J., Novák, P., Pollok, K., Langenhorst, F., Roeder, M. v., Lenchuk, O., Mollenhauer, D. & Adelhelm, P. (2018). Graphite as Cointercalation Electrode for Sodium-Ion Batteries: Electrode Dynamics and the Missing Solid Electrolyte Interphase (SEI). *Advanced Energy Materials,* 8, [16], 1702724. https://doi.org/10.1002/aenm.201702724

Jache, B. & Adelhelm, P. (2014). Use of Graphite as a Highly Reversible Electrode with Superior Cycle Life for Sodium-Ion Batteries by Making Use of Co-Intercalation Phenomena. *Angewandte Chemie,* 126, [38], 10333-10337. https://doi.org/10.1002/ange.201403734

Moriwake, H., Kuwabara, A., Fisher, C. A. J. & Ikuhara, Y. (2017). Why is sodium-intercalated graphite unstable? *Rsc Advances,* 7, [58], 36550-36554. https://doi.org/10.1039/C7RA06777A

Nayak, P. K., Yang, L., Brehm, W. & Adelhelm, P. (2018). From lithium-ion to sodium-ion batteries: advantages, challenges, and surprises. *Angewandte Chemie International Edition,* 57, [1], 102-120. https://doi.org/10.1002/anie.201703772

Carbon 2022

# Influence of microwave power, weight, humidity and activated carbon added in microwave assisted pine chips pyrolysis for bio-carbon production

**Iván Esteve-Adell[1], Patricia Pérez Llamas[1], Mayte Gil-Agustí[1], Leire Zubizarreta[1], Alfredo Quijano-López[1,2] and Marta García-Pellicer[2]**

[1]Instituto Tecnológico de la Energía (ITE). Avenida Juan de la Cierva, 24, 46980, Paterna, Valencia, Spain

Email: ivan.esteve@ite.es

[2]ITE, Universitat Politècnica de València, Camino de Vera s/n Edificio 6C, 46022, Valencia, Spain

**Keywords**

Bio-carbon, biomass, microwave-assisted pyrolysis.

## INTRODUCTION

The generation of biomass waste in different sectors such as agriculture and forestry, urban or water purification plants is becoming a problem with serious consequences at the environmental level and from the economic point of view related to the costs derived from its management. The energy transition towards a better and more efficient energy production, is paving the way towards the use of waste generated in certain sectors, as energy sources or as raw materials for transformation into other valuable products. Traditional thermal transformation of biomass using pyrolysis to obtain biocarbons has been extensively used for many years. These high valuable biocarbons are of great interest in applications in different sectors such as energy storage, water effluents and gas streams purification. However, pyrolysis is a time and energy consuming process due to the low heating rates of electrical furnaces and the high energy necessary to reach the desired temperature.

In this context, microwave-assisted transformation of biomass residues into valuable biocarbons has encouraged extensive research due to the heating advantages against traditional thermochemical processes. Microwave technology offers a reduction in waste volume, high heating rate, selective heating, increased capability for testing in-situ due to possibility of portable equipment and low energy consumption compared to traditional pyrolytic processes.

Biomass is generally a poor microwave absorber. Therefore, in microwave-assisted biomass pyrolysis the introduction of carbonaceous additives, as microwave absorbing substances, is necessary to enhance the microwave absorption capacity and reach the desired temperatures quickly and effectively. In this work, the influence different parameters, such as microwave power, biomass amount, humidity and wt% of activated carbon on the pyrolysis temperature have been studied.

## EXPERIMENTAL

The biomass and activated carbon used in the microwave-assisted biomass pyrolysis were previously dried overnight in a stove oven at 105 ºC. The biomass particle size was less than 1 mm and the activated carbon was sieved between 20-150 µm particle size. Before the microwave-assisted pyrolysis reaction, the system with the dry sample was inerted with $N_2$.

To study the effect of microwave power, the rest of the pyrolysis parameters were fixed: 5wt% of activated carbon, same samples mass and samples previously dried.

On the other hand, to study the influence of humidity the samples were previously dried and subsequently the corresponding amount of water was added. The water was weighed and added to the mixture of biomass and activated carbon. Final sample humidity was also measured by thermobalance to check the value.

## RESULTS

The obtained results have shown that the reaction temperature increases with the amount of sample, the moisture content, the wt% of activated carbon and the microwave power.

The humidity increased the microwave-assisted pyrolysis temperature, achieving up to 556ºC with 50wt% of humidity samples. However, the heating rate observed was slow, around 7ºC/min.

Biomass amount increased the final temperature of the sample with fast heating rate.

The 1000 W and 700 W microwave power increased the temperature around 250-300 ºC. No difference was observed within these two powers.

Activated carbon wt% was the most important parameter to increase the microwave absorption capacity of pine chips. The final temperature in a microwave-assisted pyrolysis with 10wt% of activated carbon was 498 ºC and its heating rate was about 8 ºC/min.

In FIGURE 1 it can be seen the influence of microwave power and wt% of activated carbon in the microwave-assisted pyrolysis.

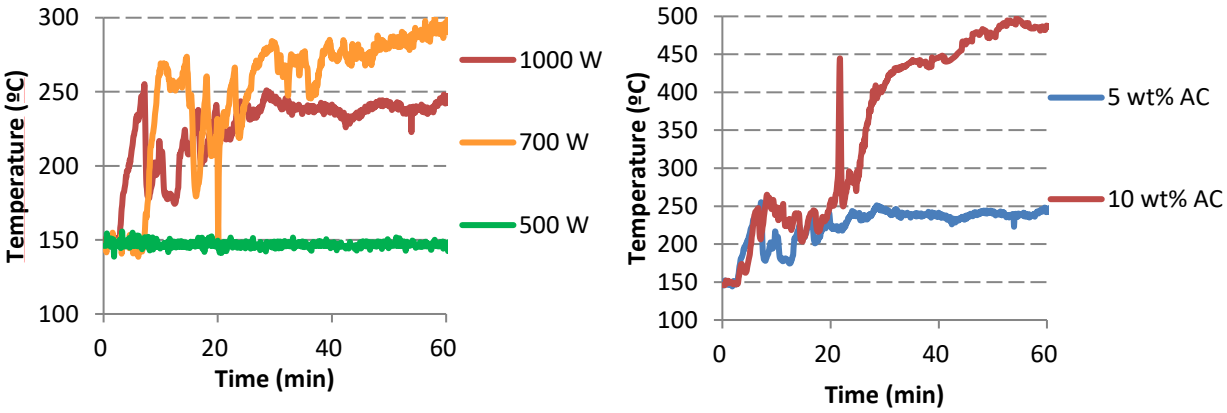


**FIGURE 1:** Influence of microwave power (left) and wt% of activated carbon (right) in the temperature of microwave-assisted biomass pyrolysis of pine chips.

## CONCLUSIONS

The obtained results have shown that the addition of activated carbon increases the microwave absorption capacity of the pine chips, producing an increase in the temperature reached and lowering the time necessary for a good biomass to biocarbon transformation.

**Acknowledgements**

This research was funded by the Centro de Desarrollo Tecnológico Industrial-CDTI within the Cervera call (ALMAGRID Project-CER-20191006) and Generalitat Valenciana -IVACE and FEDER (CIRCULARCARBON-IMIDEC/2019/10).

**References**

Jing Li, Jianjun Dai, Guangqing Liu, Hedong Zhang, Zuopeng Gao, Jie Fu, Yanfeng He and Yan Huang. (2016). Biochar from microwave pyrolysis of biomass: A review. *Biomass and Bioenergy,* 94, 228-244.

Jing Sun, Wenlong Wang and Qinyan Yue. (2016). Review on Microwave-Matter Interaction Fundaments and Efficient Microwave-Associated Heating Strategies. *Materials*, 9, [4], 231.

Li Longjun, Ma Xiaoqian, Xu Qing and hu Zhifeng. (2013). Influence of microwave power, metal oxides and metal saltson the pyrolysis of algae. *Bioresource Technology,* 469-474.

María T. Martín, Ana B. Sanz, Leonor Nozal, Flor Castro, Raúl Alonso, Juan L. Aguirre, Sergio D. González, M. Paz Matía, José L. Novela, Manuel Peinado and Juan J. Vaquero. (2017). Microwave-assisted pyrolysis of Mediterranean forest biomass waste: Bioproduct characterization. *Journal of Analytical and Applied Pyrolysis,* 278-285.

Paola A. Mello, Ricardo A. Guarnieri. (2014). Microwave Heating. *Microwave-Assisted Sample Preparation for Trace Element Determination,* 59-75.

Yu-Fong Huang, Pei-Te Chiueh, Shang-Lien Lo. (2016). A review on microwave pyrolysis of lignocellulosic biomass. *Sustainable Environment Research*, 26, [3], 103-109.

Carbon 2022

# Scaling up from lab to screw reactor slow pyrolysis pilot plant the production of sustainable carbon from biomass waste

**Iván Esteve-Adell[1,*], Patricia Perez-Llamas[1], Leire Zubizarreta[1] , Mayte Gil-Agustí[1], Marta García-Pellicer[1], Alfredo Quijano-Lopez[1, 2]**

[1] Instituto Tecnológico de la Energía (ITE), Avenida Juan de la Cierva, 24 46980 Paterna, Valencia, Spain

Email: ivan.esteve@ite.es

[2] Instituto de Tecnología Eléctrica, Universitat Politècnica de València. Camino de Vera, s/n 46022 Valencia, Spain

**Keywords**
bio-carbon, biomass, slow pyrolysis, pilot plant, sustainability

## INTRODUCTION

The search for new production forms of carbonaceous materials from renewable and sustainable sources is a field of research of great interest nowadays. The production of sustainable carbonaceous materials from residues coming from forestry, agricultural or other sectors has been widely demonstrated. Such transformation procedures allow to obtain carbonaceous materials with tuned properties for different fields of application such as energy storage, water filtration and gas purification. For the use of these sustainable carbonaceous materials to become a reality, it is necessary to scale up to have production at an industrial level. The control of the production process variables is of great importance for an adequate parameterization of the pyrolysis plant so that the transformation of the waste occurs in an effective and efficient way to obtain a good quality carbon material.

In this context, this work shows the work carried out in the scaling-up of the production of sustainable activated carbon from forestry residues. Data obtained from the laboratory scale production of sustainable activated carbon was used to develop a semi-continuous slow pyrolysis plant.

## EXPERIMENTAL

The developed pilot plant has a 2-meter tubular furnace where a temperature gradient can be programmed. Five differentiated heating zones can be controlled where the different biomass transformation steps take place progressively. The feed and dosage flow as well as the residence time are variables that have been evaluated to determine their influence on the produced carbons. The properties of biochar and activated carbon (porosity, specific surface area, pore types and ash content) as a function of feed rates, temperatures, residence time and gas flow rates have been evaluated.

## RESULTS

The results of this study show that the developed pyrolysis pilot plant can operate with a feed rate between 1 and 5 kg/h depending on the density of the starting biomass, being able to feed particles of up to 60 mm. For biomass with a density of less than 0.3 g/cm$^3$, the maximum feed rate reached is 1 kg/h. However, for high-density biomass (>0.6g/cm$^3$) feed rates increase to 5 kg/h. The maximum operating temperature is 950ºC, which allows physical activation of the carbons with $CO_2$.

The selected temperatures for bio-carbon production are obtained from the biomass thermogravimetric decomposition profile, where the different transformation steps can be calculated (FIGURE 1).

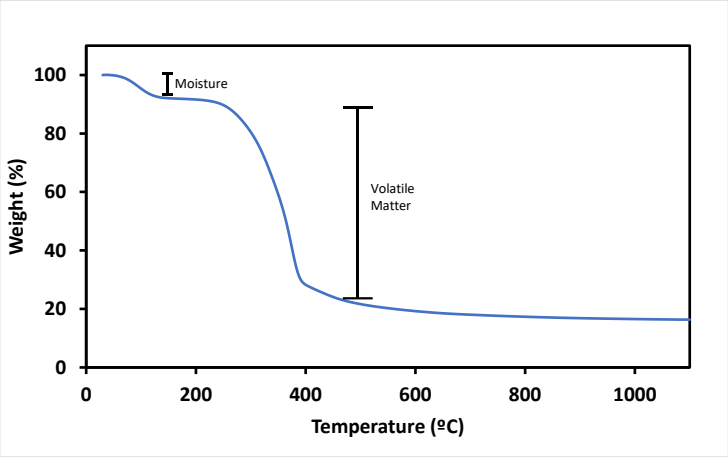


**FIGURE 1.** Thermogravimetric decomposition profile for pine wood under $N_2$ atmosphere.

Different gradient temperatures were used for pine wood pyrolysis between 150 and 550ºC. In a set of experiments for evaluation of the temperature gradient on the pine wood pyrolysis, the five heating zones of the oven were programmed with the temperatures showed in TABLE 1. A production of 30% biochar was obtained for all the experiments. However, differences on the bio-oil and bio-gas yield were observed. When the residence time at 550ºC is higher, the bio-oil cracking increases producing an increase of the bio-gas production. On the other hand, when the pine wood spends more time in the temperature range between 250-350ºC and the heating rate in that range is slower, the production of bio-oil increases up to 41% yield.

**TABLE 1.** Reaction conditions product yields for a set of experiments with pine wood.

| Reaction | Temperature gradient (ºC) | % biochar | % bio-oil | % bio-gas |
|---|---|---|---|---|
| 1 | 150-250-350-450-550 | 28 | 36 | 36 |
| 2 | 250-300-350-450-550 | 30 | 41 | 30 |
| 3 | 250-350-450-550-550 | 31 | 29 | 40 |

The characterization of biochar obtained after pyrolysis shows that higher amount of volatile matter was removed when the residence time at 550ºC is 30 minutes (Figure 1).

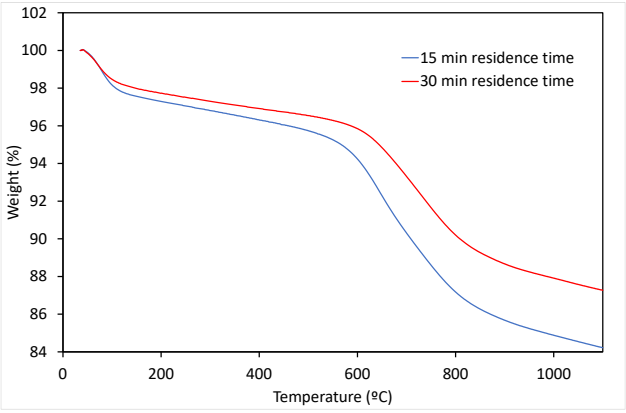


**FIGURE 2**: Thermogravimetric decomposition profile of pine wood biochar acquired under $N_2$ atmosphere after different pyrolysis residence time.

A second step allows the activation of biochar using $CO_2$ as physical activating agent. Adjusting gas flow and residence time the textural properties of AC can be tuned. These results show that the developed screw reactor for slow pyrolysis pilot plant is a versatile production line which allows to parametrization of all the variables taking place in any thermochemical transformation process allowing the production either biochar and activated carbons coming from different biomass wastes with tuned physicochemical and morphological properties.
Thanks to the digitization of the entire pilot plant and its integration with renewable energy sources, it has allowed an evaluation of energy consumption and optimization of all the variables of the biomass transformation process into carbon for improved process efficiency.

## CONCLUSIONS

This study demonstrates the possibility of producing sustainable carbon from biomass wastes coming from other sectors that can replace the different activated carbons currently used in Europe from third countries.

**Acknowledgements**

This research was funded by the Conselleria de Innovación, Universidades, Ciencia y Sociedad Digital (SINCLAIR CONV21/DGINN/09) and Generalitat Valenciana –IVACE and FEDER (CIRCULARCARBON- IMIDEC/2019/10).

**References**

Di Stasi, C., Greco, G., Canavesi, R. L. S., Izquierdo, M. T., Fierro, V., Celzard, A., Gonzalez, B., and Manya, J. J. (2021). Influence of activation conditions on textural properties and performance of activated biochars for pyrolysis vapors upgrading. *Fuel*, 289, 119759. https://doi.org/10.1016/j.fuel.2020.119759

Sygula, E., Swiechowski, K., Hejna, m., Kunaszyk, I., Bialowiec, A. (2021). Municipal Solid Waste Thermal Analysis—Pyrolysis Kinetics and Decomposition Reactions. *Energies*, 14(5), 4510. https://doi.org/10.3390/en14154510

Xu, Z. and Xu, Z. (2020). The rational design of biomass-derived carbon materials towards next-generation energy storage: A review. *Renewable and Sustainable Energy Reviews*, 134, 110308. https://doi.org/10.1016/j.rser.2020.110308

Carbon 2022

# Imidacloprid removal using activated carbons

**J. Farrando-Pérez, A. Garcia-Ripoll, E. Oliveira Jardim, J. Silvestre-Albero**
Inorganic Chemistry Department, University Materials Institute, University of Alicante, Spain
Email: erika.jardim@ua.es

**Keywords**
Activated carbons, adsorption, imidacloprid

## INTRODUCTION

For decades, human beings have produced and used various types of chemical products both for their daily comfort and for the development of the industrial activity. In recent years, water analysis has found the presence of many pollutants in water, which are directly related to numerous health problems in both animals and humans [1]. One of the most prominent groups of pollutants is pesticides, which are not only harmful to living beings but also cannot be easily and effectively eliminated from water systems [2]. Imidacloprid, a pesticide belonging to the neonicotinoid group, is mainly used for insect and pest control, both in agriculture and in parks and lawns, etc [3]. Exposure to this substance in high doses can lead to degenerative changes in vital organs of the body. The main problem with imidacloprid is its ability to accumulate in nature, which makes most of the removal techniques used (advanced oxidation, photocatalytic degradation, nano-membrane filtration, ozonation, etc.) unsuitable as they generate equally harmful by-products [4]. For this reason, much research has been focussed on the use of adsorption to remove the compound from water, rather than degradation. Adsorption using nanoporous materials has several advantages such as low cost, reasonable removal values, the high surface area available, and many active sites for adsorption [5]. One of the most widely used adsorbents in water treatment is activated carbon. Due to the slow kinetics in a liquid phase, activated carbons must be designed with a proper porous structure combining micropores (adsorption sites) and mesopores (diffusional channels). Based on these premises, the main goal of the present study is the evaluation of the adsorption performance of a micro/mesoporous activated carbon, RGC-30 (from Nuchar), in the removal of imidacloprid in a liquid phase.

## EXPERIMENTAL

Imidacloprid quantification was performed based on a UV-Vis spectroscopy method. A 100 ppm stock solution was prepared to dissolve 0.1 g of Imidacloprid in 1000 ml of ultrapure water. The calibration curve was developed by measuring concentrations from 1 to 50 ppm using the UV-Vis Spectrophotometer. Measurements were made at a fixed wavelength (270 nm) with 3 cycles of measurements with an interval of 5 seconds between each cycle. To evaluate the adsorption process, adsorbent dosage and volume of solution studies were carried out to determine the effect of these parameters on the process. The adsorbent dosage effect was investigated by adding different amounts of RGC-30 as an adsorbent to the fixed concentration of Imidacloprid solutions (from 5 to 30 mg). The volume effect was investigated by adding the same amount of RGC-30 ( 5mg) to different volumes (from 50 to 100 ml) of Imidacloprid solutions. All experiments were left under stirring until equilibrium was reached. Aliquots were taken at different times to evaluate the kinetic behavior of RGC-30. The activated carbon reaches complete adsorption equilibrium after 48 hours.

## RESULTS AND DISCUSSION

The adsorption results are displayed in Fig. 1. As it can be observed, the adsorption kinetics are very promising with more than 70 % removal in less than 10 h. Interestingly, the amount of imidacloprid adsorbed does not scale with the amount of sorbent incorporated. In general, the adsorption capacity at equilibrium (mg/g) decreases with the amount of RGC-30, except for the experiment with 2.5 mg. Most probably at a low carbon dose, diffusional limitations are important, thus limiting the adsorption performance. A closer look at the removal capacity shows that 30 mg is able to remove 100 % of the pesticide in less than 10 h. A much smaller amount of sorbent (5 mg) exhibits an optimum performance with close to 92 % removal efficiency after 25 h and a total capacity of ca. 500 mg/g. In the case of the effect of the volume of the initial solution, the results were as expected. An increase in the concentration of pesticide molecules present in the medium causes an increase in the adsorption capacity of the adsorbent, while the performance is worse under diluted conditions.

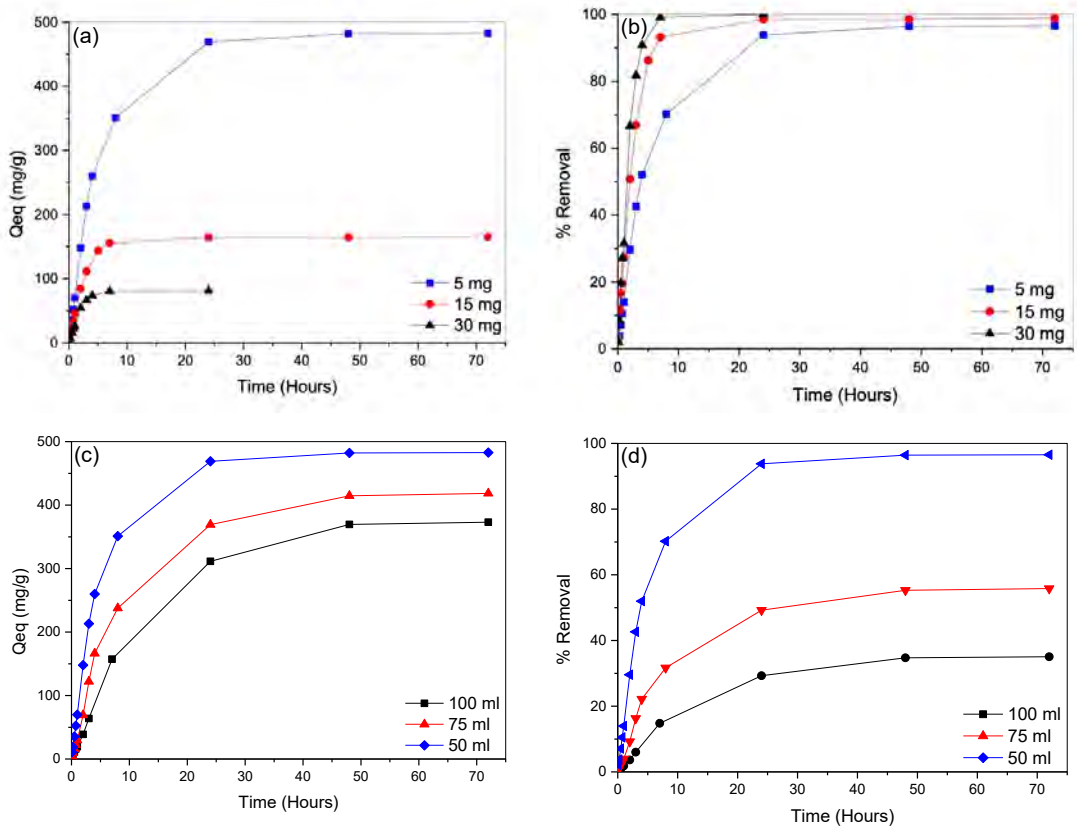


**FIGURE 1**: Effect of (a-b) amount of RGC-30 incorporated and (c-d) volume of the initial solution of Imidacloprid in the adsorption performance (amount adsorbed at equilibrium - Qeq, and removal percentage). Experiments are performed at 25ºC.

## CONCLUSIONS

These results anticipate that an activated carbon with a properly designed porous structure combining micro and mesopores exhibits a promising performance for the removal of pesticides with high efficiency (close to 100 %), excellent kinetics (less than 10 h), and a high adsorption capacity (up to 500 mg/g).

**Acknowledgements**

Authors acknowledge financial support from the MINECO (Projects PID2019-108453GB-C21 and PCI2020-111968/ERANET-M/3D-Photocat).

**References**

Gupta, V.K., Gupta, B., Rastogi, A., Agarwal, S., Nayak, A. (2011). Pesticides removal from wastewater by activated carbon prepared from waste rubber tire. Water Res., 45, [13] 4047-4055. https://doi.org/10.1016/j.watres.2011.05.016

Nault, B.A., Taylor, A.G., Urwiler, M., Rabaey, T., Hutchison, W.D. (2004). Neonicotinoid seed treatments for managing potato leafhopper infestations in snap bean. *Crop Protect*., 23, [2], 147-154. https://doi.org/10.1016/j.cropro.2003.08.002

Segura, C., Zaror, C., Mansilla, H.D., Mondaca, M.A. (2008). Imidacloprid oxidation by photo-Fenton reaction. *J. Hazard Mater.*, 150, [3], 679-686. https://doi.org/10.1016/j.jhazmat.2007.05.018

Singh, S., Kaushal, S., Kaur, J., Kaur, G., Mittal, S.K., Singh, P. (2021). CaFu MOF as an efficient adsorbent for simultaneous removal of imidacloprid pesticide and cadmium ions from wastewater. *Chemosphere*, 272, 129648. https://doi.org/10.1016/j.chemosphere.2021.129648

Yong Kim, K., Dominic Ekpe, O., Lee, H.J., Oh, J.E., J. (2020) Perfluoroalkyl substances and pharmaceuticals removal in full-scale drinking water treatment plants. *Hazard. Mater.,* 400, 123235. 10.1016/j.jhazmat.2020.123235

Carbon 2022

# Application of Carbon gel-$TiO_2$ nanocomposites as chemoresistive VOC´s sensors

**M.D. Fernández-Ramos [a,c], L.F. Capitán-Vallvey [a,c], L.M. Pastrana-Martínez [b,c], S. Morales-Torres [b,c], F.J. Maldonado-Hódar*[bc]**

[a] *ECsens. Department of Analytical Chemistry, University of Granada, Granada 18071 (Spain).*
[b] *NanoTech – Nanomaterials and Sustainable Chemical Technologies. Department of Inorganic Chemistry, University of Granada, Granada 18071 (Spain).*
[c] *Unit of Excellence in Chemistry applied to Biomedicine and the Environment of the University of Granada.*
Email: fjmaldon@ugr.es

**Keywords**
Carbon gel, carbon gel-$TiO_2$ composites, chemoresistive sensors, Volatile Organic Compounds (VOC´s), pollutant detection.

## INTRODUCTION

In recent decades, air quality and air pollution control have been the main lines of action in EU policies on environment, human health and well-being. Therefore, it is vitally important to have methods for determining gases and toxic components in the atmosphere that allow information to be obtained quickly, reliably and economically. There are also many other economic sectors where the strict control of the atmosphere composition is a key factor, such as facilities for the storage or transport of climacteric products to avoid premature ripening and the disposal of such products, among others [Paul, 2014]. Therefore, there is considerable interest in developing new materials and methods to obtain gas sensors with better analytical characteristics, in particular good adsorption, sensitivity, selectivity and thermodynamic stability. Carbon-$TiO_2$ composites can be prepared using different synthesis procedures and combinations with many carbon phases available, with different loadings and using thermal treatments to fit the crystallographic $TiO_2$ phases. These composites are important functional materials with excellent physicochemical properties and have been applied in the field of catalysis [Hamad, 2019], including photocatalysis, electrochemical applications in supercapacitors and sodium ion batteries. Nevertheless, research into the gas sensing properties of carbon-doped $TiO_2$ is limited. In this study, we demonstrate the successful features of resistive sensors to determination of ammonium gas based on carbon gel-$TiO_2$ composites.

## EXPERIMIMENTAL

The synthesis of the carbon gel-$TiO_2$ nanocomposites was carried out by a fitted sol-gel process in a three-neck balloon using a mixture of resorcinol (R)-formaldehyde (F) as the precursor of the organic fraction and tetrabutyl orthotitanate (TBTi, 97 wt%.) as the $TiO_2$ precursor [Maldonado-Hódar, 2000]. The resistive gas sensor was prepared on a clean glass slide (2.5 x 2.5 cm) by screen printing two 10 mm x 2 mm silver electrodes on it with a separation of 1.5 mm (Figure 1). For the determination of sensor response, experiments were performed inside a homemade plastic climate chamber where the sensor was

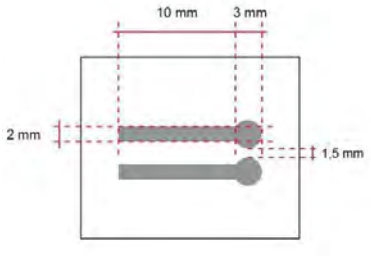


**Figure 1.** Representation of the silver electrodes used as support of the carbon gel-$TiO_2$ nanocomposite films for resistive gas sensors.

introduced and connected to the electrometer. A UV lamp VL-6MC 6 W (1.4 mW/cm$^2$) (λ = 312 nm) is placed in the lid of the box. The gas or vapour input and electrical connections are located on the side.

**RESULTS AND DISSCUSSION**

Carbon gel-$TiO_2$ nanocomposites with a $TiO_2$ content ranging between 27-84% wt. were synthetized by sol-gel method. The physicochemical properties of materials were exhaustively determined by complementary techniques and the synergism between phases was pointed out. The thermogravimetric analysis of the pyrolysis processes denoted the formation of weaker bonds in the composites. After thermal treatment, the carbon phase presented a micro-macroporous structure with a surface area of ca. 500 $m^2 . g^{-1}$ while the neat $TiO_2$ showed a low porosity. The surface area in the composites increased up to 700 $m^2 . g^{-1}$ at low $TiO_2$ content but decreases with higher $TiO_2$ content. A developed mesoporous volume was observed for composites with $TiO_2$ content around 50% wt., in this case, the pore size distribution changing from macroporous to bimodal macro-mesoporous character. The morphology of the prepared materials showed a well distribution of $TiO_2$ nanoparticles in the composites; only the sample with a high $TiO_2$ content (i.e., 84% wt.) showed a XRD-pattern denoting a certain sintering and diffraction peaks corresponding to a mixture of anatase-rutile phases. The morphology and distribution of $TiO_2$ in the composites were analysed by SEM/TEM-EDS imaging and mapping (Figure 2). Surface composition was analysed by XPS experiments and the results are collected in Table 1.

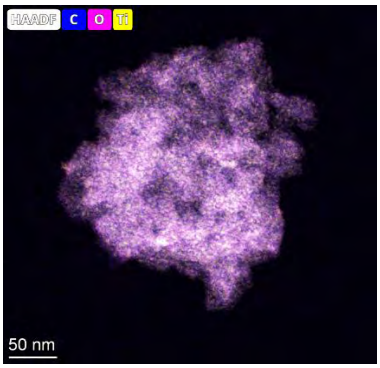


**Figure 2.** TEM-EDS mapping of 30Ti composite

**Table 1.** Bulk and surface composition of the RF-$TiO_2$ composites carbonized at 900 ºC

| Composite | $TiO_2$ (% wt.) | Surface composition by XPS | | |
|---|---|---|---|---|
| | | C (%) | Ti (%) | O (%) |
| 10Ti | 27 | 91.2 | 1.5 | 7.3 |
| 20Ti | 41 | 82.8 | 4.5 | 12.7 |
| 30Ti | 54 | 76.1 | 6.4 | 17.5 |
| 50Ti | 84 | 68.7 | 8.4 | 22.9 |

The resistance of the films of pure phases and composites in air and dark/UV conditions at a potential difference of 1.0 V was determined (Table 2). Conductivity increased with $TiO_2$ content and under UV radiation. Resistivity was also determined in the presence of different gases with concentrations in the range 0-1000 ppm. The gases tested were ammonia ($NH_3$), carbon dioxide ($CO_2$), ethanol ($C_2H_5OH$), methanol ($CH_3OH$), butanol ($C_4H_{10}O$) and ethyl acetate ($C_4H_8O_2$). The response of the resistive sensor is expressed as response sensitivity, S (%), increasing linearly as increasing concentrations of the gas. In Figure 3 is showed the evolution of the response changing the butanol concentration, as an example. The sensor response is obtained at room temperature and under dark/UV irradiation. The results showed that the increase of the $TiO_2$ content in the composite trigger a higher response to the analyte. The sensor based on carbon-$TiO_2$ nanocomposite with 84% wt. of $TiO_2$ presented a good sensing performance in terms of sensitivity (sensor response ~18.8 for 100 ppm $NH_3$), selectivity (selectivity factor for $NH_3$ is about ~5.8 against $C_4H_8O_2$, $C_4H_{10}O$ and ~4.5 for $CO_2$, $CH_3OH$, $C_2H_5OH$), stability (both long-term and short-term) and influence of humidity. The prepared film possesses the advantages of low power consumption, cost-effective and detection ability for VOCs detection, but is more specific for $NH_3$ sensing.

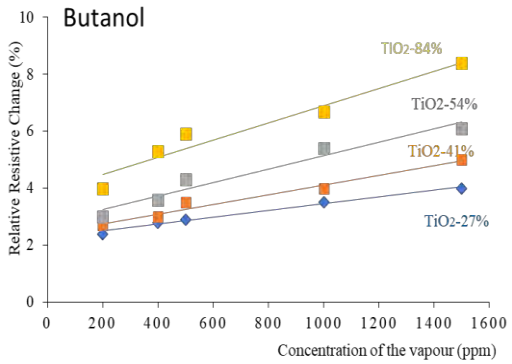


**Figure 3.** Evolution of the resistivity changes as a function of the butanol concentration.

**Table 2.** Influence of UV light on the resistance value of different materials in air.

| Material | Electrical Resistance (kΩ) | |
|---|---|---|
| | Dark | UV |
| C | 34228.3 ± 32.5 | 32725.0 ± 36.3 |
| $TiO_2$ | 90.7 ± 17.2 | 85.2 ± 12.4 |
| P25 | 119.1 ± 8.2 | 100.4 ± 6.2 |
| 10Ti | 25540.0 ± 22.1 | 24021.3 ± 18.3 |
| 20Ti | 9236.3 ± 7.3 | 8205.1 ± 8.2 |
| 30Ti | 5432.6 ± 6.5 | 4302.1 ± 7.2 |
| 50Ti | 528.7 ± 4.6 | 430.2 ± 3.8 |

## CONCLUSIONS

Carbon gel-$TiO_2$ nanocomposites have been proposed as sensing materials. The C-X$TiO_2$ exhibits different gas sensing to ammonia, ethanol, methanol, butanol, ethyl acetate and carbon dioxide at ambient temperature and under UV illumination. The resistive sensor behaves like an n-type semiconductor. Carbon doped with 84% $TiO_2$ has the best sensor properties: good selectivity towards ammonia (100 ppm, S = 18), low response and recovery times (50 and 170 s, respectively), stability over time and a low influence of humidity on the response with a low applied voltage of 1.0 V.


## Acknowledgements

This work was financially supported by the PCI2020-112045 project from MCIN/AEI/10.13039/501100011033 and European Union Next Generation EU/PRTR, as part of the PRIMA Programme (Nano4Fresh project). S.M.T. (RYC-2019-026634-I) and L.M.P.M. (RYC-2016-19347) acknowledge the MICIN/AEI/10.13039/501100011033 and the European Social Found (FSE) "El FSE invierte en tu futuro" for a Ramón y Cajal research contracts.


## References


Hamad H., Castelo-Quibén, J., Morales-Torres, S., Carrasco-Marín, F., Pérez-Cadenas, A.F. Maldonado-Hódar, F.J. (2018) On the Interactions and Synergism between Phases of Carbon⁻Phosphorus⁻Titanium Composites Synthetized from Cellulose for the Removal of the Orange-G Dye, Materials (Basel), 11 1766. https://dx.doi.org/10.3390%2Fma11091766

Maldonado-Hódar, F.J., Moreno-Castilla, C., Rivera-Utrilla, J. (2000) Synthesis, pore texture and surface acid–base character of $TiO_2$/carbon composite xerogels and aerogels and their carbonized derivatives, Applied Catalysis A: General, 203, 151-9. https://doi.org/10.1016/S0926-860X(00)00480-4

Paul, V., Pandey, R., Role of internal atmosphere on fruit ripening and storability--a review, (2014) Journal of Food Science and Technology, 51 1223-50. https://dx.doi.org/10.1007%2Fs13197-011-0583-x

Carbon 2022

# Roles of surface chemistry and texture of activated carbons in $CO_2$ capture as a function of operational conditions

**Vanessa Fierro[a], Rafael Canevesi[a], Sebastien Schaefer[a], M.T. Izquierdo[b] and Alain Celzard[a]**
[a]Université de Lorraine, CNRS, F-88000, Épinal, France
[b]Instituto de Carboquímica, Zaragoza E-50018, Spain
Email: Vanessa.Fierro@univ-lorraine.fr

**Keywords**
$CO_2$ capture; activated carbons; textural properties; heteroatom content

## INTRODUCTION

$CO_2$ capture and storage (CCS) is expected to reduce industrial $CO_2$ by about 20% by 2050 (Han *et al.*, 2019). Among the various CCS technologies, adsorption has an important role to play because of its low energy consumption, ease of use and high robustness. Zeolites, metal-organic frameworks (MOFs), covalent metal-organic frameworks (COFs), carbon materials, among others, have been proposed as $CO_2$ adsorbents. Activated carbons (ACs) are one of the best solutions for CCS (García-Díez *et al.*, 2019), especially those doped with nitrogen, which increases the AC basicity and thus the $CO_2$ affinity (Canevesi *et al.*, 2022). Furthermore, AC texture can be tailored depending on the activation conditions because $CO_2$ adsorption capacities are related to the amount of micropores, *i.e.*, pores narrower than 2 nm (Marco-Lozar *et al.*, 2014).

Most $CO_2$ adsorption studies are performed in commercial manometric devices at 273K and up to 1 bar. However, CCS is usually performed after combustion and thus at temperatures well above 298K. As the increase in temperature is unfavorable to adsorption, the effect of temperature, textural properties and surface chemistry should be analysed together. To this end, this study analyses the effect of textual properties and heteroatoms content as a function of temperature. We used three commercial ACs doped with nitrogen by a chemical treatment with urea, assisted or not by a preliminary oxidation in order to increase their reactivity. Their textural properties and elemental compositions were studied, and their $CO_2$ adsorption isotherms at three different temperatures (273, 298 and 313K) were obtained up to 25 bar.

## MATERIALS AND METHODS

Three commercial ACs named MSP-20X (Kansai Coke & Chemicals, JAPAN), MSC-30 (Kansai Coke & Chemicals, JAPAN), and CW30 (Silcarbon & Aktivkohle, GERMANY) were used in this study. These ACs were selected for the diversity of their porous structures, with BET areas ranging from 1736 to 3200 $m^2\ g^{-1}$ and micropore fractions ranging from 40 to 95%. The commercial ACs were doped with oxygen and/or nitrogen usig the following three methods: (1) Oxygen-doped materials were prepared by oxidising 3g of AC with 30mL of hydrogen peroxide solution (31%, VWR) at room temperature; (2) Nitrogen-doped carbons were obtained by mixing ground urea and powdered AC, using a urea/AC weight ratio of 1 or 2. After mixing, the blend was subjected to heat treatment in a tube furnace heated to 623K under synthetic air atmosphere. The final temperature was maintained for 3 h. The materials were finally washed with hot water to neutral pH and dried for 24 h in a ventilated oven at 378K; (3) The O-N doped carbons were obtained by mixing 1g of the O-doped carbons with urea powder, using the same protocol as described above. The chemical and textural characteristics of the surface of the pristine and doped materials were obtained by XPS and physisorption techniques. The bulk composition was obtained by elemental analysis. High-pressure $CO_2$ adsorption isotherms were measured up to 25 bar and at three different temperatures (273, 298 and 323 K).

The contributions of textural properties and surface chemistry to the $CO_2$ adsorption capacity were evaluated as follows. First, based on PSDs, the pore volumes $V_i$ ($cm^3/g$) of the materials were divided into four classes according to their pore size L (nm): $V_{L<0.5}$, $V_{0.5<L<0.7}$, $V_{0.7<L<2}$, $V_{L>2}$; a coefficient representing the contribution to adsorption was assigned to each range. Then, the contribution of the surface chemistry was attributed to oxygen and nitrogen contents ($C_{N+O}$), obtained by XPS. Therefore, the $CO_2$ adsorption capacity, q (mol $kg^{-1}$), was represented mathematically as follows:

$$q = a_1 V_{L<0.5} + a_2 V_{0.5<L<0.7} + a_3 V_{0.7<L<2} + a_4 V_{L>2} + b C_{N+O}$$

**RESULTS AND DISCUSSION**

The pristine and doped MSP-20X and MSC-30 materials showed type Ia and Ib nitrogen isotherms, while the pristine and doped CW30 materials showed a type IV nitrogen isotherm with a hysteresis loop at a relative pressures above 0.50. Urea treatment induced a progressive decrease in surface area and average micropore size, as evidenced by changes in the knee angle of the nitrogen isotherm at low relative pressures ($p/p_0 < 0.2$), as well as the pore size distribution calculated by 2D Non-Local Density Functional Theory. Bulk composition analysis showed that the oxygen content increased significantly after oxidation wit $H_2O_2$, and the O content favoured nitrogen doping. The highest nitrogen bulk content, up to 16.5 wt %, was obtained with materials pre-oxidised with hydrogen peroxide and then subjected to urea treatment. N and O doping decreased the surface area, probably due to steric hindrance and deformation, affecting supermicropores and mesopores. XPS analysis showed that the grafted O groups were mainly in carbonyl form, while the N groups were pyridinic and pyrrolic. Furthermore, the non-proportionality between the oxygen and nitrogen contents on the surface and in the bulk could indicate the creation of clusters, probably localized in the larger pores. The latter hypothesis can be advanced due to a more significant volume reduction in the mesopore region after N doping, although N doping always produce a decrease in surface area.

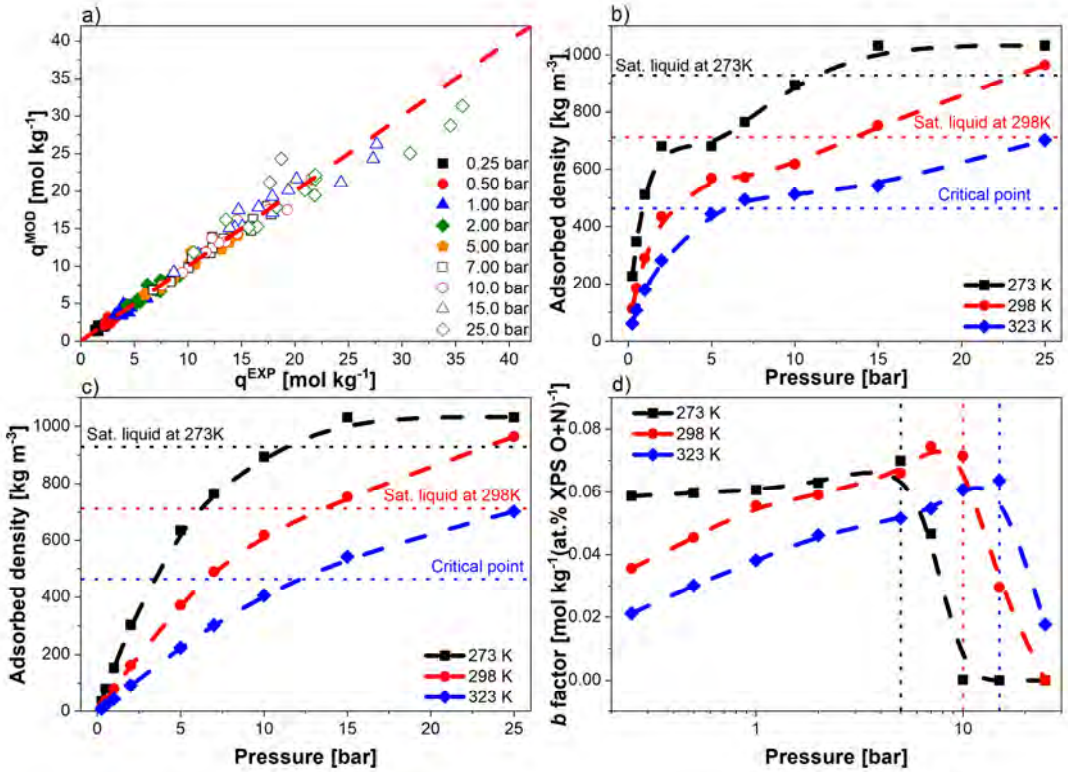


**FIGURE 1**: (a) Model fitting efficiency; (b) adsorbed density in pores below 0.5nm and (c) in mesopores (*i.e.*, larger than 2.0nm); (d) effect of heteroatom content at different temperatures.

The $CO_2$ adsorption capacity at high pressures was strongly affected by the surface area, so that the N-doped carbons had lower capacities than the pristine ones at high pressures. However, the doping

had a positive effect on the Henry's constant, which accounts for adsorption at lower pressures. The polynomial expression showed good efficiency in fitting the experimental data at all evaluated temperatures and pressures (Fig. 1a), although some discrepancies are observed at 25 bar. Since the regression coefficients ($a_1$, $a_2$, $a_3$ and $a_4$) are representative of the adsorbed phase density for each pore diameter, we estimated the average $CO_2$ density in micropores with diameters less than 0.5 nm (Fig. 1b) and mesopores (Fig. 1c). Narrow micropores are able to produce densities above that of supercritical $CO_2$ at lower pressures than mesopores. At 273K, the term b, related to the contribution of the heteroatom content, increases up to 5 bars (see Fig. 1d), which means that there is a shift from a surface chemistry-controlled behaviour to a pore texture-controlled behaviour at 5 bars. When increasing the temperature from 273 to 323 K, this shift occurs at increasing pressures: 10 bar at 298K and 15 bar at 323 K.

## CONCLUSIONS

Three activated carbons (ACs) were efficiently doped with O and N and the highest bulk nitrogen content, up to 16.5 wt %, was obtained with an AC pre-oxidised with hydrogen peroxide and then subjected to urea treatment. N and O doping decreased the surface area, probably due to steric hindrance and deformation, affecting supermicropores and mesopores. We simultaneously took into account the surface chemistry and the texture of all materials to study $CO_2$ adsorption at 3 temperatures up to 25 bar. We concluded that the presence of heteroatoms, such as N or O, on the surface of ACs promotes $CO_2$ uptake due to specific interactions at pressures below 5 bar at 273K. The shift from surface chemistry-controlled to pore texture-controlled behaviour occurs at increasing pressures from 5 to 15 bar when increasing temperature from 273 to 323 K.

**Acknowledgements**

The French research team thanks ANR-15-IDEX-04-LUE and the TALiSMAN project (2019-000215), financed by the European Regional Development Fund (ERDF).

**References**

Canevesi, R.L.S. *et al.* (2022) 'Roles of Surface Chemistry and Texture of Nanoporous Activated Carbons in CO2 Capture', *ACS Applied Nano Materials*, 5(3), pp. 3843–3854. doi:10.1021/acsanm.1c04474.

García-Díez, E. *et al.* (2019) 'Novel Porous Carbons Derived from Coal Tar Rejects: Assessment of the Role of Pore Texture in CO2 Capture under Realistic Postcombustion Operating Temperatures', *ACS Applied Materials & Interfaces*, 11(40), pp. 36789–36799. doi:10.1021/acsami.9b13247.

Han, J. *et al.* (2019) 'The N-doped activated carbon derived from sugarcane bagasse for CO2 adsorption', *Industrial Crops and Products*, 128, pp. 290–297. doi:https://doi.org/10.1016/j.indcrop.2018.11.028.

Marco-Lozar, J.P. *et al.* (2014) 'Sorbent design for CO2 capture under different flue gas conditions', *Carbon*, 72, pp. 125–134. doi:10.1016/j.carbon.2014.01.064.

Carbon 2022

# Preparation of MEAs of $LaMn_{0.7}Co_{0.3}O_3$/Carbon Black for oxygen reduction reaction

**J.X. Flores-Lasluisa[1], T. Servais[2], D. Cazorla-Amorós[3], N. Job[2], E. Morallón[1]**

*[1]Dept. Química Física e Instituto Universitario de Materiales, Universidad de Alicante. Ap. 99, E-03080, Alicante, Spain*

Email: jhony.flores@ua.es

*[2]Dept. Chemical Engineering, Liège Université, B6a, allée du 6 août 11, 4000 Liège, Belgium*

*[3]Dept. Química Inorgánica e Instituto Universitario de Materiales, Universidad de Alicante. Ap. 99, E-03080, Alicante, Spain*

**Keywords**

MEAs, carbon black, alkaline medium, perovskite oxides.

## INTRODUCTION

Fuel cells and metal-air batteries are promising devices employed for the conversion of chemical energy into electrical energy, facilitating the transition towards a more sustainable world and decreasing the use of fossil fuels. However, the oxygen reduction reaction (ORR) that occurs in the cathode presents sluggish kinetics; electrodes thus generally use Pt-based electrocatalysts due to their great catalytic performance, but Pt is scarce and expensive. Perovskite metal oxides such as $LaBO_3$ (B being a *3d* transition metal) are attractive to substitute platinum-based materials because their physicochemical and electrochemical properties can be tailored, modifying their catalytic response towards ORR (Sunarso et al., 2012)(Ashok et al., 2018). However, these materials need to be studied in alkaline conditions due to their instability in acidic medium. Among the different B-site cations, Mn and Co are the most active for ORR, even though it was reported that Co-doped $LaMnO_3$ perovskite have a better performance (Flores-Lasluisa et al., 2020). However, perovskite metal oxide materials exhibit both low electrochemical active surface area and low electrical conductivity, which limits their catalytic activity. Therefore, they need to be employed together with carbon materials that mitigate these drawbacks. Previously to the characterization of the materials in a fuel cell station, it is essential to prepare Membrane-Electrode-Assemblies (MEAs) (Kruusenberg et al., 2012). However, this is a challenging process due to several problems related to the reproducibility in assembling, the poor knowledge of fuel cells in alkaline conditions and the low stability of the alkaline membrane (Zheng et al., 2021)(Mustain et al., 2020). In this investigation, we propose a synthesis of perovskite/carbon black materials, which were employed for the preparation of MEAs to test them in alkaline membrane fuel cells (AMFCs).

## EXPERIMENTAL

The perovskite metal oxides were synthesized by a sol-gel method described elsewhere (Flores-Lasluisa et al., 2020). The metal oxides were characterized by different physicochemical techniques such as XRD, XPS, EDX, TEM, and SEM. To measure the electroactivity of the as-synthesized materials, they were firstly mixed with carbon black (Vulcan). The selection of the material for the preparation of MEAs was based on its electrocatalytic behaviour in ORR studied by LSV using a rotating ring-disk electrode (RRDE). To prepare MEAs, it is necessary to make a catalyst ink to deposit it on the gas diffusion layer (GDL) using a doctor blade technique. The ink is prepared by stirring and sonicating the catalyst and the anionic ionomer (30 wt.%) in NMP. However, it is important to reduce the size of the metal oxide particles by employing a ball-milling approach, and then, the metal oxide material was physically mixed with Vulcan using a mortar (ratio 1:1). The alkaline membrane used to prepare the MEAs is the commercial Fumapem FAA-3-50. The resulting MEAs were characterized by electrochemical techniques such as polarization curves and electrochemical impedance spectroscopy

(EIS) experiments. To compare with a commercial reference, platinum-based MEAs were also prepared using a commertial 60 wt.% Pt/C material.

## RESULTS AND DISCUSSION

The degree of cobalt substitution in $LaMnO_3$ perovskite has a significant impact on the physicochemical properties. It was observed that increasing the amount of cobalt changes the crystal structure, enlarges the crystallite size and increases the number of active sites for the ORR (Flores-Lasluisa et al., 2020). The $LaMn_{0.7}Co_{0.3}O_3$ perovskite material was selected for the preparation of MEAs due to its great performance in ORR as analysed in RRDE configuration (Fig. 1a). Its great catalytic behaviour was associated with several parameters (Flores-Lasluisa et al., 2020): (i) the presence of two redox pairs which favour the electron transfer, (ii) the optimal concentration of $Mn^{3+}/Mn^{4+}$ which can catalyse in a different way the ORR, and (iii) the synergistic effect produced between the metal oxide and the carbon black. Although the preparation of alkaline MEAs can be tricky due to the lack of proper protocols, it was accomplished for the perovskite-based and Pt/C materials and the results are displayed in Fig. 1b. Firstly, it can be observed that the performance in power density terms is more than twice lower in the case of the perovskite-based MEA compared to the commercial Pt/C catalyst; however, this can be enhanced by using a different mixing method that may improve the electron transfer between both components or by improving the ink deposition on GDLs. Whatever catalyst considered, the alkaline MEAs are unstable with the number of cycles which is probably due to the poisoning of the alkaline membrane by $CO_2$ present in the atmosphere and in the hydrogen feed (Zheng et al., 2021). Therefore, a better protocol to activate and use the membrane is needed to avoid its deterioration before use in the fuel cell.

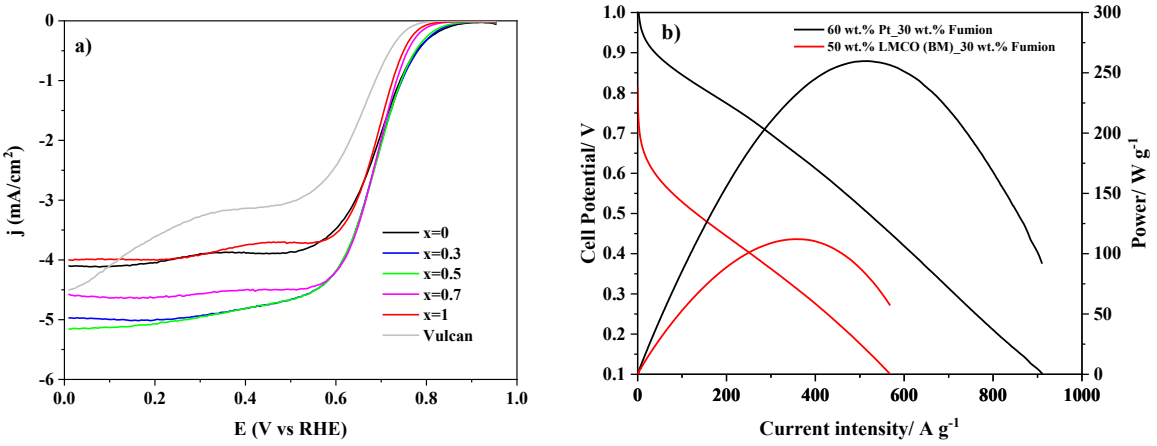


**FIGURE 1**: a) RDE liner sweep voltammograms for $LaMn_{1-x}Co_xO_3$ perovskite/Vulcan (1:1: mass ratio) in 0.1 M KOH saturated with $O_2$ at 1600 rpm; b) Comparison of the polarization curves and power vs. current curves of $LaMn_{0.7}Co_{0.3}O_3$/Vulcan- and Pt/C-based MEAs. The current and power are related to amount of active phase in each catalyst. Relative humidity of 100% at 50 ºC with $H_2$/Air gases with a flow rate of 300 mL $min^{-1}$ both gases.

## CONCLUSIONS

The low cobalt substitution in $LaMnO_3$ perovskite enhances significantly the electrocatalytic performance in ORR due to the increase in electrical conductivity and active surface sites. Moreover, the carbon black material increases the catalytic activity of the perovskite metal oxide material due to a synergistic effect between both components that favours the electron transfer. The perovskite-based MEAs shows a modest, but improvable activity compared to the Pt-based MEAs, being the mixing method, ink deposition and the membrane activation protocol, important aspects that have to be optimized for the successful development of alkaline MEAs.

**Acknowledgements**
The authors thank MCI/AEI and FEDER, UE (PID2019-105923RB-I00 project) for the financial support. J.X.F.-L. gratefully acknowledges MINECO for the financial support through an FPI contract (BES-2017-081598).

**References**
Ashok, A., Kumar, A., Bhosale, R.R., Almomani, F., Malik, S.S., Suslov, S. & Tarlochan, F. (2018) Combustion synthesis of bifunctional LaMO3 (M = Cr, Mn, Fe, Co, Ni) perovskites for oxygen reduction and oxygen evolution reaction in alkaline media. *Journal of Electroanalytical Chemistry*. 809 (August 2017), 22–30. doi:10.1016/j.jelechem.2017.12.043.
Flores-Lasluisa, J.X., Huerta, F., Cazorla-Amorós, D. & Morallon, E. (2020) Carbon Material and Cobalt-Substitution Effects in the Electrochemical Behavior of LaMnO3 for ORR and OER. *Nanomaterials*. 10 (12), 2394. doi:10.3390/nano10122394.
Kruusenberg, I., Matisen, L., Shah, Q., Kannan, A.M. & Tammeveski, K. (2012) Non-platinum cathode catalysts for alkaline membrane fuel cells. *International Journal of Hydrogen Energy*. 37 (5), 4406–4412. doi:10.1016/j.ijhydene.2011.11.143.
Mustain, W.E., Chatenet, M., Page, M. & Kim, Y.S. (2020) *Environmental Science Durability challenges of anion exchange membrane fuel cells*. 17–19. doi:10.1039/d0ee01133a.
Sunarso, J., Torriero, A.A.J., Zhou, W., Howlett, P.C. & Forsyth, M. (2012) Oxygen Reduction Reaction Activity of La-Based Perovskite Oxides in Alkaline Medium: A Thin-Film Rotating Ring-Disk Electrode Study. *The Journal of Physical Chemistry C*. 116 (9), 5827–5834. doi:10.1021/jp211946n.
Zheng, Y., Nicole, L., Col, I., Hassan, N.U., Williams, E.R., Stefik, M., Lamanna, J.M., Hussey, D.S. & Mustain, W.E. (2021) *Effect of Membrane Properties on the Carbonation of Anion Exchange Membrane Fuel Cells*. (1).

Carbon 2022

# Outstanding electrocatalytic activity towards ORR of thermally treated multi-walled carbon nanotubes

**J.X. Flores-Lasluisa[1], D. Cazorla-Amorós[2], E. Morallón[1]**

[1]*Dept. Química Física e Instituto Universitario de Materiales, Universidad de Alicante. Ap. 99, E-03080, Alicante, Spain*

Email: jhony.flores@ua.es

[2]*Dept. Química Inorgánica e Instituto Universitario de Materiales, Universidad de Alicante. Ap. 99, E-03080, Alicante, Spain*

**Keywords**

MWCNTs, oxygen reduction reaction, carbon defects

## INTRODUCTION

Fuel cells and metal-air batteries are promising devices to transform chemical energy into electrical energy, suppressing the use of fossil fuels as the main energy sources. However, the reactions that occur in these devices, especially the oxygen reduction reaction (ORR), exhibit sluggish kinetics. Therefore, it is necessary the use of catalysts, being the commercial ones based on Pt. These are the most catalytic, but they are expensive and non-abundant. Thus, it is essential to develop materials based on low-cost and abundant elements. Among the different alternatives, metal-free carbon-based materials are attractive as catalysts for ORR. In these catalysts, defects and heteroatoms are responsible for the active sites. The defects can be produced in three different ways (Quílez-Bermejo et al., 2020)(Yan et al., 2018): (i) defects by doping with heteroatoms (N, S or B), (ii) defects by doping with atomic metal species and (iii) defects created by physical or chemical methods. The latter is the most interesting method because materials with great performance can be developed without the need for doping with any other element (Gabe et al., 2019) (Waki et al., 2014) and in which carbon structural defects determine the catalytic activity. In this investigation, we propose the development of defective carbon materials as ORR catalysts by treating commercial multi-walled carbon nanotubes (MWCNTs) with two different acidic procedures and a posterior heat treatment.

## EXPERIMENTAL

The MWCNTs selected for this investigation were commercial nanotubes with 99 % and 95 % of purity. Before their use, the MWCNTs were purified with 5 M HCl to eliminate metal traces. Later, they were treated with 3 M $HNO_3$ and heat-treated at 920 ºC in a $N_2$ atmosphere for 30 min. The as-synthesized carbon materials were named MW99_P and MW95_P for pristine materials, and MW99_T and MW95_T for the as-obtained materials. The carbon materials were characterized by different physicochemical techniques such as XPS, TEM, EDX, $N_2$ adsorption isotherms, TPD and Raman spectroscopy. The Active Surface Area (ASA) was determined following a previously used procedure (Gabe et al., 2019).

The electrochemical activity of the as-synthesized materials was characterized by cyclic voltammetry (CV) and the activity of the materials was studied by linear sweep voltammetry (LSV) using a rotating ring-disk electrode (RRDE).

## RESULTS AND DISCUSSION

Firstly, the removal of metal traces was assessed by EDX analysis, indicating that for the MW99_T it was successful, while for the MW95_T it was reduced considerably. The microstructure of the samples analyzed by TEM revealed that the as-synthesized materials have some important features such as remaining nanoparticles (MW95_T) and broken fringes, being the latter responsible for increasing the

number of edge carbon atoms that are active for ORR (Tao et al., 2016) (Radovic et al., 2020). Raman spectroscopy confirms an increase of carbon defects in the as-synthesized materials; thus, the catalytic activity is expected to be enhanced (Jiang et al., 2015). Moreover, the active surface area (ASA) and the electroactive area of the synthesized materials increase significantly compared to the pristine materials. Thus, both acidic and thermal treatments increase the number of active sites for ORR, which is a consequence of the generation of defects.

The cyclic voltammograms of the carbon materials show that the double-layer capacitance for the as-synthesized materials increases significantly compared to the pristine ones, especially for the MW99_T. This might be related to the increase in the surface area of the as-synthesized carbon materials, which can also provide a higher content of available surface for the ORR. The electrocatalytic activity of the samples was analyzed by LSV and the results are displayed in Figure 1. Figure 1a shows that the as-synthesized materials outperform the pristine materials, especially in the MW99-based materials. The enhancement is related to the generation of active sites resulting from topological defects, carbon defects and edge carbon atoms, which can adsorb $O_2$ molecules and proceed with the reduction. Moreover, the number of electrons through which the reaction occurs is close to the 4-electron pathway for the sample MW99_T. The high limiting current observed for this material can be a consequence of the surface roughness produced by the carbon material although this aspect needs further research.

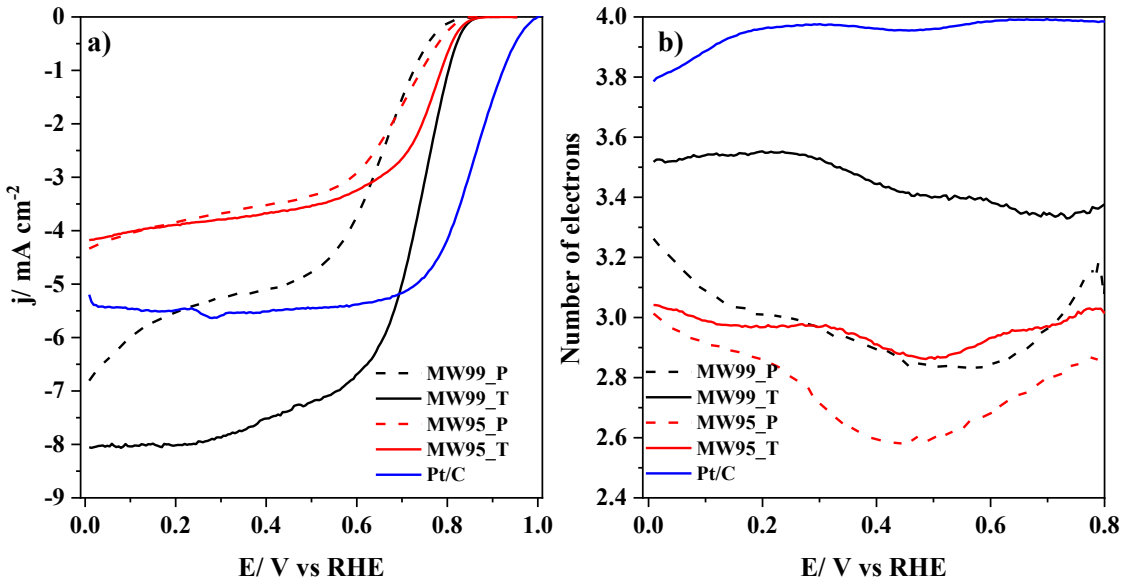


**FIGURE 1**: a) RDE linear sweep voltammograms for carbon nanotube materials in 0.1 M KOH solution saturated with $O_2$ at 1600 rpm, v= 5 mV/s; b) Number of electrons involved in ORR at increasing potential obtained by using the current measured at the ring electrode.

## CONCLUSIONS

The as-synthesized materials obtained by applying both acidic and thermal treatment to MWCNT produces highly defective carbon materials. These treatments have strong impact on the physicochemical properties such as the increase of surface area, active surface area, electroactive area and double-layer capacitance. Moreover, Raman spectroscopy demonstrates the generation of defects in the carbon materials, which agrees with the TEM observations. As defects can be active sites for ORR, the as-synthesized materials have a great catalytic performance, especially the MW99_T material. Therefore, MW99-T sample can be a promising material to substitute the commercial Pt-based materials.

**Acknowledgements**
The authors thank MCI/AEI and FEDER, UE (PID2019-105923RB-I00, RTI2018-095291-B-I00 projects) for the financial support. J.X.F.-L. gratefully acknowledges MINECO for the financial support through an FPI contract (BES-2017-081598).

**References**

Gabe, A., Ruiz-Rosas, R., Morallón, E. & Cazorla-Amorós, D. (2019) Understanding of oxygen reduction reaction by examining carbon-oxygen gasification reaction and carbon active sites on metal and heteroatoms free carbon materials of different porosities and structures. *Carbon*. 148, 430–440. doi:10.1016/j.carbon.2019.03.092.

Jiang, Y., Yang, L., Sun, T., Zhao, J., Lyu, Z., Zhuo, O., Wang, X., Wu, Q., Ma, J. & Hu, Z. (2015) Significant Contribution of Intrinsic Carbon Defects to Oxygen Reduction Activity. *ACS Catalysis*. 5 (11), 6707–6712. doi:10.1021/acscatal.5b01835.

Quílez-Bermejo, J., Morallón, E. & Cazorla-Amorós, D. (2020) Metal-free heteroatom-doped carbon-based catalysts for ORR: A critical assessment about the role of heteroatoms. *Carbon*. 165, 434–454. doi:10.1016/j.carbon.2020.04.068.

Radovic, L.R., Salgado-Casanova, A.J.A. & Mora-Vilches, C. V. (2020) On the active sites for the oxygen reduction reaction catalyzed by graphene-based materials. *Carbon*. 156, 389–398. doi:10.1016/j.carbon.2019.09.059.

Tao, L., Wang, Q., Dou, S., Ma, Z., Huo, J., Wang, S. & Dai, L. (2016) Edge-rich and dopant-free graphene as a highly efficient metal-free electrocatalyst for the oxygen reduction reaction. *Chemical Communications*. 52 (13), 2764–2767. doi:10.1039/c5cc09173j.

Waki, K., Wong, R.A., Oktaviano, H.S., Fujio, T., Nagai, T., Kimoto, K. & Yamada, K. (2014) Non-nitrogen doped and non-metal oxygen reduction electrocatalysts based on carbon nanotubes: Mechanism and origin of ORR activity. *Energy and Environmental Science*. 7 (6), 1950–1958. doi:10.1039/c3ee43743d.

Yan, X., Jia, Y. & Yao, X. (2018) Defects on carbons for electrocatalytic oxygen reduction. *Chemical Society Reviews*. 47 (20), 7628–7658. doi:10.1039/C7CS00690J.

20 C 22 arbon 2022

# Performance of C/*c*Si Hybrids and Composites as Anode Material in Li-ion Batteries

**Samantha L. Flores-López, Sara F. Villanueva, Belén Lobato, Lucía dos Santos-Gómez[2], Natalia Rey-Raap[2], Ignacio Cameán, Ana B. García, Ana Arenillas**

Institute of Carbon Science and Technology (INCAR) CSIC, Francisco Pintado Fe 26, 33011 Oviedo, Spain
Email: samantha.f@incar.csic.es

[2]Department of Physical and Analytical Chemistry, University of Oviedo–CINN-CSIC, 33006-Oviedo, Spain

**Keywords**
C/Si hybrids, C/Si composites, Li-ion Batteries

## INTRODUCTION

In the development of advanced devices to improve energy utilization, lithium-ion batteries play an important role as power source due to their remarkable characteristics as low weight, compact size, high energy density, longevity and versatility. However, their optimization based on a higher energy density and better rate performance is still necessary. In this scenario, studies have been carried out on different materials capable of acting as an anode due to their ion intercalation or alloying capacity, being the most successful those involving ordered nanostructures based on carbon and silicon compounds (Shi et al., 2021). The structure of the based-carbon materials has a great influence on the reversibility of the lithium intercalation and electronic conductivity, while the crystalline silicon (*c*Si) has an electrochemically active structure that enhances the specific capacity. However, using C/Si materials in lithium-ion batteries, the aim is to combine the properties of both species (Pedrayes, 2016). While the contribution of carbon seeks to provide a stable structure that allows the transport of lithium without collapse, the *c*Si species provides a high capacity, enhancing the general performance (Zhang et al., 2016). In this work, C/*c*Si materials obtained by two different approaches (i.e. hybrid and composites), were characterized and evaluated as potential anode materials for lithium-ion batteries. The main differences conferred during the synthesis process of the materials revealed an important role in their electrochemical performance.

## EXPERIMENTAL

In both, hybrid and composites materials, the carbon contribution comes from pyrolysis of resorcinol-formaldehyde (RF) species, while silicon comes from tetraethylorthosilicate (TEOS). Using these reactants as precursors, RF, Si and hybrid gels were synthesized via microwave heating, through a one-pot, quick and efficient process. Synthesis variables such as molar ratio of reagents, volume of catalyst and dilution ratio were employed to design their properties. In the case of hybrid materials, AEAPTMES as catalyst and molar ratios R/F=0.5, D=5.6 y EtOH/TEOS=4.7 were employed, whilst R/TEOS was adjusted in 0.1 or 0.5 to modify the Si content. For comparison with hybrids, Si gel was synthesized following a similar procedure (i.e. molar ratios and basic conditions), whilst RF gels were designed based on a comparable pore size. Hybrid and RF gels were carbonized under $N_2$ atmosphere at 1000°C for 2h.

To obtain the C/*c*Si materials, C/$SiO_2$ hybrid gel or a physical mixture of carbon and silica gels (i.e. composite with the same C:$SiO_2$ proportion than hybrids) were powdered and homogeneously mixed with Mg to carry out a magnesiothermic reduction. This reduction was performed at 750°C

under Ar atmosphere for 12h. The heating ramp and Si:Mg ratio were optimized with hybrid samples. Samples were washed with HCl 1M to eliminate sub-products.
The reduced materials were evaluated with adsorption-desorption $N_2$ isotherms to determine $S_{BET}$, and pore volumes. X-ray diffraction was employed to analyze the crystalline compounds formed, whilst XPS and SEM/EDX were employed to determine their chemical composition.
Finally, the C/*c*Si were studied as anodes in Li-ion batteries. For the electrochemical experiments, two-electrode (working, WE, and counter, CE) Swagelok-type cells were used. The WE composition was 70% wt. of active material, 20% wt. of NaCMC and 10% wt. of carbon black. A metallic lithium disc was the CE. WE and CE were separated by two microfiber glass discs soaked with 150 µl of electrolyte $LiPF_6$. Galvanostatic cycling tests of the cells were carried out in a BioLogic Potenciostat, in the 0.003-2.1 V and 0.01-0.9 V voltage ranges, at 500 mA $g^{-1}$ during 200 charge-discharge cycles. As a reference, electrodes composed of the same carbon and a commercial *c*Si (nanocrystalline silicon 97%, Strem Chemicals) were also tested.

**RESULTS AND DISCUSSION**

From the results obtained with the magnesiothermic reduction of hybrid materials, it was concluded that the most effective via to obtain the *c*Si specie is the use of materials with higher Si content, slow heating ramp and a Mg:Si ratio slightly above the stoichiometric one. After these treatments, around 10% wt. of *c*Si was developed on these samples and, in most cases, the crystalline specie SiC was formed. Due to the macroporous character of the hybrid precursors (c.a. 4 µm), materials with Si crystalline structures well distributed on an accessible matrix were obtained. However, the magnesiothermic treatment of composites produced different results. Unlike hybrid materials, in the case of composites, the absence of Si-C bonds increases the formation of Si with high crystallinity (see Figure 1a). In this case, crystalline SiC is not formed when a macroporous gel of high pore size is employed (c.a. 4µm) due to the low interaction between carbon and silica components. However, when the pore size decreases to 100nm, similar XRD profile and percentage composition are obtained (see Figure 1b). In terms of porous properties, small differences were observed between hybrid and composite reduced samples.

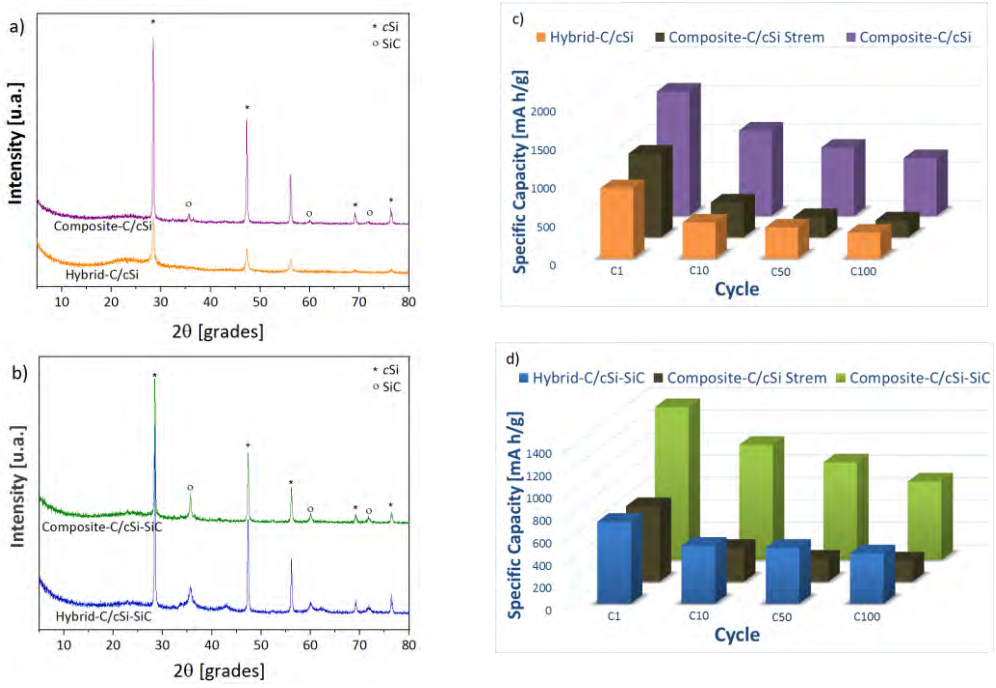


**FIGURE 1:** a,b) XRD patterns of hybrid and composite materials after reduction treatments. c,d) Specific capacity from cycles 1th, 10th, 50th and 100th of the materials.

The electrochemical performance of reduced materials was defined mainly by its constituent crystalline species. The presence of SiC should provide higher capacity retention, however, this benefit is better appreciated in the case of the hybrid-*C/c*Si-SiC material. On the other hand, *c*Si was determinant to increase the capacity of the material, especially for composites. In comparison with hybrids, the presence of individual species in composites precursors leads to high crystalline structures with better distribution, which impacts positively on their electrochemical performance (see Figures 1c and d). However, competitive performances can be achieved with both types of materials, as their capabilities are superior to those of commercial C/*c*Si Strem composite.

## CONCLUSIONS

The use of hybrid materials as the precursor of C/cSi materials with electrochemical purposes has some advantages in terms of processing time and cost. However, the arrangement of the different chemical bonds presents in this hybrid structure limits its availability during the reduction processes. On the other hand, when similar quantities of the same components are used in a composite, the efficiency of this process increases, favoring not only the crystalline properties of the final material but also their electrochemical performance. Therefore, composites are a more promising option in the development of anode materials for lithium-ion batteries.

**Acknowledgements**

Authors thanks the financial support received from Ministerio de Ciencia e Innovación de España and European Union NextGeneration EU/PRTR with the projects PCI2020-112039 MCIN/AEI-10.13039/501100011033 and PID2020-113001RB-I00 MCIN/AEI-10.13039/501100011033. NRR and LdSG are grateful for their postdoctoral grants funded by Ministerio de Ciencia e Innovación de España (IJC2019-040875-I and IJC2020-044746-I). SLF gratefully acknowledges to Principality of Asturias for their pre-doctoral grant through Severo Ochoa Program.

**References**

Pedrayes, N.C., 2016. Materiales anódicos alternativos para el desarrollo de baterías de ion-litio sostenibles. Universidad de Oviedo, España.

Shi, Q., Zhou, J., Ullah, S., Yang, X., Tokarska, K., Trzebicka, B., Ta, H.Q., Rümmeli, M.H., 2021. A review of recent developments in Si/C composite materials for Li-ion batteries. Energy Storage Materials 34, 735–754. https://doi.org/10.1016/j.ensm.2020.10.026

Zhang, L., Liu, X., Zhao, Q., Dou, S., Liu, H., Huang, Y., Hu, X., 2016. Si-containing precursors for Si-based anode materials of Li-ion batteries: A review. Energy Storage Materials 4, 92–102. https://doi.org/10.1016/j.ensm.2016.01.011

Carbon 2022

# Novel Ordered Carbon Materials for the Analysis of Aromatic Compounds

**Samantha L. Flores-López, Lucía dos Santos-Gómez[2], J. Angel Menéndez, Ana Arenillas and Miguel A. Montes-Morán**

Institute of Carbon Science and Technology (INCAR), CSIC, Francisco Pintado Fe 26, 33011 Oviedo, Spain
Email: samantha.f@incar.csic.es

[2]Department of Physical and Analytical Chemistry, University of Oviedo–CINN-CSIC, 33006-Oviedo, Spain

**Keywords**
Ordered carbon materials, Solid phase extraction, Chromatography

## INTRODUCTION

Carbon-based materials with graphene and other ordered structures have a significant potential in different analytical techniques. Their porous properties, thermal stability and adsorption capacity make them suitable for sample preparation and separation processes (Zheng et al., 2021). Thanks to their good adsorption capacity, graphene aerogels (GA) have achieved notable success in this field for their use in environmental applications. Specifically, some recent studies have unveiled the potential of graphene sponges (GS) as solid-phase extraction (SPE) materials (Wang et al., 2018). However, GS present some disadvantages including long synthesis processes and their low mechanical strength. This leads to a continuous search for more robust, easier to produce or cheaper materials. In this work, we present a new, more efficient synthesis process of GA with a similar structure to GS, but showing better mechanical properties due to the incorporation of resorcinol-formaldehyde (RF) gels in their structure. These materials have been evaluated in SPE processes for the purification/concentration of benzotriazoles with promising results.

## EXPERIMENTAL

Synthesis of GA materials was carried out through the sol-gel method assisted by microwave heating. Precursor solutions were prepared by using R (Indspec 99%), F (Merck 37%) and a graphene oxide (GO) suspension as solvent. The molar ratio R/F =0.5 and dilution ratio D = 200 were fixed, whilst different concentrations of the GO suspension were employed (i.e. 5 and 10 mg/L) to adjust the final graphene content to 40% and 60% wt. Gelling and curing of the RF mixtures were carried out at 85°C under microwave heating for 3h. Freeze drying was employed to obtain high porous gels. A GS was synthesized by direct lyophilization of the graphene oxide suspension and used for comparison. Samples were heated at 1000°C for 2h under $N_2$ atmosphere. Additionally, the sample with 40% wt. of graphene was treated at 2000°C for 1h (G-GA-40%). The resultant materials were characterized by $N_2$ adsorption-desorption isotherms (-196°C), XRD and SEM.

For SPE experiments, cartridges with 15 or 80 mg of our materials were prepared. Cartridges were washed with water and methanol prior use. Single solutions or mixtures of three benzotriazoles (UV-P, UV-329 and UV-234) were used to evaluate the retention/elution capacity of our materials and to perform concentration and solvent change tests. Methanol was used as solvent. For retention/elution test, cartridges were charged with 25mL of single solution (2500µg/L), and eluted with 12.5mL of acetone or acetonitrile. Materials with the best performance were used in a concentration test with mixtures of benzotriazoles. In this case, cartridges with 15mg of material were charged, and different volumes of eluent were employed to determine the optimum

extraction. In all cases, bezotriazoles were determined in a HPLC-UV Agilent 1100 Series. Isocratic elution (0.7 mL/min) of MeOH:$H_2O$ 95:5 or 90:10 was performed with a C18 column, with an injection volume of 20 µL and λ of 340 nm.

## RESULTS AND DISCUSSION

The GA obtained show a morphology comparable to that of GS. However, in this case the graphene sheets show a network with a certain order thanks to the presence of the RF gel, which acts as a binder. All GA present a macroporous structure, whose specific surface area and microporosity varying with the graphene content and the thermal treatment applied (Table 1). The GO reduction and, consequently, the formation of graphitic planes was confirmed by XRD (band at 25° 2θ, Figure 1). These ordered structures increase with the graphene content, but are considerably developed when the additional treatment at higher temperature is applied (Figure 1). Results obtained in the retention/elution tests show how the performance of the materials is determined by the specific surface available, micropore volume and the degree of ordering. The retention capacity of the materials was around 1.7-2.4 µg/mg being the highest one for GA-40% and the smallest one for G-GA-40%. For elution capacity (Figure 2), sample GA-60% and G- GA-40% show the best performance, comparable o higher to that of GS. The best solvent to elute samples was acetone, with the maximum recovery at 1000 µL of eluent volume.

**TABLE 1.** Specific surface area and micropore volume.

| Sample | $S_{BET}$ ($m^2/g$) | $V_{micro}$ ($cm^3/g$) |
|---|---|---|
| GS | 203 | 0.04 |
| GA-40% | 247 | 0.06 |
| GA-60% | 164 | 0.03 |
| G-GA-40% | 51 | 0.02 |

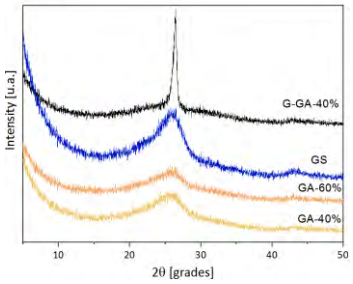


**FIGURE 1:** XRD pattern of AG samples.

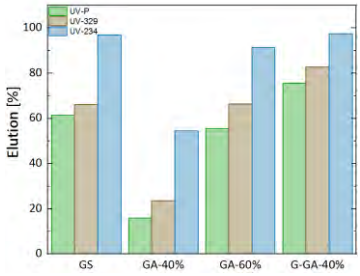


**FIGURE 2:** Elution capacity.

## CONCLUSIONS

These novel graphene-based carbon materials are promising materials for their use in the analysis of aromatic compounds (benzotriazoles). These GA presented an effective adsorption/desorption process for molecules of this family, making them attractive for purification and separation applications. Moreover, when compared with GS, the addition of RF species implies a simpler synthesis process rendering GA samples that can be handled better thanks to their lower graphene content and their reinforced RF structure.


### Acknowledgements

This work was financed by Ministerio de Ciencia e Innovación de España and European Union NextGeneration EU/PRTR (PCI2020-112039 MCIN/AEI-10.13039/501100011033, PID2020-115334GB-I00 MCIN/AEI-10.13039/501100011033 y PID2020-113001RB-I00 MCIN/AEI-10.13039/501100011033). LdSG and SLF gratefully acknowledges to Ministerio de Ciencia e Innovación de España and Principality of Asturias for their post and predoctoral grants (IJC2020-044746-I and Severo Ochoa Program).


### References


Wang, X., Wang, J., Du, T., Kou, H., Du, X., Lu, X., 2018. Determination of six benzotriazole ultraviolet filters in water and cosmetic samples by graphene sponge-based solid-phase extraction followed by high-performance liquid chromatography. Anal Bioanal Chem 410, 6955–6962. https://doi.org/10.1007/s00216-018-1301-6

Zheng, X., Zhao, Y., Wenwu, Zheng, H., Gao, L., 2021. Application of graphene and its compounds in pretreatment of environmental samples. IOP Conf. Ser.: Earth Environ. Sci. 687, 012064. https://doi.org/10.1088/1755-1315/687/1/012064

Carbon 2022

# Nitrogen-rich carbon for redox-active capacitor with a high-frequency response

**Elżbieta Frąckowiak[1], Adam Ślesiński[1], Justyna Piwek[1], Krzysztof Fic[1], Sergio Aina[2], Alen Vizintin[3], Blaz Tratnik[3], Elena Tchernychova[3], Maria Pilar Lobera[2], Robert Dominko[3], Maria Bernechea[2]**

[1] Institute of Chemistry and Technical Electrochemistry, Poznan University of Technology, 60-965 Poznan, Poland

[2] Instituto de Nanociencia y Materiales de Aragón (INMA) CSIC-Universidad de Zaragoza, Department of Chemical and Environmental Engineering, University of Zaragoza, Campus Río Ebro-Edificio I+D, C/ Mariano Esquillor S/N, 50018 Zaragoza, Spain

[3] National Institute of Chemistry, Hajdrihova 19, 1000 Ljubljana, Slovenia

Email: elzbieta.frackowiak@put.poznan.pl

**Keywords**
electrochemical capacitor, high frequency response, redox active compounds

Electrochemical capacitors (ECs) are energy storage devices capable to operate over many thousands of cycles. Their energy storage phenomenon is based on electrostatic attractions of respective ions within porous activated carbon electrodes. Beside superior power rates, ECs still suffer from relatively low energy density values especially when compared to traditional batteries. Therefore, one of the main research goal is focused on energy density enhancement. The strategy can be realized by increasing the operation voltage (U) or by improvement of capacitance (C) via introduction of redox-active materials to the EC system. It has been reported that additional contribution to the capacitance can be achieved thanks to the pseudocapacitance originated from heteroatoms present in the electrode material (mainly nitrogen, sulfur, oxygen and iodide). Another option is to utilize redox-active electrolytes (e.g. iodides, selenocyanates or thiocyanates).

In this work, we present the good performance of EC system based on nitrogen-rich carbon prepared from adenine precursor via soft-templating method (AdeKZ)[1]. The special properties can originate from the advantageous nanostructure visible in TEM image (Figure 1). It is compared to the commercially available carbon YP50F. AdeKZ exhibits less disordered and dense structure of the graphene layers than YP50F. The presence of mesopores as well as supermicropores enables to obtain wide diffusion paths, while keeping high specific surface area.

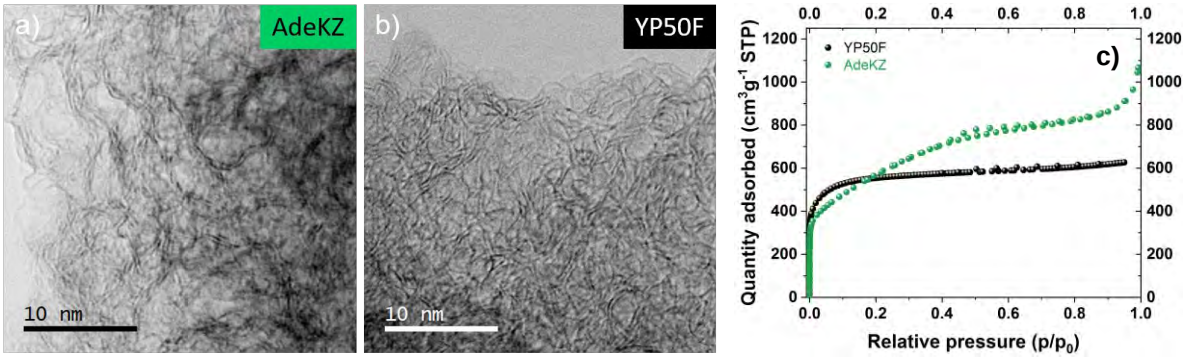


Figure 1: TEM images of: a) AdeKZ; b) YP50F at high magnification; c) nitrogen sorption isotherms

AdeKZ carbon contains 5.5% of nitrogen, mainly in the quaternary type (401.0 eV, 54.9%), pyridinic (398.3 eV, 28.9%) and in much less concentration pyrrolic one (399.5 eV, 16.2%) as shown in Figure 2a. The presence of pyridine, pyrrole and quaternary N enhances the capacitance of the system with N-rich carbon. Pyrrolic and pyridinic N contributes to the pseudocapacitance due to their e- donor behaviour while the positive charge of quaternary N improves the electron transfer.

The carbon enriched in N (AdeKZ) is characterized by the enhanced capacitance, good conductivity and wettability in relation to YP50F. The performance of two-electrode capacitor operating in 1 mol $L^{-1}$ $Li_2SO_4$ electrolyte (at 1.5 V) is presented in Figure 2b. The interesting parameters of the carbon is not only the superior gravimetric capacitance comparing to commercial carbon (130 F $g^{-1}$ *vs.* 100 F $g^{-1}$), but also the high frequency response (107 F $g^{-1}$ *vs.* 42 F $g^{-1}$ at 1 Hz).

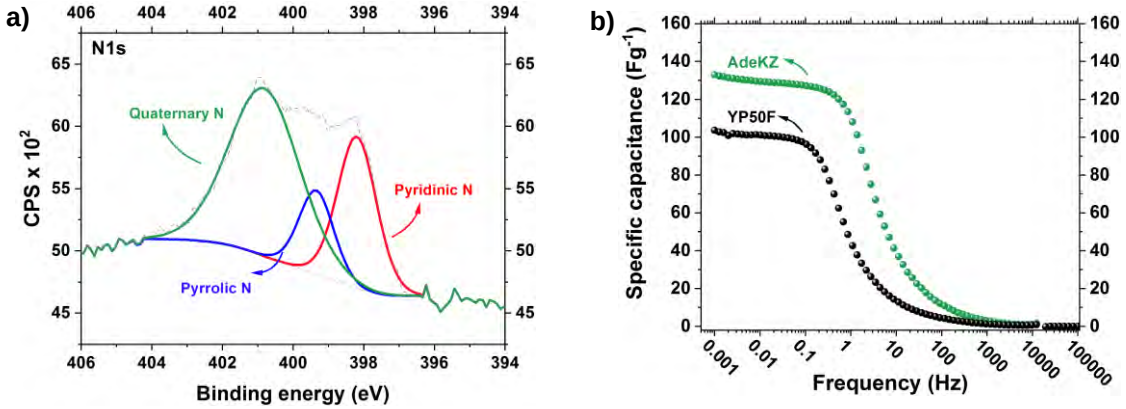


Figure 2: a) XPS deconvolution of N1s region for AdeKZ, b) Electrochemical impedance spectra (capacitance vs. frequency) recorded at 0 V for the AC/AC capacitors: YP50F (black), AdeKZ (green) in 1 mol $L^{-1}$ $Li_2SO_4$

Additionally, in order to increase the overall ECs capacitance, bismuth sulfide ($Bi_2S_3$) nanocrystals were introduced to carbon matrix. It has been proven that activity of sulphur on the negative electrode is achieved only when mercaptopropionic acid (MPA) linker between carbon and nanocrystals is used. MPA is a crucial compound for attachment of sulphide to carbon. The asymmetric capacitor system with various amount of $Bi_2S_3$ (5%-15%) in the negative electrodes were tested exhibiting higher capacitance values than pure carbon. Furthermore, in order to compensate the charge on the negative side, 1 mol $L^{-1}$ KI redox-active electrolyte was applied. The capacitance increased from 105 F $g^{-1}$ with 1 mol $L^{-1}$ $Li_2SO_4$ to 265 F $g^{-1}$ in 1 mol $L^{-1}$ KI electrolyte. Various concentrations of KI were tested (0.5 - 2 mol $L^{-1}$) proving that the higher concentration of iodide, the higher the capacitance. A long-term stability and self-discharge phenomena have been investigated. It has been demonstrated that hybridized EC system based on bi-redox activity (sulfur and iodide) exhibits well-balanced solution having both high energy and high power density. Embedding the sulphur activity inside the carbon matrix and application of iodide-based aqueous electrolyte allows a stable system without cross-mixing effect of two redox couples to be achieved.

*Acknowledgement: The authors would like to acknowledge the M-ERA.NET (NOEL) project.*

REFERENCE

[1] J. Piwek, A. Slesinski, K. Fic, S. Aina, A. Vizintin, B. Tratnik, E. Tchernychova, M. P. Lobera, M. Bernechea, R. Dominko, E. Frackowiak, High frequency response of adenine-derived carbon in aqueous electrochemical capacitor, Electrochimica Acta, (2022) 140649.

20 C 22 arbon 2022

# Bio-based porous carbon pre-forms for the manufacture of high-performance composites

**Christian Fuerst[1], Christoph Unterweger[1], Matthias Mihalic[1], Christopher Wallis[2], Erich Neubauer[2]**
[1]Wood K plus - Kompetenzzentrum Holz GmbH, Altenbergerstrasse 69, 4040 Linz, Austria
Email: c.fuerst@wood-kplus.at

[2]RHP Technology GmbH, Forschungs- und Technologiezentrum, 2444 Seibersdorf, Austria

**Keywords**
Porous carbon, bio-based, high-performance composites.

## INTRODUCTION

Global warming and the depletion of fossil fuels force a transition to renewable energies and resources. This also requires a reorientation in the field of material development. Carbon composites in a wide variety of forms play a central role in this process, since their properties such as high mechanical strength, low specific weight, high-temperature resistance and excellent chemical resistance make them key components in materials development (Vanholme, 2013). The majority of carbon fibers and related materials is based on polyacrylnitrile (PAN) and pitch precursors – both fossil raw materials. Bio-based carbon fibers are industrially only used in small quantities (Park, 2015). In this work the preparation of bio-based porous carbon pre-forms is presented which can be transformed in subsequent steps to high-performance composites like carbon reinforced ceramics (CMCs, Ceramic Matrix Composites) and metal alloys (MMCs, Metal Matrix Composites) and carbon-fiber reinforced carbons (CFCs). Green bodies from novel thermoset-based natural-fiber composites (NFCs) using injection moulding, 3D-printing, extrusion and pressing techniques are prepared. In a subsequent carbonization step these NFC green-bodies are transformed into porous carbon pre-forms, which can further be processed into MMCs, CMCs and CFCs by infiltration with metals, semi-metals and carbon-rich bio-based binders. Material characterization is done along the process chain.

## MATERIALS AND METHODS

For the preparation of the NFCs cellulose fibers (length (L)/diameter (D)-ratio of 30; e.g. Tencel FCP) and wood flour (L/D-ratio up to 3; e.g. Arbocel C100) were used as fiber components. The thermoset matrix was based on novolac and urotropin as hardener. Optionally matrices based on the lignin Indulin AT were used. Low density polyethylene (LDPE) and Mowital (polyvinylbutyral) acted as thermoplastic components. As processing aids stearates and fatty acid derivatives were used. The compounding took place on a Cincinnati Fiberex Konos 38, a counter-rotating conical twin-screw extruder, and a Brabender DSE20/40 twin screw extruder. Injection moulding of green-bodies was done on a Wittmann-Battenfeld SmartPower 120/350 injection moulding machine and profile-extrusion on a Cincinnati Fiberex Konos 38 (Mihalic, 2019).
3D-printing of green-bodies was performed on an EXAM feedstock printer from AIM 3D GmbH. Pressing experiments were performed on a Fontijne LabEcon 300 press. Carbonization, heat treatments as well as infiltration experiments were carried out in a GERO HTK-8 furnace. Hot pressing under different atmospheres was conducted in furnaces of FCT Systeme GmbH. Micrographs for the evaluation of the homogeneity and porosity (e.g. carbons) and for the phase analysis (e.g. carbon/silicon/silicon carbide (C/Si/SiC); C/copper (Cu)) of the specimens were taken of embedded and polished samples by light optical microscopy (LOM) with an Olympus device. Mechanical testing was performed according to ISO 178 on a Messphysik BETA5 universal testing machine. Density

measurements were performed applying Archimedes´ principle. Thermal diffusivity was determined by heat flow thermography with the laser-flash method.

**RESULTS AND DISCUSSION**

Novolac-based compounds with 30 wt% natural fiber content and 12 wt% LDPE offer a processing window of around 5 minutes at 150 °C and therefore can be shaped to NFC green-bodies by different techniques: on the one hand by injection moulding with pressures ranging up to 2000 bars as well as by 3D-printing at zero pressure. Carbonization of these green-bodies leads to porous carbon templates with densities between 0.6-0.75 g $m^{-2}$. **FIGURE 1** shows 3D-printed cups, an injection moulded plate and the porous carbon template thereof with a representative micrograph for those porous carbons derived from 30 wt% fiber reinforced green-bodies.


**FIGURE 1**: 3D-printed cups, novolac-based (left), lignin-based (middle-left), injection moulded plate (middle), corresponding porous carbon plate (middle-right), micrograph of porous carbons (white: carbon, right).

Compounds with a natural fiber content > 40 wt% can be processed by pressing and extrusion only - for injection moulding the necessary pressures get too high and in 3D-printing the flowability is too low and friction too high. With fiber contents of 50 wt% in the green-bodies densities of the porous carbon templates reach 0.85-0.95 g $m^{-2}$. **FIGURE 2** shows a pressed plate and extruded profiles with their corresponding porous carbon templates and a micrograph for those porous carbons derived from 50 wt% fiber reinforced green-bodies. One can see a clear difference to the micrograph in **FIGURE 1**.


**FIGURE 2**: pressed board (left), corresponding porous carbon (middle-left), extruded NFC profiles with corresponding porous carbons (middle, middle-right), micrograph of porous carbons (white: carbon, right).

CMCs were prepared by liquid silicon infiltration of the porous carbons at 1600 °C in vacuum. The density of the porous carbon determines the grade of the C/Si/SiC-ceramics (see **FIGURE 3**). The carbons derived from green-bodies with 50 wt% natural fiber content reach much higher SiC contents than those with 30 wt% fiber content. **TABLE 1** shows an overview of the reached properties.

**TABLE 1**: properties of CMCs realized by liquid silicon infiltration of porous carbons (C/Si/SiC-ceramics)

| *fiber content [wt%] | density carbon [g $cm^{-3}$] | porosity carbon [vol%] | SiC [vol%] | Si [vol%] | C [vol%] | Pores [vol%] | bending strength [MPa] | bending modulus [GPa] | density ceramic [g $cm^{-3}$] |
|---|---|---|---|---|---|---|---|---|---|
| 30 | 0.72 | 49.8 | 65.3 | 26.1 | 7.8 | 0.8 | 107 | 149 | 2.78 |
| 50 | 0.87 | 40.0 | 85.1 | 8.3 | 4.5 | 2.1 | 231 | 141 | 2.96 |
| 50 | 0.91 | 37.2 | 89.2 | 5.1 | 4.3 | 1.4 | 245 | 184 | 3.03 |

* in green-bodies

MMCs were prepared by pressing and hot pressing techniques. 50/50 wt% mixtures of copper powder and natural fibers (Tencel FCP, Arbocel C100) were pressed with 100 MPa to pellets which were carbonized at 900 °C. The resulting specimens were densified and heat treated at 1000 °C and 50 MPa under a reducing atmosphere (see **FIGURE 3**). The fiber structure of the carbonized Tencel FCP with a high L/D-ratio and their flexibility result in a much better heat conductivity compared to the brittle carbonized wood flour Arbocel C100 with a low L/D-ratio (see **TABLE 2**).
Comparable Cu-MMCs with PAN-based CF reach 150 W $m^{-1}$ $K^{-1}$ but with only 40 vol% CF (Neubauer, 2003). Reducing CF volume increases the heat conductivity. Based on that it can be concluded that a Tencel based Cu-MMC with a reduced CF-content of 40 vol% (in this work: 56 vol%, 112 W $m^{-1}$ $K^{-1}$) would be quite similar in the properties compared to a PAN-CF Cu-MMC with 40 vol% CF-content.

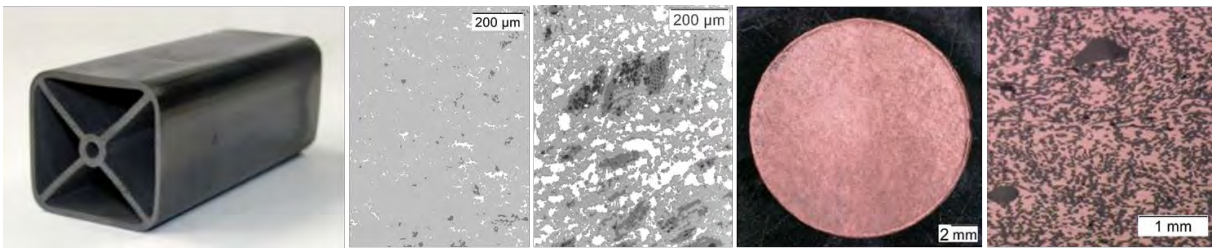


**FIGURE 3**: C/Si/SiC-ceramic profile (left); micrographs (SiC: light grey, C: dark grey, Si: white): C/Si/SiC with high SiC-content (green-body with 50 wt% fiber content) (middle-left), C/Si/SiC with high Si-content (green-body with 30 wt% fiber content) (middle); Cu/C-MMC (middle-right), micrograph of Cu/C-MMC (Cu: reddish, right).

**TABLE 2**: properties of MMCs, copper reinforced with bio-based carbon fibers

| | density | Cu / CF-content | | thermal diffusivity | heat conductivity* |
|---|---|---|---|---|---|
| | [g $cm^{-3}$] | [wt%] | [vol%] | [$m^2$ $s^{-1}$] | [W $m^{-1}$ $K^{-1}$] |
| **Tencel + Cu** | 4,67 | 83 / 17 | 44 / 56 | $34{,}8*10^{-6}$ | 112 |
| **Arbocel C100 + Cu** | 4,78 | 80 / 20 | 39 / 61 | $17{,}3*10^{-6}$ | 55 |

* calculated

## CONCLUSIONS

Thermoset-based NFC are prepared by injection moulding, 3D-printing, extrusion and pressing techniques. A carbonization of these NFC green-bodies leads to porous carbon pre-forms. Further processing to CMCs by liquid silicon infiltration leads to C/Si/SiC-ceramics. The fiber content in the green-bodies determines in the end the grade of the final CMCs. MMCs have been prepared by pressing techniques and heat treatment from copper and natural fibers. The fiber structure of viscose derived Cu/C-MMCs is superior to the particle structure of wood and leads to competitive heat conductivities. The focus in the following work lies in developing MMCs by infiltration with metals and CFCs by infiltration with carbon-rich bio-based binders into porous carbon forms.

**Acknowledgements**

This work was conducted within the project BioC4HiTech funded through the program Production of the Future by the Austrian Research Promotion Agency (FFG).

**References**

Mihalic, M., Soares de Sousa, F., Burzic, I., Hinterreiter, A., Stifter, D. and Fürst, C. (2019). Morphology and Characterisation of Novolac-LDPE Based Mixtures as Matrix for Injection Moulded Green Bodies for Bio-based SiC Ceramics. *Ceramics*, 2, 536–550. https://doi.org/10.3390/ceramics2030041.

Neubauer, E (2003). Optimierung der Grenzfläche in Kupfer-Kohlefaser-Verbundwerkstoffen. Phd thesis, TU Wien.

Park, S.J., and Heo, G. Y. (2015). Carbon Fibers. *Springer Series in Materials Science*, 210, 31-66.

Vanholme, B., Desmet, T., Ronsse, F., Rabaey, K., Van Breusegem, F., De Mey, M., and Boerjan, W. (2013). Towards a carbon-negative sustainable bio-based economy. *Frontiers in plant science*, 4, 174ff.

# Carbon-Polydopamine-Ru composites towards Palm oil valorization

Sebastián Gámez[1*], Ernesto de la Torre[2] and Eric M. Gaigneaux[1]
[1] Institute of Condensed Matter and Nanosciences, Université catholique de Louvain, Place Pasteur 1, L4.01.09, 1348 Louvain-la-Neuve, Belgium
[2] Department of Extractive Metallurgy, Escuela Politécnica Nacional, Ladron de Guevera E11-253, Quito 170517, Ecuador
*sebastian.gamez@uclouvain.be

## Introduction

Nowadays, palm oil is an interesting raw material because of its low price and high content in unsaturated fatty acids (UFAs) [1]. UFAs can be employed as a novel source of chemical base materials for several industries (e.g. foods, polymers, cosmetics) [2]. Amid them, oleic (18:1 n-9) and linoleic (18:2 n-9,12) acids are the most abundant UFAs within palm oil and can be used for the production of azelaic acid via oxidative cleavage of their carbon-carbon double bond(s). Azelaic acid is commonly used as main ingredient for creams to cure cutaneous malignant melanoma [3]. On one hand oxidative cleavage is up to now carried out on pure UFAs, by ozonolysis or homogenous catalysis. Moreover, there are no example in the literature about the oxidative cleavage of a real vegetable oil [4]. On the other hand, current heterogeneous catalysts display poor activity due to the poor contact among the UFA and the active phase [4]. Our work with oxidized carbon black (CBO) modified with polydopamine (PDA) and Ru has proven to be efficient in the oxidative cleavage of pure oleic acid via a not frequent boomerang catalytic mechanism [5]: the functional groups of PDA release Ru ions in the reaction medium where they are oxidized by $NaIO_4$ into $Ru(VIII)O_4$ (the active species for the oxidative cleavage), then once the reaction ends PDA recovers Ru species allowing to re-use the catalyst multiple times. Based on this success, we extended our investigation on the application of this catalyst in the oxidative cleavage of UFAs of a real palm oil, the idea being to observe whether it is still possible to perform the cleavage reaction efficiently on the complex mixture of fatty acids (FAs) that a real oil represents using CBO and carbon nanoparticles (CCN) as supports. In our presentation, we will report on both steps of our investigation.

## Materials and Methods

Carbon black was purchased from Degussa while CCN were synthesized by submitting a glucose solution to hydrothermal treatment. PDA was deposited on both carbon supports by *in situ* polymerization of dopamine hydrochloride under alkaline conditions. Afterwards, a $RuCl_3.H_2O$ solution was used to deposit Ru (2 wt%) on the PDA-modified supports by wet impregnation. Prior oxidative cleavage, palm oil was derivatized with KOH-MeOH and HCl-MeOH solutions in order to hydrolyze the triglycerides and transform the free FAs into methyl esters. The organic fraction was dissolved in ethyl acetate and incorporated in the mixture of our catalytic system consisting in $H_2O$/MeCN/AcOEt (4/2/1) along with the synthesized composites and $NaIO_4$. The reaction was carried out at room temperature and monitored by Gas Chromatography, UV-Vis and NMR spectroscopy. Recycling tests and hot-filtration tests were carried out to assess the catalysts stability.

## Results and Discussion

The assessed palm oil contained 41% of oleic acid and 9% of linoleic acid. CBO-Ru(2%) resulted to be more active (Fig. 1a) than CCN-Ru(2%) in the oxidative cleavage of UFAs, demonstrating that a macroporous material (Fig. 1e) is preferable when the substrates are large molecules like oleic or linoleic acid. Catalysts synthesized with PDA presented higher catalytic activity reaching complete conversions in 7 hours (Fig. 1a). Recycling tests demonstrated that PDA catalysts maintained its catalytic activity after 5 runs (Fig. 2b) even though Ru ions were detected in the reaction medium during the Hot-filtration test and UV-Vis monitoring (Fig. 1d and Fig. 1f). These results confirmed the PDA benefits observed for the oxidative cleavage of pure oleic acid [5].

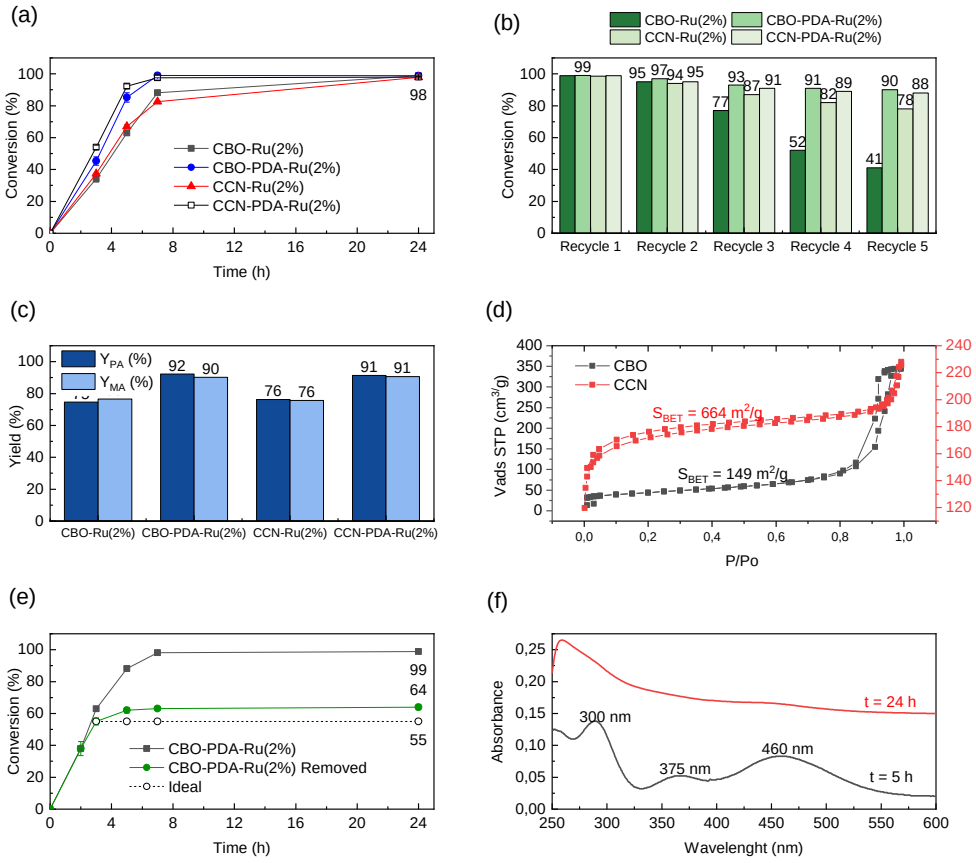


**Figure 1.** a) Catalytic activity of synthesized composites; b) Recycling tests; c) Yield of pelargonic (PA) and azelaic (AA) acid; d) Hot-filtration test with CBO-PDA-Ru(2%) e) $N_2$ physisorption isotherms; f) UV-Vis spectra of oxidative cleavage medium at reaction times of 3 and 24 h.

With real palm oil, as was observed in the experiments with pure oleic acid, PDA catalysts also behave boomerang wise as explained above. The rest of fatty acids within the oil did not affect the catalysts performances and in addition working with a real oil allowed boosting the production of azelaic acid thanks to other UFAs than oleic acid. We will thus demonstrate that the proposed catalytic system can successfully perform the oxidative cleavage of a real oil.

## Significance

Our home-developed Ru-PDA-modified carbon catalysts perform the oxidative cleavage of UFAs within a real oil under soft and sustainable conditions. This opens a novel route to the production of a high value-added product with medicinal applications from a cheap feedstock as palm oil. This might also have positive societal consequences for the development of poor countries where palm oil (and similar) is abundant.

## References

[1] Andi, N et al., European Journal of Lipid Science and Technology, 109, 422-432 (2007).
[2] Mamat, H et al., Food Chemistry, 9, 731-736 (2005).
[3] Fitton, et al., Drugs 41, 780–798 (1991).
[4] Kerenkan, A et al., Catal. Sci. Technol., 6, 971-987 (2016).
[5] Gámez, S et al., Chemical Engineering Journal, 427, 131820 (2022).

Carbon 2022

# Activated Carbon for Hydrogen Storage: Optimization of Synthesis Conditions

**Ximena García, Claudia Ulloa[2], Alejandro Karelovic, Francisca Troncoso, Daniel Parra and Karin Walter**

Carbon and Catalysis Laboratory (Carbocat), Department of Chemical Engineering, Universidad de Concepción, P.O. Box 160-C, Concepción, Chile

Email: xgarcia@udec.cl

[2]Department of Environmental Engineering and EULA Chile Centre, Universidad de Concepción, P.O. Box 160-C, Chile

**Keywords**

Hydrogen storage, activated carbon, chemical activation.

## INTRODUCTION

The worsening of the climate crisis during the past decade has promoted the replacement of oil-based fuels with cleaner energy sources with low or no $CO_2$ emissions, such as hydrogen.

Even though the use of hydrogen offers multiple advantages, there are several challenges in the implementation of a hydrogen economy, which include economic and technological factors, particularly, the storage of hydrogen for onboard applications. Any technological alternative should consider not only safety issues, but also, volumetric capacity, stability, heat transfer, recharge time and feasible temperatures. According to the US-DOE, the ultimate storage parameters should be at least 5.5 wt.% and 0.040 kg $H_2$/L (DOE, 2017). Although multiple types of storage technologies are available, this goal have not yet been fully fulfilled. Nevertheless, the most promising characteristics, for onboard applications, are exhibited by solid-storage materials, such as hydrides, MOFs and carbonaceous materials (Nazir et al., 2020). Therefore, extensive research on this type of materials is being done. In this context, the current study focuses on the evaluation of activated carbons prepared from coal as hydrogen storage material.

## METODOLOGY

Different activated carbons were prepared by chemical activation, using a bituminous coal (Biobío region, Chile) as precursor. Activation parameters such as activating agent (NaOH, KOH), temperature (650-800 °C), time (0.5, 1.5, 2.0 h), hydroxide:coal ratio (3:1, 4:1, 5:1) and preparation method (wet impregnation, physical blending) were varied. Additional evaluated parameters were a high temperature heat treatment (1700 °C, 2h) after activation and, the incorporation of nitrogen through a hydrothermal synthesis (N-precursor: $NH_3$, parameters tested: concentration of $NH_3$ in the solution (10, 15, 20, 25 wt.%) and synthesis time (3, 6, 12, 24 h)). The resulting activated carbons were characterized by $N_2$ adsorption/desorption isotherms (77 K, 0-1 bar) and the hydrogen adsorption capacity was evaluated using a volumetric method at 77 K and 0-1 bar.

## RESULTS AND DISCUSSION

Optimal synthesis conditions (high BET area and micropore volume, $V_{micro}$) differ depending upon the activation agent (Figure 1). Nonetheless, both activating agents performed at their best using longer activation times (2 h) and a hydroxide:coal ratio of 4:1. The main differences were observed for the activation temperature and preparation method. 650 °C and wet impregnation were the most successful conditions when activating with NaOH, whereas for KOH, these were 750°C, and blending

as the preparation method. Using these conditions, BET areas up to 2700 $m^2/g$ were achieved, with pore size distribution showing a high $V_{micro}/V_{total}$ ratio.

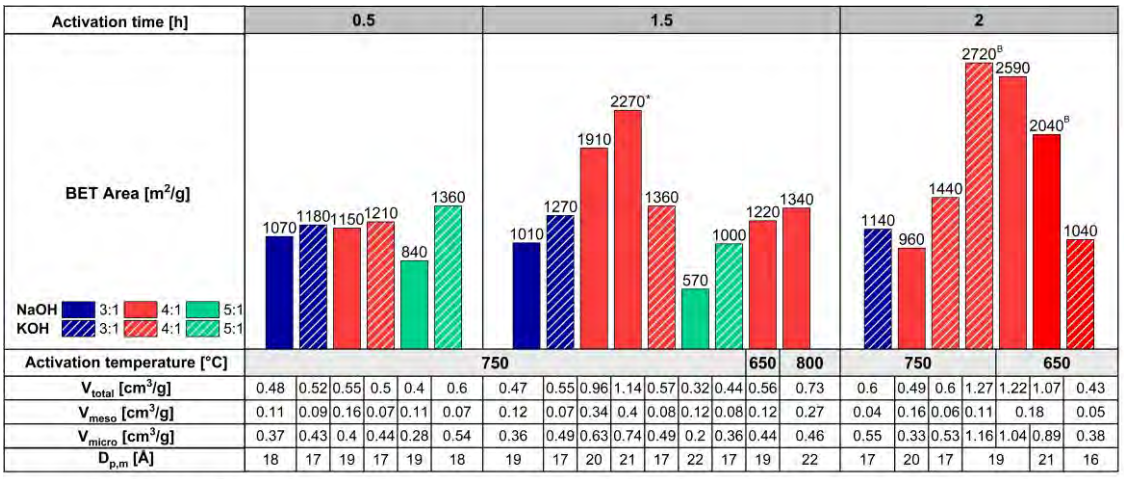


| Activation time [h] | 0.5 | | | | | | 1.5 | | | | | | | | | 2 | | | | | | |
|---|---|---|---|---|---|---|---|---|---|---|---|---|---|---|---|---|---|---|---|---|---|---|
| Activation temperature [°C] | 750 | | | | | | 750 | | | | | | 650 | 800 | | 750 | | | | 650 | | |
| $V_{total}$ [$cm^3/g$] | 0.48 | 0.52 | 0.55 | 0.5 | 0.4 | 0.6 | 0.47 | 0.55 | 0.96 | 1.14 | 0.57 | 0.32 | 0.44 | 0.56 | 0.73 | 0.6 | 0.49 | 0.6 | 1.27 | 1.22 | 1.07 | 0.43 |
| $V_{meso}$ [$cm^3/g$] | 0.11 | 0.09 | 0.16 | 0.07 | 0.11 | 0.07 | 0.12 | 0.07 | 0.34 | 0.4 | 0.08 | 0.12 | 0.08 | 0.12 | 0.27 | 0.04 | 0.16 | 0.06 | 0.11 | 0.18 | | 0.05 |
| $V_{micro}$ [$cm^3/g$] | 0.37 | 0.43 | 0.4 | 0.44 | 0.28 | 0.54 | 0.36 | 0.49 | 0.63 | 0.74 | 0.49 | 0.2 | 0.36 | 0.44 | 0.46 | 0.55 | 0.33 | 0.53 | 1.16 | 1.04 | 0.89 | 0.38 |
| $D_{p,m}$ [Å] | 18 | 17 | 19 | 17 | 19 | 18 | 19 | 17 | 20 | 21 | 17 | 22 | 17 | 19 | 22 | 17 | 20 | 17 | 19 | 21 | | 16 |

*Nitrogen flow: 800 [ml/min], [B]Preparation method: blending, $V_{total}$: total pore volume, $V_{meso}$: mesopore volume, $V_{micro}$: micropore volume, $D_{p,m}$: mean particle size.

**FIGURE 1**: Summary of the assayed conditions tested

According to literature, a higher surface polarization is reported to be beneficial for the hydrogen storage capacity (Ströbel et al. 2016) and a higher basicity should promote the adsorption of acid gases (Sousa et al. 2013). Consequently, further tests were performed to assess the effect of a high temperature heat treatment (to attempt an increase in the polarization of the surface) and the incorporation of nitrogen (to increase the basicity of the surface) in the textural properties and storage capacity. Selected results are shown in Figure 2.

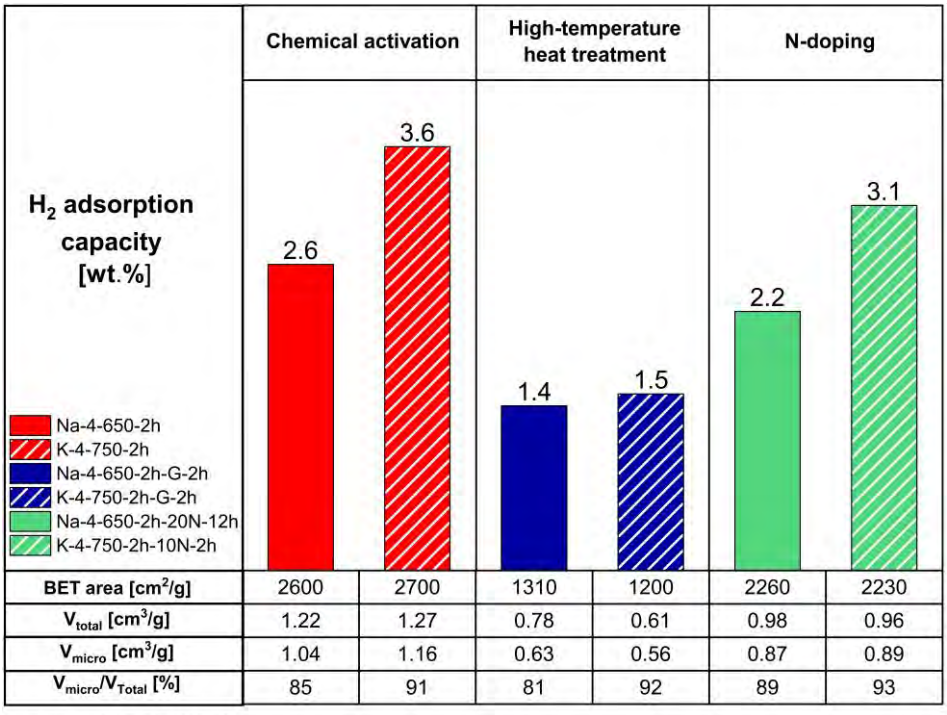


| | Chemical activation | | High-temperature heat treatment | | N-doping | |
|---|---|---|---|---|---|---|
| BET area [$cm^2/g$] | 2600 | 2700 | 1310 | 1200 | 2260 | 2230 |
| $V_{total}$ [$cm^3/g$] | 1.22 | 1.27 | 0.78 | 0.61 | 0.98 | 0.96 |
| $V_{micro}$ [$cm^3/g$] | 1.04 | 1.16 | 0.63 | 0.56 | 0.87 | 0.89 |
| $V_{micro}/V_{Total}$ [%] | 85 | 91 | 81 | 92 | 89 | 93 |

Notation: **A-R-T-t-XN/G-Yh**
A: Activating agent (Na for NaOH, K for KOH); R: Hydroxide:coal ratio; T: Activation temperature; t: activation time; XN: Ammonia concentration or G: High-temperature heat treatment; Yh: Hydrothermal synthesis time

**FIGURE 2**: Textural properties and storage capacity for selected samples.

The high-temperature treatment decreased both, the BET area and $V_{micro}$, by 40-50%, but did not markedly affect the $V_{micro}/V_{total}$ ratio, when compared to the activated starting material, i.e., without any further treatment. Nitrogen doping also decreased the BET area (by 13-15%) and $V_{micro}$ (by 15-25%), as expected, but the $V_{micro}/V_{total}$ ratio slightly increased. Unfortunately, none of these procedures improved the results (regarding $H_2$ adsorption capacity) achieved by only chemically activating, since maximum capacities were lower than 3.6 wt.%. In accordance with Luo et al. (2017), a slight dependency between the hydrogen storage capacity and the N-content was observed, nonetheless, this effect was not as pronounced as that presented by these authors, since our starting material, a bituminous coal, had a higher initial N-content (1.1 wt.%) in comparison to theirs (0.3 wt.%).

## CONCLUSIONS

We succeeded in optimizing activation parameters which resulted in two activated carbons with promising textural properties for hydrogen storage. Even though a high temperature treatment and the incorporation of nitrogen did not benefit the hydrogen adsorption capacity as expected, these trends could change if conditions closer to application, i.e. higher temperatures and pressures, are used. These will be assayed shortly. Moreover, further surface modifications are planned, such as the incorporation of metals and other heteroatoms, which we expect will enhance the hydrogen storage capacity. Additionally, to account for reproducibility and repeatability, synthesizing larger batches of activated carbons are currently being processed.

**Acknowledgements**

The authors thank Prof. Dr. Néstor Escalona, Josefa Pinto and Adrien Boulard (Pontificia Universidad Católica) and Prof. Gina Pecchi and María José Soto (Universidad de Concepción) for the adsorption measurements. Funding, through ANID FONDEF program (Grant No. ID20I10008) is gratefully acknowledge.

**References**

Luo, L., Chen, T., Zhao, W., and Fan, M. (2017). Hydrothermal doping of nitrogen in bamboo-based super activated carbon for hydrogen storage. *BioResources*, 12, [3], 6237-6250. https://doi.org/10.15376/biores.12.3.6237-6250

Nazir, H., Muthuswamy, N., Louis, C., Jose, S., Prakash, J., Buan, M.E., Flox, C., Chavan, S., Shi, X., Kauranen, P., Kallio, T., Maia, G., Tammeveski, K., Lymperopoulos, N., Carcadea, E., Veziroglu, E., Iranzo, A., Kannan, A.M. (2020). Is the H2 economy realizable in the foreseeable future? Part II: H2 storage, transportation, and distribution. *International Journal of Hydrogen Energy*, 45, 20693-20708. https://doi.org/https://doi.org/10.1016/j.ijhydene.2020.05.241

Sousa, J.P.S., Pereira, M.F.R., Figuereido J.L. (2013). Modified activated carbon as catalyst for NO oxidation. *Fuel Processing Technology*, 106, 727-733-. https://doi.org/10.1016/j.fuproc.2012.10.008

Ströbel, R., Garche, J., Moseley, P. T., Jörissen, L., & Wolf, G. (2006). Hydrogen storage by carbon materials. *Journal of Power Sources*, 159, [2], 781–801. https://doi.org/10.1016/j.jpowsour.2006.03.047

U.S. Department of Energy (2017). DOE Technical Targets for Onboard Hydrogen Storage for Light-Duty Vehicles. https://www.energy.gov/eere/fuelcells/doe-technical-targets-onboard-hydrogen-storage-light-duty-vehicles

Carbon 2022

# Submicron-diameter carbon fibers by electrospinning of lignin as adsorbents for phenol removal

**Francisco J. García-Mateos, M.C. Gutiérrez, Ramiro Ruiz-Rosas, Juana María Rosas, José Rodríguez-Mirasol, Tomás Cordero**

Departamento de Ingeniería Química, Facultad de Ciencias, Universidad de Málaga, Andalucía Tech., Campus de Teatinos s/n, 29010 Málaga, España

Email: garciamateos@uma.es

**Keywords**

lignin, electrospinning, liquid phase adsorption, phenol.

## INTRODUCTION

Activated carbons are widely used in liquid phase adsorption process due to their high specific surface area and low cost. In this process, pollutants have to diffuse through the activated carbon porosity to be adsorbed on the micropores surface. Sometimes, and depending on the micropore size, diffusional problems might limit the adsorption process. This problem can be avoided by using porous carbon materials with very accessible microporosity, such as submicron size microporous carbon fibers, which could be an interesting alternative in adsorption processes (Brasquet, 1997). Lignin is one of the main biopolymer of plants, which can be obtained as a coproduct in the papermaking and biofuel industries. Lignin is also an excellent precursor for the preparation of highly valued carbon materials, due to its high carbon and aromatic content, high availability, and reduced cost. The electrospinning of lignin solutions makes possible the preparation of porous carbon fibers in a simple way. In this work, the used of lignin-derived carbon fibers as adsorbent for phenol removal has been studied.

## EXPERIMENTAL

Carbon fibers were prepared by a coaxial configuration of the electrospinning set up (Lallave, 2007) by using lignin/ethanol or $H_3PO_4$/lignin/ethanol solutions with a weight ratios of 1/1 or 0.3/1/1, respectively. Pure lignin fibers were stabilized in air at 200 ºC for 60 h, with a heating rate of 0.08 ºC/min, while phosphorus-containing lignin fibers were stabilized by using a heating rate of 1 ºC/min and keeping the final temperature for only 1 h. Finally, stabilized fibers were carbonized at 900 ºC, in a $N_2$ flow of 150 $cm^3$/min, to obtain pure and P-containing carbon fibers, CF900 and PCF900, respectively. A granular activated carbon, with similar texture and chemical parameters than phosphorus-containing carbon fibers was prepared by chemical activation of lignin with $H_3PO_4$ with a $H_3PO_4$/lignin ratio of 1 (ACP900), in order to check the influence of the adsorbent morphology and pore arrangement and connectivity on phenol adsorption. Equilibrium and kinetics adsorption experiments were carried out in a batch system at 15, 25 and 35 ºC. Dynamic adsorption experiments at different phenol concentrations and temperatures were also studied in a fixed-bed column by using a flow rate of 5 mL/min and 200 mg of carbon fibers. Finally, a desorption study was carried out in the same column system by using water at 25 and 80 ºC.

## RESULTS AND DISCUSSION

Submicron size carbon fibers were obtained by carbonization of electrospun lignin fibers. Table 1 shows the textural parameters and chemical composition of the carbon materials used in this work. Pure carbon fibers with $A_{BET}$ of 840 $m^2/g$ and narrow microporosity ($V_t^{N2}/V_{DR}^{CO2}$ = 0.87) were obtained. The incorporation of $H_3PO_4$ produced carbon fibers with wider microporosity ($V_t^{N2}/V_{DR}^{CO2}$ = 1.44), along with an increase of ca. 20% in $A_{BET}$ (1140 $m^2/g$). Figure 1a represents the effect of the carbon morphology on the phenol adsorption kinetics, showing faster phenol adsorption rate in carbon fibers

(fiber diameter of 3 μm) compared to that of granular activated carbon (particle diameter of 300 μm). Adsorption isotherms determined at temperatures from 15 to 35 ºC revealed that phenol adsorption was an exothermic process (see Figure 1b for the case of PCF900). Figure 1c shows the breakthrough curves for phenol adsorption on PCF900 carbon fibers at three different inlet phenol concentrations, obtaining the typical S-shape curves. The bed utilization efficiency (defined as total adsorption capacity/adsorption capacity until bed service time) was higher for carbon fibers than for granular activated carbon (being 77 and 71% for CF900 and PCF900, respectively, and 32% for ACP900), confirming the higher phenol adsorption rate on carbon fibers. The amount of phenol desorbed from CF900 and PCF900 during the regeneration step at 25 ºC was 15.4 and 53.0 %, respectively. An increase in desorption temperature (80ºC) provided higher carbon fibers regeneration (100% for PCF and 85% for CF).

***Table* 1.** Textural parameters and chemical composition by XPS of the activated carbon

| Samples | Textural parameters | | | | Chemical surface composition by XPS (%) | | |
|---|---|---|---|---|---|---|---|
| | $A_{BET}$ ($m^2/g$) | $V_t^{N2}$ ($cm^3/g$) | $V_{meso}$ ($cm^3/g$) | $V_{DR}^{CO2}$ ($cm^3/g$) | C | O | P |
| CF900 | 840 | 0.33 | 0.01 | 0.38 | 95.9 | 4.1 | 0 |
| PCF900 | 1143 | 0.49 | 0.02 | 0.34 | 90.2 | 7.4 | 2.4 |
| ACP900 | 1210 | 0.48 | 0.025 | 0.34 | 85.0 | 12.3 | 2.7 |

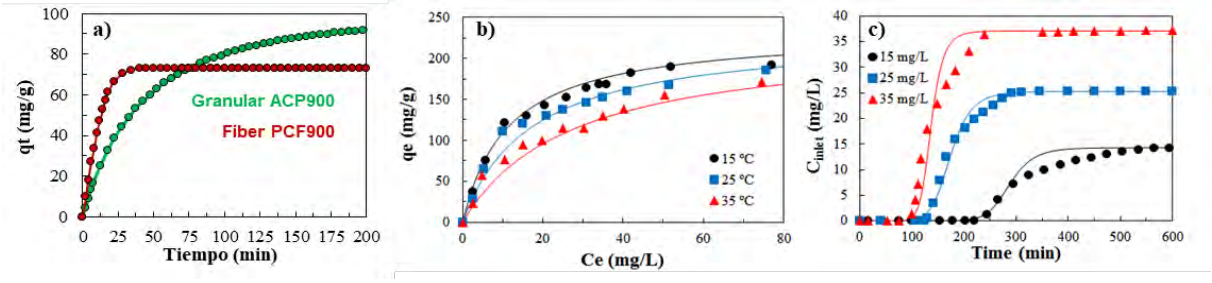


**FIGURE 1.** a) Phenol adsorption kinetics on ACP900 and PCF900; b) Phenol adsorption isotherms at different temperatures and c) breakthrough curves at different inlet concentrations (w: 200 mg, Q: 5 mL/min) on P-containing carbon fibers.

## CONCLUSIONS

Submicrometric lignin-derived carbon fibers were prepared by electrospinning of lignin solution. The incorporation of $H_3PO_4$ to the initial lignin solution shortened the carbon fibers preparation time and produce carbon fibers with wider microposity, which resulted in faster phenol adsorption rate than that observed for granular activated carbon. In addition, the regeneration of phosphorus-containing carbon fibers is faster than that observed for the pure carbon fibres at the desorption temperatures studied.

**Acknowledgements**

The authors wish to thank MICINN (RTI2018-097555-B-100) and Junta de Andalucía (UMA18-FEDERJA-110 and P18-RT-4592) for financial support.

**References**

Brasquet, C., Le Cloirec, P. (1997). Adsorption onto activated carbon fibers: Application to water and air treatments. *Carbon*. 35, (9), 1307-1313.

Lallave M., Bedia, J., Ruiz-Rosas R., Rodríguez-Mirasol J., Cordero T., Otero J.C., Marquez M., Barrero A., Loscertales I.G. (2007). Filled and hollow carbon nanofibers by coaxial electrospining of Alcell lignin without binder polymers. *Advanced Materials*, 19, (23), 4292-4296.

Carbon 2022

# Basic carbon catalysts by partial gasification of magnesium lignosulfonate chars with $CO_2$

**Miguel García-Rollán, Francisco J. García-Mateos, Ramiro Ruiz-Rosas, Juana María Rosas, José Rodríguez-Mirasol, Tomás Cordero**

Departamento de Ingeniería Química, Facultad de Ciencias, Universidad de Málaga, Andalucía Tech., Campus de Teatinos s/n, 29010 Málaga, España

Email: garciamateos@uma.es

**Keywords**

Biomass, lignin, catalyst, dehydrogenation, alcohols.

## INTRODUCTION

Lignin is the main by-product of lignocellulosic biorefineries, mainly used as a fuel for energy production. The production of activated carbons (AC) could be an interesting alternative to its combustion. Among the technical lignins, lignosulphonates stand out for their high and varied content of inorganic matter, which can eventually be exploited for the preparation of AC catalysts. Some reactions used to produce biofuels in ligno-cellulosic biorefineries, such as aldol condensation, require basic catalysts (Huber, 2006). Thus, the kinetics of the partial gasification of a magnesium lignosulphonate (L) derived char for the preparation of carbon-based catalysts with basic character was studied in this work.

## EXPERIMENTAL

L was carbonized at temperatures from 500 to 900 °C in a horizontal tubular furnace with a heating rate of 10 °C/min and with a constant flow of inert gas (150 $cm^3$STP/ min). The char obtained at the highest temperature, i.e., 900 °C (L900), was submitted to a gasification kinietic study with $CO_2$ in a thermobalance, at temperatures from 725 to 800 °C. According to the results of the kinetic study, an AC, L900G, was obtained by partial gasification of L900 with $CO_2$. In order to assess the basicity of the carbon materials, 2-propanol dehydrogenation experiments were carried out in a fixed bed reactor (73 $g_{AC}$·s/ $mmol_{2\text{-propanol}}$).

## RESULTS AND DISCUSSION

L carbonization process produces hollow carbon spheres with yields between 43 and 28 %, Table 1. The char obtained at 500 °C (L500) presents an almost negligible porosity, while narrow microporosity ($V_{DR}^{CO2} > V_S^{N2}$) is observed for L700 and L900 samples, Table 1. As expected, the alkaline and alkaline-earth cations in the parent L sample are incorporated into the char, with Mg contents as high as 14 %, Table 1. At carbonization temperatures above 700 °C (L700 and L900), the formation of magnesium oxide species is observed by XPS and confirmed by XRD (Periclase structure). The presence of small amounts of K and Ca, Table 1, which are well-known gasification catalysts, is another advantage of using L as raw material, since K and other alkalis can not only catalyse the partial $CO_2$ gasification of the char, but also promote a higher basicity in the final AC than the one obtained only by MgO. In this sense, an isothermal kinetic study of the gasification of the char at temperatures between 725 to 800 °C was carried out. Random pore model provides a better description of the gasification rate of L900 up to a conversion of about 50%.

In accordance with the kinetic model prediction for achieving a burn-off of 25%, an AC was prepared by partial gasification with $CO_2$ at 750 °C for 30 min, resulting in an AC with a 50% increase of specific surface area ($A_{BET}$= 720 $m^2$/g). The physical activation also produces a widening in the porosity ($V_{meso}$, Table 1), facilitating the access of the reagents to the active sites dispersed on the carbon surface. It

also produces a relative increase in the concentration of magnesium oxide, Table 1, which remains homogeneously dispersed over the entire surface of the catalyst, as confirmed by TEM analyses. Physical activation with $CO_2$ seems to favour sintering of MgO crystallites, with an average size determined from XRD profiles that moves from 6.0 nm in L900 to 8.5 nm in L900G.

***Table* 1.** Preparation yields, chemical composition and textural parameters of the samples

| Samples | Preparation Yields (% d.a.f.) | XRF (%) | | | Textural parameters | | | |
|---|---|---|---|---|---|---|---|---|
| | | Mg | K | Ca | $A_{BET}$ $m^2/g$ | $V_s$ $cm^3/g$ | $V_{meso}$ $cm^3/g$ | $V_{DR}$ $cm^3/g$ |
| L500 | 42.7 | 8.6 | 0.9 | 0.4 | 1 | <0.01 | <0.01 | 0.01 |
| L700 | 31.7 | 12.7 | 1.3 | 0.6 | 390 | 0.15 | <0.01 | 0.17 |
| L900 | 28.0 | 14.4 | 1.5 | 0.7 | 465 | 0.19 | <0.01 | 0.18 |
| L900G | 21.0 | 15.3 | 2.2 | 0.9 | 720 | 0.25 | 0.12 | 0.18 |

The 2-propanol catalytic decomposition reaction was used to characterize the basic/acid character of the catalysts (Bedia, 2010). L900G presents the highest activity of all the catalysts evaluated, with steady-state conversions of 2-propanol higher than 50% at 400 ºC, providing also the highest selectivity towards acetone (almost 100%), at all temperatures range studied, Figure 1.B. This result evidences the prominent basic character of this catalyst. On the other hand, L900 shows the highest performance of the involved chars, starting the 2-propanol decomposition at a significantly lower temperature than that for L700.

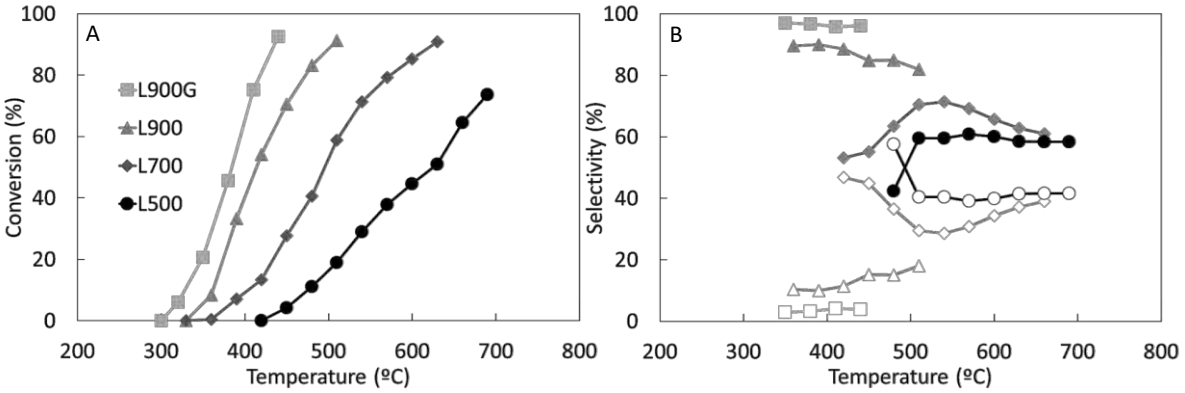


**FIGURE 1.** Evolution of the steady-state conversions of 2-propanol (A) and selectivity to acetone (filled marks) and propylene (hollow marks) (B) with the temperature for all the carbonaceous materials.

## CONCLUSIONS

The partial gasification of the magnesium lignosulfonate with $CO_2$ produces an increase of the activated carbon porosity with very well distributed and dispersed MgO particles on its surface. The biomass origin and these properties make this material a more sustainable catalyst, highly selective towards the dehydrogenation of alcohols (basic character) and, therefore, with a high potential to be used in different reaction framed in the lignocellulosic biorefinery environment.

**Acknowledgements**

The authors wish to thank MICINN (RTI2018-097555-B-100) and Junta de Andalucía (UMA18-FEDERJA-110 and P18-RT-4592) for financial support. M.G.R. acknowledges the assistance of MICINN through an FPU Grant (FPU 18/01402).

**References**

Bedia J., Rosas J.M., Vera D., Rodríguez-Mirasol J., Cordero T., Isopropanol decomposition on carbon based acid and basic catalysts, Catalysis Today. 158 (2010) 89–96. https://doi.org/10.1016/j.cattod.2010.04.043

Huber G. W., Iborra S., Corma A., Synthesis of Transportation Fuels from Biomass: Chemistry, Catalysts, and Engineering, Chem. Rev. 2006, 106, 9, 4044–4098. https://doi.org/10.1021/cr068360d

Carbon 2022

# Designing Novel Nanocomposites of Titanate Nanotubes with S- and N-doped Graphite Oxide Derivatives: Elevating the Photocatalytic Selective Oxidation of 5-hydroxymethylfurfural to 2,5-diformylfuran

**Dimitrios A. Giannakoudakis[1,*], Zoi-Lina Koutsogianni[1], Ioanna Ntekouli[1], Juan Carlos Colmenares[2], Konstantinos Triantafyllidis[1,3]**

[1] Department of Chemistry, Aristotle University of Thessaloniki, Thessaloniki, Greece
[2] Institute of Physical Chemistry, Polish Academy of Sciences, Kasprzaka 44/52, Warsaw, Poland
[3] Center for Interdisciplinary Research and Innovation (CIRI-AUTH), Balkan Center, 10th km Thessaloniki-Thermi Rd, P.O. Box 8318, 57001 Thessaloniki, Greece
Email: dagchem@gmail.com

**Keywords**
Biomass valorization, 5-hydroxymethylfurfural photocatalytic oxidation, titanate nanotubes composites with graphite oxide.

## INTRODUCTION

To satisfy the augment demands in merchandises and fuels by adapting modern and sustainable approaches is an epitactic challenge. One strategy that concentrates the research attention is the massively transformation of abundantly available and renewable feedstocks, like biomass or organic wastes, to valuable chemicals (Behling et al., 2016). Hence, the development of proficient, environmental-friendly, and innovative processes for catalytic synthesis of biomass derived chemicals is of a paramount importance. Considering that an enormous amount of energy is radiated to earth from sun, to develop solar light assisted catalytic methods is concluded within the modern and state-of-the-art concepts of circular (bio)economy. Within this context, to achieve effective heterogeneous photocatalytic biomass or organic wastes valorization, the precisely design of novel nanomaterials play a key role (Giannakoudakis et al., 2022). Titanium dioxide based materials represent a promising class of semiconductor materials and were studied broadly as photocatalysts for the photocatalytic synthetic/upgrading processes. More recently, 1-D nanostructures, such as titanate nanotubes (TiO-NTbs) derived from scrolled titanate nanosheets ($H_2Ti_3O_7$), presented to possess elevated photoreactivity against various organic pollutants in aqueous matrixes (Giannakoudakis et al., 2020) as well as for toxic vapors in air like the chemical warfare agent mustard gas surrogate (2-chloroethyl ethyl sulfide, CEES) (Giannakoudakis et al., 2021).

## SCOPE

In this work, we focused on the ultrasound-assisted/hydrothermal synthesis and physicochemical characterization of titanium oxide nanotubes (TiO-NTbs) and their nanocomposites with (reduced) graphite oxide (rGO), as well as chemically modified counterparts, in order to study their photocatalytic activity for the selective partial and additive-free oxidation of a cellulose/hemicellulose derived compound, 5-hydroxymethylfurfural (5-HMF) to 2,5-diformylfuran (DFF). All the experiments, for the herein mentioned as HMF-2-DFF process, were performed at ambient conditions using low power LED-emitted light (ultraviolet, 365 nm). Optimization of the rGO phase was achieved by synthesizing nanocomposites using different initial amount of the graphitic phase, namely 1, 10, and 20 wt%, with the derived nanomaterials to be referred as TiGO1%, TiGO10%, and TiGO20% respectively. The main steps of the synthetic process, the main physicochemical features as well as improvement of the HMF to DFF selectivity in the case of the TiGO10% are illustrated is **Figure 1**. Going a step ahead, nanocomposite of TiO-NTbs with sulfur and/or nitrogen doped graphene oxide were synthesized, characterized, and evaluated for the partial photo-oxidation of HMF.

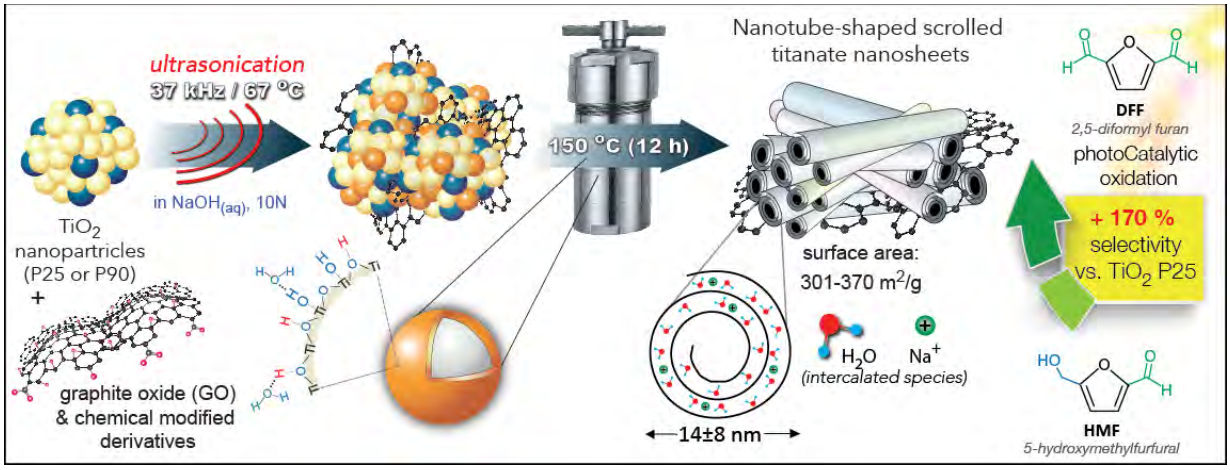


**Figure 1.** The involved steps of the synthesis of the composites consisting of titanate nanotubes and graphite oxide derivatives utilized for the additive-free photocatalytic selective partial oxidation of 5-hydroxymethylfurfural to 2,5-diformylfuran.

**RESULTS & DISCUSSION**

The characterizations revealed the successful formation of the nanocomposites and the synergistic effects on the physicochemical features as was also reported previously (Giannakoudakis et al., 2021). The HR-TEM images showed the presence of scrolled titanate tubular-shaped nanoparticles (open-ended nanotubes) for all samples, with the external diameter, internal channel size, and length to be 17 ± 5 nm, 4–11 nm and 50 to 150 nm, respectively. The addition on graphite phase did not alter the crystallographic structure or the shape of the nanotubes, since the XRD patterns were similar for all materials. The composite TiGO10% showed the highest porosity parameters values, with the specific surface area to be 360 $m^2/g$ compared to 300 $m^2/g$ for the pure nanotubes, with both values to be assumed as remarkable for metal oxide-based materials. Analogue increment was observed for the total pore volume (+17 %). Based on thermal analysis tests, the amount of the rGO phases were estimated as around 1, 4, and 8 % for TiGO-1%, TiGO-10%, TiGO-20%, respectively. An important change on the optical features was that the composites were capable to absorb light within the visible range, although the band gap of all materials was similar.

The results regarding the photocatalytic activity for the HMF to DFF selective oxidation (HMF conversion, DFF selectivity and DFF yield) are presented in **Figure 2**. The first outcome is that the nanotubes revealed a lower HMF conversion compared to $TiO_2$ P25, but on the contrary, the selectivity to DFF was 58% higher. The most pronounced positive impact was observed for the nanocomposite TiGO10% that revealed +72% and +170% higher DFF selectivity compared to the commercial and pure nanotubes, respectively, and hence the highest DFF yield.

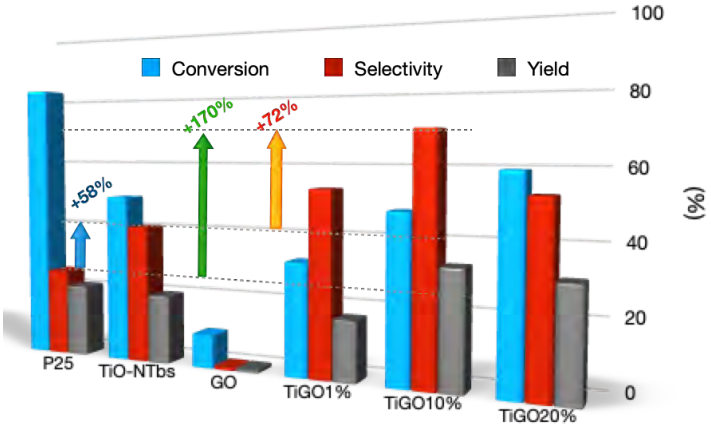


**Figure 2.** The results of the photocatalytic HMF to DFF oxidation after 1 h of irradiation with low-power UV light.

To further enhance the DFF selectivity and yield of the HMF-2-DFF photocatalytic selective oxidation, sulfur and/or nitrogen doped graphite oxide counterparts (after treatment with urea ($CO(NH_2)_2$) or sulfanilic acid ($NH_2$-$C_6H_4SO_3H$)) were additionally used for the synthesis of novel nanocomposites. The composites obtained using sulfanilic acid treated GO is referred to as TiGOSa-10%, while the one after urea treated GO, TiGOUr-10%, since 10 wt.% of the initial carbonaceous phase was used. TiGOSa-10% showed the lowest textural features in between all the other composites with the same amount of graphite-phase. The surface pH of TiGOSa-10% was also the lowest (3.3) compared to pure nanotubes (7.4), TiGO-10% (4.6) and TiGOUr-10% (4.8). On the regards of HMF-2-DFF photocatalytic activity of TiGO-10%, TiGOUr-10%, and TiGOSa-10%, the former showed the lowest DFF yield and the latter the highest, which was enhanced by ~33% comparing to TiGO-10%.
In order to conclude regarding the involved mechanisms, various additional tests were performed by varying specific in each case parameters. The main outcome was that different reaction pathways are catalyzed by the commercial $TiO_2$ nanoparticles and different ones by titanium oxide nanotubes. The presence of molecular dissolved oxygen plays a key role, as well as the pre-adsorbed humidity. Another worth to pointed out conclusion was that the reaction is self-catalyzed since the presence of photo-catalytically formed DFF promote the HMF conversion.

## CONCLUSIONS

The main outcome is that titanium oxide nanotubes (TiO-NTbs) revealed better selectivity for the photocatalytic HMF partial oxidation to DFF compared to the benchmark commercial $TiO_2$ P25 nanoparticles. The selectivity as well as the total DFF yield can be further increased by designing novel nanocomposite of TiO-NTbs with a small amount of reduced graphite oxide. Chemical pre-treatment of graphite oxide can have an additional positive effect, since the composite obtained after GO was pre-treated with sulfanilic acid (for doping with S and N) showed the greatest DFF yield in between all the herein tested nanocatalysts.

### References


Behling, R., Valange, S., Chatel, G., (2016). Heterogeneous catalytic oxidation for lignin valorization into valuable chemicals: What results? What limitations? What trends? Green Chem. 18, 1839–1854. https://doi.org/10.1039/c5gc03061g

Giannakoudakis DA, Zormpa FF, Margellou AG, et al (2022). Carbon-Based Nanocatalysts (CnCs) for Biomass Valorization and Hazardous Organics Remediation. Nanomaterials 12:1679. https://doi.org/10.3390/nano12101679

Giannakoudakis DA, Chatel G, Colmenares JC (2020). Mechanochemical Forces as a Synthetic Tool for Zero- and One-Dimensional Titanium Oxide-Based Nano-photocatalysts. Top Curr Chem 378:2. https://doi.org/10.1007/s41061-019-0262-3

Giannakoudakis DA, Vikrant K, LaGrow AP, et al (2021). Scrolled titanate nanosheet composites with reduced graphite oxide for photocatalytic and adsorptive removal of toxic vapors. Chem Eng J 415:128907. https://doi.org/10.1016/j.cej.2021.128907

Carbon 2022

# Biomass-derived Activated Carbons for the Desulfurization of Model Fuels: Importance of Carbon Surface Chemistry and Antagonistic Effect by the Presence of Aromatics

**Dimitrios A. Giannakoudakis[1], Eleni D. Salonikidou[1], Eleni A. Deliyanni[1], Svetlana Bashkova[2], Konstantinos S. Triantafyllidis[1,3]**

[1] Department of Chemistry, Aristotle University of Thessaloniki, University Campus, Thessaloniki, Greece

[2] Department of Chemistry and Biochemistry, Fairleigh Dickinson University, Madison, NJ 07940, USA

[3] Center for Interdisciplinary Research and Innovation (CIRI-AUTH), Balkan Center, 10th km Thessaloniki-Thermi Rd, P.O. Box 8318, 57001 Thessaloniki, Greece

Email: dagchem@gmail.com

**Keywords**
Deep liquid desulfurization, biomass-derived activated carbons, carbonization temperature, effect of aromatics, model diesel fuel.

## INTRODUCTION

Adsorptive desulfurization of liquid fuels has been suggested as a sustainable, effective, low-cost and easy to operate in real-life technique, especially taking into account the new strict restrictions of sulfur in transportation fuels and the high consumption of costly hydrogen used in the industrially applied method of hydrodesulfurization (Tan *et al.*, 2018). Towards obtaining low sulfur content, the research for low-cost and efficient, green-oriented adsorbents, like activated carbons, for the deep desulfurization of liquid fuels is an ongoing active research goal (Kampouraki *et al.*, 2019; Kakamouka *et al.*, 2022).

## SCOPE

Herein, we illustrate the potential of biomass-derived activated porous carbons using cashew nut shells as an abundantly available and renewable precursor. The chemical activation with phosphoric acid at four different carbonization temperatures (400-700 °C), in order to tailor the impact of carbonization/activation on the physicochemical properties and the surface chemical functionality has been explored. The desulfurization efficiency of the obtained biomass materials was evaluated under ambient batch conditions using a model diesel fuel, consisting of 4,6-dimethyldibenzothiophene (4,6-DMDBT, 20 ppmwS), dibenzothiophene (DBT, 20 ppmwS), benzene (801 ppmw) as a mono-aromatic and naphthalene (7323 ppmw) as a di-aromatic compound, dissolved in hexadecane, while a low amount of adsorbent (400 mL fuel per g of adsorbent) was used at each experiment. Various simpler model solutions were also examined in order to determine the impact and the antagonistic effects by the presence of aromatic compounds on the desulfurization process.

## RESULTS

It was observed that the synthesis of the activated carbons at various carbonization/activation temperatures led to materials with different physiochemical features, as it can be observed at **Figure 1**, indicating the importance of the production process. The increment of pyrolysis temperature had a positive impact on the textural properties of the carbons up to 600 °C, and a negative effect on the surface functional groups, especially of the acidic ones.

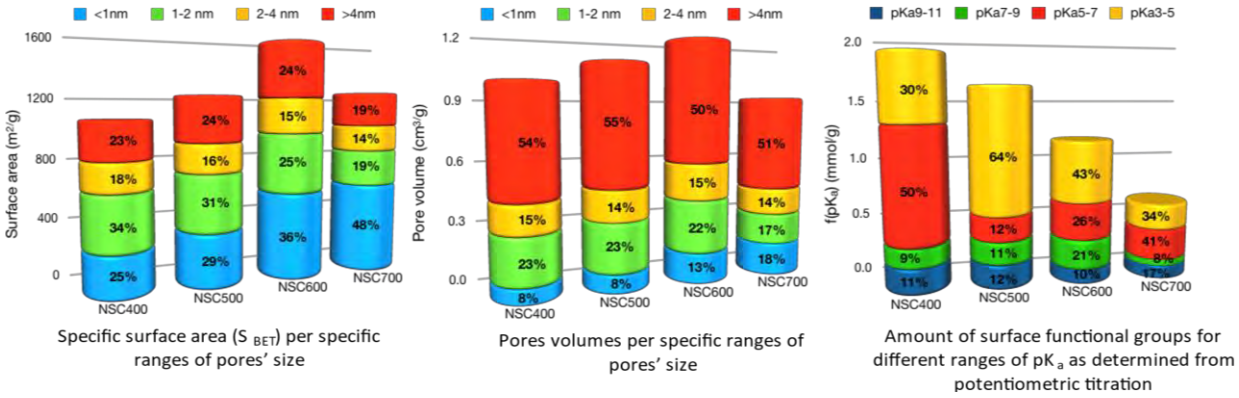


**FIGURE 1**: Main physicochemical features of the biomass-derived activated carbons.

In addition, the adsorption capacities for the four activated carbons, presented in **Figure 2** as the removal of 4,6-DMDBT from hexadecane, did not follow a specific trend/correlation related to the pyrolysis temperature, mainly due to the alteration of the size and volume of pores and of the density of the surface functional groups. The activated carbon synthesized at 600°C, which contains the highest number of carboxylic surface groups, displayed the greatest adsorptive removal of DBT and 4,6-DMDBT. It is also worth noting that nutshell-derived carbons NSC600 and NSC700 showed higher desulfurization efficiency than the benchmark commercial wood-based nanoporous carbon BAX. The addition of aromatic components in the model fuel, negatively affected the removal of 4,6-DMDBT from 52.5% in pure hexadecane to 46.1% for the best performing carbon, as seen in **Figure 2**, revealing the antagonistic character of the aromatics.

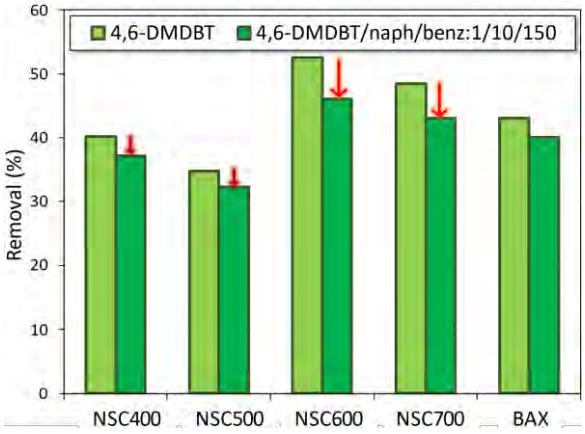


**FIGURE 2**. Adsorptive removal of 4,6-DMDBT in hexadecane with and without the presence of aromatic compounds for the activated carbons derived from nut-shell after different carbonization/activation temperature; conditions: 25 mg activated carbon, 10 ml model fuel, 20 ppmwS, T=25 °C, 170 rpm, t=3 h, $n_{4,6\text{-DMDBT}}/n_{naph}/n_{benzene}$=1/10/150.

Going a step forward and preparing a more complex model diesel fuel with the addition of both sulfur compounds and both aromatic compounds, indicated that the co-existence of DBT in the mixed model diesel fuel dropped the removal of 4,6-DMDBT to 37.3% (**Figure 3**), implying that even though up to a certain extend the two organosulfur molecules compete with each other in the adsorption on the available sites of the carbon, they mainly are adsorbed on different adsorption sites. Another observation is that the removal efficiencies for 4,6-DMDBT are higher than for DBT.

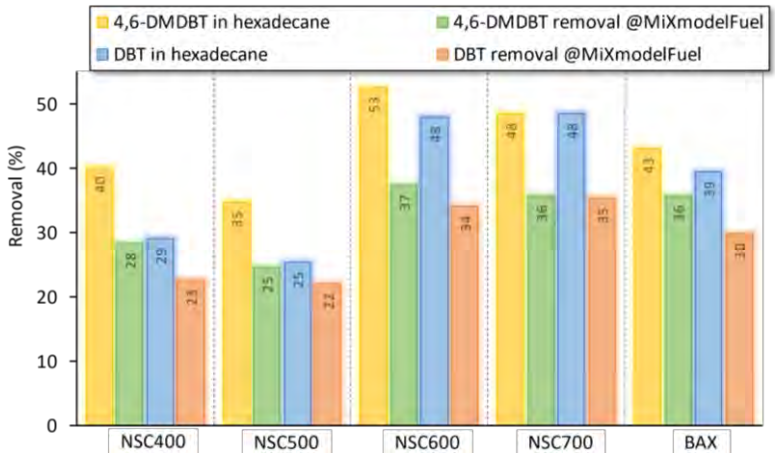


**FIGURE 3**: Adsorptive removal of 4,6-DMDBT and DBT in hexadecane, separately and in the mixed model fuel, for the activated carbons; conditions: 400 mL/g, 20 ppmwS 4,6-DMDBT + 20ppmwS DBT, T = 25 °C, 170 rpm, t = 3 h, $n_{4,6\text{-DMDBT}}/n_{DBT}/n_{naph}/n_{benzene}$ =1/1/10/150, 801 ppmw naphthalene, 7323 ppmw benzene.

## CONCLUSIONS

In the current work, biomass (cashew nut shells) derived activated nanoporous carbons were synthesized at different carbonization/activation temperature and were used as adsorbents for the deep desulfurization of model diesel fuels. The results elucidated that the carbonization temperature affects the physicochemical properties: the highest values of the textural features was found for carbonization at 600 °C, while the highest surface chemistry heterogeneity at 400 °C. It was revealed that in the desulfurization process both textural features and surface chemistry matter and that there is a complicated correlation between the carbonization temperature, the physicochemical features, and the adsorption performances. This leads to the conclusion that for the design of the best-performing desulfurization carbon various factors like biomass precursor and synthesis should be taken into account. Finally, the presence of naphthalene and benzene limits the desulfurization efficiency partially and the two sulfur molecules exhibit mostly different adsorption active sites.

**Acknowledgements**

This research has been co-financed by the European Regional Development Fund of the European Union and Greek national funds through the Operational Program Competitiveness, Entrepreneurship and Innovation (EPAnEK 2014-2020), under the Action "RESEARCH–CREATE–INNOVATE B' CALL" (Project: DESULFUR, code: T2EΔK-01976).

**References**

Kakamouka, K. et al. (2022). Dynamic/column tests for dibenzothiophene (DBT) removal using chemically functionalized carbons: exploring the effect of physicochemical features and breakthrough modeling. Colloids and Surfaces A: Physicochemical and Engineering Aspects, p. 128597. doi: 10.1016/j.colsurfa.2022.128597.

Kampouraki, Z. C. et al. (2019). Catalytic oxidative desulfurization of a 4,6-DMDBT containing model fuel by metal-free activated carbons: The key role of surface chemistry. Green Chemistry, 21(24), pp. 6685–6698. doi: 10.1039/c9gc03234g.

Tan, P. et al. (2018). Design and fabrication of nanoporous adsorbents for the removal of aromatic sulfur compounds. Journal of Materials Chemistry A, 6(47), pp. 23978–24012. doi: 10.1039/c8ta09184f.

Carbon 2022

# The effect of nacre-inspired coating on the tensile properties of carbon fibre composite

**Rupam Gogoi[a#], Francois De Luca[b], David B. Anthony[a,c], and Milo Shaffer[a,d*]**
a: Department of Chemistry, Imperial College London, UK
b: Department of Chemical Engineering, Imperial College London, UK
c: Department of Aeronautics, Imperial College London, UK
d: Department of Materials, Imperial College London, UK
# Presenting author, E-mail: rgogoi@ic.ac.uk
* Corresponding author, E-mail: m.shaffer@imperial.ac.uk

**Keywords**
Nanostructured coating; Bio-mimicking; Fibre-matrix interphase

## INTRODUCTION

Carbon fibre (CF) has shown tremendous potential as an alternative material for the construction of lightweight and high-strength composites commonly known as CF reinforced polymer (CFRP). Yet, there is a concerning design limitation in such material which arises from its poor toughness leading to a catastrophic failure. Although, energy absorption in composite materials is manifested through various toughening mechanism such as fibre-matrix debonding and friction post debonding, fibre pull-out, stress relief at the interphase etc., yet it is brittle in nature with very low strain to failure.
In addition to low toughness, CFRP do not reflect the true inherent strength of the CF, implying limited exploitation of the reinforcing fibre. The strength of a composite material depends on the effective load transfer from the matrix to the fibre under the application of load. The effective load transfer is therefore dependent on the interphase and the fibre-matrix interfacial adhesion. From previous studies, it has been observed that surface modifications of CF have the potential in improving the fibre-matrix interfacial adhesion, and hence, bulk mechanical properties of composites under tensile and flexural loads (Sharma, 2014). However, increasing the interfacial strength improves composite strength and stiffness it reduces the toughness. To tackle both these drawbacks, an optimized nanostructured interphase, inspired by natural nacre was developed in the current study to increase the toughness by alleviating local stress concentration, whilst maintaining effective load transfer (De Luca, 2018). The nanostructured interphase in the form of a coating on CF was produced by layer-by-layer (LbL) deposition of hexagonal layered double hydroxide (LDH) platelets as the inorganic phase and soft poly (sodium 4-styrene sulfonate) (PSS) polyelectrolyte as the organic phase, thus mimicking a brick-and-mortar nanostructure analogues to the natural nacre system. The hypothesis is that an ordered multilayer structure can absorb the energy released by fiber breaks, via multiple crack deflections in the layered interphase structure, spreading along the length of the fibers; progressive fiber debonding/slippage, mediated by strain hardening of the interphase layer in shear, can then allow local stress relaxation without excessive debonding. Together, these effects may potentially delay the correlation of fiber breaks in a composite and hence increase its ultimate strength and exhibit a pseudo-ductile failure.

## RESULTS AND DISCUSSION

The LbL process is based on electrostatic forces and requires the substrate to have a high surface charge density. For successful deposition and adequate adhesion, the surface charge density of the as revied industrially oxidized, unsized CF was increased by oxidation using $O_2$ plasma treatment initially and subsequent immersion in 0.1 M $KMnO_4$ (Fig. 1A). At high pH, the oxidises obtained on the CF surface dissociate, resulting in an increased negative surface charge density. The measured

ζ-potentials increased in magnitude from −19 mV for as received CF to −58 mV observed for the oxidised CF. To have a high electrostatic interaction among fibre surface and coating the pH was maintained at 10 for all the solutions and suspensions in LbL deposition, where the ζ-potential was most negative.

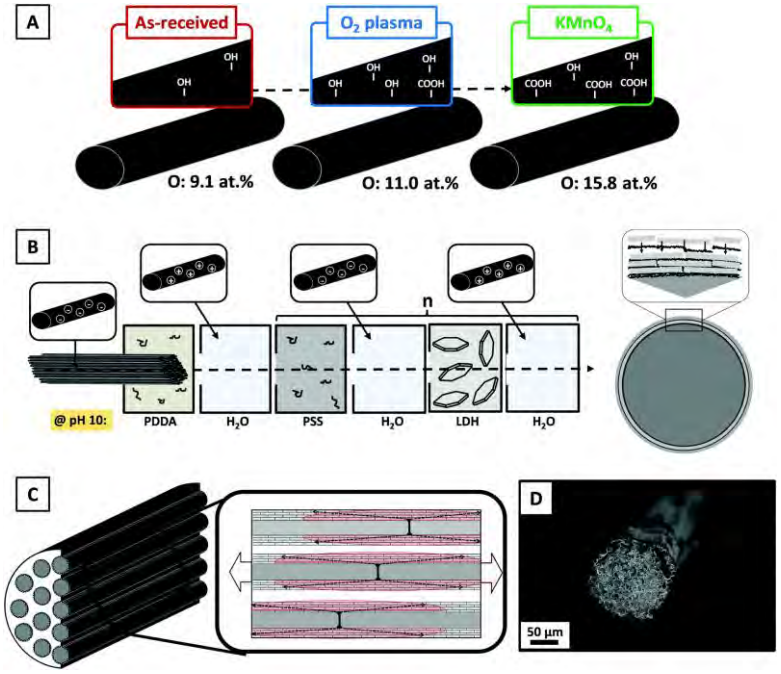


**Fig. 1.** Schematic diagram showing the modification of the as-received unsized carbon fibers, coating deposition and small composite manufacture: the as-received carbon fiber surfaces were functionalized with low-pressure $O_2$ plasma treatment and subsequently further oxidized in KMnO4 (A). PDDA(PSS/LDH)n "brick-and-mortar" nanostructures were assembled, by LbL at pH 10, on all the individual carbon fibers within a bundle (B). The composite containing coated carbon fibers was intended to fail via crack deflection (in red) and sliding within the volume of the anisotropic nanostructured interphase (C). SEM micrograph of a composite cross-section made of coated carbon fibers (D).

Coating of CF was done by sequential LbL dipping process, as illustrated in Fig. 1B. A soft, cationic poly (diallyl dimethyl ammonium chloride) (PDDA) precursor layer was found to promote the adhesion of the coating to the fiber, avoiding direct contact between the stiff, positively charged platelets and rigid carbon fiber surfaces. The negatively charged fiber surfaces were first coated with a positive PDDA buffer layer, before repeatedly applying (PSS/LDH) bilayers.

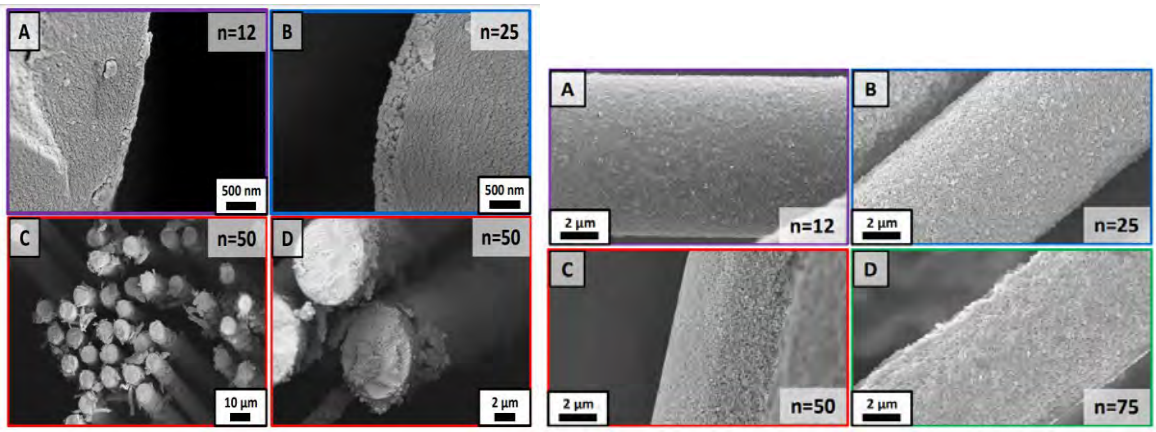


**Fig. 2**: Cross-section (left image) and surface (right image) of nanostructured coatings deposited on a bundle of unsized CF. SEM micrographs of carbon fibers coated with PDDA/$(PSS/LDH)_n$ coating. n=12 (A), n=25 (B) and n=50 (C and D).

SEM in Fig. 2 showed that the PDDA/(PSS/LDH)$_n$ coatings were homogeneous across all the fibers within the bundles. The self-limiting nature of the LbL process means that each individual fiber within the bundle can be coated simultaneously, accelerating production and allowing small unidirectional model composites, consisting of several hundred coated carbon fibers in epoxy to be manufactured (Fig. 1C and D).

The apparent interfacial shear strength (IFSS) and ability of the fiber to progressively slide during the debonding process were investigated from single-fibre pull-out (SFPO) test (Fig. 3A and B). Stable fiber slippage was quantified by defining the debonding length ratio (DLR) as the ratio between the distance that the fiber slides prior to full debonding ($l_d$) over the fiber length embedded in epoxy ($l_e$). The IFSS was determined from a plot of maximum force against embedded area (Fig. 3A). Both IFSS and DLR were significantly improved by the presence of the nanostructured coating, relative to the control fibers, reaching maxima of 59.5 ± 3.9 MPa (+84%) and 0.17 ± 0.02 (+89%), respectively, for the fibers coated with a 0.4 µm thick PDDA/(PSS/LDH)$_{25}$ layer. Further increases in the interphase thickness resulted in a relative drop of the IFSS and DLR, most likely due to a reduction of the radial clamping force exerted on the fiber by the epoxy matrix, as a result of the compliance of the coating.

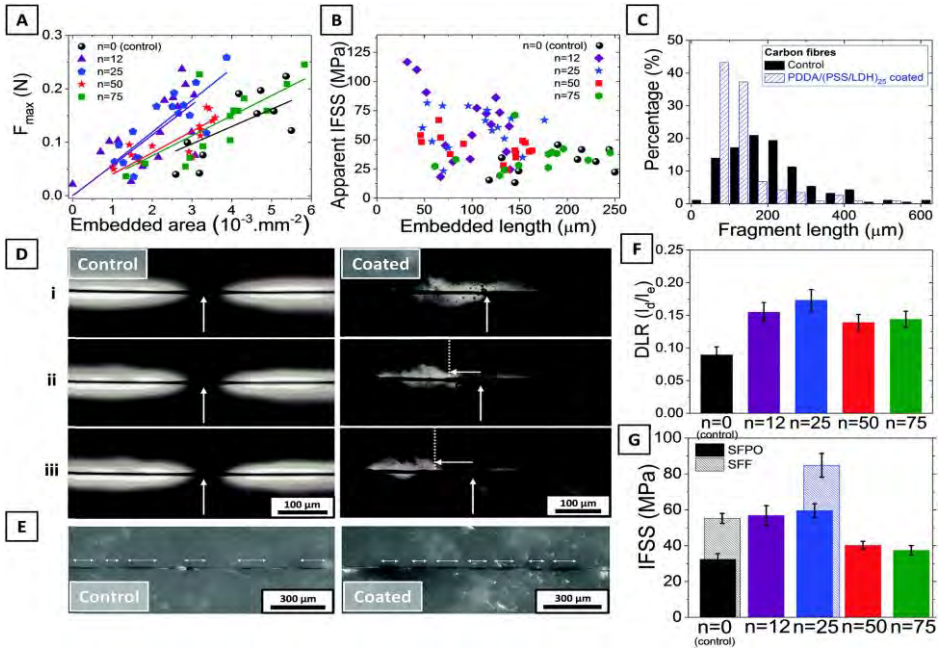


**Fig. 3.** Maximum force ($F_{max}$) applied to single fibers as a function of fiber embedded area in the epoxy matrix (A), apparent IFSS = $f(l_e)$ of control fibers and fibers coated with PDDA/(PSS/LDH)$_n$ of varying thickness (B) and histogram distribution of fiber fragment length for control and PDDA/(PSS/LDH)$_{25}$ coated fibers obtained by single fiber fragmentation tests (C). Optical images of in situ fragmentation of control and PDDA/(PSS/LDH)$_{25}$ coated (D) carbon fibers using cross-polarized light in transmission at +1.2% and +2.4% strain (i, ii and iii, respectively); vertical arrows pinpoint fiber fragments and horizontal arrows and the dashed line highlight progressive sliding of the fiber. Optical images of control and PDDA/(PSS/LDH)$_{25}$ coated carbon fibers using non-polarized light in transmission mode after the fragmentation test (E); horizontal arrows show fiber fragments. Debonding length ratio (DLR) and IFSS of carbon fibers coated with different PDDA/(PSS/LDH)$_n$ coating thicknesses determined by single fiber tests in epoxy (F and G, respectively).

Under single fiber fragmentation tests (SFFT), the control fibers exhibited an intense and large stress field near each fiber break, which remained relatively unchanged when strain increased (Fig. 3D(i–iii)); in contrast, the PDDA/(PSS/LDH)$_{25}$ coated fibers presented a less intense stress field, spread along the length of the fiber (Fig. 3C and D). Upon increasing the macroscopic strain, the stress field was observed to propagate progressively along the fiber, accompanied by a noticeable further reduction in intensity of the stress field. The weaker initial stress field can be attributed to crack

deflection within the nanostructured “brick-and-mortar” interphase, while the reduction in its intensity can be attributed to progressive slippage of the fiber, through plastic deformation of the interphase. IFSS values estimated using Kelly-Tyson model (Kelly, 1965), which were 55.2 ± 2.8 and 84.8 ± 6.6 MPa respectively for the control and PDDA/(PSS/LDH)$_{25}$ coated fibers.

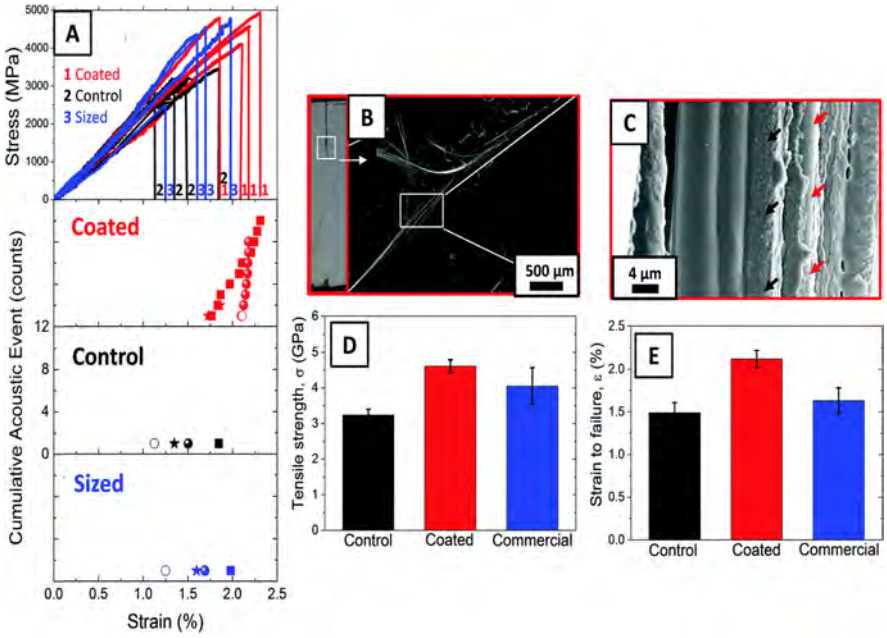


**Fig. 4.** Stress–strain curves and associated cumulative distributions of acoustic emission events occurring during tensile tests of impregnated fiber tow composites containing control fibers, coated fibers (with “brick-and-mortar” PDDA/(PSS/LDH)$_{25}$ nanostructured coating), and sized fibers (A). Low and high magnification SEM micrographs, accompanied by high-speed video stills, of fracture surfaces of impregnated fiber tow composites containing coated fibers (B and C, respectively) – red and white arrows pinpoint locations where the coating is removed and still adhered to the surface of the fibers, respectively. Tensile strength and strain-to-failure of the composites containing control, coated and sized fibers (D and E, respectively).

The tensile properties and fracture behavior of small unidirectional model composites were compared against control fibers, and the optimum PDDA/(PSS/LDH)$_{25}$ coated fibers, as well as additional samples prepared with as-received commercially sized PAN-based fibers (called “sized fibers” in the following). The tensile stress–strain responses of these tow composites were recorded and correlated with acoustic events (AEs), indicative of fiber breaks (Fig. 4A) occurring during the tensile test. In order to minimize any effect of varying fiber volume fractions and, therefore, allow for a fair comparison of the different composite specimens, the load applied to the material was converted into a stress normalized to the cross-sectional area of the total fiber content in the composite. This approach provides a clearer indication of the fiber dominated tensile properties, which determine the tensile properties of unidirectional tow composites. The elastic modulus was determined to be similar for all types of fiber composites, roughly 230 GPa; the similarity to the expected elastic modulus of AS4 carbon fibers (231 GPa) confirms the robustness and consistency of the composite preparation and testing. The tensile strength of the tow composites containing the nanostructured interphase increased from 3235 ± 160 MPa to 4607 ± 391 MPa, as compared to composites containing the control fibers (Fig. 4D). The increased tensile strength of the coated fibers was accompanied by an increased strain-to-failure from 1.49 ± 0.12% to 2.12% ± 0.10% (Fig. 4E). More importantly, the strength and strain to failure of the coated fiber composites also exceeded the values for the sized fibers (4048 ± 523 MPa and 1.63 ± 0.15%, respectively). Only a single AE event was detected for the composites based on control or sized fibers, which was associated with the final composite failure. However, for the composites containing coated fibers, additional AE

events were detected, prior to failure. This observation is consistent with a larger number of independent fiber breaks occurring in the hierarchical composites, due to a successful reduction in local stress concentrations in neighbouring fibers. The associated delay in the formation of a critical cluster of fiber breaks can explain the improved ultimate tensile strength and strain to failure of the composites.

**CONCLUSIONS**

An entirely new class of nanostructured fiber sizing was designed and successfully implemented. A 0.4 µm thick "brick-and-mortar" PDDA/$(PSS/LDH)_{25}$ nanostructured coating was found to offer the greatest improvements in IFSS and DLR, as determined by single fiber pull-out. In fragmentation tests, the local stresses associated with fiber fragmentation appeared reduced and diffused. When the optimum coating was used as the interphase in unidirectional impregnated fiber tow model composites, the new system provided higher ultimate strength and strain-to-failure than composites containing either bare unsized treated carbon fibers ("control fibers") or the as-received commercially sized carbon fibers ("sized fibers"). Acoustic emission recorded a higher number of fiber breaks within the hierarchical composites prior to the final catastrophic failure, indicative of the occurrence of multiple isolated fiber breaks. The nanostructured "brick-and-mortar" interphase appears to have isolated fiber breaks within the composite, delaying the formation of a critical cluster, leading to improved tensile properties compared to the composite containing commercial fibers.

**REFERENCES**

De Luca, F., Clancy, A. J., Carrero, N. R., Anthony, D. B., De Luca, H. G., Shaffer, M. S., & Bismarck, A. (2018). Increasing carbon fiber composite strength with a nanostructured "brick-and-mortar" interphase. Materials Horizons, 5(4), 668-674.

Kelly, A., & Tyson, A. W. (1965). Tensile properties of fibre-reinforced metals: copper/tungsten and copper/molybdenum. Journal of the Mechanics and Physics of Solids, 13(6), 329-350.

Sharma, M., Gao, S., Mäder, E., Sharma, H., Wei, L. Y., & Bijwe, J. (2014). Carbon fiber surfaces and composite interphases. Composites Science and Technology, 102, 35-50.

Carbon 2022

# On the use of carbon black for enhanced production of hydrogen peroxide towards hazardous organics degradation in water

**Alicia Gomis-Berenguer[1], Marina Fedoseeva[1], Ana Casanova[1] and Jesus Iniesta[1,2]**
[1] Institute of Electrochemistry, University of Alicante, Alicante, Spain
Email: alicia.gomis@ua.es

[2] Physical Chemistry Department, University of Alicante, Alicante, Spain

**Keywords**
Carbon black, cathodes, hydrogen peroxide generation.

## INTRODUCTION

In the past decade, the increasing demands of the society for decontaminating water from various sources, coupled with increasingly stringent environmental regulations, have driven the development of new purification technologies to complement the existing physical-chemical and biological methods. In this sense, the advanced oxidation processes (AOPs) take advantages of producing high oxidizing species (e.g., free hydroxyl radical) to provoke the organic contaminants removal in those cases where conventional treatment methods are inefficient to achieve the desired levels of decontamination.

The oxidizing power of $H_2O_2$ can be enhanced by the generation of powerful hydroxyl radicals ($^{\bullet}OH$), on so-called electro-Fenton processes, with the action of iron catalyst in slightly acidic medium. The $H_2O_2$ generation, on a cathode through the electrochemical reduction of oxygen, is an attractive method from the perspective that it may be in-situ generated with a relatively low energy cost and without formation of toxic byproducts, being a promising tool to remove organic pollutants in aqueous media (Sirés, 2014). Recently, several carbonaceous electrodes have been tested as cathodes, such as carbon felt, graphite felt, carbon sponge or carbon cloths, due to their relatively low cost, environmental compatibility and high working current density for the generation of $H_2O_2$. However, it is still difficult to find a material with an appropriate cost-benefit balance and a satisfactory activity, selectivity, and production rate of $H_2O_2$; consequently, considerable efforts are needed to enhance the electrochemical activity of carbonaceous cathodes (Petrucci, 2016; Brillas, 2009).

Accordingly, the purpose of this work is the evaluation of the electrocatalytic activity towards $H_2O_2$ generation at various carbon materials (e.g., carbon blacks) impregnated on a carbon cloth support using PTFE as binder.

## EXPERIMENTAL SECTION

The commercial carbon black (CB, Vulcan XC72R) was oxidised by $HNO_3$ treatment at 120 °C during 90 min (sample labelled CBox). The cathodes were prepared by impregnation of a commercial carbon cloth (24.75 $cm^2$) with a mixture of carbon black (pristine or oxidised), 2 g/L, and PTFE, 5 g/L, in a solvent (EtOH:$H_2O$ 1:2.5 wt.). After the impregnation in an ultrasonic bath, the carbon cloth was dry at 80 °C until constant weight and sintered at 350 °C for 30 min.

All electrochemical tests were performed at room temperature in a three-electrode undivided cell magnetically stirred. The cathode was the above-mentioned electrode, a BDD electrode (Boron Doped Diamond) was employed as anode, and Ag/AgCl electrode was used as reference electrode. The background electrolyte was 0.05 M $Na_2SO_4$ (pH = 3), with continuous flow of $O_2$. Samples were withdrawn from the electrochemical cell at desired time and the amount of $H_2O_2$ generated was

evaluated by determining the absorbance of yellow pertitanic acid complex, as result of the reaction between $H_2O_2$ and potassium titanium oxalate in acid solution, at wavelength of 400 nm.

## RESULTS

The $H_2O_2$ concentration was measured using the pristine and modified carbon cloths (carbon cloth impregnated with PTFE is also included for comparison) by means of chronoamperometry to evaluate the performance of CB and CBox at different applied potentials (-0.7; -0.8 and -1.0 V *vs.* Ag/AgCl). Figure 1 shows the evolution of the $H_2O_2$ generation as function of time for all the cathodes, applying a constant potential of -0.7 V. After 120 min the pristine carbon cloth is able to generate 21 ppm of $H_2O_2$, while the carbon cloth-CBox produces three times higher amount (67 ppm), unveiling a beneficial effect of the presence of oxygenated groups on the electrode material. In terms of generated current, also an important increase is observed from -0.6 (pristine carbon cloth) to -0.8 and -1.4 mA/cm$^2$ for carbon cloth-CB and carbon cloth-CBox, respectively, corroborating the higher electrocatalytic activity of the oxidised carbon black.

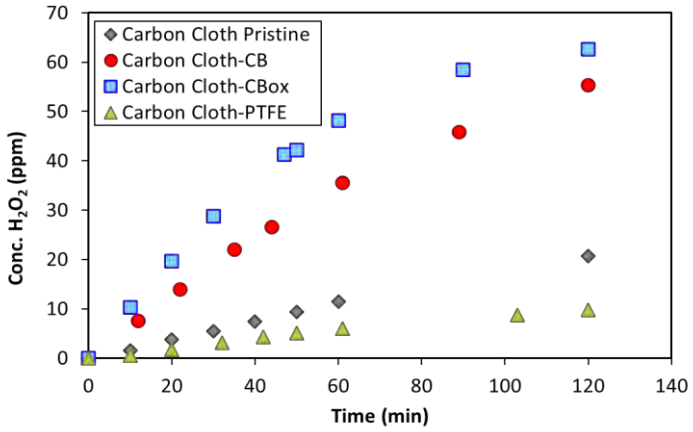


**FIGURE 1**: Hydrogen peroxide production as function of time on the carbon cloth pristine and modified with CB, CBox and PTFE under continuous flow of $O_2$ applying a constant potential of -0.7 V. Background electrolyte, 0.050 M $Na_2SO_4$ pH = 3.

## CONCLUSIONS

In this work, we have explored the influence of the functional groups and structural features of carbon black as cathodes for the $H_2O_2$ generation by chronoamperometry. Our study shows that the oxidation of CB results in the increase of oxygen content showing an important enhanced of $H_2O_2$ production under the studied conditions. This effective improvement opens a variety of applications in the field of environmental remediation for the fabricated carbon-based cathodes.


### Acknowledgements

The financial support of the Spanish MINICINN (project PID2019-108136RB-C32) is acknowledged. A.G-B. thanks European Union NextGenerationEU (ZAMBRANO21-10) for the funding.


### References


Brillas, E., Sirés, I. and Oturan, M.A. (2009). Electro-Fenton process and related electrochemical technologies based on Fenton's reaction chemistry. *Chem. Rev.* 109, 6570. https://doi.org/10.1021/cr900136g

Petrucci, E., Da Pozzo, A., Di Palma, L.D. (2016). On the ability to electrogenerate hydrogen peroxide and to regenerate ferrous ions of three selected carbon-based cathodes for electro Fenton processes. *Chemical Engineering Journal,* 283, 750. https://doi.org/10.1016/j.cej.2015.08.030

Sirés, I., Brillas, E., Oturan, M.A., Rodrigo and M.A., Panizza, M. (2014) Electrochemical advanced oxidation processes: today and tomorrow. A review. *Environmental science and pollution research*, 21, 8336. https://doi.org/10.1007/s11356-014-2783-1

20 C 22 arbon 2022

# Electrochemical impedance spectroscopy to analyse the semiconducting behavior of metal-free porous carbons

**Alicia Gomis-Berenguer[1,2], Jesus Iniesta[1,3] and Conchi O. Ania[2]**
[1] Institute of Electrochemistry, University of Alicante, Alicante, Spain
[2] CEMHTI, CNRS (UPR 3079), University of Orléans, 45071, Orléans, France
[3]Physical Chemistry Department, University of Alicante, Alicante, Spain
Email: alicia.gomis@ua.es

**Keywords**
microporous carbon, intrinsic photoresponse, water splitting.

## INTRODUCTION

The objective of this communication is to gain some insight on the semiconducting behavior of metal-free porous carbons with different textural properties and chemical functionalization by using electrochemical impedance spectroscopy (EIS), in analogy to the methods applied to characterize conventional semiconductors based on transition metal oxides. The goal is to analyze the role of the porosity and surface chemistry to the charge distribution within the electrode surface, and the ion accessibility to the porous network. The Mott-Schottky (M-S) representation of the experimental EIS data allowed explaining the relationship between the photovoltages and photocurrent transients recorded under irradiation for different metal-free porous carbons and their physicochemical features (e.g., surface area, electric conductivity, hydrophobicity character, $sp^2/sp^3$ ratio, zero charge potential). Additionally, the M-S plots have also been used to determine the n- or p-type semiconductor character of the different studied carbons, to quantify the density of charge carriers, as well as the flat band potential so as to estimate the position of the conduction and valence band edge potentials.

## EXPERIMENTAL

*Synthesis*: The synthesis of nanoporous carbon materials were addressed in previous work performed by Ania and co-workers (Parra, 2004; Velasco, 2012). Briefly, nanoporous carbon were denoted as Q= microporous, hydrophobic carbon material, with 12 % ash (from bituminous coal, under steam activation); F= microporous, hydrophobic carbon material, with no ashes (from lignocellulose) and P= microporous, hydrophobic nanoporous carbon, with no ashes (from plastic waste derived, under $CO_2$ activation. *Preparation of nanoporous carbon thin film electrodes:* Titanium (Ti) foil was cleaned with acetone and then thoroughly rinsed with deionized water. For the preparation of the nanoporous carbons thin film based electrodes, a slurry formed by nanoporous carbon materials, PVDF and carbon black (CB) (with a weight ratio of 85:10:5) in N-methylpyrrolidone was blended for 10 min and then coated onto a Ti foil of 1.0 $cm^2$. Then, the electrode was dried at 120 °C for 1 h until a constant weight was obtained. The coating of the carbonaceous slurry onto the Ti foil was repeated twice to get an average thickness of about 150 µm with very homogeneous surfaces. All electrodes were weighed to determine the nanoporous carbon thin film deposited onto the Ti substrate and then were equilibrated for one day in 0.1 M $Na_2SO_4$ aqueous solution adjusted at pH 2.0 with sulphuric acid prior to the electrochemical and photoelectrochemical measurements. *Electrochemical and photoelectrochemical experiments:* The electrochemical characterization of the nanoporous carbon thin films supported on Ti (called z-C), where z stands for the different type of the nanoporous carbons, F, Q and P, respectively, was performed using a three-electrode configuration quartz cell, using a z-C electrode as a working electrode. The nanoporous carbon thin film electrode is intimately placed onto

the quartz plane window of the electrochemical cell. A graphite rod was used as a counter electrode placed out of the irradiation light path. A Ag/AgCl//KCl (saturate) electrode was used as reference electrode via a lugging. Solution was made up of 0.1 M $Na_2SO_4$ pH 2.0. All experiments were carried out at r.t. and when necessary, solutions were de-oxygenated by using a nitrogen stream before the illumination. Cyclic voltammetry (CV) chronoamperommetry (CA), open circuit photovoltages (OCP) and electrochemical impedance measurements were carried out using a Bio-logic potentiostat.

**RESULTS**

In the absence of a redox probe system, the OCP is a parameter strongly linked to the nature of the carbon (Nakamura, 1993), in this case, values ranged from -66 to +61 mV. The transient photocurrent response of the studied photoelectrodes under on/off illumination conditions at various bias potentials (i.e. +200 and -400 mV) is shown in Figure 1. Impedance spectra were recorded in order to clarify the dominant electrochemical processes that take place at the electrode/electrolyte interface, and particularly to gain insight on the contribution of both the mesopores and micropores to the electrochemical performance (see Figure 2).

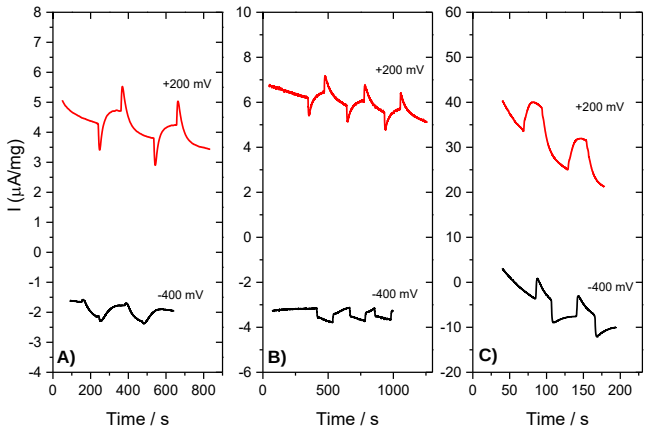


**FIGURE 1**: Photocurrent transients of the z-C/Ti electrodes in 0.1 M $Na_2SO_4$ pH 2.0 solutions under UV-light irradiation using a 125 W Hg lamp. (A) Q-C/Ti, (B) P-C/Ti, (C) F-C/Ti.

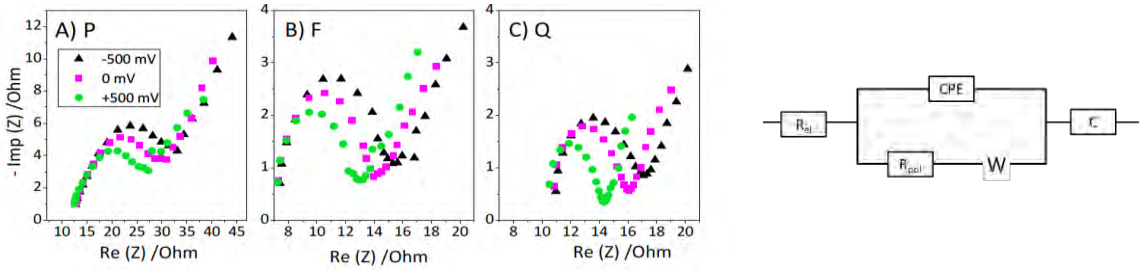


**FIGURE 2**: Nyquist plots at various bias potentials (-500, 0 and +500 mV vs Ag/AgCl) for the nanoporous carbons A) P, B) F and C) Q (mass electrode: 16, 7.4 and 11.5 mg for P, F and Q, respectively). The equivalent circuit used for fitting the impedance data.

**CONCLUSIONS**

The nature of the carbonaceous material and the structural properties determined by the presence of defects or heteroatoms on the nanoporous carbons brings enhanced photocatalytic activity water splitting. In this respect, the presence of defects and here the presence of heteroatoms like oxygen, can entrap and stabilize holes or positive charges by electrostatic incorporation, while the graphene like regions present in the nanoporous carbons can enhance the local electron density due to the photogenerated electrons. In the light of the results, the F sample exhibits the highest oxygen content which can have a huge impact on the entrapped holes on the carbonaceous material and therefore on a lower recombination of the exciton and finally an enhanced photocurrent. On the other side, the

photocurrent response shows an opposite behaviour for the P-C/Ti and Q-C/Ti electrodes, which exhibit negative photocurrents in the potential bias between -800 and +200 mV; this behaviour could be adscribed to a lower content of oxygen for the P sample and the highest $I_D/I_G$ ratios.

**Acknowledgements**

JI thank MINICINN, Spain (project CTQ2016- 76231-C2-2-R) for financial support. The financial support of the European Research Council through a Consolidator Grant (684161) is acknowledged.

**References**

Parra, J.B., Ania, C.O., Arenillas, A., Rubiera, F., Palacios, J.M. and Pis, J.J. (2004). Textural development and hydrogen adsorption of carbon materials from PET waste. *J. Alloys Compd.*, 379, 280-289, doi:10.1016/j.jallcom.2004.02.044.

Nakamura, M.; Nakanishi, M. and Yamamoto, K. (1996). Influence of physical properties of activated carbons on characteristics of electric double-layer capacitors. *J. Power Sources*, 60, 225-231, doi:10.1016/s0378-7753(96)80015-2.

Velasco, L.F.; Fonseca, I.M.; Parra, J.B.; Lima, J.C. and Ania, C.O. (2012). Photochemical behaviour of activated carbons under UV irradiation. *Carbon*, 50, 249-258, doi:10.1016/j.carbon.2011.08.042.

Carbon 2022

# The importance of N-doping on CNT as catalyst support for $CO_2$ methanation reaction

**Liliana P. L. Gonçalves,[1,2,3] Maria Meledina,[4,5] Alexander Meledin,[4,5] Dmitri Y. Petrovykh,[1] Juliana P. S. Sousa,[1] O. Salomé G. P. Soares,[2,3] Yury V. Kolen'ko,*[1] M. Fernando R. Pereira*[2,3]**

[1] LSRE-LCM - Laboratory of Separation and Reaction Engineering – Laboratory of Catalysis and Materials, Faculty of Engineering, University of Porto, Rua Dr. Roberto Frias, 4200-465 Porto, Portugal.

Email: fpereira@fe.up.pt

[2] ALiCE - Associate Laboratory in Chemical Engineering, Faculty of Engineering, University of Porto, Rua Dr. Roberto Frias, 4200-465 Porto, Portugal

[3] RWTH Aachen University, Central Facility for Electron Microscopy, Aachen, Germany

[4] Ernst Ruska Centre for Microscopy and Spectroscopy with Electrons, Jülich, Germany

**Keywords**

Carbon nanotubes, $CO_2$ methanation, N-doping, HAADF-STEM.

## INTRODUCTION

$CO_2$ methanation is the reaction in which carbon dioxide ($CO_2$) reacts with hydrogen ($H_2$) to form methane ($CH_4$) (Sabatier, P., & Senderens, 1902). $CO_2$ is considered the main contributor to the greenhouse effect, and $CO_2$ emissions have risen in recent years; therefore, $CO_2$ methanation presents a great opportunity to combat $CO_2$ emissions by converting it into $CH_4$ with $H_2$ produced using renewable energy. This reaction is the most energetically advantageous reaction to valorize $CO_2$ as a carbon source regarding thermodynamics.

Several transition metals have been studied as catalysts for $CO_2$ methanation, and emphasis is given to supported Ni catalysts owing to the optimal combination of activity, selectivity and cost. Furthermore, it was proved that the used support can influence the activity and selectivity of the catalysts, which implies that it can be an interesting toolbox for tailoring the performance of the catalyst (Ashok *et al.*, 2020).

Among the used supports, metal oxides are the prevalent ones; however, carbon materials have also been studied, but in less extent. It has been reported that the presence of N-groups can enhance the catalytic performance of carbon materials in this reaction, mainly for two reasons: it can improve the Ni dispersion by providing binding sites for Ni stabilization, and it can improve the $CO_2$ adsorption capacity (Gödde *et al.*, 2021).

Therefore, the main goal of this work was to develop new catalysts for $CO_2$ methanation, which present higher activity at lower temperatures since there is the need to perform the reaction at low temperature to improve the flexibility of the operation. N-doped multiwalled carbon nanotubes (CNT) were prepared by a simple physical method and Ni-based catalysts (15 wt% Ni) were synthesized, supported both on pristine carbon nanotubes (Ni/CNT) and N-doped CNT (Ni/CNT–N). Their catalytic properties in methanation reaction were investigated and compared and the materials were fully characterized in order to understand the reason for improving the catalytic performance by N-doping the supporting material (Gonçalves *et al.*, 2022).

## METHODOLOGY

Pristine and N-doped multiwalled CNT (Nanocyl-3100) were used as supporting materials for Ni catalysts. The N-doping was performed by a simple method using ball milling, where CNT and melamine (N-precursor) were co-ball milled in a closed pot for 4 h. After that, the mixture was

annealed at 600 °C for 1 h under $N_2$ resulting in the N-doped CNT supporting material (CNT−N). Ni catalysts supported on CNT and CNT−N were prepared by incipient wetness impregnation (IWI) method and reduced under $H_2$ at 400 °C.

The resultant supports and catalysts, namely CNT, CNT−N, Ni/CNT and Ni/CNT−N were fully characterized and the activity, selectivity, and stability of the catalysts in $CO_2$ methanation were evaluated in a Microactivity XS15 system (PID Eng & Tech), using a fixed bed quartz reactor ($d_{int}$ = 1 cm). Each catalyst (100 mg) was pre-treated *in situ* under $H_2$ flow, and after that, a temperature ramp was performed under reaction conditions ($Q$ = 100 $cm^3$ $min^{-1}$, $CO_2$ : $H_2$ : He = 10 : 40 : 50, $P$ = 1 bar,). The isothermal time on stream (TOS) experiments were conducted under the same reaction conditions to evaluate the stability of the catalysts.

## RESULTS AND DISCUSSION

The characterization of Ni/CNT and Ni/CNT–N demonstrated that both samples presented similar textural properties (Table 1). However, the samples showed different surface area accounting for metallic Ni, with Ni/CNT–N exhibiting a higher surface area of the metallic component.

**TABLE 1:** Textural Properties and $H_2$-chemisorption results of Ni/CNT and Ni/CNT–N.

| | $S_{BET}$ ($m^2$ $g^{-1}$) | $d_P$ (nm) | $V_P$ ($cm^3$ $g^{-1}$) | $V_{micro}$ ($cm^3$ $g^{-1}$) | $H_2$ chemisobed (µmol $g^{-1}$) | Metallic Ni surface area ($m^2$ $g_{cat}^{-1}$) |
|---|---|---|---|---|---|---|
| Ni/CNT | 213 | 3.2 | 0.378 | ≈0.0 | 3.3 | 0.3 |
| Ni/CNT–N | 225 | 3.2 | 0.442 | ≈0.0 | 14.1 | 1.1 |

Ni/CNT–N exhibited higher conversion ($X$) and selectivity to methane ($S_{CH4}$) at a lower temperature than Ni/CNT during the $CO_2$ methanation reaction. This sample reached a maximum of $X$ = 81% and $S_{CH4}$ = 99% at 400 °C, which is close to the thermodynamic equilibrium values (Figure 1a,b). Furthermore, both samples presented high stability over 48 h with no apparent loss in conversion.

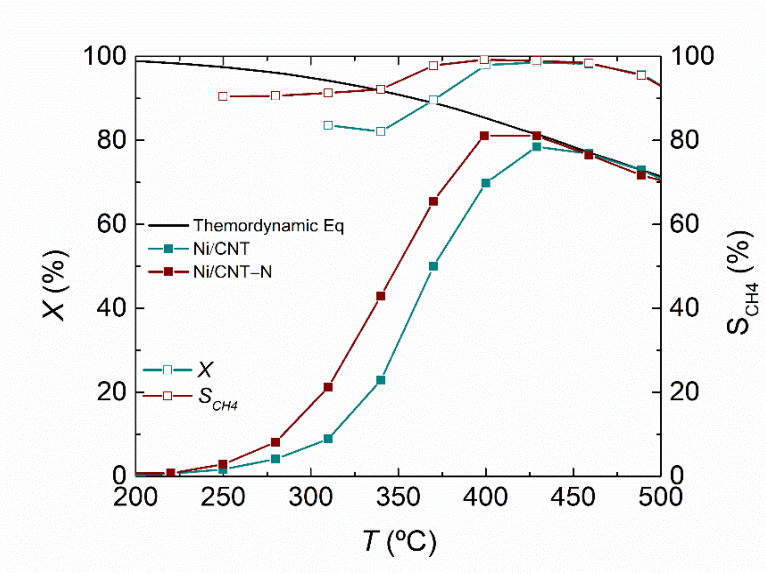


**FIGURE 1**: $CO_2$ conversion ($X$) and $CH_4$ selectivity ($S_{CH4}$) at different temperatures for Ni/CNT and Ni/CNT–N.

It was observed by HR-STEM that in the case of the Ni/CNT–N catalyst, besides Ni NPs, atomically dispersed Ni was also found dispersed over the surface of CNT–N, which were not observed in the case of Ni/CNT. It is believed that N-doping provides more sites not only for $CO_2$ uptake but also for Ni anchoring, leading to the formation of Ni single sites together with the Ni NPs, and thus increasing the available surface area of the catalytically active metal, thus boosting the performance of the catalyst.

## CONCLUSIONS

Ni-based catalysts (15 wt% Ni) supported on CNT and N-doped CNT were synthesized with the aim to develop active and selective catalysts. Their catalytic properties in methanation reaction were investigated and compared, and it was concluded that Ni/CNT–N presented higher conversion and selectivity to methane at a lower temperature than Ni/CNT, which could be attributed to the formation of Ni single sites together with the Ni NPs on the surface of CNT–N, leading to an increase in the available metallic surface area and boosting the performance of the catalyst and also to an increase in the $CO_2$ adsorption capacity of the support.

**Acknowledgements**

L.P.L. Gonçalves is thankful for the support of FCT PhD grant SFRH/BD/128986/2017. This work was financially supported by project Move2LowC - POCI-01-0247-FEDER-046117 funded by ERDF through COMPETE 2020, by Project HyGreen&LowEmissions, reference NORTE-01-0145-FEDER-000077, Co-financed by the European Regional Development Fund (FEDER), through the North Portugal Regional Operational Programme (NORTE2020), and by LA/P/0045/2020 (ALiCE), UIDB/50020/2020 and UIDP/50020/2020 (LSRE-LCM), funded by national funds through FCT/MCTES (PIDDAC). OSGPS acknowledges FCT funding CEECINST/00049/2018.

**References**

Ashok, J. *et al.* (2020) 'A review of recent catalyst advances in $CO_2$ methanation processes', *Catalysis Today*, 356(May), pp. 471–489. doi: 10.1016/j.cattod.2020.07.023.

Gödde, J. *et al.* (2021) 'Nickel nanoparticles supported on nitrogen–doped carbon nanotubes are a highly active, selective and stable CO2 methanation catalyst', *Journal of Energy Chemistry*, 54, pp. 323–331. doi: 10.1016/j.jechem.2020.06.007.

Gonçalves, L. P. L. *et al.* (2022) 'Understanding the importance of N-doping for CNT-supported Ni catalysts for CO2 methanation', *Carbon*, 195, pp. 35–43. doi: 10.1016/j.carbon.2022.03.059.

Sabatier, P., & Senderens, J. B. (1902) 'Nouvelles synthèses du mèthane', *Comptes Rendus Hebdomadaires des Séances de l'Académie des Sciences*, 134, pp. 514–516.

Carbon 2022

# Adsorption of Emerging Pollutants using Activated Carbon derived from Waste Scrap Tires

**Lisdelys González-Rodríguez[1], Claudia Ulloa Tesser[2*], Carla Araya[2] and Ximena García[3]**
[1]Facultad de Ingeniería y Negocios, Universidad de las Américas, Concepción Chile
[2]Facultad de Ciencias Ambientales, [3]Facultad de Ingeniería
Universidad de Concepción, Concepción, Chile
*Email: claudiaulloa@udec.cl

**Keywords:** waste tires, activated carbon, emerging water pollutants

## INTRODUCTION

Water pollution represents a problem of great magnitude due to its impact on the environment. Among the most relevant anthropogenic pollutants are the emerging pollutants (EPs), which include pharmaceuticals, personal care products, and agrochemicals. These substances have negative effects on human health such as neurotoxicity, reproductive toxicity, metabolic interference, and antibiotic resistance (Bachman, 2021). They are present in natural waters as well as in urban wastewater. The removal of EPs requires advanced technologies that complement current treatment systems. Among these is adsorption on activated carbons (Sotello, 2012). Recent research has focused on the development of AC derived from cheap and abundant residual carbonaceous materials. Among these materials highlights the pyrolytic char, a by-product of the pyrolysis of end of life-tires. The objective of this study was to produce activated carbon from pyrolytic tire char and to evaluate its performance in the adsorption of atrazine, caffeine, carbamazepine, sulfamethoxazole, and ibuprofen in aqueous single and multicomponent systems.

## MATERIALS AND METHODS

Pyrolytic char was supplied by Arrigoni Ambiental SpA to be used as a precursor material for the synthesis of tire-derived activated carbon (TAC). TAC was produced by physical activation ($CO_2$, 1000°C, 2.5h) and characterized by BET surface area ($N_2$, 77 K), FTIR, SEM, and point of zero charge pH ($pH_{pzc}$). Target EPs such as Atrazine (ATZ, 95%), Carbamazepine (CBZ, 98%), Caffeine (CAF, 99%), Sulfamethoxazole (SMX, 98%) and Ibuprofen (IBU, 98%) were purchase from Sigma Aldrich and Acros Organics. All the reagent used has analytical purity. Five stock solutions of 1000 mg $L^{-1}$ (ATZ, CBZ, CAF, SMX, and IBU) were prepared in methanol. The working solutions of a single compound and mix were obtained by diluting the stock solution with distilled water until a concentration of 5 mg $L^{-1}$. The pH of the solutions was controlled using phosphate buffer (1 mM) pH 7.2. Batch adsorption tests were carried out in single and multi-component solutions (5 mg/l, pH 7, 168 hours, dosage: 10-190 mg/l). In addition, kinetic tests were performed (pH 7, 10 hours, dosage 40 and 100 mg/l). The residual concentrations of EPs were determined by High-Pressure Liquid Chromatography (HPLC).

## RESULTS AND DISCUSSION

The specific surface area (BET), and micropore volume of TAC were 339 $m^2g^{-1}$ and 0.14 $cm^3g^{-1}$, respectively. FTIR spectrum indicates mainly the presence of acidic functional groups such as carboxylic, hydroxyl, and aldehyde or ketone group and stretching vibration of $CH_2$ group. However, $pH_{pzc}$ = 7.4 suggested that the TAC has amphoteric nature, allowing acidic and basic groups to co-exist on the surface. Figures 1a, b shows the experimental adsorption data adjusted with the best model in single and multicomponent systems, respectively. In single-component tests, the equilibrium adsorption capacity varied between 74.40-49.29 $mgg^{-1}$, while in the multicomponent system, the maximum adsorption capacity showed ranges between 43.08-12.80 $mgg^{-1}$. In both systems the maximum adsorption capacity order was ATZ>CBZ>CAF>SMX>IBU.

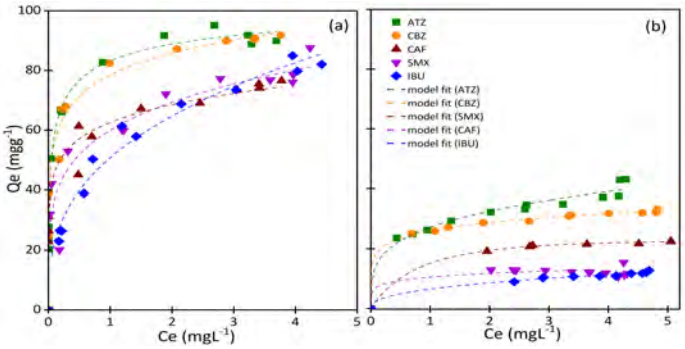


**FIGURE 1**. Best model fits from (a) single solute system and (b) multipollutant system (pH: 7; initial concentration: 5 $mgL^{-1}$; agitation speed: 130 rpm).

Figures 2a, b displays the rate of EPs adsorption in single and multicomponent systems, respectively (Dosage: 100 mg/l). In both systems and for all compounds, the adsorption capacity increased rapidly during the first hours, followed by a gradual rise. The removal percentage varied between 95.94-63.30% and 52.72-10.87% in single and multipollutant systems, respectively.

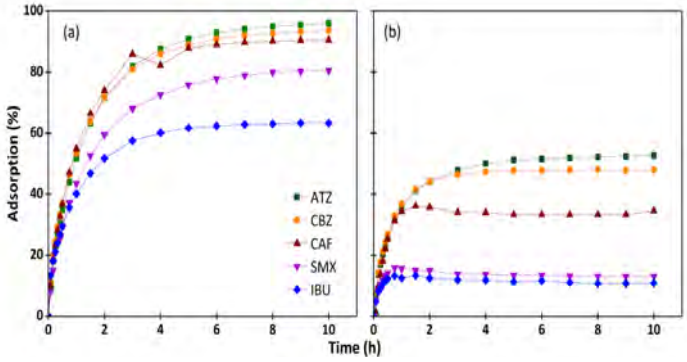


**FIGURE 2**. Removal efficiency of (a) single solute system and (b) multipollutant system (contact time: 10 h; initial concentration: 5 $mgL^{-1}$, adsorbent dose: 0.1 $gL^{-1}$

## CONCLUSIONS

Through physical activation, a low-cost and environmentally friendly adsorbent based on tire pyrolytic char was developed. The activated carbon displays a surface area of 339 $m^2g^{-1}$ and amphoteric nature ($pH_{pzc}$ = 7.4). The experimental results presented in this work showed the adsorption capacity of adsorbent carbon to remove ATZ, CAF, CBZ, IBU, and SMX from aqueous solutions.

**Acknowledgments**

The authors wish to thank the technical laboratory staff working at the EULA Center and the Faculty of Chemical Sciences, University of Concepción. Funding, through ANID FONDEF program (Grant No. ID20I10008) is gratefully acknowledge.

Bachmann SAL, Calvete T, Féris LA (2021). Caffeine removal from aqueous media by adsorption: An overview of adsorbents evolution and the kinetic, equilibrium and thermodynamic studies. *Sci Total Environ* 767, 144229. https://doi.org/10.1016/j.scitotenv.2020.144229.

Sotelo JL, Rodríguez AR, Mateos MM, Hernández SD, Torrellas SA, Rodríguez JG (2012). Adsorption of pharmaceutical compounds and an endocrine disruptor from aqueous solutions by carbon materials. *J Environ Sci Heal - Part B Pestic Food Contam Agric Wastes* 47, 640–52. https://doi.org/10.1080/03601234.2012.668462.

Carbon 2022

# Carbon quantum dots produced from orange peel, their reduction degree, and the feasibility of their application on photovoltaic devices

**A. S., González-Vera[1], C. O. Ania[2], C.A. Pineda-Arellano[3], J. Matos[4], C. Nieto-Delgado[1], L. F., Cházaro-Ruiz[1], J. R. Rangel-Méndez[1]**

[1]División de Ciencias Ambientales, Instituto Potosino de Investigación Científica y Tecnológica A.C., Camino a la Presa de San José 2055, Lomas 4ta Sección, C.P. 78216 San Luis Potosí, S.L.P., México.
Email : andrea.gonzalez@ipicyt.edu.mx

[2] POR2E Group, CEMTHI (CNRS UPR 3079) Université d'Orléans, 45071, Orléans, France. [3] CONACYT-Centro de Investigaciones en Óptica, A.C., Unidad Aguascalientes, Prol. Constitución 607, Fracc. Reserva Loma Bonita, Aguascalientes, Ags., 20200. México. [4] Instituto de Ciencias Químicas Aplicadas, Facultad de Ingeniería, Universidad Autónoma de Chile, 8900000 Santiago, Chile.

**Keywords**
Carbon Quantum Dots, Quantum Dot Sensitized Solar Cells, Electrochemical reduction.

## INTRODUCTION

Carbon quantum dots (CQDs) are a new class of zero-dimensional nanomaterial that possess photoluminescent features, with potential application on quantum dot-sensitized solar cells (QDSSC) (Gao, 2020). The QDSSC provide a technically and economically feasible alternative to current photovoltaic cells.

CQDs can be produced from different precursors and their characteristics strongly depend on the synthesis conditions and purification process. For instance, it has been reported that the oxidation degree of the CQDs has a significant effect in their photoluminescence features (Liu, 2017). Furthermore, the purification of CQDs has also been reported as an important parameter that influence the electron transport capacity and quantum yield of CQDs (Lu, 2014). Consequently, it is necessary to understand and correlate their physicochemical and photoelectrochemical capabilities to apply these materials.

Our research group has recently explored the synthesis of CQDs from a renewable carbon source (orange peel) by a microwave assisted (MWA) hydrothermal method (Olmos-Moya, 2022). The use of orange peel allows to reduce manufacturing costs and environmental impact; nevertheless, the purification step is a challenge due to its heterogeneous composition. In this context, the objective of this work is to investigate three purification methods for the preparation of CQDs from orange peels.

## METHODS

CQDs were prepared through a MWA hydrothermal synthesis; briefly, 100 mg of orange peel powders were suspended in 15 mL of deionized water and placed in the microwave oven (Nanowave 400 Anton Paar GmbH) at 220 °C for 30 minutes, under stirring of 1000 rpm (maximum power 700 W). The obtained dispersion was filtered (Millex-GS, 0.22 µm) to remove the large carbon particles. The purification of the CQDs was performed by: i) extraction in $CHCl_3$ as reported elsewhere (Zhu, 2021); ii) extraction with $(CH_3)_2CO$, and iii) pre-treatment of the orange peel in 1 M HCl solution. In the former, the dispersion after the microwave treatment was sequentially filtered with polyethersulfone membranes (0.1 µm, 30 kDa, 10 kDa, 5 kDa). The filtrated solution was lyophilized, and the resulting powder was dispersed in $CH_3CH_2OH$, and centrifugated at 14000 rpm for 15

minutes to recover the supernatant. All the purified-CQDs were further centrifuged at 3000 rpm and 60 °C to finally obtain CQDs in a powder form (Figure 1).

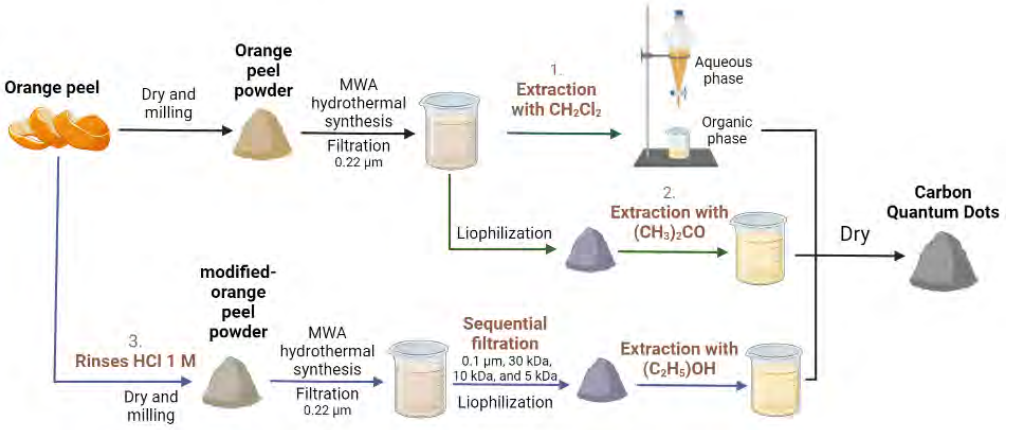


**FIGURE 1**: Methods of synthesis and purification of CQDs.

## RESULTS

The characterization of the CQDs after the different purification processes demonstrated that the extractions with $CHCl_3$ and $(CH_3)_2CO$ are not enough effective to completely eliminate the organic and inorganic remnant compounds. On the other hand, the third method allowed to obtain a fluorescent nanomaterial, easily resuspended in polar solvents. The UV-VIS spectrum of this powder (Figure 2C) shows a band at 280 nm, attributed to the $\pi - \pi^*$ transitions; it also exhibited fluorescence at around 430 nm, and an average hydrodynamic diameter of 2.5 nm (Figure 2D). The Raman spectrum shows the characteristic D and G bands of carbon materials, located around 1349 and 1571 $cm^{-1}$, respectively ($I_D/I_G$ of 0.89). FTIR characterization showed the presence bands associated with -O-H, -N-H, -C=C, -C-H, -C-O, -C=O, -C-OH and -COOH functional groups.

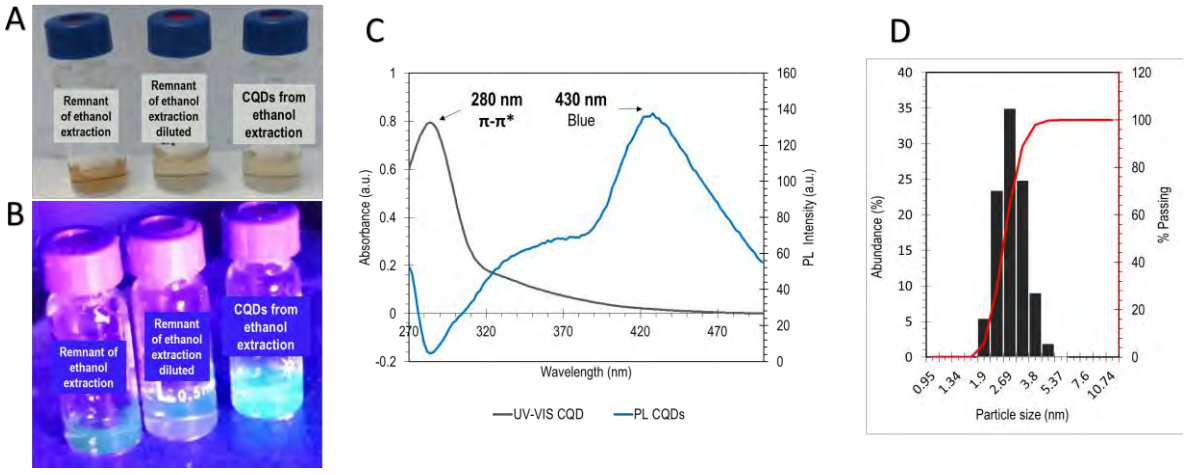


**FIGURE 2**: CQDs obtained from the extraction with ethanol under visible (A) and UV (380 nm) light (B), UV-Vis and photoluminescence spectra (C), and particle size analysis by Dynamic Light Scattering (D) of the as obtained CQDs suspended in water

## CONCLUSIONS

We have successfully developed a purification method for the preparation of photoluminescence of CQDs from orange peels, consisting in a pre-treatment of the carbon precursor in acid conditions before the hydrothermal transformation. The obtained CQDs showed interesting photoluminescent features in the blue region, and a rich surface functionalization. The materials obtained are candidates to obtain environmentally friendly CQD solar cells.

**Acknowledgements**

This work was funded by CONACYT-Fondos Sectoriales-SENE (grant 245467) and SEP-CONACYT-ANUIES-ECOS NORD Francia-México (grants 315202, M20P01). González-Vera thanks CONACyT for her PhD scholarship (CVU: 821870). The authors thank to LAMBAMA, LINAN and IPICYT laboratories for the facilities and the technical support (Rocha, Isaacs, Vidriales, Iris Peña, Silva, Becerril, and Rivera).

**References**

Gao, N., Huang, L., Li, T., Song, J., Hu, H., Liu, Y., Ramakrishna, S., (2020) Application of carbon dots in dye-sensitized solar cells: A review. Journal of Applied Polymer Science. https://doi.org/10.1002/app.48443

Liu, M. L., Yang, L., Li, R. S., Chen, B. bin, Liu, H., & Huang, C. Z. (2017). Large-scale simultaneous synthesis of highly photoluminescent green amorphous carbon nanodots and yellow crystalline graphene quantum dots at room temperature. Green Chemistry, 19(15), 3611–3617. https://doi.org/10.1039/c7gc01236e

Lu, Y., Wang, J., Yuan, H., Xiao, D., (2014) Separation of carbon quantum dots on a C18 column by binary gradient elution via HPLC. Analytical Methods 6, 8124–8128. https://doi.org/10.1039/c4ay01052c

Olmos-Moya, P.M., Velazquez-Martinez, S., Pineda-Arellano, C., Rangel-Mendez, J.R., Chazaro-Ruiz, L.F., (2022) High added value functionalized carbon quantum dots synthetized from orange peels by assisted microwave solvothermal method and their performance as photosensitizer of mesoporous TiO2 photoelectrodes. Carbon N Y 187, 216–229. https://doi.org/10.1016/j.carbon.2021.11.003

Zhu, J., Wu, C., Cui, Y., Li, D., Zhang, Y., Xu, J., Li, C., Iqbal, S., Cao, M., (2021) Blue-emitting carbon quantum dots: Ultrafast microwave synthesis, purification and strong fluorescence in organic solvents. Colloids and Surfaces A: Physicochemical and Engineering Aspects 623. https://doi.org/10.1016/j.colsurfa.2021.126673

Carbon 2022

# Evaluation of large diameter mesophase petroleum pitch fiber stabilization by thermal analysis and infrared spectroscopy

**Caroline J. B. Guimarães, Priscila Sieira, Alcino P. Aguiar[2] and Alexandre T. Castro**
Seção de Tecnologia de Materiais de Carbono, Centro Tecnológico do Exército, Rio de Janeiro, Brasil
Email: caroljovine@gmail.com

[2]Seção de Química, Instituto Militar de Engenharia, Rio de Janeiro, Brasil

**Keywords**
Mesophase petroleum pitch, stabilization, large diameter.

## INTRODUCTION

Petroleum pitch has been used as a low-cost carbon fiber precursor (Wei, 2022). Among fabrications steps, thermal stabilization has a prime influence on carbon fiber's physical properties, at which fundamental chemical changes occur in the precursor (Peng, 2021). However, these changes are complex and poorly defined because the pitch is chemically heterogeneous (Jana, 2022). Therefore, this study aims to monitor the stabilization by thermogravimetric analysis (TGA) and Fourier transform infrared photoacoustic spectroscopy (FTIR/PAS).

## MATERIALS AND METHODS

This study used a pitch with 90 vol% mesophase that had insoluble content in toluene and quinoline, 73.3% and 71.4%, respectively, and a 303 °C softening point. Multiple stabilization treatments were monitored by thermogravimetric analysis equipment, using a mesophase petroleum pitch fiber of 54.1 ± 1.5 µm diameter. The stabilized filaments were characterized by FTIR/PAS spectroscopy. The carbonization was under nitrogen at 3 °C/min to 1500 °C. Mechanicals and electrical properties were determined by averaging 15 randomly chosen filaments following ASTM C1557 (4 mm gauge length) and DC four-point probe method, respectively. The carbon fiber's surface morphology was observed at SEM EVO-10 (Zeiss).

## RESULTS

Experimental setup, carbon fibers' physical properties, and mass variation (Δm) after stabilization are displayed in Table 1.

**TABLE 1**: Carbon fiber physical properties and mass variation.

| Exp. | Temperature (°C) | Heating rate (°C/min) | Residence time (min) | Tensile strength (GPa) | Modulus (GPa) | Electrical conductivity (kS/m) | Δm (%) |
|---|---|---|---|---|---|---|---|
| 1 | 300 | 0.5 | 300 | 1.12 ± 0.09 | 70 ± 5 | 147± 27 | 6.5 |
| 2 | 300 | 1.0 | 180 | 0.99 ± 0.07 | 67 ± 6 | 135± 15 | 6.3 |
| 3 | 300 | 1.5 | 300 | 0.98 ± 0.10 | 65 ± 2 | 133 ± 4 | 6.3 |
| 4 | 300 | 0.5 | 60 | 0.87 ± 0.11 | 61 ± 6 | 118 ± 6 | 5.8 |
| 5 | 270 | 0.5 | 120 | 0.75 ± 0.05 | 56 ± 5 | 106± 8 | 5.5 |
| 6 | 270 | 5.0 | 220 | 0.72 ± 0.05 | 55 ± 6 | 104± 9 | 5.3 |
| 7 | 300 | 1.5 | 60 | 0.62 ± 0.08 | 50 ± 4 | 94 ± 7 | 4.6 |
| 8 | 270 | 5.0 | 120 | 0.59 ± 0.06 | 48 ± 9 | 90 ± 9 | 4.1 |
| 9 | 270 | 25 | 120 | 0.49 ± 0.07 | 45 ± 7 | 85 ± 6 | 3.6 |
| 10 | 350 | 10 | 60 | 0.47 ± 0.05 | 41 ± 4 | 79 ± 12 | 2.9 |
| 11 | 270 | 5.0 | 20 | 0.43 ± 0.06 | 37 ± 6 | 75 ± 10 | 2.0 |

Figure 1 shows that carbon fiber's physical properties increase slightly with increasing mass variation after stabilization, according to an exponentially increasing function, with a 0.99 coefficients of determination.

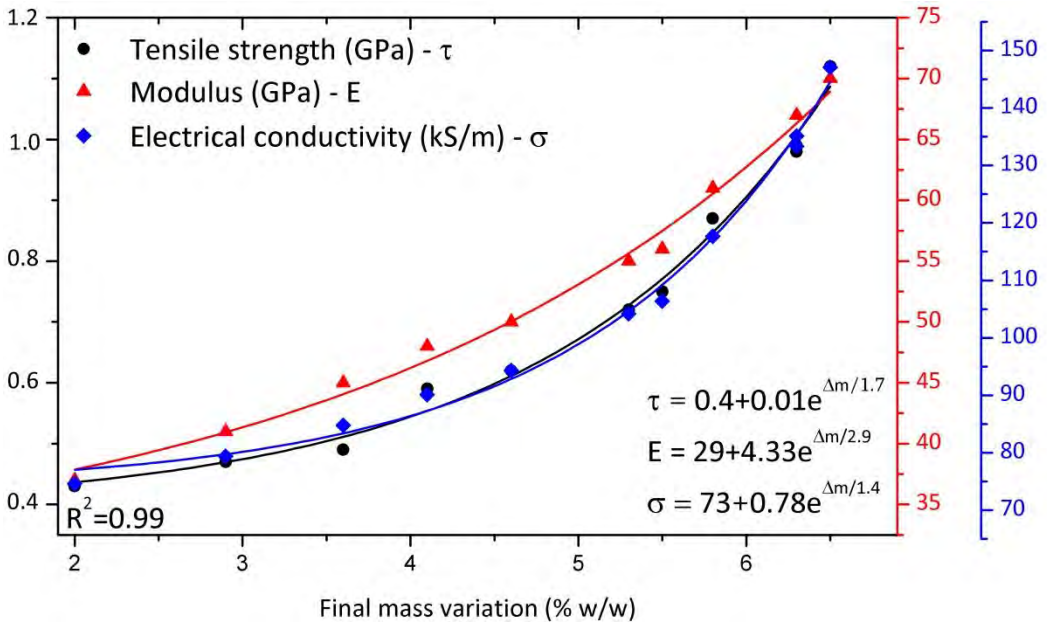


**FIGURE 1**: Carbon fiber physical properties function as the percentage mass variation during the stabilization.

**FTIR/PAS spectroscopy**

Figure 2 shows normalized FTIR/PAS spectra of as-spun and stabilized fibers. Between 1800 – 1450 $cm^{-1}$ appears bands whose intensity increase as the mass variation increases, attributed to the formation of conjugated and unconjugated carboxyls, confirming that the fiber structure underwent a reticulation process. In addition, the 870 $cm^{-1}$ band becomes weaker than the 815 and 750 $cm^{-1}$ bands as the mass gain increases. This spectral pattern reveals that, among the aromatic hydrogens, those isolated in the aromatic rings are the most oxidation susceptible.

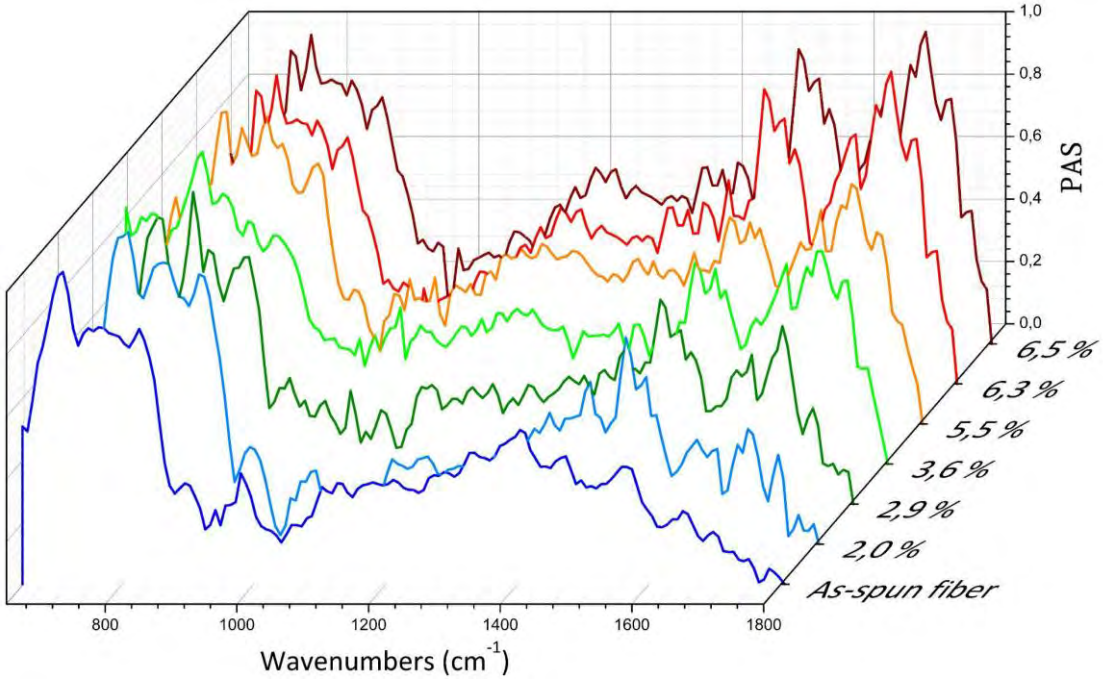


**FIGURE 2**: FTIR/PAS spectra of original and different degrees of oxidized mesophase pitch fiber.

**Carbon fiber microstructure**

Figure 3 shows the representative microstructure of experiments 1 and 7. The carbon fibers cross-section from experiment 1, Figure 3a, presents a homogeneous microstructure along the entire diameter. Thus, experiment 1 stabilization conditions turned the pitch fiber into an infusible material, without causing structural damage, in concordance with its physical properties (Table 1). In the micrographs from experiment 7, it is possible to correlate tensile strength reduction with voids caused by volatilization during the carbonization process (Figure 3b), so this fiber was insufficiently stabilized.

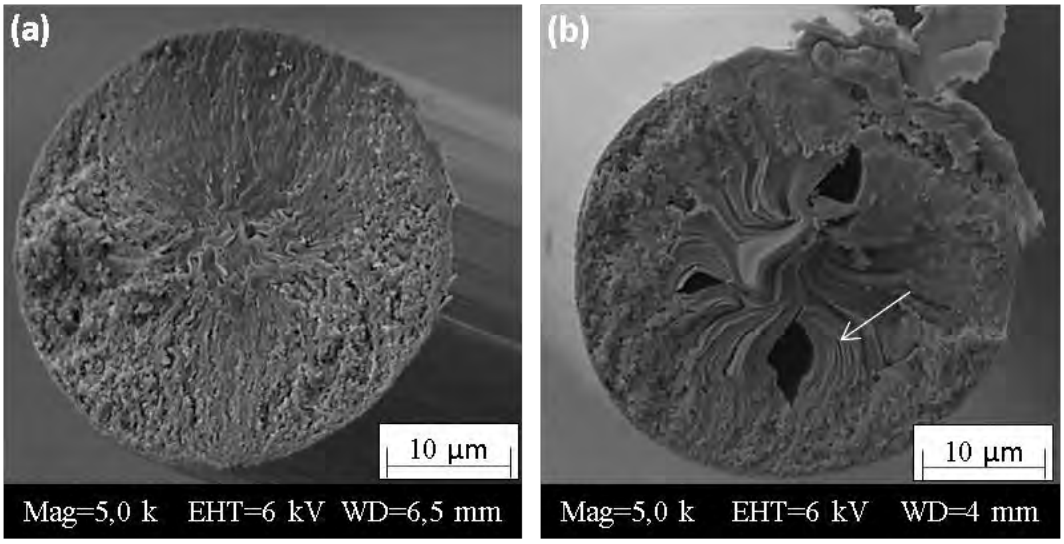


**FIGURE 3**: Carbon fibers cross-section.

**CONCLUSIONS**

The stabilization monitoring by thermogravimetry showed that a mass increase of around 6.5 % can adequately stabilize a mesophase petroleum pitch fiber with a ~ 54 µm diameter. In addition, the mass variation from TG curves showed a good correlation with carbon fiber physical properties, with a 0.99 coefficient of determination. With the association of TG curves, micrographs, and FTIR/PAS spectra, it can be verified that the increase in mass during stabilization promotes oxygenated group formation, specifically conjugated esters which transform pitch fiber into an infusible material.

**Acknowledgements**

We thank Centro Tecnológico do Exército (CTEx) and Instituto Militar de Engenharia (IME).

**References**

Wei, Y., Chen, J., Zhao, H., & Zang, X. (2022). Pressure-Strengthened Carbon Fibers from Mesophase Pitch Carbonization Processes. *The Journal of Physical Chemistry Letters*, 13(14), 3283-3289. https://doi.org/10.1021/acs.jpclett.2c00664

Peng, Y., Tan, R., Liu, Y., Yang, J., Li, Y., Li, J., ... & Shi, K. (2021). Mesophase Pitch-Based Carbon Fibers: Accelerated Stabilization of Pitch Fibers under Effective Plasma Irradiation-Assisted Modification. *Materials*, 14(21), 6382. https://doi.org/10.3390/ma14216382

Jana, A., Zhu, T., Wang, Y., Adams, J. J., Kearney, L. T., Naskar, A. K., ... & Ferralis, N. (2022). Atoms to fibers: Identifying novel processing methods in the synthesis of pitch-based carbon fibers. *Science advances*, 8(11), eabn1905. https://doi.org/10.1126/sciadv.abn1905

Carbon 2022

# Definitive screening design (DSD) as a tool to study bone char properties at different pyrolysis conditions

**Diego Felipe Hernández-Barreto, Liliana Giraldo[2] and Juan Carlos Moreno-Piraján**
Chemistry Department – Faculty of Science, Universidad de los Andes, Bogotá, Colombia
Email: df.hernandez14@uniandes.edu.co

[2]Chemistry Department, Universidad Nacional de Colombia, Bogotá, Colombia

**Keywords**
Pyrolysis, bone char, screening design.

## INTRODUCTION

Screening designs are used to identify the key factors that affect process variables and process quality, to reduce the quantity of factors under study and the number of experimental runs. In comparison to full – factorial designs, where investigators use all possible combinations of factor levels, in screening designs it is assumed that not all factors are relatively important, but just few factors control process quality. There are three types of screening designs that are typically used: 2-Level fractional factorial, Plackett-Burman, and Definitive Screening Designs (DSD); of which DSD is the only one that provides information about the second order terms (quadratic and 2-way interactions), without further sequential experimental runs (Antony, 2003).

Bone char is a material obtained by the pyrolysis of bone residues, and it is commonly used in adsorption in aqueous phase. Bone char's adsorption capacity depends on its textural and physicochemical properties, which in turn depend on the conditions used during pyrolysis process (Azeem *et al.*, 2022). The present work has the aim to show preliminary results of dependence of bone char's characteristics and properties, with pyrolysis conditions, by means of DSD analysis.

## METHODOLOGY

Bone wastes were collected from a local butcher shop in Bogotá, Colombia. They were washed, crushed, sieved, and dried previous thermal treatment. Bone char was prepared on a tubular furnace Barnstead Thermolyne 21100, using a fixed gas rate flow of 200 $mL.min^{-1}$ for all experimental runs. A DSD was proposed to study the effect of five factors (A: Temperature, B: Time (dwelling), C: Heating rate, D: Particle size, E: Atmosphere), each one with three levels, except for atmosphere which has only two categorical levels. The effect of this factors was studied over different properties of bone char such as carbon content, Ca/P ratio, BET surface area, $pH_{PZC}$, and immersion enthalpy ($\Delta H_{imm}$) in glyphosate solution. The DSD was composed by 14 runs and 2 central points, and it was obtained and analysed using Minitab19® software.

BET surface area was calculated from the nitrogen physisorption isotherm at 77 K, that was measured using the gas sorption analyser Quantachrome Autosorb IQ2. Carbon, calcium, and phosphorus content was determined by SEM-EDS analysis, performed on a TESCAN LYRA3 FIB-SEM microscope equipped with a microanalysis system of EDS. Point of zero charge ($pH_{PZC}$) was determined following the salt addition method with slight modifications. Finally, immersion enthalpy was measured with a Calvet type microcalorimeter of local construction, using 200 mg of each bone char and 10 mL of glyphosate solution of 100 ppm.

**RESULTS**

In general, for most of the response variables the significant factors are temperature and atmosphere. However, other factors such as particle size and dwelling time are significant for $pH_{PZC}$ and Ca/P ratio respectively. Heating rate was the only factor that did not affect any of the studied variables, so for future experiments this factor could be fixed in its higher value (5 $K.min^{-1}$), to spend less time during the pyrolysis.

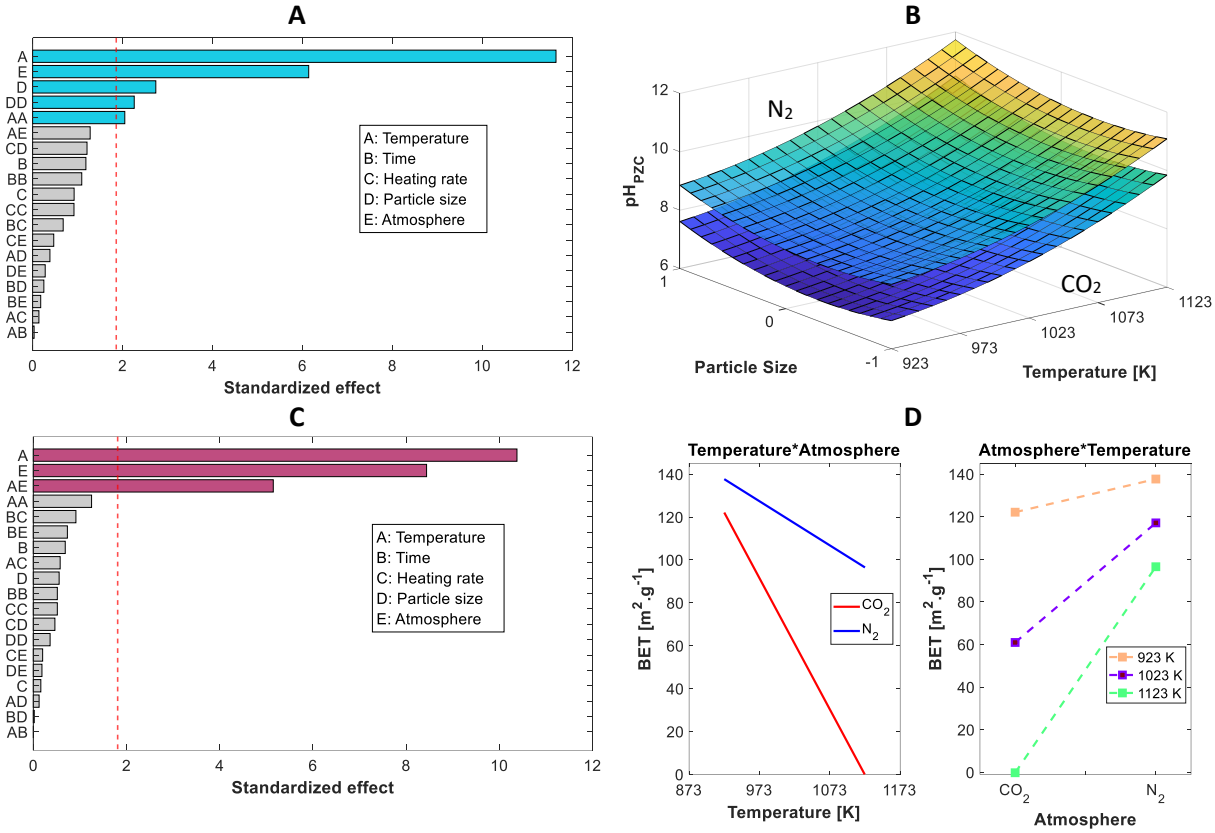


**FIGURE 1: A)** Pareto chart for $pH_{PZC}$, **B)** Response surface of $pH_{PZC}$ vs Temperature vs Particle size, **C)** Pareto chart for BET surface area and **D)** Interaction effects for BET surface area.

In **FIGURE 1A** the Pareto chart for $pH_{PZC}$ is shown. As it is evident the significant factors (p value < 0.05) for this property are temperature, atmosphere, and particle size. In addition, there are quadratic terms that are also significant such as temperature$^2$ and particle size$^2$. As it was determined, there are quadratic terms that are significant, so the model includes these terms and let us to build two response surfaces as presented in **FIGURE 1B**. The regression equation for this model is the following

$$\mathbf{pH_{PZC}} = 24 - 0.0561\mathrm{A} + 0.324\mathrm{D} + 0.621\mathrm{E} + 4.7 \times 10^{-5}\mathrm{A}^2 + 0.515\mathrm{E}^2 \qquad \textbf{[1]}$$

Response surfaces show that for both atmospheres, $pH_{PZC}$ increases with temperature rising and with particle size increment. It is relevant to highlight that the surface presents curvature due to the presence of quadratic terms, that are significant in the model. These results described the behaviour of $pH_{PZC}$ at the different pyrolysis conditions, showing that there is a minimum of $pH_{PZC}$ when temperature is at 1023 K and particle size at the intermediate level (0). In contrast, the highest $pH_{PZC}$ was found at the highest temperature (1123 K) and particle size (1). Finally, the effect of the atmosphere over this property was that bone chars prepared in $CO_2$ are more acidic than the ones prepared in $N_2$ (higher $pH_{PZC}$ value).

On the other hand, in the **FIGURE 1C**, the Pareto chart for BET surface area shows that temperature and atmosphere are the significant factors (p value < 0.05), as well as the 2-way interaction of these factors. In the **FIGURE 1D** the interaction effect plots are presented, and it is evident that BET surface area decreases with a temperature rising for both atmospheres, and that the mean value of BET area is lower for the bone chars obtained under $CO_2$. The interaction between these two factors is observed in the slopes of the plot "Temperature*Atmosphere", in which $CO_2$ line has a steeper slope, indicating a stronger effect of temperature over BET area under this atmosphere. Similarly, in the plot "Atmosphere*Temperature" it is noticeable that the slope of the line 1123 K is the highest in comparison with the other two temperature lines. This means that at the highest temperature the atmosphere effect is stronger than the effect at lower temperatures. The results and behaviour obtained for BET surface area are very similar to those obtained for $\Delta H_{imm}$ in glyphosate solution. This implies that there is an interaction between glyphosate and bone chars' surface, that depends on the BET area as well as on the surface chemistry of the material; suggesting that bone char is a potential adsorbent of glyphosate in aqueous solution.

The principal reason of the obtained behaviour is due to the thermal degradation reactions that are promoted in both atmospheres ($N_2$ and $CO_2$). Nitrogen is an inert atmosphere that allows carbonization to take place, while $CO_2$ is a partially oxidative atmosphere which promotes gasification reactions. In addition, a higher temperature results in loss of porosity which is directly related to BET surface area (Rojas-Mayorga *et al.*, 2013). In the case of $pH_{PZC}$ its behaviour is related to the surface functional groups present in bone chars. In this case, higher pyrolysis temperature results in bone chars with lower content of oxygenated functional groups and therefore with higher basicity.

## CONCLUSIONS

A DSD is a powerful tool to study the dependence of the bone char properties on the pyrolysis conditions. The advantage of this experimental design is the information that can be obtained with a reduced number of runs, including principal effects, 2-way interaction effects and quadratic effects, without performing other new experimental runs. In conclusion, the factors that are statistically significant in most of the properties of bone chars are temperature and pyrolysis. In some cases, particle size and dwelling time are significant; and in contrast, the heating rate has not a significant effect in the bone char characteristics. This allows us to focus on the relevant process variables, reducing time spend and economic cost.

**Acknowledgements**

The authors thank to *Facultad de Ciencias* of *Universidad de los Andes* for the funding through the project INV-2020-104-2062. In addition, *Fondo de Apoyo Financiero para Doctorados* of *Universidad de los Andes* is thankfully acknowledge.

**References**

Antony, J. (2003) 'Screening designs', *Design of Experiments for Engineers and Scientists*. Butterworth-Heinemann, pp. 44–53. doi: 10.1016/B978-075064709-0/50006-5.

Azeem, M. *et al.* (2022) 'Removal of potentially toxic elements from contaminated soil and water using bone char compared to plant- and bone-derived biochars: A review', *Journal of Hazardous Materials*, 427. doi: 10.1016/j.jhazmat.2021.128131.

Rojas-Mayorga, C. K. *et al.* (2013) 'Optimization of pyrolysis conditions and adsorption properties of bone char for fluoride removal from water', *Journal of Analytical and Applied Pyrolysis*. Elsevier B.V., 104, pp. 10–18. doi: 10.1016/j.jaap.2013.09.018.

Carbon 2022

# Are Nanotubes Circular?

**Anthony Impellizerri[1], Abraao C. Torres-Dias[2], Emmanuel Picheau[3], Laure Noé[2], Alain Pénicaud[3], Pascal Puech[2], Marc Monthioux[2], Chris Ewels[1]**

[1] Institut des Matériaux de Nantes Jean Rouxel (IMN), UMR-6502 CNRS, Université de Nantes, 44000 Nantes, France
Email: chris.ewels@cnrs-imn.fr

[2]Centre d'Elaboration des Matériaux et d'Etudes Structurales (CEMES), UPR8011 CNRS, Université de Toulouse, CEDEX 04, 31055 Toulouse, France
[3]Centre de Recherche Paul Pascal (CRPP), UMR5031 CNRS, Université de Bordeaux, 33600 Pessac, France

**Keywords**
Arc-electric nanotubes, thermal contraction, radial buckling, cross-section, distortion, intercalation, Iodine.

## INTRODUCTION

The conventional picture of a carbon nanotube is an elongated tubular structure with circular cross-section. However, this is not always the case, for example carbon nanotubes with a limited number of walls (1-2) are forced to adopt non-circular cross-section upon the constraining effect of filling material (Rybkovskiy 2022), and tubes with diameters much larger than usual and large interior cavities can spontaneously flatten (Impellizzeri 2019). We demonstrate here that as well as these examples, arc-discharge multi-walled carbon nanotubes actually have asymmetric buckling along their axis due to thermal contraction after growth.

### Thermal Contraction after synthesis causes MWCNTs to buckle along their length

When multi-walled carbon nanotubes are grown by the electric arc process, the temperatures in the growth zone are typically of the order 3000-3800K. At this temperature range we should expect expansion of the carbon lattice as compared to room temperature. The in-plane coefficient of thermal expansion of graphitic systems is almost zero (lattice variation from 300 to 3500°C is $7.10^{-4}$ nm) but the out-of-plane coefficient is around $30.10^{-6}$/K, and as a result this means that at electric arc growth temperatures the equilibrium interlayer spacing is around 3.75 Å (see Figure 1 left). When growing layered graphite this layer spacing can then reduce as the material cools, reaching its stable room temperature value of 3.335 Å. However, when growing tubular structures, it is not possible to reduce the tube diameter once it is synthesised, since this would involve loss of carbon material. How then can multiwalled carbon nanotubes manage to adopt this interlayer shrinkage?

The answer appears to be that they buckle on one side of the tube, i.e. they no longer maintain a fully circular cross-section. Localised buckling allows the rest of the tube to adopt the preferred interlayer spacing and localises the excess material in a bulge along one side of the nanotube (Figure 1 top right). This can be seen in high-resolution transmission electron microscopy (HRTEM) images of as-purchased nanotubes from both Mer Corp. and Sigma Aldrich, as variations in the interlayer spacing in some tubes, but localised to only side of the tube. This local buckling creates a cavity along the length of the tube, and we were able to demonstrate this by oxidising away the tube tips and then filling the cavities with Iodine. This can be clearly observed in both HRTEM and high-angle annular dark field images, the Iodine forming lines along one side only of the nanotube, between the nanotube graphenic layers. Counting the layer numbers on both sides of the projected nanotube

image confirms that Iodine is intercalated rather than substitutional (Cefas Torres-Dias 2022). We have confirmed and explained this intercalation behaviour with DFT calculations (Figure 1 bottom right). **Our full publication on this work is available open source at (Cefas Torres-Dias, 2022).**

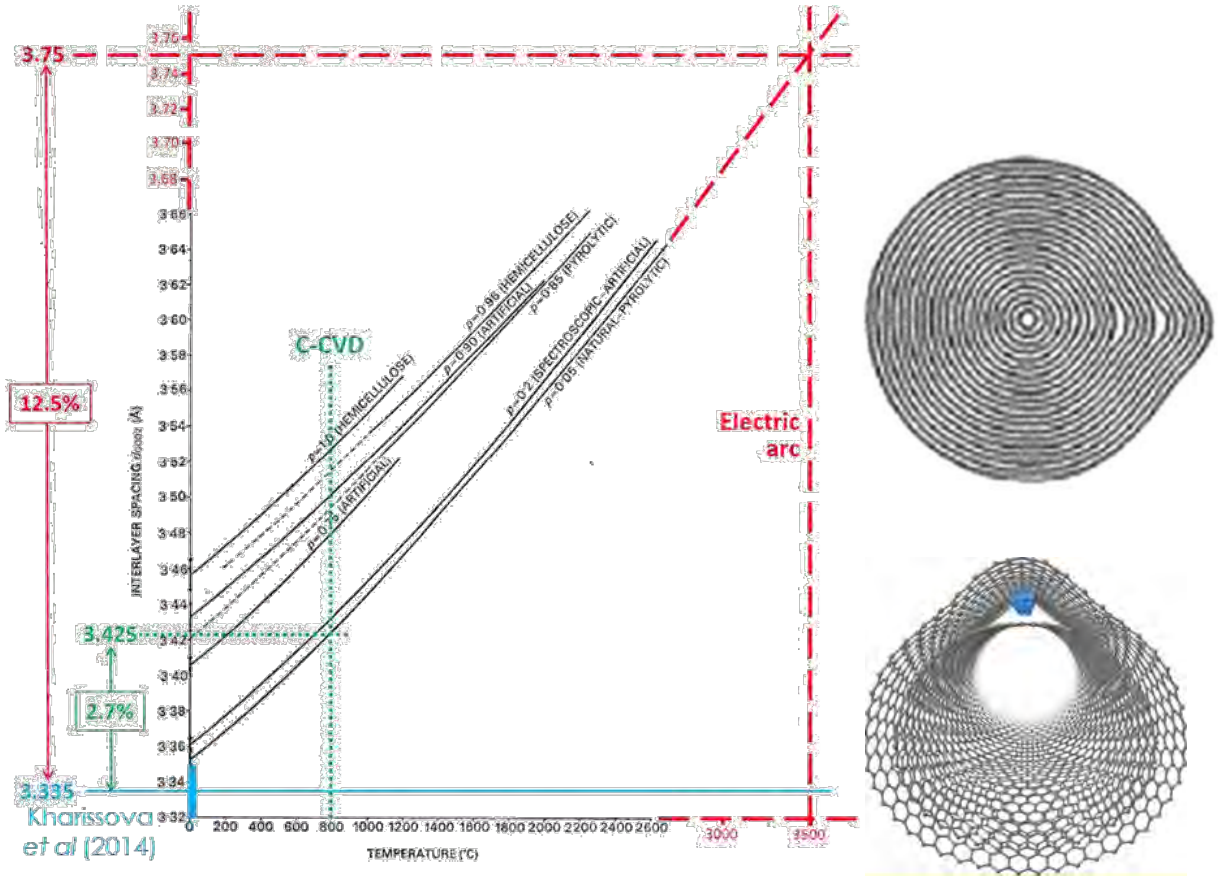


**FIGURE 1**: (Left) Coefficient of thermal expansion (CTE) for a range of graphenic materials (Original Image taken from Kellett 1971, Modified image from Cefas Torres-Dias 2022). Nanotube growth temperatures are marked, indicating likely interlayer spacing lattice expansion of around 12.5% during electric arc nanotube synthesis as compared to room temperature spacing of 3.335Å. (Top-right) Effect of van der Waals interactions on concentric graphenes with spacing initially larger than equilibrium (Huang 2011). (Bottom-right) Iodine intercalation into off-centered axial buckles is thermodynamically stable and seen experimentally (Cefas Torres-Dias 2022).

**Acknowledgements**

We thank the CCIPL (Centre de Calculs Intensifs des Pays de la Loire), where many of the calculations were performed. This research received funding from the 'EdgeFiller' project (grant # ANR-16-CE24-0008-02) and the 'OPIFCat' project (grant # ANR-20-CE08-0026).

**References**

Cefas Torres-Dias A., Impellizzeri, A., Picheau E., Noé, L., Pénicaud A., Ewels. C., Monthioux, M. (2022). Asymmetrical cross-sectional buckling in arc-prepared multi-wall carbon nanotubes revealed by iodine filling. *MDPI* C, 8 [1], 10. DOI: https://doi.org/10.3390/c8010010

Huang, X., Liang, W., Zhang, S., (2011). Radial corrugations of Multi-Walled Carbon Nanotubes driven by Inter-wall nonbonding interactions. *Nanoscale Res Lett*, 6, 53. https://doi.org/10.1007/s11671-010-9801-0

Impellizzeri, A., Briddon, P., Ewels, C.P. (2019) Stacking- and chirality-dependent collapse of single-walled carbon nanotubes: A large-scale density-functional study. *Phys. Rev. B*, 100 [11] 115410.

Kellett, E.A.; Richards, B.P. (1971) The c-axis thermal expansion of carbons and graphites. *J. Appl. Cryst.* 4, 1–8.

Rybkovskiy, D.V., Koroteev, V.O., Impellizzeri, A., Vorfolomeeva, A.A., Gerasimov, E.Yu., Okotrub, A.V., Chuvilin, A., Bulusheva, L.G., Ewels, C.P. (2022). "Missing" one-dimensional red-phosphorus chains encapsulated within single-walled carbon nanotubes. *ACS Nano* 16 [4], 6002-6012.

Carbon 2022

# Synergistic effect of hydrothermal co-carbonization of agricultural and urban waste on hydrochar fuel characteristics

**R.P. Ipiales[1,2], I. Sanchis[1], E. Diaz[1], E. Diaz-Portuondo[2], A.F. Mohedano[1], M.A. de la Rubia[1]**

[1]Chemical Engineering Department, Universidad Autónoma de Madrid, 28049 Madrid, Spain

[2]Arquimea-Agrotech, 28400 Collado Villalba, Madrid, Spain

Email: pipiales@arquimea.com

**Keywords**

Combustion properties, hydrochar, hydrothermal co-carbonization, livestock waste, municipal waste.

## INTRODUCTION

Hydrothermal carbonization (HTC) is a technology that transform wet biomass into biofuel under moderate temperatures (180 – 250 °C), short residence times (5 – 120 min) and autogenous pressure. The main product is a carbonaceous solid, called hydrochar (HC), with suitable properties to be used as biofuel (Villamil *et al.*, 2019). The main problem of some hydrochar to be used as biofuels lies in their high N, S, and ash contents according to regulations (ISO/TS 17225-8, 2016). N and S, can release $NO_X$, $SO_X$ during combustion and/or leading corrosion and fouling of boilers, especially in hydrochar from sewage sludge, animal manure or microalgae (Brown et al., 2020), in contrast of the hydrochar obtained from lignocellulosic biomass or biowaste (Zhang *et al*., 2017). Therefore, blending different biomasses by hydrothermal co-carbonization (co-HTC) would be a good option to find synergy and improve the fuel quality of individual materials. This study aims to explore the feasibility of producing a high-quality hydrochar via co-HTC, blending livestock waste (poultry litter (PL) and swine manure (SM)) with municipal waste (garden and park waste (GPW) and biowaste (BW)) to i) evaluate the mixing ratio of each waste to optimize the hydrochar yield ($Y_{HC}$), carbon content, higher heating value (HHV) and energy yield ($E_{yield}$); and ii) analyse the combustion behaviour of the obtained hydrochars.

## MATERIALS AND METHODS

HTC tests were conducted (at 180 ºC, 1h) in an electrically heated 4 L ZipperClave® pressure vessel loaded with 1.5 kg of SM, PL, GPW or BW and in the case of co-HTC 1.2 kg of blended of the different feedstock (SM:GPW, PL:GPW and PL:BW) at different ratios (3:1, 1:1 and 1:3, w:w). The biomass:water ratio was kept at 20:80 for each test. The hydrochar from plain HTC were called as HC followed by feedstock acronym (HC-SM, HC-PL, HC-GPW and HC-BW) and co-hydrochar (co-HC) from co-HTC according to ratio blend (i.e., HC-SM3:GPW1 is the co-hydrochar from co-HTC of 75% of SM and 25% of GPW w:w). Feedstock and hydrochar were evaluated according to standard ISO 17225-8 (HHV > 17 MJ $kg^{-1}$; volatile matter < 75%; N < 3%; S < 0.5 and ash < 20%) for industrial biofuel use.

## RESULTS

Table 1 shows the energy and combustion characteristics of the feedstock and hydrochar in all the runs carried out. The HTC process proved to be a suitable method to increase the carbon content (6 – 10 %) and HHV (5 – 12%) in resulted hydrochar compared to the feedstock. As expected, hydrochar from livestock waste (HC-SM and HC-PL ) did not reach characteristics to be used as biofuel (ISO/TS 17225-8, 2016). In addition, their $Y_{HC}$ due to the high portion of high hydrolysable compounds such as protein, fat, and carbohydrate were low. As also expected, hydrochar from GPW and BW showed suitable characteristics for its use at industrial level fulfilling all the requirements of ISO standard and with larger $Y_{HC}$ and $E_{yield}$. Co-HTC of livestock waste with municipal waste (SM-GPW, PL-GPW and PL-BW) resulted in hydrochar with suitable fuel characteristics, being the mixing containing ≥ 50 wt.% of GPW or BW which showed the best increment in C content 20 – 40%, HHV (> 17 MJ $kg^{-1}$) as well as minimal N, S, and ash content. Therefore, Co-HC fulfil the ISO standard requirements, allowing the use of these HC without any restrictions with the exception of HC-PL3:GPW1 and HC-PL3:BW1 due to N > 3%.

**Table 1.** Energy characteristics and combustion properties of the feedstock and hydrochars

| | C (%) | N (%) | S (%) | $Y_{HC}$ (%) | HHV (MJ $kg^{-1}$) | $E_{yield}$ (%) | VM (%) | Ash (%) | SI | FI | Ea (kJ $mol^{-1}$) | CCI·$10^7$ ($min^{-2}$ $°C^{-3}$) |
|---|---|---|---|---|---|---|---|---|---|---|---|---|
| **SM** | 35.3 | 2.4 | 0.7 | - | 14.1 | - | 60.0 | 24.3 | 83.7 | 505.2 | 80.6 | 9.2 |
| **PL** | 38.6 | 3.5 | 0.8 | - | 15.5 | - | 74.6 | 18.5 | 35.2 | 129.4 | 58.6 | 4.8 |
| **GPW** | 46.9 | 0.9 | 0.4 | - | 19.7 | - | 76.5 | 5.1 | 4.7 | 20.7 | 61.6 | 7.8 |
| **BW** | 40.9 | 1.7 | 0.2 | - | 17.0 | - | 76.3 | 18.6 | 4.4 | 21.3 | 56.6 | 4.5 |
| **HC-SM** | 37.3 | 1.9 | 0.7 | 54.4 | 15.5 | 58.5 | 53.9 | 31.6 | 11.0 | 54.3 | 67.8 | 6.2 |
| **HC-PL** | 42.8 | 4.0 | 0.6 | 64.5 | 17.4 | 72.7 | 75.3 | 17.0 | 56.5 | 311.7 | 62.3 | 6.3 |
| **HC-GPW** | 49.8 | 1.3 | 0.2 | 87.0 | 20.7 | 91.4 | 67.1 | 3.3 | 33.1 | 81.2 | 62.3 | 7.8 |
| **HC-BW** | 44.5 | 2.3 | 0.2 | 84.0 | 18.6 | 92.0 | 0.0 | 12.3 | 31.4 | 138.6 | 64.6 | 6.4 |
| **HC-SM3-GPW1** | 43.3 | 1.8 | 0.3 | 47.5 | 17.9 | 57.0 | 67.3 | 21.1 | 25.1 | 16.1 | 60.6 | 9.2 |
| **HC-SM1-GPW1** | 45.0 | 1.8 | 0.3 | 51.7 | 19.5 | 59.7 | 64.8 | 19.1 | 19.3 | 18.1 | 56.5 | 8.5 |
| **HC-SM1-GPW3** | 48.2 | 2.3 | 0.2 | 71.7 | 19.9 | 75.6 | 70.9 | 12.0 | 1.6 | 9.4 | 58.1 | 10.1 |
| **HC-PL3:GPW1** | 46.2 | 4.0 | 0.3 | 73.0 | 19.0 | 79.4 | 75.3 | 15.8 | 0.9 | 6.4 | 62.3 | 8.3 |
| **HC-PL1:GPW1** | 47.9 | 3.0 | 0.2 | 76.5 | 19.2 | 83.3 | 72.8 | 11.3 | 5.2 | 23.3 | 64.5 | 8.1 |
| **HC-PL1:GPW3** | 48.0 | 2.4 | 0.2 | 77.5 | 19.5 | 83.8 | 71.4 | 7.9 | 2.6 | 27.8 | 68.6 | 8.5 |
| **HC-PL3:BW1** | 42.7 | 3.9 | 0.3 | 68.0 | 17.2 | 73.4 | 70.7 | 12.4 | 9.5 | 9.1 | 61.3 | 8.2 |
| **HC-PL1:BW1** | 43.6 | 2.8 | 0.2 | 73.0 | 17.8 | 78.4 | 73.1 | 8.9 | 0.7 | 0.7 | 63.7 | 8.0 |
| **HC-PL1:BW3** | 44.5 | 2.3 | 0.2 | 72.5 | 18.6 | 77.7 | 76.2 | 4.9 | 0.2 | 0.2 | 65.8 | 7.6 |

Fouling index (FI) and slagging index (SI) are related to rapid ash agglomeration, formation of eutectic mixtures that melt with the boiler walls and corrosion as well as energy losses during the combustion (Brown *et al.*, 2020). Hydrochar obtained by plain HTC decreased FI and SI compared to raw SM and PL, although not enough to avoid the above problems. Co-HC (HC-SM:GPW, HC-PL-GPW and HC-PL:BW) reduced both indexes to values considered low and medium propensity. The combustion behaviour showed a minimal variation in energy activation however, the combustibility index showed a gradual increment which shows that co-HCs are more stable materials in combustion than plain HC.

## CONCLUSIONS

The HTC of SM and PL showed slightly improves in the energy characteristics, but not enough to fulfil the ISO standard to be used as biofuel due to their high N, S, and ash content. Moreover, these materials could cause several drawbacks during combustion. Co-HTC improved the energy characteristics and combustion properties compared with plain hydrochar with higher energy densification, fulfilling the ISO standard. Also showed lower ash agglomeration propensity and better combustion behaviour, proving that blending biomass waste with poor characteristics as livestock waste with a more noble biomass as municipal waste can improve the obtained hydrochar, achieving strong synergies to produce more environmentally friendly biofuels.

**Acknowledgements**

Authors greatly appreciate funding from Spain's MINECO (PID2019-108445RB-I00, PDC2021-120755-I00), Madrid Regional Government (Project S2018/EMT-4344) and Grupo Kerbest company. R.P. Ipiales acknowledges financial support from Community of Madrid (IND2019/AMB-17092) and Arquimea-Agrotech Company.

**References**

Brown, A. E. *et al.* (2020) 'An Assessment of Different Integration Strategies of Hydrothermal Carbonisation and Anaerobic Digestion of Water Hyacinth', *Energies*, 13, 5983, pp. 1–26. doi: 10.3390/en13225983.

ISO/TS 17225-8 (2016) *International organization for standardization ISO/TS 17225-8. Solid biofuels — Fuel specifications and classes. Graded thermally treated and densified biomass fuels. First edition*. USA.

Villamil, J. A. *et al.* (2019) 'Technologies for wastewater sludge utilization and energy production: Hydrothermal carbonization of lignocellulosic biomass and sewage sludge', in *Wastewater Treatment Residues as Resources for Biorefinery Products and Biofuels*, pp. 133–153. doi: 10.1016/B978-0-12-816204-0.00007-2.

Zhang, X., Zhang, L. and Li, A. (2017) 'Hydrothermal co-carbonization of sewage sludge and pinewood sawdust for nutrient-rich hydrochar production: Synergistic effects and products characterization', *Journal of Environmental Management*, 201, pp. 52–62. doi: 10.1016/j.jenvman.2017.06.018.

Carbon 2022

# Graphene-based electrocatalysts for ORR synthesized by electrochemical methods

**Cristian Jaimes-Paez[1], Diego Cazorla-Amorós[2], Emilia Morallón[1]**
[1]Departamento de Química Física and Instituto Universitario de Materiales de Alicante (IUMA), University of Alicante, Ap. 99, 03080, Alicante, Spain
Email: cristian.jaimes11@ua.es

[2]Departamento de Química Inorgánica and Instituto Universitario de Materiales de Alicante (IUMA), University of Alicante, Ap. 99, 03080, Alicante, Spain

**Keywords**
Cathodic graphene, electrochemical, ORR.

## INTRODUCTION

The need to replace combustion engines has led to the development of promising new technologies like fuel cells and electrolysers that require the use of electrocatalytic materials and in which carbon nanomaterials play an essential role (Dai et al., 2012). Graphene is a carbon nanomaterial which has remarkable properties, for this reason its study has grown exponentially. The development of scalable methods to produce large, processable amounts of high-quality graphene-based materials is essential to bridge the gap between laboratory study and commercial applications (Najafabadi & Gyenge, 2015). The production of graphene-based materials by electrochemical exfoliation of graphite is a simple, cost-effective and environmentally friendly method for the large-scale production of high-quality graphene (Abdelkader et al., 2015). The oxygen reduction reaction (ORR) is a fundamental process in electrochemistry and its slow kinetics is undoubtedly one of the main drawbacks for the large-scale commercialization of fuel cell technology. Then, the development of electrocatalysts for ORR is of great importance and constitutes a central issue in the sustainable energy and environmental scenario(Shao et al., 2016).

In this study, we propose the use of a high-quality graphene-based material synthesized by electrochemical method, through cathodic expansion, as a support of Pt nanoparticles. These nanoparticles have been incorporated by a simple and straightforward one-step stirring method. The electrocatalyst obtained consists of nanometre size Pt nanoparticles well distributed in the graphene-based material with an excellent catalytic activity to ORR compared to a commercial catalyst.

## EXPERIMENTAL

The synthesis of graphene-based material was performed by cathodic expansion of graphite sheets, after an initial immersion in $H_2SO_4$ (95-98%). The immersion time was between 0 and 72 h. Then, the obtained material was subjected to an electrochemical expansion step during 1 h, and two voltages (i.e., 10 and 15 V) were studied. For the electrochemical treatment, a graphite sheet was used as cathode and a platinized titanium mesh as anode and 0.1 M $K_2SO_4$ solution was used as electrolyte. After the electrochemical treatment, sonication and centrifugation stages were carried out. The incorporation of Pt nanoparticles has been performed on selected graphene-based material dispersions using a specific volume of 3 mM $H_2(PtCl_6).6H_2O$ as Pt precursor to achieve a final metal content of 10 wt. %. The samples were characterized by physicochemical and electrochemical techniques.

## RESULTS AND DISCUSSION

The optimum conditions to reach the higher concentration are: 50 h in the immersion time; after that, using 15 V at the electrochemical expansion and three sonication and centrifugation steps. With these conditions of synthesis, the morphology of the materials corresponds to few-layer graphene material. The dimensions of the layer are between 1 to 10 µm. Carbon content of the graphene-based material higher than 97 wt.% and oxygen content below 2 wt.%. By Raman spectroscopy the structural quality of the graphene-based material was analysed, the results corroborate that the cathodic expansion produces a material with low presence of oxygen groups and the number in the synthesised materials is 2 or 3 layers.

Furthermore, the incorporation of Pt by stirring method without the addition of reducing agent was the best way to produce a Pt/Graphene-based material with an average particle size of 1 nm and with an excellent distribution. The carbon material itself facilitates the reduction of the Pt precursor to $Pt^0$. Moreover, the desired amount of Pt was reached by this method (10 wt.%).

Figure 1 shows the results for the graphene-based electrocatalyst in alkaline and acid media for ORR. In which the material with the highest electrocatalytic activity is the one obtained by incorporating Pt during stirring and without reducing agent (Gr-5/Pt-S) which achieve a limiting current density and onset potential similar to that of the commercial Pt/C catalyst. But using only half of wight of platinum.

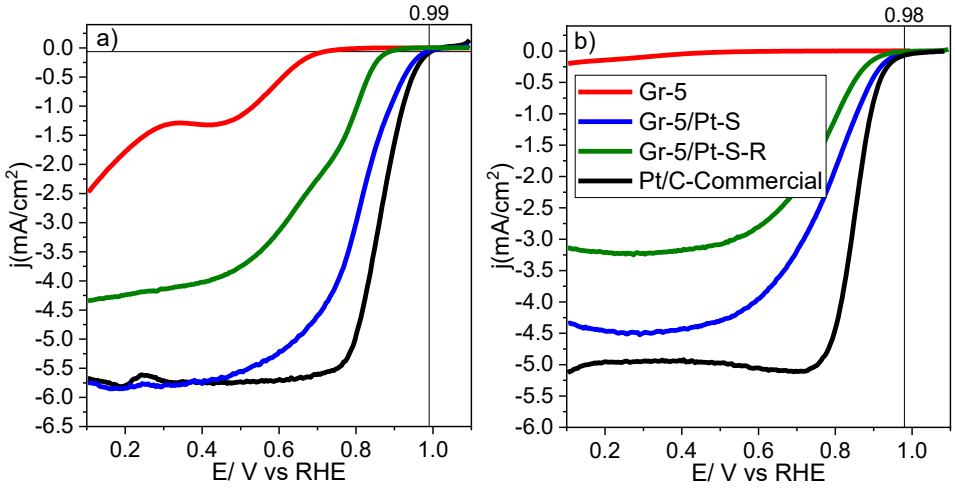


**FIGURE 1**: Linear sweep voltammograms obtained with the rotating disc electrode for the graphene-based samples in a) 0.1 M KOH, b) 0.5 M $H_2SO_4$. Saturated with O2 at 1600 rpm.

## CONCLUSIONS

Graphene-based materials were synthesized by electrochemical exfoliation method (cathodic expansion), obtaining few layer graphene dispersions with a low oxidation degree. The optimal experimental conditions to obtain the highest concentration without altering the properties were stablished. For the synthesis of the Pt electrocatalysts for ORR, the study of the incorporation of platinum was done in each of the steps of the FLG synthesis. The incorporation of platinum in the FLG dispersion with stirring and without using any reducing and protecting agents, produced a 10wt.% Pt catalyst with an average particle size of 1nm and with an excellent distribution on the graphene-based material support. The easiness of the synthesis is determined by the presence of the graphene-based material that acts as both reducing and protecting agent.

Finally, this electrocatalyst has an excellent behaviour in both acid and alkaline medium, with high onset potential and excellent limit current density for the ORR, which significantly improves the commercial Pt/C material that contains a 20 wt.% of Pt.

**Acknowledgements**
The authors would like to thank the Spanish Ministry of Science and Innovation and FEDER (PID2019-105923RB-I00, RTI2018-095291-B-I00) and the Generalitat Valenciana (GRISOLIA/2020/114) for the financial support.

**References**

Abdelkader, A.M., Cooper, A.J., Dryfe, R.A.W. & Kinloch, I.A. (2015) How to get between the sheets: A review of recent works on the electrochemical exfoliation of graphene materials from bulk graphite. Nanoscale. 7 (16), 6944–6956. doi:10.1039/c4nr06942k.

Dai, L., Chang, D.W., Baek, J.B. & Lu, W. (2012) Carbon nanomaterials for advanced energy conversion and storage. Small. 8 (8), 1130–1166. doi:10.1002/smll.201101594.

Najafabadi, A.T. & Gyenge, E. (2015) Synergistic production of graphene microsheets by simultaneous anodic and cathodic electro-exfoliation of graphitic electrodes in aprotic ionic liquids. Carbon. 84 (1), 449–459. doi:10.1016/j.carbon.2014.12.041.

Shao, M., Chang, Q., Dodelet, J.P. & Chenitz, R. (2016) Recent Advances in Electrocatalysts for Oxygen Reduction Reaction. Chemical Reviews. 116 (6), 3594–3657. doi:10.1021/acs.chemrev.5b00462.

Carbon 2022

# Electrochemical characterization of carbonaceous electrode materials under the co-intercalation phenomenon

**Knut Arne Janßen, Guillermo A. Ferrero, Gustav Åvall, Youhyun Son and Philipp Adelhelm[2]**
Humboldt Universität zu Berlin, Department for Physical Chemistry, Berlin, Germany
Email: janssekn@hu-berlin.de

[2]Helmholtz-Zentrum Berlin für Materialien und Energie, Berlin, Germany

**Keywords**
electrochemical impedance spectroscopy, co-intercalation, carbon

## INTRODUCTION

The so called "co-intercalation" process, where the charge carrying ions are intercalated together with the solvation shell comes along with various favorable features such as a high reversibility, high coulombic efficiency and especially an excellent rate capability – caused by the absence of the desolvation step (Jache, 2014).

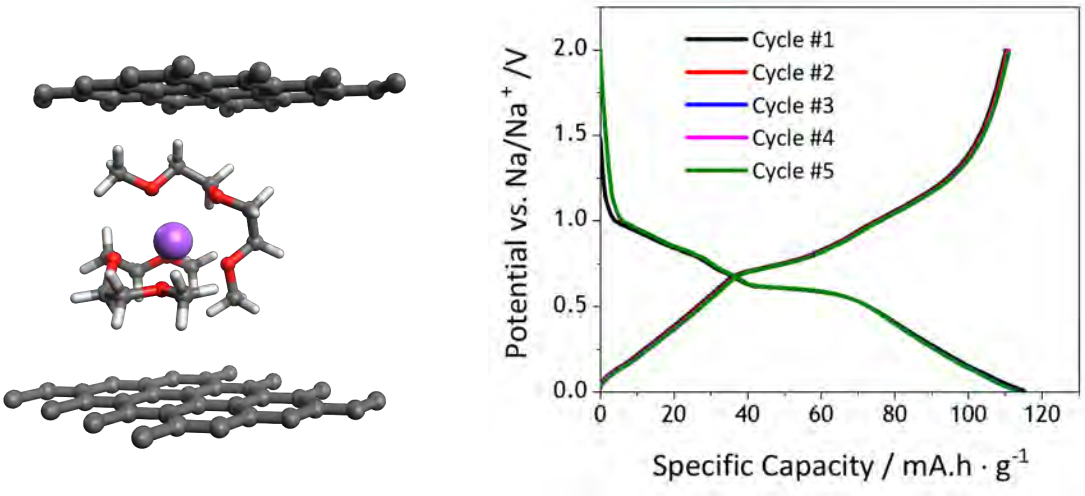


**FIGURE 1**: $Na^+(diglyme)_2$ complex intercalated into graphite (l.) and potential profile for the de-/sodiation in the co-intercalation process (r.).

The material behavior of this system has already been thoroughly investigated for different carbonaceous electrodes (e.g., graphite, hard carbon) with x-ray diffraction (XRD), scanning electron microscopy (SEM) and dilatometry by this group in the past. These examinations showed a huge expansion in the case of graphite that leads to exfoliation without delamination (Göktas, 2018).

Though this process has been investigated a lot in the past, a thorough electrochemical analysis is still missing. By doing supportive electrochemical measurements (electrochemical impedance spectroscopy (EIS) and galvanostatic intermittent titration (GITT)) we could deconvolute the contributions of several features of this system to the outstanding performance measured.

## METHOD

The kinetical properties were in a first step determined, measuring impedance spectroscopy. The results were evaluated by utilizing a transmission line model (TLM). The application of a TLM is especially suited to describe the behavior of porous electrodes.

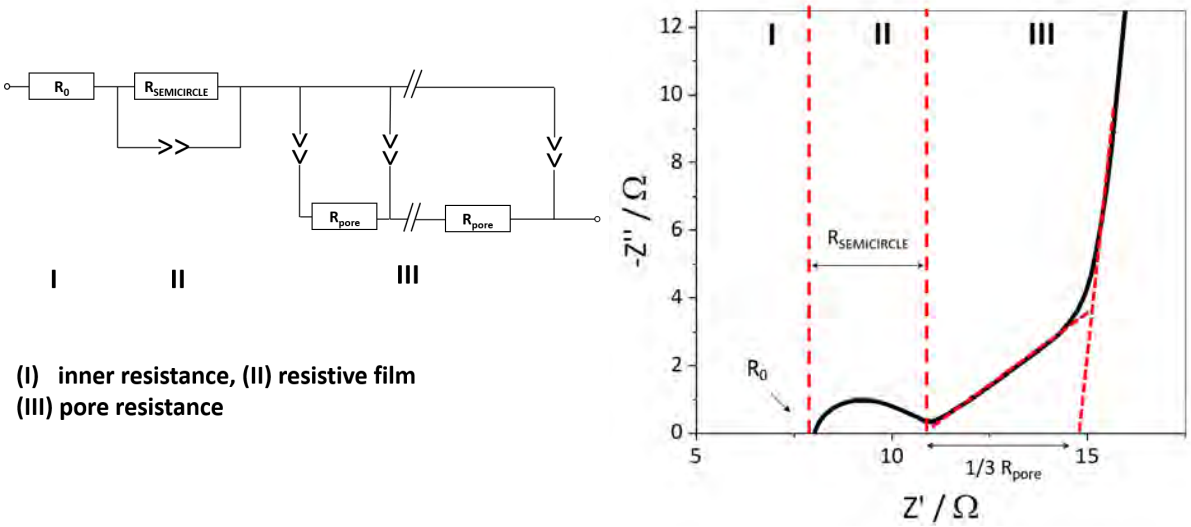


**FIGURE 2**: Equivalent circuit of the applied transmission line model (l.) and Nyquist-diagram with attributed signals in blocking condition (r.).

## EXPERIMENTAL

Several properties of the examined system can be deducted if the contributions of the single kinetic processes to the impedance spectrum are attributed carefully by varying influencing parameters in the setup (electrolyte/electrode).

With this approach and by varying the setup regarding the electrolyte composition of the electrode, the role of resistive feature that might be attributed to a resistive film (SEI) and the effect of the volume expansion of the graphite lattice on the kinetics could be deciphered by determining the changes of the pore resistance, the interfacial resistance, and the charge-transfer.

To study how the variation of the electrolyte composition effects the kinetics, additives like Fluoroethylene carbonate (FEC) have been added to a diglyme based electrolyte in various amounts to form an SEI. FEC precycled samples were subsequently harvested and cycled in a pure glyme based setup to show the reversibility of this resistive feature.

## CONCLUSION

The unique properties of the co-intercalation process and the deconvolution of the effects in the experimental setup enabled a detailed attribution of various frequency dependent impedance signals to single kinetical processes.

By varying the composition of the electrolyte an artificial resistive film could be established under the addition of FEC, leading to blocking behavior. Cycling experiments in a pure glyme based setup showed the reversibility of this feature while undergoing a co-intercalation process.

**Acknowledgements**
Project supported by the European Research Council (ERC) under the European Union's Horizon 2020 research and innovation programme (grant agreement no. 864698, SEED)

**References**

Jache, B., & Adelhelm, P. (2014). Use of graphite as a highly reversible electrode with superior cycle life for sodium-ion batteries by making use of co-intercalation phenomena. *Angewandte Chemie International Edition*, *53*(38), 10169–10173. https://doi.org/10.1002/anie.201403734

Göktas, M., Bolli, C., Berg, E. J., Novák, P., Pollok, K., Langenhorst, F., Roeder, M. v., Lenchuk, O., Mollenhauer, D., & Adelhelm, P. (2018). Graphite as co-intercalation electrode for sodium-ion batteries: Electrode dynamics and the missing solid electrolyte interphase (SEI). *Advanced Energy Materials*, *8*(16), 1702724. https://doi.org/10.1002/aenm.201702724

Carbon 2022

# Mechanism of Alignment Enhancement of CNT Fibres by AC Electric Fields

**Philipp A. Kloza and James A. Elliott**
Department of Materials Science & Metallurgy, University of Cambridge, 27 Charles Babbage Road, Cambridge, UK, CB3 0FS
Email: pak37@cam.ac.uk

**Keywords**
carbon nanotubes, alignment, FCCVD

## INTRODUCTION

The large-scale production of highly aligned carbon nanotubes (CNTs) represents a desirable research goal due to their exceptional electrical and mechanical properties in the alignment direction. Here, we focus on aligning CNTs with AC electric fields *in situ* during synthesis using the floating catalyst vapour deposition (FCCVD) method; a scalable and continuous manufacturing technique (Li, Kinloch and Windle, 2004).

Experiments show that freely suspended CNTs can be substantially aligned using AC electric fields in the radio frequency regime (Zhou et al., 2006). However, so far, no theoretical explanation for the observed higher efficacy of alignment using alternating current (AC) electric fields compared to using direct current (DC) fields has been given in the literature. We propose that axial currents generated by the AC field, together with the subsequently induced magnetic fields, are mainly responsible for the observed increase in the CNT alignment.

## Z-PINCH STIFFENING

### Mechanism

Here, we describe the "z-pinch" effect which arises from Lorentz forces due to electromagnetic interactions in a CNT exposed to an external electric AC field. Modelling of the current-carrying modes within a single-walled CNT (SWCNT) suggests that substantial current is achieved for radio frequency AC fields (Burke, 2002).

This axial electric current then induces a circumferential magnetic field in the CNT. In turn, the current experiences a Lorentz force due to the magnetic field which can be modelled as a pressure acting on the wall of the CNT. The name z-pinch refers to this "pinching" of the CNT about its z-axis. An illustration of the z-pinch effect is shown in Figure 1.

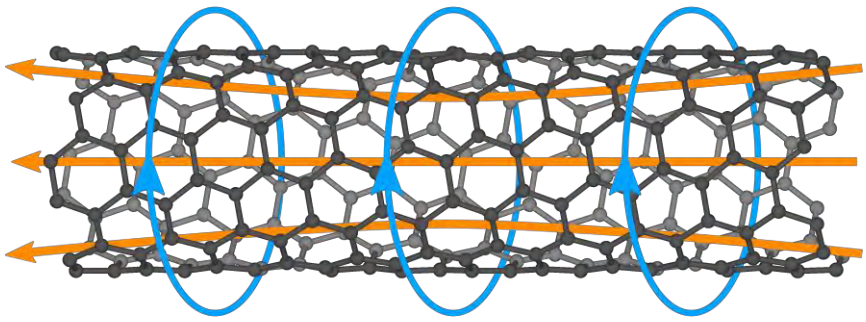

**FIGURE 1**: SWCNT with axial current (orange) and induced magnetic field (blue).

By considering a curved CNT with a constant Lorentz pressure acting on its surface, one can show that the z-pinch effect leads to a restoring force acting against the curvature, effectively stiffening the CNT, and thus facilitating alignment.

**Theoretical Model**

Our mathematical model of a freely suspended individual CNT in an AC electric field extends the worm-like chain (WLC) model for one-dimensional macromolecules. The model further extends our previous work on DC field alignment (Kloza and Elliott, 2020) to account for the z-pinch effect. The CNT is modelled as a one-dimensional curve parametrised in terms of the contour length $s$. We show that the free energy of the system is a functional of the tangent vector $\hat{t}(s)$ and is given by:

$$F[\hat{\mathbf{t}}(s)] = \int_0^L \mathrm{d}\, s \left[\frac{a}{2}\left(\frac{\mathrm{d}\hat{\mathbf{t}}(s)}{\mathrm{d}s}\right)^2 - \frac{\varepsilon_0 A}{2}(\hat{\mathbf{t}}(s)\cdot\mathbf{E})^2\right] - \frac{\mu_0 J^2}{8\pi}\left[\int_0^{L/2}\mathrm{d}\, s\, \hat{\mathbf{t}}(0)\cdot\hat{\mathbf{t}}(s) + \int_{L/2}^{L}\mathrm{d}s\, \hat{\mathbf{t}}(L)\cdot\hat{\mathbf{t}}(s)\right]. \quad [1]$$

The functional accounts for bending, polarsiation and z-pinch stiffening of the CNT via the first, second and final two terms of the functional, respectively. In the functional, $a$, $L$ and $A$ stand for the bending stiffness, the length and cross-sectional area of the CNT, respectively, and $J$ is the electric current inside the CNT. Appropriate averages can be calculated by employing a harmonic approximation to the functional and using standard methods from Gaussian statistical field theory (Landau and Lifshitz, 1980).

**RESULTS**

The main measure for alignment used in our study is the two-dimensional (Chebyshev) order parameter which can be readily measured in experiments using SEM imaging:

$$T_2 = 2\langle\cos\theta_{2D}\rangle - 1. \quad [2]$$

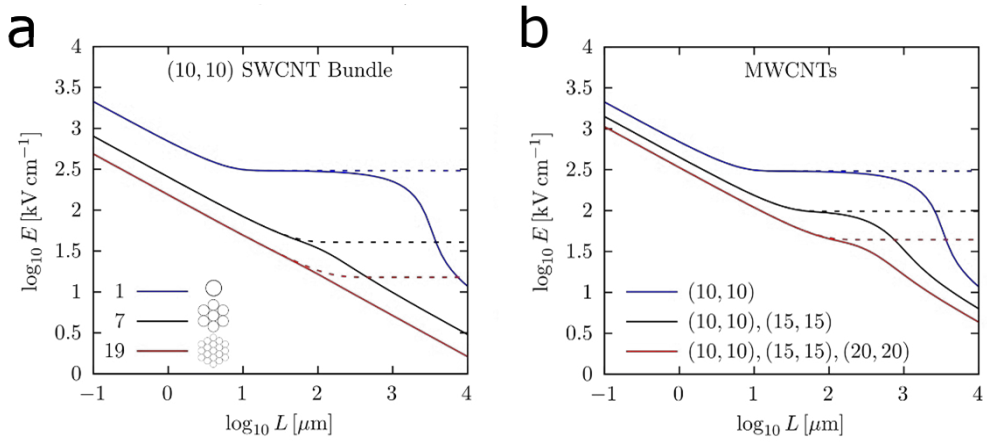


**FIGURE 2**: Electric field strength necessary to reach $T_2 = 0.5$ versus CNT length for SWCNT bundles (a) and MWCNTs (b). Solid and dashed lines show values with and without z-pinch, respectively.

For bundles of SWCNTs and individual multi-walled CNTs (MWCNTs), we calculated the electric field strength necessary to reach an order parameter $T_2 = 0.5$ which indicates substantial alignment. The results in Figure 2 show that without the z-pinch effect, the CNTs transition from rigid to elastic behaviour once they reach a critical length. Once the behaviour becomes elastic, an increase in length does not lead to an increase in coupling to the electric field. When z-pinch stiffening is considered, the transition from rigid to elastic behaviour is removed, thus reducing the electric field strength necessary for alignment by over an order of magnitude for CNTs with lengths exceeding $300\ \mu\mathrm{m}$. This indicates that AC-field-induced z-pinch stiffening is a key factor in facilitating electric field alignment of CNTs and explains the improved performance of AC versus DC field alignment.

**Acknowledgements**

P.A. Kloza gratefully acknowledges the Cambridge Commonwealth, European & International Trust and the Engineering and Physical Sciences Research Council (EPSRC) for funding to conduct this research under auspices of the Centre for Doctoral Training in Computational Methods for Materials Science, EP/L015552/1.

**References**

Burke, P. (2002), 'Luttinger liquid theory as a model of the gigahertz electrical properties of carbon nanotubes', IEEE Transactions on Nanotechnology 1(3), 129–144. https://doi.org/10.1109/TNANO.2002.806823

Kloza, P. A. & Elliott, J. A. (2020), 'Freely suspended semiflexible chains in a strong aligning field: Simple closed-form solutions for the small-angle approximation', Macromolecular Theory and Simulations 29(6), 2000049. https://doi.org/10.1002/mats.202000049

Landau, L. & Lifshitz, E. (1980), Statistical Physics, third edn, Butterworth-Heinemann, Oxford, UK. ISBN 978-0-08-057046-4.

Li, Y.-L., Kinloch, I. A. & Windle, A. H. (2004), 'Direct spinning of carbon nanotube fibres from chemical vapor deposition synthesis', Science 304(5668), 276–278. https://doi.org/10.1126/science.1094982

Zhou, Z., Wan, D., Dou, X., Song, L., Zhou, W. & Xie, S. (2006), 'Postgrowth alignment of SWCNTs by an electric field', Carbon 44(1), 170–173. https://doi.org/10.1016/j.carbon.2005.08.015

Carbon 2022

# Ultra-permeable graphene-zeolite membranes for hydrogen separation

Radovan Kukobat,[1,2] Motomu Sakai,[3,4] Hideki Tanaka,[1] Hayato Otsuka,[1] Masahiko Matsukata,[3,4] Takuya Hayashi[5] and Katsumi Kaneko*[1]

[1]Research Initiative for Supra-Materials, Shinshu University, Nagano 380-8553, Japan
[2]Center for Biomedical Research, Faculty of Medicine, University of Banja Luka, Bosnia and Herzegovina
[3] School of Advanced Science and Engineering, Waseda University, Tokyo, JAPAN
[4]Research Organization for Nano and Life Innovation, Waseda University, Tokyo, Japan
[5]Department of Electrical Engineering, Shinshu University, Nagano, Japan

e-mail for corrrespondence: kkaneko@shinshu-u.ac.jp

**KEYWORDS** Colloidal graphene, membrane, hydrogen separation

## INTRODUCTION

$H_2$ is a significant industrial target for clean energy generation and intensive $CO_2$ reduction., and it is mainly produced through steam reforming of natural gas. The energy-saving recovery of $H_2$ from refinery streams containing $H_2$, $CH_4$, and light hydrocarbons is ultimately aimed at consistently reducing $CO_2$ emissions. The recovery of $H_2$ from refinery gases via membrane separation is more favorable than distillation with regard to energy consumption and reduction of $CO_2$ emissions. In particular, thermally stable membranes are preferred for an energy-saving process for $H_2$ separation. The efficient separation of $H_2$ from $CH_4$ and light hydrocarbons for clean energy applications remains a technical challenge in membrane science.

## RESULTS AND DISCUSSION

To address this issue, we prepared a graphene-wrapped MFI (G-MFI) molecular-sieving membrane. Figure 1(a) shows the SEM and TEM images of G-MFI. The SEM image clearly shows that zeolite crystals are wrapped with graphenes and the graphene-wrapped zeolite particles are associated with each other. Then, the graphene-wrapped zeolite membrane has no cracks to show the excellent sieving properties. Also Figure 1 (b) shows the structure of graphene wrapping zeolite crystal. We can observe many nanowindows[1)] whose size is in the range of 0.5 nm to 2.5 nm; $H_2$ and $CH_4$ molecules can

permeate freely through the nanowindows. Figure 2 shows the Robeson plot for $H_2/CH_4$. This indicates explicitly that the graphene-wrapped zeolite membrane induces the ultrafast separation of $H_2$ from $CH_4$ at a permeability reaching $5.8 \times 10^6$ barrers at a single gas selectivity of 245 and mixed gas selectivity of 50. Our results set a new upper bound for $H_2$ separation[2]. There are interfacial spaces between colloidal graphene and zeolite crystal surfaces whose width is less than 0.4 nm, which can separate quite efficiently $H_2$ from $CH_4$. Molecular dynamics simulation studies supported this novel separation mechanism using a simplified model that a zeolite rod was coated with single wall carbon nanotube having the nanoscale entrance and exit; the permeation depended on the crystal face of zeolite. The zeolite crystals wrapped with graphenes form an aggregated porous membrane without leakage. The porous structure induces unusually high permeance for $H_2$ with keeping high selectivity, as described above. Here, colloidal graphenes used for wrapping zeolite crystals have nanowindows[1] of about 1 nm in size which was evaluated by analysis of high-resolution transmission electron microscopic images. Consequently, gas molecules such as $H_2$ can permeate freely the nanowindows to move to the interfacial spaces between the graphene and zeolite crystal face, where highly selective permeation of $H_2$ occurs[3]. This graphene-wrapped fine-crystal membranes exhibit excellent separation characteristics for $CO_2/CH_4$ as well as $H_2/CH_4$. [2]

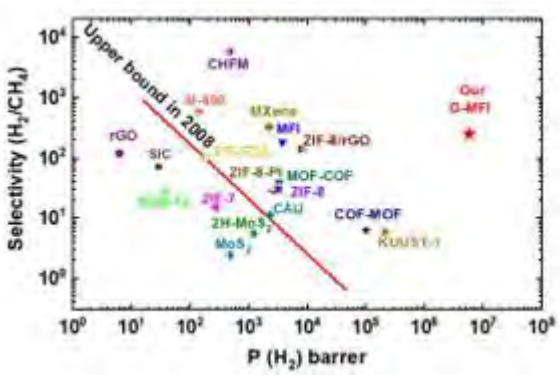


Fig. 1. Robeson plot of G/MFI for $H_2/CH_4$

This work was supported by JST-CREST "Creation of Innovative Functional Materials with Advanced Properties by Hyper-nanospace Design" and Kotobuki Holdings Co.

**REFERENCES**

1. Vallejos-Burgos, F., Coudert, F.-X., Kaneko, K. (2018). Air separation with graphene mediated nanowindow-rim concerted motion. *Nature Comm*. 9, 1812-1821.
2. Kukobat, R., Sakai,M., Tanaka,H., Otsuka, H., Vallejos-Burgos, F., Lastoskie, C., Matsukata, M., Sakai, Y., Yoshida, K., Hayashi, T., Kaneko, K. (2022). Ultrapermeable 2D-channeled graphene-wrapped zeolite molecular sieving 5 membranes for hydrogen separation, *Sci. Adv.*, 8, 3521, 1-11.
3. Kukobat, R., Sakai, M., Furuse, A., Otsuka, H., Tanaka, H., Hayashi, T., Matsukata, M., . Kaneko, K. (2022). Apatite–Graphene Interface Channel-Aided Rapid and Selective $H_2$ Permeation, *J. Phys. Chem. C*. 126, 3653-3660.

Carbon 2022

# N,S Doped Biomass Based Highly Porous Carbon and its Environmentally Relevant Application Potential

**Krisztina László[1]*, Samantha K. Samaniego Andrade[1], István Bakos[2], Miklós Mohai[2], Attila Farkas[3], János Madarász[4]**

[1]Department of Physical Chemistry and Materials Science, Budapest University of Technology and Economics

Email: laszlo.krisztina@vbk.bme.hu

[2]Institute of Materials and Environmental Chemistry, Research Centre for Natural Sciences, Eötvös Loránd Research Network

[3]Department of Organic Chemistry and Technology, Budapest University of Technology and Economics

[4]Department of Inorganic and Analytical Chemistry, Budapest University of Technology and Economics

**Keywords**
graphene oxide; gas separation; oxygen reduction reaction (ORR)

## INTRODUCTION

Carrageenan is a natural polysaccharide extracted from a red seaweed species (Rhodophyceae) with water or aqueous alkali. Regarding its chemical structure (Figure 1), carrageenan is a sulfated polygalactan with a content of 25% - 30% ester-sulfate groups. The sugar units in the chemical structure, sulfur content and the associated sodium, potassium, and/or calcium cations jointly determine the properties of the carrageenan and the carbon materials derived from it (Michel et al, 1997). N atoms incorporated into high surface area carbon materials significantly increase their catalytic and electrocatalytic activity (Voitko et al, 2015). The synergistic effect of heteroatom doping, induction of defects and well-developed porous structure have proved effective to enhance the physical chemical properties of carbon materials and increasing their potential for environmental related applications such as electrocatalysis or biogas separation. In our work, the intrinsic sulfur content of carrageenan works as S dopant while the inorganic mineral content simultaneously serves as template and activation agent. N doping is achieved by adding urea in the synthesis process. The formation of defects results from the thermal treatment given to the materials.

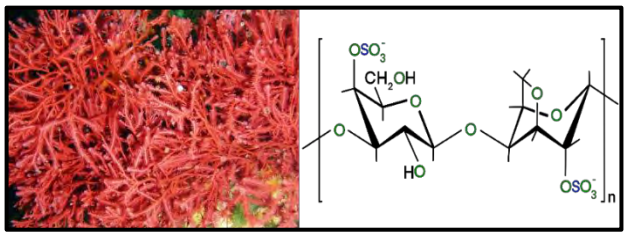


**FIGURE 1**. Red seaweed and i-carrageenan chain unit

Our aim is to produce a metal-free porous carbon and to reveal its potential as electrode in oxygen reduction reaction (ORR) or as adsorbent in biogas upgrading (separation of $CO_2$ from $CH_4$) (Andrade et al, 2021). To achieve the best performance the electric and thermal conductivity of the carbons graphene oxide (GO) was added in the reaction mixture. GO incorporated into the porous polymer framework could be reduced under thermal treatment and converted to graphene like layers, which might enhance the physical-chemical properties of the porous carbon and enhance its performance in the above-mentioned applications.

## MATERIALS AND METHODS

Graphene oxide doped N, S containing carbon cryogels were synthesized following the method of Li et al. (2018) with the addition of aqueous GO suspension early in the process followed by urea as N

source and carrageenan in a mass ratio of 1:1. The GO content varied in the 50 - 200 mg/4 g precursor mixture range. The annealed carbons were labeled as CA, CAGO50, CAGO100, CAGO200 according to the amount of GO added. Nitrogen adsorption measurements (77 K) were performed to study the morphology of the samples. $CO_2$ and $CH_4$ adsorption was measured at 273 K. The surface chemistry was studied by X-ray photoelectron spectroscopy (XPS) and Raman spectroscopy. The electrocatalytic activity of the carbons was tested in ORR in alkaline media. The biogas separation performance was estimated from the single gas adsorption isotherms according to the Ideal Adsorbed Solution Theory (IAST).

**RESULTS AND DISCUSSION**

$N_2$ adsorption isotherms (Fig. 1) showed GO has a benign effect on the adsorption properties. There was a significant enhancement of surface area and almost doubled the pore volume seen by $N_2$ adsorption, but only up to 100 mg GO used, 200 mg caused a negative effect. The pore size distribution functions showed that the more significant development of the porosity occurs in the lower mesopore region for all samples. On the other hand, pore size distribution functions from $CO_2$ adsorption data revealed the ultra-microporous content in all samples. These ultra-micropores are relevant because they have been reported as beneficial in ORR (de Falco et al, 2021; Bandosz, 2022). XPS results revealed that the heteroatom content in all samples is around 10 %, and that the O/C and N/C ratios systematically change with the GO added. Data from Raman spectroscopy confirmed that the addition of GO enhances the formation of defects in the carbon framework.

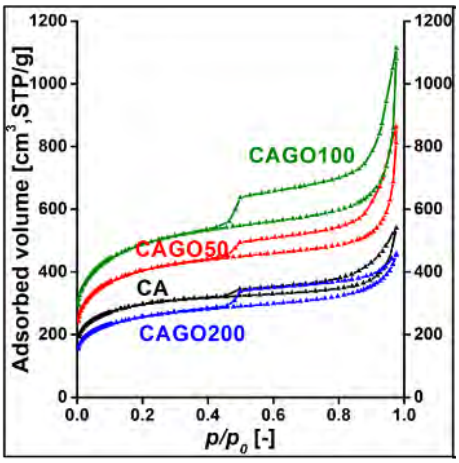


**FIGURE 1** $N_2$ adsorption/desorption isotherms

Each carbon was tested as electrode in ORR. The Koutecky-Levich plots revealed that the undoped CA and CAGO50 carbons seem to follow the 4 $e^-$ mechanism. The combination of hierarchical porous structure, the ultra-micropores, heteroatoms content and the enhanced number of defects may be responsible for the better performance of CA and CAGO50 in ORR. All samples adsorb $CO_2$ better than $CH_4$ along the whole pressure range. The more significant difference in the selectivity values occurs in the low-pressure range. Samples CA and CAGO100 showed the highest selectivity and have the best potential for biogas upgrading.

**CONCLUSIONS**

GO doped N,S containing highly porous carbons were successfully synthesized with the addition of GO affecting both the morphology and surface chemistry of the carbons depending on the amount of GO added. CA and CAGO50 showed the best performance in ORR and might follow the 4 $e^-$ mechanism. All carbon samples adsorb $CO_2$ better than $CH_4$ being CA and CAGO100 the ones with the highest selectivity especially at low pressure.

**Acknowledgements**

The financial support of the National Research, Development and Innovation Office (grant # 2020-3.1.1-ZFR-KVG-2020-00006) and the National Research, Development, and Innovation Fund of Hungary (grant # TKP2021-NVA-02) is acknowledged.

**References**

Andrade, S. K. S.; Bakos, I.; Dobos, G.; Farkas, A.; Kiss, G.; Klébert, Sz.; Madarász, J.; László, K: Biomass related highly porous metal free carbon for gas storage and electrocatalytic applications. Materials, 2021, 14, 3488. DOI: 10.3390/ma14133488

Bandosz T.J.. Revealing the impact of small pores on oxygen reduction on carbon electrocatalysts: A journey through recent findings. Carbon, 2022, 188, 289-304. DOI: 10.1016/j.carbon.2021.11.071

Falco, G.; Florent, M.; Jagiello, J.; Cheng, Y; Daemen, L.L.; Ramirez-Cuesta, A-J.; Bandosz, T.J.: Alternative view of oxygen reduction on porous carbon electrocatalysts: The substance of complex oxygen-surface interactions. iScience, 2021, 24, 3, 102216. DOI: 10.1016/j.isci.2021.102216

Li, D.; Jia, Y.; Chang, G.; Chen, J.; Liu, H.; Wang, J.; Hu, Y.; Xia, Y.; Yang, D.; Yao, X. A defect-driven metal-free electrocatalyst for oxygen reduction in acidic electrolyte. Chem 2018, 4, 2345–2356.
Michel, A.-S.; Mestdagh, M.M.; Axelos, M.A.V. Physico-chemical properties of carrageenan gels in presence of various cations. Int. J. Biol. Macromol. 1997, 21, 195–500.
Voitko, K.; Tóth, A.; Demianenko, E.; Dobos, G.; Berke, B.; Bakalinska, O.; Grebenyuk, A.; Tombácz, E.; Kuts, V.; Tarasenko, Y.; et al. Catalytic performance of carbon nanotubes in H2O2 decomposition: Experimental and quantum chemical study. J. Colloid Interface Sci. 2015, 437, 283–290.

Carbon 2022

# Aging of Concentrated Aqueous Graphene Oxide Suspension

**Krisztina László[1], Benjámin Gyarmati[1], Shereen Farah[1], Attila Farkas[2] and Miklós Mohai[3]**

[1]Department of Physical Chemistry and Materials Science, Budapest University of Technology and Economics , Hungary

Email: laszlo.krisztina@vbk.bme.hu

[2]Department of Organic Chemistry and Technology, Budapest University of Technology and Economics , Hungary

[3]Eötvös Loránt Research Network ,Research Centre for Natural Sciences, , Budapest, Hungary

**Keywords**
rheology; Raman spectroscopy; XPS

## INTRODUCTION

Graphene oxide (GO) has been widely used as a precursor to prepare chemically converted graphene, but recently, it has gained its own recognition, as its application is continuously increasing. Much of the processing of GO based devices occurs in dispersed form, which explains the commercialization of its suspensions. Aging of these suspensions can, however, affect the shelf life and thus their application potential. Here in we investigate 10 mg/mL aqueous GO suspensions over a two-year time scale. To reveal the change of microstructure of GO suspensions, the rheological behavior of the suspensions was followed in oscillatory and transient shear measurements. The dynamic moduli and the viscosity increased with age, particularly within the first year. Raman spectroscopic results reveal that the change in the rheological behaviors with age results from a slow oxidation process occurring in the highly acidic aqueous medium during the relatively long-term storage. The (over)oxidized layers may peel off spontaneously or with high shear stress, resulting in enhancement of the viscosity (Gyarmati et al, 2022).

## MATERIALS AND METHODS

Graphene oxide (GO) was obtained from natural graphite following an “improved” Hummers’ method (Hummers, 1958; Marcano, 2010). Three 10 mg/mL of aqueous GO suspensions were produced with 1 year time gap and stored in sealed amber bottles at 25 °C, avoiding agitation. Samples are distinguished as 0 y, 1 y and 2 y. Rheological studies were performed using 25 mm-diameter parallel plate geometry with a measuring gap of 300 µm and at 25 ± 0.01 °C. Raman spectra of the GO suspensions were evaluated in the range of 800-3000 $cm^{-1}$.

## RESULTS AND DISCUSSION

GO in liquid media develops a microstructure (isotropic fluid, glass, gel and liquid-crystalline states) influenced also by the concentration of GO. In our system GO concentration is above the percolation threshold, i.e., where the sheets start to touch each other. The microstructure of a concentrated suspension may evolve over time, therefore, various rheological methods were applied to follow the change in this microstructure. This paper discusses the results of the oscillatory and transient measurements. The former method gives information about the storage modulus (G' represents the elastic response of the material), and the loss modulus (G'' describes the viscous character). While transient ones are related to the recovery of the material. We found that the long-term storage of the aqueous GO suspensions strengthens the 3D structure and a possibly alters the GO flakes.

To reveal the potential changes of the platelets themselves during long-term storage, the three batches were also studied by Raman spectroscopy. The first order region of the spectra of all GO samples contains the D (defect band) and G bands (vibrations of the $sp^2$ building blocks) beside the D' (disordered graphitic lattices) and the D'' (amorphous phases) bands. Whereas the second order

region consists of the 2D (structural order) and the combined G* band. The intensity *I* ratio of the D and G bands is widely used to follow the defects while that for the 2D and G bands is related to the number of layers. The systematic increase of the intensity ratios $I_D/I_G$ and the $I_{2D}/I_G$ implies an increase of the defects and decrease of the number of layers, respectively. This suggests a slow oxidation process of the most upper GO layers making them more vulnerable to be peeled off. During the long-term storage, the dissolved oxygen present in the intrinsically acidic medium can act as oxidizing agent, as corroborated by X-ray photoelectron spectroscopy (XPS). The shearing off was confirmed by powder XRD.

**CONCLUSIONS**

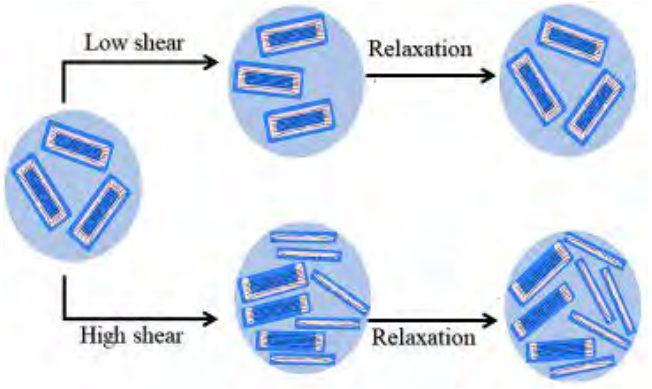


**FIGURE 1** Proposed mechanism of the microstructural changes

The rheological measurements of the aged samples suggests a microstructural change. A very fast relaxation was confirmed by the plateau viscosity, that was reached within a short time. At low shear rates (≤100 $s^{-1}$) (Figure 1, upper panel), the structure can be recovered. An irreversible increase of the viscosity was observed at high shear rates (≥1000 $s^{-1}$) (Figure 1, lower panel) that suggest a microstructural change that is related to a process in which the highly oxidized external GO sheets are peeled off from the flakes. As a consequence new surfaces are born that adsorb water from the bulk phase, resulting in an increase in viscosity. The aged samples display a microstructural change, similar to that under high-shear load. The results of the complementary Raman spectroscopy indicate that the alteration in the rheological behavior is the result of a slow oxidation process that occurs in the highly acidic aqueous medium during long-term storage and leads to spontaneous peeling of the external sheets from the flakes. The oxidation process was confirmed XPS analysis.

**Acknowledgements**

We extend our warm thanks to Madarász, J. for the XRD analysis, and to Bosznai, G. for his invaluable technical assistance. This research was performed within the frame of the OTKA grant K 128410 and FK 138029 from the National Research, Development and Innovation Office (NRDI) and funded by the National Research, Development, and Innovation Fund of Hungary under Grants TKP2021-EGA-02. Financial support from VEKOP-2.3.2-16-2017-00013 is acknowledged. The VEKOP project is supported by the EU and by Hungary, co-financed by the European Regional Development Fund. The work is also part of the EU project NANOMED (H2020-MSCA-RISE-2016, #734641). S. Farah is grateful to the Stipendium Hungaricum scholarship program, the Ministry of Higher Education and Research Sudan as well as University of Khartoum, Sudan for their financial support.

**References**

Gyarmati B, Farah S, Farkas A, Sáfrán G, Voelker-Pop LM, László K. Long-Term Aging of Concentrated Aqueous Graphene Oxide Suspensions Seen by Rheology and Raman Spectroscopy. Nanomaterials. **2022**, 12, 916. doi: 10.3390/nano12060916

Hummers, W.S., Jr.; Offeman, R.E. Preparation of graphitic oxide. J. Am. Chem. Soc. **1958**, 80, 1339−1339. doi: 10.1021/ja01539a017

Marcano, D.C.; Kosynkin, D.V.; Berlin, J.M.; Sinitskii, A.; Sun, Z.; Slesarev, A.; Alemany, L.B.; Lu, W.; Tour, J.M. Improved synthesis of graphene oxide. ACS Nano **2010**, 4, 4806–4814. doi: 10.1021/nn1006368

# ENCAPSULATED IONIC LIQUIDS (ENIL) FOR $CO_2/CH_4$ SEPARATION USING FIXED BED COLUMNS

**J. Lemus, C. Paramio, D. Hospital-Benito, C. Moya, R. Santiago, A. Belinchón, E. Hernández, P. Navarro, J. Palomar**

*Departamento de Ingeniería Química/ Universidad Autónoma de Madrid/ 28049 Madrid*

**E-mail: jesus.lemus@uam.es*

***Key words:*** $CO_2$ capture, encapsulated ionic liquids, activated carbon, fixed bed columns.

## Introduction

Ionic liquids (ILs) are being investigated as solvents in $CO_2$ capture and there are a large number of ILs analyzed for this purpose [1]. An important factor in $CO_2$ capture with ILs is the kinetic one. ILs generally present a high viscosity compared to traditional organic solvents. Available data indicate that $CO_2$ absorption phenomena are mainly controlled by mass transfer, increasing in the case of chemical absorption, where the reaction products increase the viscosity of the medium. In this context, encapsulated ionic liquids (ENIL) [2], are presented, which consist of carbon microcapsules (particle diameter around 800 nm) with a porous shell and a hollow core filled with IL, in quantities even above 80 % by mass.

## Experimental procedure

In the present work, 6 ILs were used, and they were introduced into porous carbon capsules, which were prepared as in previous works of the group [3]. These absorbent materials were used in $CO_2$ capture. First, experiments were carried out with 2 grams of ENIL to treat a continuous stream through the fixed bed composed of a mixture of different concentrations of $CO_2/CH_4/N_2$, with a constant flow rate of 16 NmL/min, at 30ºC and 1 bar of total pressure. $CO_2$ solubility measurements ($W_{CO2}$, $mol_{CO2}/kg_{ENIL}$) were also obtained with the different ENIL in a high-pressure sorption gravimetric analyzer (ISOSORP GAS LP-flow, Rubotherm).

## Results

The thermodynamic (equilibrium) behavior of the 6 ENIL materials in $CO_2$ capture was tested by gravimetric measurements and fixed-bed experiments. The $CO_2$ chemical absorption isotherms were obtained for the ENIL materials from 0.03 to 1 bar $CO_2$ partial pressure at 30ºC (Figure 1). These comparisons allow us to validate both methodologies, with fixed-bed column results obtained up to 0.4 bar of $CO_2$ partial pressure and from 0.3 to 1 bar for gravimetric measurements. The capture of $CO_2$ in this operating range is due to the chemical capture of $CO_2$ by each IL. Analyzing the nature of the ILs, it can be verified that those based on acetate present the highest capture of $CO_2$, reaching a solubility of 1 mol/kg, followed by those based on cyanopyrrole anion (solubility in $CO_2$ of 0.6 mol/kg) and finally, the amino acid derivatives, which showed a $CO_2$ solubility of about 0.4 mol/kg at 1 bar $CO_2$ partial pressure.

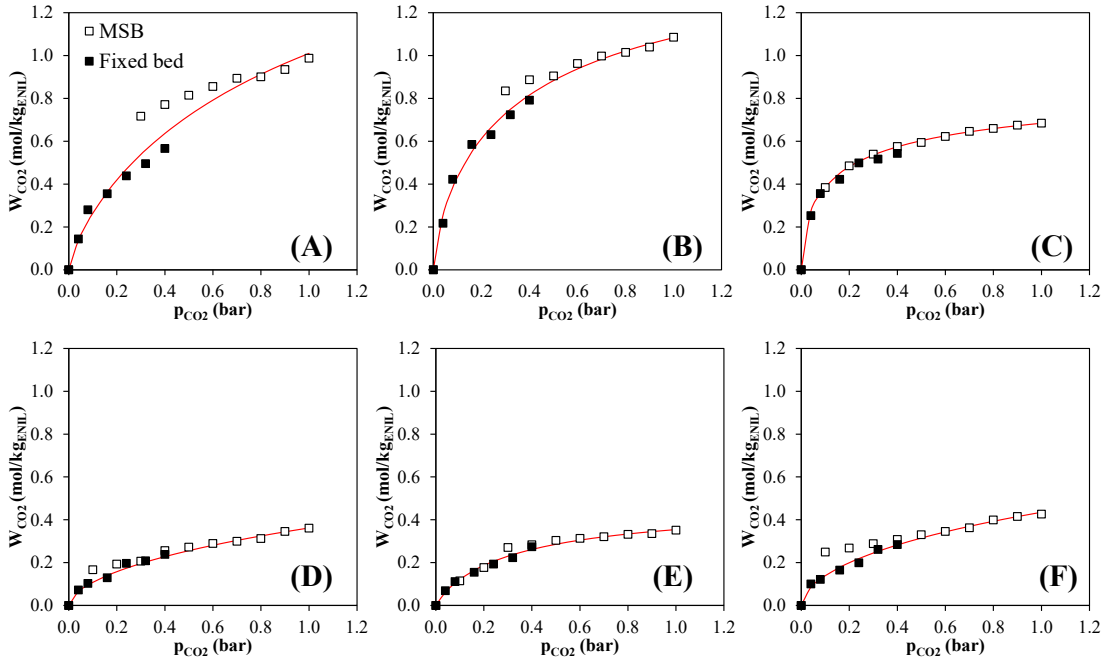


**Figure 1.** $CO_2$ isotherms of ENIL material with different ILs (A) [Emim][Acetate], (B) [Bmim][Acetate], (C) [$P_{66614}$][CNPyrr], (D) [Bmim][GLY], (E) [Bmim][MET], y (F) [Bmim][PRO] at 30ºC and different CO2 partial pressures. The points correspond to the experimental data (white squares obtained by MSB and black squares obtained in a fixed bed).

## Conclusions

In this work, 6 ENIL materials for the selective separation of $CO_2$ from $CO_2/CH_4/N_2$ streams were prepared and evaluated by gravimetric and fixed-bed measurements. First, 6 ENIL materials were prepared, with about 70% by weight of IL inside the capsules, to be used as absorbent material. All ENIL materials showed high $CO_2$ solubility and negligible $CH_4$ retention, with acetate anion-based ENIL materials showing higher $CO_2$ solubility. The experimental breakthrough curves were fitted to the Yoon and Nelson and LDF models. It was shown that the kinetics of the process is controlled by the thermodynamics of $CO_2$ capture, since ILs with lower solubility in $CO_2$ showed higher kinetic constants, but when normalizing this parameter, the results were similar.

**Acknowledgments:** The authors thank the Ministerio de Ciencia e Innovación (projects PID2020-118259RB-I00 and PDC2021-120881-I00) and the Comunidad de Madrid (project P2018/EMT4348) for the financial support and the Centro de Computación Científica de la Universidad Autónoma de Madrid for the computational facilities.

## References

[1] Palomar, J.; Larriba, M.; Lemus, J.; Moreno, D.; Santiago, R.; Moya, C.; de Riva, J.; Pedrosa, G., Demonstrating the key role of kinetics over thermodynamics in the selection of ionic liquids for CO2 physical absorption. Sep. Pur. Tech. 2019; 213:578-586.

[2] Palomar, J.; Lemus, J.; Alonso-Morales, N.; Bedia, J.; Gilarranz, M. A.; Rodriguez, J. J., Encapsulated ionic liquids (ENILs): from continuous to discrete liquid phase. Chem Commun. 2012; 48(80): 10046-10048.

[3] Lemus, J.; Da Silva F, F. A.; Palomar, J.; Carvalho, P. J.; Coutinho, J. A. P., Solubility of carbon dioxide in encapsulated ionic liquids. Sep. Pur. Tech. 2018; 196: 41-46.

20 C 22 arbon 2022

# 3D porous carbon structures using whey as a green precursor

**Raúl Llamas Unzueta*, Miguel A. Montes Morán, J. Angel Menéndez**
Instituto de Ciencia y Tecnología del Carbono (INCAR-CSIC) c/ Francisco Pintado Fe, 26, 33011 Oviedo
Email: r.llamas@incar.csic.es

**Keywords**
Porous carbons, additive manufacturing, whey.

## INTRODUCTION

The manufacturing of porous carbons has evolved significantly over the last decades. Nowadays, key parameters such as pore size distribution or surface chemistry of those materials can be controlled and adapted to the user requirements. However, despite these great improvements at the nanometric scale, the macroscopic design of these materials remains a challenge.

In recent years, additive manufacturing techniques have emerged changing the paradigm in material design and development. Most commonly used materials for these purposes are thermoplastic polymers, but metals and ceramics have been also manufactured with these techniques. However, regarding carbon precursors, thermal processes are often incompatible with shape stability, so precursors frequently need thermosetting binders or other additives to avoid shape collapse during the carbonisation or activation processes.

Whey is a by-product from the dairy industry. Currently, a large part of the total production of whey becomes a surplus, causing management problems and associated pollution episodes due to its high biological and chemical oxygen demand (BOD, COD). Whey contains mainly lactose and some remaining milk proteins, a mixture that behaves as a thermosetting resin when heated, thus preserving the original shape (aside from a similar shrinkage in the three dimensions) after carbonisation (Llamas-Unzueta et al. 2021a). The aim of this work is to show how whey powders and pastes can be easily used in common additive manufacturing techniques such as Direct Ink Writing (DIW) or Selective Laser Sintering (SLS) for producing 3D porous carbon pieces.

## EXPERIMENTAL

Different pieces were prepared from (i) whey powders and (ii) whey pastes with a solids content of 75wt%. These pieces were manufactured using 3 different techniques, namely conventional casting and SLS in the case of whey powders; and DIW in the case of whey pastes. The rheological properties of the paste were characterised by Small Amplitude Oscillatory tests (SAOS). The printed pieces were carbonised under $N_2$ at 850°C. The mineral matter was removed by washing the carbon pieces with HCl and HF. The carbon pieces were activated with $CO_2$ at 850°C. The porous structure of these materials was characterised using $N_2$ isotherms at -196°C and Hg intrusion. Compressive tests were also carried out to assess the mechanical resistance of the carbonised pieces.

## RESULTS AND DISCUSSION

SAOS tests of the whey paste show a shear-thinning behaviour and good viscoelastic properties for being extruded in any conventional DIW 3D printing device. In amplitude sweep tests, the paste show a yield stress of ca. 1100 Pa, and the dominant solid behaviour lasts up to 2400 Pa (crossover point). After 24h at room temperature, the pieces are dry, solid and easy to handle. In the case of

casting and SLS, the powder particles stick together (pseudo-sintering) around 150°C, resulting also into mechanically stable pieces. For every technique, whey acts as a thermosetting resin with no shape modification at high temperatures. This is attributed to the reaction between lactose and whey proteins (non-enzymatic glycation) favoured by temperatures below 200°C. This thermosetting behaviour allows the carbonisation and the obtention of 3D printed porous carbon pieces (Figure 1). During carbonisation, there is a linear shrinkage of 23±2% in the three dimensions. Both before and after carbonisation, the pieces are easy to machine. The carbon pieces are mainly macroporous with porosities around 60%. The compressive strength, exceeding 14 MPa, is excellent for such a porous material, and they have an elasticity modulus between 4 and 4.5 GPa. Whey carbons present a high ash content (15 wt%) mainly composed by K, P and Ca species. These salts induce an incipient in vitro bioactivity. This bioactivity, together with an adequate porosity, non-cytotoxic behaviour and excellent mechanical properties, places whey carbons as good candidates to be used in bone scaffolds (Llamas-Unzueta et al. 2021b). The mineral matter present in carbonised pieces can be reduced from a 15 wt% to <1 wt% by acid washing. A network of micro and mesopores results after that ash reduction, with washed 3D carbons having BET areas up to 500 $m^2/g$. These 3D carbons can be further activated with $CO_2$, obtaining activated pieces with BET areas of 1200 $m^2/g$. These 3D printed whey derived carbons are suitable for being used both in traditional applications for this type of material (filters, membranes) and in novel ones (manufacturing of bone scaffolds).

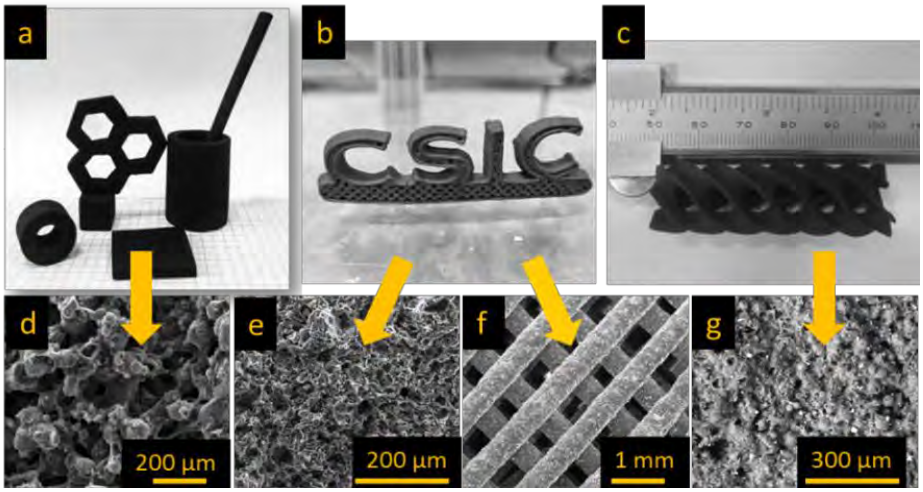


**FIGURE 1**: Macro and microscopic aspect of carbonised whey pieces obtained by casting (a, d), DIW (b, e, f) and SLS (c, g).

## CONCLUSIONS

Results presented in this work show the viability of whey as a precursor for porous carbons structures produced by casting and 3D printing techniques. The proper rheology of whey/water pastes and the pseudo-sintering behaviour of whey powder particles make DIW and SLS the most appropriate techniques for additive manufacturing of this material. The most significant advantage of whey carbons is their mechanical resistance, so it overcomes other similar materials such as porous ceramics or activated carbons. Designing porous carbons morphology may potentially result into application improvements, opening new possibilities for porous carbon materials, such as tissue engineering, out from their traditional applications.

**Acknowledgements**

The authors gratefully acknowledge the financial support received from the Ministerio de Ciencia e Innovación (MCIN/AEI/10.13039/501100011033) (Project PID2020-115334GB-I00) and Principado de Asturias (FICYT) -

European Union (FEDER) (Project PCTI-Asturias IDI/2021/000015). J. Angel Menéndez and Miguel Montes are members of the SusPlast PTI+ of the Spanish National Research Council (CSIC).

**References**

Llamas-Unzueta, R., Menéndez, J. A., Ramirez-Montoya, L. A., Vina, J., Argüelles, A., and Montes-Moran, M. A. (2021). 3-D structured porous carbons with virtually any shape from whey powders. *Carbon*, 175, 403-412. https://doi.org/10.1016/j.carbon.2021.01.021

Llamas-Unzueta, R., Suárez, M., Fernández, A., Díaz, R., Montes-Morán, M. A., & Menéndez, J. A. (2021). Whey-Derived Porous Carbon Scaffolds for Bone Tissue Engineering. *Biomedicines*, 9(9), 1091. https://doi.org/10.3390/biomedicines9091091

Carbon 2022

# Influence of Oxygen Surface Groups on Bacteria/Carbon Interaction in Microbial Electrochemical Fluidized-Bed Reactors

**María Llorente[1,2], Raúl Berenguer[3,]*, and Abraham Esteve-Núñez[1,2]**

[1] Chemical Engineering Department, Universidad de Alcalá, Alcalá de Henares, Spain
[2] IMDEA Agua, Parque Tecnológico de la Universidad de Alcalá, 28805, Alcalá de Henares, Spain
[1] Instituto Universitario de Materiales, Departamento de Química Física, Universidad de Alicante UA, Apartado 99, 03080-Alicante, Spain
*Email: raul.berenguer@ua.es

**Keywords**
electroactive microorganism, surface chemistry, fluidized-bed reactors

## INTRODUCTION

The use of conductive carbon materials to speed up the extracellular electron transfer (EET) in certain bacteria, so-called electroactive, is essential for microbial electrochemical technologies (METs). We reported a new concept in bacteria-electrode interaction based on glassy carbon-supported electroactive planktonic (individual) living cells, that enabled the practical application of Microbial Electrochemical Fluidized Bed Reactors (ME-FBR), e.g. in wastewater treatment (Tejedor-Sanz, 2017). To now, the role of carbon properties involved in this interaction is unknown. This work studies the influence of oxygen surface groups in the interaction and electron transfer between two different carbon materials and Geobacter cells, and their effect on ME-FBR performance.

## EXPERIMENTAL

Commercial glassy carbon (GC) particles (0.63-1.00 mm) were oxidized under different conditions, namely, boiling 65% $HNO_3$ for different times or saturated $(NH_4)_2S_2O_8$ in 1 M $H_2SO_4$ for 24 h. For comparison purposes, commercial activated carbon (AC) particles (1.00-1.20 mm) were oxidized with the same procedures. The original and oxidized materials were characterized by XPS, TPD, gas adsorption, Raman, SEM and cyclic voltammetry. Next, the materials were tested as fluidized-bed electrodes (20 mL), polarized at +0.2 V (Ag/AgCl/Cl-(sat.)), in an anoxic culture medium of electroactive Geobacter Sulfurreducens growing on acetate (20 mM) as sole electron donor and carbon source. The tubular reactor (150 mL) was operated under batch and continuous mode, and a platinized titanium and graphite rod were used as counter electrode and current collector of carbon particles (working electrode), respectively (Fig. 1A). Electrical current production and acetate concentration were monitored with time to calculate the coulombic efficiency and biodegradation rate, respectively. Moreover, the microbial protein concentration and the optical density at 600 nm of the reactor medium were followed. The materials and supported bacteria were also analysed by cyclic voltammetry, SEM, and confocal microscopy before and after different times of the studied electrogenic treatments.

## RESULTS

As observed in Table 1, the AC presents a microporous structure with a high specific surface area and relatively large oxygen content, while the GC shows no microporosity and a considerably lower O content. The oxidation treatment significantly increases the surface O wt% on both materials, but it causes almost no effects on their surface morphology (from SEM) and GC microstructure (from

Raman). However, the severe oxidation of AC significantly reduces its microporosity (Table 1) and induces in some microstructural defects (from Raman).

**TABLE 1**: Textural properties and surface chemical composition of the different carbonaceous materials.

| | $N_2$ Adsorption-desorption (-196 ºC) | | | | $CO_2$ Adsorption (0 ºC) | | XPS | |
|---|---|---|---|---|---|---|---|---|
| Sample | $A_{BET}$ ($m^2/g$) | $V_{0.995}$ ($cm^3/g$) | $V_{DR}(N_2)$ ($cm^3/g$) | Vmes ($cm^3/g$) | $A_{DR}(CO_2)$ ($m^2/g$) | $V_{DR}(CO_2)$ ($cm^3/g$) | C (wt.%) | O (wt.%) |
| GC | ~1 | 0.003 | 0.001 | 0.002 | -- | --- | 95.7 | 4.3 |
| GC-ox | ~1 | 0.001 | 0.000 | 0.001 | --- | --- | 92.9 | 7.1 |
| AC | 1112 | 311 | 0.437 | 0.042 | 1068 | 0.460 | 87.8 | 12.2 |
| AC-ox | 828 | 246 | 0.314 | 0.065 | 835 | 0.360 | 65.9 | 33.7 |

Figure 1B shows that, in the presence of Geobacter (inoculated), the functionalized GC exhibits superior voltammetric response than the pristine one, demonstrating that the introduced surface oxygen groups promote e-transfer with Geobacter. This enhanced activity results in enhanced current production and acetate biodegradation rate (figures not shown). Interestingly, SEM and confocal laser SEM reveal a change from planktonic- to biofilm-like bacteria-electrode interaction on glassy carbon after functionalization. The maintained current production observed only for the functionalized GC working under continuous regime, which minimizes planktonic bacteria in the medium, strongly supports the occurrence of this new interaction.

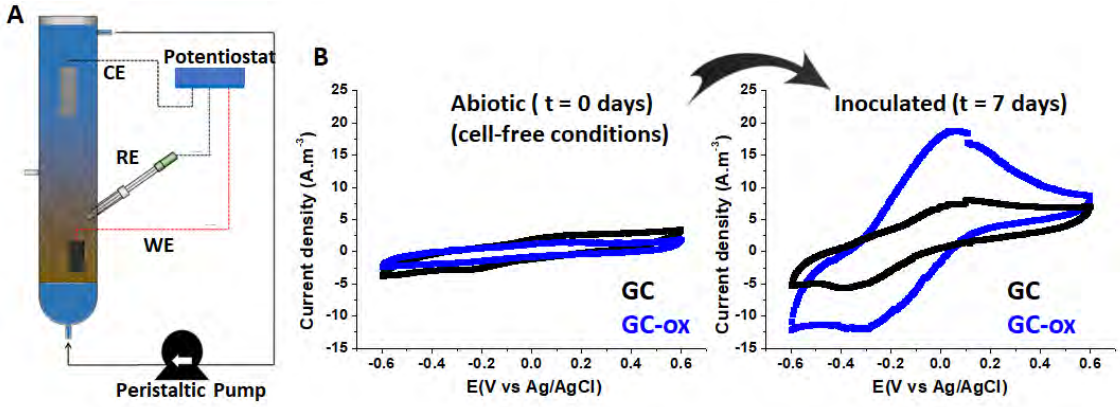


**FIGURE 1**: (A) Scheme of the experimental set-up of the ME-FBR reactor; (B) voltammetric response of the fluidized anodes before and after polarization at +0.4 V and 7 days of inoculation (v = 5 mV/s).

## CONCLUSIONS

We demonstrate that the controlled oxidation of the GC promotes e-transfer with Geobacter, but the strong effects caused on the AC properties seem to restrict it. The found results demonstrate that carbon properties remarkably affect their interaction with electroactive bacteria. The functionalization of carbon materials seems to be a promising strategy to improve the performance of Microbial Electrochemical Fluidized Bed Reactors (ME-FBR).

**Acknowledgements**

The authors thank MINECO and FEDER funds (Ramon y Cajal contract (RYC-2017-23618) and MET-FLUID project (RTI2018-101974-B-C-21)) for financial support.

**References**

Tejedor-Sanz, S., Quejigo, J. R., Berná, A., Esteve-Núñez, A. (2017). The Planktonic Relationship. Between Fluid-Like Electrodes and Bacteria: Wiring in Motion. ChemSusChem 10, 693-700.

Carbon 2022

# Nanotubes from Atlantis

**Sharali Malik**
Karlsruhe Institute of Technology (KIT), Institute of Quantum Materials and Technology (IQMT), Hermann von Helmholtz Platz 1, D-76131 Karlsruhe, Germany.
Email: sharali.malik@kit.edu

**Keywords**
Branched Carbon Nanotubes, Nanocomposites, Carbon Nanostructures, COST Action CA19118 EsSENce.

**ABSTRACT**
Nanosized carbon materials such as Carbon nanotubes (CNTs) provide the possibility to achieve, in terms of tensile strength and Young's modulus, incredibly strong materials. Therefore, the fabrication of nanocomposites with CNTs offers the potential for applications in electronics, medicine, defence and aerospace. Furthermore, it has been shown that having branched CNT structures is a promising way forward in terms of providing structures with enhanced mechanical properties. However, in order to realize this, mass production techniques at reasonable costs are needed. One possibility is the chemical vapour deposition (CVD) method which involves the decomposition of a hydrocarbon e.g. benzene, ethylene, methane, etc. over catalytically active metal deposited on or inside a support such as silica, alumina or titania. Here we report a simple and industrially scalable CVD process to manufacture long single-walled carbon nanotubes (SWNTs), branched multi-walled carbon nanotubes (b-MWNTs) and multi-walled carbon nanotubes (MWNTs) using the abundant pumice from the Akrotiri volcanoes on the Greek island of Santorini (Figure 1) to catalyse the transformation of the carbon in methane ($CH_4$) into CNT materials (Malik, 2018).

**FIGURE 1**: View into the caldera of the Greek island of Santorini (pic. S. Malik)

## INTRODUCTION

Santorini is the site of one of the largest volcanic eruptions in recent prehistory, the Minoan eruption, which occurred about 3,500 years ago. In the 1860s, excavation for volcanic ash and pumice as building materials for the Suez Canal project in Egypt uncovered the Minoan settlement of Akrotiri on Santorini which is claimed to resemble Plato's description of the legendary lost city of Atlantis (Plato, 360BC).

Composites of nanotubes and, e.g. an organic polymer matrix should be stronger, lighter, have increased tensile strength compared to conventional composites and according to Ajayan and Tour, "are on the cusp of commercial exploitation as the multifunctional component of the next generation of composite materials". This means that seemingly futuristic sounding ideas such as a "Space Elevator" may become possible (Clarke, 1979). This elevator could be used to transport materials from Earth to space more cheaply than by rocket. For this a 35,000 kilometer cable from the Earth's surface to a platform in geosynchronous orbit is required and carbon nanotube composites have all the hallmarks of being made of "the right stuff". However, significant challenges to overcome are the cost of production and poor CNT-polymer matrix adhesion. In fibre reinforced composites, mechanical properties such as tensile strength and elastic modulus depend on fibre pull-out energy which is influenced by fibre-length distribution, fibre-orientation distribution and interfacial stress transfer properties. In CNT-polymer composites, the adhesion between CNTs and the polymer matrix controls how effective the reinforcement can be and is thus the critical factor in the ultimate performance of the composite. A drawback is that the atomically smooth surfaces of CNTs results in poor matrix adhesion. Ideally, the CNTs need to be long, aligned and well dispersed in the matrix. These challenges can be overcome if branched CNTs are used since these have been shown to have high fibre pull-out energy which means that they are potentially are ideal matrix reinforcement material.

## CONCLUSIONS

Although many CNT-polymer applications currently use CVD-MWNTs more cost-effective ways to achieve this are always desirable. Thus, the b-MWNTs described here have the potential to be ideal reinforcement materials for composites as they could be manufactured simply and cheaply.

At the time of writing, only about 30% of the Akrotiri sites had been excavated by archeologists. It is fascinating to think that the volcanic material removed could be used in the process to fabricate fibres which could be used in the Space Elevator project. Thus not only will "Atlantis" be rising from the waves but reaching for the stars.

**Acknowledgements**

S.M. acknowledges support by the Helmholtz Association via the Helmholtz Program - Natural, Artificial and Cognitive Information Processing (NACIP), http://www.nacip.kit.edu

**References**

Clarke, A. C. (1979). The Fountains of Paradise. Victor Gollancz (UK), Harcourt Brace Jovanovich (US). ISBN 0-575-02520-4

Malik, S. (2018). Nanotubes from Atlantis: Magnetite in pumice as a catalyst for the growth of carbon nanotubes. *Polyhedron*, 152, 90-93. https://doi.org/10.1016/j.poly.2018.06.033

Plato (360 BC). Timeaus and Critias. http://classics.mit.edu/Plato/timaeus.html

20 C 22 arbon 2022

# Carbon Nanotubes Functionalized with Phosphate Ligands for Effective Grafting of Iron Phthalocyanines as Electrocatalysts for Oxygen Reduction Reaction

**B. Martínez-Sánchez[1], D. Cazorla-Amorós[2] and E. Morallón[1]**
[1]Departamento de Química Física and Instituto Universitario de Materiales de Alicante (IUMA), University of Alicante, Ap. 99, 03080, Alicante, Spain
[2]Departamento de Química Inorgánica and Instituto Universitario de Materiales de Alicante (IUMA), University of Alicante, Ap. 99, 03080, Alicante, Spain
Email: beatriz.ms@ua.es

**Keywords**
Iron Phthalocyanine; Oxygen Reduction Reaction; Phosphate Axial Ligand

## INTRODUCTION

The oxygen reduction reaction (ORR) is of great relevance in many renewable and energy-saving technologies, such as fuel cells (Zion et al., 2018). To solve the sluggish nature of the ORR kinetics, it is necessary to design more efficient alternatives to the state-of-the-art electrocatalysts based on precious metals. On this search, iron phthalocyanines (FePc) supported on nanostructured carbon materials have emerged as extraordinary electrocatalysts (Zagal and Koper, 2016). Particularly, carbon nanotubes (CNTs) have placed into the focus of recent studies for the immobilization of catalysts because of their fast electron delivery to the ORR active sites and their intrinsic properties (Nakashima and Fujigaya, 2019). The catalytic activity, selectivity and long-term stability of FePc can be positively modulated by strong interactions with the carbon support. One promising strategy consists of the incorporation of coordination sites to anchor metals by a functional polymer wrapping on the CNTs. In this work, we present the synthesis of composite materials based on non-pyrolyzed FePc immobilized on modified CNTs with a low content of metal (~1 wt. % Fe). Two different structures of CNTs are studied as supports, Single-Walled Carbon Nanotubes (SWCNTs) and Herringbone Carbon Nanotubes (hCNTs). Phosphate species electrochemically incorporated on CNTs at the experimental conditions used (Martínez-Sánchez et al., 2022) have been employed as suitable axial ligands for FePc, that leads to improved activity, stability and selectivity towards the ORR.

## EXPERIMENTAL METHODOLOGY

The procedure for the electrochemical functionalization of CNTs with the *ortho*-aminophenylphosphonic acid (2APPA) has been scaled-up from our previous work (Martínez-Sánchez et al., 2022) by cyclic voltammetry (CV) procedure. The optimal upper potential limit conditions were employed to achieve the highest incorporation of N and P species on the CNTs, that is, at 1.2 V and 1.4 V with SWCNTs and hCNTs, respectively, resulting in SWCNT-f and hCNT-f samples, respectively. Iron phthalocyanines were supported onto the CNTs by using the incipient wetness impregnation method in order to obtain a nominal metal loading of 1 wt. %, resulting in FePc/SWCNT and FePc/hCNT samples. The same procedure was done onto CNT-f materials, thus resulting in FePc/SWCNT-f and FePc/hCNT-f samples. Different characterization techniques have been used to study physico-chemical, morphological and electrochemical properties of synthesized materials, including Fourier Transform Infrared (FTIR) spectroscopy, X-ray photoelectron spectroscopy (XPS), Raman spectroscopy, transmission and field emission scanning electron microscopy (TEM and FESEM, respectively) equipped with an EDX microanalysis system, as well as

cyclic voltammetry (CV). The electrocatalytic performance of the materials towards the ORR was studied in 0.1 M KOH $O_2$-saturated electrolyte by linear sweep voltammetry (LSV). The experimental results were also supported by Density Functional Theory (DFT) computational calculations.

## RESULTS AND DISCUSSION

### Physico-chemical and Morphological Characterization of FePc/CNT and FePc/CNT-f composites

SWCNTs and hCNTs were previously modified in a highly controlled way by electrochemical methods in the presence of 2APPA monomers, thus introducing oligomeric materials on the carbon support which contain neutral amine/amide and phosphate species. Then, both the unmodified and functionalized CNTs were decorated with FePc molecules via a facile wet impregnation method. The presence of Fe-containing species detected by XPS analysis corroborates the incorporation of FePc molecules on CNTs, where the mass percentage obtained is close to the nominal value (1 wt. % Fe). Experimental results reveal that the presence of such N and P-related functional moieties on carbon supports is conductive to strengthening the interaction between FePc and both types of CNTs. This is especially evident in Fe2p XPS spectra deconvolutions, which could validate the axial coordination between the central iron atom and ligands incorporated in the carbon support. Moreover, these interactions lead to a more homogeneous dispersion of FePc macrocycles, as observed by TEM and FESEM images, as well as by Raman experiments. This suggests an effective five-coordination system by binding with axial phosphate ligands, as corroborated later by computational calculations, together with the influence of N functionalities, which could boost the ORR performance.

### Electrochemical Studies

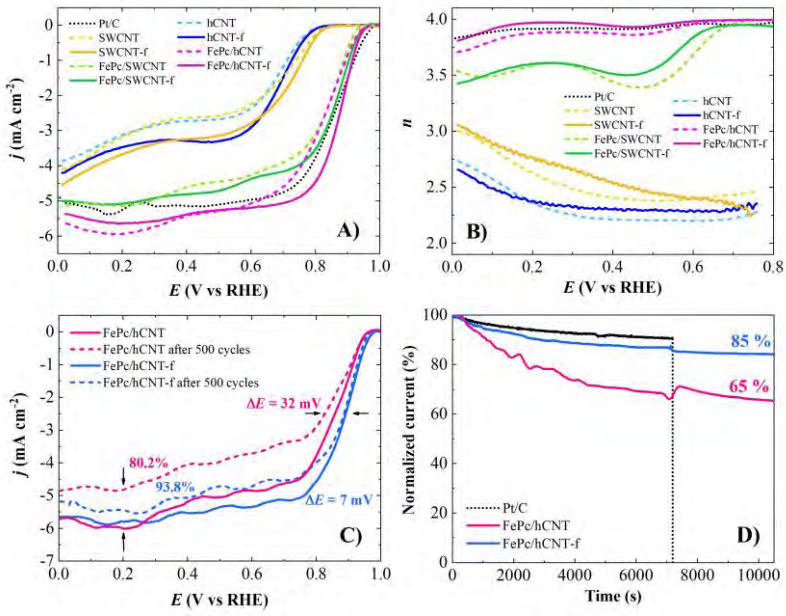


**FIGURE 1**: A) LSV for ORR at 5 mV $s^{-1}$, B) number of electrons transferred (*n*) per oxygen molecule during the ORR for Pt/C, SWCNT, SWCNT-f, FePc/SWCNT, FePc/SWCNT-f, hCNT, hCNT-f, FePc/hCNT and FePc/hCNT-f catalysts. C) LSV (at 5 mV $s^{-1}$) durability test of FePc/hCNT and FePc/hCNT-f before and after 500 cycles at 50 mV $s^{-1}$ and a rotation rate of 1600 rpm. D) Chronoamperometric curves (Normalized *j* vs. time) of FePc/hCNT, FePc/hCNT-f and Pt/C electrode at 0.65 V. All measurements were performed in $O_2$-saturated 0.1 M KOH solution and rotation rate of 1600 rpm (T=25ºC).

Firstly, cyclic voltammetry studies were carried out in $N_2$ and $O_2$-saturated 0.1 M KOH electrolyte as a preliminary step for the catalytic study towards the ORR. Next, RRDE experiments were employed to gain further insights into ORR performance of the as-prepared composites. FIGURE 1 (A and B) reveals that a clear improvement of the ORR performance is seen for all FePc/CNT catalysts with respect to the samples in the absence of FePc. Nevertheless, better results are observed for electrochemically functionalized carbon nanotubes supports in terms of half-wave potential ($E_{1/2}$), number of electrons transferred (*n*) and selectivity towards the most energy efficient four-electron process for the ORR in alkaline medium, which is induced by the synergistic effects between both components after the possible axial interactions. Therefore, promising catalytic results are shown even with low amount of iron in the samples, where $MN_4$ sites have been proven as the real active sites for the ORR. Interestingly, the support has a considerable influence on the catalytic results, where hCNTs combined with FePc have shown the best catalytic results in this case, possibly due to the presence of highly reactive sites in the support. Strong interactions also have a positive effect on the long-term stability of the active sites as seen in FIGURE 1 (C and D). In addition, FePc/hCNT and FePc/hCNT-f are practically insensitive to the presence of methanol in the electrolyte, whereas commercial Pt/C electrocatalyst is affected by a deactivation of the active sites towards the ORR.

**Computational Studies**

The interaction of FePc molecules with functionalized carbon nanotubes results in a strong interaction of the central iron atom and a phosphoryl oxygen. Interestingly, this structure seems to be more stable than that of FePc onto an unmodified CNT. Such strong interactions gave rise to a molecular reorganization by breaking the symmetry of electronic density that favors the oxygen reduction by stabilizing the catalytic centers and lowering the stability of ORR intermediates.

**CONCLUSIONS**

This work has explored the electrochemical modification of nanostructured carbon material supports with functional moieties, that can efficiently interact with FePc molecules, as an interesting approach for the improvement of the ORR electrocatalytic activity and stability in alkaline medium, where hCNTs combined with FePc have shown the best catalytic results. Therefore, the enhancement of the catalytic performance is mainly related to the synergistic catalysis of modified carbon supports and metallic complexes through the axial coordination between FePc and phosphate groups. This approach offers a new alternative for better ORR performance and inspires for designing new FePc-based materials with high electrocatalytic activity, selectivity, stability and methanol-tolerance, showing a competitive performance comparable to the commercial catalysts.

**Acknowledgements**

B.M.-S. thanks the Ministry of Universities of Spain for the FPU grant (FPU18/05127). The authors thank MCI/AEI and FEDER, UE (PID2019-105923RB-I00, RTI2018-095291-B-I00 projects) for the financial support.

**References**

Martínez-Sánchez, B., Quilez-Bermejo, J., San Fabián, E., Cazorla-Amorós, D., Morallon, E., 2022. On the mechanism of electrochemical functionalization of carbon nanotubes with different structures with aminophenylphosphonic acid isomers. An experimental and computational approach. J. Mater. Chem. A. https://doi.org/10.1039/D1TA10322A

Nakashima, N., Fujigaya, T., 2019. Carbon Nanotube-Based Fuel Cell Catalysts-Comparison with Carbon Black. pp. 1–28. https://doi.org/10.1007/978-3-319-92917-0_1

Zagal, J.H., Koper, M.T.M., 2016. Reactivity Descriptors for the Activity of Molecular MN4 Catalysts for the Oxygen Reduction Reaction. Angew. Chemie 128, 14726–14738. https://doi.org/10.1002/ange.201604311

Zion, N., Friedman, A., Levy, N., Elbaz, L., 2018. Bioinspired Electrocatalysis of Oxygen Reduction Reaction in Fuel Cells Using Molecular Catalysts. Adv. Mater. 30, 1800406. https://doi.org/10.1002/adma.201800406

Carbon 2022

# On the Mechanism of the Electrochemical Functionalization of Carbon Nanotubes with Aminophenylphosphonic Acid Isomers. An Experimental and Computational Approach.

**B. Martínez-Sánchez[1], J. Quílez-Bermejo[2], E. San-Fabián[1], D. Cazorla-Amorós[2] and E. Morallón[1]**
[1]Departamento de Química Física and Instituto Universitario de Materiales de Alicante (IUMA), University of Alicante, Ap. 99, 03080, Alicante, Spain
[2]Departamento de Química Inorgánica and Instituto Universitario de Materiales de Alicante (IUMA), University of Alicante, Ap. 99, 03080, Alicante, Spain
Email: beatriz.ms@ua.es

**Keywords**
Carbon Nanotubes; Electrochemical Functionalization; Mechanism

## INTRODUCTION

Carbon materials have played a crucial role in the development of nanotechnology over the last years. Among all the structures, carbon nanotubes (CNTs) arise as key materials due to their astonishing mechanical, physico-chemical and electronic properties, thermal stability, as well as large accessible surface area (Inagaki et al., 2014). Functionalization of CNTs is one of the most widespread procedures to modify their properties, driving towards more manageable multifunctional materials. Here, electrochemical methods are a well-suited tool for the tailorable design of functionalized CNTs with a precise control over the composition and functionalities (González-Gaitán et al., 2015). To understand the mechanism of the electrochemical modification of CNTs with organic aromatic molecules, it is important to predict the adsorption process on the surface of CNTs and the expected chemical structures. In the present work, we have faced this target through an experimental and theoretical approach, including electrochemical functionalization of CNTs with different structural arrangement, such as Single-Walled Carbon Nanotubes and Herringbone Carbon Nanotubes (SWCNTs and hCNTs, respectively), in the presence of phosphorus and nitrogen-containing monomers, 2- and 4-aminophenylphosphonic acid isomers (2APPA and 4APPA, respectively).

## EXPERIMENTAL METHODOLOGY

The electrochemical functionalization of SWCNTs and hCNTs was achieved by submitting the sample to anodic oxidation by cyclic voltammetry (CV) in acidic aqueous electrolyte in the presence of 2APPA or 4APPA isomer, as well as in the presence of aniline (ANI) for comparison purposes. Upper potential limit was varied in order to analyze its influence in the functionalization (1.0 V, 1.2 V, 1.4 V, 1.6 V and 1.8 V vs RHE). Different electrochemical, morphological and physico-chemical techniques were used to characterize the resulting samples. In order to deepen into the mechanism, the experimental results were supported by computational calculations, what allow us to get a theoretical view to shed light on important factors about the mechanism of functionalization.

## RESULTS AND DISCUSSION

The electrochemical functionalization of SWCNTs and hCNTs has been carried out in presence of aminophenylphosphonic acid isomers (2APPA or 4APPA), with an excellent level of control regarding the N and P species incorporated by carefully selecting the potential in the electrochemical oxidation conditions. FIGURE 1 shows the electrochemical characterization by CV of CNTs modified at 1.2 V

and 1.4 V with N and P species (2APPA and 4APPA in blue and red lines, respectively) in a monomer-free acidic electrolyte. Higher oxidation potentials lead to defects and film degradation due to the over-oxidation of the polymer structure. Electrochemical responses of unmodified CNTs (dashed lines), as well as those of CNTs modified with ANI (green lines) have also been displayed for comparison purposes. The development of electroactive species with N and P moieties onto CNTs surface is confirmed by the presence of several redox processes, different from the rectangular capacitive shape of non-electrochemically modified CNTs and from the responses of CNTs modified with ANI. Interestingly, low potential redox processes, at around 0.10 V and 0.31 V, seem to be related with phenazine-ring-type structures (Kellenberger et al., 2011), which suggests that 4APPA promotes this sort of branched chains; while the more similar voltammetric profiles of 2APPA and ANI suggest the development of more linear chains associated with short oligomers and derivatives (Kuznetsov et al., 2019). In addition, X-ray photoelectron spectroscopy (XPS) analysis determined a maximum heteroatom incorporation of *ca*. 2.3-2.6 at. % N and 1.4-1.6 at. % P when 2APPA is used with both carbon materials, as consequence of the linear polymeric growth. However, the polymeric product obtained with 4APPA is much more limited due to its branched structure.

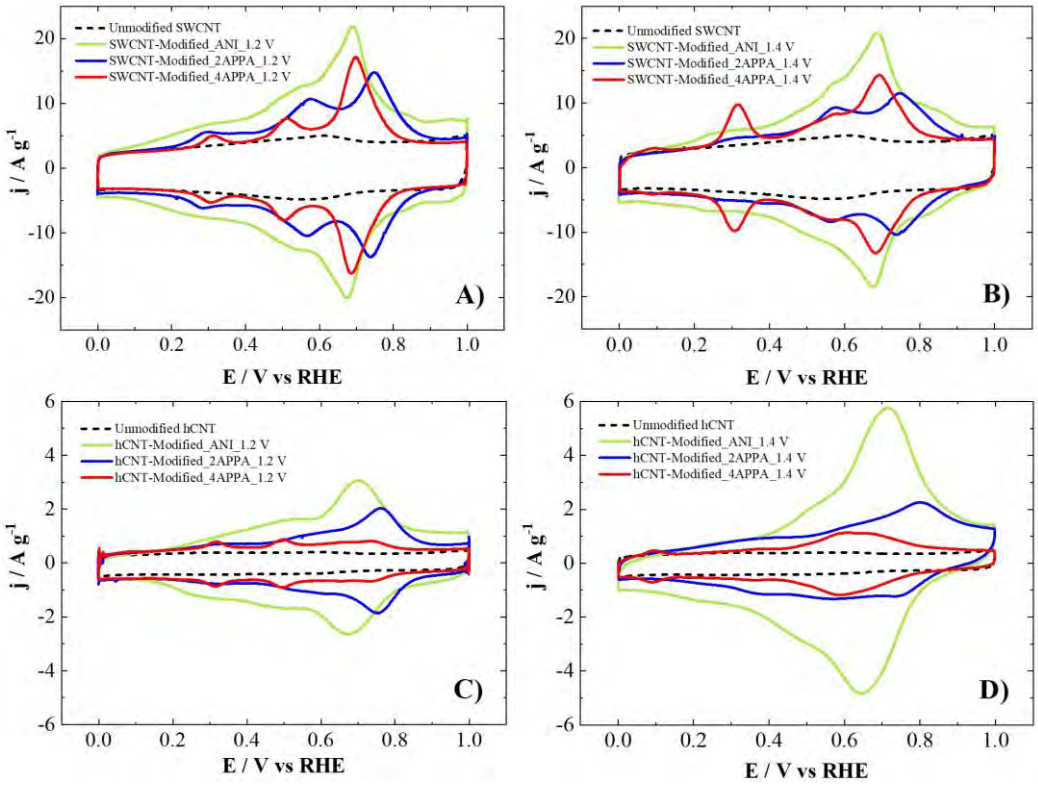


**FIGURE 1**: Cyclic voltammograms of A, B) SWCNT and C, D) hCNT unmodified (dashed lines) and electrochemically modified at A, C) 1.2 V and B, D) 1.4 V with 1 mM ANI (green lines), 1 mM 2APPA (blue lines) and 1 mM 4APPA (red lines), in acid medium (0.5 M $H_2SO_4$) free of monomers at 50 mV $s^{-1}$. $10^{th}$ cycle.

Interestingly, electrochemical characterization, XPS analysis, Raman spectroscopy and transmission electron microscopy (TEM) suggest that SWCNTs favor the correct adsorption of the monomers onto the CNTs wall through interaction with the π electrons of the walls, followed by the oligomeric growth, while hCNTs promote a covalent attachment of the monomers and short-chains formation according to their heterogeneity and higher reactivity, where a high functionalization level can be reached but the development of polymers is not favored. Local attachment of radicals could take place at the most reactive sites, giving rise to a heterogeneous distribution of functionalities with no apparent damage in the structure of CNTs, as seen in FIGURE 2.

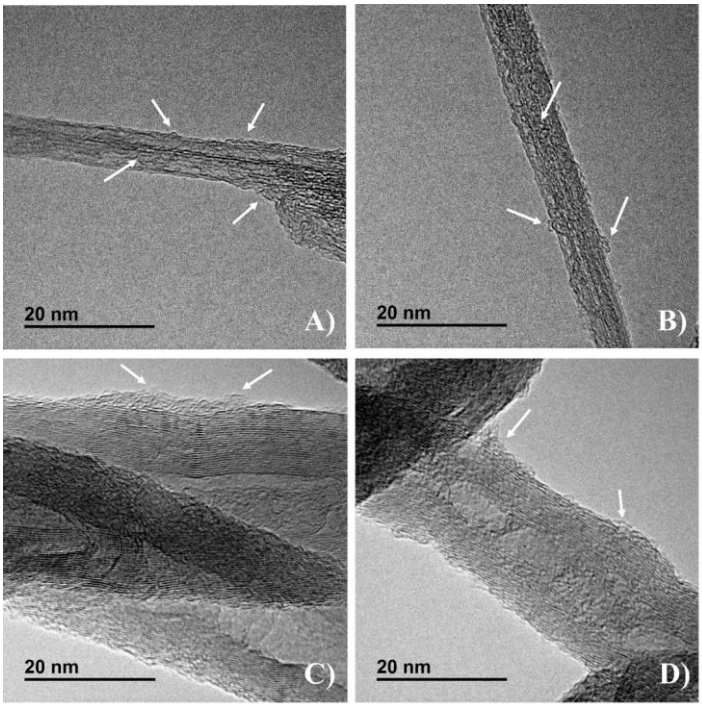


**FIGURE 2**: TEM images of A, B) SWCNT and C, D) hCNT electrochemically modified with A, C) 2APPA and B, D) 4APPA at 1.4 V (vs RHE). White arrows mark amorphous material associated with the oligomers.

Modelling results support these findings and help us to gain a deeper understanding of the functionalization mechanism of CNTs with different structures.

## CONCLUSIONS

Electrochemical functionalization of SWCNTs and hCNTs has been successfully performed with 2APPA and 4APPA. Modification of CNTs with 2APPA provides a higher presence of N and P heteroatoms under the optimal conditions (1.2 and 1.4 V vs RHE), which can be a promising methodology to develop electrocatalysts and electrocatalysts support for next-generation electrochemical energy devices. Computational calculations have confirmed the experimental results obtained, which allow us to shed more light on the mechanisms of the electrochemical functionalization of CNT with phosphorus and nitrogen-containing polymers.

**Acknowledgements**

B.M.-S. thanks the Ministry of Universities of Spain for the FPU grant (FPU18/05127). The authors thank MICINN and FEDER (projects PID2019-105923RB-I00 and RTI2018-095291-B-I00) for the financial support.

**References**

González-Gaitán, C., Ruiz-Rosas, R., Morallón, E., Cazorla-Amorós, D., 2015. Electrochemical Methods to Functionalize Carbon Materials, in: Thakur, V.K., Thakur, M.K. (Eds.), Chemical Functionalization of Carbon Nanomaterials: Chemistry and Applications. CRC Press, p. 32.

Inagaki, M., Kang, F., Toyoda, M., Konno, H., 2014. Advanced materials science and engineering of carbon. MRS Bull. https://doi.org/10.1557/mrs.2014.271

Kellenberger, A., Dmitrieva, E., Dunsch, L., 2011. The stabilization of charged states at phenazine-like units in polyaniline under p-doping: An in situ ATR-FTIR spectroelectrochemical study. Phys. Chem. Chem. Phys. 13, 3411–3420. https://doi.org/10.1039/c0cp01264e

Kuznetsov, A.N., Ayupov, A.B., Yeletsky, P.M., Lebedeva, M. V., 2019. Influence of monomer content on course of aniline polymerization in presence of high surface area carbon. J. Electroanal. Chem. 835, 73–80. https://doi.org/10.1016/j.jelechem.2018.12.057

Carbon 2022

# Electrically Enhanced Adsorption of Fluoride in Aqueous Solution Using Activated Carbon Electrodes Modified with La(III)

**D. Ricardo Martinez-Vargas[1], E. R. Larios-Durán[2], J. Rene Rangel-Mendez[1]*, Luis F. Chazaro-Ruiz[1]***
[1]División de Ciencias Ambientales del Instituto Potosino de Investigación Científica y Tecnológica, Camino a la Presa San José 2055, Col. Lomas 4a sección, San Luis Potosí, S.L.P, México.
[2] Departamento de Ingeniería Química. Universidad de Guadalajara, CUCEI, Guadalajara 44430, Jalisco, Mexico.
Email: luis.chazaro@ipicyt.edu.mx, rene@ipicyt.edu.mx,

**Keywords**
Fluoride electrosorption; lanthanum-activated carbon electrode; polarization profiles.

## INTRODUCTION

Chronic and excessive fluoride consumption has important implications for human health. the World Health Organization (Fawell, 2006) established a maximum concentration limit of 1.5 ppm in waters for human consumption. On the other hand, the USEPA's enforceable standard in public water supplies is 4.0 ppm, with a secondary maximum contaminant level of 2.0 mg/L in areas that have high levels of naturally occurring fluoride, while the Department of Health and Human Services recommends an optimal level of only 0.7 ppm. For this, several methods have been implemented to decrease its concentration of fluoride in drinking water to the previous limits, such as adsorption, coagulation, filtration, ion-exchange, electroflocculation, electrocoagulation, electrodialysis, among other processes. Electrosorption has been implemented in water for the selective removal of specific ions. La(III) has been widely implemented for the adsorption of hard bases, such as fluoride because it presents not only high affinity but high adsorption capacities and velocities towards this anion. In addition, La(III) presents low toxicity and bio accumulation, which depends on the dose, the uptake forms (free cation or ion pair, cluster or crystal size, etc.) and its physicochemical properties. Lanthanum has been previously immobilized on a commercial activated carbon for fluoride adsorption. In this work fluoride electrosorption was studied using activated carbon impregnated with three La(III) percentages: La-0.5%, La-1.5% and La-2.0% [1] to explore the influence of the amount of lanthanum on the electrosorption process.

## RESULTS AND DISCUSSION

The formed lanthanum clusters decreased the surface area, pore volume and electrical conductivity of the adsorbents as a function of increasing the lanthanum content in the matrices. The deprotonation of lanthanum hydroxyls at the working conditions increased the input of negative surface charges, reflected in the acidification and anodization of their points ($pH_{PZC} < 5$) and potentials ($E_{PZC} > 0.1$ V) of zero charge, respectively, compared to those of the pristine carbon ($pH_{PZC} = 8.5$ and $E_{PZC} = 0$ V). Electrosorption was evaluated by applying 0.8 V (*vs.* Ag/AgCl/3M NaCl) in two polarization profiles: (i) polarizing from the beginning and (ii) polarizing after the adsorption equilibrium. For La-0.5%, the same removal (~3 mg $g^{-1}$) was reached independently of the profile, although the first profile (i) promoted a faster rate. For La-1.5%, the second profile (ii) increased by 50% its removal (~9 mg $g^{-1}$), compared to the first (i) profile (~6 mg $g^{-1}$). This was interpreted as a difference in the available polarizable surface before and after fluoride adsorption, attributed to an electrical blockage due to the excess of negative charges from the La(III) clusters. In addition, La-1.5% presented a higher and faster charging by the second profile (ii), while the charging processes

of La-0.5% were very similar for both profiles. Then, the polarization profile could also increase the performance of electrodes that undergo synergistic changes in their surface charges. Table 1 presents the adsorption and electrosorption rates in mg $g^{-}$ $h^{-1}$, where the differences in kinetics were appreciated.

**TABLE 1**. Removal velocities by adsorption and electrosorption in mg $g^{-}$ $h^{-1}$ (M = 0.25 g, V = 0.5 L, $C_0$ = 20 ppm $F^{-}$, $pH_0$ = 7, rpm = 120-130, T = 25 °C).

| | Conventional adsorption | Electrosorption (0.8 V *vs.* Ag/AgCl/3 M NaCl) |
|---|---|---|
| GAC | 0.615 | 1.32 |
| La-0.5% | 2.863 | 4.714 |
| La-1.5% | 9.785 | 7.61 |
| La-2.0% | 17.169 | 8.928 |

Desorption by reversing the polarization to -0.5 V was attained. During the cyclic performance, La-0.5% released a small amount of La(III), and the surface of both carbons oxidized during their anodic polarization, corroborated by measurements of $pH_{PZC}$, the open circuit potentials and electrochemical impedance spectroscopy analysis (Martinez-Vargas, 2021 and 2022).

Selectivity was explored by evaluating kinetics against anions of environmental relevance (nitrate, chloride, phosphate, sulfate and arsenate) in equimolar concentrations and only for the carbons La-0.5% and La-1.5%. It was observed that nitrate and chloride were practically not competing with fluoride for the modified carbon La-0.5% and its fluoride removal was not affected by the presence of these anions. Nevertheless, the other anions decreased the fluoride removal for this same modified carbon to only 6.8, 4.8 and 4.2% in the presence of sulfate, phosphate, and arsenate, respectively. All these reported removals and the subsequent ones were computed at t = 60 minutes, unless stated different. On the other hand, the modified carbon La-1.5% presented a significant decrease in its fluoride removal by all competing anions in binary solutions ($F^{-}$ *vs.* anion), even in the presence of chloride and nitrate, which decreased its removal down to 13.9% and 17.3%. As with La-0.5%, the species with higher charge presented higher competition and decreased the most its removal down to 13.6%, 9.5% and 4% in the presence of sulfate, phosphate and arsenate, respectively. A similar effect was observed for the removal velocities.

## CONCLUSIONS

The addition of La(III) increased the number of sorption sites, increasing their adsorption capacity. Nevertheless, the electrical polarization of the modified electrodes promoted contrasting results. The electrical polarization of the modified activated carbons only benefited the carbon with the lowest La(III) content, increasing its removal capacity and kinetics, independently of the polarization profile. On the other hand, the other two carbons with higher La(III) content presented a similar or lower removal than that obtained by conventional adsorption (without polarizing the electrode). Even when La-1.5% presented a similar removal by conventional adsorption and electrosorption (polarized from the beginning), its polarization after the adsorption equilibrium promoted higher removal than by both processes individually. La-0.5% presented a mixture of adsorption (well-dispersed La(III) clusters) and electrosorption (electrically polarizable surface) sites for allocating the

studied anions at the studied conditions. The divalent anions presented higher competition towards fluoride, probably not only by electrostatic interactions, but also by chemisorption to La(III) clusters

**Acknowledgements**
The authors thank to CONACyT for the PhD scholarship [CVU No. 478185] and for the financial support (project CONACyT Atención a problemas nacionales, PDCPN-2015-789). We also appreciate the technical support of Ma. Carmen Rocha-Medina and Ma. Guadalupe Ortega Salazar from LANBAMA, and Elizabeth Isaacs Páez.

**References**

Fawell, J. K. (2006). World Health Organization., Fluoride in drinking-water. https://doi.org/10.1007/BF01783490. World Health Organization (2011), Guidelines for Drinking-Water Quality, in: Geneva. World Health Organization (Ed.), Fourth edi, 2011.

Martinez-Vargas, D. R., J. Rene Rangel-Mendez, J. R., Luis F. Chazaro-Ruiz, L., F. (2021). Correlation between physicochemical and electrochemical properties of an activated carbon doped with lanthanum for fluoride electrosorption,

*Separation and Purification Technology*, 268, 118702. https://doi.org/10.1016/j.seppur.2021.118702.

Martinez-Vargas, D. R., J. Rene Rangel-Mendez, J. R., Luis F. Chazaro-Ruiz, L., F. (2022). Fluoride electrosorption by hybrid La(III)-activated carbon electrodes under the influence of the La(III) content and the polarization profile,

*Journal of Environmental Chemical Engineering*, 10 [1], 106926. https://doi.org/10.1016/j.jece.2021.106926.

Carbon 2022

# Preparation of Solvent Component of Spinnable Mesophase Pitch Using Ethylene Bottom Oil as Raw Material

**Takashi Mashio[1], Taisei Tomaru[1], Hiroki Shimanoe[2], Koji Nakabayashi[1, 2], Jin Miyawaki[1, 2], Seong-Ho Yoon[1, 2]**

[1]Interdisciplinary Graduate School of Engineering Science, Kyushu University, Kasuga, Fukuoka 816-8580, Japan.

[2]Institute of Materials Chemistry and Engineering, Kyushu University, Kasuga, Fukuoka 816-8580, Japan.

E-mail: mashio.takashi.746@s.kyushu-u.ac.jp

**Keywords**
Spinnable mesophase pitch, lyotropic liquid crystalline solution, solvent component

## INTRODUCTION

Recently, we have proposed the following two new concepts regarding molecular species in spinnable mesophase pitch (SMP) (Shimanoe, 2022). (1) SMP exhibiting 100 vol% optical anisotropic contents is a lyotropic liquid crystalline solution which is composed of mesogen component showing 100 vol% optical anisotropy and solvent component showing 100 vol% optical isotropic. (2) The mesogen component consists of molecular stacking units of planar molecules having none or only one methyl side chain in the C (002) direction, and the solvent component has a function of dissolving and dispersing the mesogen stacking units. This previous study has clarified the role of the two components of SMP in the formation of anisotropic textures. However, the effect of the molecular species constituting each functional component of SMP has not been clarified in detail.

Therefore, we tried to understand the molecular properties of the mesogen component and the solvent component. In this study, we first focused on the solvent component. As a raw material of solvent components, ethylene bottom oil (EO) was used. To modify molecular structures of the solvent components, an addition of slurry oil (SO) or coal tar (CT) to EO was also tried. These prepared solvent components were mixed with the mesogen component (tetrahydrofuran insoluble component of AR pitch (AR-THFI)) to obtain various SMPs. Then, the influence of the solvent component pitch on properties of the prepared SMPs was evaluated.

## EXPERIMENTAL

1) Solvent fractionation of mesogen component (AR-THFI) and preparation of EO-derived solvent components

In this study, AR-THFI was fractionated at 50°C and used as a mesogen component. Hexane soluble component of EO (EO-HS) was used as the raw material for the solvent components. In addition, EO-HS with 30 wt% SO-HS added and EO-HS with 30 wt% CT added were also used as raw materials. These raw materials were heat-treated at 390°C for 6 h under autogenous

**TABLE 1:** Properties of prepared EO-derived solvent components.

| Sample | Yield (wt%)[1] | H/C[2] | $H_{aro}/H_{ali}$[3] | $f_a$[4] | AMW[5] |
|---|---|---|---|---|---|
| AR-THFS | — | 0.73 | 1.0 | 0.61 | 400 |
| EOp | 14.1 | 0.70 | 1.2 | 0.71 | 408 |
| SO-EOp | 16.8 | 0.70 | 1.1 | 0.73 | 409 |
| CT-EOp | 22.6 | 0.68 | 1.7 | 0.80 | 475 |

[1] Final yield after heat treatment and TLE treatment.
[2] H/C obtained from elemental analysis.
[3] $H_{aro}/H_{ali}$ obtained from $^1$H-NMR. [4] $f_a$ : aromaticity obtained from $^{13}$C-NMR.
[5] AMW : Average molecular weight obtained from MALDI-TOF/MS.

pressure using an autoclave. Next, these samples were heat-treated at 300°C for 5 h under vacuum to remove low molecular weight species in the samples. Finally, the softening point of these samples was adjusted to 140°C by thin layer evaporation (TLE). The obtained solvent components are denoted as "EOp", "SO-EOp" and "CT-EOp", respectively.

2) Preparation of MP by mixing AR-THFI and EO-derived solvent components

AR-THFI and each prepared solvent components were mixed at a weight ratio of 7/3, 5/5 or 3/7. Then, the mixture was annealed at 370°C for 10 min in $N_2$ atmosphere with stirring.

3) Analysis of EO-derived solvent components and SMPs

The prepared EO-derived solvent components were investigated by elemental composition analysis, molecular weight measurement by MALDI-TOF/MS, and chemical structure analysis by $^{1}$H-NMR and $^{13}$C-NMR. In addition, SMPs were observed using a polarizing microscope, and the anisotropic content was calculated.

## RESULTS AND DISCUSSION

**TABLE 1** shows results of molecular characteristics of prepared EO-derived solvent components. The yield, carbon aromaticity ($f_a$) and average molecular weight (AMW) of SO-EOp and CT-EOp showed the higher values compared to those of EOp. From these results, it is understood that the addition of CT and SO to EO can increase the polycyclic structure of the prepared SO-EOp and CT-EOp. Especially, CT-EOp showed much higher values than the other two, suggesting that CT-EOp had well-developed polyaromatic condensed hydrocarbons with shorter alkyl side chains.

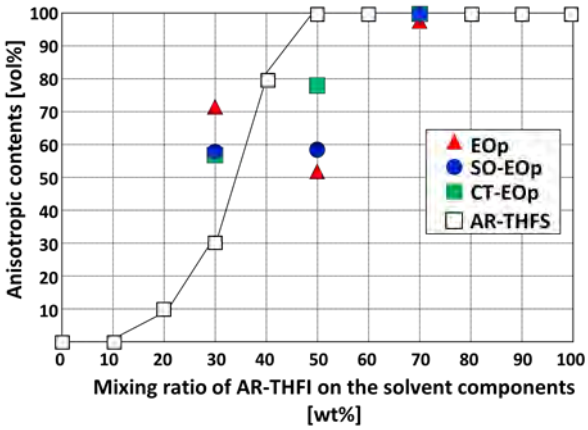


**FIGURE 1:** Changes of anisotropic contents of prepared SMPs by mixing ratio of AR-THFI/solvent component.

**FIGURE 1** shows the changes of anisotropic contents evaluated from the polarizing microscope images according to the mixing ratios of AR-THFI/solvent components. All EO-derived solvent components showed the higher threshold concentrations (TCs) for the revelation of full anisotropic contents of the obtained SMPs compared to AR-THFS as a solvent component, which meant that AR-THFS played better performance compared to EO-derived ones as a solvent and confirmed that the molecular similarity was the most important factor for solvent performance. EOp from EO-HS only needed higher TC compared to the others because it failed to express 100 vol% anisotropy even at the mixing ratio of AR-THFI/EOp = 7/3. The solvent performance of EO-derived solvent components were in the order of CT-EOp > SO-EOp > EOp at AR-THFI/EOp = 5/5, and EOp > SO-EOp ≥ CT-EOp at AR-THFI/EOp = 3/7.

## CONCLUSION

EO-derived solvent components (EOp, SO-EOp and CT-EOp) showed higher TCs compared to AR-THFS for expressing the 100 vol% anisotropic texture. The additions of CT and SO to EO enabled to decrease TCs. CT-EOp showed better solvent performance at the ratio of 5/5, but EOp did better at the ratio of 3/7. The exact cause of this phenomena is currently under investigation.

### Reference

H. Shimanoe, T. Mashio, H. Nakashima, S. Ko, Y.-P. Jeon, K. Nakabayashi, J. Miyawaki, S.-H. Yoon, (2022). Correlation between molecular stacking and anisotropic texture in spinnable mesophase pitch. *Carbon*, 192, 395-404. https://doi.org/10.1016/j.carbon.2022.02.062

Carbon 2022

# Effect of Heat Treatment Method on the Preparation of Solvent Component for the Spinnable Mesophase Pitch

**Takashi Mashio[1], Taisei Tomaru[1], Hiroki Shimanoe[2], Koji Nakabayashi[1, 2], Jin Miyawaki[1, 2], Seong-Ho Yoon[1, 2]**

[1]Interdisciplinary Graduate School of Engineering Science, Kyushu University, Kasuga, Fukuoka 816-8580, Japan.

[2]Institute of Materials Chemistry and Engineering, Kyushu University, Kasuga, Fukuoka 816-8580, Japan.

E-mail: mashio.takashi.746@s.kyushu-u.ac.jp

**Keywords**
Spinnable mesophase pitch, lyotropic liquid crystalline solution, heat treatment

## INTRODUCTION

Recently, we have founded that spinnable mesophase pitch (SMP) is a lyotropic liquid crystalline solution, which is composed of mesogen and solvent components (Shimanoe, 2022). Such a fact means that SMP usually contains about over 30 wt% of isotropic solvent component and whole melt properties of SMP depends on contents of mesogen and solvent components. However, the effect of the molecular species in raw materials of solvent component has not been elucidated in detail. Therefore, we tried to understand the molecular structural effects on SMP. In this study, we first focused on the molecular structure of solvent component on the revelation of anisotropic texture of SMP. A variety of solvent components were prepared using slurry oil (SO) as a raw material under various treatment conditions. For the exact evaluation of solvent components, we used the mesogen component of tetrahydrofuran-insoluble component of AR pitch (AR-THFI) through the solvent fractionation of a well-known SMP, AR pitch.

## EXPERIMENTAL

1) Extraction of mesogen component (AR-THFI) and preparation of SO-derived solvent components

AR-THFI, which is a mesogen component, was fractionated from AR pitch using THF at 50°C according to reference. The solvent components were prepared using THF-soluble fraction of SO (SO-THFS) as a raw material under various heat treatment conditions. Three types of heat treatments were performed on SO-THFS; atmospheric, vacuum, and pressurized conditions. The heat treatment temperature and time were “380°C for 3 h” and “410°C for 1 h”. After the heat treatment, the softening point of heat-treated samples was adjusted to 140°C by thin layer evaporation (TLE) to obtain the SO-derived solvent component (SOp). Hereinafter, SOp samples prepared by atmospheric pressure heat treatment, vacuum heat treatment, and pressurized heat treatment are denoted as "SO380", “SOHP380”, and “SOLP380”, respectively.

**TABLE 1:** Yield and properties of prepared SOp.

| Sample | Yield [wt%][1] | H/C[2] | $H_{aro}/H_{ali}$[3] | $f_a$[4] | AMW[5] |
|---|---|---|---|---|---|
| AR-THFS | — | 0.73 | 1.0 | 0.61 | 400 |
| SO380 | 17.7 | 0.70 | 0.98 | 0.69 | 415 |
| SOHP380 | 20.1 | 0.68 | 1.1 | 0.71 | 412 |
| SOLP380 | 14.8 | 0.70 | 0.97 | 0.69 | 385 |
| SO410 | 20.9 | 0.67 | 1.0 | 0.70 | 398 |
| SOHP410 | 15.1 | 0.69 | 1.00 | 0.71 | 413 |
| SOLP410 | 17.1 | 0.67 | 0.94 | 0.69 | 375 |

[1] Final yield after heat treatment and TLE treatment.
[2] H/C obtained from elemental analysis.
[3] $H_{aro}/H_{ali}$ obtained from $^1$H-NMR. [4] $f_a$ : aromaticity obtained from $^{13}$C-NMR.
[5] AMW : Average molecular weight obtained from MALDI-TOF/MS.

2) Preparation of mesophase pitch by mixing AR-THFI and SOp

AR-THFI and each prepared solvent component were mixed at a weight ratio of 7/3, 6/4, 5/5 or 3/7. Then, the mixture was annealed at 340°C for 30 min in $N_2$ atmosphere with stirring.

3) Analysis of SOp and mesophase pitches

The prepared SOp was examined by elemental composition analysis, molecular weight measurement by MALDI-TOF/MS, and chemical structure analysis by $^{1}$H-NMR and $^{13}$C-NMR. In addition, the AR-THFI/SOp mesophase pitches were observed using a polarizing microscope, and the anisotropic content was calculated.

## RESULTS AND DISCUSSION

**TABLE 1** summarizes the yield and the molecular characteristics of SOp as solvent components. Compared to AR-THFS, SOp was composed of more highly polycondensed molecules. The yields of SOp heat-treated at 380°C and 410°C were in the order of SOHP380 > SO380 > SOLP380 and SO410 > SOLP410 > SOHP410. Such results might suggest that the main reaction at 380°C was polymerization but at 410°C it was polycondensation after de-alkylation. The anisotropic contents calculated from the polarizing microscope images were plotted against the mixing ratio of AR-THFI and SOp (**FIGURE 1**). At first, compared to that of AR-THFS, the obtained SMPs mixed with various SOp showed higher threshold concentration (TC) of 70 wt% to express the entire anisotropic texture. Such results suggested that the AR-THFS could play better performance as a solvent component compared to SOp and also implied that the similarity of molecular structure was the most important factor as the solvent component. Among SOp-380s, SOHP380 showed a little better anisotropic content compared to the others. Compared to SOp-380s and SOp-410s, the largest difference was shown in the anisotropic contents of the obtained SMPs with AR-THFI/SOp = 3/7. The obtained SMPs by mixing with SOp-380s showed around 30 vol% of anisotropic textures, and they were very similar with SMP of AR-THFI/AR-THFS = 3/7. However, the obtained SMPs by mixing with SOp-410s showed much higher anisotropic contents of up to 50 vol% regardless of heat treatment methods. From these results, we can suggest that SOp-410s can play higher performances as a solvent for mesogen in lyotropic liquid crystalline system compared to SOp-380s. Nevertheless, we did not still clearly elucidate why the obtained SMPs with higher mesogen concentration did not show the differences in the anisotropy expression regardless of the different heat treatment methods of the solvent components. We dare to challenge continuously to understand the exact roles of solvent component in SMP.

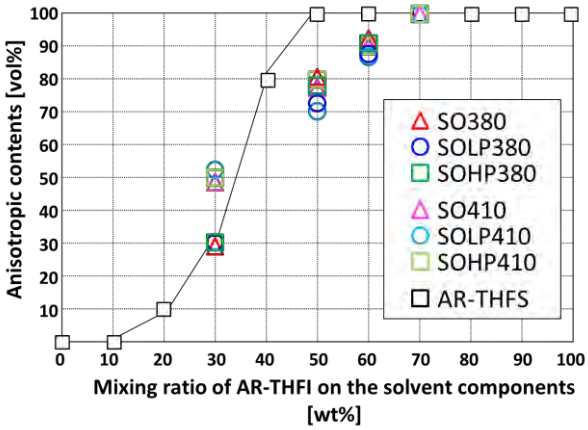


**FIGURE 1:** Changes of anisotropic contents of prepared mesophase pitches by mixing ratio of AR-THFI/SOp.

## CONCLUSION

We tried to prepare the solvent components of SMP using SO as a raw material. Compared to original solvent component of AR pitch, namely AR-THFS, SOp needed higher TC. Heat treatment method did not show a big difference in solvent property but SOp from higher heat treatment temperature at 410°C showed higher anisotropic contents in the mixing ratio of AR-THFI/SOp = 3/7.

**Reference**

H. Shimanoe, T. Mashio, H. Nakashima, S. Ko, Y.-P. Jeon, K. Nakabayashi, J. Miyawaki, S.-H. Yoon, (2022). Correlation between molecular stacking and anisotropic texture in spinnable mesophase pitch. *Carbon*, 192, 395-404. https://doi.org/10.1016/j.carbon.2022.02.062

Carbon 2022

# Ethylene conversion on carbon-supported NiMo catalysts: Pore confining effect and changes in selectivity during hydrotreatment reaction

**Juan Matos[1,*], Ana Arenillas[2], Po S. Poon[3]**
[1]Instituto de Ciencias Químicas Aplicadas, Facultad de Ingeniería, Universidad Autónoma de Chile, 8900000 Santiago, Chile.
[2] Instituto de Ciencia y Tecnología del Carbono (INCAR), CSIC, Oviedo, España.
[3] Unidad de Desarrollo Tecnológico (UDT), Universidad de Concepción, Chile.

*Corresponding author. Email: juan.matos@uautonoma.cl (J. Matos)

**Keywords**
Pore confining; NiMo catalysts; Ethylene conversion.

## INTRODUCTION

The design of industrial catalysts for superior performance in certain applications, and for the development of novel processes, requires a proper understanding of the catalyst surface structure and the various surface processes that may occur on the catalysts during reaction. Nanoporous carbons are being increasingly used as a support of Ni-based catalysts [1,2] because they have interesting features such as high surface areas with a controlled pore volume distribution, average pore size, and tailored surface chemistry. In this work, the influence of the physicochemical properties of a nanoporous carbon upon the catalytic activity and selectivity of NiMo-based catalysts on the conversion of ethylene was verified and compared against a mesopore carbon.

## EXPERIMENTAL

Pine bark (PB) was selected as carbon precursor for the synthesis of activated carbon (AC). PB was heated in a flow-continuous tubular reactor under $N_2$ flow (20 psi, 100 mL $min^{-1}$) up to 800°C and then physically activated at this temperature by 1 h by $CO_2$ flow (20 psi, 10 mL $min^{-1}$). Ni-, Mo-, and NiMo-based catalysts were prepared by wetness impregnation method of the AC [1] and denoted as Ni/AC, Mo/AC and NiMo/AC, respectively. Metal concentrations in solutions were estimated to produce 10 wt% $MoO_3$ in Mo/AC, 5 wt% NiO in Ni/AC, and ca. 10 wt% $MoO_3$ + 3 wt% NiO in the case of NiMo/AC catalysts. A carefully characterization of the materials including gas adsorption, scanning and transmission electron microscopy (SEM, TEM) and X-ray photoelectronic spectroscopy (XPS) was performed. Samples were submitted to *in situ* reducing pre-treatments under $H_2$ flow at 300°C for 10 min (mild reduction) and 500°C for 60 min (strong reduction) before activity tests. The hydrogenation of ethylene was carried out on carbon-supported Ni, Mo, and NiMo catalysts at 300°C. The results were interpreted in terms of the hydrogenating/hydrogenolytic activity, catalytic stability and coking of catalysts [2].

## RESULTS AND DISCUSSION

Table 1 shows a summary of the most relevant characteristics of catalysts as well as a summary of the kinetic parameters and activity/selectivity results. Activity and evolution of products (methane and ethane) as function of the final temperature of two reducing pre-treatments indicate that ultramicropores carbon-supported NiMo catalysts has much more tolerance to coke deposition and therefore they are less prone to suffer deactivations than catalysts based on micro-mesopores framework. The evolution of multiwall carbon nanotubes was correlated both with the activity and

changes in selectivity of the main products. The apparent rate constants and the initial rates of carbon formation were estimated as an attempt to provide a better understanding of the influence of chemical surface functionalities and of textural properties of carbons. A correlation was found between these kinetic parameters of coke formation and the catalytic behaviour of catalysts. The results indicate nanoporous carbon promotes higher activities over longer periods of operation, at least, for the hydrogenation of simple unsaturated hydrocarbons such as ethylene.

**Table 1.** Summary of textural properties and activity/selectivity trends of NiMo/AC catalysts. Values of textural properties are referred to raw and after reaction (post). Values of conversion and yields of $CH_4$ and $C_2H_6$ are referred to values observed at initial and steady-state conditions.

| Sample | $S_{BET}$ ($m^2\ g^{-1}$) [a] | $V_{tot}$ ($cm^3\ g^{-1}$) [b] | $V_{NLDFT}$ ($cm^3\ g^{-1}$) [c] | $V_{mic}$ ($cm^3\ g^{-1}$) [d] | $V_{meso}$ ($cm^3\ g^{-1}$) [e] | $C_{PT300}$ (%)[f] | $C_{PT500}$ (%)[f] | $Y_{CH4-300}$ (%)[g] | $Y_{CH4-500}$ (%)[g] | $Y_{C2H6-300}$ (%)[h] | $Y_{C2H6-500}$ (%)[h] |
|---|---|---|---|---|---|---|---|---|---|---|---|
| AC | 706 | 0.425 | 0.383 | 0.367 | 0.058 | 0 | 0 | 0 | 0 | 0 | 0 |
| Mo/AC | 544 | 0.467 | 0.428 | 0.293 | 0.174 | 26 | 25 | 0 | 0 | 0 | 0 |
| Ni/AC | 556 | 0.460 | 0.421 | 0.288 | 0.172 | 86 | 99 | 12 | 5 | 42 | 79 |
| NiMo/AC | 443 | 0.376 | 0.344 | 0.236 | 0.140 | 62 | 66 | 6 | 1 | 41 | 51 |

[a] BET specific surface area; [b] Total volume of pores estimated a $P/P_0$ = 0.99; [c] Pore volume estimated from non-local density functional theory; [d] Micropore volume estimated from Dubinin-Radushkevich model; [e] Mesopore volume estimated from $V_{tot}$ - $V_{mic}$; [f] Steady-state condition´s conversion of ethylene for the pretreatment of catalysts at 300°C and 500°C; [g] Steady-state condition´s yield of $CH_4$ for the pretreatment of catalysts at 300°C and 500°C; ; [g] Initial and steady-state condition´s yield of $C_2H_6$ for the pretreatment of catalysts at 300°C and 500°C.

## CONCLUSIONS

It can be suggested that textural properties of activated carbon led to different products during the catalytic conversion of ethylene in presence of $H_2$. The evolution of products can be assigned to the magnitude of the pore confining effect. This effect permits to suggest that Ni/AC and NiMo/AC catalysts does not suffer deactivation due to a high production of multiwalled carbon nanotubes permitting the diffusion of active Ni nanoparticles from the pore framework to a more exposed location in the catalysts.

**Acknowledgements**

J. Matos and P.S. Poon thanks the financial support of ANID-PIA/APOYO CCTE AFB170007; ANID-FONDECYT 1190591; ANID-FONDEF ID19I10003; and ANID-FONDEF ID15I20321 projects.

**References**

Matos, J; Laine, J. (2003). Ethylene conversion on activated carbon supported NiMo catalysts: Effect of the support. Applied Catalysis A: General 241, 25-38.

Matos, J; Arenillas, A; Poon, P. S. (2022). Pore confining effect and changes in selectivity during hydrotreatment reaction on NiMo-based catalysts: Texture vs. surface chemistry properties. Under Preparation..

Carbon 2022

# Pine tannin-derived biochars as supercapacitor electrodes

**Juan Matos[1,*], Sara Perez-Rodriguez[2,*], Oscar Pinto[3], Maria T. Izquierdo[2], Po S. Poon[4], Alain Celzard[2], Vanessa Fierro[2,*]**

[1]Instituto de Ciencias Químicas Aplicadas, Facultad de Ingeniería, Universidad Autónoma de Chile, 8900000 Santiago, Chile.

[2] Université de Lorraine, CNRS, IJL, F-88000, Epinal, France

[3] Departamento de Ingeniería Química, Facultad de Ingeniería, Universidad de Concepción, Barrio Universitario s/n, Chile.

[4] Unidad de Desarrollo Tecnológico (UDT), Universidad de Concepción, Concepción, Chile.

*Corresponding authors. Emails: juan.matos@uautonoma.cl (J. Matos); sara.perez-rodriguez@univ-lorraine.fr (S. Pérez-Rodríguez); Vanessa.Fierro@univ-lorraine.fr (V. Fierro).

**Keywords**
Pine bark; Tannin-derived biochar; Electrochemical capacitor.

## INTRODUCTION

In recent years, many efforts have been made to develop highly efficient electrochemical capacitors, also called supercapacitors (SCs). Several approaches have been proposed, such as the development of nanostructured carbon materials with a high surface area and hierarchical porosity to increase the specific capacitance and reduce the diffusion resistance thanks to a well-connected porosity, and thus obtain high-rate capabilities. The surface chemistry of porous carbons can be tailored by introducing heteroatoms (such as O, N or S) as a strategy to improve electrochemical performance through surface redox reactions. A further attempt to develop "greener" and more competitive SCs has been made by using widely available agricultural/wood waste as precursors of activated carbons. Similarly, pine tannins have also been proposed as low-cost, non-toxic, and renewable precursors for the synthesis of carbon materials (Sanchez-Sanchez *et al*., 2017). The objective of this work is to show that a biochar, which is a by-product of the pyrolysis of pine tannins for oil production, can be used as SC electrode after activation with KOH (Perez-Rodriguez, *et al*., 2021).

## EXPERIMENTAL

Activated carbons (ACs) were prepared from a pine Tannin-derived BioChar (TBC) by chemical activation with KOH at 650° C for 1h under $N_2$ flow (20 psi, 100 mL $min^{-1}$). Different weight ratios of KOH to biochar ($R = W_{KOH}/W_{biochar}$) from 0.3 to 3.6 were used. The corresponding samples were labelled as TBC-KR, and characterized by proximate and elemental analysis, gas adsorption/desorption, transmission electron microscopy (TEM), X-ray photoelectronic spectroscopy (XPS), and Raman spectroscopy. Electrochemical measurements were carried out with a Biologic VMP3 workstation using symmetrical two-electrode Swagelok-type cells. The electrodes (5 mm in diameter) were prepared from a paste containing the ground AC materials, polytetrafluoroethylene (PTFE) binder (60 wt.% suspension in water) and carbon black, in a weight ratio of 85:10:5. The total mass loading of the resultant electrodes was about 10.7 mg $cm^{-2}$ (ca. 9 mg $cm^{-2}$ of effective carbon material), which is comparable to commercial standards (ca. 10 mg $cm^{-2}$). The carbon electrodes were impregnated for one week in the electrolyte, an aqueous solution of 1M $H_2SO_4$. Cyclic voltammetry (CV) tests were carried out in the 0 - 0.9 V range at scan rates increasing from 5 to 100 mV $s^{-1}$. Further details have been reported elsewhere (Perez-Rodriguez, *et al*., 2021).

## RESULTS AND DISCUSSION

Table 1 shows a summary of the results obtained for TBC-K2.8 and TBC-K3.6 samples. The resulting ACs presented highly developed specific surface areas of up to 2457 $m^2 g^{-1}$, well-connected porosity, and high oxygen content, leading to enhanced electrochemical performance when used as supercapacitor electrodes in a 1 M $H_2SO_4$ aqueous electrolyte. Galvanostatic charge/discharge experiments evidenced that the best material achieved a maximum electrode capacitance of 232 F $g^{-1}$ (at 0.5 A $g^{-1}$) using commercial mass loadings (i.e., about 10 mg $cm^{-2}$). In addition, long cycling stability with 92 to 94% residual capacitance after 10,000 cycles at 5 A $g^{-1}$ was achieved. The Ragone plot (not shown here) demonstrated that the samples TBC-K2.8 and TBC-K3.6 exhibit the highest specific energies across the entire specific power range, confirming the improved storage performance of these materials (Perez-Rodriguez, et al., 2021). Their specific energies present a maximum of 5.4 and 6.7 W h $kg^{-1}$, respectively, at the specific power of ca. 110 W $kg^{-1}$ (0.5 A $g^{-1}$).

**Table 1.** Summary of tannin-derived carbon electrodes synthesized by pyrolysis and KOH activation for symmetrical supercapacitors in aqueous acid medium.

| Samples | Yield (%) [a] | $A_{BET}$ ($m^2 g^{-1}$) [b] | $C_{e,1}$ (F $g^{-1}$) [c] | $C_{e,2}$ (F $g^{-1}$) [c] | $C_{ret}$ (%) [d] |
|---|---|---|---|---|---|
| TBC-K2.8 | 26 | 2187 | 200 (0.5 A $g^{-1}$) | 120 (10 A $g^{-1}$) | 92 |
| TBC-K3.6 | 21 | 2457 | 232 (0.5 A $g^{-1}$) | 124 (10 A $g^{-1}$) | 94 |

[a] Final yield including the carbonization and the activation processes; [b] Specific areas determined by the BET method for comparison purposes. [c] Specific cell capacitances at the current density indicated in brackets. $C_{e,1}$ and $C_{e,2}$ are defined as the specific capacitances at the lowest and highest current density, respectively; [d] Capacitance retention after 10 000 cycles at 5 A $g^{-1}$.

## CONCLUSIONS

Microporous ACs with outstanding BET areas (up to ca. 2450 $m^2 g^{-1}$) were obtained by direct activation of pine tannin-derived biochar with KOH at 650 °C. Activation using KOH to biochar mass ratios of 2.8 and 3.6 led to a good compromise between high surface areas and adequate pore size distributions, resulting in a high electrochemical specific capacitance (up to 220-230 F $g^{-1}$ at 0.5 A $g^{-1}$). The materials presented long-term stability, retaining 92 and 94% of the initial energy storage after 10000 cycles at 5 A $g^{-1}$. Therefore, the upgrading of biochars derived from the pyrolysis of pine tannin as SCs electrodes has great potential for their commercial use as electrochemical energy storage devices.

**Acknowledgements**

J. Matos and P.S. Poon thanks the financial support of the Franco-Chilean network BIOCval2E (REDES-170004 project); ANID-PIA/APOYO CCTE AFB170007; ANID-FONDECYT 1190591; ANID-FONDEF ID19I10003; and ANID-FONDEF ID15I20321. This study was partly supported by the French PIA project ‘‘Lorraine Université d’Excellence”, reference ANR-15-IDEX-04-LUE and the TALiSMAN project funded by ERDF. O. Pinto thanks ANID – Subdirección de Capital Humano/Doctorado, # 2019/21190633.

**References**

Perez-Rodriguez, S., Pinto, O., Izquierdo, M. T., Segura, C., Poon, P. S., Celzard, A., Matos, J., Fierro, V. (2021). Upgrading of pine tannin biochars as electrochemical capacitor electrodes, J. Coll. Inter. Science 601, 863-876.

Sanchez-Sanchez, A., Izquierdo, M. T., Mathieu, S., González-Álvarez, J., Celzard, A., Fierro, V. (2017). Outstanding electrochemical performance of highly N- and O-doped carbons derived from pine tannin, Green Chem. 19, 2653–2665.

Carbon 2022

# Carbon-protective effect on Cu-based Catalysts for Solar driven Photocatalysis

**Juan Matos[1,*], Paula Muñoz-Flores[2], Po S. Poon[3], Conchi O. Ania[4,*]**
[1]Instituto de Ciencias Químicas Aplicadas, Facultad de Ingeniería, Universidad Autónoma de Chile, 8900000 Santiago, Chile.
[2] Faculty of Engineering, University of Concepcion, Concepcion, Chile
[3] Unidad de Desarrollo Tecnológico (UDT), Universidad de Concepción, Chile.
[4] CEMHTI, CNRS (UPR 3079), Université d'Orléans, 45071 Orléans, France

*Corresponding authors.
Emails: juan.matos@uautonoma.cl (J. Matos); conchi.ania@cnrs-orleans.fr (C.O. Ania)

**Keywords**
Carbon-protection; Cu-based catalysts; Solar-driven Photocatalysis.

## INTRODUCTION

Tartrazine -also known as yellow 5 (Y5)- is a synthetic azo dye used and accepted as a safe food additive in Europe and in US, frequently found in wastewaters derived from the food industry. Owing to some contradictory studies about its impact on health and its possible carcinogenic effects (Kapadia, 1998), the removal of Y5 from water courses has become an issue of concern. Heterogeneous photocatalysis is an effective solution for the degradation of azo dyes from wastewater, being $TiO_2$ the benchmark catalyst. However, $TiO_2$ presents important limitations such as a low surface area and limited absorptivity under solar irradiation (ca. 5–8%). This has triggered the interest for alternative semiconductors. Among them, Cu-based oxides have received much attention since copper is an abundant raw element. In this work we perform a comparative study of the catalytic performance of a C-containing Cu-based photocatalyst under artificial and natural solar light, in two photoreactor configurations.

## EXPERIMENTAL

The C-containing Cu-based photocatalyst was prepared by a two-step procedure using furfural as carbon source and copper (II) acetylacetonate as copper precursor (Muñoz-Flores, 2022a). The catalyst was labelled as Cu@C, and it was characterized by proximate and elemental analysis, gas adsorption, X-ray diffraction, and scanning and transmission electron microscopy. The performance of Cu@C catalyst for the degradation of Y5 dye was evaluated in at lab-scale in a batch slurry reactor under (artificial) simulated solar light. The optimized operating conditions (e.g., catalyst loading, dye initial concentration) were applied for the degradation at pilot scale using a compound parabolic collector (CPC) photoreactor (Muñoz-Flores, 2022b). The results under both configurations were compared using different kinetic models.

## RESULTS AND DISCUSSION

Initially, the stability of the copper photocatalyst towards the leaching of the metallic species was evaluated in dark and irradiation conditions. Data revealed that the incorporation of a carbon phase in the photocatalyst prevents the lixiviation of the Cu-species (Muñoz-Flores, 2022a). The prepared Cu@C catalyst is composed by ca. 20 wt.% of carbon and a nominal fraction of Cu of ca. 33 wt.%. XRD patterns showed Cu, CuO and $Cu_2O$ as the main crystalline phases; these are also considered the

photoactive sites of the Cu@C sample, based on the optical characterisation (e.g., a well-defined absorption edge above 600 nm ascribed to $Cu_2O$ in the diffuse reflectance spectroscopy). Important parameters such as dark adsorption capacity, catalyst´s loading and initial concentration of Y5 were optimized under artificial light following the kinetics of degradation of the dye. These optimized conditions were applied also at pilot scale in a compound parabolic collector (CPC) photoreactor. Data revealed between 2.2 – 2.9 times faster degradation kinetics of tartrazine using the CPC photoreactor under natural solar light than in a slurry reactor under artificial solar light (Table 1). This behaviour is ascribed to the combination of photoactive copper species and the carbon phase in the catalyst (boosting sunlight absorption) and the moderate photon flux conditions in the CPC (minimizing recombination). This is of paramount importance since most of the photocatalytic tests designed to evaluate the activity of novel materials are carried out under simulated solar light and disregard the impact of photon flux in outdoor conditions.

**Table 1.** Summary of adsorption in the dark and kinetic parameters of the photocatalytic degradation of Y5 using artificial UV-vis and natural solar irradiation. Initial concentration 2 ppm and 0.25 g $L^{-1}$ catalyst loading.

| Type of Irradiation | $\eta_{ads}$ ($\mu$mol $g^{-1}$) [a] | $k_{app}$ x $10^{-3}$ ($min^{-1}$) [b] | $R_1^2$ [c] | $k_2$ x $10^{+2}$ (L $mol^{-1}$ $min^{-1}$) [d] | $R_2^2$ [e] | $n_{deg}$ (%) [f] |
|---|---|---|---|---|---|---|
| Natural solar irradiation | 15.3 ± 0.3 | 5.5 ± 0.1 | 0.997 | 32.7 ± 0.9 | 0.968 | 100 |
| Artificial irradiation | 16.6 ± 0.5 | 2.5 ± 0.2 | 0.916 | 11.4 ± 0.8 | 0.932 | 63 |

[a] Y5 adsorption in the dark after 60 min; [b] 1st-order apparent rate-constant obtained from: $Ln(C_o/C_t) = k_{app} \cdot t$; [c] Quadratic factor according to a 1st-order reaction-rate; [d] 2nd-order apparent rate-constant obtained from: $(1/[C_t]) = [(1/[C_{Eq}] + k_2.t]$; [e] Quadratic factor according to a second-order reaction-rate; [f] Y5 conversion after 420 min irradiation defined by $n_{deg} = [1 - (C_t/C_o)].100$.

## CONCLUSIONS

The photocatalyst was stable under natural solar irradiation in a continuous-flow CPC photoreactor. This is attributed to the protector role of the carbon matrix preventing the lixiviation of the copper species to the solution. Its photocatalytic performance is faster in natural solar light than under artificial irradiation. Overall, the prepared Cu@C photocatalyst is an economically sustainable, locally available and efficient material to be applied for the degradation of Y5 dye from wastewater effluents by adsorption and heterogeneous photocatalysis under natural solar irradiation.

**Acknowledgements**

This research is ascribed to the cooperation framework between CNRS and Autonomous University of Chile. Financial support from the Region Centre Val de Loire (APR-IA, PRESERVE grant), the Franco-Chilean network BIOCval2E (REDES-170004 project) and grants ANID-PIA/APOYO CCTE AFB170007, ANID-FONDECYT 1190591 is acknowledged.

**References**

Kapadia, G. J.; Tokuda, H.; Sridhar, R.; Balasubramanian, V.; Takayasu, J.; Bu, P.; Enjo, F.; Takasaki, M.; Konoshima, T.; Nishino, H. (1998). Cancer chemopreventive activity of synthetic colorants used in foods, pharmaceuticals and cosmetic preparations. Cancer Lett. 129, 87–95.

Muñoz-Flores, P.; Poon, P. S.; Sepulveda, C.; Ania, C. O.; Matos J. (2022). Photocatalytic Performance of Carbon-Containing CuMo-based Catalysts under Sunlight Illumination. Catalysts 12, 46.

Muñoz-Flores, P.; Poon, P. S.; Ania, C. O.; Matos J. (2022). Performance of a C-containing Cu-based photocatalyst for the degradation of tartrazine: comparison of performance in a slurry and CPC photoreactor under artificial and natural solar light. Journal of Colloid and Interface Science. 623, 646-659.

Carbon 2022

# Computational simulation of prismatic edge dislocations in graphite

**James G. McHugh[1,2], Pavlos Mouratidis[3], Anthony Impellizzeri[4], Kenny Jolley[3], Dogan Erbahar[5], Chris P .Ewels[4]**

[1] Department of Physics and Astronomy, University of Manchester, Manchester Department of Physics and Astronomy, University of Manchester, National Graphene Institute, University of Manchester, Manchester, UK

[2] National Graphene Institute, University of Manchester, Manchester, UK

Email: james.mchugh@manchester.ac.uk

[3] Department of Chemistry, Loughborough University, Loughborough, LE11 3TU, UK

[4] Universite de Nantes, CNRS, Institut des Materiaux Jean Rouxel, IMN, F-44000, Nantes, France

[5] Faculty of Engineering, Department of Mechanical Engineering, Ümraniye, 34775, Istanbul, Turkey

**Keywords**

DFT, Prismatic edge, Dislocation, Graphite, Klein, Zigzag, Armchair, Bernal

## INTRODUCTION

Despite having been the subject of intense study for over 60 years, the behaviour of graphite subject to damage such as irradiation has remained relatively poor, and there is little detailed atomistic understanding of many of the type of defects which can occur. Dislocations, which are a central concept in materials science, dictate the plastic deformation and damage evolution in materials. In layered materials such as graphite there are two general types of interlayer dislocations: basal dislocations, which accommodate strain within the basal plane, and prismatic dislocations, where an extra half-sheet of graphene is incorporated in bulk graphite. Using quantum mechanical density functional theory (DFT) calculations, we have examined different structural configurations of the prismatic dislocation core in graphite and evaluated the structure, energetics, and mobility (McHugh, 2022). The interaction of prismatic dislocation with point defects is considered, and the implications for material damage are considered.

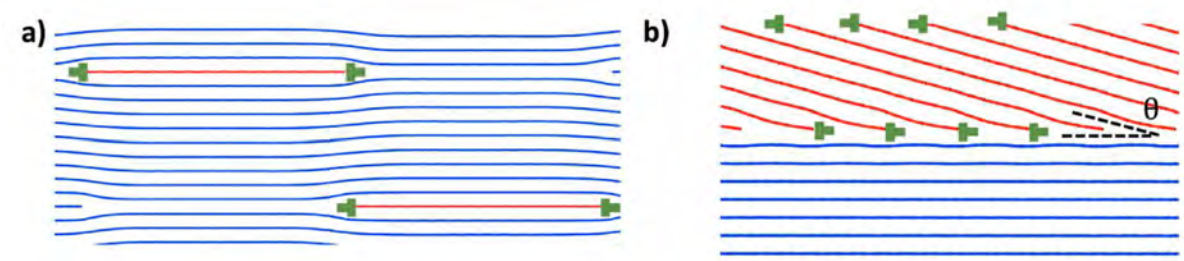


**FIGURE 1**: Schematic image of DFT supercells: **a)** containing isolated prismatic dislocation dipoles and **b)** grain boundary configurations.

## METHODS

DFT calculations have been performed using the Quantum ESPRESSO (Giannozzi, 2009) ab-initio suite. All cells have been constructed with a net Burgers vector of zero (see Figure 1), such that the lowest energy configuration of every cell is thus Bernal AB graphite. Formation energies are then

calculated relative to Bernal graphite. Point defect interactions have been considered using both bulk and “isolated” DFT supercells (Figure 2).

**RESULTS**

We find close energetic interplay between bonded and "free-standing" core structures in both zigzag and armchair directions, where a reconstructed stable zigzag core is identified. In both c-axis grain boundaries and prismatic dislocation pile-up configuration, we find novel metastable structures which may be important for energy storage in irradiated graphite, and which produce notable agreement with TEM images.

Calculations of point defects in the vicinity of the prismatic dislocation core are found to markedly lower the corresponding formation energy, suggesting that they are a significant source and sink for point-defect creation and diffusion (see Figure 2), due to the lowered barriers for $sp^3$ bonding and bond rotations in comparison to perfect material.

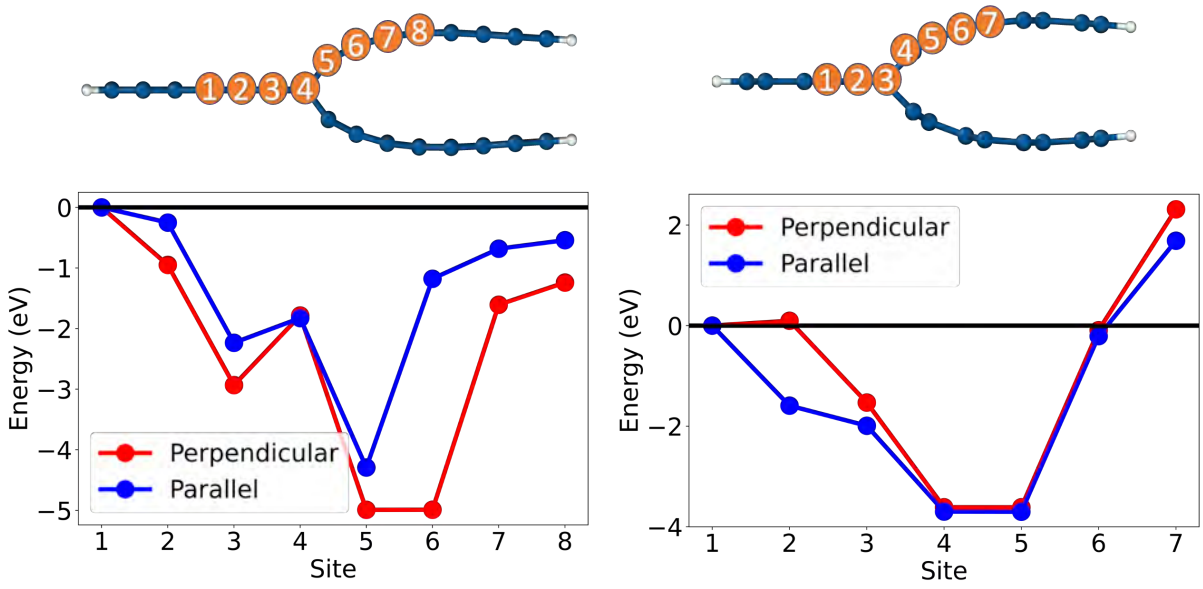


**FIGURE 2**: Vacancy formation energy as a function of position across a prismatic dislocation core, for dislocation cores along the **a)** armchair and **b)** zigzag crystallographic directions.

**CONCLUSIONS**

Our calculations show that the prismatic edge is a significant source and sink for point-defect creation and diffusion, where $sp^3$ bonds and bond rotations can happen with markedly lowered barriers in comparison to perfect material. This has implications for radiation damage, dimensional change, graphite magnetism, heat capacity, melting, and lubricity.

**Acknowledgements**

This work was supported by the United Kingdom EPSRC grant EP/R005745/1, Mechanisms of Retention and Transport of Fission Products in Virgin and Irradiated Nuclear Graphite. Kenny Jolley and Pavlos Mouratidis also gratefully acknowledge funds from EDF energy generation 2016-2021. The authors gratefully acknowledge the use of Athena at HPC Midlands+, which was funded by the EPSRC grant EP/P020232/1 as part of the HPC Midlands+ consortium. CE and AI acknowledge ANR-16-CE24-0008-01 “EdgeFiller” and ANR-20-CE08-0026 “OPIFCat” for funding. DE acknowledges support from the TUBITAK-2219 postdoctoral research abroad fund.

**References**

James G.McHugh, Pavlos Mouratidis, Anthony Impellizzeri, Kenny Jolley, Dogan Erbahard, and Chris P. Ewels. (2022). Prismatic edge dislocations in graphite. *Carbon*, 188, 401-419 https://doi.org/10.1016/j.carbon.2021.11.072

P. Giannozzi, et. al. (2009), QUANTUM ESPRESSO: a modular and open-source software project for quantum simulations of materials, *J. Phys.: Condens. Matter 21*, 395502 (2009) http://dx.doi.org/10.1088/0953-8984/21/39/395502

20 C 22 arbon 2022

# Reuse of activated carbon exhausted with pharmaceutical compounds: effect of adsorbate, particle size and thermal regeneration process

**Ana S. Mestre, Filipe M. Leandro, Ana P. Carvalho**
Centro de Química Estrutural, Institute of Molecular Sciences, Departamento de Química e Bioquímica, Faculdade de Ciências, Universidade de Lisboa, 1749-016 Lisboa, Portugal
Email: asmestre@fc.ul.pt

**Keywords**
Spent activated carbon; Regeneration; Water treatment

## INTRODUCTION

A major challenge of technologies employing adsorption onto activated carbons (ACs) is associated with extending their lifetime and the management of the spent adsorbents (Mestre et al. 2022). Nowadays, wastewater treatment is responsible for the largest amounts of exhausted granular ACs (GACs), and it is expected to growth, mainly driven by the need to remove contaminants of emergent concern, including pharmaceuticals. For this purpose, ACs adsorption and ozonation are considered consolidated technologies (Rizzo et al. 2019), with confirmed cost-efficient elimination of organic microcontaminants and toxicity in several full-scale wastewater treatment plants (WWTPs), namely in Switzerland and Germany (Mestre et al. 2022). Once the quality of the treated effluent reaches a critical point by falling below the required minimum, the loaded GAC must be replaced by fresh or regenerated GAC. Herein we address the effect of the regeneration procedure – thermal under $N_2$ flow *versus* reactivation with steam – on the effectiveness of regeneration of a commercial GAC saturated with caffeine or paracetamol to assess the influence of the adsorbate (Figure 1).

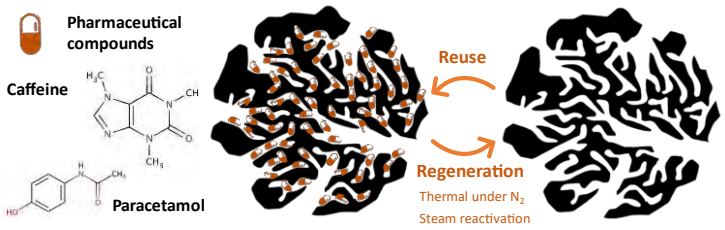


**FIGURE 1**: Chemical structure of studied pharmaceuticals and graphical illustration of the work.

## EXPERIMENTAL

The commercial GAC830 from Cabot/Norti was crushed and sieving to obtain particles with dimensions between 300 – 420 µm and 600 – 850 µm, the textural and surface properties were characterized by $N_2$ adsorption at -196 ºC and determination of the pH at the point of zero charge ($pH_{PZC}$). The adsorption of each pharmaceutical compound was assessed through single-solute kinetic and equilibrium assays. All solutions were prepared in ultrapure water. GAC samples exhausted with the target pharmaceuticals were regenerated at 600 ºC for 1 h under $N_2$ flow or under steam. The regenerated samples were characterized and re-used under the same experimental conditions to evaluate the regeneration.

## RESULTS AND DISCUSSION

For the activated carbon exhausted with caffeine and thermally regenerated, the particles with the largest particle size (600-850 µm) allow attaining removal efficiencies of 96% and 92% in, respectively,

the 1st and 2nd reuse/regeneration cycle. These values are slightly higher than those obtained for the smaller particle size granules (300-425 µm) with 92% and 85%. Besides the higher performance in the reuse, the larger particle size also allows lower mass loss percentages (27-31% *versus* 35-63%). In any case, after the 2nd reuse/regeneration cycle with caffeine, the $N_2$ isotherms of the materials are still coincident with that of the fresh adsorbent, and no variation was detected on the $pH_{PZC}$. For the material exhausted with paracetamol, the thermal regeneration is less effective since after the 1st and 2nd reuse/regeneration cycles the regeneration efficiency ranges between 50-60%. $N_2$ adsorption isotherms of the materials exhausted with paracetamol and further regenerated present a downward shift compared with the fresh material, indicating the loss of porosity mainly in the micropore region. For GAC with 600-850 µm the regeneration efficiency depends both on the regeneration method and on the pharmaceutical compound (Figure 2). For caffeine the exhausted GAC is successfully regenerated under $N_2$ flow during 4 consecutive cycles (> 90% recovery of adsorption capacity), for paracetamol the regeneration with the same procedure only 50% of the adsorption capacity is recovered after the 2nd cycle. For saturation with caffeine, steam reactivation allows improving the performance in the 1st cycle but lead to a gradual decrease of regeneration efficiency and performance for consecutive cycles.

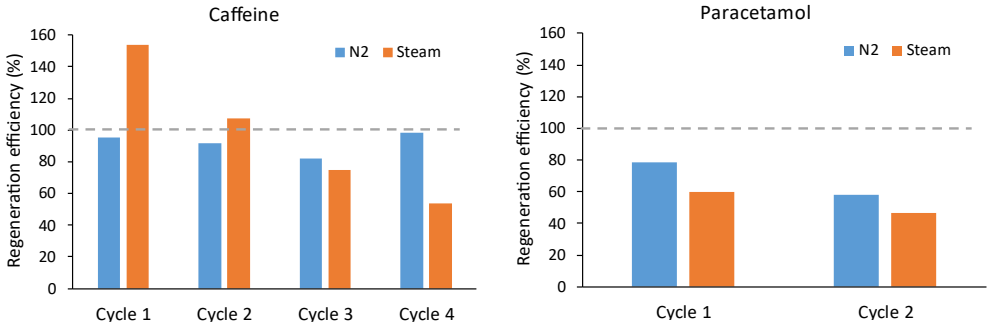


**FIGURE 2**. Influence of the regeneration method (thermal under $N_2$ and steam reactivation) on the regeneration efficiency of fraction 600-850 µm of the GAC exhausted with caffeine or paracetamol.

## CONCLUSIONS

Regeneration efficiency is dependent on the adsorbed pharmaceuticals with the pore network exhausted with caffeine being more effectively recovered by thermal regeneration or reactivation.

**Acknowledgements**

This work was supported by Fundação para a Ciência e a Tecnologia (FCT)/MCTES through national funds (PIDDAC) - UIDB/00100/2020, UIDP/00100/2020, and PTDC/EQU-EQU/6024/2020 (Project EMPOWER+). Ana S. Mestre thanks FCT for the Assistant Research contract CEECIND/01371/2017 (Embrace Project). The authors acknowledge Salmon & Cia for providing the commercial activated carbon Norit GAC830.

**References**

Mestre, A. S., Campinas, M., Viegas, R. M. C., Mesquita, E., Carvalho, A. P., & Rosa, M. J. (2022) Chapter 17 - Activated carbons in full-scale advanced wastewater treatment. In D. Giannakoudakis, L. Meili, & I. Anastopoulos (Eds.), Advanced Materials for Sustainable Environmental Remediation (pp. 433-475), Elsevier, Amsterdam, Netherlands. ISBN 978-0-323-90485-8. https://doi.org/10.1016/B978-0-323-90485-8.00001-1

Rizzo, L., Malato, S., Antakyali, D., Beretsou, V. G., Đolić, M. B., Gernjak, W., Heath, E., Ivancev-Tumbas, I., Karaolia, P., Lado Ribeiro, A. R., Mascolo, G., McArdell, C. S., Schaar, H., Silva, A. M. T., & Fatta-Kassinos, D. (2019). Consolidated vs new advanced treatment methods for the removal of contaminants of emerging concern from urban wastewater [Review]. Science of The Total Environment, 655, 986-1008. https://doi.org/10.1016/j.scitotenv.2018.11.265

Carbon 2022

# Electrodes For Redox Flow Batteries Based On Carbon Felt Modified With Advanced Carbon Materials

**A. J. Molina-Serrano[1], J. M. Luque-Centeno[1], D. Sebastián[1], C. Alegre[1], F. Carrasco-Marín[2], M. J Lázaro[1]**

[1]Instituto de Carboquímica, c/ Miguel Luesma Castán nº 4, 50018, Zaragoza, Spain
Email: mlazaro@icb.csic.es

[2] Facultad de Ciencias, Universidad de Granada. Avenida de Fuente Nueva, s/n, 18071, Granada

**Keywords**
Carbon felts, advanced carbon materials, electrodes, redox flow batteries

## INTRODUCTION

Vanadium redox flow batteries (VRFB) are one of the most efficient technologies for large-scale energy storage due to their modular design that favours their scalability. Furthermore, the use of vanadium species as electrolytes has unique advantages such as: elimination of cross-contamination through the membrane, short response time, and long shelf life (Kim *et al.*, 2015).

One of the critical components of VRFBs are the electrodes that contribute to the performance of the battery. On the electroactive surface of the electrodes, the electrochemical reactions responsible for the generation of electricity are carried out. However, improvements are still required to lower the costs of VRFBs and improve their specific power and energy (Pellow *et al.*, 2015; H. Zhang, X. Li, 2018).

The objective of the present work is the modification of commercial carbon felts with graphene oxide (GO), and Polyethylene Glycol (PEG). Thanks to the oxidizing power of PEG, the aim of this work is to obtain a carbon felt surface functionalized with oxygen groups, and increase the catalytic activity of the felts towards the reduction and oxidation reactions of vanadium, by the action of graphene oxide.

## EXPERIMENTAL

To carry out the modification of carbon commercial felts (GFD 4.6 IW1), supplied by Sigracell, we designed a method of modifying the surface of the felt with GO, synthesized by the modified Hummers method (Marcano *et al.*, 2010) and PEG. This method consists of impregnation cycles in a suspension of GO and PEG followed by drying in an oven at 75 $^{0}$C and finally in a pyrolysis in an atmosphere of $N_2$ at 800 $^{0}$C.

The physical-chemical characterization of the materials has been carried out by elemental analysis, X-ray diffraction (XRD), Raman spectroscopy, X-ray photoelectron spectroscopy (XPS) and scanning electron microscopy (SEM). In addition, the electrocatalytic activity of the felts has been determined in a three-electrode cell, using the felt as a working electrode, an Ag/AgCl (3 M KCl) reference electrode and a graphite bar as a counter electrode. The measurements have been carried out using an electrolyte with a concentration of 0.05 M of $VOSO_4$ in medium 1M $H_2SO_4$ solution.

**RESULTS AND DISCUSSION**

In the physical-chemical characterization (by XPS and elemental analysis), it can be seen how the amount of oxygen in the materials increases with the number of deposition cycles of GO-PEG (Figure 1).

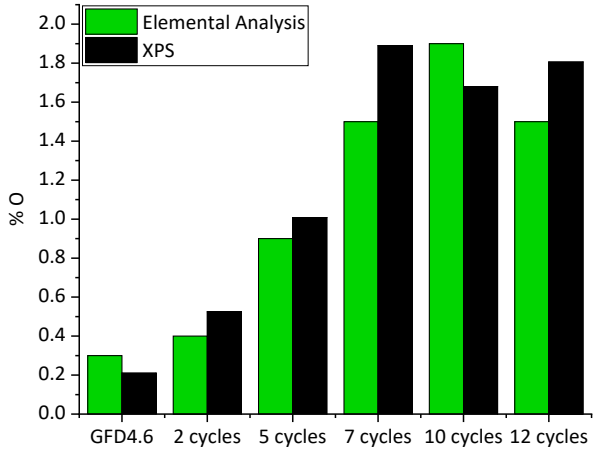


**FIGURE 1:** Mass percentage of oxygen determined by elemental analysis (green) and XPS (black).

In the scanning electron microscopy images shown in Figure 2, it can be seen how the GO deposited on the fibers of the felt increases with the deposition cycles, favouring the conductivity of the material and increasing its surface.

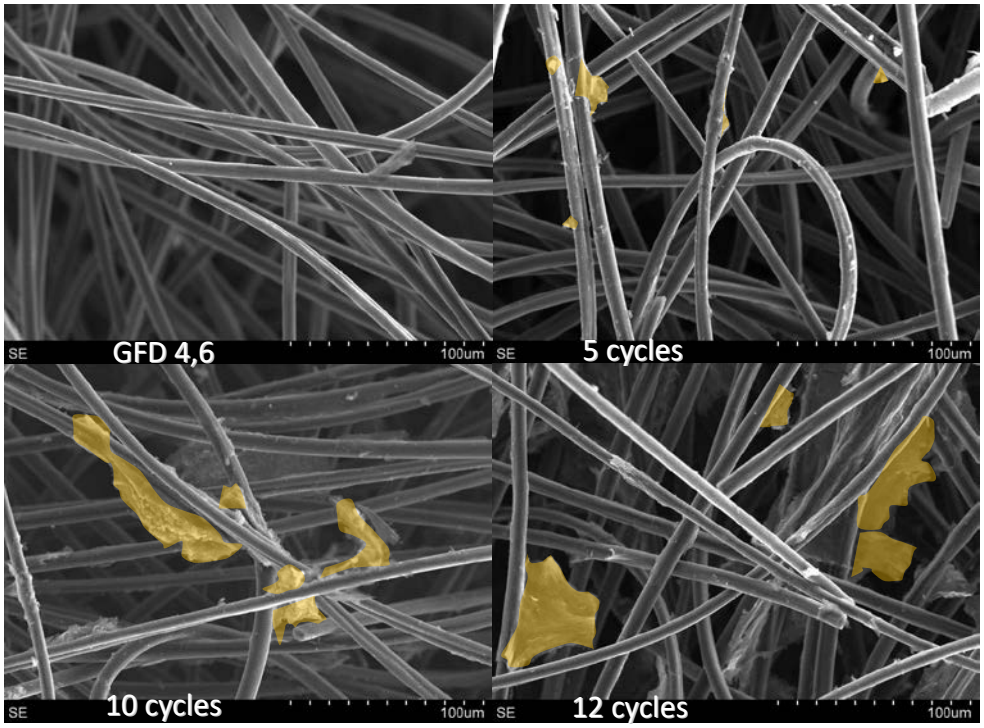


***FIGURE 2:*** *Scanning electron microscopy images, highlighting the deposited GO in yellow.*

Carbon felts functionalized with graphene and oxygen present a decrease in the overpotential (Figure 3) necessary for oxidation and reduction reactions, both in the negative electrode ($V^{2+}/V^{3+}$)

and in the positive electrode ($VO^{2+}/VO_2^+$), compared to with the unmodified felt, thus improving the efficiency of the battery.

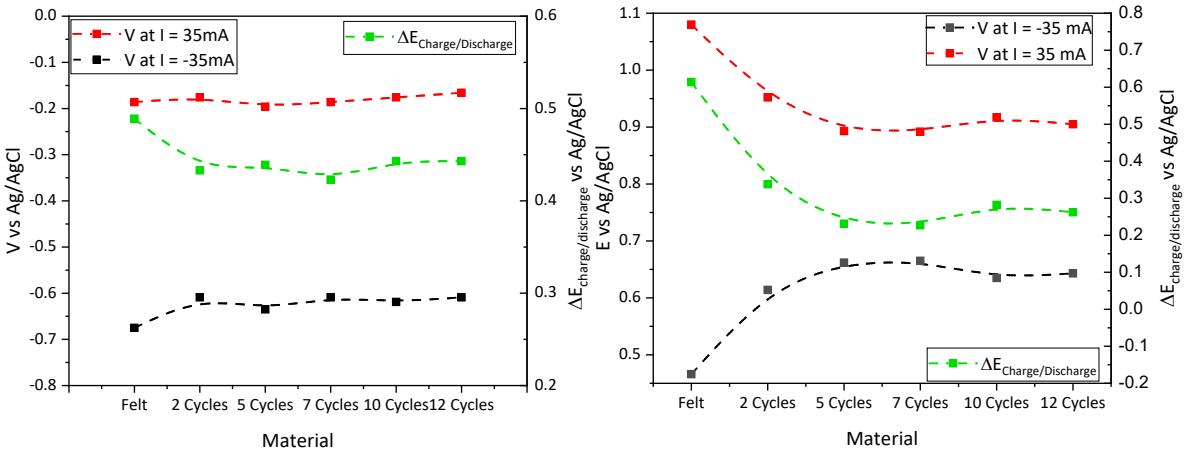


***FIGURE 3:*** *Potential at a current density of ±35 mAcm$^{-2}$ (oxidation/reduction) and potential difference for the charge versus discharge reaction for felts with different impregnations cycles for the pair $V^{2+}/V^{3+}$ (left) and for $VO^{2+}/VO_2^+$ (right). Determined by cyclic voltammetry at 5 mV/s in aqueous solution of 0.05 M $VOSO_4$ in 1 M $H_2SO_4$*

## CONCLUSIONS

• Carbon felts have been modified with graphene and polyetilenglycol through a cycle-based synthesis that allows modifying the amount of graphene deposited.

• All the materials obtained improve the electrocatalytic behaviour of the commercial material for both the positive and negative electrodes.

• The amount of graphene that offers the best results in a 3-electrode cell has been optimized.


### Acknowledgements

The authors acknowledge the funding from the Spanish National Research Council for the PTI Flowbat project. A. J. Molina-Serrano thanks the Ministry of Education for his predoctoral contract FPU Ref: FPU20/04400. In addition, authors acknowledge the funding from the Government of Aragon to the research group T06-20R.


### References


H. Zhang, X. Li, J. Z. (2018) *Redox Flow Batteries. Fundamentals and Applications*. CRC Press.

Kim, K. J. *et al.* (2015) 'A technology review of electrodes and reaction mechanisms in vanadium redox flow batteries', *Journal of Materials Chemistry A*. Royal Society of Chemistry, 3(33), pp. 16913–16933. https://doi.org/10.1039/c5ta02613j.

Marcano, D. C. *et al.* (2010) 'Improved synthesis of graphene oxide', *ACS Nano*, 4(8), pp. 4806–4814. https://doi.org/10.1021/nn1006368.

Pellow, M. A. *et al.* (2015) 'Hydrogen or batteries for grid storage? A net energy analysis', *Energy and Environmental Science*. Royal Society of Chemistry, 8(7), pp. 1938–1952. https://doi.org/10.1039/c4ee04041d.

20 C 22 arbon 2022

# The Existence and Role of a Liquid Phase in CVD Deposition Mechanisms of Pyrolytic Carbons

**Marc Monthioux, Germercy Paredes[2], Thierry Ondarçuhu[3] and Fabrice Piazza[2]**
Centre d'Elaboration des Matériaux et d'Etudes Structurales (CEMES), CNRS, Université de Toulouse, Toulouse, France.
Email: marc.monthioux@cemes.fr

[2]Laboratorio de Nanociencia, Pontificia Universidad Católica Madre y Maestra (PUCMM), Santiago de Los Caballeros, Dominican Republic
[3]Institut de Mécanique des Fluides de Toulouse (IMFT), CNRS, Université de Toulouse, Toulouse, France

**Keywords**
Time of Flight CVD, Physics of wetting, Carbon micro-/nano-cones

## INTRODUCTION

Pyrolytic carbons (PyC) make a family of graphenic carbon solids prepared by chemical vapour deposition (CVD) and exhibiting a variety of texture (isotropy/anisotropy) and nanotexture (crystallite dimensions and slight misorientations) which are exploited in many high-tech applications as coatings or composite matrices. As typical of CVD processes, the mechanisms of PyC deposition mainly involve an organic gaseous feedstock, temperature conditions high enough to break the precursor molecules, and a substrate. The primary cracking process generates a solid carbon deposit (the PyC) on the one hand, and radicals on the other hand. Then secondary processes may happen, namely radical recombination into new species, which may crack in turn and contribute to the PyC deposition and the formation of new radicals. In this process, the co-formation of a liquid phase has been debated for long. Investigating nanosized pyrolytic carbon deposits by a time-of-flight CVD process onto carbon nanotubes had suggested that the existence of a transient liquid phase was likely (Monthioux, 2006). However, a clear demonstration was missing. A decisive step for addressing this issue is to check whether the behaviour of liquids wetting wires and the related physics are able to provide explanations accounting for all the observations. This is what was done in this work. **A full version of this work was published in Paredes (2021).**

## EXPERIMENTAL

The CVD process was based on a horizontal, tubular furnace fed with a mixture of $CH_4$ and $H_2$. Multi-wall carbon nanotubes (MWCNTs) are grown first using standard conditions (iron catalyst, 1100°C). The catalyst dispersion and total flow rate make that the MWCNTs grow individually and more or less aligned parallel to the flow direction. Then, the temperature in the isothermal zone is increased up to 1400°C and the $CH_4/H_2$ ratio is changed so that to deposit PyC onto the MWCNTs for about 2 hours. The "time-of-flight" nature of the deposition comes from the extended isothermal zone which allows the gas phase to "mature" while travelling downstream. Figure 1a shows what the early PyC deposit looks like (after few-minute deposition), Figures 1b to 1d provide examples of the resulting all-graphene morphologies obtained at various time-of-flight conditions.

## DEPOSITION MECHANISMS

Figure 2 summarizes the various steps the occurrence of which were discussed in Paredes (2021). ***Step 0*** corresponds to the catalytic growth of a primary MWCNT and sketches the complexity of the

surrounding gas phase chemical composition (as a consequence of the ToF-CVD conditions) *i.e.*, including radicals, polyaromatic hydrocarbons (PAHs) and light hydrocarbons.

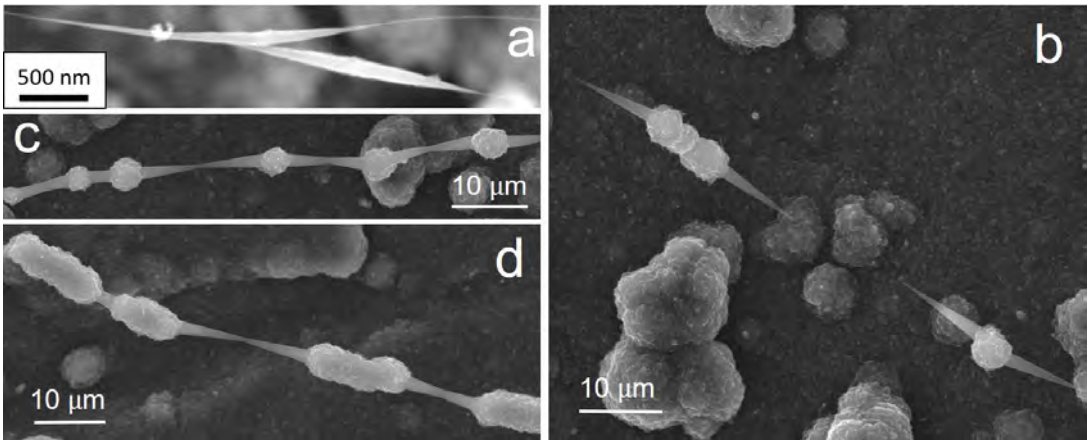


**FIGURE 1:** Examples of the complex graphenic morphologies that form when PyC is deposited onto CNTs at 1400°C by ToF-CVD. (a) After few-minute deposition. (b) to (d) After 2 hours at different time-of-flight conditions.

During ***Step 1***, the gas phase condenses as a cylinder of PAH-rich organic liquid around the CNT. Then (***Step 2***), the liquid film is immediately subjected to the effect of the so-called Plateau-Rayleigh instability (PRI) which breaks the liquid film and forms nanosized, axisymmetric elongated droplets periodically displayed along the CNT; calculations show that the PRI applies within few microseconds; the rheological behaviour of the liquid may vary with the time-of-flight conditions and generate various morphologies of the elongated droplets, subsequently resulting in either beads or short fibre segments after a 2-hour growth; importantly, surface tensions make the PAHs to align parallel to the CNT surface.

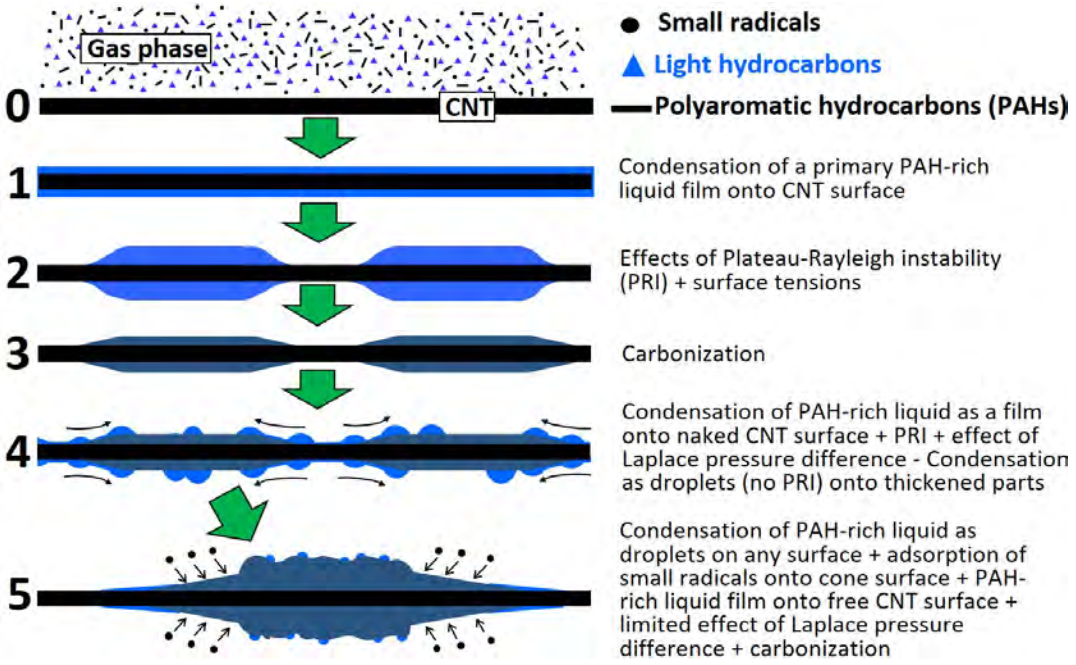


**FIGURE 2:** Sketch of the growth scenario for carbon objects as shown in Figure 1. Elements are not at scale, and the successive steps do not correspond to equal time-periods. The figure is extensively modified from Paredes (2021).

Then, carbonisation proceeds (***Step 3***), forming primary cones made of concentric graphene cylinders which are as shorter as they are more external, making the whole morphology spindle-like (as imaged in Figure 1a); this induces the occurrence of graphene edges at the conical part surface, which make adsorption sites; as a well-known mechanism in pyrolytic carbon deposition processes, radicals may then chemisorb at the conical part surface from this step, resulting in the longitudinal growth of the primary morphology. Meanwhile (***Step 4***), the PAH-containing liquid can keep depositing everywhere; when depositing on the thickened parts of the CNT (starting with the thickest part of the primary spindle-like morphology), a cylindrical liquid film can no longer form, as the diameter has become is too large; consequently, PAHs deposit under another form instead, possibly as individual droplets, or as individual entities; on the other hand, when depositing on the still-naked parts of the CNT, a liquid cylinder can still condense, but the contacts of the cylindrical liquid film with the conical parts make that the droplets created by the PRI are subjected to a Laplace pressure difference; this makes the axisymmetric droplets to migrate towards the larger diameters of the cone parts, leaving the CNT surface naked again; however, the migration stops once the droplets reach the cone part where the diameter is too large for the droplets to remain axisymmetric; therefore, the more the cones grow, the shorter the droplet migration is. During ***Step 5***, the carbonization proceeds while Step-4 events keep going; PAHs not subjected to the PRI do not align well, resulting in somewhat isotropically-displayed distorted graphenes, making the thicker part mostly grow from the PAHs both in thickness and length with a rough surface (the fibre segment-/bead-like part); on the other hand, in droplets resulting from the PRI (*i.e.*, formed on the naked part of the CNT), PAHs are subjected to surface tensions and resulting graphenes align well, hence the concentric display of graphenes, the presence of many graphene free-edges at the cone surface, and the smooth surface. From this step, the cones mostly grow from the radicals, although few PAHs may deposit in a dispersed manner and serve as nuclei for the subsequent growth of scroll-like concentric graphenes thanks to the radical chemisorption (Paredes, 2022), while the fibre segment-/bead-part mostly grows from the PAHs.

## CONCLUSION

Considering the physics of wetting strings by a liquid does apply to our system in spite of both the high temperature and the nanoscale, *i.e.*, far beyond the condition range usually investigated for wetting phenomena, and far beyond the condition range usually considered for the existence of organic liquids. From a practical point of view, as the resulting material is a solid, all-graphenic carbon material, the work demonstrates that using wetting physics in high temperature CVD can be a way to dramatically modify the surface energetics and the nano/microscale morphology of carbon nanofilaments, here forming carbon nanotube-supported complex morphologies which include graphenic carbon nanocones. The statement is assumed to also apply to other chemical systems.

**Acknowledgements**

This study was supported by the EUR grant NanoX n° ANR-17-EURE-0009, the CNRS-funded International Research Project NEWCA, the Government of Aragon (project DGA E13-20R), the Spanish MICINN (PID2019-104739GB-100/AEI/10.13039/501100011033), the European Union H2020 programs “ESTEEM3” (Grant number 823717), and the “Graphene Flagship” CORE 3 (Grant number 881603), and the Pontificia Universidad Católica Madre y Maestra (Santiago, Dominican Republic).

**References**

Monthioux, M., Allouche, H. and Jacobsen, R. L. (2006). Chemical vapour deposition of pyrolytic carbon on carbon nanotubes. Part 3. Growth mechanisms. *Carbon*, 44, 3183-3194. https://doi.org/10.1016/j.carbon.2006.07.001

Paredes, G., Ondarçuhu, T., Monthioux, M. and Piazza, F. (2021). Unveiling the existence and role of a liquid phase in a high temperature (1400 °C) pyrolytic carbon deposition process. *Carbon Trends*, 5, 10017. https://doi.org/10.1016/j.cartre.2021.100117

Paredes, G., Wang, R., Puech, P., Seine, G., Leyssale, J.-M., Arenal, R., Masseboeuf, A., Piazza, F. and Monthioux, M. (2022). The texture, structure, and nanotexture of ToF-CVD-prepared carbon micro-/nano-cones. The World Conference on Carbon "Carbon-2022", London (UK), July 3-8, Oral #NKDR105.

20 C 22 arbon 2022

# Influence of the Micro and Mesoporosity of the Different Nanoporous Carbons in $CO_2$ Capture

**Kiara Montiel-Centeno, Deicy Barrera, Jhonny Villarroel-Rocha, José J. Arroyo-Gomez and Karim Sapag**

Laboratory of Porous Solids, Institute of Applied Physics, CONICET-UNSL, San Luis, Argentina

Email: sapag@unsl.edu.ar

**Keywords**

Carbon materials, carbon dioxide, textural properties

## INTRODUCTION

One of the most relevant topics to address a "Cleaner Future" is Carbon Capture and Sequestration, where the molecule in the crosshairs of this subject is $CO_2$ (Vaz *et al.,* 2022). Several processes are considered in the $CO_2$ capture, where adsorption represents a cleaner and more affordable technology (Sattari *et al.*, 2021). Carbon materials with pore sizes from a few angstroms to a few nanometers have been highlighted among the different porous adsorbents to $CO_2$ capture. The influence of these textural properties on $CO_2$ adsorption needs to be studied.

This work presents the synthesis and analysis of a series of carbon materials with different textural properties used in the carbon dioxide capture at 308 K and up to 10 bar. Textural properties of more than twenty nanoporous carbons obtained with varying synthesis methods were compared and correlated with the carbon dioxide uptake. This series includes biomass-based carbons with chemical or physical activation and ordered templated carbons.

## MATERIALS AND METHODS

### Synthesis of carbon nanoporous materials

The series of materials presented in this work include activated carbons (AC) and templated carbons (TC). The AC were obtained from biomass and were chemically activated. Also, three physically activated commercial AC were tested. The TC were obtained using the nanocasting technique (Janus *et al.*, 2020), where different inorganic templates such as mesoporous silica and zeolites were impregnated with different carbon sources (e.g., sucrose, furfuryl alcohol) to synthesize the carbon material within the template pores and then remove the template. In this work, only the most representative samples of the series of carbons are presented: two AC (Vulcan and Maxsorb) and six TC (CN-Zeo, CMK-3, CMK-5_1, CMK-9, CMK-5_2, and Macro_2). These materials presented the extreme and mean values in the textural properties and the application studies.

### Textural characterization and Application

$N_2$ adsorption-desorption isotherms were measured at 77 K using a manometric Micromeritics ASAP 2000 analyzer. The samples were previously degassed in a vacuum at 200 °C for 12 h. The textural properties such as specific surface area ($S_{BET}$), total pore volume ($V_{TP}$), micropores volumes ($V_{\mu P}$), primary mesopores ($V_{PMP}$), and pore size distribution (PSD) were calculated from the $N_2$ isotherm data, and using the methods reported elsewhere (Montiel-Centeno *et al.*, 2019). $CO_2$ capture measurements were carried out at 308 K and up to 10 bar, using manometric equipment Micromeritics ASAP 2050. Before analysis, the samples were degassed at 200 °C for 6 h.

## RESULTS AND DISCUSSION

The textural characterization studies (Figure 1a) revealed that most TC materials presented isotherms Type IV, except CN-Zeo, which showed isotherm Type II(b). The AC exhibited isotherms Type I,

according to the IUPAC classification (Thommes *et al.*, 2015). Likewise, these isotherms showed different hysteresis loops types, H2-a (for CMK-3 and CMK-5), H2-b (for Macro-2), H3 (for CN-Zeo), and H4 (for Maxsorb), which are characteristics of mesoporous materials. The CMK-9 sample did not present hysteresis; however, using the $\alpha_S$-plot method, it was determined that this material is micro-mesoporous. From the $N_2$ isotherms data, the textural properties of these materials were determined, and the results are presented in Table 1. This table shows that the AC Maxsorb presented the highest $S_{BET}$ and $V_{\mu P}$ in all series of materials; on the contrary, the AC Vulcan presented the lowest $S_{BET}$ and $V_{TP}$. On the other hand, TC Macro-2 exhibited the highest values of $V_{TP}$ and $V_{PMP}$, and this same material was the only one that did not reveal micropores.

Figure 1b presents the PSD of the AC and TC. It is observed that these materials exhibited bimodal distributions with the presence of pores in the microporous and mesoporous regions, except Macro-2, which presented a single contribution in the mesoporous region. The mesopore's size varied between 2-10 nm, where the Macro-2 sample presented the largest mesopores and the Maxsorb the smallest. Likewise, the size of the micropores of the AC and TC was found to be between 0.5-2 nm (see inset box).

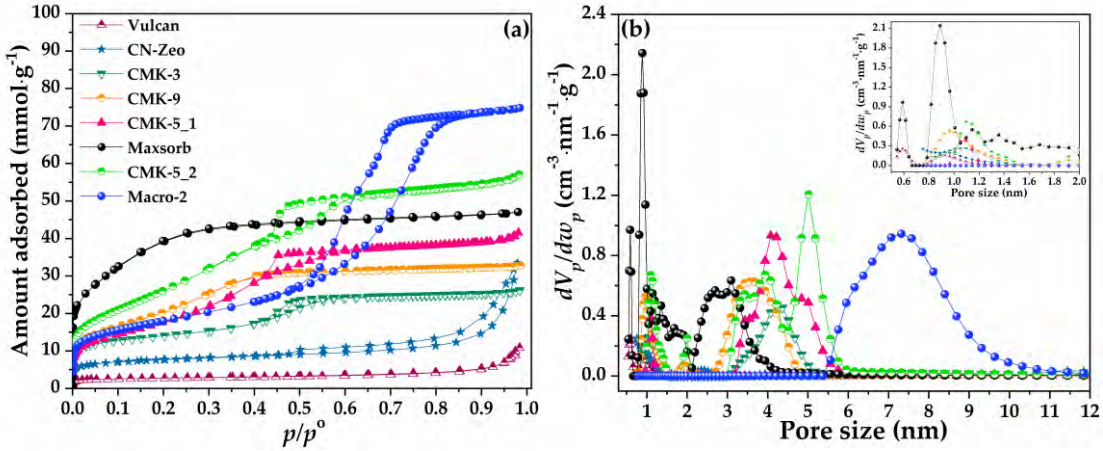


**FIGURE 1**: (a) $N_2$ ads-des isotherms at 77 K and (b) PSD of nanoporous carbons.

**TABLE 1**: Textural properties of nanoporous carbons.

| Sample | $S_{BET}$ ($m^2/g$) | $S_{MP}$ ($m^2/g$) | $V_{\mu P}$ ($cm^3/g$) | $V_{PMP}$ ($cm^3/g$) | $V_{TP}$ ($cm^3/g$) | $AdC_{CO_2}$ (mmol/g) |
|---|---|---|---|---|---|---|
| Vulcan | 230 | 70 | 0.06 | 0.30 | 0.36 | 1.61 |
| CN-Zeo | 660 | 240 | 0.16 | 0.84 | 1.00 | 3.09 |
| CMK-3 | 1090 | 510 | 0.20 | 0.70 | 0.90 | 6.13 |
| CMK-9 | 1580 | 950 | 0.20 | 0.93 | 1.13 | 6.15 |
| CMK-5_1 | 1420 | 1310 | 0.06 | 1.38 | 1.44 | 5.04 |
| Maxsorb | 3250 | 1860 | 0.71 | 0.91 | 1.63 | 8.32 |
| CMK-5_2 | 2200 | 1890 | 0.19 | 1.78 | 1.97 | 7.08 |
| Macro-2 | 1440 | 1440 | 0 | 2.59 | 2.59 | 5.81 |

Figure 2 shows the $CO_2$ adsorption isotherms of the series of carbons under study. Under the analysis conditions (10 bar and 308 K), the AC and TC isotherms have different $CO_2$ adsorption capacities ($AdC_{CO2}$). The results show that the Maxsorb presented the highest $AdC_{CO_2}$ (8.32 mmol/g), followed by the CMK-5_2 (7.08 mmol/g). On the other hand, the Vulcan carbon presented the lowest adsorption capacity (1.61 mmol/g). This is, the $AdC_{CO_2}$ of the AC and TC studied were: Maxsorb > CMK-5_2 > CMK-9 > CMK-3 > Macro-2 > CMK-5_1 > CN-Zeo > Vulcan. Based on these results, the materials with the highest specific surface areas had the highest adsorption capacities. In addition, a good correlation was found with the specific surface area of the mesopores where the TC Macro-2, with the absence

of micropores, presented an $AdC_{CO_2}$ like that of the CMK-3 (highly microporous). This result may indicate that the $AdC_{CO2}$ of the AC and TC obtained will depend not only on the micropores, as is usually reported (Gomez-Delgado *et al.*, 2022; Serafin *et al.*, 2022), but also that the mesopores play an important role. This result agrees with a work we reported earlier (Montiel-Centeno *et al.*, 2019).

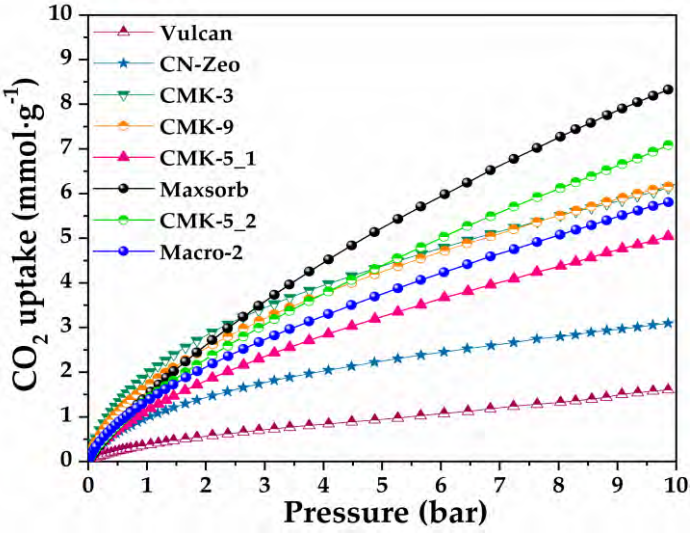


**FIGURE 2**: $CO_2$ adsorption isotherms at 308 K up to 10 bar for the nanoporous carbons.

## CONCLUSIONS

The carbon materials presented in this work had a good performance in the $CO_2$ capture. The materials with the highest specific surface area adsorbed the largest amount of $CO_2$, regardless of whether it is an activated or templated carbon. This study revealed that not only the micropores could influence the adsorption capacity of $CO_2$ but also the mesopores.


### Acknowledgments

The authors thank UNSL and CONICET (Argentina) for the subsidies and scholarships awarded.


### References


Gomez-Delgado, E., Nunell G.V., Cukierman A. L. and Bonelli P. (2022). Influence of the carbonization atmosphere on the development of highly microporous adsorbents tailored to $CO_2$ capture. *Journal of the Energy Institute*, 102, 184–189. doi: 10.1016/J.JOEI.2022.03.003.

Janus, P., Janus, R., Dudek, B., Drozdek, M., Silvestre-Albero, A., Rodríguez-Reinoso, F. and Kustrowski, P. (2020). On mechanism of formation of SBA-15/furfuryl alcohol-derived mesoporous carbon replicas and its relationship with catalytic activity in oxidative dehydrogenation of ethylbenzene. *Microporous and Mesoporous Materials*, 299, 110118. doi: 10.1016/j.micromeso.2020.110118.

Montiel-Centeno, K., Barrera, D. Villarroel-Rocha, J., Moreno, S. and Sapag, K. (2019). Hierarchical nanostructured carbons as $CO_2$ adsorbents. *Adsorption*, 25 [7], 1287–1297. doi: 10.1007/s10450-019-00089-3.

Sattari, A., Ramazani, A., Aghahosseini, H. and Aroua, M. (2021). The application of polymer containing materials in $CO_2$ capturing via absorption and adsorption methods. *Journal of $CO_2$ Utilization*, 48, 101526. doi: 10.1016/J.JCOU.2021.101526.

Serafin, Nazzal, J., Kaminska, A., Paszkiewicz, O. and Michhalkiewicz, B. (2022). Management of surgical mask waste to activated carbons for $CO_2$ capture. *Journal of $CO_2$ Utilization*, 59, 101970. doi: 10.1016/J.JCOU.2022.101970.

Thommes, M., Kaneko, K., Neimark, A., Olivier, J., Rodríguez-Reinoso, F., Rouquerol, J. and Sing, K. (2015). Physisorption of gases, with special reference to the evaluation of surface area and pore size distribution (IUPAC Technical Report). *Pure and Applied Chemistry*, 87, [7], 1051–1069. doi: 10.1515/pac-2014-1117.

Vaz, S., Rodrigues de Souza, A. P. and Lobo Baeta, B. E. (2022). Technologies for carbon dioxide capture: A review applied to energy sectors. *Cleaner Engineering and Technology*, 8, 100456. doi: 10.1016/J.CLET.2022.100456.

Carbon 2022

# Effect of Cobalt Species supported on CNTs towards the Oxygen Evolution Reaction

**Rafael G. Morais[1,2], Natalia Rey-Raap[3], José Luís Figueiredo[1,2], M. Fernando R. Pereira[1,2]**

[1] LSRE-LCM - Laboratory of Separation and Reaction Engineering – Laboratory of Catalysis and Materials, Faculty of Engineering, University of Porto, Rua Dr. Roberto Frias, 4200-465 Porto, Portugal, E-mail: (rgm@fe.up.pt)

[2] ALiCE - Associate Laboratory in Chemical Engineering, Faculty of Engineering, University of Porto, Rua Dr. Roberto Frias, 4200-465 Porto, Portugal

[3] Department of Physical and Analytical Chemistry, Oviedo University-CINN, 33006, Oviedo, Spain

**Keywords**
Carbon Nanotubes, Oxygen Evolution Reaction, Cobalt.

## INTRODUCTION

The rising urgency to shift the global energy production from fossil fuels to green renewable energies requires the optimization of the most promising storage and conversion devices for potential large-scale commercialization within the next years. An interesting strategy is the development of a unique system that could combine storage and conversion devices and, therefore, achieve maximum energy efficiency. One of the most promising systems in this area is the unitized regenerative fuel cell (URFC), which combines both an electrolyzer, which converts electrical energy into chemical energy when energy production surpasses its demand, and a fuel cell that converts the chemical energy produced by the electrolyzer into electrical energy upon necessity (Pu et al., 2021). One of the main challenges of the URFC is the sluggish kinetics of its oxygen reactions (oxygen evolution and reduction reactions, OER and ORR, respectively) that hinder the overall kinetics of the device. Thus, the design of a cheap and highly efficient electrocatalyst is necessary to achieve a competitive technology. Nowadays, the main benchmark catalysts are noble metals such as Pt, Ru and Ir, which are scarce and very expensive. Therefore, tailoring a widely-available and low-cost carbon material represents an interesting alternative to the current commercial catalysts (Qian et al., 2017). In this work, cobalt nitrate was incorporated on carbon nanotubes (CNT). This sample underwent a thermal treatment at different temperatures and under different atmospheres ($N_2$ or $H_2$) resulting in several catalysts with different cobalt species. These catalysts were then mainly tested towards the OER as the synergy between carbon and cobalt has been reported to enhance the catalyst's conductivity and overall OER electrochemical performance. XRD characterizations indicate that, in an inert atmosphere, increasing the treatment temperature at a low-temperature range (185-350 °C) slightly decreased the overall oxidized cobalt content, while further increasing the temperature up to 900 °C, the main cobalt species are modified. The treatments performed under $H_2$ atmosphere resulted in materials with lower cobalt species in comparison to those treated under $N_2$. Overall, an increase of the thermal treatment temperature and a $H_2$ atmosphere led to a decrease of oxidized cobalt species and, consequently, an increase of the total cobalt contribution due to the lower oxygen content. In the OER, samples treated under $H_2$ atmosphere presented the highest electrochemical performance, providing a current density of 10 mA $cm^{-2}$ at 1.63 V. Therefore, tailoring of carbon electrocatalysts with the most efficient and electroactive cobalt species towards the OER (in this case, metallic cobalt obtained by the reduction of cobalt oxides) is essential to achieve the best electrochemical performances. Moreover, these results demonstrate

that it is possible to achieve interesting OER performances using a carbon support, a very cheap cobalt precursor and employing low temperatures (185 °C) to minimize the production costs and environmental impact. The most electroactive sample towards OER was further tailored to probe its performance towards the oxygen reduction reaction (ORR). Three different methodologies were used to incorporate iron on the carbon material using iron(ii)phthalocyanine (FePc) as a precursor: i) incorporation of FePc on the Co-doped CNT, ii) incorporation of FePc on the CNT and posterior incorporation of cobalt on the Fe-doped sample and iii) physical mixture of the Fe-doped sample and the Co-doped sample using a 1:1 mass ratio. The bimetallic samples showed remarkable ORR activity, even better than the Pt/C ORR benchmark catalyst. Moreover, all samples tested presented long-term durability and high methanol resistance (superior to 90%) surpassing one of the biggest challenges towards large scale application. Regarding bifunctionality, a potential gap between both ORR and OER of 0.76 V was achieved for the most electroactive sample, which is similar to state-of-the-art carbon materials. Therefore, the carbon materials prepared are suited for upscale testing to probe their capability to replace noble metals at industrially more relevant applications.

## CONCLUSIONS

Highly electroactive Co-doped carbon nanotubes were used as electrocatalysts towards the oxygen evolution reaction by using a low-cost precursor and simple incorporation techniques. Furthermore, bifunctional oxygen electrocatalysts were prepared by mixing the most electroactive Co-CNT sample with a Fe-CNT sample that presented higher electroactivity towards ORR than the commercial Pt/C. The Fe,Co-doped sample displayed very high bifunctional oxygen electroactivity, which was comparable to the best state-of-the-art carbon materials while using green methodologies and low production costs, remarking high up-scaling potential towards producing carbon materials for green energy applications.

**Acknowledgements**

This work was financially supported by Project "BiCat4Energy" with reference PTDC/EQU-EQU/1707/2020. It was also supported by LA/P/0045/2020 (ALiCE), UIDB/50020/2020 and UIDP/50020/2020 (LSRE-LCM), funded by national funds through FCT/MCTES (PIDDAC). RGM acknowledges the Research Grant from FCT (2020.06422.BD).

**References**

Pu, Z., Zhang, G., Hassanpour, A., Zheng, D., Wang, S., Liao, S., Chen, Z. & Sun, S. 2021. Regenerative fuel cells: Recent progress, challenges, perspectives and their applications for space energy system. *Applied Energy*, 283**,** 116376. https://doi.org/10.1016/j.apenergy.2020.116376

Qian, Y., Hu, Z., Ge, X., Yang, S., Peng, Y., Kang, Z., Liu, Z., Lee, J. Y. & Zhao, D. 2017. A metal-free ORR/OER bifunctional electrocatalyst derived from metal-organic frameworks for rechargeable Zn-Air batteries. *Carbon*, 111**,** 641-650. https://doi.org/10.1016/j.carbon.2016.10.046

Carbon 2022

# "Efficient Production Of 5-Hydroxymethylfurfural (HMF) From Sucrose In Water Promoted By S And N-doped Carbon Catalysts"

**Katarzyna Morawa Eblagon[1,2*], Rafael Gomes Morais[1,2], Anna Malaika[3], Manuel Alejandro Castro Bravo[3], Natalia Rey-Raap [4], M. Fernando R. Pereira[1,2], José Luís Figueiredo[1,2]**

[1]Laboratory of Separation and Reaction Engineering - Laboratory of Catalysis and Materials (LSRE-LCM), Department of Chemical Engineering, Faculty of Engineering, University of Porto, Portugal

[2] ALiCE - Associate Laboratory in Chemical Engineering, Faculty of Engineering, University of Porto, Rua Dr. Roberto Frias, 4200-465 Porto, Portugal

[3]Faculty of Chemistry
Adam Mickiewicz University in Poznań, Uniwersytetu Poznańskiego 8, 61-614 Poznań, Poland

[4]Department of Physical and Analytical Chemistry, University of Oviedo-CINN-CSIC, 33006-Oviedo, Spain

E-mail: keblagon@fe.up.pt

**Keywords**
5-hydroxymethylfurfural; hydrochar; biomass; dehydration

## INTRODUCTION

Hydroxymethylfurfural (HMF) is a suitable building block for producing many value-added fine chemicals, biopolymer precursors, and biofuels (Chheda, 2007). However, the current high production costs of HMF limit its competitiveness with existing alternatives at an industrial scale. The development of cheaper and environmentally friendly catalytic systems is urgently needed for the commercialization of HMF to become a reality.

HMF can be obtained by acid-catalyzed dehydration of hexoses and their polymers. Even though fructose is the optimum feedstock for HMF production, sucrose is the preferred substrate for viable commercial-scale applications due to its higher availability and low price. The production of HMF from sucrose involves a complex reaction network including hydrolysis of sucrose to glucose and fructose (catalyzed by acidic sites), followed by isomerization of glucose to fructose (facilitated by Lewis sites) and finally, fructose dehydration to HMF (on acidic sites) (Davidson, 2021). Interestingly, biochar catalysts functionalized with basic nitrogen sites showed great activity in glucose isomerisation to fructose (Chen, 2018), but have not been tested yet in glucose dehydration to HMF.

## EXPERIMENTAL

In the present work, the conversion of sucrose to HMF was studied for the first time applying carbon catalysts having a combination of acidic and basic functionalities. The catalysts were prepared via facile one-step hydrothermal carbonization of glucose at 180 °C, using thiourea as a sole doping source of nitrogen (i.e., basic sites) and sulfur functionalities (i.e., acidic sites). The influence of the length of the hydrothermal treatment (12 and 24 h) and the amount of thiourea dopant (0.5 – 3 g) on the chemical properties of the bifunctional catalysts were studied. Selected materials were also carbonized and ball-milled. A reference catalyst containing only nitrogen functionalities was prepared by substituting thiourea with urea. For the sake of comparison, a pure glucose solution was also hydrothermally treated. The obtained samples were abbreviated according to the scheme:

*CG_aT or U_t_c_b*, in which: CG - carbon from glucose, a - amount of doping source in grams, T - thiourea, U - urea, t - time of hydrothermal carbonization, c - carbonized, b - ball-milled.

**RESULTS**

The SEM images of CG_1T_12h and CG_1U_12h are shown in Figure 1. These images revealed spherical particles with a strong tendency to aggregation and cross-linking. The size of particles in hydrochar doped with thiourea was not uniform and contained larger particles (with diameter of around 7-12 µm) along with much smaller aggregated particles (see Figure 1 A). On the other hand, hydrochar functionalized with urea (see Figure 1B) showed more uniform particles with an average diameter of 5-7 µm.

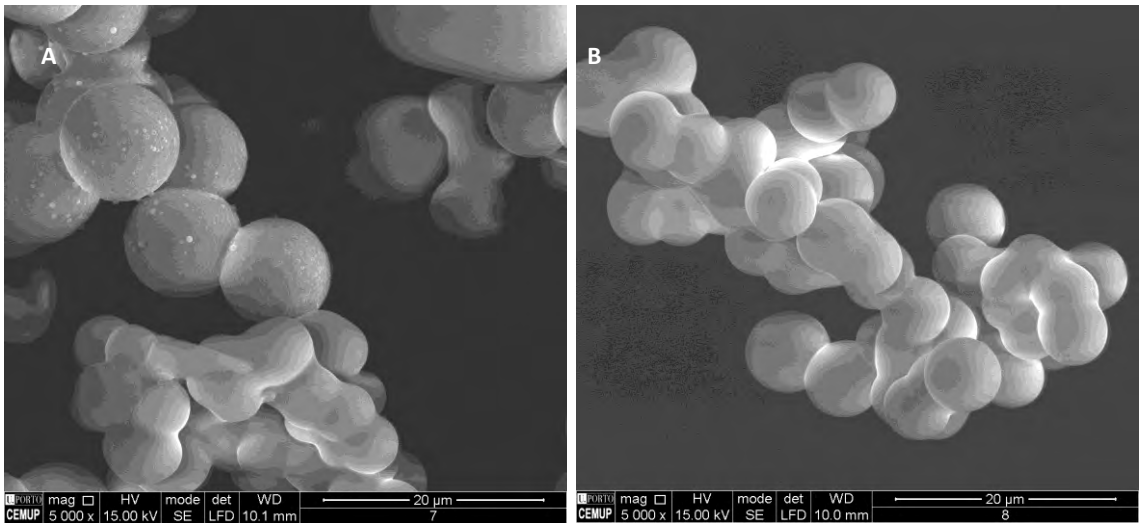


**FIGURE 1**: SEM image of CG_1T_12h A), and CG_1U_12h B).

The prepared hydrochars contained large amounts of oxygen (10 – 23 wt%), nitrogen (5 – 10 wt%), and sulfur (1.5 – 6 wt%) in bulk, and the amounts of N and S were proportional to the quantity of thiourea used. Both carbonization and ball-milling significantly decreased the amounts of S, and O, whereas nitrogen moieties were fairly stable. XPS analysis of the surfaces showed that longer HTC time increased the amount of oxygen on the surface and slightly decreased the amount of sulfur. The doping with urea introduced 5.5 wt% of nitrogen into the surface of the hydrochars. Moreover, the results showed that ball-milling introduced oxygen groups mostly to the surface of the carbons.

The total acidity ($A_{tot}$) of samples was measured using a potentiometric back titration method. The highest $A_{tot}$ of 2.32 mmol$H^+$/g was shown by the unmodified material (i.e., CG) sample. Hydrothermal carbonization of glucose with thiourea for 12 h resulted in the sample with a slightly decreased acidity (2.26 mmol$H^+$/g) compared to CG. The increase of HTC time from 12 to 24 h resulted in the drop of $A_{tot}$ to 1.64 mmol$H^+$/g. The carbonization of the samples, due to removal of the functional groups, decreased the acidity to about 0.03 mmol$H^+$/g in both cases.

The prepared materials were tested in sucrose dehydration to HMF in water, in microwave and batch reactors at 180 °C for 2 h. The highest HMF yield of 35.5% was obtained in the reaction over the catalyst containing the right combination of basic and acidic sites. Moreover, $–SO_3H$ groups were found to be more selective acid sites for fructose dehydration than –OH and –COOH functionalities. The influence of temperature, catalyst loading, and type of atmosphere on the reaction kinetics was studied. The $CO_2$ atmosphere was found to have a negative effect on the selectivity to HMF, whereas similar results were obtained under $N_2$ or air. A simple kinetic model for sucrose dehydration to HMF was developed and fitted using the concentration-time profiles of the substrate and products, agreeing well with the experimental results and helping to elucidate the major reaction pathways for

each catalyst. Within this model, it was shown that HMF is produced mainly via the dehydration of fructose and glucose is mostly converted to side products.

## CONCLUSIONS

Overall, the obtained results showed that sucrose is a promising feedstock for large-scale production of HMF because it is cheap and naturally available unlike fructose and easier to process than sugars obtained from lignocellulosic biomass.

**Acknowledgements**

Financed by projects: Base-UIDB/50020/2020 and Programmatic-UIDP/50020/2020 Funding of LSRE-LCM, funded by national funds through FCT/MCTES (PIDDAC). K.M.E. acknowledges funding from FCT under DL57/2016 Transitory Norm Programme. M.A.C.B. acknowledges Erasmus+ funded by European Union.

**References**

Chen, S., Yu, I. K. M., Cho D-W., Song, H., Tsang, D.C., Tessonnier, W. J.-P., Sik Ok, Y., Poon, C. S. (2018). Selective glucose isomerization to fructose via a nitrogen-doped solid base catalyst derived from spent coffee grounds. *ACS Sustainable Chemistry and Engineering*, 6, 16113–16120. https://doi.org/10.1021/acssuschemeng.8b02752

Chheda, J. N., Román-Leshkov, Y. J., Dumesic, A. (2007). Production of 5-hydroxymethylfurfural and furfural by dehydration of biomass-derived mono- and poly-saccharides. *Green Chemistry*, 9, 342–3502. https://doi.org/10.1039/B611568C

Davidson, M. G., Elgie, S., Parsons, S. T., Young, J. (2021). Production of HMF, FDCA and their derived products: a review of life cycle assessment (LCA) and techno-economic analysis (TEA) studies. *Green Chemistry*, 23, 3154-3171. https://doi.org/10.1039/D1GC00721A

Carbon 2022

# Modelling of dislocations and ripplocations in graphite

**Pavlos Mouratidis[1], James G. McHugh[2,3] and Kenny Jolley[1]**
[1]Department of Chemistry, Loughborough University, Epinal Way, Loughborough, UK, LE11 3TU
Email: P.Mouratidis@lboro.ac.uk

[2]Departnmrnt of Physics and Astronomy, The University of Manchester, Oxford Rd, Manchester, UK, M13 9PL
[3]National Graphene Institute, The University of Manchester, Oxford Rd, Manchester, UK, M13 9PL

**Keywords**
Dislocations, ripplocations, graphite.

## INTRODUCTION

In this work density functional theory (DFT) and molecular dynamics (MD) methods have been employed to investigate the properties of one-dimensional line defects such as basal dislocations and ripplocations. The proposed term *ripplocation* defect derives from its double nature of surface ripple and basal dislocation glide (Kushima, 2015. Gruber, 2016). Properties of these defects such as: formation energies, core widths and heights have been analysed. It has been observed that the energy, width and height of the ripplocations scales sublinearly, compared to quadratic scaling of the dislocations against Burger's vector. While dislocations relax in-plane expanding their core widths to release the strain energy, ripplocations release their strain energy by buckling out-of-plane and by keeping almost the same average bond length throughout the ripple (McHugh, 2021). It has been found that for surface ripples consisting of two or more perfect lattice transitions, ripplocation formation becomes energetically more favourable compared to dislocation (McHugh, 2021). In bulk graphite a defect called *ruck and tuck* (Heggie, 2011) is formed by the progressive pile-up of many more perfect lattice transitions. The formation energy of the ruck and tuck due to the basal dislocation climb and the formation of the almost stable prismatic dislocation loop does not change with increasing material pile-up (McHugh, 2021). The same approach has been extended to two dimensions and new peculiarities of a defect which we call *wrinklocation* have emerged.

## METHOD

Surface ripplocations are initially considered in bilayer graphene, bilayer hBN and bilayer $MoS_2$. We have employed the DFT method to optimise these structures. The supercells are created by the addition of extra material in the top layer of each bilayer structure, while the bottom layer has been held fixed. The ripplocation number, $n=b/b_0$, (where $b_0$ is the magnitude of a perfect Burger's vector equal to one periodic lattice transition, while b is the magnitude of multiple Burger's vectors in the pile-up, $b=b_0$, $2b_0$, *etc*) is a distinctive property, which constitutes to several extra unit cells or Burger's vectors on the top layer. In fig 1 (a) an example of optimised in DFT bilayer graphene supercells up to n=4 can be seen. In fig 1 (b) the same approach has been applied to hBN bilayer and $MoS_2$. It can be seen that the formation energy is sublinear against n. In fig 1 (c) the same approach extended to bulk graphite, where for $n<3$ the graphene layer is buckled, for $n>3$ it forms a stable ruck and tuck defect and the formation energy becomes almost constant, fig 1 (d).

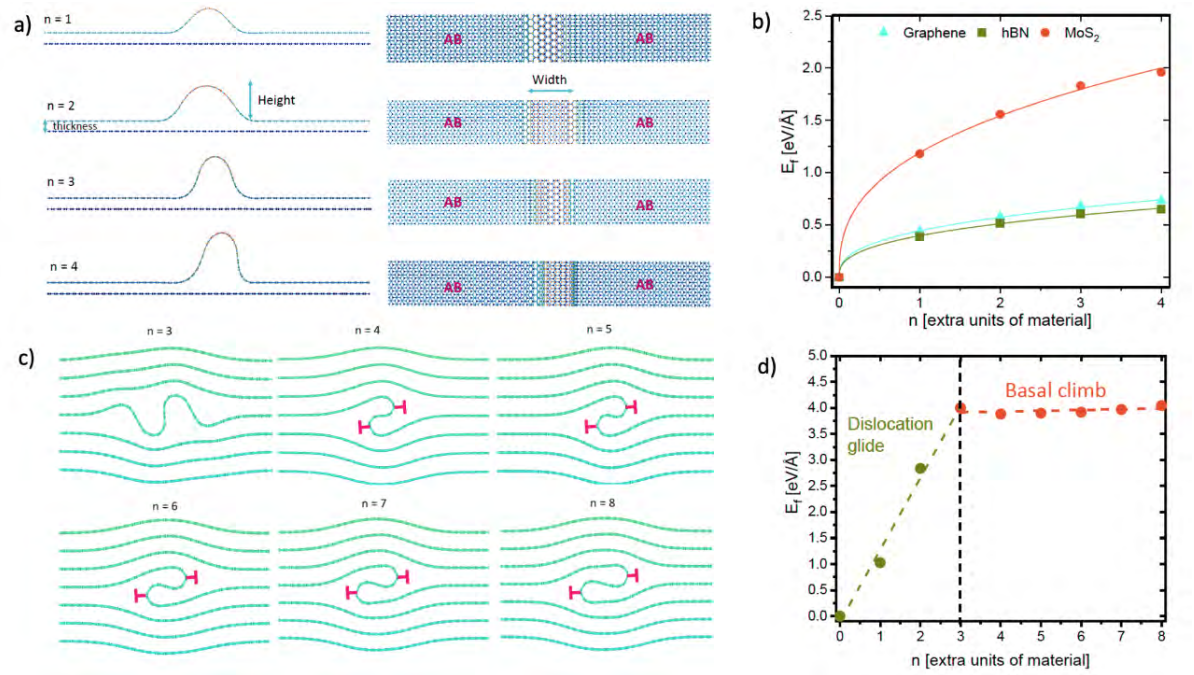


**FIGURE 1**: (a) Supercells of surface ripplocations in bilayer graphene created by the addition of an extra unit cell of material to the top layer optimised in DFT. For the n = 1, width of the ripple is 1.9 nm and height 1.1 nm, n = 2 width is 2.3 nm and height 1.4 nm, n = 3 width is 2.1 nm and height 1.6 nm, n = 4 width is 1.9 nm and height 1.8 nm. (b) Compared to dislocations, the formation energy of ripplocations follows a sublinear scaling against extra material or Burger's vector for all layered materials. (c) Supercells of bulk ripplocations in graphite optimised in MD. Pile-up for different values of additional material n, in a single graphene layer of bulk graphite, resulting in the ruck and tuck defect structure. The ruck and tuck defect structure at n = 4 forms a stable dipole of a prismatic dislocation loop. (d) Dislocation glide - ruck and tuck defect formation energy showing a basal climb after n=3.

**RESULTS**

Extending the model discussed above to two dimensions, a defect which we call wrinklocation can be defined. In that case there is a double in-plane number of [n,m] extra unit cells of material. In case of bilayers these types of defects create superlattice-like twisted bilayer structures (Lu, 2013). This introduces rotational disorder by creating patterns of partial dislocation networks consisting of AA stacked dislocation nodes and transitions from AB to AC stackings, fig 2 (a).

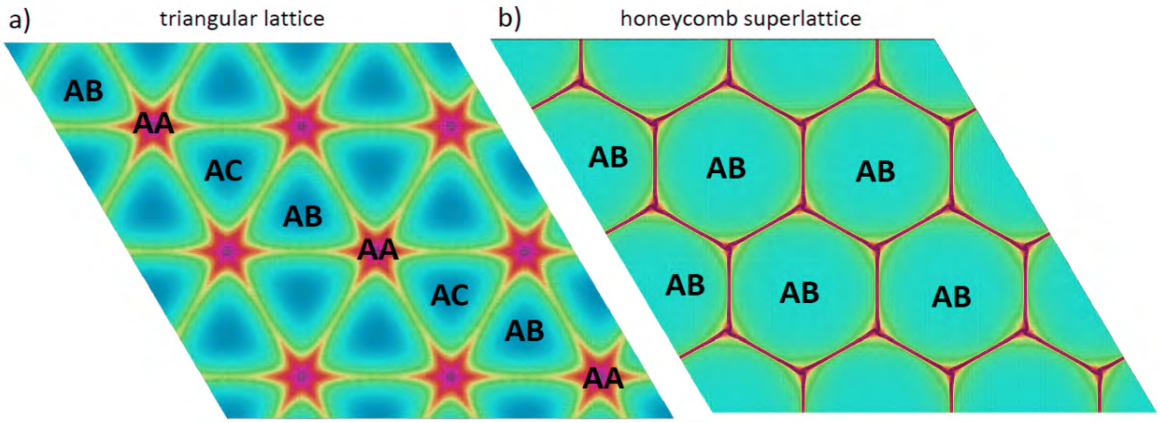


**FIGURE 2**: (a) Illustration of an optimised in MD bilayer graphene triangular supercell of [1,1] additional unit cells creating a Moiré like pattern of partial basal dislocation networks transitioning from AB to AC staking through the AA stacking. (b) Illustration of optimised [5,5] supercell of extra unit cells resulting in a honeycomb like superlattice of ripplocation networks meeting at wrinklocation nodes.

In fig 2 (b) the [5,5] the supercell relaxed into a graphene-like honeycomb superlattice, where ripplocation networks join at three folded nodes, which are the actual wrinklocation defects. In figure 3 (a), the optimised geometries of [1,1] to [20,20] supercells are presented (n=m). All supercells up to [4,4] relaxed into partial dislocation networks while the formation energy is quadratic against [n,m]. After that point the supercells relaxed into graphene-like superlattices, and the formation energy becomes sublinear.

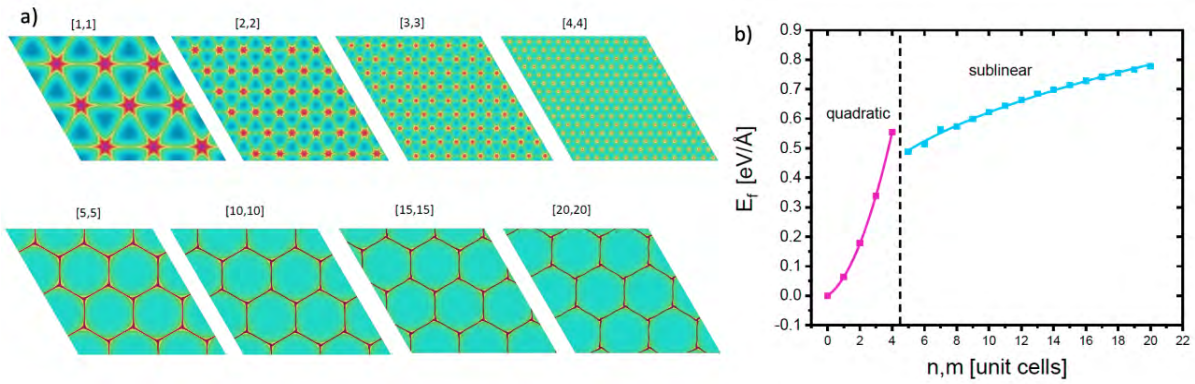


**FIGURE 3**: (a) Illustration of optimised bilayer graphene supercells in MD of [1,1] extra unit cells up to [20,20]. After the [4,4] extra unit cells, the optimised supercells transition to a honeycomb-like superlattices of ripplocations meeting at wrinklocation nodes. (b) Formation energy vs extra unit cells of material [n,m]. The transition between the triangular lattice and honeycomb-like superlattice phase happens between [4,4] and [5,5]. For the triangular phase the energy dependence is quadratic due to the presence of partial dislocation networks, while for the superlattice phase the energy becomes sublinear.

## CONCLUSIONS

The ruck and tuck defect proposed by Heggie (2011) has been observed in irradiated graphite by means of transition electron macroscopy in 2020 (Johns, 2020). This is strong evidence that these type of line defects exist in graphite and could play a vital role in developing new models for the radiation-induced dimensional change of nuclear graphite. Dislocations and ripplocations nucleated by irradiation rapidly propagate into the bulk, due to the strong in-plane bonding the in-plane strain induces out-of-plane buckling.


### Acknowledgements

P. Mouratidis and K. Jolley acknowledge funding from EDF Energy, and the UK EPSRC grant EP/V050281/1. J. G. McHugh acknowledges the UK EPSRC grant EP/R005745/1. All authors acknowledge the HPC Midlands facility at Loughborough University, funded by EPSRC grant EP/P020232/1.


### References


Gruber, J., Lang, A. C., Griggs, J., Taheri, M. L., Tucker, M. L., Barsoum, M. W. Evidence for Bulk Ripplocations in Layered Solids. (2016). *Sci. Rep.* 6, 33451. https://doi.org/10.1038/srep33451

Heggie, M. I., Suarez-Martinez, I., Davidson, C., Haffenden, G. (2011). Buckle, ruck and tuck: A proposed new model for the response of graphite to neutron irradiation. *Journal of Nuclear Materials* 413, 3, 150-155. https://doi.org/10.1016/j.jnucmat.2011.04.015

Johns, S., He, L., Kane, J. J., Windes, W. E., Ubic, R., Karthik, C., (2020). Experimental evidence for 'buckle, ruck and tuck' in neutron irradiated graphite. *Carbon* 159, 15, 119-121 https://doi.org/10.1016/j.carbon.2019.12.028

Kushima, A., Qian, X., Zhao, P., Zhang, S., Li, J. (2015). Ripplocations in van der Waals Layers. *Nano Lett.* 15, 2, 1302–1308. https://doi.org/10.1021/nl5045082

Lu, C. C., Lin Y. C., Liu, Z., Yeh, C. H., Suenaga, K., Chiu, P. W. (2013). Twisting Bilayer Graphene Superlattices. *ACS Nano* 7, 3, 2587–2594. https://doi.org/10.1021/nn3059828

McHugh, G. J., Mouratidis, P., Jolley, K. (2011). Ripplocations in layered materials: Sublinear scaling and climb. *Phys.Rev. B* 103, 195436. https://doi.org/10.1103/PhysRevB.103.195436

20 C 22 arbon 2022

# Title of Paper: Understanding the X-ray and Raman Signatures of Cellulose-Derived Carbons

**Petros k. Mubari[1,2], Théotime Beguerie[2], Marc Monthioux[1], Elsa Weiss-Hortala[2], Ange Nzihou[2], and Pascal Puech[1]**

[1]Centre d'Elaboration des Matériaux et d'Etudes Structurales (CEMES), CNRS, Université de Toulouse, 29 Rue Jeanne Marvig, CEDEX 04, 31055 Toulouse, France
Email: petros.mubari@mines-albi.fr

[2]IMT Mines Albi, UMR CNRS 5302, Centre RAPSODEE, Campus Jarlard, Université de Toulouse, CEDEX 09, 81013 Albi, France

**Keywords**
Carbonisation ; X-Ray Diffraction ; Raman.

## INTRODUCTION

In graphenic carbon materials, the apparent sizes of the average crystallite determined by X-Ray Diffraction (XRD), $L_a$ (in-plane size), and $L_c$ (size along the stacking of graphenes), are usually used to denote the degree of order. With disordered graphenic carbons, the presence of cross-linking chemical functions in the organic precursor hinders the alignment of polyaromatic molecules during primary carbonisation. The coherent graphene stacks (crystallites) remain with small $L_a$ and are misoriented with respect to each other, which makes the material unable to acquire the graphite (Bernal) structure, even if heat-treated at graphitisation temperature. In some poorly organised carbons, such as from cellulose, an XRD peak may appear below the inter-graphene diffraction peak, the origin of which has not yet been understood in the literature. The crystallinity of carbon materials has been increasingly determined by Raman spectroscopy as an alternative to XRD. It is not of common knowledge that, despite the parameter name being the same, these techniques do not measure the same $L_a$. It is, therefore, important to compare and discuss what the differences are.

## EXPERIMENTAL

Two test samples of cellulose carbonised at 1000 and 1800 °C at a heating rate of 2 C°/min were investigated by conjugating the outcomes from XRD, Raman spectroscopy, and high-resolution transmission electron microscopy (HRTEM), because they were identified as milestone samples in the course of carbonisation, with interesting differences.

Raw XRD diffractograms exhibit an intense background, presumably due to a variety of X-photon interactions with the matter (Compton effect, absorption, polarization, etc.). Hence, they were treated for removing the background using continuously decreasing functions, which is a routine procedure for X-ray pattern analysis. The resulting diffraction profiles obtained from experiments were fitted using a pseudo-Voigt function for the peaks appearing at $2\theta \approx 13°$ and $2\theta \approx 24°$, and specific parameterised functions were used for the peaks at $2\theta \approx 43°$ and $2\theta \approx 80°$ in MATLAB® (Puech,2019). The interplanar spacing was calculated using the $2\theta \approx 24°$ peak position labelled 001. We decided to use this notation 001 because the material remained turbostratic, whereas both 002 and 003 were only valid for the Bernal and rhombohedral graphite structures, respectively. The graphenic crystallite sizes $L_c$ was directly obtained from the Scherrer equation applied to the 001 peak. $L_a$ (pertaining to the 10 asymmetric band for turbostratic carbons) and were obtained as a

parameter of the parametrised function. We simulated the diffraction patterns for small graphene stacks (turbostratic) with $L_a$ = 0.7, 1, 2, and 3 nm, with the number of layers ranging from 1 to 5.
For Raman Spectroscopy, the experimental spectra were fitted with a D band which was decomposed in two contributions and a G band for obtaining accurate values for the respective intensities as well as the linewidths.

**RESULTS AND DISCUSSION**

Considering different scenarios and modelling the XRD diffractogram in each case, we find a consistent explanation of the additional peak at 2θ ≈ 13°. This peak, as shown by our modelled spectra, designated in this study as small graphene–crystallite (SGC) peak, is not a mark for amorphous carbon, but a mark of poorly organised graphenic carbon (i.e., with low nanotexture). It is specifically due to crystallites involving an odd but limited number (typically three) of carbon layers with $L_a$ in the range of 1–2 nm. It does not mean that this presence is exclusive, and crystallites with an even number of layers (two and four) may be present as well, although destructive interference effects do not allow them to contribute to this peak.

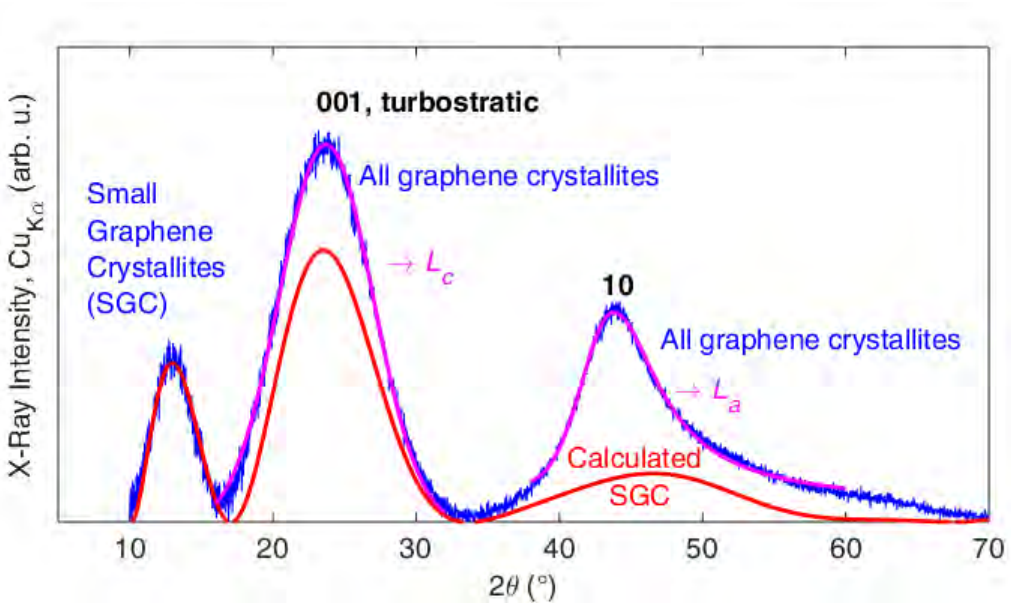


**FIGURE 1**: Calculated X-ray diffraction pattern (red curve) and experimental pattern (blue curve) after background removal normalised to the small graphene crystallite (SGC) peak (blue, noisy line). The position of the SGC peak is dependent on $L_a$.

The XRD profiles of the carbonised cellulose samples differ in the background intensity upon temperature increase. It is worth noting that the decrease in the background intensity is consistent with the assignment of at least part of the background to disorder, as claimed by (Kang, 2018), as it is expected that disorder decreases as the carbonisation temperature increases. $L_a$ increase with increasing the carbonisation temperature from 1.85 to 3.22nm.
With Raman spectroscopy, the $L_a$ values obtained from the intensity ratio ID/IG are in the order of 1.42 (Ferrari,2000) and 2.45 nm (Tuinstra, 1970) at 1000 and 1800 ◦C, respectively, whereas the $L_a$ values derived from the confinement model using FWHMD (Puech,2016) are much higher with a factor of 2 and 3.5, respectively. Although $L_a$ is an important indicator of the development of the graphenic domains, none of the $L_a$ obtained should be taken as a universal value because the different techniques do not measure the same feature. $L_a$ obtained from XRD is strictly dependent on the planarity of the graphene. Moreover, we showed that several sizes are visible in the X-ray diffraction patterns. Hence, it is a direct measurement of the average in-plane dimension of the parallel coherent graphene stacks (the genuine crystallites). Should a defect be present in the in-

plane graphene lattice while not deforming significantly the orientation of the graphene involved (as for defects such as 5–7 pairs or vacancies for instance), the $L_a$, as seen by XRD, will not be affected. For the Raman, the "$L_a$" designation, which is initially a crystallographic term, is not appropriate. $L_a$ from Raman not only depends on the in-plane graphene dimension (which is inversely proportional to the number of peripheral defects), but also on the occurrence of local defects dispersed throughout the graphene lattice. The more defective the cellulose-derived carbons are, the more broadened the D band becomes. However, this is not always true in terms of intensity due to the resonance effect and change in behaviour around $L_a$ = 2 nm. The higher $L_a$ values obtained from Raman (through the confinement model) with respect to XRD are a result of the overall presence of distortions in the graphenes at 1000 °C, followed by the structural improvement in the graphene sheets due to the healing of local (in-lattice) defects, to which the Raman signal is sensitive whilst the XRD signal is not (or less). $L_a$ obtained from the intensity ratio ID/IG give values closer to that from XRD than the confinement model. This can be understood as follows: correlations between $L_a$ and ID/IG are based on several kinds of samples from various origins and treatments, with $L_a$ determined by X-ray diffraction, leading to an average behaviour, eventually not suitable for a specific series of materials. On the contrary, the confinement model (Puech,2016) does not use XRD data, and was based on studying a homogenous sample series. However, even if other models (Cançado, 2017) now also propose to correlate ID/IG, and the FWHMs of D and G as the confinement model did, no model can account for all the Raman spectra available in the literature so far.

## CONCLUSIONS

The arguments developed in this talk explain which characteristics are deduced from the signal obtained by each of the characterisation techniques, how they are related to physics phenomena, and in which way they differ from each other; hence, our conclusions are quite general and, therefore, are valid for all kind of graphenic materials. An important conclusion of the work is that the XRD peak corresponding to a scattering angle of ~13 (Cu X-ray source), the origin of which was not understood in the literature so far, is now fully explained.

**Acknowledgements**

This work was funded by a Université Fédérale de Midi-Pyrénées scholarship, the French "Programme Investissements d'Avenir" (ANR-10-LABEX-22-01 SOLSTICE grant) is acknowledged for its support in the work on cellulose carbonisation. We thank N. Ratel-Ramond for his help in X-ray diffraction experiments.

**References**

Cançado, L.G.; Da Silva, M.G.; Ferreira, E.H.M.; Hof, F.; Kampioti, K.; Huang, K.; Jorio, A. Disentangling contributions of point and line defects in the Raman spectra of graphene-related materials. 2D Mater. 2017, 4, 025039.

Ferrari, A.C.; Robertson, J. Interpretation of Raman spectra of disordered and amorphous carbon. Phys. Rev. B 2000, 61,14095–14107. https://doi.org/10.1103/PhysRevB.61.14095

Kang, D.S.; Lee, S.M.; Lee, S.H.; Roh, J.S. X-ray diffraction analysis of the crystallinity of phenolic resin-derived carbon as a function of the heating rate during the carbonization process. Carbon Lett. 2018, 27, 108–111.

Puech, P.; Plewa, J.-M.; Mallet-Ladeira, P.; Monthioux, M. Spatial confinement model applied to phonons in disordered graphenebased carbons. Carbon 2016, 105, 275–281. https://doi.org/10.1016/j.carbon.2016.04.048

Puech, P.; Dabrowska, A.; Ratel-Ramond, N.; Vignoles, G.L.; Monthioux, M. New insight on carbonisation and graphitization mechanisms as obtained from a bottom-up analytical approach of X-ray diffraction patterns. Carbon 2019, 147, 602–611. https://doi.org/10.1016/j.carbon.2019.03.013

Tuinstra, F.; Koenig, J. Raman Spectrum of Graphite. J. Chem. Phys. 1970, 53, 1126–1130. https://doi.org/10.1063/1.1674108

Carbon 2022

# Synthesis of Novel Carbon Gel Microhoneycombs Using Stereolithographically Printed Templates

**Shin R. Mukai[1,2], Takuya Sugawara[2] and Shinichiroh Iwamura[1,2]**
[1]Faculty of Engineering, Hokkaido University, Sapporo, Japan
Email: smukai@eng.hokudai.ac.jp

[2]Graduate School of Chemical Sciences and Engineering, Hokkaido University, Sapporo, Japan

**Keywords**
Microhoneycomb, Carbon Gel, Stereolithography

## INTRODUCTION

A microhoneycomb, a monolith having straight and aligned microchannels within it, is one example of an ideal morphology for porous materials, as the trade-off relationship between inner-accessibility and resistance against fluid flows can be avoided. Although it was not quite easy to mould porous materials into such a microstructured monolith, the authors previously showed that sol-gel derived materials could be moulded into the form of a microhoneycomb by freezing their precursor hydrogels unidirectionally (Mukai et al., 2004). We also showed that sol-gel derived monoliths with a similar structure can be obtained using thermoplastic fibers as a sacrificial template (Takahashi et al., 2019). Both methods allow the easy synthesis of microhoneycombs, but the flexibility of the dimensions of microhoneycombs obtained through both methods is quite limited.

In this work, we attempted to develop an easy and versatile method to synthesize microhoneycombs of porous carbons. Our idea was to use a stereolithography 3D printer to print the sacrificial template needed for moulding. If a UV-curable and thermally degradable resin is used for template printing, it is expected that the template can be easily removed during carbonization and voids with a structure identical to the template will be left behind.

## EXPERIMENTAL

Templates needed to synthesize cylindrical microhoneycombs were 3D printed using commercially available inks, and a specially formulated ink. The obtained templates were set in properly sized tubes, and a RF sol prepared from resorcinol, formaldehyde and water using sodium carbonate as the catalyst was introduced into the tubes. After the sols transformed into monolithic gels, the monoliths were removed from the tubes and were freeze-dried. Template removal and carbonization of the monoliths were conducted simultaneously by heating the samples up to 1273 K in vacuum. Part of the monoliths were activated using $CO_2$.

The morphology of the obtained microhoneycombs was examined using a scanning electron microscope. Porous properties of the obtained monoliths were evaluated through nitrogen adsorption experiments. The hydraulic resistance the microhoneycombs cause was evaluated by measuring the pressure drop which occurs when water was passed through the microhoneycombs.

## RESULTS AND DISCUSSION

Templates printed using commercially available inks were difficult to remove, and most of the microchannels of the resulting microhoneycombs were blocked by residues originating from them. Therefore, an ink that allows accurate printing of a template which hardly leaves residues behind

when thermally treated was specially formulated by carefully selecting the monomer, photoinitiator and UV-absorption enhancer which compose it.

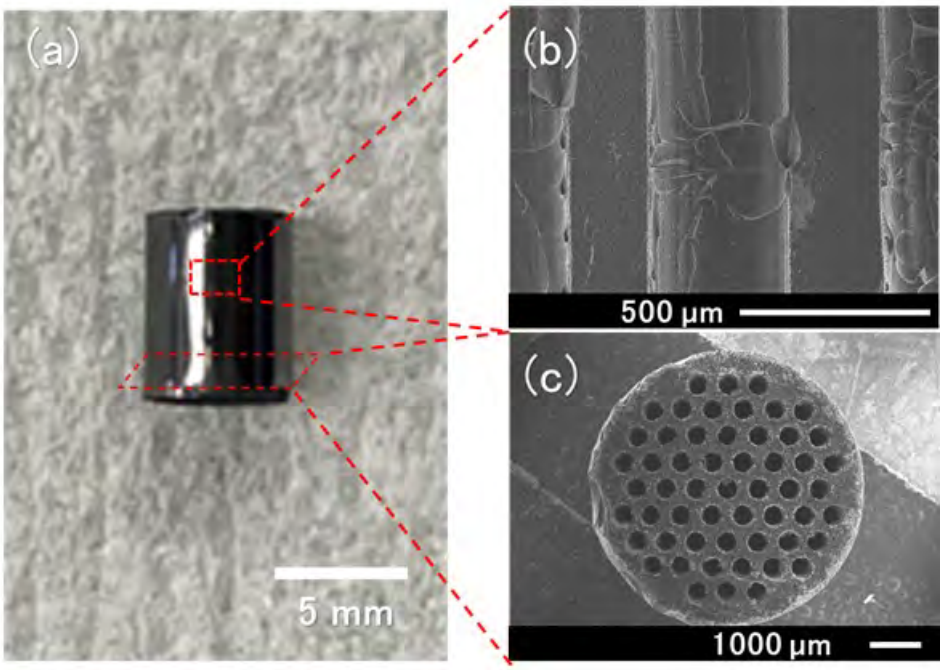


FIGURE 1: (a) Photograph, (b) vertical-sectional micrograph and (c) cross-sectional micrograph of a typical carbon gel microhoneycomb

Figure 1 shows a photograph and micrographs of a typical carbon gel monolith obtained using the template printed from the developed ink. It can be confirmed that the carbon gel was successfully moulded into the form of a microhoneycomb. The diameter of the cylinders which configure the template, and the distance between the cylinders could be reduced to about 100 µm, indicating that microhoneycombs having a channel size, and channel wall thickness both about 100 µm can be easily obtained.

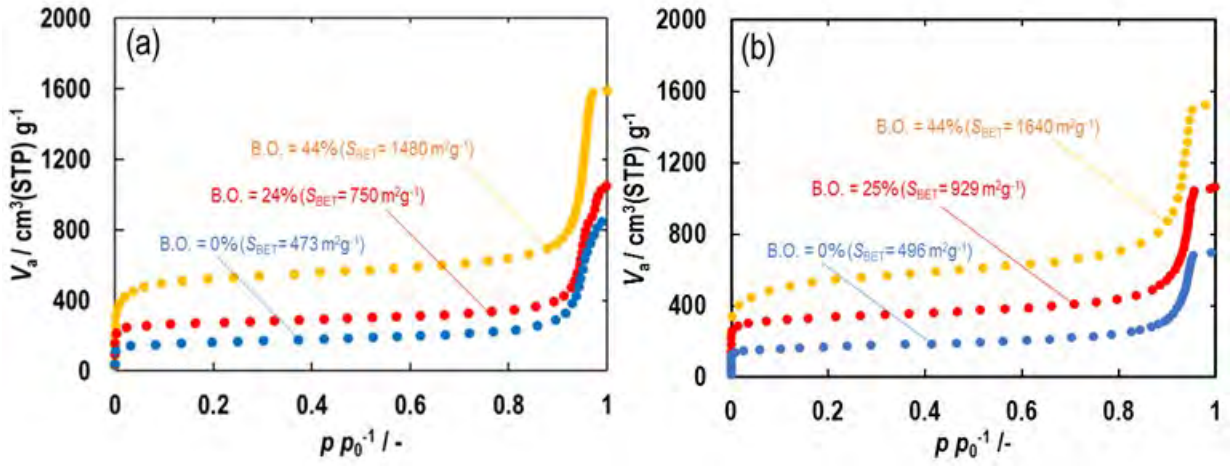


FIGURE 2: Nitrogen adsorption isotherms of typical samples
((a) carbon gel microhoneycombs, (b) carbon gel particles)

Figure 2 shows nitrogen adsorption isotherms of carbon gel microhoneycombs activated to different degrees. Those of carbon gels synthesized from an identical starting solution but in the form of particles are also shown for comparison. Slight differences can be observed, but it was confirmed

that the microhoneycombs have the micro/mesoporosity which is characteristic of conventional carbon gels. Therefore, the obtained microhoneycombs have a unique hierarchical pore system of micro-, meso- and macropores (microchannels of the microhoneycomb) similar to microhoneycombs obtained through previously developed methods.

Through pressure drop measurements, it was confirmed that the resistance a microhoneycomb causes is much lower than that a column packed with particles having the same diffusion path length as the microhoneycomb causes. Therefore, it was confirmed that short diffusion path lengths and a low resistance against fluid flows are also compatible in microhoneycombs obtained through the developed method.

## CONCLUSIONS

Through this work, it was confirmed that monolithic microhoneycombs can be easily obtained using templates printed using a stereolithography 3D printer.

**Acknowledgements**

A part of this work was supported by the Japan Society for the Promotion of Science (JSPS), Grant-in-Aid for Scientific Research (B) 19H02503(2019) and 22H01854(2022).

**References**

Mukai, S. R., Nishihara, H. and Tamon, H. (2004). Formation of monolithic silica gel microhoneycombs (SMHs) using pseudosteady state growth of microstructural ice crystals. *Chem. Commun.*, 874-875. https://doi.org/10.1039/b316597c

Takahashi, K., Yoshida, S., Urkasame, K., Iwamura, S., Ogino, I. and Mukai, S. R. (2019). Carbon gel monoliths with introduced straight microchannels for phenol adsorption. *Adsorption*, 25, [6], 1241-1249. https://doi.org/10.1007/s10450-018-00007-z

Carbon 2022

# Electrocatalytic activity of carbon materials from varied origins for the production of $H_2O_2$

**M.Muñoz Morales[1,2] J.Llanos[2] and Conchi Ania[1]**
CEMHTI, CNRS (UPR 3079), Université d'Orléans, 45071 Orléans, France
.
Email: Martin.Munoz@uclm.es

[2]Department of Chemical Engineering. Faculty of Chemical Sciences & Technologies. University of Castilla La Mancha. Campus Universitario s/n 13071 Ciudad Real

**Keywords**
Electrocatalytic activity, cathode carbon materials, hydrogen peroxide

## INTRODUCTION

Hydrogen peroxide is a chemical widely produced because of their strategic relevance in many industrial sectors such as the paper and pump industry, chemical synthesis, textile, and water treatment, among others ( C. W. Jones and J. H. Clark, 1999).

Concerning of environmental applications, $H_2O_2$ is a mild oxidant and, upon activation, generates reactive oxygen species that let us to degrade many refractory pollutants. Recently, in-situ production of $H_2O_2$ were carried out using an electrochemical cell through the $2e^-$ oxygen reduction reaction (ORR) at room temperature and atmospheric pressure. Role of the cathode material is essential in this process to avoid competitive reactions and possible mass-transfer limitations.

For this application many carbon-based electrodes have been tested considering their unique structure and electronic properties, such as graphite felt (Özcan, Şahin et al., 2008) reticulated vitreous carbon (Ramírez-Pereda, Álvarez-Gallegos et al., 2018), activated carbon or carbon paper (Li, Song et al. 2019), with different advantages and disadvantages. Among them, the use of hydrochars has been explored because they have shown potential to transform biological wastes into a substitute for petroleum-based electrodes and catalyst supports. Besides, hydrothermal carbonization is carried out at low temperature than pyrolysis without any drying step. Some efforts have also been carried out to study the influence of their structural characteristics as porosity, electrical conductivity and surface functionalization on different applications of carbon materials but there is still a lack of understanding on the correlation between the physicochemical and structural characteristics of carbon materials and their electrocatalytic capacity in the electrochemical generation of hydrogen peroxide (Nair, Kumaravel et al., 2021).

In view of above, the aim of this work was to perform a screening of carbon cathodes showing varied composition and varied electronic, porous and structural properties, for the electrochemical production of $H_2O_2$, including those that come from phytoremediation wastes that contain metallic ions (Cd, Pb, Zn, Cu) that could have catalytic interest. They were selected based on their different structural and textural properties. Furthermore, electrocatalytic performance was evaluated on relatively large (i. e. 2 cm x 2 cm) cathodes, higher than most studies from the literature reporting adequateness of carbon materials for this application.

## MATERIALS AND METHODS

A series of carbon materials was used for the fabrication of the cathodes covering graphite, carbon black, graphene and derivatives, carbon nanotubes and nanofibers, petroleum coke and nanoporous carbons. Catalytic inks were elaborated based on these materials to be casted on carbonaceous supports. Samples of hydrochars from biomass were synthesized at 200 °C using a ratio of 166 g/mL,

washed several times with warm water and dried at 80 °C. Then, further activation of hydrochars were carried out with a thermal activation via pyrolysis.
The selected carbon materials were thoroughly characterized using various techniques (e.g., gas adsorption isotherms, elemental analysis, Raman spectroscopy) to evaluate their physicochemical and structural features.
A preliminary electrochemical characterization of carbon powders was carried out with a linear sweep voltammetry (LSV) using a glassy carbon electrode (GCE, 5.0 mm diameter, Goodfellow, UK) as support. Linear sweep voltammetry (LSV) was recorded by a potentiostat (BioLogic) at a scan rate of 10 mV $s^{-1}$ in a three-electrode configuration, the prepared X/GC electrodes were used as working electrodes, a graphite rod (ca. 0.385 $cm^2$) as counter and saturated calomel electrode (SCE) as reference electrode. LSV was ranged from 0.2V to -1.2V vs SCE to covering the specific potential in which $H_2O_2$ is theoretically produced.
For the electrocatalytic assay for hydrogen peroxide generation, a 2 x 2 $cm^2$ Toray carbon paper (TGPH-120, thickness 0.19 mm) was used as electrode substrate as shown in the figure 1. These electrodes were labelled as X/TP.

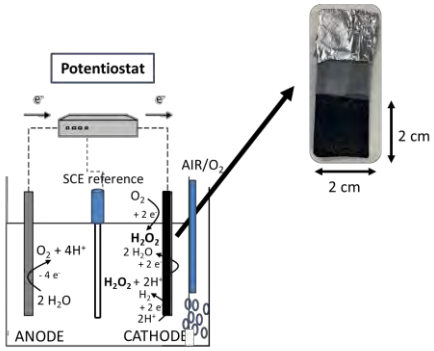


**Figure 1.** Electrochemical undivided cell for $H_2O_2$ production. (Cathode: Toray paper 4 $cm^2$ ; Anode: graphite rod 4.2 $cm^2$ and Reference electrode: SCE. Potentiostatic mode: -0.9 v vs SCE 0.05M $Na_2SO_4$ as electrolyte.

The production of $H_2O_2$ was performed in an undivided cell (0.1L) at room temperature, using 0.05 M $Na_2SO_4$ as electrolyte. The 2 x 2 $cm^2$ Toray papers with the catalytic inks were used as cathode, and a graphite rod as anode (active surface 4.2 $cm^2$). The electrolysis was done in a potentiostatic mode, with an applied potential of -0.9 mV vs SCE using a potentiostat/galvanostat. A continuous supply of oxygen was applied by bubbling air under stirring using a magnetic bar. The concentration of $H_2O_2$ was measured by following the concentration of the complex formed between $H_2O_2$ and $Ti^{4+}$ measuring the absorbance at 408 nm on a spectrophotometer (Pérez, Galia et al., 2017).

**RESULTS AND DISCUSSIONS**

To start with, Van Krevelem diagram of the selected carbons provided a helpful group classification of carbon materials in connection with their origin, and compositional evolution (thermal history) according to their atomic H/C and O/C ratios. Lower H/C and O/C ratios indicate a high degree of aromaticity and low polarity, so that higher electronic conductivity is expected and at converse, high H/C and O/C ratio indicate lower aromaticity due to functionalization. Thermogravimetric analysis were assessed with hydrochars to determine main components obtained after thermal treatments proposed.
LSVs were carried out with glassy carbon cathodes in $O_2$-saturated electrolyte in a stirred cells and in He-saturated electrolyte to observe the influence of availability of oxygen in the cathodic reduction peaks with different materials tested. As expected, better results were obtained with oxygen using activated carbon and nanocarbons casted on GC. Then, these experiments were carried out in 2 x 2 Toray Paper electrodes to confirm the production of $H_2O_2$ measuring their concentration.
The influence of electrocatalytic properties of carbon materials on their structural and textural properties shows a complex effect on microporosity because it helps to generate hydrogen peroxide

thanks to the presence of triple electrolyte/electrode/oxygen interfaces. Relevance of electrical conductivity was confirmed because their higher values reduced ohmic losses during the process and also the generation of byproducts. Thermal treatments carried out with hydrochars obtained from biomass wastes showed that both conductivity and current efficiency increase to generate $H_2O_2$ more efficiently. However, similar results were observed for non-conductive materials and low conductive materials (≈ 40 %) so also structural order of carbons were evaluated with Raman spectroscopy to identify their relationship with the rest of properties. Results were compared with carbon felts that commonly were used for this application and finally the evaluation of energy consumption of these electrodes with the catalytic ink and carbon felts indicated a reduction higher than 50 % in the overall electric power consumed.

## CONCLUSIONS

From this work, the following conclusions can be drawn:

- Current efficiency of carbon materials casted on Toray Papers is ranged between 0.3 and 0.8 and their efficiency is higher than the use of conventional carbon felt.
- Biomass-derived hydrochars can be a real sustainable alternative to modify the surface of carbonaceous electrode to electrochemically produce $H_2O_2$.
- Any parameter seems to be 'critical' in this process but the relationship between all of them showed an improvement of $H_2O_2$ production with carbon nanotubes and carbon nanofibers casted on TP.

**Acknowledgements**

Financial support from the Region Centre Val de Loire (APR-IA, PRESERVE grant), Junta de Comunidades de Castilla-La Mancha´s (project SBPLY/19/180501/000254) and the Spanish Ministry of Science and Innovation through (project PID2019-107282RB-I00) is acknowledged.

**References**

Applications of Hydrogen Peroxide and Derivatives. (1999) C. W. Jones and J. H. Clark, The Royal Society of Chemistry**:** 1-264. https://doi.org/10.1039/9781847550132

Li, J., D. Song, K. Du, Z. Wang and C. Zhao (2019). "Performance of graphite felt as a cathode and anode in the electro-Fenton process." RSC Advances 9(66): https://doi.org/10.1039/C9RA07525A

Nair, K. M., V. Kumaravel and S. C. Pillai (2021). "Carbonaceous cathode materials for electro-Fenton technology: Mechanism, kinetics, recent advances, opportunities and challenges." Chemosphere 269: 129325.https://doi.org/10.1016/j.chemosphere.2020.129325

Özcan, A., Y. Şahin, A. Savaş Koparal and M. A. Oturan (2008). "Carbon sponge as a new cathode material for the electro-Fenton process: Comparison with carbon felt cathode and application to degradation of synthetic dye basic blue 3 in aqueous medium." Journal of Electroanalytical Chemistry 616(1): 71-78.https://doi.org/10.1016/j.jelechem.2008.01.002

Pérez, J. F., A. Galia, M. A. Rodrigo, J. Llanos, S. Sabatino, C. Sáez, B. Schiavo and O. Scialdone (2017). "Effect of pressure on the electrochemical generation of hydrogen peroxide in undivided cells on carbon felt electrodes." Electrochimica Acta 248: 169-177.https://doi.org/10.1016/j.electacta.2017.07.116

Ramírez-Pereda, B., A. Álvarez-Gallegos, J. G. Rangel-Peraza and Y. A. Bustos-Terrones (2018). "Kinetics of Acid Orange 7 oxidation by using carbon fiber and reticulated vitreous carbon in an electro-Fenton process." Journal of Environmental Management 213: 279-287.https://doi.org/10.1016/j.jenvman.2018.01.022

Carbon 2022

# Manufacture of Carbon Materials with High Nitrogen Content

**Javier Narciso[1,2]*, Manuel Martínez-Escandell[1], Enrique V. Ramos-Fernández [1] and Yuli Betancourt[1]**

[1]Laboratorio de Materiales Avanzados, Departamento de Química Inorgánica, Instituto Universitario de Materiales de Alicante, Universidad de Alicante, Alicante, Spain.
[2]Instituto de Investigación Sanitaria y Biomédica de Alicante (ISABIAL), Alicante, Spain.
Email: narciso@ua.es

**Keywords**
Activated carbon; $CO_2$ adsorption; N-doped porous carbon.

## INTRODUCTION

Carbon foams are very interesting materials since depending on the precursor they can be good insulators or good thermal conductors to be used in active or passive heat sinks. Regarding the foams of great thermal conductivity, they have been developed mainly from Mesophase Pitch. It is well known that synthetic mesophase pitch shows the most ordered graphitic structure, and therefore, will be those that present the greatest thermal conductivity once graphitized. Currently, carbon fibers with thermal conductivity of 1100 W/ mK in the direction of the fiber, called K1100, patented by Professor Isao Mochida, that have been produced from Mitsubishi AR pitch (obtained from naphthalene) can be found in the market. Graphitic foams of great thermal conductivity obtained from the same mesophase pitch by pyrolysis under controlled pressure can also be found in the market. The main problem with this pitch is that during pyrolysis process it suffers an expansion that can reach an increase of volume of 4000%, which must be controlled. In the manufacture of carbon fibers, this is achieved through a stabilization process with air, of the spun pitch, between 150-250ºC, producing cross-linking with oxygen and, therefore, an increase in average molecular weight, preventing the expansion that occurs within pyrolysis process. In the case of carbon foams, they are pyrolysed in a method equivalent to hot-pressing, where it allows an expansion between 50-100%, producing foams with 50 -70% porosity. One problem they present is the fact that the expansion is not totally homogeneous, and there is also a certain orientation of the fluid domains in the direction of the volatiles exit resulting in an anisotropic structure. In the present investigation, a technique similar to the one used with carbon fibers, but in this case the pitch foams will be made by using a Gas Pressure Infiltration technique developed in Alicante for the manufacture of composite materials. The method consists in using a NaCl template, which will later dissolved in water. In this way the foam will be generated. Therefore, pore size can be controlled and porosity volumes between 40 and 70% can be obtained. The average pore size is very important, since it determines the average size of the ligaments, and therefore the time needed for air stabilization. Another important aspect is the rheology of the process, since the pitch is not a Newtonian fluid, the viscosity depends on the shear stress, and this in turn controls the size of the fluid domains. Therefore, the infiltration process must be thoroughly controlled. For this, a previous study of the rheology of the process has been carried out to know the shear stress relationship with the size of the mesophase domains.

## EXPERIMENTAL

Synthetic mesophase pitch obtained by catalytic polymerization of naphthalene (AR24) was kindly supplied by Mitsubishi Gas Chemical Company. This pitch is 100 % anisotropy with at softening point of 292 °C. Steady shear rheology measurements were performed using a Rheometrics RDS II Dynamic Spectrometer. Measurements were made at temperatures in the range of 275 C to 320 C. All steady

measurements were made using cone-plate geometry. The plate diameter was 25 mm and the cone angle 0.1 radians with a 0.05 mm gap. Prior testing, a small cylindrical sample (0.5 cm3) of mesophase pitch was formed by vacuum pelletization.
After quenching the sample was sectioned and mounted in epoxy resin afterwards the sample was polished following the standard metallograpy procedures. The samples were analyzed using a reflected polarized light optical microscope (Olimpus). The microscope has coupled and image analysis (Enterprise 861000). Quantitative assessments of the size of the domains of the mesophase pitch were assessed using a point-counting technique based on 700 points statistically selected.

**RESULTS**

Figure 1 show steady shear flow curves over a range of temperatures for the AR mesophases. This figure clearly represents the Region I and II of the shear behaviour of liquid crystal. In Region I the rheological behaviour of the mesophase in all temperatures followed a power law with an index of 0.5 approximately. These results are consistent with predictions of a model developed by Marrucci for LCPs. Thus Marrucci´s model was used to estimate the average elastic constants of the mesophase pitches, K, based on their flow curves in regions I and II and the quiescent state domain size.

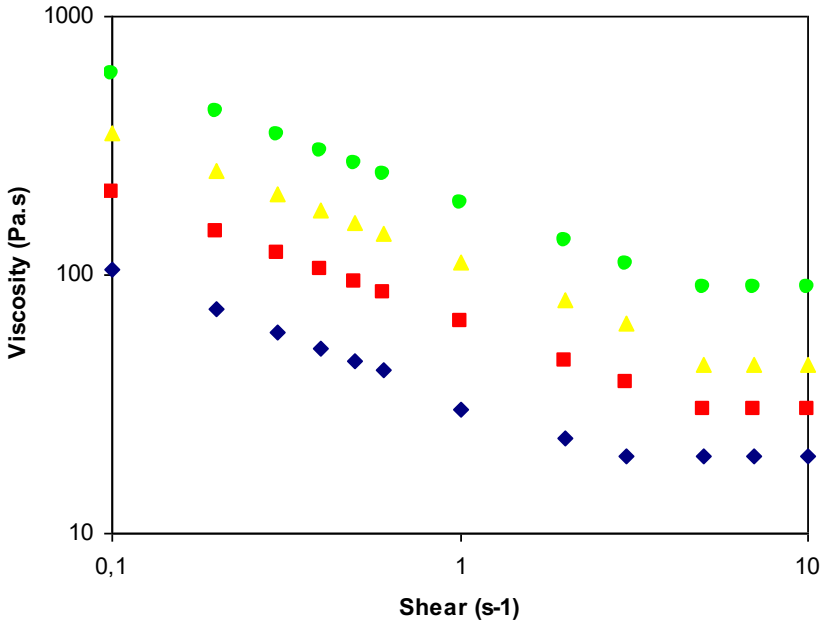


**Figure 1**. Flow curves for AR mesophase as a function of temperature

When the calculated elastic constants we can determine the evolution of the size of the domains of the mesophase pitch at functions of the shear rate. The flow-induces structures and sizes predicted by Marrucci´s model as illustrated in Fig 2. Note that the predictions reported in Figure 2 were computed for the Ar mesophase at 300 ºC. At this temperature, the analysis of the flow curve presented in Fig 2 shows that viscosity in the Newtonian region is 30 Pa·s and the average elastic constant is 1.8 $10^{-8}$ N. The experimental size of the domain in the quiescent state is around 20 microns. The Figure 2 clearly shows the good agreement between the prediction and the experimental results of measure of the domain of the quenching mesophase. To illustrate the evolution Figure 3 shows two pictures of the mesophase shearing at different rate, where, we can observe how decrease the domain when increase the shear rate.

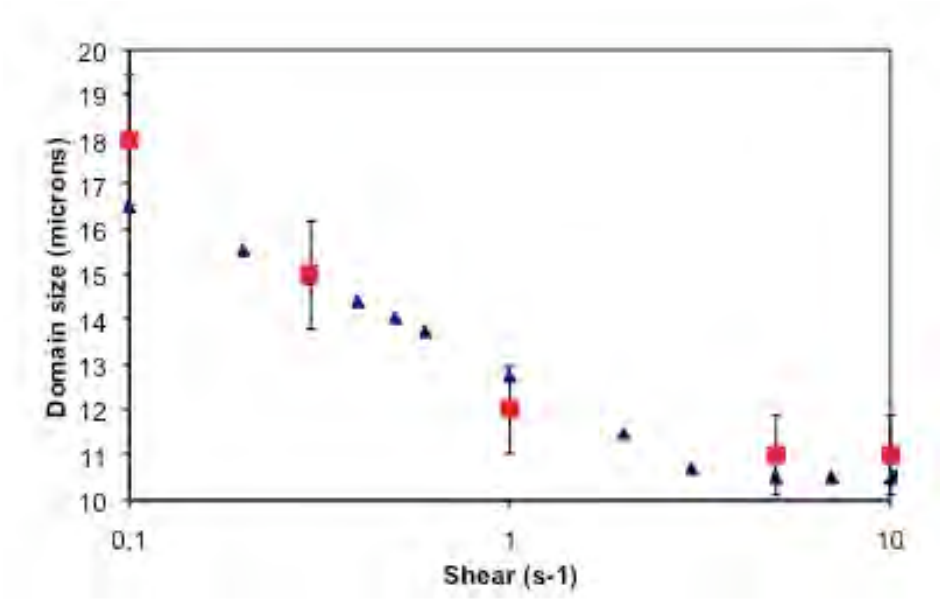


***Figure 2.*** *Comparison of predicted (using Marrucci´s model) and the measured domain size during shear flow of the AR mesophase (at 300 ºC).*

In summary, the steady shear experiments suggested that the mesophase pitches studied exhibited a polydomain structure similar to that many liquids crystalline polymers. The size of this structure decreased as the mesophase pitch was subjected to increasing rates of shear. A model developed by Marrucci was used to estimate the elastic constants of these materials and predict the size of the structure induced by shear flow.

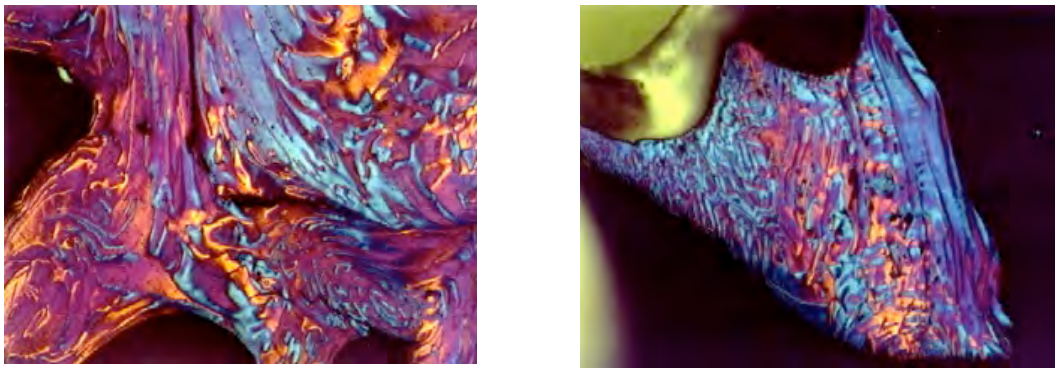

***Figure 3.*** *Evolution of optical texture of the AR mesophase pitch during shear flow at 300 C. a) quiescent state b) after shearing at 10 $s^{-1}$*

**Acknowledgements**
Authors acknowledge financial support by “Ministerio de Ciencia e Innovación” of Spain through the project PID2020-116998RB-I00.

Carbon 2022

# Fabrication of lignin based carbon fibers from wood wastes by electrospinning method

**Nazhipkyzy M.[1,2*] , Maltay A.[1,2] , Sultakhan Sh.[1,2], Assylkhanova D.[1,2], Zhaparova A.[1,2], Issanbekova A.[1,2] , Mansurov Z.[1,2]**

[1]Institute of Combustion Problems, 050012 Almaty, Kazakhstan
[2]Al - Farabi Kazakh National University, 050040 Almaty, Kazakhstan
Email*: meruert82@mail.ru

**Keywords**
Lignin, carbon fibers, electrospinning.

## INTRODUCTION

Lignin is the most abundant aromatic biopolymer, accounting for up to 30% of organic carbon on Earth, and thus can be considered as a potential renewable feedstock for the production of energy supplements and aromatic chemicals (Agarwal, 2005; Barsberg, 2011). Lignin is a natural aromatic polymer, which ranks second after cellulose. Physico-chemical property of the resulting lignin depends on the source, as well as on the extraction method. Lignin is currently used in the production of low-cost carbon fiber. In this work, we synthesized lignin using the organosolv method, this method allows us to obtain high-quality lignin and lower process temperatures with shorter completion time. Synthesized lignin is used to obtain lignin nanofibers by electrospinning. In contrast to the known methods for extracting lignin and methods for obtaining inexpensive electrospun fibers, using this method for synthesizing lignin, continuous fibers with a nanoscale diameter can be obtained.

In the work for the synthesis of lignin, household wood waste is used, as well as agricultural waste (sawdust from unclassified trees). Extraction of lignin from sawdust of unclassified trees was carried out by treatment with a mixture of formic and acetic acids. Electrospinning is a suitable top-down technique for preparing polymer fibers using high voltage electric fields and solutions of a chosen polymer with adequate viscosity and conductivity. The main advantages of the electrospinning method are the simplicity of the process, and the use of high temperatures is also not required (Xiaofei, 2016). Solutions were prepared by stirring until complete dissolution of the components using a magnetic stirrer at 40°C. To achieve a suitable operating condition, the flow rate (0.4 to 0.8 ml/h), distance (10, 15, 18 cm) and voltage (10 to 25 kV) of electrospinning were varied depending on the concentration of lignin. In the process of preparation, the electrospinning solution we can observe that the viscosity changes slowly over time as polyacrylonitrile (PAN) dissolves in added dimethylformamide (DMF). Also the colour gets more uniform over time (becoming slightly darker than initially). The main problem while trying to adjust the perfect concentration of solid phase dissolved in the liquid was to determine the narrow window of viable viscosity.

Infra-Red, nuclear magnetic resonance (NMR) analysis of lignin was performed, as well as, obtained lignin fibers investigated by thermogravimetric (TGA) and energy-dispersive X-ray (EDX) analysis. To determine the surface morphological features of lignin fibers, scanning electron microscopy (SEM) of the Quanta 200i 3D brand (FEI, USA) was used. During SEM, the electron beam is directed to the analyzed sample. As a result of the interaction, low-energy secondary electrons are generated, which are collected by a secondary electron detector. In this way, images of the morphology of the analyzed area of the sample are obtained. SEM images of samples are carried out at the following shooting parameters: accelerating voltage 15 keV, working distance 10 mm. The

elemental composition of nanofibers was also determined by X-ray microanalysis in a scanning electron microscope. Energy-dispersive spectroscopy of samples is carried out at the following shooting parameters: accelerating voltage 20 keV, working distance 15 mm. Figure 1 shows the results of the analysis of lignin fibers by physicochemical methods.

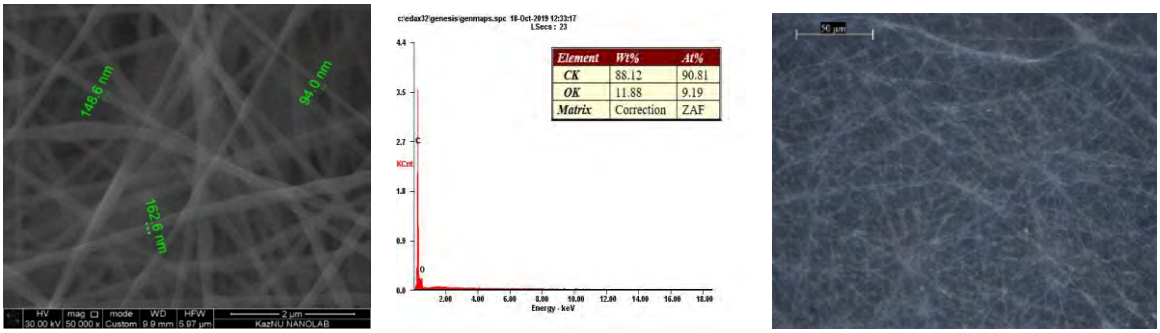


a – SEM image b – elemental analysis c – optical image

**FIGURE 1**: Analysis of the resulting nanofibers by various physicochemical methods

SEM analysis of the samples shows that nanosized fibers are formed at a concentration of 8% PAN polymer in the range from 94 to 162 nm. The acquired fibers have sufficiently low diameter (~ 100 nm) that should become even smaller after the carbonization, which induces that the parameters used in the process of electrospinning are close to being optimal. Elemental analysis results show a carbon content of 88.12%.

## CONCLUSIONS

Summarizing the above, we can conclude that household wood waste, as well as agricultural waste (sawdust from unclassified trees) were used for the synthesis of lignin. Also, a technique has been developed for extracting lignin and obtaining low-cost electrospun fibers from lignin with high performance characteristics that can be used for energy storage systems. Because lignin is an inexpensive, abundant, and green polymer, incorporating it into carbon blends increases the scalability of such materials in energy storage applications.

**Acknowledgements**

This research was supported by the Ministry of Education and Science of the Republic of Kazakhstan in the framework of the project AP08856321.

**References**

Agarwal W.P., Rainer R.S., Pandey A.K., Ralph S.A., Hirt K.S. and Atallah R.H. Raman Spectra of Model Lignin Compounds // 59th Annual Conference and Exhibition of the 13th ISWFPC, Appita Inc. – 2005.

Barsberg S., Larsen L. Environmental Effects on the Lignin Model Monomer, Vanillyl Alcohol, Studied by Raman Spectroscopy // J. Phys. Chem. B 115, 39. – 2011. – P.11470-11480.

Xiaofei Tian, Zhen Fang, Richard L. Smith Jr., Zhenqiang Wu, Mingyou Liu. Properties, Chemical Characteristics and Application of Lignin and Its Derivatives. – 2016. – pp.3-33.

Carbon 2022

# Biomass-derived Carbon Quantum Dots via Continuous Hydrothermal Flow Synthesis for nano-sensing applications

**Kiem Giap Nguyen, Ioan Alexandru Bragau, Suela Kellici, and Tariq Sajjad**

School of Engineering, London South Bank University, 103 Borough Road, London, SE1 0AA

Email: Nguyenk6@lsbu.ac.uk

**Key word**: Biomass, carbon dots, nanosensors.

Carbon quantum dots (CQDs) are derived from biomass that suggested a green route in synthesising carbon nanomaterial. Although a broad range of raw biomass materials (leaves, coffee grounds, etc.) can be used in producing CQDs, generally these synthetic routes are associated with poor control of the CQDs particle size, quality and homogeneity of the product(Cailotto *et al.*, 2018). Therefore, materials of known elemental origin that allow better control of the properties and consequently applications are desirable. Typically, the production of CQDs via bottom-up methods involves lengthy reaction times (from a few hours up to 48 hours) and high consumption of energy. Therefore, a new approach for the synthesis of CQDs from biomass related precursor that minimizes the process duration and energy consumption along with delivering fine control of the particle size and other properties are needed. In addition, the light-emitting mechanism of CDs is still not well understood which requires a deeper understanding of the origin of light-emitting and influence factors.

In this work, we employed the continuous hydrothermal flow synthesis (CHFS) is primarily water-based. The CHFS allows the designing or tailoring of the nanoparticles for specific functions based on the nucleation and surface functional process (Baragau *et al.*, 2021). The comparison between CHFS and the traditional hydrothermal process has shown that CHFS consumed less energy and time, yet it produced a higher homogenous quality product (Kellici *et al.*, 2018). This research employed a systematic dopant process to fabricate nitrogen-doped carbon quantum dots (N-CQDs). To investigate the structure as well as the physical, chemical and optical properties of the nanoparticles, techniques such as High-Resolution Transmission Electron Microscopy (HRTEM), Raman (particle size and morphology), UV-Vis (absorption), Time-resolved photoluminescence (TRPL) spectroscopy (optical properties); X-ray photoelectron spectroscopy (XPS), FT-IR (composition, functional groups). In addition, the integrating sphere will be used to measure the Q Y which will then be combined with an excited-state lifetime to determine the radiative rate (or non-radiative losses).

As the N-CQDs showed significant enhancement in fluorescence emission properties and higher quantum yield, 9.6% for N-CQDs, while the glucose-CQDs were 0.3%. Although Nitrogen-doping is the most common method employed to enhance the photoluminescence properties of the CQDs(Manioudakis *et al.*, 2019). However, the origin of the fluorescent improvement remains open for disputation and will be discussed in this work. With the stability of working in a wide range of pH (2-11), the N-CQDs were applied as a nano-sensor for highly toxic chromium (VI) ions. Furthermore, the quenching mechanism of N-CQDs was confirmed as an Inner Filter Effect (IFE) by the obtained result from spectroscopic and fluorescent lifetime analysis. The results revealed that the nitrogen-doping process has changed the overall electronic structure of N-CQDs resulting in the enhancement of the optical properties as well as the performance of the nano-sensor.

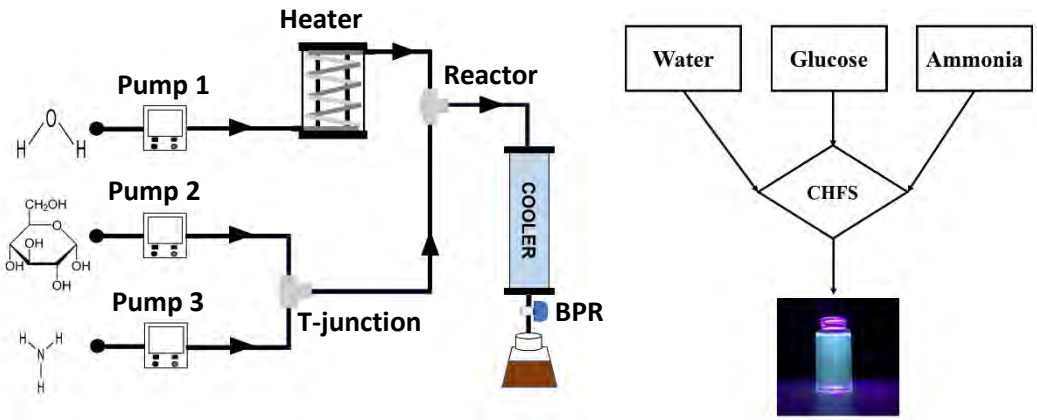


**FIGURE 1:** *Schematic of Continuous Hydrothermal Flow Synthesis (CHFS) process used to synthesize N-doped carbon quantum dots (NCQDs).*

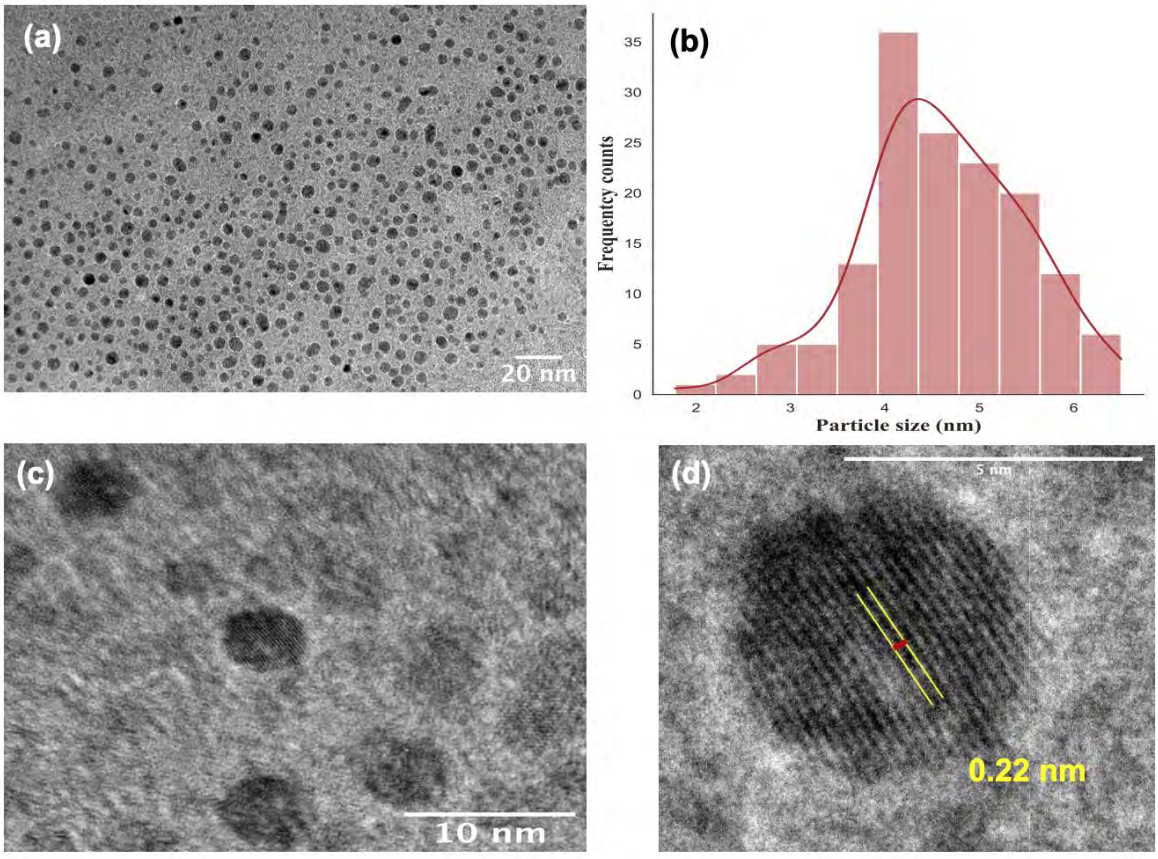


**FIGURE 2.** *HRTEM images of N-CQDs at different magnification and scale: (a) 20 nm, (c) 10 nm, (b) particle size Gaussian distribution histogram, (d) graphitic core lattice. The N-CQDs have commonly a particle size of 4.60 ± 0.87 nm.*

References

Baragau, I. A. *et al.* (2021) 'Efficient Continuous Hydrothermal Flow Synthesis of Carbon Quantum Dots from a Targeted Biomass Precursor for On-Off Metal Ions Nanosensing', *ACS Sustainable Chemistry and Engineering*, 9(6), pp. 2559–2569. doi: 10.1021/acssuschemeng.0c08594.

Cailotto, S. *et al.* (2018) 'Carbon Dots from Sugars and Ascorbic Acid: Role of the Precursors on Morphology, Properties, Toxicity, and Drug Uptake', *ACS Medicinal Chemistry Letters*, 9(8), pp. 832–837. doi: 10.1021/acsmedchemlett.8b00240.

Kellici, S. *et al.* (2018) 'Continuous hydrothermal flow synthesis of graphene quantum dots', *Reaction Chemistry and Engineering*, 3(6), pp. 949–958. doi: 10.1039/c8re00158h.

Manioudakis, J. *et al.* (2019) 'Effects of nitrogen-doping on the photophysical properties of carbon dots', *Journal of Materials Chemistry C*, 7(4), pp. 853–862. doi: 10.1039/c8tc04821e.

Carbon 2022

# Preparation of porous carbon derived from HPC (Hyper-coal) and examination of EDLC performance, and discussion of factors affecting their characteristics

**Shota Okuma[1], Toshinori Inoue[2], Naoki Kikuchi[2], Maki Hamaguchi[2], Masahiro Toyoda[1]**
[1]Department of Applied Chemistry, Graduate School of Engineering, Oita University,
700 Dannoharu, Oita 870-1192, Japan
Email: Toyoda22@oita-u.ac.jp

[2]Mechanical Engineering Research Laboratory, Kobe Steel, Ltd., Japan

**Keywords**
Hyper Coal, Precipitation method, EDLC

## INTRODUCTION

Hyper-Coal (HPC) is a thermally extracted ash-free component of coal, which is soluble in organic solvents. Carbon precursor can be prepared by precipitating at HPC solution and treating it with heat to obtain carbon powder. Without activation, the carbon powder possesses porosity, particularly micropores. Additionally, the carbon powder exhibits large capacitance when applied to electric double layer capacitor (EDLC) electrode. So far, high-grade coal derived from bituminous coal has been used in the previous reported (H. Watanabe et al. , 2020), its high specific surface area led to high capacitance. High grade coal (B-HPC) derived from bituminous coal contains a high aromatic carbon content and stacked hexagonal carbon network, giving it high crystallinity. Compared with the previously reported B-HPC derived from bituminous coal, SB-HPC derived from sub- bituminous coal has lower aromatic carbon content, smaller aromatic ring size, lower crystallinity, and higher oxygen content. Therefore, carbon powder prepared from SB-HPC is expected to have a larger specific surface area and higher capacitance than that from B-HPC. This study evaluates the pore characteristic and EDLC capacitance of carbon powder form the precipitation method using SB-HPC as the starting material. Futher, ther study compares the crystallinity of SB-HPC and B-HPC derived carbon powder.

## MATERIAL AND METHOD

SB-HPC was used as the starting material. HPC powder with a particle size of less than 250 μm was dissolved in pyridine to prepare the HPC solution. The resulting a solution poured into water as a poor solvent for precipitating HPC. The obtained HPC powder was infusibilized for 1 h at 300 °C under air environment before being carbonized for 30 min at 900 °C under nitrogen atmosphere. Surface characteristics were measured using a nitrogen adsorption/desorption measuring device at 77 K. Further, using the adsorption isotherm obtained from the nitrogen adsorption/desorption measurement, the specific surface area was determined from $\alpha_s$ analysis method. The electrodes were prepared using carbon powder, acetylene black, and PTFE in an 8:1:1 weight raito. EDLC characteristics were evaluated using a three-electrode cell with a sulfuric acid aqueous solution as the electrolyte. Galvanostatic charge/discharge measurements were conducted at current densities ranging from 50-1000 mA $g^{-1}$. The capacitance at each current density was determined in the discharge curve produced from galvanostatic charge/discharge measurement and ranged from 0.2 to 0.8 V. Carbon powder derived from SB-HPC and B-HPC was treated with heat for 30 min in argon atmosphere at 2000 °C, 2400 °C, 2800 °C to obtain graphitized carbon powder. The crystallinity of the powder was evaluated using XRD and TEM observation. The sample code was (type of HPC)-(heat treatment temperature).

## RESULTS AND DISCUSSION

Figure 1 shows the nitrogen adsorption/desorption isotherms of the carbon powder derived from SB-HPC and B-HPC. Because the adsorption amount of SB-900 at relative pressure $P/P_o \approx 0$ was larger than that of B-900, it was suggested that SB-900 had abundant micropores. The specific surface area obtained from the $\alpha_s$ analysis of SB-900 was 737 $m^2 g^{-1}$, which was larger than B-HPC (400 $m^2 g^{-1}$). Figure 2 shows the charge/discharge measurements obtained for SB-900 and B-900 at a current density at 50 mA $g^{-1}$. The capacitance per unit mass calculated from the discharge curve in the range of 0.2 to 0.8 V was 286 F $g^{-1}$ for SB-HPC, and 210 F $g^{-1}$ for B-900, its capacitance of SB-900 was higher than that of B-900. Therefore carbon powder derived from SB-900 has larger specific surface area and higher capacitance than B-HPC. Figure 3 shows the TEM images of graphitized carbon powder of SB-HPC and B-HPC at 2800 °C. Hexagonal carbon layer stacking structure was developed through graphitization in both SB-2800 and B-2800, and there were different in developing the stacking structure. B-2800 developed a shell with a hollow center. In contrast, SB-2800 developed a stacking structure oriented in various directions. It was considered that the development of crystallinity was more difficult in SB-2800 than in B-2800. Therefore, it was suggested that carbon powder made with SB-HPC had a lower crystallinity, resulting in larger specific surface area and higher capacitance than that made with B-HPC. Additionally, element analysis results show that the starting material in SB-HPC obtained from lower grade coal contains a high amount of oxygen, which contributes to an increase in pseudo-capacitance.

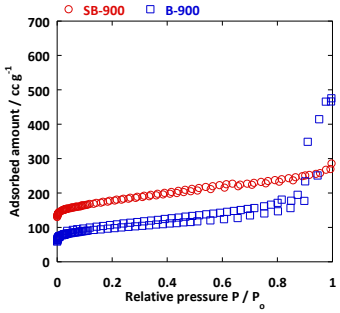


**FIGURE 1:** $N_2$ adsorption and desorption isotherms of SB-900 and B-900

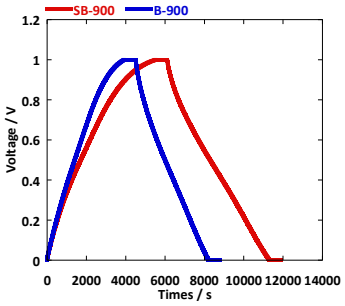


**FIGURE 2:** Galvanostatic charge/ discharge curves of SB-900 and B-900

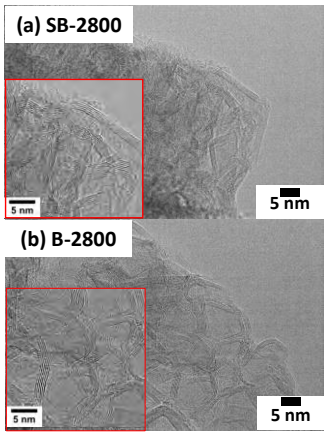


**FIGURE 3:** Carbon 002 lattice image of SB-2800 and B-2800

## CONCLUSION

In this study, pore characteristic and EDLC capacitance of carbon powder was obtained from the precipitation method using SB-HPC as starting material were evaluated, and the difference between carbon powder of SB-HPC and B-HPC was compared with crystallinity. The specific surface area of the resulting carbon powder was 737 $m^2 g^{-1}$, which was larger than that of the carbon powder obtained B-HPC (400 $m^2 g^{-1}$). The capacitance per unit mass was 286 F $g^{-1}$, when carbon powder was applied to the EDLC electrode, which was higher than that using B-HPC. Considering these factors, carbon powder using SB-HPC has lower crystallinity than that using B-HPC. This is because SB-HPC was containing more oxygen components in the starting material from B-HPC. Furthermore, TEM results from high-temperature heat-treatment demonstrate that the carbon material formed from SB-HPC has a lower graphite structure and crystallinity than B-HPC, despite being heat-treated at the same treatment temperature.

## REFERENCES

H. Watanabe, T. Inoue, N. Kikuchi, M. Hamaguchi, T. Tsumura and M. Toyoda, (2020). EDLC Characteristics of Carbon Materials Prepared from Coal Extract. *Electrochemistry*, 88, [3], 119-126.

https://doi.org/10.5796/electrochemistry.20-63011

Carbon 2022

# Perspectives on the near surface disposal of irradiated reactor graphite: Case study of the Chernobyl NPP, Ukraine

**Yuriy O. Olkhovyk[1], Sergey V. Mikhalovsky[2] and Andrew B. Cundy[3]**
[1]Institute of Environmental Geochemistry, 34a, Prospect Palladina, Kyiv, Ukraine, 02000
[2]ANAMAD Ltd, Sussex Innovation Centre, Falmer, Brighton, UK, BN1 9SB
[3]School of Ocean and Earth Science, University of Southampton, Southampton, UK, SO14 3ZH
Email: [1]yolkhovyk@ukr.net; [2]sergey.mikhalovsky@anamad.co.uk; [3]A.Cundy@noc.soton.ac.uk

## INTRODUCTION

Currently works are ongoing in the Chernobyl Exclusion Zone (ChEZ) on the site of the Chernobyl Nuclear Power Plant (NPP) to complete the final closure and conservation of the power units 1-3. These units have high-power channel-type nuclear power reactors (RBMK), in which the active zone contains a nuclear graphite cylinder of 7-m height and 8-m diameter serving as a moderator. During its operation, the graphite cylinder becomes radioactive with increasing specific activity due to the formation and accumulation of the radionuclide $^{14}C$ with a long half-life of 5730 years. The experimentally determined specific activity of $^{14}C$ for the graphite in similar RBMK reactors used at the Leningrad NPP (Russia) was $(4\text{-}7)*10^5$ Bq/g (Pavliuk, et al., 2021). Additionally, other radionuclides, mainly $^{36}Cl$ (half-life $3.01x10^5$ y.) and $^{60}Co$ (5.3 y), formed due to the activation of technological impurities in the graphite, spills of fission products and fragments of the nuclear fuel caused by various failures or accidents contribute to the radioactivity of the irradiated graphite. The dose rate of the reactor graphite γ-radiation in such power units could reach 600 μSv/s at a distance of 0.5 m. It presents a long-term radiological hazard (Metcalfe and Tzelepi, 2019).

## DISCUSSION

The main problem of decommissioning power units with RBMK reactors is the choice of the optimal method of disposing of large volumes of irradiated graphite. The total amount of irradiated reactor graphite (IRG) contained in units 1-3 of the Chornobyl NPP is estimated to be 5700 tonnes. It has as much $^{14}C$ as would have been formed by an explosion of a 3.3 Mt nuclear bomb.

As a material, graphite has some unique properties. It is chemically stable and resistant to ionising radiation in dry environments, however in the presence of water graphite increases its reactivity. The radiolysis of water caused by $^{14}C$ β-decay with maximum energy of 156 keV generates soluble oxygenated carbon species, which are products of reactions between chemically active ions and radicals with the graphite surface enriched with radiocarbon. The rate of formation of such products is very low. It has been estimated that the daily rate of release of radiocarbon from the irradiated graphite in the RBMK reactor upon its contact with water is $2*10^{-8} – 2*10^{-9}$ g/cm$^2$ or $10^{-5}$-$10^{-6}$ % (Pavliuk, et al., 2021). However, taking into account the high total activity of $^{14}C$ in IRG, even this seemingly negligible rate of leaching can result in significant environmental contamination with radiocarbon. Furthermore, the water penetrating the storage sites could carry mixomycetes (*Acremonium, Arthrinium, Paecilomyces spp,* etc) capable of intensifying graphite corrosion thus increasing the specific activity of the water infiltrating graphite blocks (Sobotovich, et al., 1996). The accelerated biodegradation of IRG debris released in April 1986 after the Chernobyl NPP accident was confirmed

by the difference in radiocarbon dating of the ecosystems of the river Prypyat', tributary to the river Dnipro, which was affected by the accident and the unaffected Dnipro (Dnieper).

The radiological hazards of radiocarbon are associated with its high migration potential in the environment and intake by humans via inhalation and oral routes. Even in the early days of nuclear weapons testing it was noticed that the release of radiocarbon in the atmosphere could be the cause of rising number of malignant neoplasms (Sakharov, 1990). The release of radiocarbon in the environment would increase the number of transmutations $^{14}C \rightarrow {}^{14}N$ through radioactive $\beta$-decay; and radiocarbon incorporated in the human body induces DNA damage and genetic mutations via ionising radiation (Penninckx, et al., 2021).

The potentially dangerous radiological and genetic impact of radiocarbon requires applying methods of IRG handling which prevent its release into the atmosphere. So far, no satisfactory strategy for solving this problem has been suggested. To date, two alternative approaches have been considered: (i) pre-treatment of graphite by extracting mobile radionuclides using different physical or chemical methods, and (ii) immobilisation of mobile radionuclides which prevents or diminishes their release. Another method, burning irradiated graphite, is hardly acceptable as it generates large volumes of secondary wastes. According to IAEA (2016), most countries consider geological disposal as their preferred option rather than IRG deactivation. This choice is justified by the absence of technologies capable of achieving 99.9% purification of IRG from the radioisotope $^{14}C$ with minimal formation of solid secondary waste, which would be stable for tens of thousands of years.

At present, the possibility of near-surface disposal of radioactive waste on-site of the Chernobyl NPP power units and the object "Shelter" by forming a mound in which the radioactive debris are covered with inert materials (a so-called "Green Mound" technology), is debated (Stel'makh et al., 2016). In this case, the protection of the storage structures against the ionising radiation and unauthorised access is achieved by creating a multi-metre layer of inert materials, and the structures containing radioactive materials are permanently inaccessible to groundwater. However, over the long storage periods required, natural factors such as the evolution and migration of the Prypyat' river, and seismic activity, could significantly impact the near-surface disposal sites.

The formation of artificial barriers made of quartz sand and local low quality clay is insufficient for the isolation of radiocarbon and other radionuclides with long half-lives against natural water precipitation which is typical for Ukrainian woodland areas. Barriers made of concrete and bulk clay could not withstand the environmental factors long enough to prevent radiocarbon migration outside the storage site. Due to the high porosity of IRG and the possibility of radiocarbon leaching, the collective dose which the residents of surrounding territories could receive with food and drinking water from radioactive contamination has been estimated at 30-40 Sv/y.

Another powerful mechanism of the destruction of site structures, which has not been considered, is the impact of the vicinity of "Green mounds" to the Prypyat' riverbed. The latter is characterised by free meandering and fast river bank erosion which is likely to cause erosion of the near-surface storage sites.

For the "Green Mound" scenario, risks associated with the impact of climate changes become more likely and higher because of the vulnerability of near-surface objects to external environmental factors. Taking into account the long half-lives of the dose-forming radioisotopes, the terms of operation of protective barriers are comparable with the timeline of global climatic changes. The potential impact of regional and global climate changes and possible climatic extremes on the intensity of geomorphological changes at the "Green Mound" sites require careful consideration. Current models of climate change, which calculate insolation using the Milankovitch astronomical cyclic theory, suggest a high likelihood of the next glacial period occurring in 50-60 thousand years. This could lead to dramatic changes in the geomorphological landscape of the region, which was formed under the influence of the Dnipro or Riss glaciation, a major event during the Quaternary period. Such changes could destroy the near-surface sites of disposal of highly active radioactive wastes containing isotopes

with long half-life. Conversely, future trajectories of global heating suggest increased risks of extreme climatic events, prolonged drying or desertification, and increased regional temperatures, which also pose significant risk to the integrity of near-surface disposal sites. All these arguments lead to the conclusion that the safety of the near-surface disposal sites located in the inner ChEZ cannot be guaranteed over a longer term of tens of thousands of years.

## CONCLUSIONS

A deep geological disposal facility (GDF) seems the optimal and viable option for storing the irradiated reactor graphite from ChNPP (IFEP, 2019). Taking into account the high migration potential of carbon compounds and the absence of effective geological barriers, the migration of $^{14}C$ from the GDF wil be determined by the regional regime of the underground waters. The GDF for graphite should be located in deep horizons of slow water exchange. The IEG storage safety could be improved by creating additional engineered barriers on the surface of the graphite blocks which prevents them from any contact with underground water. A promising candidate material for engineering such a barrier is a microlayer of a ceramic SiC composite. This has proven chemical and radiation stability under external environmental factors, which has already been utilised for manufacturing granulated nuclear fuel, and which may contribute to limiting environmental exchange from contaminated graphite during interim storage.

**Acknowledgements**

The authors acknowledge financial support from the National Nuclear User Facility EXACT (Next Generation Accelerated Characterisation Technologies), via the UK Engineering and Physical Sciences Research Council (grant EP/T011548/1). AC acknowledges additional support from the TRANSCEND (TRANsformative SCience and Engineering for Nuclear Decommissioning) consortium (EPSRC grant number EP/S01019X/1). YO acknowledges the support of the Institute of Environmental Geochemistry, National Academy of Sciences of Ukraine.

**References**

International Atomic Energy Agency (2016). Processing of irradiated graphite to meet acceptance criteria for waste disposal. IAEA-TECDOC-1790, 1-148. ISBN:978-92-0-104016-9.

International Features, Events and Processes (IFEP) List for the Deep Geological Disposal of Radioactive Waste: Version 3.0. (2019). *Radioactive Waste Management*, NEA/RWM/R. 1 July 2019.

Metcalfe, M. and Tzelepi, A. (2019). The significance of carbon 14 in graphite reactor components at end of generation. *Journal of Environmental Protection*, 10, 118-129.

Pavliuk, A.O., Kotlyarevskiy, S.G., Kan, R.I., Volkova, A.G. and Zakharova, E.V. (2021). [Experimental studies of long-living $^{14}C$ and $^{36}Cl$ radionuclides leaching from irradiated graphite]. *Radiochemistry,* 63, [2], 149-159. (in Russian).

Penninckx, S., Pariset, E., Cekanaviciute, E. and Costes, S.V. (2021). Quantification of radiation-induced DNA double strand break repair foci to evaluate and predict biological responses to ionizing radiation. *NAR Cancer*, 3, [4], zcab046.

Sakharov, A.D. (1990). Radioactive carbon from nuclear explosions and nonthreshold biological effects. *Science and Global Security*, 1, [3-4], 175-187.

Sobotovich, E.V., Skripkin, V.V. and Zhdanova N.N. (1996). [Transformation of reactor graphite of the Chernobyl accident discharge in biogeochemical systems]. *Dopovídí NAN Ukraïni* [Proceedings of NAS of Ukraine], [11], 173-176.

Stel'makh, D.A., Kuchynsky, V.K., Platonenko, A.M. (2016). [On-site storage scenario for decommissioning of the Chernobyl NPP objects. [*Ядерна та радіаційна безпека. [Nuclear and Radiation Safety],* 1(69), 57-63. (in Ukrainian).

Carbon 2022

# Combined Neutron and X-Ray Microtomography for Tracking Local Hydrogen and Carbon+Oxygen Distributions in Biomass Pyrolysis

**Frederik Ossler[1], Emanuel Larsson[2], Stephen Hall[2], Cyrille Couture[3], Alessandro Tengattini[3], Charles E.A. Finney[4]**

[1]Combustion Physics, Lund University, Lund, Sweden

Email: frederik.ossler@forbrf.lth.se

[2]Division of Solid Mechanics, Lund University, Sweden

[3]Institut Laue-Langevin ILL, Grenoble, France

[4]Oak Ridge National Laboratory, Oak Ridge, Tennessee USA

**Keywords**

Neutron tomography, X-ray microtomography, biomass pyrolysis

## INTRODUCTION

Biomass is a significant source for renewable hydrogen-rich green energy and for advanced carbon materials as part of a sustainable-energy strategy. Hydrogen (H) and carbon (C) are key elements of study to understand how one can convert hydrogen into fuel and carbon into materials, so that one can achieve the right balance of product yields, e.g., in terms of economic value. In previous studies utilizing in-situ 2D neutron imaging, we recorded how H was released from lignocellulosic biomass undergoing pyrolysis and carbonization up to 1000 °C. It was found that the content of H decreased to only a few percent at 800–1000 °C pyrolysis temperatures relative to that of pristine wood [Ossler et al]. Comparing 3D neutron and X-ray microtomography (NCT and XCT) results of fully pyrolyzed and pristine samples, we observed that the contrast in the neutron images increased for the carbonized samples, suggesting that H would be concentrated at the surface of the carbonized material structure. The spatial resolution was limited to > 80 µm, so finer detail in the 3D distribution was lacking. To achieve higher-resolution correlation of local H and C density variations, we performed combined NCT and XCT measurements on pristine and pyrolyzed samples of different biomass materials, including pine and beech wood at a resolution better than 10 µm at the NeXT beamline at the Institut Laue-Langevin (ILL), Grenoble, France [Tengattini et al.]. Pristine, partially carbonized, and fully carbonized samples were prepared and analyzed by combined NCT and XCT without further treatment

## EXPERIMENTAL

NCT and XCT measurements of wood samples which had undergone complete or partial carbonization was performed at the NeXT facility. A description of the beamline and its performance is given in [Tengattini et al.]. Beech dowels with diameters of 8 and 10 mm and nominal lengths 1 cm were analysed. Measurements were also performed on pine dowels and other biomass or biomass-derived samples. The same sample set up was used for NCT and XCT, where the neutron and X-ray beams were orthogonally aligned. The two scans were performed one after another to achieve optimum conditions for comparative studies between NCT and XCT results. In some occasions a fully carbonized sample and a partially carbonized sample were glued one on top of the other so that we could obtain comparative information at different levels and degrees of carbonization from a single scan.

Two types of carbonization were performed prior to sample scanning: (S1) Rapid pyrolysis at 800 °C (measured under operation without a sample) in atmospheric nitrogen flow inside a heating coil. The temperature was ramped up for around 2 minutes and then held for 10 minutes. The current was then switched off, and the sample was allowed to cool to room temperature before it was handled. The

weight of the samples was measured before and after pyrolysis. The samples were then brought to and measured at ILL 2–3 days later without further treatment; (S2) Another sample from the same dowel was wrapped in aluminium foil and heated on one end with a butane lighter torch so that a carbonization gradient was obtained. The foil was then removed and the sample allowed to rest before being glued onto one end of the fully carbonized sample (S1) before being glued onto the holder used for the measurements.

In **Fig. 1** we have reported details of beech dowels (10 mm diameter), one partially burnt (lower, S2) and another more extensively pyrolyzed (upper, S1).

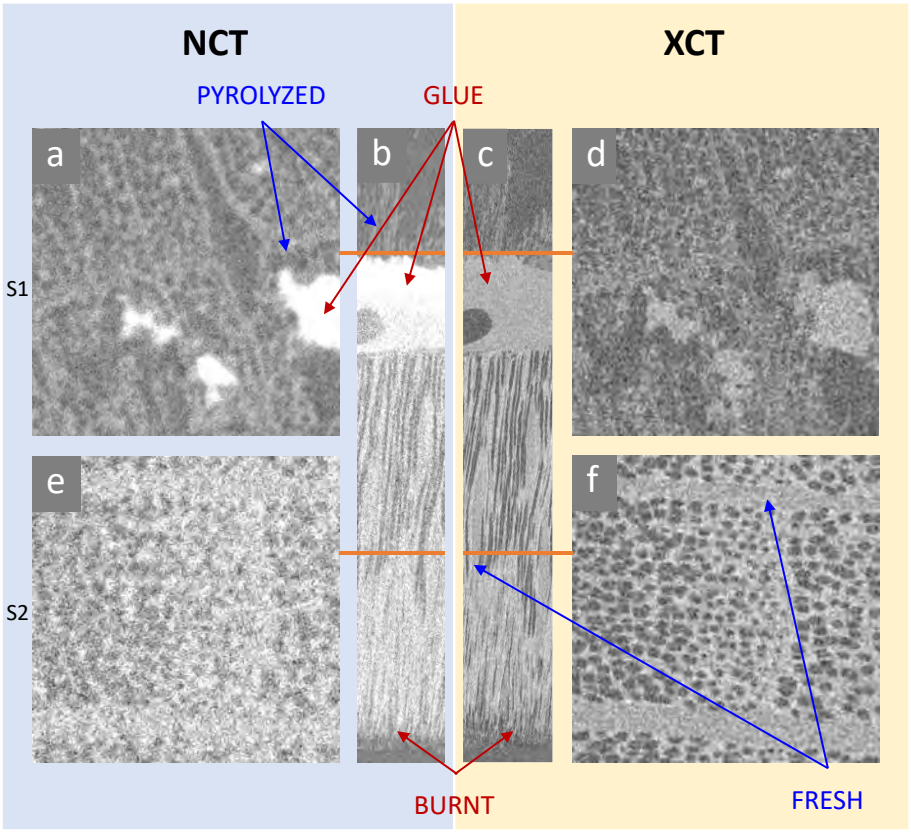


**FIGURE 1** *Comparison of NCT (left) and XCT (right). (a) and (b) show* x–y *and* y–z *cut planes from NCT. (c) and (d) show the corresponding cut planes from XCT. (e) and (f) show* x–y *cut plane of the fresh part of the partially burnt sample (S2). The pyrolyzed (S1) and partially burnt (S2) samples were adhered with plastic glue. The square pictures are 241×241 and 213×213 in pixels for NCT and XCT, respectively, and correspond to sides of 1.9 and 2.0 mm. (a), (d), (e) and (f) are from cut planes across the grains of the wood and char, and (b) and (c) show vertical cut planes along the grain. No enhancement of the images was done after reconstruction.*

Tomographic images were reconstructed from the radiographs, and a first analysis was performed on the reconstructed slices. In this way the 3D distribution of the local attenuation coefficients, $\mu$, for the neutrons and X-rays were estimated. As the main atomic species are H, C, and O, we can obtain information on the local relative abundance of these species throughout the samples. The linear attenuation coefficients $\mu$ for both neutrons and X-rays depend on the attenuation cross sections, $\sigma_i$ (which are slightly wavelength dependent), and number concentrations, $n_i$, of respective species:

$$\mu_{\text{Neutrons}} = \sigma_{H,N} \times n_H + \sigma_{C,N} \times n_C + \sigma_{O,N} \times n_O \quad (1)$$

$$\mu_{\text{X-rays}} = \sigma_{H,X} \times n_H + \sigma_{C,X} \times n_C + \sigma_{O,X} \times n_O \quad (2)$$

To completely retrieve $n_i$, we would need a third independent equation. This is not easily obtained, but a first-pass approximation might include the specific cross sections and expected trends in changes of mol% with the degree of pyrolysis process. At room temperature, unprocessed beech wood has a mol% around 46, 33, and 21 [Ossler et al., and references therein]. The mol% of H and O gradually decrease with pyrolysis temperature, while that of C increases. Nitrogen concentration is negligible in beech wood. The neutron attenuation cross sections for H, C, and O as used in previous pyrolysis studies are 82.5, 5.556, and 4.232 barn (1 barn = $10^{-24}$ cm$^2$), respectively for 2.6 Å wavelength [Ossler et al.], close to the peak wavelength of NeXT, 2.8 Å [Tengattini et al]. The corresponding X-ray attenuation coefficients for 100 keV are 0.493, 3.02, and 4.12 barn, respectively [from the NIST web-site: https://physics.nist.gov/cgi-bin/Xcom/xcom2]. Local variations in composition can be considerable in a sample, and it is therefore convenient to consider the relative variations of elements in the groups H and C+O when comparing neutron and X-ray tomographies. For fresh wood, the attenuation is dominated by H for neutrons and by C and O for X-rays. We see that NCT gives less contrast than XCT. The reason is not clear although increased (multiple) scattering from hydrogen could be an explanation. For the carbonized wood, on the average, only a smaller fraction of mol% of the sample is from H compared to C, which can be expected to be around 80% or more. The white areas observed in **Fig. 1** for neutrons are from polymer-based glue (H-rich, potentially this can be used for calibration if the density of the glue is known), and appear very strongly in the NCT because of the glue's relatively high H content. However, one can see in (a) and (b) that the carbonized material shows regions with particularly thicker lines than for (c) and (d), even if the resolution on the very small white areas in (a) and (d) have similar structure resolutions. This would mean that the widening of the lines in (a) is most probably due to hydrogen. We cannot yet say what the chemical nature of H is — it could be water from ambient humidity or hydrogen-rich chemical groups bound to the carbon surface.

## CONCLUSIONS

Comparing the reconstructed NCT and XCT images we found that the pristine samples showed contrast with similar spatial variations between the two techniques, although XCT showed less marked contrast. Clear differences were found for the pyrolyzed samples: NCT showed higher contrast with distinct connected linear structure in the material with higher dynamic range than for the XCT. The linear structures in the NCT followed the structures in the XCT images but were more accentuated and wider, in particular at the edges of the carbon structure, primarily resulting from the XCT image contrast. We also investigated gradually burnt parts of the wood samples, which showed intermediate variations. Despite the fact that the average H density is expected to be low in the pyrolyzed samples, considerable concentrations are found in localized regions of the material. The nature of the high surface density of H is not yet understood.

**Acknowledgements**

We acknowledge and are grateful for the support from the Physics Department, Lund University; Institut Laue-Langevin for the assistance and allowing access for experiments at the NeXT beamline. This work has been partly authored by UT-Battelle, LLC, under contract DE-AC05-00OR22725 with the US Department of Energy (DOE).

**References**

Ossler, F., Finney C. E. A., Warren, J. M.; Bilheux, J.-C., Zhang, Y., Mills, R. A., Santodonato, L. J., Bilheux, H. Z. (2021]. Dynamics of hydrogen loss and structural changes in pyrolyzing biomass utilizing neutron imaging. *Carbon*, 176 , 511–529. https://doi.org/10.1016/j.carbon.2020.11.060

Tengattini, A., Lenoir, N., Andò, E., Giroud, B., Duncan A., Beaucour, J., Viggiani, G. NeXT-Grenoble, the Neutron and X-ray tomograph in Grenoble; *Nuclear Inst. and Methods in Physics Research, A 968 (2020) 163939.* https://doi.org/10.1016/j.nima.2020.163939

20 C 22 arbon 2022

# On The Surprisingly High Order Of The Graphene Structure Of Non-Graphitic Carbons (NGCs) Determined By Wide-Angle Neutron Scattering (WANS)

**Oliver Osswald and Bernd M. Smarsly**
Justus-Liebig University Giessen, Institute of Physical Chemistry
Heinrich-Buff-Ring 17, 35392 Giessen, Germany
Email: oliver.osswald@phys.chemie.uni-giessen.de

**Keywords**

- Microstructure Analysis
- Wide-angle neutron scattering (WANS)
- Non-graphitic carbon

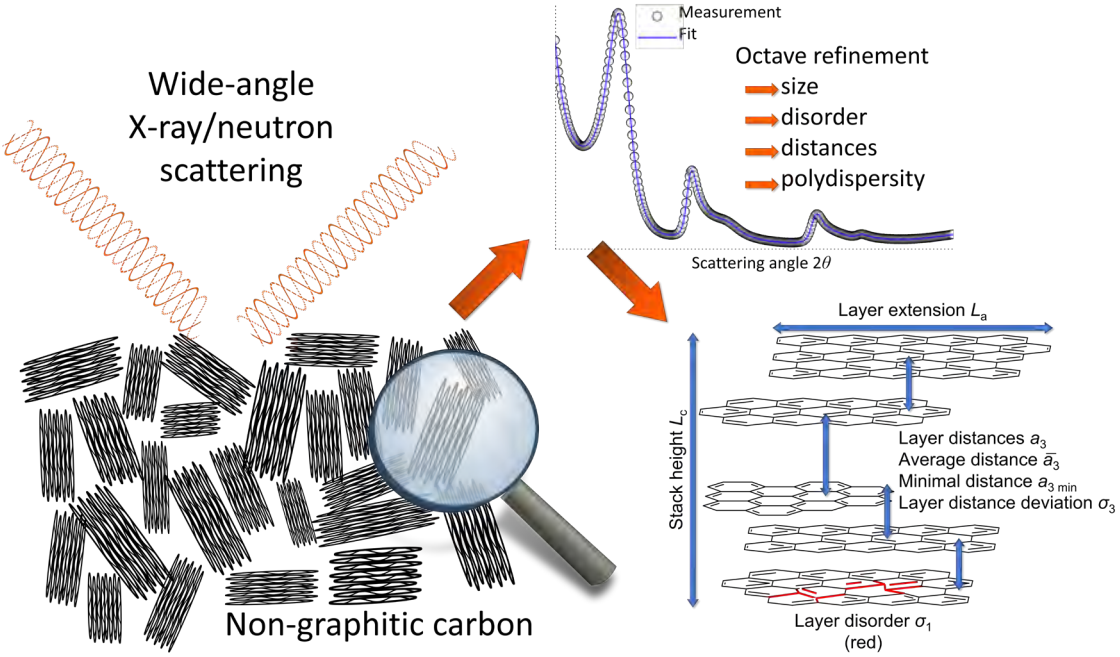


**FIGURE 1**: Determination of the microstructure by refining wide-angle X-ray/neutron scattering using *Octave*. The layers have an intrinsic disorder, which is exemplarily marked in the bottom layer (red).

## ABSTRACT

Non-graphitic carbons (NGCs) like glassy carbons, coal tar pitches and activated carbon consists of small graphene layers building stacks in a turbostratic order (Figure 1). Both structure types, the single graphene sheets as well as the stacks feature significant structural disorder, which can be analyzed by wide-angle X-ray and neutron scattering (WAXS/WANS). A suitable algorithm to evaluate and analyze such X-ray scattering data was introduced by Ruland & Smarsly in 2002 and used by multiple studies (Badaczewski et al. 2019 & 2020, Faber et al. 2014, Loeh et al. 2016 & 2018, Pfaff et al. 2018 & 2019). Pfaff, Badaczewski et al. expanded this model for neutron scattering in 2019 and showed the principal possibility to also analyze such scattering data in a meaningful way.

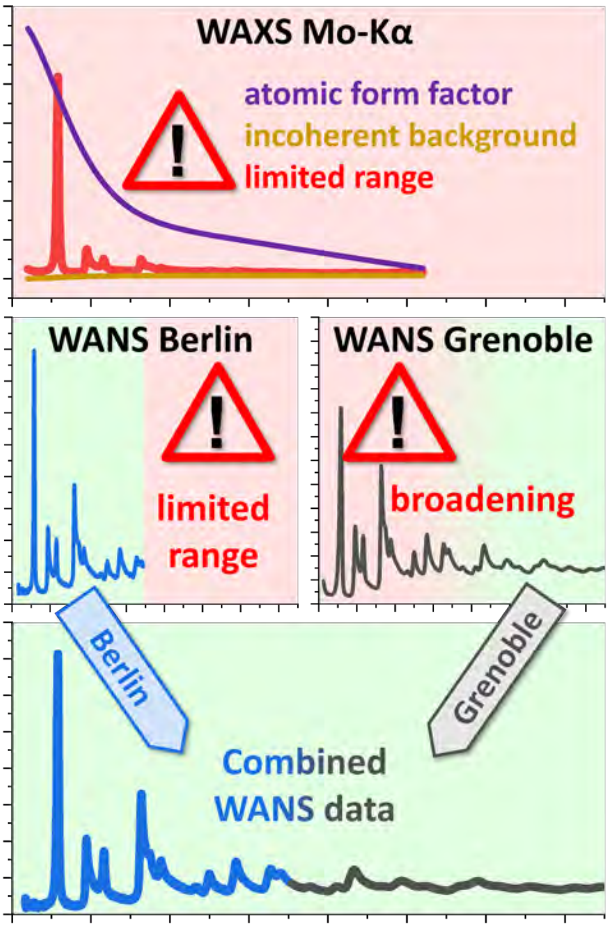


**FIGURE 2**: Wide-angle X-ray scattering (WAXS) suffers from different features: Beside the incoherent background, which must be considered exactly, the damping of the atomic form factor and the limited measuring range prevent the analysis of higher-order reflections. The wide-angle neutron scattering (WANS) data von Berlin suffers from the limited measurement range and the WANS data from Grenoble from the experimental broadening at low values of the scattering values s, so only a combination of both WANS measurements can lead to a detailed microstructure analysis.

Here, first we present a free software tool operated in Octave for the refinement of wide-angle X-ray and neutron scattering (WAXS/WANS) data of non-graphitic carbons (NGCs) on Windows, MacOS and Linux. The refinement script is based on the evaluation approach of Ruland & Smarsly (2002). As result, up to 14 physically meaningful parameters like the layer extension $L_a$, the stack height $L_c$ and the degree of disorder of the graphenes ($\sigma_1$) and their stacking ($\sigma_3$) are obtained through a fitting routine. In addition, the background based only on physically phenomena and different correction parameters like polarization and absorption can be considered. For both options, the automatic as well as manual fitting, the complex mathematical calculations are implemented and performed in the background. Due to only few settings to be made, the software was designed to be useable by inexperienced users. Beside this, the whole refinement can be tweaked and optimized for special purposes and measuring geometries, which makes it useful for all scientists dealing with the characterization of NGCs by X-ray or neutron scattering techniques.

Second, even if WANS data of NGCs have already been measured and analyzed in different studies, there are still open questions in regard to the validation with wide-angle X-ray scattering (WAXS), which is usually used for routine characterization. Generally, wide-angle X-ray scattering (WAXS) suffers from a non-negligible incoherent background, which must be considered exactly. Additionally, the damping of the atomic form factor and the limited measured range prevent the analysis of higher-ordered reflections, which are crucial for determining and distinguishing between the stack/layer size ($L_a$, $L_c$) and disorder ($\sigma_1$, $\sigma_3$). Therefore, in this study WANS measurements of three different types of carbon materials (glassy carbon made out of a phenol-formaldehyde resin (PF-R), a mesophase pitch (MP) and a low softening-point pitch (LSPP)) were performed at a low neutron wavelength to obtain WANS over a large range of the scattering vector *s*. These WANS data were combined to WANS data from previous studies of Pfaff, Badaczewski et al. in 2019. This usage of two sets of WANS data of identical materials offered the unique opportunity to determine both the interlayer and the interlayer structure as accurately as possible.

As a result (Figure 3), the previous picture from previous studies (large graphene layers with higher-order domains (dark) in overall more disordered layers (light)) from Pfaff, Badaczewski et al. (2019) needs to be changed: the graphene layers are much smaller, but consistently more highly ordered than assumed over their whole extension.

**Acknowledgements**

We acknowledge Torben Pfaff for programming the basic calculation routine in C++ and Henry E. Fischer for the explanations about the inelastic neutron scattering, data preparation and beamtime support. We would also like to thank Torben Pfaff and Felix Badaczewski for performing the WANS measurements and Marc Oliver Loeh for synthesizing the necessary samples. We also acknowledge computational resources provided by the HPC Core Facility and the HRZ of the Justus-Liebig University in Giessen/Germany. We thank Christian Bauer and Felix Badaczewski for testing and evaluating the provided *Octave* script. We also thank ILL for the allocation of neutron radiation beamtime and thankfully acknowledge the financial support from ILL.

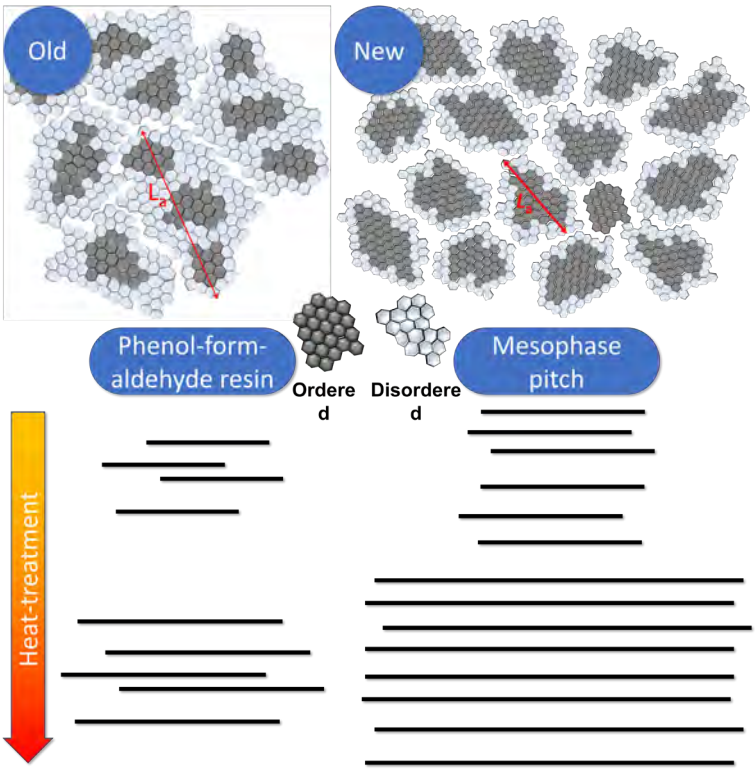


**FIGURE 3**: New insights into the microstructure of non-graphitic carbon: compared to prior studies (left) on the same materials (Pfaff, Badaczewski et al. 2019) the present analysis (right) suggests smaller, but highly ordered graphene layers.

**References**

Badaczewski, F. M., Loeh, M. O., Pfaff, T., Dobrotka, S., Wallacher, D., Clemens, D., Metz, J. and Smarsly, B. M. (2019). Peering into the structural evolution of glass-like carbons derived from phenolic resin by combining small-angle neutron scattering with an advanced evaluation method for wide-angle X-ray scattering. *Carbon*, 141, 169-181, doi.org/10.1016/j.carbon.2018.09.025

Badaczewski, F. M., Loeh, M. O., Pfaff, T., Wallacher, D., Clemens, D. and Smarsly, B. M. et al. (2020). An advanced structural characterization of templated meso-macroporous carbon monoliths by small- and wide-angle scattering techniques. *Beilstein Journal of Nanotechnology*, 11, 310-322, doi.org/10.3762/bjnano.11.23

Faber, K., Badaczewski, F. M., Oschatz, M., Mondin, G., Nickel, W., Kaskel, S. and Smarsly, B. M. (2014). In-Depth Investigation of the Carbon Microstructure of Silicon Carbide-Derived Carbons by Wide-Angle X-ray Scattering. *The Journal of Physical Chemistry C*, 118, 29, 15705-15715. doi.org/10.1021/jp502832x

Faber, K., Badaczewski, F., Ruland, W. and Smarsly, B. M. (2014). Investigation of the Microstructure of Disordered, Non-graphitic Carbons. *Zeitschrift für anorganische und allgemeine Chemie*, 640, 15, 1307-1317. doi.org/10.1002/zaac.201400210

Loeh, M. O., Badaczewski, F. M., Faber, K., Hinter, S., Bertino, M. F., Mueller, P., Metz, J. and Smarsly, B. M. (2016). Analysis of thermally induced changes in the structure of coal tar pitches by an advanced evaluation method of X-ray scattering data. *Carbon*, 109, 823-825, doi.org/10.1016/j.carbon.2016.08.031

Loeh, M. O., Badaczewski, F. M., von der Lehr, M., Ellinghaus, R., Dobrotka, S., Metz, J. and Smarsly, B. M. (2018). Hard-templating of carbon using porous $SiO_2$ monoliths revisited - Quantitative impact of spatial confinement on the microstructure evolution. *Carbon*, 129, 552-563, doi.org/10.1016/j.carbon.2017.12.044

Pfaff, T., Badaczewski, F. M., Loeh, M. O., Franz, A., Hoffemann, J.-U., Reehuis, M., Zeier, W. G. and Smarsly, B. M. (2019). Comparative Microstructural Analysis of Nongraphitic Carbons by Wide-Angle X-ray and Neutron Scattering . *The Journal of Physical Chemistry C*, 123, 33, 20532-20546, doi.org/10.1021/acs.jpcc.9b03590

Pfaff, T., Simmermacher, M. and Smarsly, B. M. (2018). *CarbX* : a program for the evaluation of wide-angle X-ray scattering data of non-graphitic carbons. *Journal of Applied Christallography*, 51, 219-229, doi.org/10.1107/S1600576718000195

Ruland, W. and Smarsly, B. M. (2002). X-ray scattering of non-graphitic carbon: an improved method of evaluation. *Journal of Applied Crystallography*, 35, 624-633. doi.org/10.1107/S0021889802011007

Carbon 2022

# Durability of Metastable Graphene Oxide Colloids

**Hayato Otsuka, Koki Urita[2], Nobutaka Honma[3], Yasushi Amako[4], Radovan Kukobat, Junzo Ukai[3], Isamu Moriguchi[2] and Katsumi Kaneko**
Research Initiative for Supra-Materials, Shinshu University, 4-17-1 Wakasato, Nagano, Japan
Email: hayat_o@shinshu-u.ac.jp

[2]Graduate School of Engineering, Nagasaki University, Japan
[3]Mobility Material Engineering Div., Toyota Motor Corporation, Japan
[4]Faculty of Science, Shinshu University, Japan

**Keywords**
Graphene oxide, ripening, metastability

## INTRODUCTION

Graphene oxide (GO) and the so-called reduced graphene oxide are promising for a wide range of applications. GO colloids are metastable and undergo spontaneous reduction in aqueous solution, which is easily recognized by the color change. The gradual change can be regarded as ripening of the graphene oxide dispersions. Therefore, the changes of the structure and properties of GO with time must be systematically clarified in order to promote generally acceptable understanding of GO without degradation. Optical absorption spectral and magnetic property analyses of GO can provide structural information on the electronic state and/or $sp^2/sp^3$ ratio of GO. We accelerated the ripening process of GO colloids by elevation of the temperature to elucidate the unstable nature from the structural aspect.

This presentation will show the presence of two unstable states in GO colloids of a quite intrinsically unstable state and metastable one. The appropriate expiration date of GO colloids is proposed and the effective stabilization method of the intrinsically unstable GO is presented.

## EXPERIMENTAL

All guaranteed reagents other than graphite were purchased from FUJIFILM Wako Pure Chem. Co. Graphene oxide colloids were prepared from Madagascar graphite by means of improved Hummers' method. 2 g of graphite was oxidized with stirring at 310 ± 2 K for 4 hours with sulfuric acid (95%, 80 ml), phosphoric acid (85%, 9 ml), and potassium permanganate (99.3%, 10 g). After the reaction for 4 hours, the mixture was diluted with water and then the oxidation reaction was quenched by adding hydrogen peroxide. The manganese residue in the GO colloids was removed by 5 times washing with 5% hydrochloric acid through centrifugation, and then GO colloids were washed with distilled water 5 times. The clear yellow brown GO colloids were obtained through washing process. Equally divided GO colloids were ripened at different temperatures of 298, 308, 333, and 348 K for 1 h to 336 h (2-week). The aliquot was sampled after ripening for different times to measure their ultraviolet-visible (UV-vis) absorption spectra and zeta potential. The residual GO colloids ripened were freeze-dried (223K, 10 Pa) by a freeze dryer (FDU-12AS, AS-ONE). Those freeze-dried GO powders were characterized by X-ray diffraction, X-ray photoelectron spectroscopy and Raman spectroscopy. Magnetic properties of the freeze-dried GO powders were also investigated.

Transmission electron microscopic (TEM) images the freeze-dried GO powders were observed after annealing at 2073 K in Ar. Electron energy-loss spectroscopy (EELS) was conducted on a specific area on the TEM image.

## RESULTS AND DISCUSSIONS

The color of GO colloids just after preparation is yellow brown. The colour darkens with ripening and the ripening at higher temperature promotes darkening. (Figure 1(a)) The colour of GO ripened at 348 K for 48 h becomes black, while the GO ripened at 298 K has still brownish colour. The colour changes of GO colloids with ripening were analyzed quantitatively by UV-vis spectra.

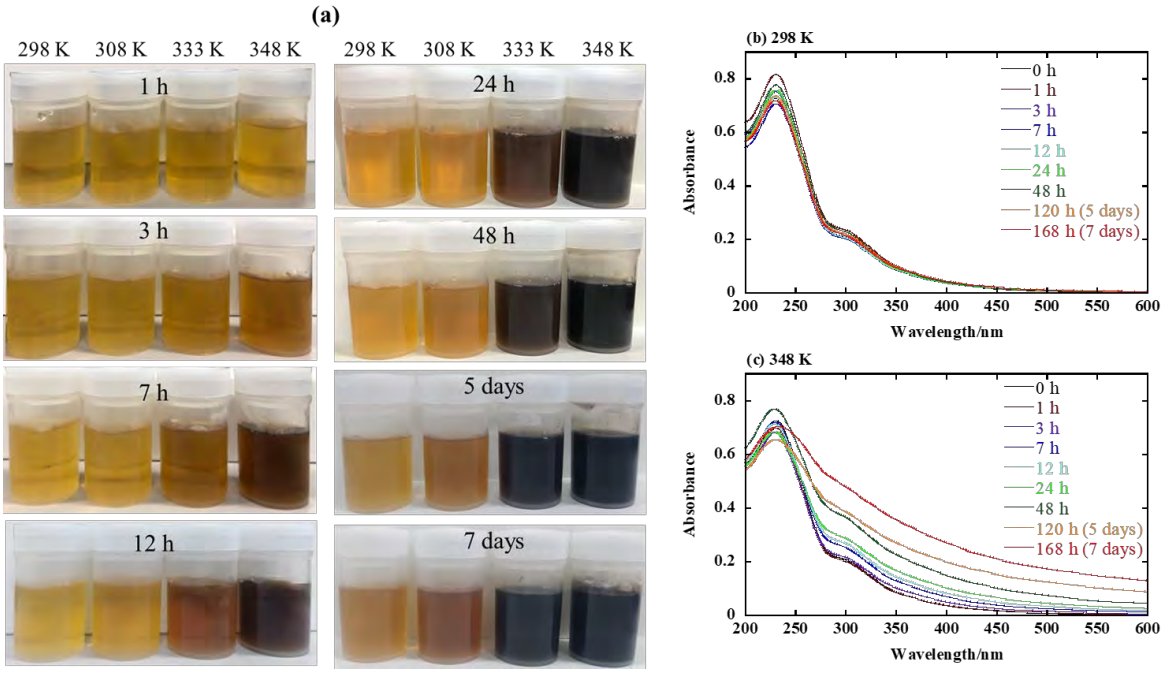


**FIGURE 1**: Pictures of GO colloids ripened at different temperatures for 1h to 7 days(a) and time variations of UV-vis absorption spectra of GO colloids ripened at 298 K(b) and 348 K(c). The ripening time: Black; 0 h, brown; 1 h, purple; 3 h, blue; 7 h, pale blue; 12 h, yellow green; 24 h, green; 48 h, orange; 120 h (5 days), and red; 168 h (7 days).

GO colloids without ripening (0 h) shows a main absorption peak at 230.4 nm assigned to $\pi \rightarrow \pi^*$ transition of aromatic C-C bonds and a broad shoulder around 300 nm assigned to $n \rightarrow \pi^*$ transition of C=O bonds. (Figure 1(b)) The absorption band of the GO colloids ripened at 348 K has a broad absorption tail in the visible region, which grows with the ripening time. (Figure 1(c)) This very broad absorption tail extending to 600 nm brings about the dark color. The systematic analysis of the $\pi \rightarrow \pi^*$ transition bands for GO colloids ripened gives a new insight on the unstable GO colloids. The GO colloids can be divided into three stages, a fresh GO which is named as an intrinsic GO (iGO), a following one metastable GO (mGO) and the last stage named transient GO (tGO) which is the initial stage of reduced GO. The details of each stage of GO colloids are explained in the presentation. This understanding enabled to evaluate durability of GO colloids. It was shown that freezing of the iGO was effective to preserve the characteristics of iGO.

## CONCLUSIONS

The spontaneous reaction of GO aqueous colloids is inevitable and undergo from just after exposure to water. The metastable state of GO colloids lasts relatively long term of a half year at room temperature, however the intrinsic GO colloids without any distinct changes in physical properties can be kept during 5 days at 298 K. The characteristics of the intrinsic GO can be preserved by the freezing state of GO colloids. Generally studied GO should be metastable GO, being not the intrinsic GO. The next stage research on unstable GO must rigorously describe the GO state from the three states evidenced in this study for common understanding of GO.

# Hydrogen-storage potential of Zn-, V-, Ni- and Li-doped fullerenes using DFT

**Andrea Oyarzún-Aravena and Hugo Ramos-Herrera**
Departamento de Ingeniería Química, Facultad de Ingeniería, Universidad de Magallanes, Punta Arenas, Chile, 6200000
Email: andrea.oyarzun@umag.cl

**Keywords**
Hydrogen storage, fullerene, metal-doped.

## INTRODUCTION

Hydrogen gas has the potential to replace fossil fuels as a clean and sustainable energy carrier. The main problem yet to solve is the development of a hydrogen storage method which is practical, safe, easy, and cost-effective. Materials-based $H_2$ storage is considered by the Unites States Department of Energy (DOE), to be a key technological option for the long-term applications, with a 5 wt% $H_2$ storage recommended for mobile applications.

In the last decades, carbon materials for hydrogen storage have received attention (Yang et al., 2012). It is possible to increase the storage capacity of graphene-based materials by the development of defects and porosity, and by chemical modifications including metal decorations and heteroatom doping (Shiraz and Tavakoli, 2017). The decoration with transition or alkali metals can affect the spillover or the kubas interactions. In the case of fullerenes, most of the studies apply computational chemistry to analyze the potential for internal storage (Pupysheva et al., 2008), and external storage including the hydrogenation or hydrides (El-Barbary, 2016) and external physisorption. Ni-, Si-, Na-, Li-, Ca-, Pd-, Pt-, and Ti-metal doped fullerenes and some composites with graphene or metallic organic frameworks have been studied. Experimental physical adsorption at 300 K and 70 bar can reach a hydrogen storage of 0.08 wt.% on untreated fullerenes, 0.51 wt.% on oxygen-treated fullerene and 0.64 wt.% on $CO_2$ activated fullerenes (Loutfy and Wexler, 2001). Doping with alkali metals can form fullerides (Mauron et al., 2012), increasing the adsorption energy to desirable values between 0.18-0.32 eV (Yoon et al., 2007). The dispersion of the metal atoms is also a relevant issue, as some metals might form clusters.

## METHODS

Density functional theory as implemented in Gaussian 16 (Frisch et al., 2016) is used to calculate the thermochemistry of Li, V, Ni, and Zn metals on the surface of $C_{60}$. After finding the ground state $MC_{60}$ isomer (Fig. 1a), the metal is analyzed for adsorption of one to five $H_2$ molecules (Fig. 1b). Finally, fullerenes covered with many metals are also evaluated (Fig. 1c). Distances and binding energies for metals and $H_2$ adsorption are reported (Fig. 1d). The calculations used the B3LYP/6-31g(d,p) and M06-2x/6-31g(d,p) functionals and basis set.

## RESULTS AND DISCUSSION

Fig. 1a shows the lowest energy locations found for the metal atom, which are labelled as ground state (g.s.). The most stable isomers are in the $\eta^5$ position for $LiC_{60}$ and $ZnC_{60}$, and $\eta^2$(6-6') for $VC_{60}$ and $NiC_{60}$. On these singly metal doped fullerenes, we adsorbed from one to five $H_2$ molecules as shown for $VC_{60}$ in Fig. 1b. Later, we studied the feasibility of each metal to cover the fullerene surface in the ground state position, finding clustering characteristics for $Zn_{12}C_{60}$ as shown in Fig, 1c, in contrast to $Li_{12}C_{60}$.

Finally we calculated hydrogen adsorption on the multiple metal-doped fullerenes as shown in Fig. 1d, reporting mean hydrogen binding energies as shown in Fig. 1e for Li and Ni. We have found that the

maximum hydrogen storage load for $Li_{12}C_{60}$, $Ni_6C_{60}$ and $V_6C_{60}$ is 8.3 wt%, 3.4 wt%, and 5.6 wt% respectively. Therefore, Li, Ni and V are possible candidates for further experiment research on metal-doped fullerenes for hydrogen storage.

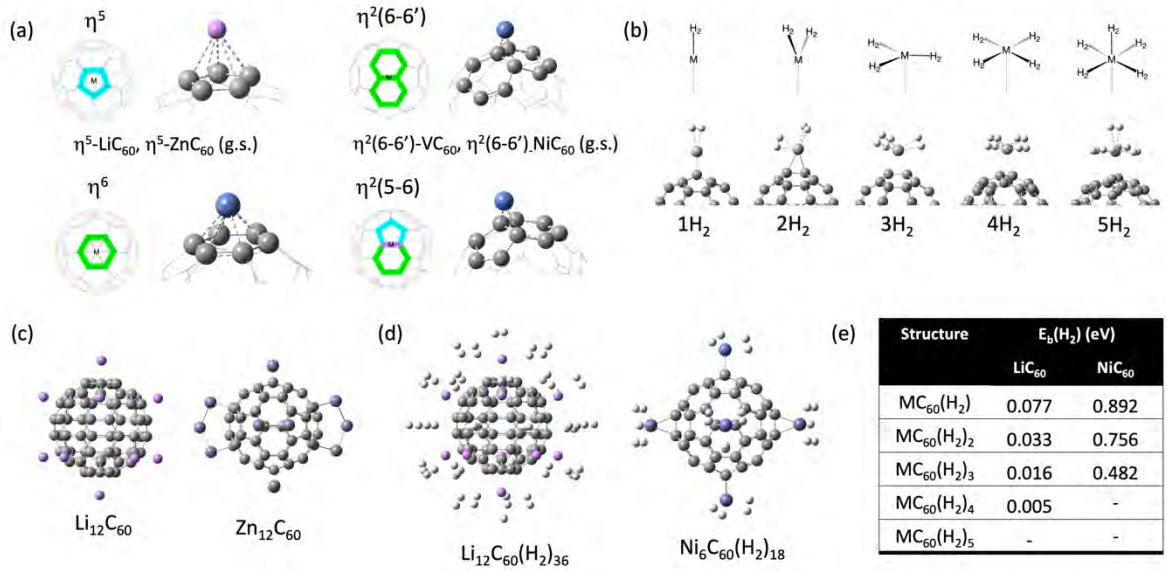


| Structure | $E_b(H_2)$ (eV) | |
|---|---|---|
| | $LiC_{60}$ | $NiC_{60}$ |
| $MC_{60}(H_2)$ | 0.077 | 0.892 |
| $MC_{60}(H_2)_2$ | 0.033 | 0.756 |
| $MC_{60}(H_2)_3$ | 0.016 | 0.482 |
| $MC_{60}(H_2)_4$ | 0.005 | - |
| $MC_{60}(H_2)_5$ | - | - |

**FIGURE 1**: (a) Ground state of $MC_{60}$, (b) one to five $H_2$ adsorbed on $VC_{60}$, (c) clustering effects of $Li_{12}C_{60}$ *vs*. $Zn_{12}C_{60}$, (d) hydrogen adsorption over $Li_{12}C_{60}(H_2)_{36}$ and $Ni_6C_{60}(H_2)_{18}$, and (e) mean $H_2$ binding energies for $LiC_{60}$ *vs*. $NiC_{60}$, all calculated with the B3LYP functional.

## CONCLUSIONS

Hydrogen adsorption on metal doped fullerenes was analyzed. Zn proved to be a poor candidate for enhancing hydrogen storage, while Ni, V, and Li show significantly greater potential for this application.


### Acknowledgements

This study has been supported by the Chilean National Research and Development Agency (ANID) through the FONDECYT Initiation Project 11170689.


### References


El-Barbary, A. A. (2016). Hydrogenation mechanism of small fullerene cages. *Int. J. Hydrogen Energy,* 41**,** [1], 375-383. https://doi.org/10.1016/j.ijhydene.2015.10.102

Frisch, M. J., Trucks, G. W., Schlegel, H. B., et al. 2016. Gaussian 16 Revision A.03. Gaussian Inc., Wallingford CT.

Loutfy, R. O. & Wexler, E. M. Feasibility of fullerene hydride as a high capacity hydrogen storage material. *In:* Mercuri, F., ed. Proceedings of the 2001 DOE Hydrogen Program Review, 2001. MER.

Mauron, P., Remhof, A., Bliersbach, A., et al. (2012). Reversible hydrogen absorption in sodium intercalated fullerenes. *Int. J. Hydrogen Energy,* 37**,** [19], 14307-14314. https://doi.org/10.1016/j.ijhydene.2012.07.045

Pupysheva, O. V., Farajian, A. A. & Yakobson, B. I. (2008). Fullerene Nanocage Capacity for Hydrogen Storage. *Nano Lett.,* 8**,** [3], 767-774. https://doi.org/10.1021/nl071436g

Shiraz, H. G. & Tavakoli, O. (2017). Investigation of graphene-based systems for hydrogen storage. *Renew. Sustain. Energy Rev.,* 74104-109. https://doi.org/10.1016/j.rser.2017.02.052

Yang, S. J., Jung, H., Kim, T., et al. (2012). Recent advances in hydrogen storage technologies based on nanoporous carbon materials. *Prog. Nat. Sci.: Mater. Int.,* 22**,** [6], 631-638. https://doi.org/10.1016/j.pnsc.2012.11.006

Yoon, M., Yang, S., Wang, E., et al. (2007). Charged Fullerenes as High-Capacity Hydrogen Storage Media. *Nano Lett.,* 7**,** [9], 2578-2583. https://doi.org/10.1021/nl070809a

# PREPARATION OF IONIC LIQUIDS SUPPORTED (SILP) ON COMMERCIAL CARBONACEOUS MATERIALS FOR $CO_2$ CAPTURE.

**C. Paramio, J. Lemus, D. Hospital-Benito, C. Moya, R. Santiago, A. Belinchón, E. Hernández, P. Navarro, J. Palomar**

*Chemical Engineering Department/ Universidad Autónoma de Madrid/ 28049 Madrid*

**E-mail: coral.paramio@uam.es*

***Keywords:*** $CO_2$ Capture, supported ionic liquids, activate carbon, fixed-bed column.

## Introduction

The reduction of $CO_2$ emissions into the atmosphere is receiving great interest from the scientific community. For this reason, there is a constant search of new solvents and materials that allow to overcome the current limitations linked to the $CO_2$ capture processes. [1]. In this context, ionic liquids (ILs) are presented as an alternative to conventional solvents, due to their excellent properties as sorbents, highlighting their high capacity and thermal stability, low toxicity, high selectivity towards $CO_2$ and a wide range of possible ionic combinations (design solvents). Nonetheless, ILs present a great viscosity, a fact that negatively affects to mass transfer phenomena [2]. Supported ionic liquids (SILP) emerge with the goal of increasing gas-liquid contact area, since IL is supported on porous materials and the amount of IL is optimized, make them an attractive alternative to neat ILs.

## Experimental procedure

In the present work, different SILP materials have been used, where activated carbon, silica and carbon cloth were selected as supports. [Bmim][Acetate] has been the chosen IL, which was confined in the supports by incipient wetness impregnation. First, fixed-bed experiments with a constant height have been carried out. The inlet stream was a mixture of $CO_2/CH_4/H_2$ at different concentrations, with a constant flow of 10 NmL/min, at 40ºC and several $CO_2$ partial pressures (1, 5 y 10 bar). In turn, CO2 solubility ($W_{CO2}$, $mol_{CO2}/kg_{LI}$) in the different supports has been measured in a gravimetric high-pressure sorption analyzer (ISOSORP GAS LP-flow, Rubotherm). Finally, Aspen Adsorption simulator were used to fit the breakthrough curves and determine the mass transfer coefficients($K_{MTC}$) [3].

## Results y discussion

In order to study the thermodynamic behavior of different SILPs, fixed-bed experiments have been carried out. The breakthrough curves have been fitted by means of a linear driving force model, implemented in Aspen Adsorption (red line), allowing to obtain the mass transfer coefficients ($K_{MTC}$). *Figure 1* shows how an increment in $CO_2$ partial pressure ($p_{CO2}$) causes an increase in breakthrough times as a consequence of a gain in absorption capacity. These breakthrough times are longer for silicas because of their high density, i.e., there is a greater bed mass for a constant height of about 19 cm. $K_{MTC}$ values are also affected by the change in $p_{CO2}$, increasing the rate of $CO_2$ uptake as pressure increase. At last, the $K_{MTC}$ value in SILP with silica is also influenced by the particle size, being higher for a smaller particle size, due to an increment in the G-L contact area.

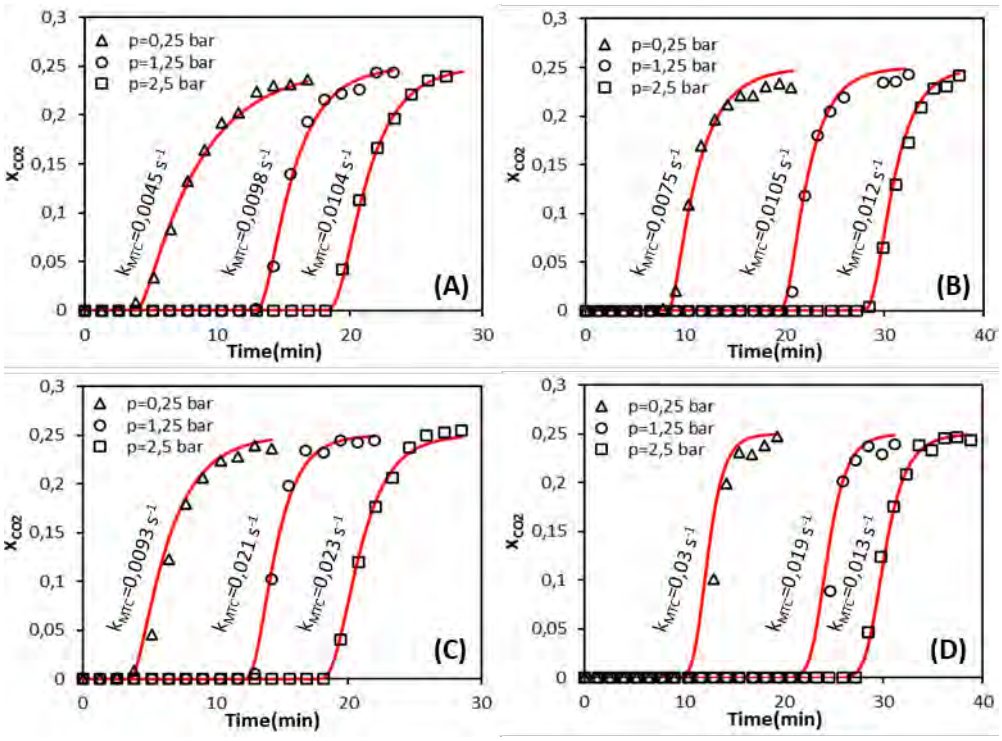


Figure 1. SILP breakthrough curves at different $CO_2$ partial pressures and at 40°C using SILP supports prepared with (A) Monolith, (B) $SiO_2$ 500 µm, (C) CAPSUPER y (D) $SiO_2$ 150 µm.

## Conclusions

Different SILP materials impregnated with [Bmim][Acetate] have been assessed in order to analyze which support is the most suitable for $CO_2$ capture processes. To evaluate these materials, fixed-bed experiments have been carried out, where the effects of $p_{CO2}$ and material density have been studied. All the materials showed longer breakthrough times as $p_{CO2}$ increased. Lastly, the breakthrough curves were fitted using a linear kinetic model implemented in Aspen Adsorption, let us to calculate the $K_{MTC}$ values. Results showed how the $K_{MTC}$ increased at higher $p_{CO2}$, i.e., the $CO_2$ absorption rate in SILP grows with $p_{CO2}$, with the medium silica being the support that presents the highest $CO_2$ uptake rates.

**Acknowledgments:** The authors thank the Ministerio de Ciencia e Innovación (projects PID2020-118259RB-I00 and PDC2021-120881-I00) and the Comunidad de Madrid (project P2018/EMT4348) for the financial support and the Centro de Computación Científica de la Universidad Autónoma de Madrid for the computational facilities.

## References

[1] M. Mier, C. Weissbart, Power markets in transition: Decarbonization, energy efficiency, and short-term demand response, Energy Econ. 86 (2020).
[2] H. Zhai, E.S. Rubin, Technical and Economic Assessments of Ionic Liquids for Pre-Combustion CO2 Capture at IGCC Power Plants, in: Energy Procedia, Elsevier Ltd, 2017: pp. 2166–2172.
[3] R. Santiago, J. Lemus, D. Hospital-Benito, C. Moya, J. Bedia, N. Alonso-Morales, J.J. Rodriguez, J. Palomar, CO2 capture by supported ionic liquid phase: Highlighting the role of the particle size, ACS Sustain. Chem. Eng. 7 (2019) 13089–13097.

Carbon 2022

# The Texture, Structure, and Nanotexture of ToF-CVD-Prepared Carbon Micro-/Nano-Cones

**Germercy Paredes[1], Rongrong Wang[2], Pascal Puech[3], Grégory Seine[3], Jean-Marc Leyssale[4], Raul Arenal[2], Aurélien Masseboeuf[3], Fabrice Piazza[1], Marc Monthioux[3]**

[1]Laboratorio de Nanociencia, Pontificia Universidad Católica Madre y Maestra, Santiago, Dominican Republic

Email: gd.paredes@ce.pucmm.edu.do

[2]Instituto de Nanociencia y Materiales de Aragon (INMA), CSIC, Universidad de Zaragoza, Spain.

[3]Centre d'Elaboration des Matériaux et d'Etudes Structurales (CEMES), UPR8011 CNRS, Université Toulouse 3, Toulouse, France.

[4]Institut des Sciences Moléculaires (ISM), UMR 5255 CNRS, Université de Bordeaux, Talence, France.

**Keywords**

Scroll texture, Growth mechanisms, Identification of defects

## INTRODUCTION

Carbon conical morphologies exhibit interesting geometrical features (*e.g.*, needle-like shape, small apex) and excellent physical properties (e.g. mechanical resistance, electrical, thermal conductivity) that make them excellent candidates for many applications such as electron emission, and near-field microscopy probes, with better performances than other carbon materials such as nanotubes (CNTs). Individual micro-/nano-cones (CnCs) were grown onto CNTs as individual supports using a Time-of-Flight Chemical Vapor Deposition (ToF-CVD) process (Allouche, 2003; Paredes, 2020). CnCs are all-graphenic micro-/nano-objects, made of a rough-surface fibre-segment with protruding smooth-surface conical parts at both ends (Figure 1a).

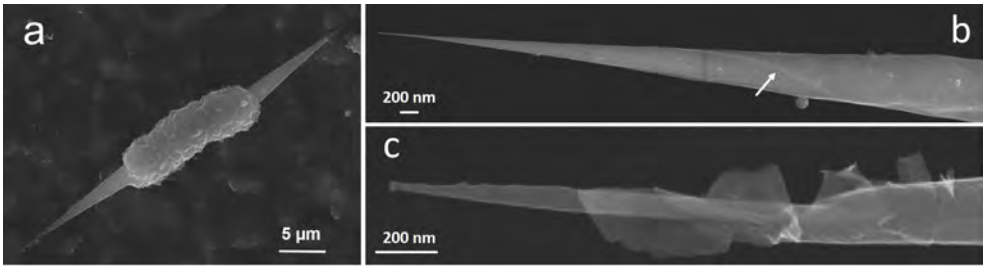


**FIGURE 1.** Scanning electron microscopy (SEM) images. (a) Example of an as-grown CnC morphology. (b) close-up on a cone end; the arrow designates a step at the cone surface, presumably a graphene edge; (c) the same cone surface as in (b) after passing a current, and showing the unwrapping of the graphene layers.

The very first steps of CnC formation were shown to be dominated by the physical behaviour of a short-lifetime polyaromatic hydrocarbon (PAH)-rich liquid wetting the CNTs (Paredes, 2021). Afterwards, the fibre-segment mostly grows from the PAHs while the conical parts mostly grow from the radicals, as both species are present in the gas phase (Paredes, 2021). The nanotexture and texture of CNCs have been partially studied, suggesting that the cones might follow a Russian-doll model with concentric graphenes parallel to the cone axis, in which many graphenes could present the same helicity (Allouche, 2005; Paredes, 2022). Consequently, the conical shape makes that the cone surface exhibits many graphene edges (which are chemisorption sites for the radicals).

However, a systematic study regarding the graphene arrangement, in particular at the cone apex, which can be a crucial aspect when considering potential applications, was still needed. In this work, we investigated the texture, structure and nanotexture of CnCs, by analysing their behaviour when passing a current through it, and by performing multiple characterization studies such as high-resolution transmission electron microscopy (HRTEM), HR-SEM, Raman spectroscopy, and molecular dynamic modelling, in order to show how actually these cones look like, particularly at the apex.

## RESULTS AND DISCUSSION

### Concentric *Versus* Scroll Growth

SEM images of the cone surface (Figure 1b) show faint, oblique lines suggesting that the graphene edges at the cone surface could adopt a spiral display, indicating a scroll configuration of the graphenes**.** This was confirmed by conducting a scaled-down duplicate of the experiment carried-out by Bacon (1960) to reveal the way graphenes were displayed in carbon whiskers. For doing so, a current of 2 nA at 1,1 V and then of 5 nA at 0,25 V was passed through the carbon cones. An unwrapping phenomenon of the cone surface was observed (Figure 1c), thereby demonstrating that the cone texture is preferably scroll-like, with the scroll turns being parallel to the cone axis as for Bacon's carbon whiskers. This explains why many of the concentric graphenes (actually scroll turns) were found to exhibit the same helicity vector. Such a spiral growth is a common way for crystals to grow rapidly when starting from a screw dislocation. However, calculations showed that the cones are made with hundreds or thousands of concentric graphenes, making unlikely that a single cone could be formed by a single, wrapped graphene. A texture as shown in Figure 2 is proposed, involving multiple intricated concentric scrolls combined with a Russian-doll model for the earliest growth step, which is consistent with the distinct roles of the radicals and the PAHs previously mentioned.

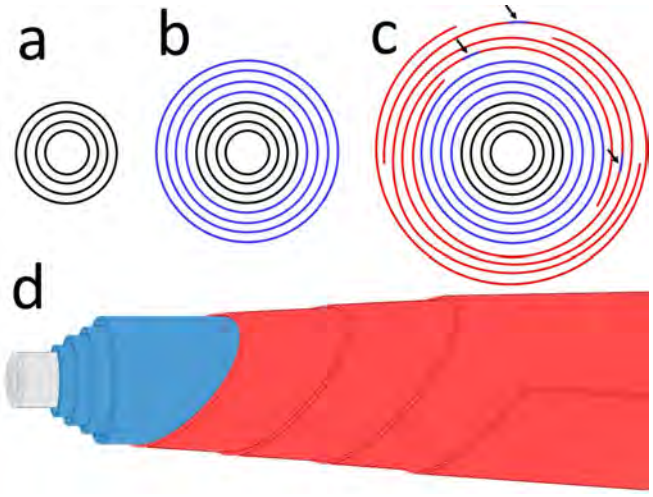


**FIGURE 2.** Sketches (cross-sections, but (d)) of the way graphenes may display during the cone formation. (a) The supporting CNT, in which graphenes are concentric (black circles) following the Russian-doll model. (b) Formation of a primary, spindle-like cone, also with the concentric, Russian-doll texture (blue circles), from the carbonisation of PAHs from the liquid phase (Paredes, 2021). (c) The inner concentric graphenes (blue circles) grow in length (perpendicular to the figure) thanks to the chemisorption of species (PAHs or radicals) to the graphene edges; meanwhile, the cone also grows both in diameter and length thanks to physisorbed then carbonised individual PAHs which act as nuclei (arrows) from which graphenes develop as scrolls (red spirals) thanks to the chemisorption of radicals to the edges. (d) Longitudinal view of a cone as seen in (c).

### At The Cone Apex

HR-TEM images of carbon cones confirmed that the cone surface exhibits many steps, most of them with a height of a single-layer graphene, although some steps are higher because made of multiple

graphenes, which are those visible by HR-SEM. The graphene nanotexture is perfect all over the cone length, despite they are several-micrometres long. A specific type of double-graphene termination was observed at the cone apex, showing that the edges of two superimposed graphenes close onto each other without exhibiting any curvature (additional to the cylindrical curvature), making the edges looking like they are zipped. It is thus different from the more common "loop" termination which looks like it is made of single graphene heavily folded on itself, and exhibiting negative curvatures at the fold in order to relax the constraints on the C-C bonds. An in-house molecular dynamics (MD) code, operating in the canonical ensemble at the synthesis temperature of the cones (1400 °C), was used to demonstrate that such a zipped graphene closure is plausible and structurally stable. It is made possible by a high number of heterocycles (*i.e.*, aromatic rings with 5, 7, and 8 carbon atoms), which are necessary to accommodate both the cylindrical curvature and the mismatch between the number of carbon atoms available at the edges of the two concentrically superimposed graphene lattices. Simulated HR-TEM images were also performed and matched well the experimental ones. Finally, Raman spectroscopy (wavelength of 632.8 nm, spot size of 0.5 µm and a power of 0.7 mW) was used to analyse cone apices. A $I_D/I_{D'}$ ratio of 1.5 was found, which is the lowest ever reported in the literature., and believed to be the signature of such zip termination. Combining this result with others from the literature, the $I_D/I_{D'}$ Raman ratio appears to be a key parameter to identify 5 different types of graphene defects with values ranging from ~1.5 to ~13.

A detailed version of the work will be published in Paredes (2022).

**CONCLUSIONS**

Individual carbon micro-/nano-cones produced by ToF-CVD at high temperature are made of perfect concentric graphenes along the cone axis, most of them following a scroll-like model. A growth mechanism involving a primary Russian-doll-type texture subsequently covered with a multiple scroll-type texture is proposed, which accounts for all the observations. A specific kind of double-graphene termination is revealed at the cone apex looking like the edges of a pair of graphenes are zipped to each other without any kind of deformation. Despite they form at 1400 °C, "zip" defects are stable at room temperature, and result from the occurrence of many aromatic heterocycles formed to allow the closing process. A specific Raman signature of zip defects is proposed, corresponding to the lowest $I_D/I_{D'}$ ever reported. Our study confirms the latter ratio as an identification parameter for a variety of defects in graphene systems.

**Acknowledgements**

This study has been supported through the EUR grant NanoX n° ANR-17-EURE-0009, the Government of Aragon (project DGA E13-20R), the Spanish MICINN (PID2019-104739GB-100/AEI/10.13039/501100011033), the European Union H2020 programs “ESTEEM3” (Grant number 823717), the “Graphene Flagship” CORE 3 (Grant number 881603), and The Pontificia Universidad Católica Madre y Maestra (Dominican Republic).

**References**

Allouche, H., Monthioux, M. and Jacobsen, R. (2003). Chemical vapor deposition of pyrolytic carbon on carbon nanotubes: (I) synthesis and morphology. *Carbon*, 41, 2897-2912.

Allouche, H. and Monthioux, M. (2005). Chemical vapor deposition of pyrolytic carbon on carbon nanotubes. Part 2. Texture and structure. *Carbon*, 43, 1265-1278.

Bacon R. (1960). Growth, structure, and properties of graphite whiskers. *J. Appl. Phys*., 31, 283-290.

Paredes, G. (2020). *Development of new probes based on carbon nanocones for near-field microscopies*. PhD Dissertation, University of Toulouse (France).

Paredes, G., Ondarçuhu, T., Monthioux, M., and Piazza, F. (2021). Unveiling the existence and role of a liquid phase in a high temperature (1400 °C) pyrolytic carbon deposition process. *Carbon Trends*, 5, 10017.

Paredes, G., Wang, R., Puech, P., Seine, G., Leyssale, J.-M., Arenal, R., Masseboeuf, A., Piazza, F. and Monthioux, M. (2022). Texture, nanotexture, and structure of carbon nanotube-supported carbon cones. (submitted).

Carbon 2022

# Quantitative self-assembly of metal-organic mesocrystal for carbon architecture with controlled pore aperture

**Jae Seo Park and Seung Jae Yang***
Department of Chemistry and Chemical Engineering, Education and Research Center for Smart Energy and Materials, Inha University, Incheon 22212, Republic of Korea
Email: sjyang@inha.ac.kr

**Keywords**
Porous carbon, Multi-scale adsorption, Bottom-up construction of carbon architecture

## INTRODUCTION

Mesocrystal, a unique aggregate composed of nanocrystals, has been considered as a design strategy for complicated structure due to their anomalous construction method (Zhu et al. 2021). In particular, mesocrystal structured from building units based on metal-organic coordination have an inherent architecture that could not be accessible in the metal-organic framework (MOF), providing great advantages for bottom-up design of materials (Hwang et al. 2019). Moreover, as a precursor for carbon materials, metal-organic mesocrystals provide enormous opportunities for hierarchical structuring through their thermal transformation into carbonaceous materials (Qiu et al. 2021). However, current synthetic and controlling routes for metal-organic mesocrystal have been hindered by complex metal-organic interaction, requiring various reaction directors such as surfactant and pH-modulator.

Herein, we suggest a mesocrystal with quantitative self-assembly behavior of metal-organic building blocks without external factors. The supersaturated metal-organic nuclei were transformed into characteristic primary structures according to the initial concentration of precursor. Subsequently, the particle-mediated attachment occurs around the respective primary structure, resulting in the formation of mesocrystal with different architectures. As transformable scaffolds, the resulting mesocrystals were thermally transformed into carbon structures. Owing to the hierarchical architecture of mesocrystals, the pore aperture of carbon structures was highly diversified, providing universal adsorption capability over a wide scale of chemicals.

## METHOD

For the synthesis of metal-organic mesocrystal, the zinc acetate dihydrate (ZAD) of 100 mM and 2,6-Naphthalenedicarboxylic acid (NDC) of 50 mM were dissolved in N-Methyl-2-Pyrrolidone (NMP). After aging at the ambient atmosphere, the white precipitates were obtained, and washed with NMP. To investigate the impact of initial nuclei density on self-assembly behavior, increased concentration of ZAD and NDC were used with identical procedure. Thermal conversion of mesocrystals was conducted at 900 °C for 3 hours with heating rate of 5 °C/min. The morphological properties were investigated by scanning electron microscopy (SEM; S-4300SE, Hitachi) and transmission electron microscopy (TEM; JEM-2100F, JEOL). The quantifying textural properties were conducted by static volumetric gas adsorption apparatus (Belsorp-max, BEL) and mercury porosimeter (AutoPore IV 9500, Micromeritics).

## RESULTS AND DISCUSSION

Depending on the reaction time, the Zn-NDC cloudy solution became clear, and a white precipitate was observed at the end of the reaction. The gravity-induced precipitation of the metal-organic nuclei forms a spontaneous primary structure, which is then converted into mesocrystals by particle attachments.

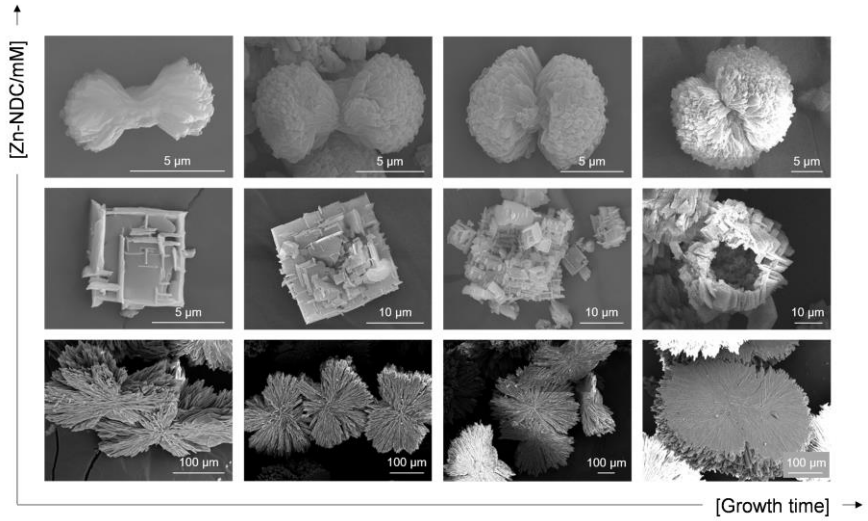


**FIGURE 1**: Ex-situ SEM analysis of mesocrystal with various initial nuclei densities.

In this synthetic route, the primary structure is crucial for subsequent structuring, as growth is continued by particle attachment to the initial structure. Based on our hypothesis, we investigated the impact of nuclei density on the primary structure and resultant mesocrystal. To improve the nucleation density, the concentrations of the initial reactants were increased. The morphological changes of mesocrystal were characterized by ex-situ SEM to elucidate differentiation according to growth time as observed in FIGURE 1. It is noteworthy that the primary structure is varied with the concentration of initial precursor, suggesting the different self-assembly behavior of Zn-NDC nuclei. In addition, the respective primary structure was differentiated into unique architecture, highlighting the importance of primary structure for the resulting morphology of mesocrystal.

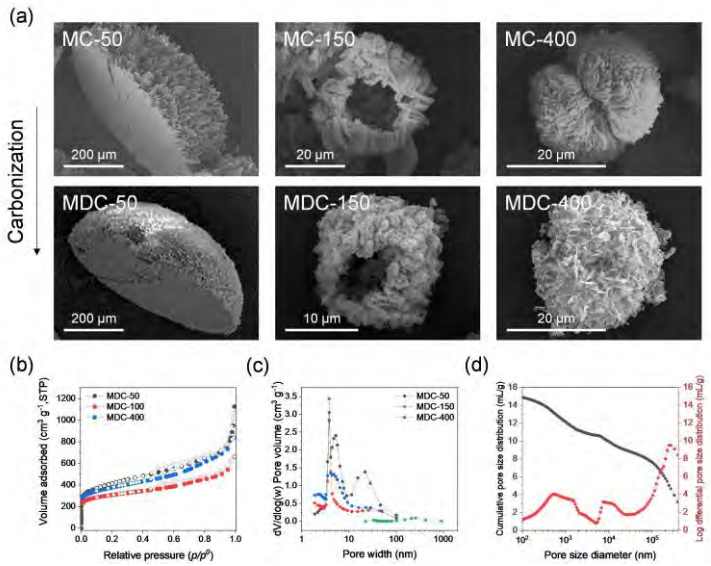


**FIGURE 2**: (a) SEM images of mesocrystals and their thermal-derivatives (samples denoted as MC-X and MDC-X according to the concentration of reactant ZAD). (b) $N_2$ adsorption-desorption, and (c) pore size distribution of MDC series. (d) Mercury intrusion results of MDC-50.

To exploit their fractal-like hierarchical structure, the thermal conversion of mesocrystal was conducted as shown in FIGURE 2(a) The inherent structure was well-preserved even after direct carbonization, contributing to the evolution of textural properties with enormous meso- and macropores. Moreover, the atomically distributed Zn-species participate in the development of micro- and mesopores (Yang et al. 2015). The $N_2$ adsorption revealed the highly developed textural properties of carbon structures (FIGURE 2(b)). The significant uptake at low relative pressure represents the existence of micropores. The hysteresis at middle relative pressure and high uptake at endpoint indicated the presence of meso- and macropore, respectively. The pore size distribution calculated from Barrett-Joyner-Halenda (BJH) exhibited the quasi-continuous pore system of the carbon structures (FIGURE 2(c)) We selected the representative carbon structures (MDC-50) for quantifying distribution and volume which is originated from macropore. Even at large size of pore scale, the MDC-50 possesses remarkable macropore volume, manifesting the high degree of structural hierarchy (FIGURE 2(d)). Further inspection of hierarchical pore system with micro-, meso-, and macropore system was performed by adsorption test for various chemicals including gas, dye, and polymers. Benefitting from diversified textural properties, the carbon structure showed universal adsorption capability for these absorbates.

## CONCLUSIONS

We demonstrate the synthesis and quantitative self-assembly of mesocrystal which can be transformed into pore-diversified carbon structures. Because of the unique construction method of mesocrystal, the different type of morphologies was realized using only single nuclei (Zn-NDC), exhibiting the polymorphism. Furthermore, the pore system of mesocrystal-derived carbons was distinctly maximized by unique structure and Zn-based pore generation. As a consequence, these carbon structures showed universal capability for a wide range of chemicals. We believe that this synthetic route can be expended for the bottom-up synthesis of carbon structures.

**Acknowledgements**

This research was supported by the Material/Parts Technology Development Program (20017548) and Technology Innovation Program (20010853) funded by the Ministry of Trade, Industry & Energy (MOTIE, Korea).

**References**

Hwang, J., Walczak, R., Oschatz, M., Tarakina, N. V. and Schmidt, B. V. (2019) 'Micro-Blooming: Hierarchically Porous Nitrogen-Doped Carbon Flowers Derived from Metal-Organic Mesocrystals', *Small*, 15(37), 1901986. https://doi.org/10.1002/smll.201901986

Qiu, X., Wang, X., He, Y., Liang, J., Liang, K., Tardy, B. L., Richardson, J. J., Hu, M., Wu, H. and Zhang, Y. (2021) 'Superstructured mesocrystals through multiple inherent molecular interactions for highly reversible sodium ion batteries', *Sci. Adv.*, 7(37), eabh3482. https://doi/10.1126/sciadv.abh3482

Yang, S. J., Antonietti, M. and Fechler, N. (2015) 'Self-assembly of metal phenolic mesocrystals and morphosynthetic transformation toward hierarchically porous carbons', *J. Am. Chem. Soc.*, 137(25), 8269-8273. https://doi.org/10.1021/jacs.5b04500

Zhu, G., Sushko, M. L., Loring, J. S., Legg, B. A., Song, M., Soltis, J. A., Huang, X., Rosso, K. M. and De Yoreo, J. J. (2021) 'Self-similar mesocrystals form via interface-driven nucleation and assembly', *Nature*, 590(7846), 416-422. https://doi.org/10.1038/s41586-021-03300-0

Carbon 2022

# A flexible and transparent supercapacitor with high specific capacitance based on layered double hydroxide@carbon nanotube film

**Ji Yong Park[1] and Seung Jae Yang[1]**
[1]Department of Chemistry and Chemical Engineering, Inha University, Incheon, 22212, Republic of Korea
Email: 22202275@inha.edu (J.Y. Park), sjyang@inha.ac.kr (S.J. Yang).

**Keywords**
NiCo- Layered double hydroxides, Carbon nanotubes, Transparent supercapacitor

## INTRODUCTION

An emerging proliferation in portable intelligent electronics is moving toward flexible and optically transparent devices, such as displays, panels, phones, tablets, and other touchable devices (Zhao et al., 2020). The ever-growing market demands are driving advances in flexible transparent power sources with excellent energy storage activity and high optical transparency under deformation conditions (Simon and Gogotsi, 2020). Owing to their high transparency and electrical conductivity, indium tin oxide (ITO) is the most widely used transparent electrode material for the last decades. However, the use of ITO has difficulties in flexible electronics due to brittle nature properties and limited resources. For these reasons, carbon nanotubes (CNTs), graphene, metal meshes, and metal nanowires have received extensive attention for alternative transparent conductive materials (Chen et al., 2019). Among these promising candidates, CNT flexible transparent conductive film (FTCF) exhibits high potential because of its outstanding optical, mechanical, and electrical properties with high environmental stability, and good flexibility (Zhou and Azumi, 2016).
In this research, we propose the direct fabrication of ultra-thin, highly conductive, and transparent CNT films based on aerogel without an additional dispersion process. Also, to enhance capacitance, we created layered double hydroxides (LDHs) using electrochemical deposition on transparent CNT skeletons because they are electrically conductive and transparent even after the deposition. We specifically used LDHs, because LDH@CNT films can not only partially solve the low conductivity of LDHs, but also results in high specific capacitance, rate performance, optical transparency, flexibility, and durability of FTCFs (Zhou and Azumi, 2016).

## METHOD

In this study, the CNT films were made by direct spinning method. Double walled CNT (DWCNT) aerogel was synthesized at 1200°C by floating catalyst chemical vapor deposition (FCCVD) process in a vertical alumina tube furnace. This DWCNT aerogel is continually wound out of the hot zone as a film by a PET film covered winding roller at the end of the tube furnace.
The NiCo-LDH@CNT film was prepared by the electrodeposition method using three-electrode system, with CNT film as the working electrode, platinum as the counter electrode, and Ag/AgCl electrode as the reference electrode (Wang et al., 2017). The prepared 1M cobalt nitrate hexahydrate and nickel nitrate hexahydrate solutions were used as the sources of Co and Ni. The electrodes were immersed in the solution for 1h, followed by electrodeposition proceeded under constant potential of -0.6 V (vs. Ag/AgCl electrode).

## RESULTS AND DISCUSSION

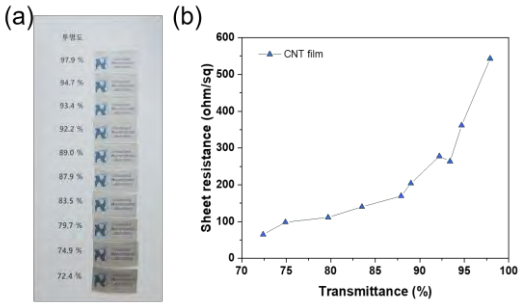


**FIGURE 1**: (a) Virtual image of with varying transparency made by direct spinning method. (b) Transmittance versus sheet resistance of CNT films

We prepared CNT films with various transparency as shown in figure 1(a). To adjust the transparency of the CNT films, we changed the winding number of CNT aerogels. In figure 2(b), As the transparency decreased, the sheet resistance ($R_s$) tended to decrease; 543 ohm/sq at 97.9 %(5r), 277 ohm/sq at 92.2 %(20r), and 140 ohm/sq at 83.5 %(40r).

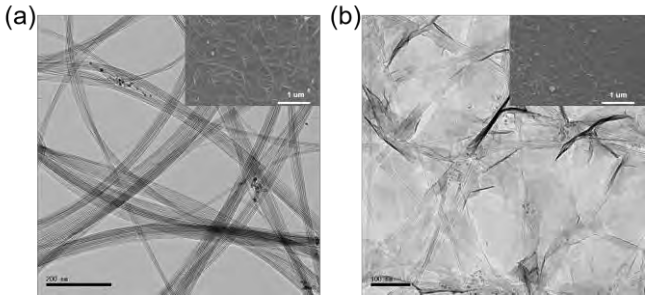


**FIGURE 2**: Tem image of (a) pristine CNT film and (b) NiCo-LDH@CNT film (inset: SEM image of corresponding film)

NiCo-LDH was synthesized through electrodeposition. The reaction mechanism of electrodeposition to prepare Ni–Co LDH is explained by the following reaction equation (Li et al., 2019).

$$NO_3^- + 7H_2O + 8e^- \rightarrow NH_4^+ + 10OH^- \quad [1]$$

$$Co^{2+} + 2OH^- \rightarrow Co(OH)_2 \quad [2]$$

$$Ni^{2+} + 2OH^- \rightarrow Ni(OH)_2 \quad [3]$$

When synthesizing the NiCo-LDH, the procedure does not require the addition of an alkali source, because hydroxide ions produced by reaction between nitrate ion and water molecules as shown in reaction [1]. The synthesized 2D NiCo-LDH (figure 2(b)) grew up in CNT bundle skeleton (figure 2(a)) with a network structure.

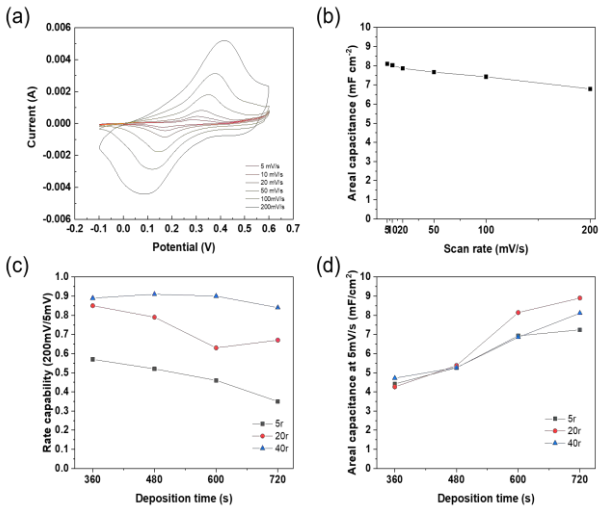


**FIGURE 3**: (a) CV curves of NiCo-LDH@CNT film (40r 720s) in potential window of -0.1 to +0.6V. (b) Areal capacitance of the electrodes calculated form the CV curves. (c) Deposition time versus rate capability (200mV/s to 5mV/s) and (d) Areal capacitance at 5mV/s about three kinds of sample with different deposition time.

Figure 3(a) displays the CV curves of NiCo-LDH@CNT film (40r 720s) at a scan rate of 5, 10, 20, 50, 100, 200 mV/s with a potential window of -0.1 to 0.6V. The electrodes have discrete faradaic redox peaks about 0.1V and 0.4V, showing that reversible valence state shifts between $Ni^{2+}/Ni^{3+}$ and $Co^{2+}/Co^{3+}$ are primarily responsible for the electrodes' electrochemical activity. Figure 3(b) illustrates the areal capacitances of the composite films calculated from the CV at various scan rate. With the increase of scan rate, the areal capacitance decreases 8.11 mF/cm$^2$ to 6.79 mF/cm$^2$. Figure 3(a) and (b) show that rate capability has improved as the amount of CNT increases, while the areal capacitance depends on the amount of LDH controlled by deposition time.

Through NiCo-LDH@CNT film, we were able to get a highly transparent and flexible supercapacitor with high-rate capability with high capacity. Furthermore, we found out the correlation between the mass ratio of CNT and LDH controlled by deposition time influencing the performance of supercapacitor, which will be a guideline to higher capacity.

## ACKNOWLEDGMENT

This research was supported by the Material/Parts Technology Development Program (20017548) and Technology Innovation Program (20010853) funded by the Ministry of Trade, Industry & Energy (MOTIE, Korea).

## REFERENCES

CHEN, J., WANG, Y., LIU, W. & MA, Y. 2019. Nano-Engineered Materials for Transparent Supercapacitors. ChemNanoMat, 6, 42-52. https://doi.org/10.1002/cnma.201900369

LI, Y., SHAN, L., SUI, Y., QI, J., WEI, F., HE, Y., MENG, Q., REN, Y. & LIU, J. 2019. Ultrathin Ni–Co LDH nanosheets grown on carbon fiber cloth via electrodeposition for high-performance supercapacitors. Journal of Materials Science: Materials in Electronics, 30, 13360-13371. https://doi.org/10.1007/s10854-019-01703-4

SIMON, P. & GOGOTSI, Y. 2020. Perspectives for electrochemical capacitors and related devices. Nat Mater, 19, 1151-1163. https://doi.org/10.1038/s41563-020-0747-z

WANG, X., LI, X., DU, X., MA, X., HAO, X., XUE, C., ZHU, H. & LI, S. 2017. Controllable Synthesis of NiCo LDH Nanosheets for Fabrication of High-Performance Supercapacitor Electrodes. Electroanalysis, 29, 1286-1293. https://doi.org/10.1002/elan.201600602

ZHAO, W., JIANG, M., WANG, W., LIU, S., HUANG, W. & ZHAO, Q. 2020. Flexible Transparent Supercapacitors: Materials and Devices. Advanced Functional Materials, 31. https://doi.org/10.1002/adfm.202009136

ZHOU, Y. & AZUMI, R. 2016. Carbon nanotube based transparent conductive films: progress, challenges, and perspectives. Sci Technol Adv Mater, 17, 493-516. https://doi.org/10.1080/14686996.2016.1214526

20 C 22 arbon 2022

# Influence of carbon support structure on cathode catalysts durability

**Miroslawa Pawlyta[1], Szymon Smykala[1], Barbara Liszka[2], Agata Blacha-Grzechnik[3]**

[1] Silesian University of Technology, Materials Research Laboratory, Konarskiego 18A, 44-100 Gliwice, Poland

Email: miroslawa.pawlyta@polsl.pl

[2] Faculty of Natural Sciences, University of Silesia in Katowice, Bedzinska 60, 41-200 Sosnowiec, Poland

[3]Faculty of Chemistry, Silesian University of Technology, Strzody 9, 44-100 Gliwice, Poland

**Keywords**

fuel cell, carbon black, catalyst, platinum, transmission electron microscopy

## INTRODUCTION

Fuel cells are one of the most attractive energy generation systems because of their high efficiency and positive impact on the environment. Fuel cells generate electricity through an electrochemical reaction of hydrogen and oxygen; unlike fossil fuels, it does not emit carbon dioxide during power production. Due to the sluggish cathode oxygen reduction reaction, the use of strong and efficient cathode catalysts is crucial for the commercialization of proton-exchange membrane fuel cells. The catalysts most commonly used for that purpose are still nanoparticles of platinum or platinum alloy deposited on carbon black (Meier, 2014). These systems operate under aggressive conditions, especially during start-up and shutdown, when the potential can reach values of up to 1.5 V, leading to carbon support degradation. The carbon support anchors the catalyst platinum nanoparticles and provides electrical connectivity. During high local-potential events, the cathode carbon support corrodes, which could cause electrical isolation of the catalyst particles. At lower potential dissolution, particle coalescence and Ostwald ripening are responsible for the degradation of platinum nanoparticles. Furthermore, the catalyst particles could be detached from the support and/or agglomerate, leading to a reduced electrochemical surface area of the catalyst. To characterize and explain the degradation of cathode catalysts, the evolution of electrocatalysts is monitored during the accelerated stress test (AST). The possibility of conducting research for carbon materials with a different degree of structure order and the possibility of research with atomic spatial resolution creates an additional opportunity to explain the impact of the carbon support structure on the durability of cathode catalysts. Our efforts focus on comparison of the catalytic system (platinum nanoparticles and carbon support) before and after durability tests, including the use of the Identical Location TEM - microscopic techniques developed to track morphological changes of the catalysts material at the nanoscale level (Meier, 2012; Zana, 2013; Arenz, 2016; Hodnik, 2019).

## MATERIALS AND METHODS

Platinum nanoparticles deposited on carbon black with different structure (spherical particle size, specific surface area, and degree of graphitization modified by hight temperature heat treatment) were used as the tested material. TEM, XRD and raman spectroscopy were used for their characterization, and next catalyst nanoparticles were deposited by formic acid reduction method (Li, 2008). Electrocatalytic activity was evaluated by the RDE methodology involves the casting of a catalyst thin-film of known concentration on the surface of a glassy carbon electrode substrate in a standard three-electrode electrochemical cell with working, counter, and reference electrodes

(Mayrhofer, 2008; Garsany, 2010). The performance of the catalysts was characterized by cyclic voltammetry (CV) and linear sweep voltammetry (LSV). The durability of the catalyst was evaluated by AST within a potential scanning range of 0.6–1.1 V at a 100 mV/s scan rate, while anticorrosion properties of the carbon black supports within a scanning potential range of 1.0–1.5 V.

**RESULTS AND CONCLUSIONS**

In order to better understand and explain the results of electrochemical studies, observations of the catalysts structure on the atomic scale were performed in parallel with the AST studies. Fig. 1 shows a comparison of high resolution TEM images before and after testing. The gold TEM microscope grid with the catalyst served as the working electrode for the electrochemical reaction carried out outside the microscope column. After completion of the measurement, the grid was removed from the reaction system and, after drying, transferred to an electron microscope for imaging. This process was repeated many times in different reaction steps and/or settings to study the evolution of the catalyst.

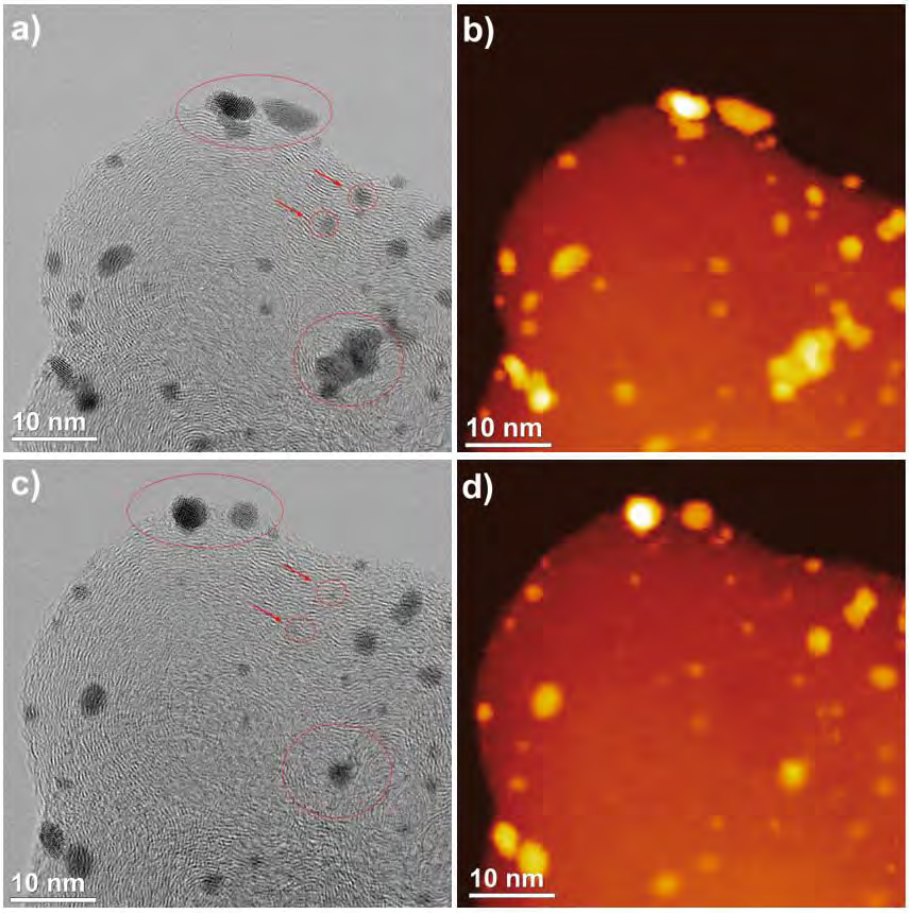


**FIGURE 1**: An examples of IL-TEM images of platinum catalyst on carbon black before (a,b) and after (c,d) 18 K potential cycles between 0.6 and 1.2V (0.1 M HClO4, 100 mV/s, $N_2$ atmosphere).

The observations made (for catalysts deposited on various carbon supports) help to explain the influence of the structure on the durability of cathode catalysts. It is also hoped that they will help in a better design of catalytic systems, enabling effective moderation of agglomeration and growth of platinum nanoparticles, and inhibiting detachment.

**Acknowledgements**

The work was created as a result of the research project No. 2019/33/B/ST5/02702 financed by the National Science Center.

**References**


Arenz, M., & Zana, A. (2016). Fuel cell catalyst degradation: Identical location electron microscopy and related methods. Nano Energy, 29, 299-313. doi.org/10.1016/j.nanoen.2016.04.027

Garsany, Y., Baturina, O. A., Swider-Lyons, K. E., & Kocha, S. S. (2010). Experimental methods for quantifying the activity of platinum electrocatalysts for the oxygen reduction reaction. Anal. Chem. 2010, 82, 6321–6328. 10.1021/ac100306c

Hodnik, N., & Cherevko, S. (2019). Spot the difference at the nanoscale: identical location electron microscopy in electrocatalysis. Current opinion in electrochemistry, 15, 73-82. doi.org/10.1016/j.coelec.2019.03.007

Li, L. H., & Zhang, W. D. (2008). Preparation of carbon nanotubes supported platinum nanoparticles by an organic colloidal process for nonenzymatic glucose sensing. Microchimica Acta, 163(3), 305-311.doi.org/10.1007/s00604-008-0016-3

Mayrhofer, K. J. J., Strmcnik, D., Blizanac, B. B., Stamenkovic, V., Arenz, M., & Markovic, N. M. (2008). Measurement of oxygen reduction activities via the rotating disc electrode method: From Pt model surfaces to carbon-supported high surface area catalysts. Electrochimica Acta, 53(7), 3181-3188. doi.org/10.1016/j.electacta.2007.11.057

Meier, J. C., Katsounaros, I., Galeano, C., Bongard, H. J., Topalov, A. A., Kostka, A., ... & Mayrhofer, K. J. (2012). Stability investigations of electrocatalysts on the nanoscale. Energy & Environmental Science, 5(11), 9319-9330. doi.org/10.1039/C2EE22550F

Meier, J. C., Galeano, C., Katsounaros, I., Witte, J., Bongard, H. J., Topalov, A. A., ... & Mayrhofer, K. J. (2014). Design criteria for stable Pt/C fuel cell catalysts. Beilstein journal of nanotechnology, 5(1), 44-67. doi:10.3762/bjnano.5.5

Zana, A., Speder, J., Roefzaad, M., Altmann, L., Bäumer, M., & Arenz, M. (2013). Probing degradation by IL-TEM: the influence of stress test conditions on the degradation mechanism. Journal of The Electrochemical Society, 160(6), F608. doi.org/10.1149/2.078306jes

20 C 22 arbon 2022

# Upgrading of biomass waste as nitrogen and iron co-doped carbons for oxygen reduction reaction electrocatalysis

**Sara Pérez-Rodríguez[1], David Sebastián[1], Cinthia Alegre[1], Tanya Tsoncheva[2], Nartzislav Petrov[2], Daniela Paneva[3] and María Jesús Lázaro[1]**

[1]Instituto de Carboquímica (CSIC), Miguel Luesma Castán 4, Zaragoza 50018 Spain
Email: mlazaro@icb.csic.es

[2]Institute of Organic Chemistry with Centre of Phytochemistry, Bulgarian Academy of Sciences, Acad. G. Bontchev str. Bl.9, Sofia 1113 Bulgaria
[3]Institute of Catalysis. Bulgarian Academy of Sciences, Acad. G. Bontchev str. Bl.11, Sofia 1113, Bulgaria

**Keywords**
Biomass waste, Fe-N-C catalysts, Oxygen Reduction Reaction.

## INTRODUCTION

Biomass from agroindustrial waste is attracting special attention as an economic, available and environmentally friendly source for applications in efficient and sustainable technologies like fuel cells. At these electrochemical systems, the oxygen reduction reaction (ORR) represents the less favourable process due to its slow kinetics. Electrocatalytic formulations based on platinum group metals (PGM) exhibit a high activity for the ORR and an adequate durability (Sui, 2017). However, the high cost and low availability of these metals, makes difficult the widespread commercialization of the fuel cells. Different approaches have been investigated to reduce/remove the PGM content, including alloying with non-precious metals, enhancing metal utilization by new supports with a well-developed porosity, or the use of non-noble transition metals. Among these catalysts, those containing transition metal atoms dispersed on a nitrogen-doped carbon framework (M-N-C, M = Fe, Co, etc.) have emerged as a promising alternative (Pérez-Rodríguez, 2021). In this work, we studied iron and nitrogen co-doped carbon materials, derived from aronia (AR), peach stones (PS) or coal tar pitch/furfural (CF), as electrocatalysts for the ORR in alkaline media.

## EXPERIMENTAL SECTION

Activated carbon materials were obtained from the bio-resources by thermal treatment in the absence of oxygen of AR, PS and CF and posterior physical activation with water vapour at 700, 750 and 850 °C for 1 h, respectively, as reported in (Pérez-Rodríguez, 2021). Fe-N-C catalysts were prepared by impregnation of the carbon materials with an iron nitrate salt as metal precursor and urea as the nitrogen source. The resultant mixture was subjected to two annealing steps at 950 °C under an inert atmosphere with an intermediate acid leaching (Pérez-Rodríguez, 2021).

The carbon materials and catalysts were characterized by different techniques, such as X-ray photoelectron spectroscopies (XPS), inductively coupled plasma atomic emission spectroscopy (ICP-AES), nitrogen physisorption, X-ray diffraction (XRD) or transmission Mössbauer spectra. The electrochemical behavior for oxygen reduction was assessed by means of a rotating disk electrode (RDE, 5 mm of diameter) in a 0.1 M NaOH electrolyte using a catalyst loading of 0.5 mg $cm^{-2}$. A commercial Pt/C (20 wt.%) was also tested for comparison purposes (0.05 mg $cm^{-2}$ Pt loading).

**RESULTS**

ICP measurements showed the incorporation of Fe in all catalysts with low contents ranging from 0.4 to 1.2 wt.% depending on the nature of the carbon precursor, whereas the generation of Fe-$N_x$ moieties was confirmed by Mössbauer and XPS measurements. Nitrogen adsorption-desorption isotherms revealed the developed microporosity of the as-synthesized activated carbons with the lowest mesopore contribution for the sample obtained from CF. Regarding structural properties, the CF-derived catalyst presented an amorphous structure, while graphitic domains were generated during the thermal treatment of the activated carbons obtained from PS and AR in the presence of iron nitrate. The catalysts presented an adequate performance for oxygen reduction, increasing following the sequence: CF << AR < PS. The PS-derived catalyst exhibited Pt-like performance for the ORR (Figure 1), with a 60 mV $dec^{-1}$ Tafel slope. These results show that a well-developed microporosity with a certain content of mesopores and the creation of graphitic domains lead to a high relative density of active sites (Fe-$N_4$ and nitrogen functionalities), which control the catalytic activity.

**CONCLUSIONS**

An easy and effective strategy for the synthesis of active Fe-N-C ORR electrocatalysts from bio-resources is proposed as an advantageous alternative to the state-of-the-art cathodes (based on PGM) in terms of lower cost and the not requirement of critical raw materials. The electrocatalysts derived from biomass waste (PS and AR) exhibited an improved performance for oxygen reduction compared to the analogous obtained from CF. Besides to the generation of Fe-N and nitrogen species, the textural properties, together with the generation of graphitic domains seem to play a key role in the electrocatalytic behaviour for oxygen reduction. The results are of interest to guide future research in the design of ORR electrocatalysts from green, abundant and low-cost precursors.

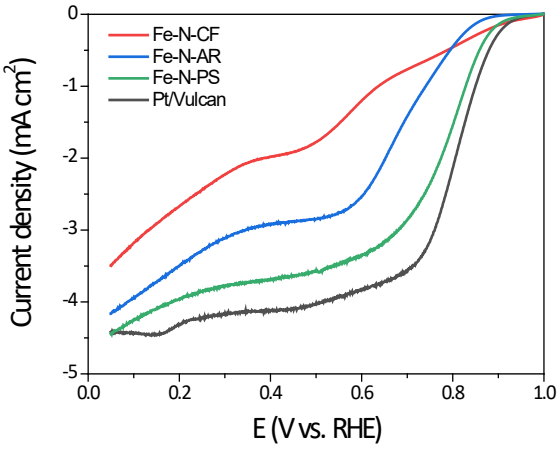


**FIGURE 1**: ORR LSV for the Fe-N-C catalysts in 0.1 M NaOH at 5 mV $s^{-1}$ and 1600 rpm

**Acknowledgements**

The authors gratefully acknowledge financial support given by the project BLOW UP "Balkans Waste to Products: transfer of NoI model to Balkan area " from EIT RAW MATERIAL EIT16320, Horizon 2020 and by Aragon Government (research group T-06).

**References**

[1] Sui, S., Wang, X., Zhou, X., Su, Y., Riffat, S., Liu, C. (2017). A comprehensive review of Pt electrocatalysts for the oxygen reduction reaction: Nanostructure, activity, mechanism and carbon support in PEM fuel cells. *J. Mater. Chem. A.* 5 1808–1825. https://doi.org/10.1039/C6TA08580F.

[2] Pérez-Rodríguez, S., Sebastián, D., Alegre, C., Tsoncheva, T., Petrov, N., Paneva, D., Lázaro, M.J. (2021). Biomass waste-derived nitrogen and iron co-doped nanoporous carbons as electrocatalysts for the oxygen reduction reaction. Electrochimica Acta. 387 138490. https://doi.org/10.1016/j.electacta.2021.138490

Carbon 2022

# Application of Carbon Nanofibers Based Catalysts in Biomass Conversion Reactions

**José Luis Pinilla, Daniel Torres, Elba Ochoa, Esther Frecha, Isabel Suelves**
Instituto de Carboquímica-CSIC. C/Miguel Luesma Castán 4. 50.018 Zaragoza (Spain)
Email: jlpinilla@icb.csic.es

**Keywords**
Carbon nanofibers, biofuels, biorefinery, catalysts, carbocatalysts.

## INTRODUCTION

Hydrogen production via catalytic decomposition (CD) of natural gas (methane) or biogas (mixture of methane and carbon dioxide) is a very interesting approach to produce $CO_x$-free hydrogen. Through this process, carbon nanofibers (CNF) are obtained as a solid product (de Llobet et al., 2015). A fundamental aspect to ensure the viability of the CD process is the pinpoint of suitable CNF applications.

Research in technologies related to a more efficient use of energy resources is an interesting niche for the use of CNF derived materials as catalysts or catalyst supports. The use of lignocellulosic biomass for the synthesis of chemicals and the generation of biofuels, in what is conceptually called biorefinery, presents a series of challenges derived mainly from the complexity of its structure and its notorious resistance to chemical transformations. CNF possess exceptional properties, including good electrical conductivity, high chemical stability in non-oxidizing media, excellent textural and mechanical properties together with the possibility of modifying their surface chemistry on demand, which may facilitate the development of catalysts that are active, selective and stable in conditions relevant for the conversion of lignocellulosic resources.

In this communication, we present the recent advances on the applications of CNF as catalysts or catalyst supports in different biorefinery relevant reactions developed at the Instituto de Carboquímica-CSIC. Thus, by using a plethora of post-treatments mainly based on acid functionalization, and the impregnation with different active phases (nickel, molybdenum carbide or noble metals), a set of different CNF supported catalysts were prepared. These catalysts were evaluated in different reactions, namely stearic acid decarbonylation, guaiacol hydrodeoxygenation (HDO), cellulose hydrolysis and cellobiose hydrolytic hydrogenation, with excellent results.

## EXPERIMENTAL

Fishbone-type carbon nanofibers (CNF) were obtained by catalytic decomposition of biogas (150 mL/min, $CH_4/CO_2$ 50% v/v) in a rotary bed reactor working at 650 °C for 4 h using a Ni:Co/γ-$Al_2O_3$ catalyst (de Llobet et al., 2015). The resulting CNF were subsequently functionalized with different acid treatments (HCl, $HNO_3$, $SOCl_2$) in order to incorporate different oxygen surface groups, useful as anchoring points and acid sites. These CNF were further used as catalytic support for different metallic phases (Pd, Ni and $Mo_2C$): (i) subnanometric Pd species prepared by immobilization of a di-μ-chloro-Bis[palladium(II) anthranilate] complex over acyl chlorinated CNF by incipient wetness impregnation with DMF were used in the decarbonylation of stearic acid; (ii) mono- (Ni and Pt) and bimetallic NiPt catalysts supported on CNF prepared by incipient wetness impregnation were used in the hydrolytic hydrogenation of cellobiose; (iii) $Mo_2C$/CNF catalysts were prepared by carbothermal hydrogen reduction and used in the HDO of guaiacol. A more severe CNF treatment based on a modification of the Hummers' method was also applied to obtain graphene oxide (GO)-derived

materials with a surface rich in S and O-groups, which were used in the hydrolysis of cellulose. Representative TEM images of the catalysts used are shown in Figure 1.

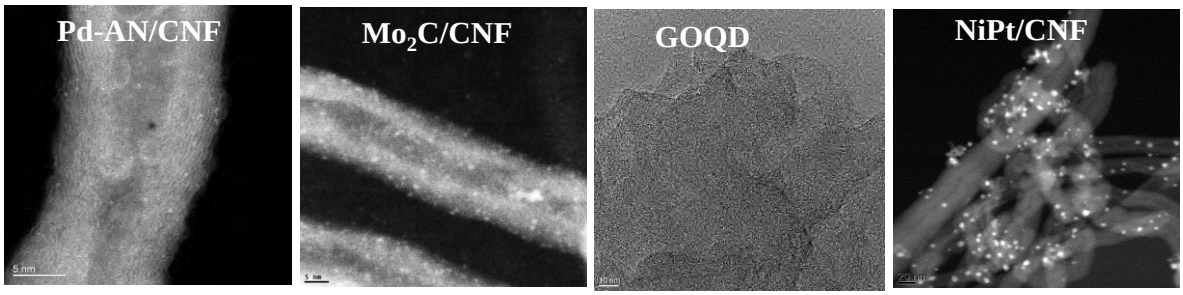


**FIGURE 1**: TEM micrographs of the CNF based catalysts used.

**RESULTS**

Production of linear α-olefins from renewable sources is gaining increasing attention because it allows the transition from the current petrochemical synthesis route to a more sustainable scenario. The atomically dispersed Pd heterogeneous catalyst supported on CNF exhibited higher catalytic efficiency for the selective decarbonylation of stearic acid to 1-heptadecene as compared to the reference homogenous catalyst, with a selectivity of 90 mol% and a TON = 484 at 140 °C (Figure 2, left) (Ochoa et al., 2020a).

The production of drop-in biofuels and/or aromatics from lignocellulosic feedstocks is crucial in order to reduce the dependency on fossil fuels and make the biorefinery concept a reality. However, bio-oil obtained from biomass pyrolysis has a high amount of oxygenated compounds, which hinders its direct use as a biofuel. Catalytic HDO allows removing oxygenated groups from bio-oils in form of water under a high $H_2$ pressure atmosphere and moderate temperatures. The impact of using different nanostructured carbon materials (CNF, carbon nanotubes (CNT), graphene oxide (GO) and activated carbon (AC)) as support for $Mo_2C$ based catalysts on the HDO of guaiacol was studied. Overall, the catalytic activity (guaiacol conversion, HDO ratio and phenol + benzene selectivity) followed this order: $Mo_2C$/CNF > $Mo_2C$/AC > $Mo_2C$/GO > $Mo_2C$/CNT (Figure 2, right). $Mo_2C$ crystal size measured by XRD, which ranged from 10.9 to 15.5 nm, was inversely proportional to the guaiacol conversion. The higher thermal stability of CNF support also accounted for the better catalytic performance (Ochoa et al., 2020b).

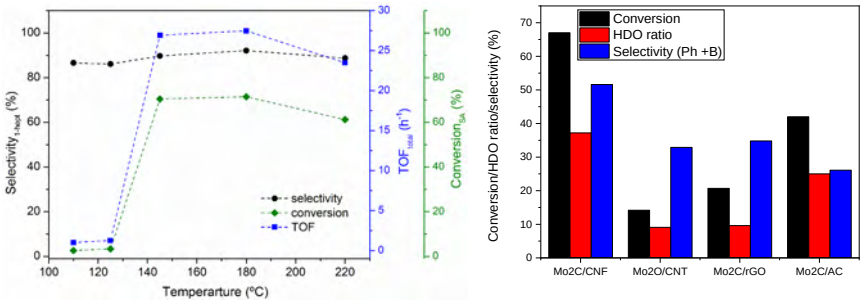


**FIGURE 2**: Results on stearic acid decarbonylation after 18 h (left) and guaiacol HDO after 2 h at 300 °C and an initial pressure of 20 bar $H_2$ (right).

In the framework of second-generation biorefinery, the robust nature of cellulose represents a bottleneck for its effective utilization graphene-based materials derived from CNF were shown to be promising catalysts for cellulose hydrolysis into glucose. A clear relationship between hydrolysis performance and the oxidation/exfoliation degree of the graphene oxide materials was found (Figure 3, left). The best results in terms of glucose yield were achieved with dimensionless structures based on GO quantum dots (GOQD), which provided sterically accessible O- and S-

functionalities in high density, overperforming other GO morphologies such as GO nanofiber (GONF) and few-layers GO (FLGO) (Frecha et al., 2021). A soft mix-milling stage (10 min) promoted the effective molecular interaction between solid cellulose and the active sites of the nanocarbon materials.

The reduction of sugars to their hydrogenated form (sorbitol) emerges as an effective chemical way to enhance the productivity of the cellulose depolymerization process. The hydrolytic hydrogenation of cellobiose into sugar alcohols was studied with mono- and bimetallic CNF supported catalysts (Figure 3, right). The addition of small amounts of Pt (0.5%) to Ni(3%)/CNF catalysts enhanced the selectivity to hydrogenation products (cellobitol and sorbitol) as compared to the monometallic counterparts (Frecha et al., 2019). Pt induced changes in the size and dispersion of the Ni phase through the formation of the corresponding alloy, and favored the reductive conditions ($H_2$ spillover from noble metal to Ni).

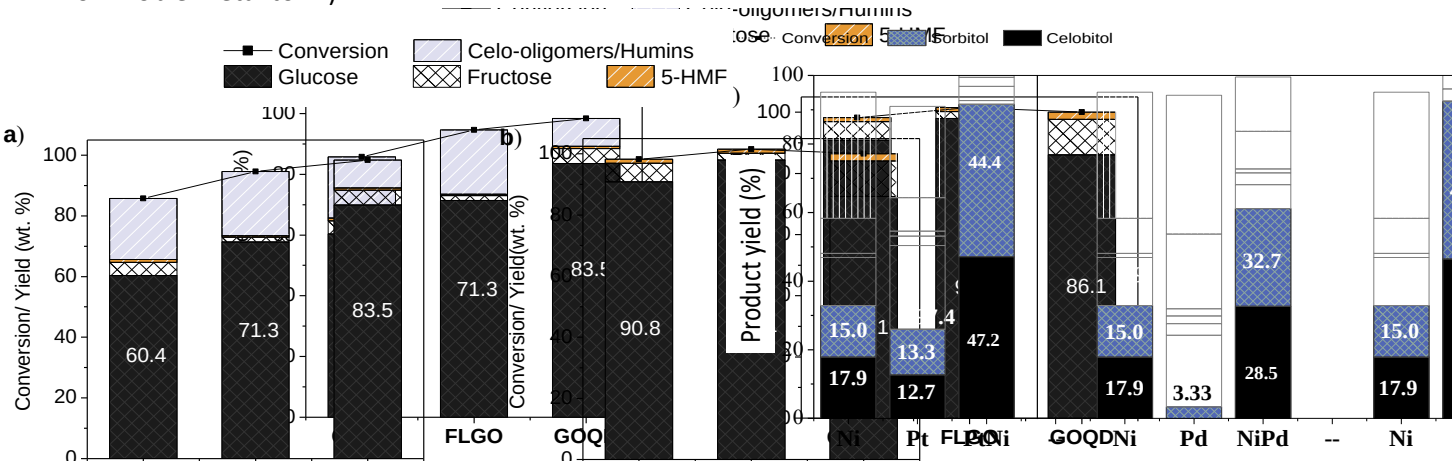


**FIGURE 3**: Results on cellulose hydrolysis after 24 h at 135 °C (left) and cellobiose hydrolytic hydrogenation after 3 h at an initial pressure of 4.0 MPa of $H_2$ and 180 °C (right).

## CONCLUSIONS

Catalysts based on CNF are presented as a very interesting option for biomass conversion reactions, which open the prospects for their use in biorefinery processes with the overriding goal to produce biofuels and chemicals of renewable origin.

**Acknowledgements**

This work was supported by the I+D+i project PID2020-115053RB-I00, funded by MCIN/ AEI/10.13039/501100011033.

**References**

De Llobet, S., Pinilla, J. L., Moliner, R. & Suelves, I. 2015. Effect of the synthesis conditions of Ni/Al2O3 catalysts on the biogas decomposition to produce $H_2$-rich gas and carbon nanofibers. *Applied Catalysis B: Environmental,* 165**,** 457-465. https://doi.org/10.1016/j.apcatb.2014.10.014

Frecha, E., Torres, D., Pueyo, A., Suelves, I. & Pinilla, J. L. 2019. Scanning different Ni-noble metal (Pt, Pd, Ru) bimetallic nanoparticles supported on carbon nanofibers for one-pot cellobiose conversion. *Applied Catalysis A: General,* 585. http://dx.doi.org/10.1016/j.apcata.2019.117182

Frecha, E., Torres, D., Suelves, I. & Pinilla, J. L. 2021. Custom-sized graphene oxide for the hydrolysis of cellulose. *Carbon,* 175**,** 429-439. https://doi.org/10.1016/j.carbon.2021.01.108

Ochoa, E., Henao, W., Fuertes, S., Torres, D., Van Haasterecht, T., Scott, E., Bitter, H., Suelves, I. & Pinilla, J. L. 2020a. Synthesis and characterization of a supported Pd complex on carbon nanofibers for the selective decarbonylation of stearic acid to 1-heptadecene: the importance of subnanometric Pd dispersion. *Catalysis Science & Technology,* 10**,** 2970-2985. https://doi.org/10.1039/D0CY00322K.

Ochoa, E., Torres, D., Pinilla, J. L. & Suelves, I. 2020b. Nanostructured carbon material effect on the synthesis of carbon-supported molybdenum carbide catalysts for guaiacol hydrodeoxygenation. *Energies,* 13. http://dx.doi.org/10.3390/en13051189

Carbon 2022

# Solid and Liquid Biomass- based Activated Carbon Hybrid Materials as Oxygen Reduction Catalysts

**A. Plavniece[1], G Dobele[1], A. Volperts[1], A. Zhurinsh[1], D. Upskuviene[2], A. Drabavicius[2], V. Jasulaitiene[2], L Tamasauskaite-Tamasiunaite[2], E. Norkus[2], Y.-C. Lin[3], Y.-W. Chen[4]**

[1]Latvian State Institute of Wood Chemistry, Riga, Latvia

Email: ance.plavniece@kki.lv

[2]Center for Physical Sciences and Technology, Vilnius, Lithuania

[3]National Cheng Kung University, Tainan, Taiwan

[4]National Central University, Taoyuan City, Taiwan

**Keywords**

Activated carbons, porous structure, oxygen reduction reaction.

## INTRODUCTION

Preparation of tailored carbon materials from biomass and its wastes by simple and up-scalable method still is a challenge. From all available biomass waste resources more than 47 million tons of wood residues is available across the EU each year (Verkerk *et al.*, 2019). At the same time developers of new innovative wood biorefinery processes face the problems with valorization of residues, e.g. in thermochemical conversion technologies char and liquid wastes are produced as by-products and can be used only as fuels. In sugar platform technologies where acids or ferments are applied for hydrolysis, lignin is obtained as a low added value by-product and the size of the market for its further utilization is far from what is need.

Hierarchical porous char, based on biomass and its components, with its unique combination of different pore sizes, has already proven its superior performance compared to traditional fossil carbon materials. For carbon materials, the role of ultramicro-, supermicro-, micro- meso- and macropores in the processes of ion diffusion, which is important for capacity and energy density, has not been sufficiently studied. The formation of a porous structure will proceed differently under the same activation conditions for the solid ligno-carbohydrate complex of wood in comparison with aromatic matrix of lignin containing liquid precursor. Activated carbons have shown promising results as electrodes for batteries and supercapacitors, and as catalysts for fuel cells, i.e. devices which are critical for enabling technologies and are at the center of vast global research and initiatives to meet the rising demand for clean, sustainable energy (Shi, 1996; Yang *et al.*, 2001; Pandolfo and Hollenkamp, 2006).

The goal of this research is synthesis of carbon materials with high specific surface and adjustable pore distribution using solid (wood) and lignin and phenolics containing liquid biorefinery wastes precursors to obtain novel hybrid composite materials for energy devices.

## MATERIALS AND METHODS

In this study to obtain hybrid carbon materials, composites from a mixture of wood and a water-insoluble lignocellulose pyrolysis tar were used as precursors. Activated carbons were synthesized via two-stage thermochemical method, using carbonization at 400 and 500 $^{o}$C and then thermochemical activation with NaOH at 800 $^{o}$C in argon atmosphere, with the aim to provide specific surface area control and, especially, tailoring of mesopores size and distribution. Nitrogen was introduced into the activated samples using dicyandiamide. The influence of precursors on materials pore structure and elemental composition, as well as on surface functional groups and ion-exchange properties, was

investigated. Activated carbons porosity, structure and composition were studied as well as their application as cathodes for oxygen reduction in fuel cells.

**RESULTS**

Precursors, i.e. wood, tar and their composites, pyrolysis volatile products were studied with the analytical pyrolysis method (Fig. 2a). The most notable difference in the content of volatile products was observed during the pyrolysis of wood and tar. The share of carbohydrate decomposition products typical for deciduous wood was 58.8% and lignin 17.8%; in the case of tar the content of carbohydrate degradation products was less - 8.9%, and the content of monomeric phenolics increases and reaches 62.1%.

The results of thermogravimetric analysis of carbonized tar and other precursors at 400°C showed that their thermal stability differs (Fig. 2b). The formation of volatile products of carbonized tar obtained at 400°C proceeds at a higher rate comparing to other samples, reaching a maximum at 444°C, their amount at 700°C is 33%. It is possible that oligomeric lignocarbohydrate complexes undergo degradation in this temperature range, the condensation of which at 400°C proceeded insufficiently. The thermal stability of the rest of the samples is almost the same, the maximum rate of formation of volatile products was observed at temperatures of 561°C. The amount of volatile products for wood and hybrid carbonizates at 700°C is approximately 10% less than for tar. Carbonization of samples at 500°C (Fig. 2c) leads to the formation of more thermally stable materials. Their destruction, according to the maximum on the DTG curves, is most active at a temperature of about 600°C. Comparison of samples shows that the most thermally stable composite is 4:4 (Fig. 2a). Wood carbonizate obtained at 500°C has a 4-6% higher amount of volatile products compared to other carbonized samples, which also indicates interaction of composite components during carbonization.

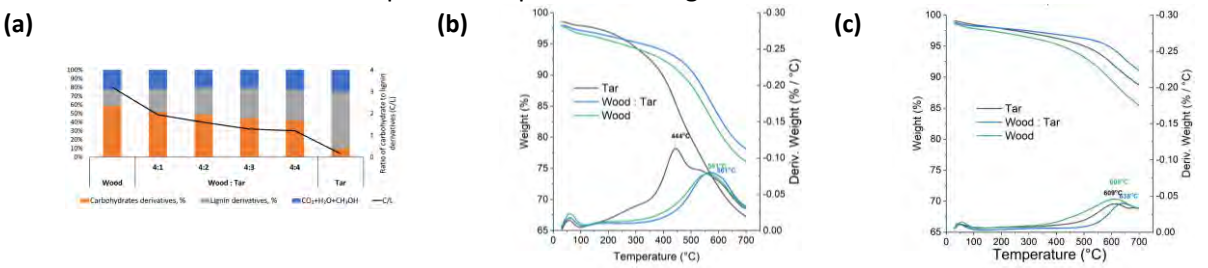


**FIGURE 2.** Composition of volatile degradation products of wood, tar and their composites determined by Py-GC/MS at 500 ° C. TG and DTG analysis of carbonizates (carbonization temperatures (b) 400 and (c) 500 ° C).

To form a porous structure, precursor samples were subjected to thermochemical treatment. The samples were tested using nitrogen sorption at 77K and the resulting isotherms are demonstrated in the Figure 3a. The shape of the isotherm for the activated samples of wood, tar and composites carbonized at 500 belongs to Type I according to IUPAC classification, which points at the predominant presence of very fine micropores. For samples carbonized at 400 ° volume of adsorbed $N_2$ increases and Type II isotherms are accompanied with visible H4 type hysteresis, when using tar as a precursor characteristic to capillary condensation and development of mesoporosity. Figure 3b compares the pore size distributions of carbon materials. The decrease in the carbonization temperature influences micropore development in activation process by increasing their width. Micropore input into the total specific volume of the tar and composite based samples carbonized at 400 ° C significantly decreases, and the volume of mesopores with a pore width of 2–4.5 nm increases. The highest mesopore volume from the total pore volume (%), respectively 56%, was observed in the case of activated sample based on 400 ° C carbonized tar precursor.

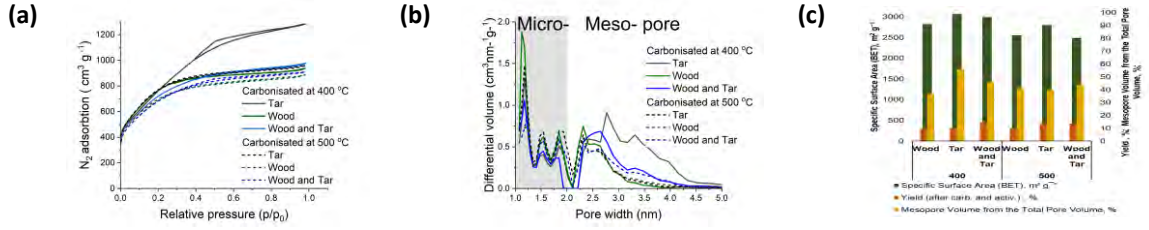

**FIGURE 3.** $N_2$ adsorption-desorption isotherms (a), pore size distribution (b) and specific surface area, mesopore volume from total pore volume as well yield comparison (c) of activated carbons based on precursors carbonized at 400° C (straight line) and 500° C (dashed line).

The surface chemical composition of N-doped activated carbons was studied using XPS. Three peaks (Fig. 4a) were determined for nitrogen: pyridinic-N, pyrrolic-N, graphitic-N, pyridine-N-oxide. Most of the nitrogen was in the pyridinic form. Raman spectroscopy (Fig. 4b) was applied to assess the structural distortion and defects in N-doped activated carbon materials. All the samples exhibit two strong bands near 1343−1348 and 1582−1606 $cm^{-1}$ and weaker band at 2685−2694 $cm^{-1}$ in the case of wood and hybrid material indicating that the material consists of few-layer graphene samples (Hao *et al.*, 2010).

Preliminary ORR performance was evaluated using the rotating disk electrode (RDE) method. Onset potential is equal approximately 1.05 V for for all samples. The diffusion-limited current density falls to slightly lower values in the case of activated carbon based on precursors carbonized at 400° C. The number of electrons transferred per $O_2$ molecule (n) was calculated using the Koutecky-Levich (K-L), and it was determined, that the reaction follows a $4e^-$ mechanism for all samples.

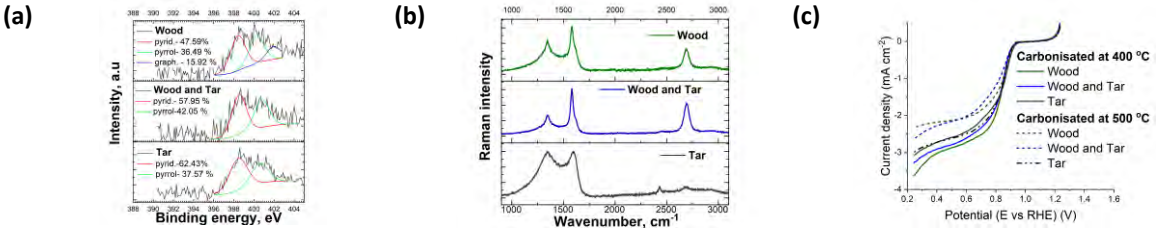


**FIGURE 4.** XPS N 1s spectra of N-doped activated carbons (a). Raman spectra of N-doped carbon-based samples (b). LSVs of N-doped activated carbons recorded at a scan rate of 10 mV $s^{-1}$ in $O_2$-saturated 1 M KOH at 1600 rpm (c).

## CONCLUSIONS

The results of this study show that using a liquid precursor for impregnation of a solid one, as well as increasing the activation temperature, increases pore width. It is possible to obtain a hybrid material with high specific surface area and more than 50% mesopore volume. Preliminary ORR performance was evaluated using the rotating disk electrode method. Onset potential was equal, approximately 1.05 V for, all samples under study. The diffusion-limited current density falls to slightly lower values in the case of N-doped activated carbon with the highest mesopore volume from the total pore volume (%), respectively 56%, i.e. in the case of activated 400 ° C carbonized tar. The number of electrons transferred per $O_2$ molecule (n) was calculated using the Koutecky-Levich (K-L), and it was determined, that the reaction follows a $4e^-$ mechanism for all samples.

**Acknowledgements**

This study was financially supported by the Lithuanian-Latvian-Taiwanese Tripartite Cooperation Program under the project “Innovate Catalysis for Sustainable Energy (ICatSE)”

**References**

Hao, Y. *et al.* (2010) ‘Probing layer number and stacking order of few-layer graphene by Raman spectroscopy’, *Small (Weinheim an der Bergstrasse, Germany)*, 6(2), pp. 195–200. doi: 10.1002/SMLL.200901173.

Pandolfo, A. G. and Hollenkamp, A. F. (2006) ‘Carbon properties and their role in supercapacitors’, *Journal of Power Sources*, 157(1), pp. 11–27. doi: 10.1016/j.jpowsour.2006.02.065.

Shi, H. (1996) ‘Activated carbons and double layer capacitance’, *Electrochimica Acta*, 41(10), pp. 1633–1639. doi: 10.1016/0013-4686(95)00416-5.

Verkerk, P. J. *et al.* (2019) ‘Spatial distribution of the potential forest biomass availability in europe’, *Forest Ecosystems*, 6(1), pp. 1–11. doi: 10.1186/S40663-019-0163-5/FIGURES/4.

Yang, K. L. *et al.* (2001) ‘Electrosorption of Ions from Aqueous Solutions by Carbon Aerogel: An Electrical Double-Layer Model’, *Langmuir*, 17(6), pp. 1961–1969. doi: 10.1021/LA001527S.

Carbon 2022

# Simulation of Anisotropic Pyrolytic Carbons Using a Polygranular Image Guided Atomistic Reconstruction Approach

F. Polewczyk[1,2], P. Lafourcade[1] and J.-M. Leyssale[2]
Email: jean-marc.leyssale@u-bordeaux.fr

[1]CEA/DAM-DIF, Bruyères-le-Châtel, France

[2]Institute of Molecular Sciences, University of Bordeaux, France

**KEYWORDS**

Molecular Dynamics (MD), Pyrocarbon, Elastic Properties

## INTRODUCTION

Pyrocarbons (pyC) are dense, anisotropic, turbostratic carbons that form the matrices of high performances carbon/carbon thermostructural composites. We propose here a new method for the generation pyC atomistic models, called polygranular image guided atomistic reconstruction (PG-IGAR), improving on the previously introduced IGAR method (Farbos, 2014). It relies on the construction of a textured 3D Voronoï tesselation image based on experimental diffraction data, which then serves as an external potential bringing the atoms to settle preferentially on the black areas during a conventional simulated annealing simulation. The method is applied to produce a large data base of models with independent variations of the structural/textural parameters ($L_a$, $L_c$, and the orientation angle of selected area electron diffraction (SAED) patterns). Elastic properties are then computed and discussed in relation with the structural/textural parameters.

## METHODS

Atomistic pyC models are constructed according to the following steps (Figure 1).

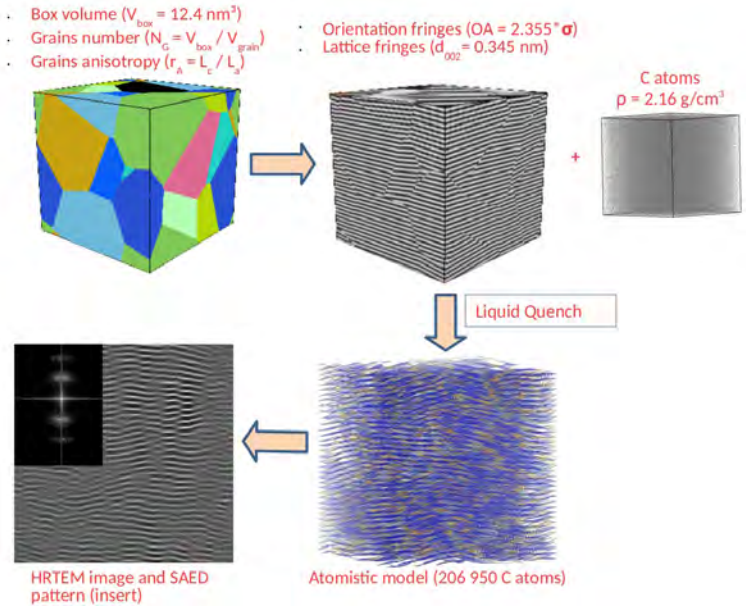


**Figure 1:** Principle of the PG-IGAR method.

First, a 3D Voronoï tessellation is created to accommodate anisotropic grains with prescribed target $L_a$ and $L_c$ values in a cubic volume of 12.5 nm width. It is then decorated with lattice fringes with prescribed interlayer distance ($d_{002}$) and a distribution of orientations following the target orientation angle OA (full width at half maximum of the OO2 arc in SAED patterns). Atomistic models are then obtained by slowly cooling a liquid of carbon atoms under the influence of a potential field derived from the grey levels of the decorated image, ranging from 0 eV (black) to 4eV (white). The second generation REBO potential (Brenner, 2002) is used to describe the interatomic interactions between C atoms. After this quench, the external field is removed and the system is relaxed at 300 K with a simulation controlled by the *LCBOPII* interatomic potential implemented in the MD code STAMP (Los, 2005).
Application of this method is presented through two parametric studies: i) the evolution of the crystallite sizes in the 1-8 nm range at fixed OA (30 degrees); and ii) the evolution of OA from 10-100 degrees at fixed crystallite sizes La=Lc. In this two studies, the density is fixed at 2.16 g/cm$^3$, close to the experimental values (Farbos, 2015).
Relaxed models are characterized using diffraction data (X-Ray, Neutron), by simulating Pair Distribution Function (PDF) and Structure Factor S(Q). A structural analysis is performed in order to quantify the amount and nature of defects composing the models. Finally, high resolution transmission electron microscopy (HRTEM) images are simulated using Dr Probe (Barthel, 2018). SAED patterns are obtained through fast Fourier transform (FFT) of the HRTEM images and the OA values extracted from the 002 arcs. Finally, elastic tensors of the models are computed using molecular dynamics simulations at small deformations.

**RESULTS AND DISCUSSION**

Only the case where we imposed crystallytes sizes equal to ($L_c$,$L_a$)=(2.5, 2.5) nm and a disorientation of 30 degrees is presented in this extended abstract (Figure 2).

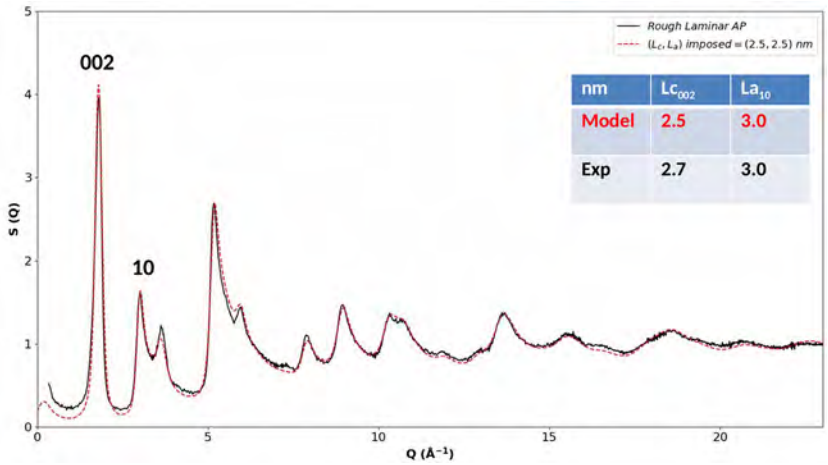


**Figure 2:** Comparison between simulated and experimental S(Q) for the Rough Laminar.

Compare to the IGAR method (Farbos, 2014), it appears that the “out of plane” organization given by the 002 peak is well reproduced. The “in plane” organization given by the 10 asymmetric band is also well reproduced. Coherence length $L_c$ is obtained by fitting the 002 peak with a Pseudo-Voigt function and coherence length $L_a$ is obtained by fitting the 10 asymmetric band with a Skewed Gaussian function. Computed values are relatively closed with experimental values.
HRTEM image and SAED pattern are simulated for 1 nm slice and the full model (Figure 3).

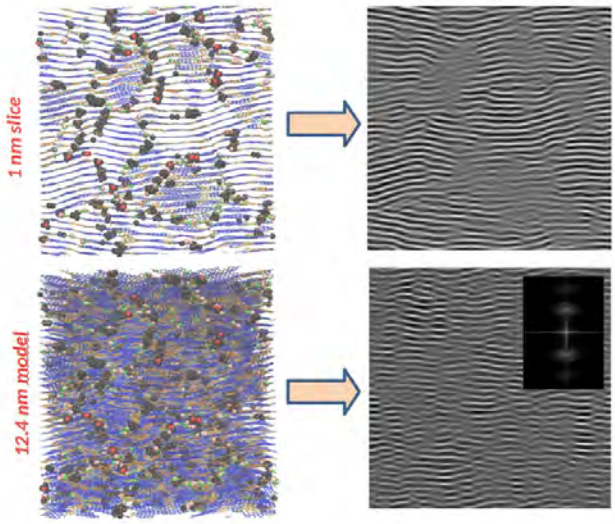


**Figure 3:** HRTEM images simulated for 1nm slice and full model. SAED pattern in insert.

For the 1 nm slice, the grains are clearly visible in the simulated HRTEM image. Indeed the slice thickness is smaller than the domain sizes. For the full model, with a thickness of 12.4 nm, grains boundaries are not clearly visible in the simulated HRTEM image and in the model snapshot. A superposition Moiré effect is observed and a smoothing effect seems to increase apparent anisotropy. Extracted OA from the SAED pattern is closed to the imposed value ($OA_{computed}$ = 34° .vs. $OA_{imposed}$ = 30°) and gives the model texture.

## CONCLUSION

To conclude, we propose a new approach to reconstruct anisotropic pyrolitic carbons. Unlike the IGAR method, this approach based on experimental diffraciton data combined with MD simulations allows to obtain several realistic models, which are directly comparable to the experimental models. Reconstructed models are validated by comparison between experimental and simulated PDF, S(Q) and HRTEM images. It permit to obtain a large database concerning pyrolitic carbons.

### Acknowledgements

Research financially supported by the French Ministry of Defense – Defence Innovation Agency

### References

Barthel, J. (2018). Dr. Probe: A software for high-resolution STEM image simulation. Ultramicroscopy, 193, 1-11. https://doi.org/10.1016/j.ultramic.2018.06.003

Brenner, D.W., Shenderova, O.A., Harrison, J.A., Stuart, S.J., Ni, B. and Sinnott, S.B. (2002). A second-generation reactive empirical bond order (REBO) potential energy expression for hydrocarbons. *Journal of Physics: Condensed Matter*, 14, [4], 783-802. https://doi.org/10.1088/0953-8984/14/4/312

Farbos, B., Weisbecker, P., Fischer, H.E., Da Costa, J.-P., Lalanne, M., Chollon, G., Germain, C. and Leyssale, J.-M. (2014). Nanoscale structure and texture of highly anisotropic pyrocarbons revisited with transmission electron microscopy, image processing, neutrons diffraction and atomistic modeling. *Carbon*, 80, 472-489. https://doi.org/10.1016/j.carbon.2014.08.087

Los, J.H., Ghiringhelli, L.M., Meijer, E.J. and Fasolino, A. (2005). Improved long-range reactive bond-order potential for carbon. I. Construction. Physical Review B, 72, [21], 214102. https://link.aps.org/doi/10.1103/PhysRevB.72.214102

Carbon 2022

# Synthesis of Graphene in a Flame on the Surface of Porous Structured Current Collector for Hybrid Supercondensers

**N.G. Prikhodko [1,2], N.B. Rakhymzhan [1], A.T.Taurbekov [1,4], A.A. Abdisattar [1,3], B.T. Lesbayev [1,4], A.B. Tolynbekov [1,4], K. Askaruly [1,3], Y. Y. Beisenova [3]**

[1] Institute of Combustion Problems, Almaty, Kazakhstan
Email: nik99951@mail.ru

[2] Almaty University of Power Engineering and Telecommunications, Almaty, Kazakhstan

[3] Satbayev University, Almaty, Kazakhstan

[4] Al-Farabi Kazakh National University, Almaty, Kazakhstan

**Keywords**
Graphene, supercapacitor, flame

## INTRODUCTION

Supercapacitors, having a practically unlimited service life and the ability to accumulate high energy capacity, attract a lot of attention from researchers. The main problems for the widespread use and commercialization of supercapacitors are high cost and low energy density. At present, graphene and its modifications are used as a carbon material in supercapacitors and studied. (Yu Bin Tan, 2013; Yeleuov, 2020). The prospect of using graphene for electrodes of supercapacitors is explained by its exceptional properties, namely: the two-dimensional structure of atomic thick with a large surface area, which does not dependent on the distribution of pores and and provides electrolyte access to both sides, high electrical conductivity; mechanical strength; chemical inertness.

The work presents the results of graphene synthesis on the porous surface of the current collector in the flame. The electrochemical precipitation of the transition metal oxide (TMO), namely $MnO_2$, was carried out on the resulting surface. The resulting structures ($MnO_2$/Flame-based-graphene/ Porous nickel current collector) were used as electrodes for hybrid supercapacitors and their electrochemical properties were studied. It is established that the layer of graphene, formed on the surface of a porous metal current collector, increases the electrical conductivity, chemical resistance to electrolytes, used in supercapacitors, and increases the specific capacitance of the capacitor at the expense of the double electric layer of carbon on the base of the graphene.

## MATERIALS AND METHODS

The paper presents a hybrid electrode for a supercapacitor that combines the advantages of an electric double layer capacitor based on graphene and a pseudosupercapacitor based on transition metal oxides.

A porous structure based on nickel is used as a current collector: porous-nickel-layer/nickel foil; nickel foam. A porous structured nickel film on a nickel foil is used as a current collector. The porous structure of the current collector improves the contact between the active material and the current collector, and the deposited graphene on the porous structure provides an electrical double layer, increasing the capacity and power density of the supercapacitor.

Results on the synthesis of graphene in a flame on the porous structure of a current collector are presented. Since the CVD method is energy-consuming, multicomponent, time-consuming and requires a high purity of the initial components, the process of graphene synthesis in a flame is

preferable. (Memon, 2011; Prikhod'ko, 2014). The process of nanostructure formation in flames takes place over a period of $10^{-5}$ to $10^{-3}$ seconds. The method of synthesis of graphene in flames is a continuous, simple and inexpensive method, and it can successfully compete with the method of CVD (Memon, 2011). Graphene was synthesized in a premixed propane/oxygen/argon flame under atmospheric conditions at a flow rate of 170/370/160 $cm^3$/min, respectively; synthesis temperature 950-980$^oC$, synthesis time 1-2 minutes; ratio C/O=0.65-0.7 (**Figure 1**).

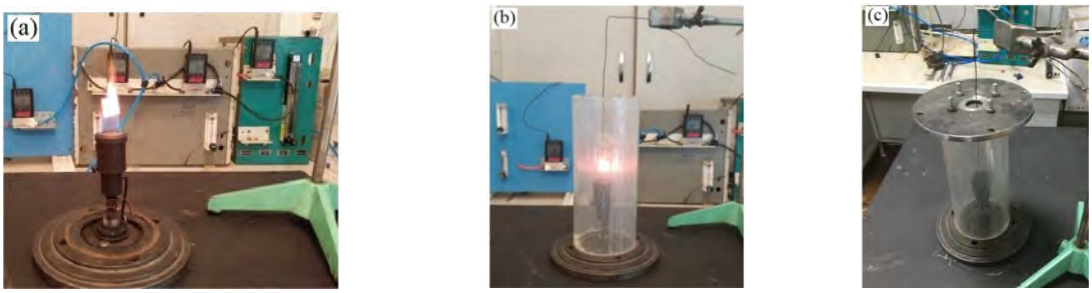


**FIGURE 1:** Photograph of a burner with a current collector in the central part of the flame: a - synthesis of graphene in open conditions; b, c - synthesis of graphene when isolating flames from atmospheric air.

A porous current collector, pretreated for 30 minutes in a 20% nitric acid solution, was placed vertically in a flame for one minute. Then it was quickly cooled in a flow of argon, after extinguishing the flame. The result is a structure of Flame-based graphene/Porous nickel current collector. Then the resulting current collector in the electrochemical method settled the micro- and meso-porous oxide of the transition metal (TMO), and it is the manganese oxide ($MnO_2$).

**RESULTS AND DISCUSSION**

The studies were carried out on a Raman spectrometer (NTEGRA Spectra, λ=473 nm). Raman spectroscopy allows to identify single and multilayer graphene, as well as its quality (Ferrari, 2006). Graphene was analyzed in three peaks: peak D at 1351 $cm^{-1}$, peak G at 1580 $cm^{-1}$, and peak2D at 2700 $cm^{-1}$. The ratio between the intensities $I_G/I_{2D}$ gives an estimate of the number of layers.It was found that 5-10 graphene layers are formed on the porous current collector ($I_G/I_{2D}$=1.5-2.2), (**Figure 2, a**).

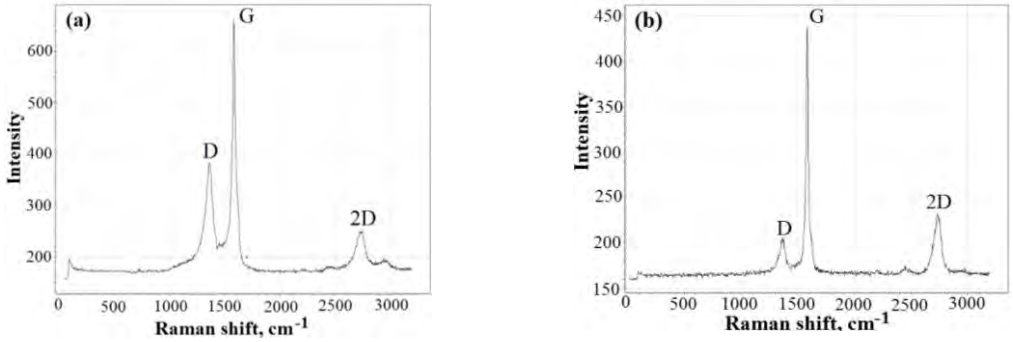


**FIGURE 2:** Raman spectra of graphene on the surface of a current collector obtained in an open flame: a - before treatment in an ultrasonic bath, $I_G/I_{2D}$ = 2.2; b - after treatment in an ultrasonic bath for 5 minutes, $I_G/I_{2D}$ = 1.5.

It turned out that during the synthesis of graphene in an open flame, the surface of the current collector is covered with a carbon structure mainly along the flame profile. However, when graphene is synthesized in a flame isolated from atmospheric air, a carbon structure is formed on the entire surface of the current collector. It is shown that the number of graphene layers during synthesis in a flame isolated from atmospheric air is also the in range of5-10 layers ($I_G/I_{2D}$=1.7-2.1).

It was found that graphene has a greater defectiveness in comparison with graphene obtained by the CVD method, and an amorphous soot structure is observed. However, when processed for 1-5 minutes in an ultrasonic bath with distilled water, the amorphous soot structure peels off and the purifiedgraphene remains on the surface of current collector. In this case, additional layers of graphene are opened, which were covered by an amorphous carbon structure and were not detected on a Raman spectrometer. It was found that after treatment in an ultrasonic bath, the number of graphene layers formed on the current collector remains unchanged (**Figure 2, b**).

It is established that the reduced time of graphene synthesis on the current collector in the flame (less than one minute), it is possible to obtain small layer graphene (less than 5 layers) with minimal defects and minimal amorphous content.

The resulting porous metal structure with graphene layers, after electrochemical growth of transition metal oxides ($MnO_2$) on it, was investigated as electrodes for hybrid supercapacitors.

Measurements of electrochemical characteristic electrodes with the structure of $MnO_2$/Flame-based-graphene/Porous nickel current collector were carried out in a three-electrode cell on the potentiostat-galvanostate of the company Elins with a module of measurement EIS (P-40X) with FRA. 3M water solution KOH was used as electrolyte. It is established that the specific capacitance of the electrode material at current density 1 A/g is equal: on the basis of $MnO_2$: without graphene - 233 F/g, with flame-based graphene - 274 F/g. Coulomb efficiency of the electrode on the basis of manganese oxide with flame-based graphene is 99% at current density of 1 A/g, which speaks of the slow process of self-discharge of supercapacitors. Preservation of electrical capacitance of cells with an electrode $MnO_2$/Flame-based-graphene/Porous nickel current collector is about 98% even after 2000 cycles, which characterizes the durability of the created electrodes and the long process of their operation.

## CONCLUSIONS

Developed a method of synthesis of graphene in flames on a Porous current collector, allowing obtaining 5-10 layers of graphene. At the same time, graphene has a large defect in the comparison with graphene, obtained by the method of CVD, and also has an amorphous sage structure. To remove the amorphous structure from the current collector, a method of ultrasonic treatment in distilled water was developed, which gave a positive result. The electrochemical characteristics of the electrodes with the structure of $MnO_2$/Flame-based-graphene/Porous nickel current collector were studied. Electrode with flame-based graphene has a higher specific capacitance and stability in long cycles in comparison with the electrode without graphene layer.

**Acknowledgements**

This research is funded by the Science Committee of the Ministry of Education and Science of the Republic of Kazakhstan (Grant No. AP08856683).

**References**

Ferrari A.C., Meyer J.C., Scardaci V., Casiraghi C., Lazzeri M., Mauri F. (2006). Raman spectrum of graphene and graphene layers. *Phys Rev Lett*, 97, 187401. https://doi.org/10.1103/PhysRevLett.97.187401

Memon N.K., Tse S.D., Al-Sharab J.F., et al. (2011). Flame synthesis of graphene films in open environments. *Carbon*, 49, 5064-5070. http://dx.doi.org/10.1016/j.carbon.2011.07.024

Prikhod'ko N.G., Lesbayev B.T., Auelkhankyzy M., Mansurov Z.A. (2014). Synthesis of Graphene Films in a Flame. *Russian Journal of Physical Chemistry B*, 8, [1], 61–64. DOI:10.1134/S1990793114010059

Yeleuov M., Seidl C., Temirgaliyeva T., Taurbekov A., Prikhodko N., Lesbayev B., Sultanov F., Daulbayev C., Kumekov S. (2020). Modified activated graphene-based carbon electrodes from rice husk for supercapacitor applications. *Energies*, 13, [18], 4943. https://doi.org/10.3390/en13184943.

Yu Bin Tan, Jong-Min Lee. (2013). Graphene for supercapacitor applications. *J. Mater. Chem. A*, 1, 14814–14843. https://doi.org/10.1039/C3TA12193C

Carbon 2022

# Restoration of Water Reservoirs Polluted with Petroleum Products Using Expanded Graphite Sorbent

**Oleksandr V Pugach, Yuriy V Kiselev, Lyudmyla A Odukalets, Maksym O Stokolos and Yuriy L. Zabulonov***
Institute of Environmental Geochemistry of National Academy of Sciences of Ukraine
*Email: 1952zyl@gmail.com

**Keywords**
Expanded graphite, water pollution, oil spillage.

## INTRODUCTION

All oil components are toxic to the environment. The aromatic fraction of oil has a carcinogenic effect and mutagenic effects. The spillage of oil products into water bodies is a serious problem for the environment and biota and could affect human health via the food chain and contamination of fresh water.

The main methods of water purification from oil products are mechanical, chemical and biological. The mechanical skimming of oil usually precedes other treatments. In chemical methods, dispersants are used to break down the oil film into smaller droplets, which then are consumed by bacteria. However, the use of dispersants may have a detrimental effect on the marine biota because the oil droplets have larger surface area than the oil film and the oil/dispersant mixture was shown to be toxic to some living organisms (Rico-Martinez, 2013). In the biological treatment, different microorganisms that can feed on oil and its products are used (Doshi, 2018). Sorption is considered an efficient method of removing oil spills as sorbent particles have high capacity for oil uptake and could be mechanically removed from the water surface. A great variety of porous materials have been tested in this application including carbons, zeolites, polymers and other sorbents. Expanded graphite was first reported in this application by Toyoda *et al*. (1998). Here we present the results of using thermally expanded graphite for oil spills sorption.

## RESULTS AND DISCUSSION

It is known that due to its hydrophobicity and oleophilicity, EG has high affinity to hydrocarbons even in aqueous environment. Unlike other hydrophobic adsorbents, EG can be easily regenerated and used repeatedly.

We designed an electrical module for manufacturing EG in situ, on the site where it should be used. (Fig. 1).

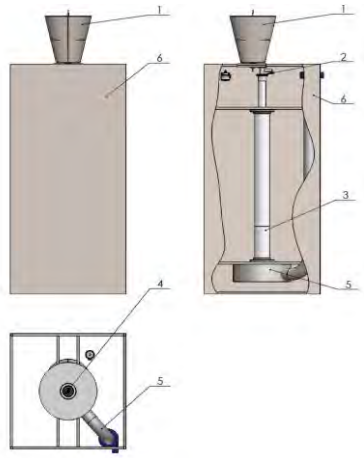


**FIGURE 1.** Schematic of the electrical reactor for EG production.

Graphite flakes are loaded through the funnel 1 and using the dosing feeder 2 into the tubular expansion reactor 3 heated to 700-900 ℃. Thermally expanded graphite is transferred to the collector 4 by aerodynamic flow through the tube 5. 6 – the reactor casing.

This module can produce 6-10 kg EG per hour, with electric energy consumption 5 kW/h. The bulk density of EG is inversely dependent on the expansion temperature, decreasing from 5 g/dm$^3$ at 700 ℃ to 3 g/dm$^3$ at 900 ℃. The productivity decreases respectively from 8 to 6 kg/h.

Some of the EG properties are given in Table 1.

**TABLE 1.** Properties of thermally expanded graphite produced in the electrical reactor.

| External Appearance | Bulk Density | Oil Capacity | Oil Capacity | Water Capacity | Regeneration, Utilisation |
|---|---|---|---|---|---|
| Black hydrophobic Powder | 3-5 g/dm$^3$ | >50 g/g | > 5 g/cm$^3$ | Absent (does not sink) | 2-3 cycles, after that additive to bitumen/asphalt |

The oil sorption capacity of EG per weight or per volume is substantially higher than that of other sorbents. In comparison with other materials, EG has a significant advantage in terms of its cost efficiency. Although its cost (approximately 10,000 USD/t) is several times more expensive than the cost per weight of other sorbents, for expanded graphite it has been estimated as 50 USD per ton of the collected oil products, whereas it is 2,350 USD for granulated vermiculite and 1,610 USD/t for peat-based sorbent Turbojet.

## CONCLUSIONS

The *in situ* production of EG makes a significant saving on transportation costs taking into account that graphite flakes expand in volume 200-400 times upon thermal treatment. For practical purposes in removing oil spills, EG could be placed in special bags made of the material similar to vapour barrier films; in this case it is practically impenetrable to water. After its use, the oil is squeezed out of the EG-filled bag by a mechanical press and the sorbent can be regenerated or utilised in other applications. Thus water could be cleaned without losing oil or its products.

**Acknowledgements**

This work was supported by the research grant of the National Academy of Sciences of Ukraine.

**References**

Doshi, B., Sillanpää, M. and Kalliola, S. (2018). A review of bio-based materials for oil spill treatment. *Water Research*, 135, 262-277.

Rico-Martínez, R., Snell, T.W. and Shearer, T.L. (2013). Synergistic toxicity of Macondo crude oil and dispersant Corexit 9500A® to the *Brachionus plicatilis* species complex (Rotifera). *Environmental Pollution,* 173, 5-10.

Toyoda, M.; Aizawa, J. and Inagaki, M. (1998). Sorption and recovery of heavy oil by using exfoliated graphite. *Desalination*, 115, 199–201.

20 C 22 arbon 2022

# Selective graphitic N enrichment of activated carbon for ORR electrocatalysts

**Javier Quílez-Bermejo[1], Sara Pérez-Rodríguez[1], Rafael Canevesi[1], Daniel Torres[1], Emilia Morallón[2], Diego Cazorla-Amorós[3], Alain Celzard[1], Vanessa Fierro[1]**

Email: javier.quilez-bermejo@univ-lorraine.ft

[1]Université de Lorraine, CNRS, F-88000, Épinal, France
[2]Departamento de Química Física and Instituto Universitario de Materiales, Universidad de Alicante, Ap. 99, 03080, Alicante, Spain
[3]Departamento de Química Inorgánica and Instituto Universitario de Materiales, Universidad de Alicante, Ap. 99, 03080, Alicante Spain

**Keywords**
Oxygen reduction reaction, electrocatalysts, activated carbon, selective enrichment, graphitic N.

## INTRODUCTION

Carbon materials have proven to be excellent electrocatalysts for the oxygen reduction reaction (ORR), which occurs in the cathode electrode of fuel cells and metal-air batteries. However, the catalytic activity of pure carbon materials is still far from the commercial performance of platinum. This is because undoped carbon layers have a homogeneous distribution of charge densities, which makes chemisorption of oxygen molecules difficult. In order to overcome this limitation, the introduction of heteroatoms is mandatory (Quílez-Bermejo, 2020). Among all heteroatoms, nitrogen (N) seems to create the most promising catalytic activities in carbon materials. Although it is known that nitrogen doping can increase the catalytic activity towards the ORR, only a few N-doped carbon materials have been found to be highly efficient for the reduction of oxygen molecules, close to the performance of platinum (Dai, 2015). Graphitic N species have shown the most promising to increase the catalytic activity of carbon materials up to the performance of platinum in alkaline medium (Gong, 2009). Nevertheless, graphitic N is mainly found in N-doped carbon materials that have been obtained by carbonization of N-containing precursors and, therefore, the textural properties, morphology and other important properties of the resulting N-doped carbon material are highly dependent on the nature of the precursor. Post-functionalization methodologies for selective graphitic N enrichment are needed to extrapolate the synthesis protocol to selective doping of other carbon materials, while retaining most of the properties of the pristine carbon material.

In this work, we prepare a highly catalytic N-doped carbon material by selective post-functionalization of a commercial activated carbon with the majority of the N in the form of graphitic species. The pristine porous carbon was first functionalized with urea under different conditions and then heat-treated at high temperatures to tailor the nitrogen functional groups. The extensive characterization shows that the different conditions of the nitrogen functionalization processes and the temperatures of the heat treatment result in a wide range of functionalization degrees and nitrogen species. The resultant N-doped carbon materials show promising catalytic activity for the oxygen reduction reaction, with strong resistance to methanol poisoning and high stability under working conditions.

## EXPERIMENTAL

A commercial activated carbon, MSC30, was functionalized using urea as a nitrogen precursor. MSC30 and urea were physically mixed in mass ratios of 1:1 and 1:2 and subjected to a first heat treatment at 350 °C in air. The resulting samples were cooled to room temperature and subsequently heat-treated in an inert atmosphere at high temperature (from 700 to 1300 °C). The samples were labelled MSC30-U1-T or MSC30-U2-T according to the carbon/urea ratio, where T is the temperature of the second heat treatment.

The materials were characterized by elemental analysis, XPS, Raman, EDX-TEM, and $N_2$ and $H_2$ adsorption isotherms. The catalytic activity tests towards the ORR were performed in a rotating ring-disk electrode (RRDE) in 0.1 M KOH solution.

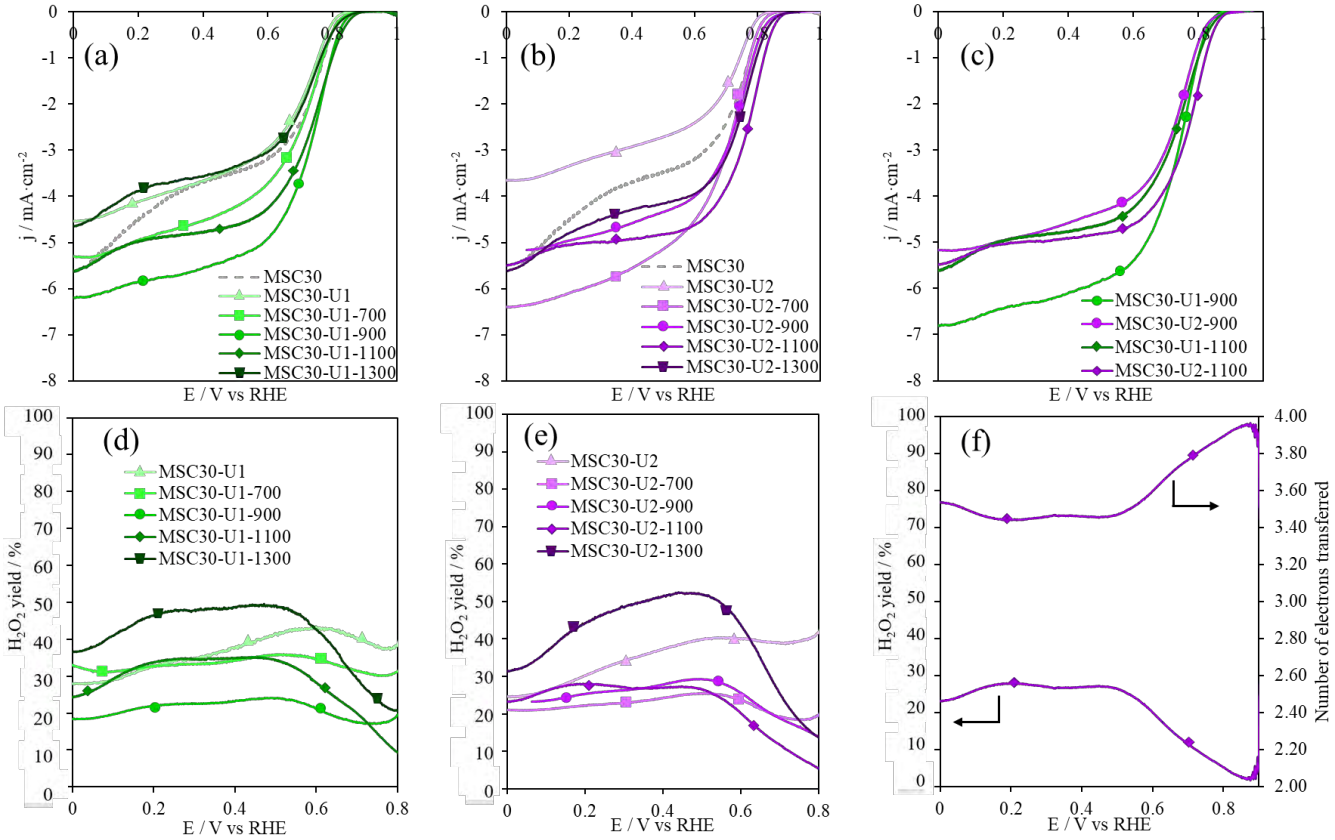


**FIGURE 1**: LSV curves and electron transfer number of MSC30-U1-T and MSC30-U2-T samples in 0.1 M KOH solution.

## RESULTS AND DISCUSSION

According to Raman spectroscopy and gas adsorption results, the textural properties and structural order were not significantly modified after the post-functionalization procedure. Regarding the surface chemistry, the activated carbons treated at the lowest temperature, 700 °C, showed a mixture of pyridines, pyrroles/pyridones and graphitic N species, with pyridines being the main contribution. With increasing temperature, the contribution of pyridines decreased while an increase in graphitic nitrogen was observed, especially for MSC30-U2-1100, in which all nitrogen is in the form of graphitic species. At 1300 °C, no nitrogen was detected in the surface chemistry of the carbon materials, regardless of the carbon/urea ratio.

Fig. 1a-c show the LSV curves before and after heat treatment of the MSC30-U1 and MSC30-U2 samples, respectively. A clear effect of pyrolysis temperature on electrochemical performance was observed. In the case of MSC30-U1-T samples, the thermal treatment at 700 °C improves the limiting current density, compared to the pristine MSC30 (dotted line). This increase in catalytic activity

continues up to 900 °C, where the optimum catalytic activity appears to be achieved. At temperatures above 900 °C, the higher the annealing temperature, the lower the current density.
For the analogous MSC30-U2 materials (Fig. 1b), the trend is slightly different. There is still an improvement in catalytic activity for the materials heat-treated at 1100 °C. The presence of this optimized electrocatalytic behaviour for oxygen reduction seems to be related to the surface chemistry of this sample, containing only graphitic-N species. The hydrogen peroxide yield, which is indicative of ORR mechanisms, is shown in Fig. 1d-f. Interestingly, all materials show low $H_2O_2$ yield at higher potentials, meaning that the number of electrons transferred is close to 4.

## CONCLUSIONS

N-doped carbon materials enriched with graphitic N were prepared by post-functionalization with urea of a commercial activated carbon. Urea and MSC30 were mixed and heat-treated to obtain N-doped carbon materials with different nitrogen contents and functional groups distributions. The high catalytic performance towards ORR of the resulting materials corroborated the key role of graphitic nitrogen in this electrochemical reaction.

**Acknowledgements**

The French research team thanks ANR-15-IDEX-04-LUE and the TALiSMAN project (2019-000215), financed by the European Regional Development Fund (ERDF). The authors from UA thank MICINN and ERDF (project RTI2018-095291-B-I00) for financial support.

**References**

Dai, L.; Xue, Y.; Qu, L.; Choi, H.J.; Baek, J.B. (2015) Metal-Free Catalysts for Oxygen Reduction Reaction, Chem. Rev. 115, 4823-4892. 10.1021/cr5003563

Gong, K.; Du, F. ; Xia, Z.; Durstock, M.; Dai, L. Nitrogen-doped carbon nanotube arrays with high electrocatalytic activity for oxygen reduction Science (2009) 323, 760-764. 10.1126/science.1168049.

Quílez-Bermejo, J.; Morallón, E.; Cazorla-Amorós, D. (2020) Metal-free heteroatom-doped carbon-based catalysts for ORR. A critical assessment about the rôle of heteroatoms Carbon. 165, 434. 10.1016/j.carbon.2020.04.068

Carbon 2022

# Effect of pore size and surface functionality of the host on the mobility and phase transitions of an ionic liquid confined in micro- and mesoporous carbons

**Paula Ratajczak[1], Zhuanpei Wang[1], Christopher Bachetzky[2], Eike Brunner[2] and Francois Béguin[1]**

ICTE, Poznan University of Technology, Berdychowo 4, 60-965 Poznan, Poland
[2]TU Dresden, Faculty of Chemistry and Food Chemistry, 01062 Dresden, Germany
Email: francois.beguin@put.poznan.pl

**Keywords**
Micro and mesoporous carbons; Ionic liquid; Mobility and phase transitions of confined ions

## INTRODUCTION

Recently, it was shown that the issue of the relatively high melting point of ionic liquids (ILs) can be resolved by their confinement either in appropriate mesoporous carbons, where the IL's melting temperature is reduced, or in microporous carbons, where, due to the IL adsorption, no phase transition is observed down to 140 K (Béguin, 2020; Singh 2011). However, when considering the development of energy storage systems as electrical double-layer capacitors (EDLCs) able to operate at low temperatures, while implementing IL electrolytes, it is necessary to simultaneously get information about the changes in phase transitions, from the bulk to the confined state of ILs, as well as in their low temperature mobility. In this context, the effect of pore size and surface functionality of the carbonaceous host on the phase transitions and mobility of a confined IL was herein studied by combining differential scanning colorimetry (DSC) and $^{1}$H Nuclear Magnetic Resonance ($^{1}$H NMR).

## EXPERIMENTAL

The surface-clean materials (i.e., with a total amount of evolved oxygen below 2.5 wt.%) were the commercially available microporous Maxsorb carbon (MSP-20X, Kansai Coke; further in the text "Maxsorb") and a home-made templated mesoporous carbon synthesized from $SiO_2$ (particle size of 12 nm) templating (further in the text "STC-12"), while adapting the conditions described by Bhandari (2015). Additionally, a carbon of identical porous texture (mesopore size of 9 nm at PSD maximum) and increased surface oxygen content (10.3 wt.%) as referred to the pristine STC-12 has been obtained by oxidation in air of the STC-12 carbon at 420 °C (further in the text "STC-12-ox420"). The three carbons were soaked with the 1-ethyl-3-methylimidazolium bis(fluorosulfonyl)imide ($[EMIm^+][FSI^-]$) IL at a filling ratio R ≈ 0.85 to provide almost complete pore filling, while avoiding excess liquid outside the pores, as reported by Ratajczak (2022).

## RESULTS AND DISCUSSION

When $[EMIm^+][FSI^-]$ was confined in the microporous carbon (IL@Maxsorb), the DSC curves (Fig. 1) were totally flat during cooling and heating, due to the adsorption of the molecules strongly interacting with the pore walls (Béguin, 2020). For the mesoporous carbon soaked with the IL (IL@STC-12), the thermograms showed freezing upon cooling, and a glass transition followed by cold crystallization and melting upon heating (Fig. 1). Two IL populations characterized by slightly different (by ~6 K) melting/freezing points were disclosed by deconvoluting the DSC signals (Fig. 1). They are attributed to two environments corresponding to: i) a monolayer of molecules in contact with the mesopore walls, hence, interacting both with the carbon walls and the neighboring molecules; ii) molecules interacting only with other molecules, i.e., close to the mesopore center.

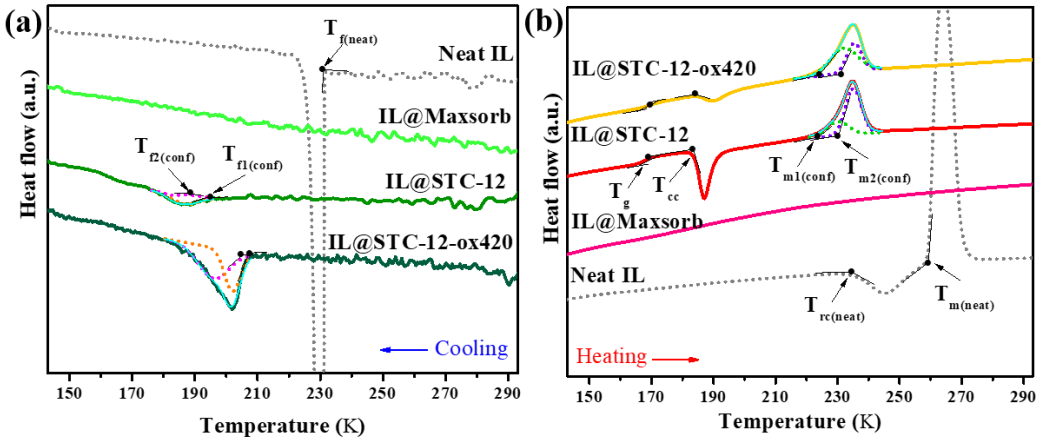


**FIGURE 1**: DSC thermograms of neat [EMIm$^+$][FSI$^-$] and [EMIm$^+$][FSI$^-$] confined in the Maxsorb, STC-12, and STC-12-ox420 carbons (IL@Maxsorb, IL@STC-12, IL@STC-12-ox420, respectively) upon (a) cooling and b) heating at 10 K min$^{-1}$. The horizontal double arrows indicate the temperature range of the first-order transitions.

With the oxidized STC-12-ox420 host, the thermograms of confined [EMIm$^+$][FSI$^-$] exhibited the same features as revealed with the pristine STC-12 carbon (Fig. 1). However, when shifting from the surface clean host (IL@STC-12) to the oxidized one (IL@STC-12-ox420), the overall specific freezing enthalpy increased, whereas the amount of heat evolved during cold-crystallization decreased. Both the freezing and cold-crystallization enthalpy values are modified by a factor of ~4, suggesting that the oxygenated functionalities (i.e., carboxylic, lactones, phenols, quinones) present on the carbon surface play the role of crystallization seeds for [EMIm$^+$][FSI$^-$] confined in the mesoporous matrix.
The room temperature $^1$H NMR spectra revealed that the mobility of [EMIm$^+$][FSI$^-$] is more restricted in the microporous carbon (IL@Maxsorb exhibited a full width at half maximum (FWHM) of 3100 Hz) than in the mesoporous carbon (FWHM of 2460 Hz for IL@STC-12) (Ratajczak, 2022). Fig. 2a shows that the linewidth of the IL@Maxsorb signal gradually increases as the temperature decreases. Noteworthy, after deconvoluting the spectra of IL@STC-12, two types of signals with considerably distinct transverse relaxation times (i.e., narrow and broad) revealed the existence of two strongly different motional regimes: (i) where the molecules are relatively mobile (narrow signal) and (ii) strongly immobilized (broad signal). Since at low temperature, the intensity of the broad signal cannot be quantitatively evaluated (due to the dead-time problem), the FWHM plot in Fig. 2 refers exclusively to the narrow signal (or a sum of narrow signals, if more than one narrow signal appears) of IL@STC-12. Interestingly, upon cooling the IL@STC-12 sample from 293 K down to about 200 K, the linewidth of the narrow signal only slightly increased (Fig. 2b), i.e., the mobility of the ions contributing to the signal remained almost unchanged. Below 200 K, the very steep increase of FWHM reveals a sudden immobilization of the IL. Hence, the temperature of ~200 K can be recognized as the freezing point of [EMIm$^+$][FSI$^-$] confined in STC-12, as already presented by DSC in Fig. 1a (however, as DSC is a dynamic method, the freezing point appears at a slightly lower temperature than 200 K). Remarkably, even after freezing of the molecules in the mesopore center, the species in contact with the pore walls remain mobile and contribute to the observed increase in width of the narrow signal (Fig. 2b) when the temperature decreases from 200 K to 193 K; below 193 K, the narrow signal is no longer observed in the spectrum (Ratajczak, 2022).

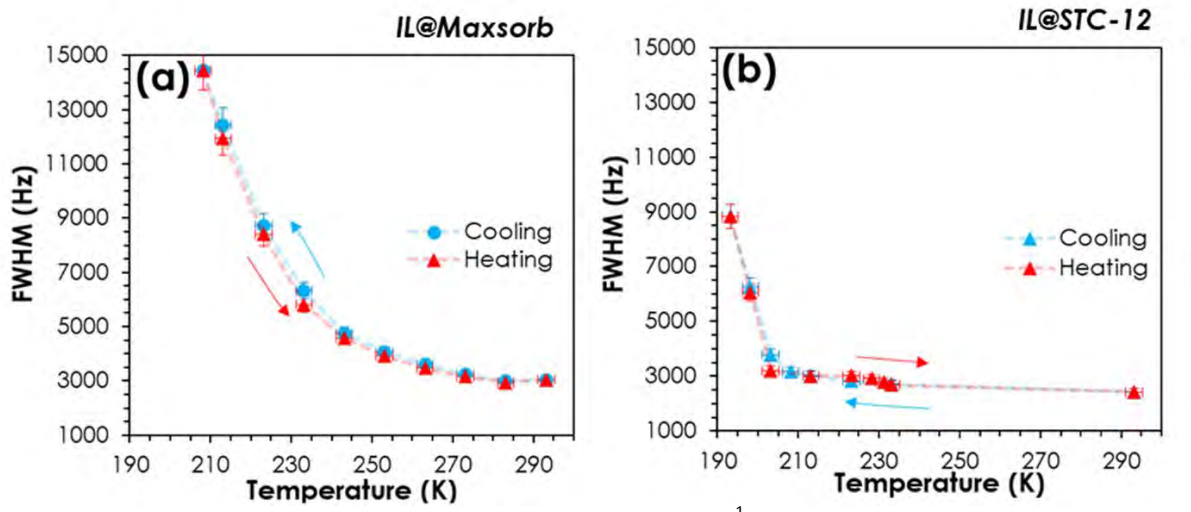


**FIGURE 2**: Full width at half-maximum (FWHM) of the narrow $^{1}$H NMR signals vs. temperature for: (a) IL@Maxsorb and (b) IL@STC-12. The subtle dashed lines are provided only to guide the eye. The error bars indicate the deviations in FWHM and temperature values by ±5% and ±2 K, respectively.

## CONCLUSION

In summary, in contrast to the neat IL, the IL confined in micropores does not freeze, whereas the IL in mesopores does not exhibit a precisely defined freezing point (~6 K wide freezing/melting temperature range) due to the ions located in vicinity of the pore walls. Upon cooling slightly below the freezing point, the ions interacting with the mesopore walls remain relatively mobile, though the ions in the proximity of the pore center (bulk-like molecules) are already frozen. Interestingly, when applying the oxidized mesoporous carbon, a part of the molecules initially in the bulk-like state, aggregate close to the pore walls and crystallize already upon cooling. Overall, the low temperature mobility and phase transitions of the IL confined in mesopores are affected by the surface functionality of the host. For developing IL-based EDLCs able to perform optimally down to 230 K, the choice of mesoporous carbons for the confinement appears as a good option to reduce the freezing/melting temperature, while keeping the mobility of ions at the same level as at room temperature (in contrast to the system with the microporous carbon host where the IL mobility is restricted already at RT). Hence, the combination of DSC and NMR is a powerful tool to predict if an applied IL-porous carbon pair is eligible to support a high-power output of energy storage systems at low temperature.

**Acknowledgements**

This work was supported by the Polish National Science Center (NCN) [UMO-2016/22/A/ST4/00092].

**References**

Béguin F., Pavlenko V, Przygocki P., Pawlyta M. and Ratajczak P (2020) Melting point depression of ionic liquids by their confinement in carbons of controlled mesoporosity, *Carbon*, 169, 501-511

Bhandari N., Dua N., Estevez L., Sahore R., Giannelis E.P. (2015) A combined salt-hard templating approach for synthesis of multi-modal porous carbons used for probing the simultaneous effects of porosity and electrode engineering on EDLC performance, *Carbon*, 87, 29-43

Ratajczak P., Bachetzky C., Wang Z., Chojnacka A., Fulik N., Pamete Yambou E., Pourhosseini S.E.M.,Brunner E. Beguin F. (2022) Mobility and phase transitions of the [$EMIm^{+}$][$FSI^{-}$] ionic liquid confined in micro- and mesoporous carbons. *J. Mater. Chem. A.,* 14, 7928-7940

Singh M. P., Singh R. K. and Chandra S. (2011) Studies on Imidazolium-Based Ionic Liquids having a Large Anion Confined in a Nanoporous Silica Gel Matrix, *J. Phys. Chem. B*, 115, 7505-7514.

Carbon 2022

# Structural-Photophysical Relationships in Atomically-Precise Distorted Nanographenes

**Marco Reale[1], A. Sciortino[1,2], M. Cannas[1], E. Maçôas[3], A. G. Campaña[4], F. Messina[1,2]**
[1]Dipartimento di Fisica e Chimica – E. Segré, Università degli Studi di Palermo, Palermo (Italy)
[2]ATeN Center, Università degli Studi di Palermo, Palermo (Italy)
[3]Centro de Química Estrutural, Instituto Superior Técnico, Lisboa (Portugal)
[4]Departamento de Química Orgánica, Universidad de Granada, Granada (Spain)
Email: marco.reale@unipa.it

**Keywords**
Luminescent Nanocarbons, Atomically-Precise Nanographenes, Structure-Properties Correlation

## INTRODUCTION

The great interest in luminescent zero-dimensional nanocarbons such as Carbon Dots (CDs) and Graphene Quantum Dots (GQDs) is driven by the wide range of interdisciplinary applications made possible by their fascinating properties and versatility (Li et. al, 2012). However, in most cases the synthetic procedures lack of an optimal control over the produced samples, giving rise to heterogeneous compounds. The high degree of inhomogeneity that affects such compounds is one of the main responsible of the intrinsic ambiguity of their optical behaviours, hampering a full understanding of their properties and their applications (Sciortino et. al, 2018).
In this perspective, in the realm of luminescent nanocarbons, novel atomically-precise nanographenes (NGs), namely polycyclic aromatic hydrocarbons (PAHs) with very large sizes (>1nm), are emerging as ideal benchmarks to study the photophysical properties of graphene-related nanomaterials (Narita et al., 2015; Drummer et al., 2021). Such NGs can be considered as a class of atomically-precise zero-dimensional nanocarbons, displaying interesting optical properties which can be vastly tailored through chemical engineering. Indeed, many chemical bottom-up synthetic strategies allow to tightly control and finely tuning the structure of monodisperse NGs, perfectly defined in terms of their size, morphology, edges and topological defects that in turn permit to modulate their photophysical properties (Dötz et al., 2000). Thus, such atomically-precise NGs represent model systems to disclose how every single structural modification is reflected on their optical characteristics. Within this context, among the several graphene nanostructures that have been reported, well-defined distorted NGs have gained a particularly great interest owing to the potential influence of such deliberately introduced structural distortion over the structure and properties of the standard $sp^2$ planar systems (Márquez et al., 2018).

## RESULTS AND DISCUSSION

Here, through a comparative study, we present the photophysical characterization of four atomically-precise distorted NGs whose chemical structures are reported in Figure 1a. In these, the distortion is caused by the controlled inclusion of a heptagon ring in their otherwise purely hexagonal networks, which is thus forced out from planarity. The three smallest NGs, namely NG1a, NG1b and NG1c, can be considered as hexabenzocoronene analogues containing a seven-membered ring at the edge of their carbon network. Each of them differs from the others for defined structural elements. More specifically, moving from NG1a to NG1b the oxygen of the peripherical carbonyl group of the tropone moiety is replaced by a methylene group, and moving from NG1a to NG1c two edge hydrogens are replaced by two bromine atoms. Instead, the largest nanographene NG2 can be

roughly considered double the size of NG1. It also contains a tropone moiety as heptagon-ring and, in addition, the presence of a helicene moiety causes a deeper distortion away from planarity making the overall structure more flexible.

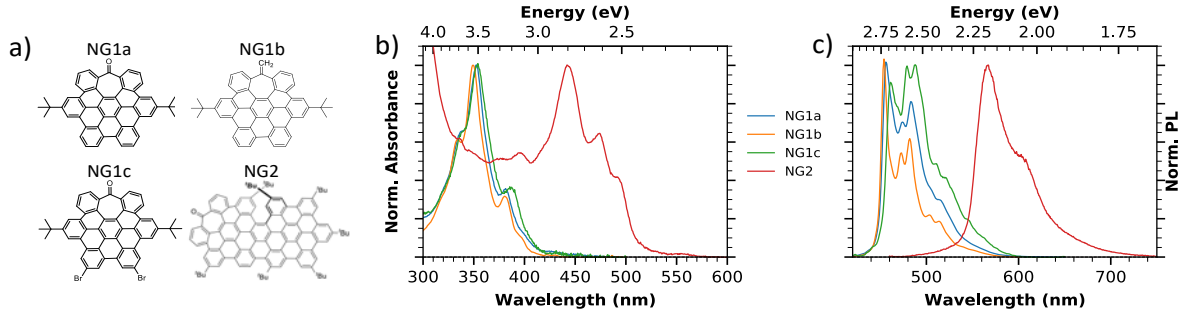


**FIGURE 1**: (a) Chemical structures, (b) normalized absorption spectra and (c) normalized steady-state emission spectra of the four atomically-precise distorted nanographenes studied.

On these compounds we executed a photophysical characterization, starting from steady-state optical properties as highlighted by Figure 1b and Figure 1c where the normalized absorption and emission spectra are shown respectively. Moreover, a thorough analysis of the described NGs permitted us to disclose their entire optical photocycle by means of the combination of several spectroscopic techniques, including time resolved photoluminescence down to ultrafast optical methods characterized by a temporal resolution of tens of femtoseconds. In particular the latter, poorly employed for the study of these systems, provided an exhaustive picture also of the earliest excited-state relaxation dynamics. Overall, thanks to the well-defined structures of the NGs, it is possible to unambiguously obtain structural-photophysical relationships.

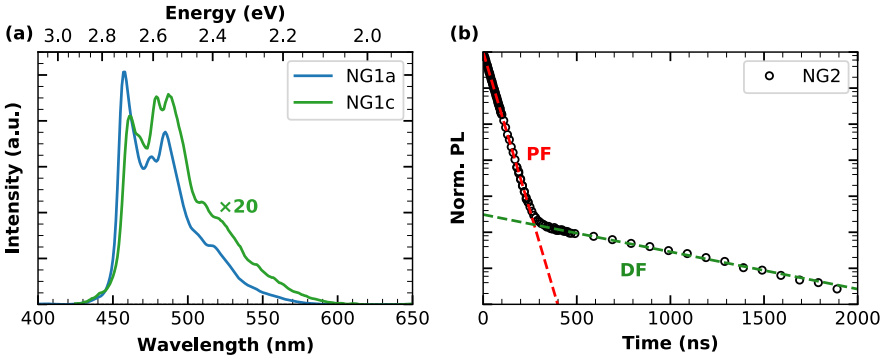


**FIGURE 2**: (a) Comparison of photoluminescence spectra of NG1a and NG1c. (b) Prompt fluorescence (PF) and delayed fluorescence (DF) contributes in time-resolved photoluminescence decay of NG2.

An explanatory example of this is provided by dramatical reduction of photoluminescence quantum yield (QY) from NG1a (QY=2%) to NG1c (QY=0.1%), as shown in Figure 2a. The knowledge of their exact structure permits to infer the emergence of a heavy-atom effect due to the introduction of two bromine atoms, as further confirmed by time-resolved optical data. In general, smallest NGs showed quite standard molecular-like photophysical characteristics. On the contrary, we had evidence that the largest distorted nanographene NG2 is characterized by a range of quite uncommon properties, such as delayed fluorescence (Figure 2b) that an appropriate investigation has allowed to associate to a triplet-triplet annihilation mechanism. Moreover, other NG2 peculiar properties include slow dynamical structural relaxations, rarely observed in traditional aromatic molecules. In fact, the synergetic effect of the saddle-shaped curvature due to the heptagon ring together with the helicity induced by the helicene might cause a particularly marked conformational flexibility responsible of the observed dynamics.

## CONCLUSIONS

Our studies revealed several important details on the photophysics of atomically-precise NGs. The differing structures of the studied compounds permitted to unequivocally relate how their optical characteristics are affected by single modifications of their well-defined structures, such as size, presence of heteroatoms or functional groups. In this perspective, we observed very strong structure-property relationships, offering promising routes to tailor NGs for specific applications.

### References


Dötz, F., Brand, J. D., Ito, S., Gherghel, L., Müllen, K. (2000). Synthesis of Large Polycyclic Aromatic Hydrocarbons: Variation of Size and Periphery. *Journal of American Chemical Society*, 122, [32], 7707–7717. https://doi.org/10.1021/ja000832x.

Drummer, M. C., Singh, V., Gupta, N., Gesiorski, J. L., Weerasooriya, R. B., Glusac, K. D. (2021). Photophysics of nanographenes: from polycyclic aromatic hydrocarbons to graphene nanoribbons. *Photosynthesis Research*, 151, 163-184. https://doi.org/10.1007/s11120-021-00838-y.

Li, H.; Kang, Z., Liu, Y., Lee, S. T. (2012). Carbon Nanodots: Synthesis, Properties and Applications. *Journal of Materials Chemistry*, 22, [46], 24230–24253. https://doi.org/10.1039/c2jm34690g.

Márquez, I. R., Castro-Fernández, S., Millán, A., Campaña, A. G. (2018). Synthesis of Distorted Nanographenes Containing Seven- and Eight-Membered Carbocycles. *Chemical Communications*, 54, [50], 6705–6718. https://doi.org/10.1039/C8CC02325E.

Narita, A., Wang, X. Y., Feng, X., Müllen, K. (2015). New Advances in Nanographene Chemistry. *Chemical Society Reviews*, 44, [18], 6616-6643. https://doi.org/10.1039/c5cs00183h.

Sciortino, A., Cannizzo, A., Messina, F. (2018). Carbon Nanodots: A Review—From the Current Understanding of the Fundamental Photophysics to the Full Control of the Optical Response. *C*, 4, [4], 67. https://doi.org/10.3390/c4040067.

Carbon 2022

# Adsorbents and photocatalysts based on activated carbons for the ethylene removal

**Ana M. Regadera-Macías, Luisa M. Pastrana-Martínez, Sergio Morales-Torres, Francisco J. Maldonado-Hódar ***

*NanoTech – Nanomaterials and Sustainable Chemical Technologies. Unit of Excellence in Chemistry applied to Biomedicine and the Environment. Department of Inorganic Chemistry. University of Granada, Granada 18071 (Spain).*

Email: fjmaldon@ugr.es

**Keywords**

Biochar, activated carbons, carbon – $TiO_2$ composites, adsorption, photocatalysts, ethylene

## INTRODUCTION

Perishable food products deteriorate since the moment they are harvested. Nowadays, associated with cold chambers of conservation, different types of atmospheres (namely, normal, modified, controlled and dynamic) are used by regulating levels of $O_2$ and $CO_2$. Ethylene ($C_2H_4$) is evolved from the stored fruits and its removal is critical because a very low concentration of $C_2H_4$ may induce fast/excessive ripening and senescence [Paul, 2014]. For that, the air from the storage room can be circulated through a sealed cartridge that is loaded with adsorbents materials or catalysts. The ethylene combustion is usually carried out using Pt-catalysts at temperatures ranging between 200 – 300 °C, thus the process requires heating the air from the usual temperature (2 – 5 °C) in the storage chambers to 200 – 300 °C in the reactors and then cooling down again. Our approach is the development of a combined system of adsorbents and photocatalysts allowing the removal of the heating step.

Activated carbons (ACs) are typically used as adsorbents or catalysts supports. They can be prepared from agricultural by-products, in a concept of circular economy, and applied as ethylene adsorbents under dynamic conditions or combined with semiconductors ($TiO_2$) with photocatalytic activity looking for a synergetic effect on the composite [Pastrana, 2018; Hamad, 2018].

## EXPERIMENTAL

Olive stones from the olive oil industry were selected as raw materials. ACs were prepared either by chemical activation with KOH in one step process, or by physical activation with $CO_2$ or steam, obtaining previously in this case a biochar by carbonization before activation (two steps process). Experimental conditions were fitted to obtain ACs with different activation degrees and physicochemical characteristics. A commercial AC (Norit) was used as a reference. Photocatalysts were prepared by hydrothermal deposition of $TiO_2$-phases on the ACs. Textural and chemical characteristics of samples were determined by complementary techniques (i.e., gasses adsorption, $pH_{PZC}$, SEM, TEM, XPS, DRX, among others). Chemically ACs exhibited surface areas larger than 1600 $m^2/g$ with developed mesoporosity. The obtained ACs were milled and sieved bellow 150 µm and packed in columns of 10 x 0.6 cm. The performance of the prepared ACs for the ethylene adsorption was evaluated by obtaining the corresponding breakthrough curves. A continuous flow of $N_2$/ethylene (10000 ppm) stream passed through the columns at a rate of 50 $cm^3/min$. The breakthrough and saturation points were defined as the volume passed when the concentration of ethylene detected at the exit of the column was $C/C_0$ = 0.02 and 0.9, respectively. The adsorptive behavior of the composites was compared with those corresponding ACs supports. The

photocatalytic performance was evaluated using both UV and VIS lamps. The analysis of reactant and products were evaluated by gas chromatography.

## RESULTS AND DISCUSSIONS

During the preparation of the biocarbon, the weight loss of the olive stone during the carbonization was 76%. Then, biochar was physically activated with $CO_2$ or steam up to 15-23%. The weight loss for direct activation with KOH ranges 92%. Steam activation (CAV-samples) at similar activation degree (13%) produces a deeper development of micropore volume and micropore width than $CO_2$-activation, leading to an increase of the $S_{BET}$ from 750 to 1300 $m^2g^{-1}$, but the most developed porosity was found for chemically activated carbons, surface reaching values higher than 1600 $m^2g^{-1}$ and total pore volume of 0.99 $cm^3g^{-1}$ (from $N_2$-adsorption at $P/P_0$=0.95). Nevertheless, when the results obtained for ethylene adsorptive performance indicate that physical activation with steam is the best option (Figure 1).

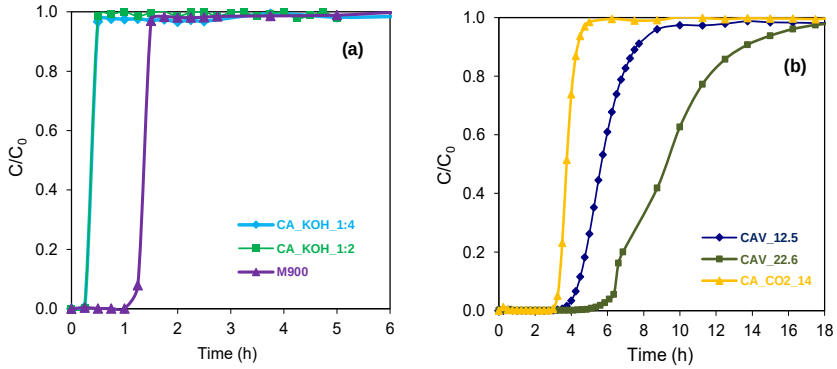


**Figure 1.** Breakthrough curves for dynamic ethylene adsorption (10000 ppm, 50 $cm^3min^{-1}$, 0.5 g of AC) obtained with activated carbons prepared by chemical activation (a) and physical activation (b).

The activated carbon with steam at 13% (CAV-13) was selected to prepare carbon-$TiO_2$ composites, taking into account that it presents a similar porosity than Norit (Figure 2a). Composites 50% $TiO_2$ - 50% carbon were prepared using both ACs. The microporosity of the composites decreased, but the mesoporosity is strongly enhanced. The morphology of the composite analysed by SEM. Figure 2c shows the formation of anatase nanoparticles inside the open porosity of CAV, becoming from the vesicular structure of the lignocellulosic raw materials (Figure 2b). This structure is destroyed aggressively in the case of KOH activation. In the experimental conditions used, the formation of $TiO_2$ nanorods is favoured (Figure 2c).

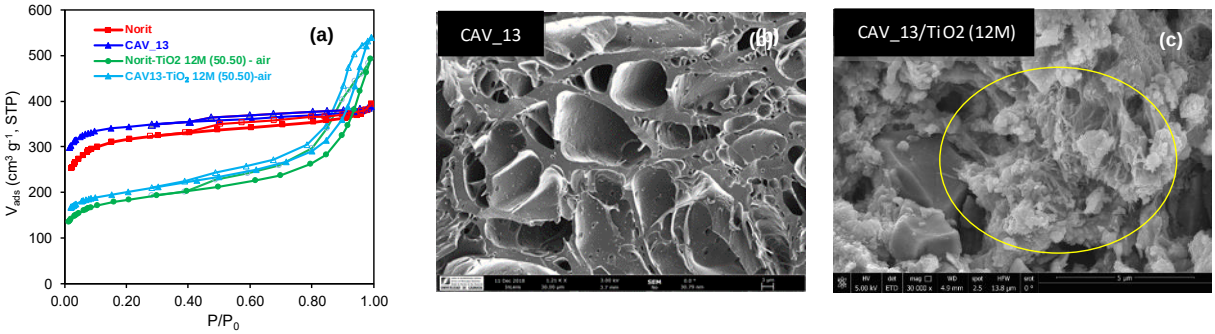


**Figure 2.** $N_2$-adsorption isotherms of ACs and ACs-$TiO_2$ composites (a), SEM images showing the morphology of steam activated carbons (b) and the composite derivative (c).

The ethylene adsorption capacity of ACs was related with the narrowest microporosity (determined from $CO_2$ isotherms), thus it was expected a smaller performance of the composites in adsorption

(Figure 3). Samples obtained from biochar exhibited a similar performance or slightly improved than those prepared with commercial ones.

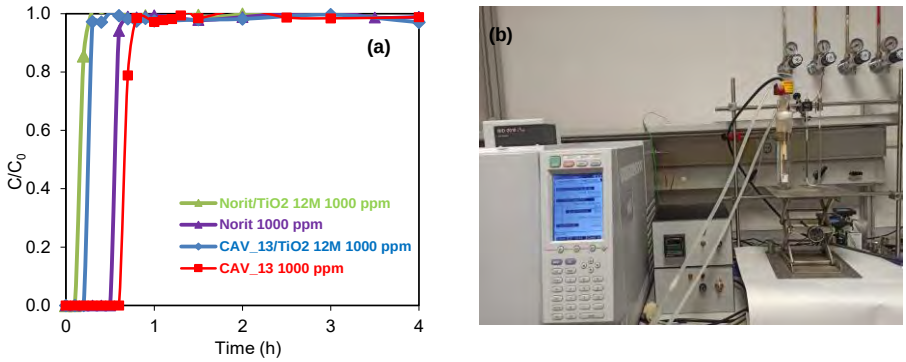


**Figure 3.** Breakthrough curves for dynamic ethylene adsorption (1000 ppm, 50 $cm^3min^{-1}$, 0.5 g of sample) using ACs vs their ACs-$TiO_2$ composites (a), preliminary photocatalytic reactor used for ethylene photo-oxidation (b).

The photocatalytic activity of the prepared composites (saturated) was previously evaluated in the degradation of emerging pollutant, i.e., paracetamol in aqueous solution using a batch reactor. The results show a conversion of paracetamol of around 90% in 6 hours under UV/vis irradiation. On the other hand, the experimental set-up for the degradation of ethylene in gas phase is shown in Figure 3b. Preliminary results showed than in spite of the reactor design/experimental conditions relevance, ethylene is oxidized selectively to $CO_2$ under UV-Vis lamp, $\lambda$ = 385 nm. Fixed bed reactors and films prepared by dip-coating of active photocatalysts are being tested.

## CONCLUSIONS

The possibility to use agricultural waste residues (olive stones) as raw materials in an integrated circular economy process for the production of suitable materials (ACs and photocatalysts) with high performance in the ethylene removal from the atmosphere of storage chambers for climacteric fruits is point out. The selection of the appropriate activation procedure (steam activation) in combination with hydrothermal deposition of photocatalytic active phases leads to materials with suitable porosity and enhanced interactions with ethylene, which favour its photocatalytic oxidation.


### Acknowledgements

This work was financially supported by the PCI2020-112045 project from MCIN/AEI/10.13039/ 501100011033 and European Union Next Generation EU/PRTR, as part of the PRIMA Programme (Nano4Fresh project). S.M.T. (RYC-2019-026634-I) and L.M.P.M. (RYC-2016-19347) acknowledge the MICIN/AEI/10.13039/501100011033 and the European Social Found (FSE) “El FSE invierte en tu futuro” for a Ramón y Cajal research contracts.


### References


Hamad H., Castelo-Quibén, J., Morales-Torres, S., Carrasco-Marín, F., Pérez-Cadenas, A.F. Maldonado-Hódar, F.J. (2018) On the Interactions and Synergism between Phases of Carbon Phosphorus Titanium Composites Synthetized from Cellulose for the Removal of the Orange-G Dye, Materials (Basel), 11 1766. https://dx.doi.org/10.3390%2Fma11091766

Pastrana-Martínez, L.M., Morales-Torres, S., Carabineiro, S.A.C., Buijnsters, J.G., Figueiredo, J.L., Silva, A.M.T et al., (2018) Photocatalytic activity of functionalized nanodiamond-$TiO_2$ composites towards water pollutants degradation under UV/Vis irradiation, Applied Surface Science, 458839-48 https://doi.org/10.1016/j.apsusc.2018.07.102

Paul, V., Pandey, R., Role of internal atmosphere on fruit ripening and storability-a review, (2014) Journal of Food Science and Technology, 51 1223-50. https://dx.doi.org/10.1007%2Fs13197-011-0583-x

Carbon 2022

# Carbons materials prepared from L-cysteine amino acid

**S. Reljic, C. Cuadrado-Collados, E. Oliveira Jardim, J. Farrando-Pérez, M. Martínez-Escandell and J. Silvestre-Albero**
Inorganic Chemistry Department, University Materials Institute, University of Alicante, Spain
Email: erika.jardim@ua.es

**Keywords**
Activated carbons, cysteine, gas adsorption

## INTRODUCTION

The activated carbon global market is continuously growing due to the versatility of these materials in industry and municipalities for cleaning purposes. Their main application involves the removal of contaminants in water and air environments [1]. The attractiveness of activated carbon as a universal adsorbent is due to its low cost, the versatility in its production, and the possibility to design the porous structure and surface chemistry upon request. Although the porous structure has a profound impact on the performance of the activated carbons (e.g., microporous activated carbons exhibit an optimum performance for gas and energy storage [2,3]), the presence of surface functionalities, although being also important, has been less explored due to the difficulty to tailor the surface chemistry [4, 5]. Non-essential amino acids can be anticipated as potential platforms to obtain carbon materials with a rich surface chemistry. Amino acids are organic compounds that contain amino (-NH2) and carboxyl (-COOH) functional groups, together with side chains that could contain other functional groups such as sulphur (e.g., cysteine & methionine). A priori these platforms could be susceptible to be converted into activated carbon, after a proper activation step, although they have never been evaluated. Based on these premises, the main goal of the present study is the preparation of activated carbon materials combining oxygen, nitrogen and sulphur functionalities starting from L-cysteine as a raw material.

## EXPERIMENTAL

In a first step, L-cysteine was spread in the alumina boat and thermally treated in a horizontal furnace at 700ºC for 2h under a N2 flow rate of 100 ml/min (heating ramp of 3ºC/min). The reaction process is a simple condensation reaction of L-cysteine under nitrogen atmosphere. After condensation the yield was 5.4 wt.%. In the second step, the condensed material was activated with CO2 (100 ml/min) at a temperature of 800ºC with the heating ramp of 3ºC/min and the activation time of 1h, 3h, 6h. An additional sample was prepared using 900ºC as activation temperature for 1h. Four different cysteine-based activated carbons (CAC) were prepared and labelled CACxy00, where x = activation time and y = activation temperature. The synthesized samples have been characterized by different techniques, such as N2 adsorption measurements at -196ºC, CO2 adsorption at 0ºC, FESEM and XPS.

## RESULTS AND DISCUSSION

The results described in Fig. 1 (right) show that, for a given activation temperature (800ºC), the porous structure of the synthesized samples scales-up with the extend of the activation treatment, i.e. activation time from 1h to 6h. Sample activated for 1h at 800ºC, i.e. CAC1800, exhibits a poorly developed porous structure, with a BET surface area ca. 140 $m^2/g$. The presence of a scarcely developed porous structure can be clearly appreciated in the $N_2$ adsorption isotherm (Type I according to the IUPAC classification), with a narrow knee at low relative pressures associated with a

purely microporous material. An extension in the activation process to 3h and 6h at 800ºC gives rise to a significant development of the porosity with a BET surface area of 600 $m^2/g$ and 1013 $m^2/g$, respectively. The CAC1900 sample exhibits a moderate BET surface area (ca. 378 $m^2/g$). Interestingly, the $N_2$ adsorption isotherms confirm that the activation treatment with $CO_2$ provides purely microporous samples, independently of the activation degree. Despite these large differences in the nitrogen adsorption performance for the three samples synthesized at 800ºC, their $CO_2$ uptake (Figure 1 right) at 0ºC and 1 bar is rather similar. This observation anticipates the presence of diffusional restrictions for N2 to access the inner porous structure in samples with a low activation degree (e.g., CAC1800). The restricted accessibility of nitrogen at -196ºC is confirmed after comparing the micropore volume (V0) and the narrow micropore volume (Vn) deduced after application of the Dubinin-Radushkevich equation to the $N_2$ and $CO_2$ isotherms, respectively. For this specific sample (CAC1800), Vn>>V0 (0.18>>0.06), thus confirming the presence of diffusional restrictions for nitrogen to access the inner porous structure at cryogenic temperatures. The presence of narrow micropores is also reflected in the more concave shape of the $CO_2$ isotherm at 0ºC. In the specific case of sample CAC3800, Vn~V0 (0.24>>0.25), thus reflecting the presence of a narrow micropore size distribution. Only sample CAC6800 possess wider micropores V0>>Vn (0.42>>0.26), although without mesoporosity. Overall, these results show that L-cysteine is an excellent platform to synthesize purely microporous activated carbons with molecular sieving properties. The XPS analysis (not shown) confirm that the synthesized carbons exhibit a rich surface chemistry containing oxygen, nitrogen, and sulphur functional groups. Their performance in the adsorption of relevant probes ($CH_4$, $C_2H_4$ and $CO_2$) will be further discussed.

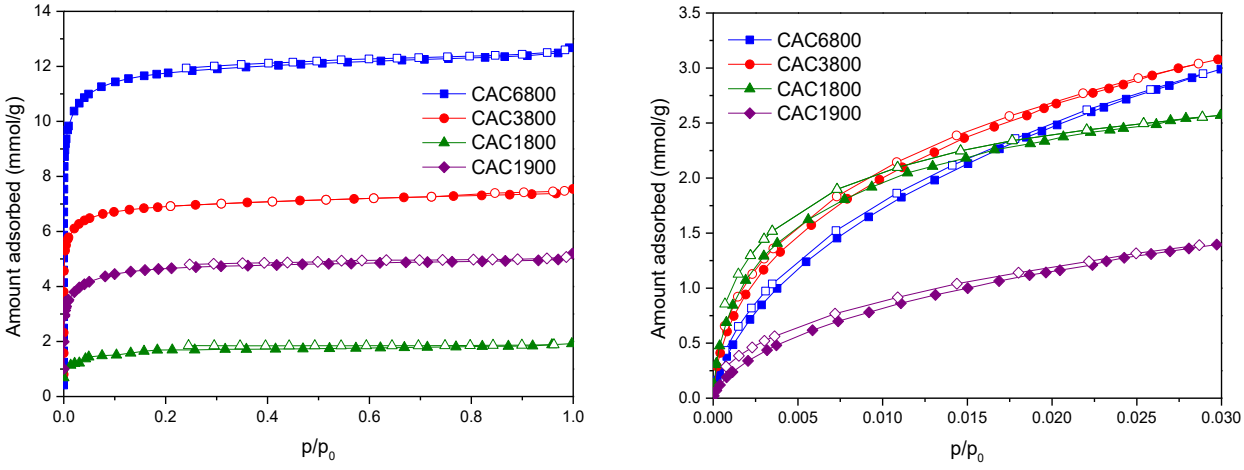


**FIGURE 1**: (left) $N_2$ adsorption/desorption isotherms at -196ºC and (right) $CO_2$ isotherms at 0ºC in the different carbon materials evaluated.

## CONCLUSIONES

A series of activated carbon materials have been successfully prepared from a non-essential amino acid, such as L-cysteine. The synthesized carbons combine a widely developed porous structure (BET surface area up to 1000 $m^2/g$) and a rich surface chemistry (mainly oxygen, nitrogen, and sulphur functionalities). Furthermore, the synthesized carbons exhibit an excellent adsorption performance for $CO_2$ (up to 3 mmol/g at 0ºC).

**Acknowledgements**

Authors acknowledge financial support from the MINECO (Projects PID2019-108453GB-C21 and PCI2020-111968/ERANET-M/3D-Photocat).

**References**

Bandosz, T. (2009). Surface chemistry of carbon materials. *Carbon materials for catalysis* (Ed. P. Serp, J.L. Figueiredo Eds.), Wiley, pp. 45-92.

Marsh, H., Rodríguez-Reinoso, F. (2006). Activated Carbon. Elsevier, London, UK. ISBN 0-08-044463-6.

Saha, D., Kienbaum, M.J. (2019). Role of oxygen, nitrogen and sulfur functionalities on the surface of nanoporous carbons in $CO_2$ adsorption: A critical review. *Microp. Mesop. Mater,* 287, 29-55. https://doi.org/10.1016/j.micromeso.2019.05.051

Sevilla, M., Mokaya, R. (2014). Energy storage applications of activated carbons: supercapacitors and hydrogen storage. *Energy & Environm. Sci.,* 7, 1250-1280. https://doi.org/10.1039/C3EE43525C

Sircar, S., Golden, T.C., Rao, M.B. (1996). Activated carbon for gas separation and storage. *Carbon,* 34, [1], (1996), 1-12. https://doi.org/10.1016/0008-6223(95)00128-X

Carbon 2022

# Catalytic layers of ex-situ modified carbon nanotubes and composites on macro-structured supports and their application in water treatment

João Restivo, Ana S. G. G. Santos, Carla A. Orge, Manuel F.R. Pereira, Olívia S.G.P. Soares
Laboratory of Separation and Reaction Engineering – Laboratory of Catalysis and Materials (LSRE-LCM), Faculty of Engineering, University of Porto, Rua Dr. Roberto Frias, 4200-465 Porto, Portugal;
ALiCE - Associate Laboratory in Chemical Engineering, Faculty of Engineering, University of Porto, Rua Dr. Roberto Frias, 4200-465 Porto, Portugal
Email: jrestivo@fe.up.pt

**Keywords**
catalytic ozonation; ball-milling; carbon nanotubes; structured catalyst; nanostructured carbon

## INTRODUCTION

Multi-walled carbon nanotubes (MWCNT) are well-known catalysts or catalyst supports for the removal of emerging organic pollutants in water (Restivo, 2013), and it has been demonstrated that their catalytic performance can be improved through tuning of their textural and chemical properties (Soares, 2015). Recently the use of mechanical methods for the modification of MWCNT has been garnering interest. Ball-milling has been used as a method to simultaneously modify their morphology and textural properties, and introduce heteroatoms, resulting in an improved catalytic performance in ozonation (Restivo, 2014).
In this work, it is demonstrated how ball-milling can further be used to prepare slurries that allow for the coating of cordierite macro-structures with no measurable material loss during application as catalysts for water treatment. Unlike common chemical vapour deposition (CVD) methods for coating of macro-structures with carbon nanomaterials, this methodology takes advantage of the potential of mechanical methods to improve the catalysts performance. The application of the resulting macro-structured catalysts is further explored in catalytic reactions for water purification.

## MATERIALS AND METHODS

As-received powder MWCNT (Nanocyl 3100) were used as received, after milling using a Retsch benchtop MM 200 ball-mill (sample CNT-BM) to reduce the particle size of the powder, after milling mixed with melamine as a nitrogen precursor (CNT-N-BM), and after milling of a previously 7 M nitric acid oxidized sample (CNT-COOH-BM). Further powder samples were prepared by incipient wetness impregnation with 1 and 5 wt.% palladium (samples 1%Pd/CNT-BM and 5%Pd/CNT-BM).

The MWCNT nanostructured catalytic layers were prepared by dip-coating (Bungard RDC21K coater; 30 mm $min^{-1}$ dipping speed, 1 min immersion, and 5 repetitions per catalyst) of pre-treated (900 ºC in air) cordierite honeycomb monolith with 60 mm height and 22 mm diameter, with 64 channels per square inch (cpsi), in a slurry prepared with the target MWCNT sample. Physical functionalization of the MWCNT surface with a hydrophilic layer using an organic surfactant (Triton X-100™, TX1) was used to prepare stable slurries for coating. The resulting structured catalysts were then rinsed with an isopropanol/acetone mixture to remove TX1 and provide access to catalytic active sites. An organic binder (PVA) was used as required to modify the properties of the slurry and provide a binding agent to the coating. Pd impregnation was additionally carried out post-synthesis of the coated structured catalysts by excess impregnation with a solution of the metal precursor, and the availability of the metal active sites for reaction was assessed by hydrogen pulse chemisorption.

The activity of the structured catalysts was evaluated in the catalytic reduction of bromate as a model inorganic pollutant using a continuously operated bubble column reactor with an inlet of 10 mL/min of a 20 ppm bromate solution.

**RESULTS**

The milling of the as-received powder MWCNT and the use of the TX1 surfactant were found to be essential to the preparation of the structured catalysts with homogeneous and stable coatings. The use of PVA was found to improve significantly the homogeneity of the coating but with reduced adhesion. Clear differences were also observed between the structured catalyst samples, in particular between the samples prepared with N-doping and oxidised with nitric acid. While a smooth and very homogeneous coating was found for the latter, the former had a more granular texture, and several slabs could be found separating from the cordierite wall. The preparation of coated structured catalysts using N-doped carbon nanotubes thus faces issues with the stability and adhesion of the MWCNT layer due to the poor dispersibility of these materials in a slurry. An alternative strategy was designed to avoid the poor dispersion of the N-doped MWCNT consisting in the preparation of a coating slurry containing a pre-milled MWCNT/melamine mixture. Thermal treatment under nitrogen at 600 ºC was carried out post-coating to promote the decomposition of melamine and integration of N-atoms into the carbon lattice, and the decomposition of the TX1 surfactant used in the slurry preparation. A much better adhesion of the carbon layer was obtained with this method due to the better dispersion of the MWCNT powder. The study of the slurry particle size and MWCNT layer adhesion allowed the construction of a correlation suggesting that the former is the main factor in the carbon layer adhesion (Figure 1).

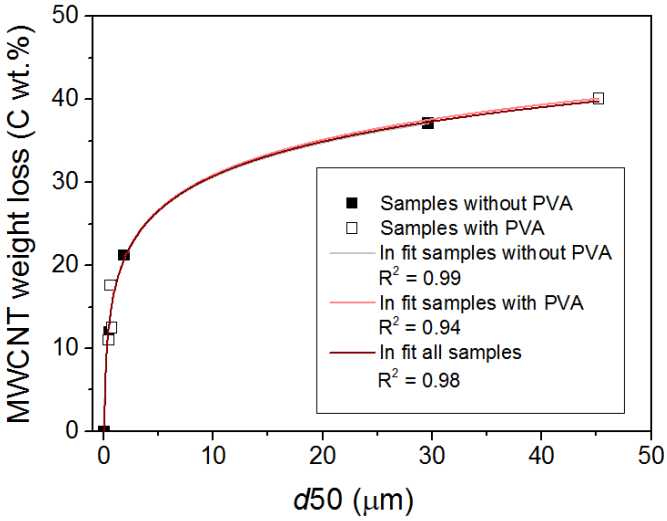


**FIGURE 1**: Carbon weight loss (as percent of total carbon content) as a function of the corresponding slurry d50 value, and natural logarithmic fit for samples without PVA, with PVA, and combination of all samples.

The catalytic performance of the structured catalysts was tested in the reduction of bromate under hydrogen (Figure 2). The post-synthesis Pd impregnated sample (WCP_wash_Pd) was found to have the largest chemisorption of hydrogen during chemisorption experiments and corresponding better performance as a bromate reduction catalyst. The difference in chemisorption and performance in comparison with the sample coated with a pre-formed Pd/MWCNT catalyst (1%Pd/WCP_wash) is explained by the uniform distribution of Pd active sites throughout the carbon layers on the latter, while Pd sites are likely accumulating towards the surface of the same layers on the former. Coating with a single layer (as opposed to the 5 layers described in the methodology) of Pd/MWCNT powder with higher Pd loading (5%Pd/WCP_wash), despite theoretically resulting in increased availability of the active metal sites towards the surface of the carbon layer, did not improve the catalysts performance. This is in part due to the formation of larger metallic particles during the powder

material synthesis. Moreover, when the same powder was coated over a previously prepared structured catalyst with 4 layers of only carbon material (i.e. no Pd), the performance was found to greatly improve, suggesting an effect of the porosity or morphology of the bottom layers on the availability of the surface metallic sites.

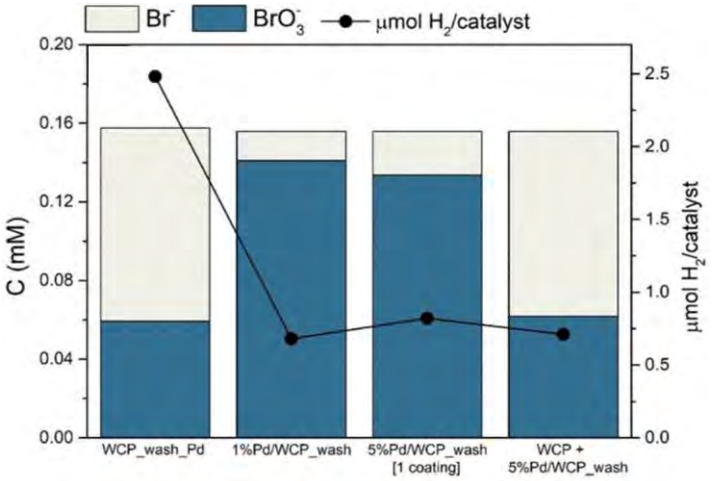


**FIGURE 2**: $BrO_3^-$ removal, $Br^-$ formation and $H_2$ chemisorption results obtained for the monometallic structured catalysts synthesized through different methodologies.

## CONCLUSIONS

A relationship between slurry particle size and adhesion of the catalytic layers to a cordierite macro-structured support is demonstrated, and strategies to allow the coating with CNT with varying properties, including CNT-containing composites, are explored. The performance of the resulting macro-structured catalysts in the removal of emerging pollutants from water is assessed and related to the properties of the CNT, the coating slurry, and the catalytic layers. The catalysts are found to be efficient as catalysts being able to obtain interesting performances in the degradation of model pollutants. The preparation conditions are of particular importance when assessing the activity of the catalysts, as the availability of active sites is found to be highly dependent on the synthesis strategies.

**Acknowledgements**

NanoCatRed (NORTE-01-0247-FEDER-045925) (ERDF –– COMPETE 2020, – NORTE 2020 and– FCT under UT Austin Portugal) and by InTreat-PTDC/EAM-AMB/31337/2017 - POCI-01-0145-FEDER-031337- (ERDF, COMPETE2020- FCT/MCTES); This work was financially supported by: LA/P/0045/2020 (ALiCE), Base-UIDB/50020/2020 and Programmatic-UIDP/50020/2020 Funding of LSRE-LCM, funded by national funds through FCT/MCTES (PIDDAC). CAO acknowledges FCT funding under DL57/2016 Transitory Norm Programme. OSGPS acknowledges FCT funding under the Scientific Employment Stimulus - Institutional Call CEECINST/00049/2018.

**References**

J. Restivo, J.J.M. Órfão, M.F.R. Pereira, E. Garcia-Bordejé, P. Roche, D. Bourdin, B. Houssais, M. Coste, S. Derrouiche, Chemical Engineering Journal. 230 (2013) 115–123.

O.S.G.P. Soares, A.G. Gonçalves, J.J. Delgado, J.J.M. Órfão, M.F.R. Pereira, Catalysis Today. 249 (2015) 199–203.

J. Restivo, R.P. Rocha, A.M.T. Silva, J.J.M. Órfão, M.F.R. Pereira, J.L. Figueiredo, Cuihua Xuebao/Chinese Journal of Catalysis. 35 (2014) 896–905.

Carbon 2022

# Graphene-doped Carbon Xerogels as Anode Materials in Sodium-ion Batteries

**Natalia Rey-Raap[1], Samantha L. Flores-López[2], Belén Lobato[2], Lucía dos Santos-Gómez[1], Ignacio Cameán[2], Ana B. García[2], and Ana Arenillas[2]**

[1] Departamento de Química Física y Analítica, Universidad de Oviedo-CINN-CSIC, 33006, Oviedo, Spain

[2] Instituto de Ciencia y Tecnología del Carbono (INCAR), CSIC, Francisco Pintado Fe 26, 33011, Oviedo, Spain

Email: nataliarey@uniovi.es

**Keywords**
Graphene oxide, porosity, electrical conductivity, electrochemical performance

## INTRODUCTION

Efficient energy production from renewable sources requires developing large-scale energy storage systems that can be integrated into the electrical distribution network. Among the different electrochemical systems, batteries are one of the most interesting alternatives due to their versatility, high power density, easy maintenance, and long cycle life. Currently, lithium-ion batteries (LIBs) are the most widespread batteries in many electric systems. However, they still have a high energy cost (€/kWh), mainly due to the lithium compounds used. To address this issue, research has focused on replacing lithium by sodium which is a more abundant and of lower cost element. Sodium-ion batteries (SIBs) required the development of new anode materials since graphite - the most common anode material in LIBs - hardly intercalates sodium ions. Therefore, different carbon materials such as soft and hard carbons or ordered mesoporous carbons have been extensively studied. Despite the great research efforts, the suitable porous and chemical properties are still not well-defined and more research is needed to develop high-performance anode materials for SIBs. In this sense, carbon gels are very promising materials as their porous and chemical properties can be easily modulated by modifying the synthesis process.

## EXPERIMENTAL

Graphene-doped carbon xerogels (GCXs) with different porous and chemical properties were synthesized by microwave heating, followed by carbonization or physical activation. GCXs were synthesized from a mixture of resorcinol (R), formaldehyde (F), and an aqueous 5 mg/ml graphene oxide suspension, using the stoichiometric R/F molar ratio (i.e., 0.5), a dilution ratio of 7.7 and a pH value of 5.0. The precursor solution was placed in a microwave oven at 85 °C for 5 h, to allow gelation, aging, and drying. After the formation of the polymeric structure, the organic sample was carbonized or activated. Both thermal treatments were performed in a tubular furnace at 1000°C for 2 h under $N_2$ and $CO_2$ atmosphere, respectively. An undoped carbon xerogel (CX) was also synthesized for comparison by the same procedure but without adding the graphene oxide suspension. The materials were tested as anodes in sodium-ion batteries. Two-electrodes Swagelok cells were assembled in a glove box using xerogels and sodium metal as working (WE) and counter (CE) electrodes, respectively. WE composition was 82 wt.% of CX, 8 wt.% of NaCMC binder and 10 wt.% of carbon black. WE and CE were separated by two microfiber glass discs soaked with 180 µl of the electrolyte (1.2M $NaPF_6$ (EC:EMC)). Galvanostatic cycling tests of the cells (CX/Na) were performed in a Biologic battery testing system BCS810, at 37.2 mA $g^{-1}$ during 160 discharge-charge cycles to evaluate their performance.

## RESULTS AND DISCUSSION

The porous properties of the xerogels were modulated by applying different thermal treatments. As expected, the surface area and the microporosity increased by carbonizing (CX) and activating (AX) the sample (600 $m^2\ g^{-1}$ and 0.24 $cm^3\ g^{-1}$, and 1400 $m^2\ g^{-1}$ and 0.57 $cm^3\ g^{-1}$, respectively) as shown in Figure 1a, while preserving the macroporous structure (mean pore size ca. 550 nm and 80% of porosity). A further graphitization of the carbonized sample (GX) improved the order of the structure removing almost all the microporosity (20 $m^2\ g^{-1}$) but also preserving the macroporous structure. Similar surface areas and micropore volumes were obtained for the graphene-doped samples. However, the mean pore size was highly increased from 550 nm to 1340 nm. This effect is due to the presence of graphene oxide which prevents the shrinkage produced during the polymerization reaction assisted by microwave heating (Canal-Rodríguez, 2017). On the other hand, the presence of graphene sheets in the final carbon structure enhanced the electrical conductivity by 20%.

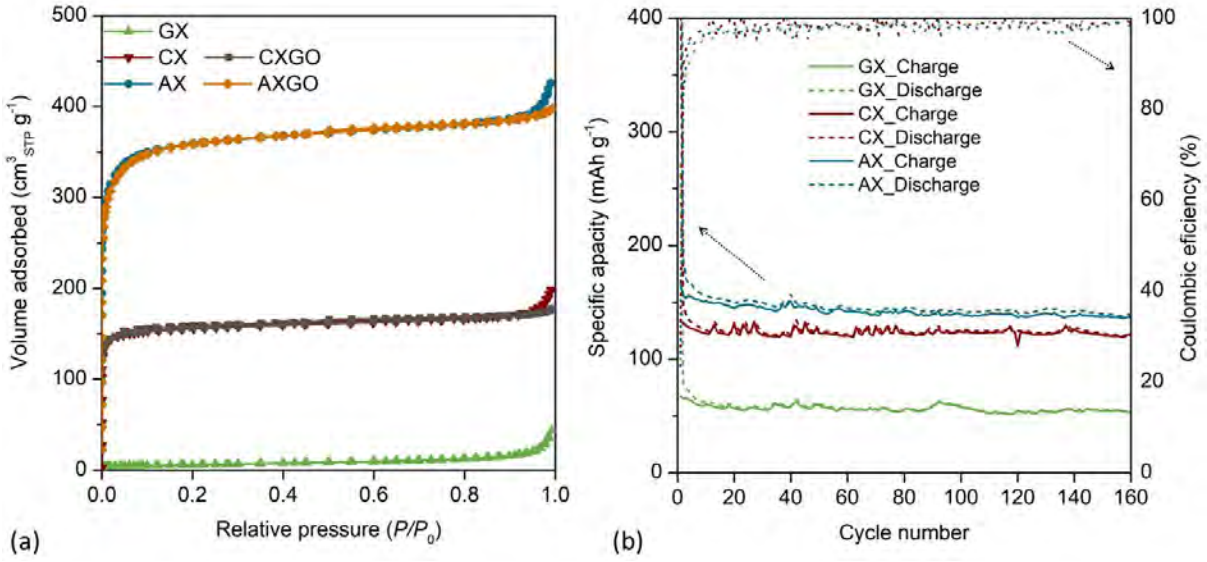


**FIGURE 1**: a) $N_2$ adsorption-desorption isotherms and b) Specific capacity and coulombic efficiency vs. cycle number

As seen in Figure 1b, the specific capacity of the CX-based anodes increases with the surface area of the active materials due to the larger number of structural defects (microporosity) on their surface. Besides, similar irreversible capacities in the first cycle were observed for all the samples, which is related to the external surface area (ca. 20 $m^2\ g^{-1}$). Previous results reported on xerogels with different pore sizes as anodes for sodium-ion batteries suggested that the storage mechanism is mainly based on the absorption of $Na^+$ ions on the material surface and in structural defects (Cuesta, 2020), which is in agreement with the results observed in Figure 1b for xerogels with different microporosity.

## CONCLUSIONS

Carbon xerogels have a competitive electrochemical performance as anode materials in sodium-ion batteries due to the successful modulation of their porous properties: large specific surface area, low external surface area, and well-developed open porosity. The activated sample delivers a capacity of ~ 140 mAh $g^{-1}$ at an electrical current density of 37.2 mA $g^{-1}$ after 160 discharge/charge cycles with excellent cycling stability and high coulombic efficiency (> 98%).

**Acknowledgments**

This work was financially supported by the Spanish Ministerio de Ciencia e Innovación and the European Union through the projects PCI2020-112039 MCIN/AEI-10.13039/501100011033 and PID2020-113001RB-I00 MCIN/AEI-10.13039/501100011033, respectively. SFL is grateful for her predoctoral grant received from the

Administración del Principado de Asturias through the “Severo Ochoa” program, and NRR and LdSG gratefully acknowledge the Ministerio de Ciencia e Innovación for her postdoctoral grant IJC2019-040875-I and IJC2020-044746-I, respectively.

**References**

Canal-Rodríguez, M., Arenillas, A., Rey-Raap, N., Ramos-Fernández, G., Martín-Gullón, I., Menéndez, J.A. (2017). Graphene-doped carbon xerogel combining high electrical conductivity and surface area for optimized aqueous supercapacitors, *Carbon*, [118], 291-298.

Cuesta, N., Cameán, I., Arenillas, A., García, A.B. (2020). Exploring the application of carbon xerogels as anodes for sodium-ion batteries, *Microporororous and Mesoporororous Materials*, [308], 110542.

Carbon 2022

# Doped Carbon Xerogels As Electrodes In Solid-State Asymmetric Supercapacitors

**Natalia Rey-Raap[1], Samantha L. Flores-López[3], Lucia dos Santos-Gómez[1], Minju Thomas[2], Francesco Lufrano[2], Ana Arenillas[3]**
Email: aapuente@incar.csic.es

[1] Department of Physical and Analytical Chemistry, Oviedo University-CINN-CSIC, Oviedo, Spain
[2] Istituto di Tecnologie Avanzate per L´Energia "Nicola Giordano", CNR-ITAE, Messina, Italy
[3] Institute of Carbon Science and Technology (INCAR), CSIC, Oviedo, Spain

**Keywords**
Carbon xerogels, sol-gel doping synthesis, electric conductivity, supercapacitors, solid-state electrolyte.

## INTRODUCTION

Energy storage is one of the main current challenges for improving hybrid electric vehicles and portable and smart devices. Among the different electrochemical energy storage devices, supercapacitors have attracted significant attention due to their high-power density, fast charge/discharge rate, and long cycle life. However, new approaches to improve the energy density of supercapacitors are still required. Carbons are commonly used as active materials in the electrodes of supercapacitors and it is already very well known that their performance is better as long as they exhibit high electrical conductivity, high-carbon purity and large specific surface area (Canal-Rodríguez, 2017). However, it is still necessary to improve the gravimetric and volumetric specific energy density in order to meet the needs of a constantly growing demand for energy and power density for these devices in the e-mobility and electronic markets.

The strategy to improve the supercapacitor's performance is to develop new combinations of their components (i.e. active materials of electrodes and electrolyte), as both components should exhibit an optimum interaction and stability. Furthermore, in this work, it is shown that the use of two different electrode materials at the positive and negative and neutral aqueous electrolyte (i.e. pH ≈7) may enlarge the operating voltage window of the device during charge/discharge processes. It is possible to use manganese oxide as positive electrode, due to its high-rate pseudocapacitive storage mechanism, and good diffusion. Moreover, it is an environmentally friendly and cost-effective material (Teng Wang, 2019). Its combination with high purity carbons with high surface area in the negative electrode produces a winning synergy between the advantages of both materials, resulting in high charge storage capacitance and long cycle life.

## MATERIALS AND CHARACTERIZATION

Carbon gels are very promising synthetic materials as they can be obtained with a great control of their physicochemical characteristics: controlled chemical composition, absence of impurities, tailored pore size distribution and high surface area. All these properties can be easily modulated by modifying the synthesis process (Rey-Raap, 2014). In this work, carbon gels were synthetized from polymerization of resorcinol (R) and formaldehyde (F), using the stoichiometric molar ratio (i.e. R/F=0.5), a dilution ratio of 5.7 and a pH of the precursor mixture of 6.5. In order to improve the electrical conductivity of the carbon gels two different precursor solutions were prepared by adding (i) urea, to incorporate nitrogen to the gel structure, or (ii) graphene oxide, which after the heat treatment it is reduced to graphene and it is also integrated into the 3D polymeric structure of the

carbon gel. Both precursor solutions were placed in a microwave oven at 85ºC for 5h, allowing gelation, ageing and drying. After the formation of the polymeric structure, the organic samples were activated in a tubular furnace at 1000 °C for 2h under $CO_2$ atmosphere, leading to a nitrogen-doped activated carbon gel (NAG) and graphene-doped activated carbon gel (GAG). These samples were employed as active materials for supercapacitor's electrodes.

Manganese oxide was prepared through a co-precipitation method by mixing manganese (II) salt with permanganate (VII) salt in an aqueous solution at room temperature. The obtained precipitate was washed several times with distilled water, filtered and dried. The dried sample was thermally treated at 200 °C for 3h.

The supercapacitors were assembled by combining the two electrodes (e.g. carbon, $MnO_2$) with a cation-exchange Aquivion membrane in sodium form. The membrane, which is obtained by ion exchange with 1M $Na_2SO_4$, would act as the solid polymer electrolyte. This membrane electrolyte brings many advantages to the supercapacitor device as there is no high-frequency semicircle in the Nyquist plot indicating no (or very low) contact resistance, better compression of the cell and so minor leakages of electrolyte, and low self-discharge of the supercapacitor, among others. Cyclic voltammetry, galvanostatic charge/discharge, electrochemical impedance spectroscopy and long-term durability tests were performed for optimizing the performance of the supercapacitors.

**RESULTS AND DISCUSSION**

The effect of the dopant (i.e. nitrogen or graphene) on the performance of the supercapacitor was evaluated in a symmetric configuration (i.e. $NAG^-/NAG^+$ and $GAG^-/GAG^+$) where both the negative and positive electrodes were composed of the same carbon gel, carbon fibres as additive and PVDF-HFP as a binder in 80, 10 and 10 wt%, respectively. The improvement of using the hybrid configuration (i.e. carbon gel in the negative electrode and $MnO_2$ in the positive electrode, $GAG^-/MnO_2^+$) was also evaluated and compared with the symmetric configuration mentioned above. According to Figure 1a, where the cyclic voltammograms of these three supercapacitors are compared, it seems to be clear that doping with graphene results in a better performance of the supercapacitor than doping with nitrogen. Moreover, the use of the hybrid configuration ($GAG^-/MnO_2^+$) of solid-state supercapacitor results in the best alternative regarding the electrode composition.

Fig. 1b shows the impedance behaviour of the capacitors, where the inset highlights the very low resistivity of all cells (intercept with x-abscissa) and also shows the absence of evident loops, which are generally attributed to charge transfer resistance and electrode-electrode and electrode-collector interface resistances. In this regard, the NAG-/NAG+ capacitor shows a higher distributed resistance, indicative of porous carbon electrodes, which appears as a typical Warburg impedance with a 45° slope in the transition region, owing to the semi-infinite diffusion of ionic species through the pores. The other two capacitors, GAG-/GAG+ and GAG-/MnO2+, have a lower Warburg impedance and a steeper vertical point distribution, more ideal of electric double-layer capacitors (EDLCs), clearly evidenced in the voltammograms of Fig. 1a. Thus, these last two show very low resistivity, an ideal EDLC character and also high rate capabilities due to the distinct and superimposed voltammograms when the scan rate is increased from 5 to 40 mVs-1 (see Fig. 1a).

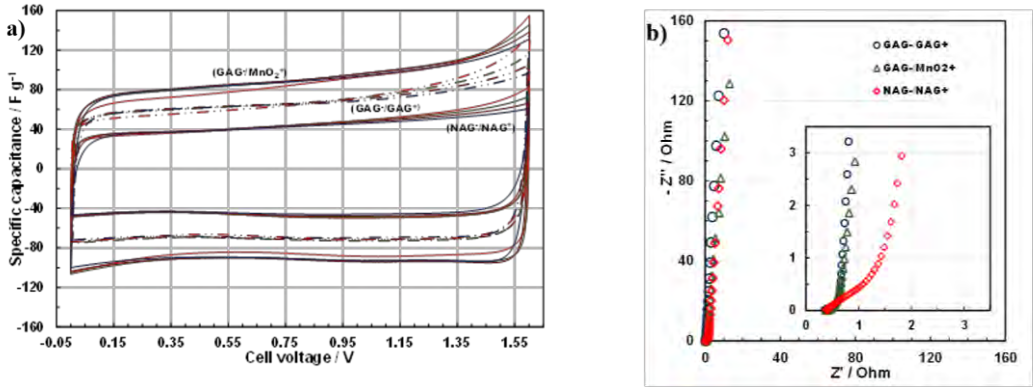


**FIGURE 1**: Cyclic voltammograms at different scan rates (a) and Nyquist plots under OCV conditions (b) for the symmetric NAG-/NAG+ and GAG-/GAG+, and hybrid $GAG^-/MnO_2^+$ supercapacitors.

In particular, the supercapacitor in hybrid configuration (GAG-/MnO2+) results in an increased gravimetric and volumetric capacity and stability even after combining 10,000 charge/discharge cycles and 140 hours of floating at 1.6 V. Some post-mortem analyses (e.g. XPS) of fresh and aged electrodes reveal that there were no noticeable structural changes and no excessive chemical changes or any degradation of GAG and $MnO_2$ electrodes after severe durability tests.

## CONCLUSIONS

Carbon gels doped may be very useful materials for optimizing the components and configuration of the new generation of supercapacitors. Introducing graphene into the 3D polymeric structure of carbon gels results in a great improvement in electric conductivity and so the performance of the supercapacitor. The hybrid configuration with the graphene-doped carbon xerogel in the negative electrode and the manganese oxide in the positive electrode seems to be the best option to obtain a substantial enhancement of both gravimetric and volumetric capacitance, as a very low loading of $MnO_2$ is needed because of its pseudocapacitance. Furthermore, the device presents a great stability at 1.6V and neutral aqueous environment which contributes to a great performance and long cycle life.

**Acknowledgements**

This research was possible thanks to the grants PID2020-113001RB-I00 and PCI2020-112039 funded by MCIN/AEI/ 10.13039/501100011033 and by the European Union NextGenerationEU/PRTR. NRR and SLFL also thanks to MICIN IJC2019-040875-I, and Principado de Asturias "Severo Ochoa" program, respectively. Besides, authors acknowledge the financial support from the INNENERMAT project. This project has received funding from EU Network M-ERA.NET (European Research Area Network for Materials Research and Innovation) Consortium.

**References**

Canal-Rodríguez, M., Arenillas, A., Rey-Raap, N., Ramos-Fernández, G., Martín-Gullón, I. and Menéndez, J.A. (1917). Graphene-doped carbon xerogel combining high electrical conductivity and surface area for optimized aqueous supercapacitors. *Carbon,* 118, 291-298.

Rey-Raap, N., Menéndez, J.A. and Arenillas, A. (2014). Simultaneous adjustment of the main chemical variables to fine-tune the porosity of carbon xerogels. *Carbon,* 78, 490-499.

T. Wang, H.C. Chen, F. Yu, X.S. Zhao, H. Wang (2019), Boosting the cycling stability of transition metal compounds-based supercapacitors, Energy Storage Mater. 16 545–573.

Carbon 2022

# One-step electrospun lignin-derived carbon fibers containing iron as Fischer-Tropsch catalyst

**Rodríguez-Cano, Miguel Ángel; García-Mateos, Francisco José; Valero-Romero, Mª José; Ruiz-Rosas, Ramiro; Rosas-Martínez, Juana María; Rodríguez-Mirasol, José; Cordero, Tomás**
Departamento de Ingeniería Química, Escuela de Ingenierías Industriales, Universidad de Málaga, Andalucía Tech, Campus de Teatinos S/n, Málaga, 29071, Spain
Email: mirasol@uma.es

**Keywords**
Lignin, carbon fibers, electrospinning, heterogenous catalysis, Fischer-Tropsch.

## INTRODUCTION

The earth suffers from an important situation of climate crisis due to the continuously increased use of fossil fuels. Biomass is a renewable source that can be used to produce synthesis gas, from which hydrocarbons such as olefins or gasolines can be obtained via Fischer-Tropsch. Fixed bed reactors used for this process suffer from pressure drops and severe heat transfer problems. A solution could be the use of structured catalysts in fibrillar morphology. The objective of this work is the preparation of iron-containing carbon submicron fiber catalysts for the Fischer-Tropsch process by electrospinning in only one step.

## MATERIALS AND METHODS

Carbon fibers were prepared by electrospinning of lignin:ethanol:iron nitrate solutions in a coaxial electrospinning configuration. The electrospun materials were stabilized in air and subsequently carbonized with a $N_2$ flow at 500, 650 and 800 ºC. The samples were denoted as FLFeX, where "X" stands for the carbonization temperature.

The prepared catalysts were tested under High Temperature Ficher-Tropsch (HTFT) conditions, 20 bar, 340 ºC, a molar $H_2$/CO ratio of 1 and a space velocity of 150 $L_{syngas}\ g_{Fe}^{-1}\ h^{-1}$. The weight of catalyst was adjusted to achieve the same iron load in the bed in each experiment.

## RESULTS AND DISCUSSION

Table 1 shows some textural properties derived from the $N_2$ adsorption isotherms at -196 ºC and $CO_2$ adsorption isotherms at 0 ºC of the samples prepared at different temperatures. Fe-containing carbon fibers catalysts prepared at 500 and 650 ºC are mainly microporous, achieving the highest $A_{BET}$ value at 650 ºC. At preparation temperature of 800 ºC, $A_{BET}$ value was reduced, meanwhile a widening of the microporosity was detected, related to the highest $V_{mic}(N_2)/V_{mic}(CO_2)$ ratio observed for FLFe800. One advantage of electrospinning technique is the excellent metal dispersion obtained on the fiber [1]. In this sense, the specific surface loading of iron ($g_{Fe}/m^2$) is reported in Table 1. This parameter reached the highest value at 800 ºC, so it could be expected that FLFe800 presents the largest number of active sites per area.

**Table 1.** Textural parameters and iron characterization of the catalysts

| Catalyst | $A_{BET}^{N2}$ ($m^2/g$) | $V_{meso,t}^{N2}$ ($cm^3/g$) | $V_t^{N2}$ / $V_{DR}^{CO2}$ | Fe ($g_{Fe}/m^2$) | Cristallite size (nm) |
|---|---|---|---|---|---|
| FLFe500 | 300 | 0.02 | 0.12 | 0.013 | - |
| FLFe650 | 510 | 0.02 | 0.10 | 0.008 | - |
| FLFe800 | 390 | 0.31 | 3.13 | 0.021 | 24.9 ($Fe_3C$)<br>44.3 ($Fe_3O_4$) |

The crystallinity was also analysed by X-ray diffraction (Figure 1). The results showed that the catalyst FLFe500 did not present any crystallite phase and only small peaks of iron oxide were observed for FLFe650, due to the low temperature of the treatment. However, cementite (i.e. iron carbide), and magnetite ($Fe_3O_4$) crystals were found in the FLFe800 sample, evidencing a stronger metal-support interaction in this catalyst, due to carburization and partial reduction of iron.

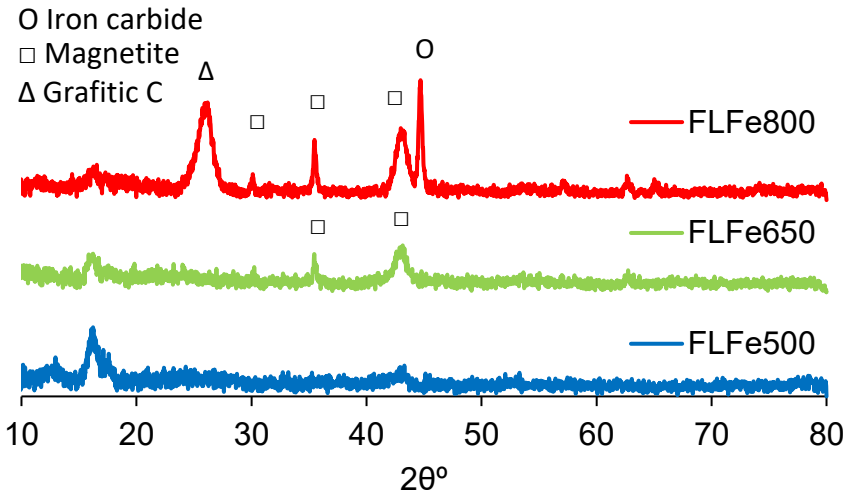


Figure 1. X-ray diffraction of catalysts FLFe500, FLFe650 and FLFe800

Figure 2 shows the CO conversion and selectivity of main products after 9 hours of reaction. As can be observed, the catalyst FLFe800 presented the highest CO conversion, in accordance with the largest surface iron load. Selectivity also shifted with the preparation temperature of the catalysts. FLFe500 and FLFe650 samples, which have narrow microporosity, promoted methane and $CO_2$ formation, due to the steric effects in narrow micropores, avoiding the growth of hydrocarbon chains. When preparation temperature was increased to 800 ºC, the product distribution was displaced to C2-C4 hydrocarbons, which could be related to the wider porosity of FLFe800. Another interesting feature of this sample was the high olefin to paraffin ratio that in the case of propylene and propane reached values close to 4, Figure 2.

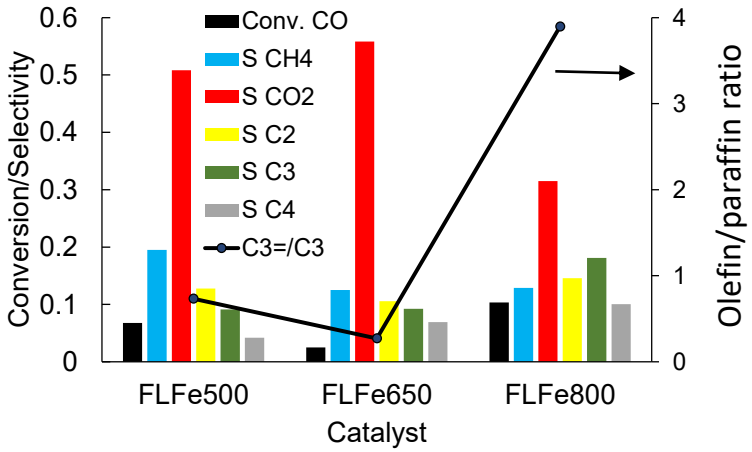


Figure 2. CO conversion and selectivity to main products for the different catalysts under High Temperature Fischer-Tropsch conditions: 20 bar, 340 ºC, $H_2$/CO=1, SV=150 $L_{syngas}$ $g_{Fe}^{-1}$ $h^{-1}$, TOS=9 h

## CONCLUSIONS

The electrospinning technique was successfully used to prepare different Fe-containing carbon submicron fiber catalysts from lignin/ethanol/iron nitrate solutions. The results showed that narrow micropores carbon fibers promoted the selectivity to $CO_2$ and $CH_4$ due to steric effects. However, the catalyst with the widest porosity and highest iron concentration on the surface, presented the highest CO conversion and the best product distribution, maximizing the C2-C4 fraction.

**Acknowledgements**

This research has been funded by Spanish Ministry of Science, Innovation and Universities and FEDER funds through RTI2018-097555-B-I00 and by Junta de Andalucía through P18-RT-4592 and UMA18-FEDERJA-110. MARC also acknowledge the PhD contract FPU18/02796 to Spanish Ministry of Science, Innovation and Universities.

**References**

[1] García-Mateos FJ, Cordero-Lanzac T, Berenguer R, Morallón E, Cazorla-Amorós D, Rodríguez-Mirasol J, Cordero T. Lignin-derived Pt supported carbon (submicron)fiber electrocatalysts for alcohol electro-oxidation. *Appl Catal B Environ* 2017; 211:18–30. https://doi.org/10.1016/j.apcatb.2017.04.008

20 C 22 arbon 2022

# On the Stability and Optical Properties of Linear Acetylenic Carbon Chains: Consequences of Quantum Anharmonicity

**Davide Romanin[1], Lorenzo Monacelli[2], Raffaello Bianco[3], Ion Errea[3], Francesco Mauri[2] and Matteo Calandra[1,4]**

Email: davide.romanin@insp.upmc.fr

[1]Sorbonne Université, CNRS, Institut des Nanosciences de Paris, UMR7588, F-75252, Paris, France
[2]Dipartimento di Fisica, Università di Roma La Sapienza, Piazzale Aldo Moro 5, I-00185 Roma, Italy
[3]Centro de Fisica de Materiales (CSIC-UPV/EHU), Manuel de Lardizabal pasealekua 5, 20018 Donostia-San Sebastiàn, Basque Country, Spain
[4]Department of Physics, University of Trento, Via Sommarive 14, 38123 Povo, Italy

**Keywords**
Low dimensionality, Anharmonicity, Optics renormalization

## INTRODUCTION

The linear acetylenic carbon chain (or carbyne) is the simplest example of a 1D carbon system and the prototype of a charge-density wave (CDW), that is broken symmetry states in solids in which the crystal acquires a periodic modulation of a given wavevector at low temperature.

As a matter of fact, at the harmonic level, it undergoes a Peierls (Peierls, 1935) phase transition from an orderered metallic phase (cumulene) to a distorted insulating phase (polyyne) due to an unstable phonon mode with momentum $2k_F$ (where $k_F$ is the Fermi momentum). Its existence is still controversial: while both the Coleman and the Mermin-Wagner-Hohenberg theorems prevent polyyne from existing at any temperature, Peierls showed that the long-range nature of interatomic forces stabilizes the distorted system.

Indeed, if one assumes small lattice displacements, in principle it is possible to recover the metallic ordered phase as temperature is increased and the corresponding insulating-to-metal phase transition is of second order. Nevertheless, recent synthesis (Shi, 2016) of ultra long carbon chains (~6000 atoms) did not show any phase transition and detected only the polyyne phase, in agreement with previous experiments on capped finite carbon chains.

In a recent work (Romanin, 2021) we re-investigated the Landau-Peierls distortion of carbyne from first principles, departing from the harmonic description of lattice dynamics and taking into account electronic correlations. We have shown that the interplay between electronic correlations and quantum anharmonicity are responsible for the absence of a polyyne-to-cumulene phase transition up to very high temperatures. Moreover, quantum and thermal fluctuations are responsible for an insulating-to-metal phase transition in the distorted phase at ~1200 K as the quasiparticle gap is gradually reduced until it is completely closed.

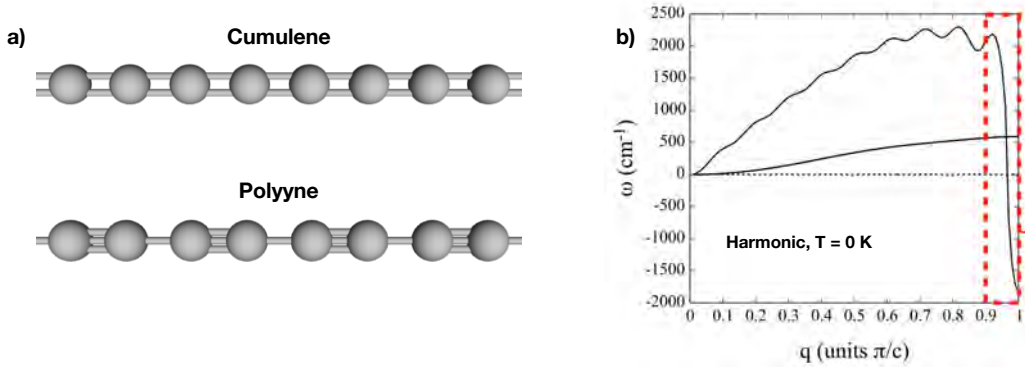


**FIGURE 1**: a) Stick-and-ball model of carbyne in its metallic ordered phase (Cumulene) and its distorted insulating phase (Polyyne); b) Phonon dispersion relation of cumulene at T = 0 K in the harmonic picture.

## COMPUTATIONAL METHODS

Density functional theory (DFT) calculations are performed using both the CAMB3LYP and the PBE0 hybrid exchange-correlation functionals and CRYSTAL code (Dovesi, 2014). CAMB3LYP is employed to model carbyne in vacuum, while PBE0 is exploited to effectively simulate the dielectric environment of a surrounding carbon nanotube. Quantum anharmonicity is taken into account via the stochastic self-consistent harmonic approximation (SSCHA, Monacelli, 2021), a method which also takes explicitly into account the quantum nature of the nuclei of carbon atoms. Finally, optical properties of the distorted phase are computed within the self-consistent GW approximation on eigenvalues only (evGW) using the Yambo code (Sangalli, 2019) and excitonic effects are then evaluated by solving the Bethe-Salpeter equation (BSE) on top of the evGW band structure (Sangalli, 2019).

## RESULTS

In Fig. 2a we plot the quantum free energy of carbyne inside the carbon nanotube (here treated in an effective way via the PBE0 functional). Quantum-anharmonicity reduces the energy gain of the polyyne phase with respect to the cumulene one by 71% already at T = 0 K. Cumulene is either an unstable (T = 0 K) or metastable (T > 0 K) phase, while polyyne is always the absolute minimum up to very large temperatures. Indeed, in Fig. 2b we show the difference between the distorted and ordered phase and the polyyne-to-cumulene phase transition is confined to an extremely high and unphysical temperature (i.e. ~3000 K). Finally, we predict that a high temperature insulator-to-metal transition occurs in the polyyne phase confined in insulating nanotubes with sufficiently large dielectric constant due to a giant quantum-anharmonic bandgap renormalization (Fig. 2c).

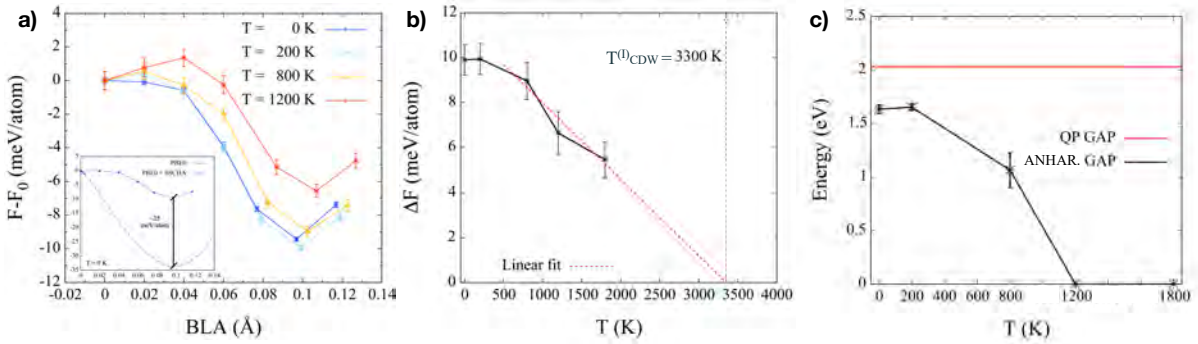


**FIGURE 2**: a) Quantum anharmonic free energy as a function of temperature. BLA is the order parameters of the CDW, i.e. the bond length alternation (the difference between the single and triple bond in the distorted insulating phase). BLA = 0 is cumulene; b) Energy difference between the polyynic and cumulenic energy minima as a function of temperature. The polyyne-to-cumulene phase transition is expected to happen at ~3000 K; c) Renormalization of the quasiparticle band gap due to quantum and thermal fluctuations. Red solid line is the harmonic band gap, while black line is the quantum anharmonic one.

## References and Citations

For references, use the Harvard System, ordered alphabetically by first author, and referenced by publication year in parentheses. See the examples at the end of this document. Within the article text itself, cite the references by (author, year). For example, “Neighbour (2008) showed that…” or “it was shown by the method (Neighbour, 2008)”.

**Acknowledgements**

The authors acknowledge support from the ANR project ACCEPT (Grant No. ANR-19-CE24-0028). This work was granted access to the HPC resources of IDRIS, CINES and TGCC under the allocation 2021-A0100912417 made by GENCI.

**References**

Dovesi, R., Orlando, R., Erba, A., Zicovich-Wilson, C. M., Civalleri, B., Casassa, S., Maschio, L., Ferrabone, M., Pierre, M. D. L., D’Arco, P., Noël, Y., Causà, M., Rérat M. and Kirtman B (2014). Crystal14: A program for the ab-initio investigation of crystalline solids. *International Journal of Quantum Chemistry*, 114, 1287–1317.

Monacelli, L., Bianco, R., Cherubini, M., Calandra, M., Errea, I. and Mauri, F (2021). The stochastic self-consistent harmonic approximation: calculating vibrational properties of materials with full quantum and anharmonic effects. *Journal of Physics: Condensed Matter*, 33, 363001.

Peierls, R. E (1935). Quelques proprietes typiques des corpses solides. *Ann. I. H. Poincare*, 5, 177−222.

Romanin, D., Monacelli, L., Bianco, R., Errea, I., Mauri, F. and Calandra, M. (2021). Dominant Role of Quantum Anharmonicity in the Stability and Optical Properties of Infinite Linear Acetylenic Carbon Chains. Journal of Physical Chemistry Letters, 12, 10339−10345.

Sangalli, D., Ferretti, A., Miranda, H., Attaccalite, C., Marri, I., Cannuccia, E., Melo, P., Marsili, M., Paleari, F., Marrazzo, A., Prandini, G., Bonfà, P., Atambo, M. O., Affinito, F., Palummo, M., Molina-Sánchez1, A., Hogan, C., Grüning, M., Varsano, D. and Marini, A. (2019). *Journal of Physics: Condensed Matter,* 31, 325902.

Shi, L., Rohringer, P., Suenaga, K., Niimi, Y., Kotakoski, J., Meyer, J. C., Peterlik, H., Wanko, M., Cahangirov, S., Rubio, A., Lapin, Z. J., Novotny, L., Ayala, P. and Pichler, T (2016). Confined linear carbon chains as a route to bulk carbyne. *Nature Materials*, 15, 634−639.

20 C 22 arbon 2022

# Higly tunable optics across a topological transition: singlet fission and negatively dispersing excitons in organic polymers

**Davide Romanin[1], Matteo Calandra[1,2] and Alex W. Chin[1]**

Email: davide.romanin@insp.upmc.fr

[1]Sorbonne Université, CNRS, Institut des Nanosciences de Paris, UMR7588, F-75252, Paris, France
[2]Department of Physics, University of Trento, Via Sommarive 14, 38123 Povo, Italy

**Keywords**
Excitons, Pi-conjugated polymers, Topological insulators.

## INTRODUCTION

Generally speaking, π-conjugated organic semiconductors form a highly promising class of materials for the development of cheap, flexible and non-toxic optoelectronic devices such as photovoltaics, sensors and solid state lighting (Bronstein, 2020). Experimental evidence (Cirera, 2020) for a topological $Z_2$ phase transition has recently been presented in a series of 1D polyacene polymers in which the monomer size and chain length could be systematically varied (See Fig. 1), representing a physical realization of the well known Su-Schrieffer-Heeger (SSH) model (Vanderbilt, 2018). As the size of the monomer increases, this transition is associated with a dramatic closing and reopening of the polymer quasiparticle gap as well as a structure transition: the central carbon ring in the monomer passes from an aromatic to quinoidal configuration, while the carbon bridge goes from polyynic to cumulenic (as seen in linear carbon chains, Romanin 2021). Nevertheless, the effects of a topological phase transition in the photophysics of such low-dimensional organic systems has, to date, remained unexplored and, based on the discussion above, could be relevant for the design of future optoelectronic devices.

In a recent work (Romanin, 2022), by employing manybody perturbation theory, we have investigated the excitonic properties across the $Z_2$ topological transition occurring in polyacene polymers. We have shown that the topological transition is accompanied by a switching from extended Mott-Wannier excitons to localized Frenkel excitations and exciton dispersions that can be tuned from gigantic bandwidth (~1.5 eV) to practically zero, simply by controlling the acene length n (Fig. 1). This extreme tunability of optical properties occurs whilst also maintaining the desirable characteristics (large exciton binding energy, strong optical absorption, large singlet-triplet splittings) for which organics are so widely used in optoelectronic applications (Citation, 2022).

## COMPUTATIONAL METHODS

Density functional theory (DFT) calculations are performed using the CAMB3LYP exchange-correlation functionals and CRYSTAL code (Dovesi, 2014). Optical properties are computed within the self-consistent GW approximation on eigenvalues only (evGW) using the Yambo code (Sangalli, 2019) and excitonic effects are then evaluated by solving the Bethe-Salpeter equation (BSE) on top of the evGW band structure (Sangalli, 2019). More computational details can be found in Romanin (2022).

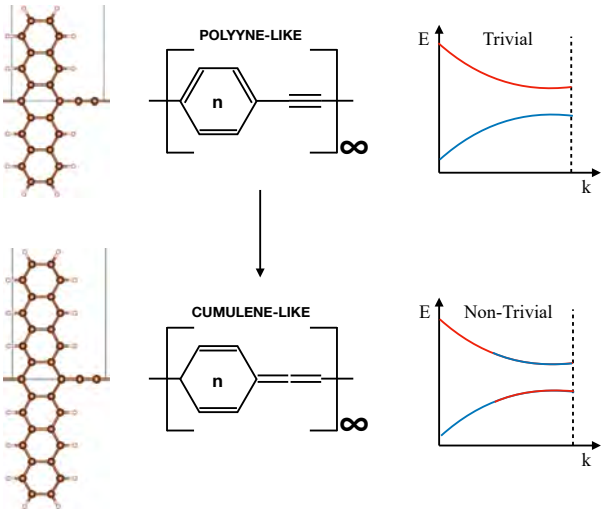


**FIGURE 1**: Schematic representation of the topological phase transition in polyacene polymers. As we increase the number of carbon rings in the central monomer, the central ring goes from being aromatic to quinoidal while the bridge passes from polyyne-like to cumulene-like. Moreover, at the border of the Brillouin zone HOMO/LUMO states exchange, due to a closing and reopening of the energy gap.

**RESULTS**

In our results, the topological phase transition happens between poly-pentacene (n=5) and poly-heptacene (n=7), setting the first as the trivial and the second as the non-trivial part insulating phase.

In Fig. 2 we report the exciton dispersion relation of. The singlet solution have been plotted together with their optical oscillator strength, being optically active excitations. The first thing that can be noticed is that the optical strength is maintained for a large part of the Brillouin zone, allowing in principle possible singlet fission processes of a singlet into a pair of triplets (i.e $T_I + T_I$ or $T_I + T_{II}$) on energetic grounds. Moreover, the bandwith of the exciton dispersion drastically goes down when crossing the topological transition, with bands that are almost dispersionless in the case of poly-heptacene.

Finally, it is interesting to notice the presence of negatively dispersive triplet excitons ($T_{II}$) in both cases. While for n=5 this is true in a region of the Brillouin zone close to the center, for n=7 the negative dispersion is attained until we reach the border of the Brillouin zone.

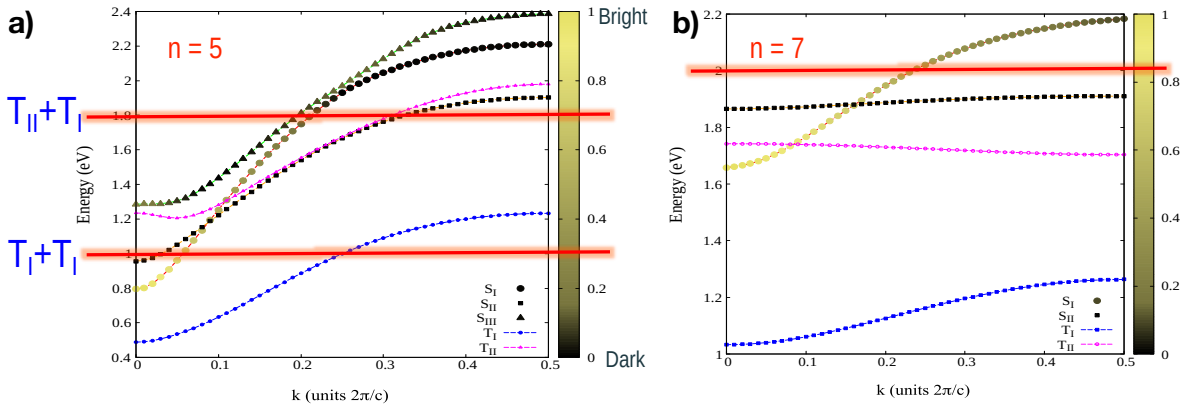


**FIGURE 2**: Exciton dispersion relation for n=5 (a-c) and n=7 (b-d). Singlet solutions (S) are plotted together with their optical oscillator strength. Red horizontal lines are the energy levels for having the fission of a singlet into a pair of triplets (i.e $T_I + T_I$ or $T_I + T_{II}$).

Finally, in Fig. 3 we report the modulus squared of the singlet exciton wavefunction as we cross the topological transition. It is possible to observe that while for n=5 the exciton is very delocalized in real space (~10 unit cells, that is ~70 Å), in the non-trivial phase the the exciton becomes extremely localized around its excited hole (~3 unit cells, that is 27 Å). Therefore we can exploit a topological phase transition to have an effective tuning mechanism between a Mott-Wannier and a Frenkel exciton, depending on the desired optoelectronic application.

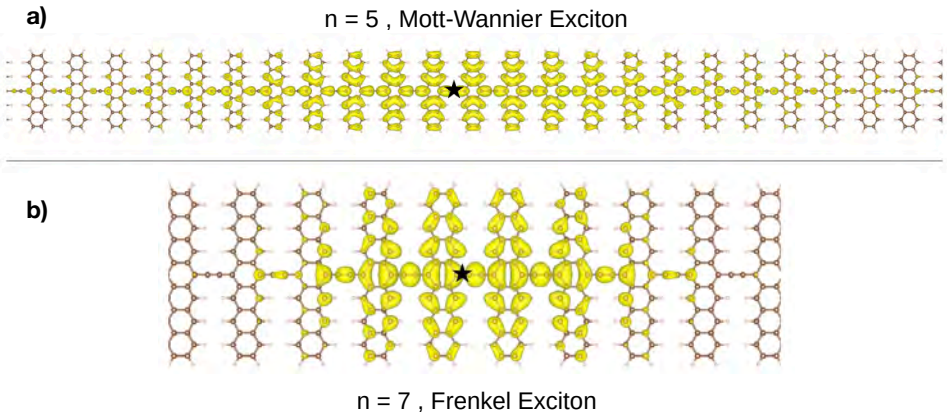


**FIGURE 3**: Modulus squared of the singlet exciton wavefunctions for n=5 (a) and n=7 (b). The black star identifies the position of the hole.

**Acknowledgements**

The authors acknowledge support from the ANR project ACCEPT (Grant No. ANR-19-CE24-0028). This work was granted access to the HPC resources of IDRIS, CINES and TGCC under the allocation 2021-A0100912417 made by GENCI.

**References**

Bronstein, H., Nielsen, C. B., Schroeder, B. C. and McCulloch, I. (2020). The role of chemical design in the performance of organic semiconductors. *Nature Reviews Chemistry* 4, 66.

Cirera, B., Sànchez-Grande,A., de la Torre, B., Santos, J., Edalatmanesh, S., Rodrìguez-Sànchez, E., Lauwaet, K., Mallada, B., Zboril,R., Miranda, R., Gröning, O., Jelinek, P., Martìn, N. and Ecija,D. (2020). Tailoring topological order and pi-conjugation to engineer quasi-metallic polymers. *Nature Nanotechnology* 15, 437.

Dovesi, R., Orlando, R., Erba, A., Zicovich-Wilson, C. M., Civalleri, B., Casassa, S., Maschio, L., Ferrabone, M., Pierre, M. D. L., D'Arco, P., Noël, Y., Causà, M., Rérat M. and Kirtman B (2014). Crystal14: A program for the ab-initio investigation of crystalline solids. *International Journal of Quantum Chemistry*, 114, 1287–1317.

Ratner, M. (2013). A brief history of molecular electronics, *Nature nanotechnology* 8, 378.

Romanin, D., Monacelli, L., Bianco, R., Errea, I., Mauri, F. and Calandra, M. (2021). Dominant Role of Quantum Anharmonicity in the Stability and Optical Properties of Infinite Linear Acetylenic Carbon Chains. Journal of Physical Chemistry Letters, 12, 10339−10345.

Romanin, D., Calandra, M. and Chin, A. W. (2022). Highly tunable optics across a topological transition in organic polymers. arXiv:2204.00321 [cond-mat.mes-hall].

Sangalli, D., Ferretti, A., Miranda, H., Attaccalite, C., Marri, I., Cannuccia, E., Melo, P., Marsili, M., Paleari, F., Marrazzo, A., Prandini, G., Bonfà, P., Atambo, M. O., Affinito, F., Palummo, M., Molina-Sánchez1, A., Hogan, C., Grüning, M., Varsano, D. and Marini, A. (2019). *Journal of Physics: Condensed Matter,* 31, 325902.

Vanderbilt, D. (2018). Berry phases in electronic structure theory: electric polarization, orbital magnetization and topological insulators (Cambridge University Press, 2018).

Carbon 2022

# CARBON MATERIALS AS CATALYSTS FOR THE SYNTHESIS OF DIPHENOLIC ACID FROM LEVULINIC ACID

**Z. Ruiz-Bernal, E.G. Tane, M.A. Lillo-Ródenas, M.C. Román-Martínez**
MCMA research group, Department of Inorganic Chemistry and Materials Institute (IUMA). Faculty of Sciences. University of Alicante, Alicante, E-03080, Spain.
Email: mcroman@ua.es

**Keywords**
Levulinic acid, carbon materials, diphenolic acid.

## INTRODUCTION

Lignocellulosic biomass has been recognized as a suitable raw material to generate fuels and high added-value chemicals. Acid hydrolysis of biomass leads to a solution that contains a significant amount of levulinic acid (LA), which can be converted into other interesting products. Among them, diphenolic acid (DPA) is a potential substitute of bisphenol A (used in the synthesis of polycarbonates and an additive in the lubricant, adhesive and paint industry) that is an endocrine disruptor. DPA can be synthesized under mild conditions by condensation of LA with phenol in the presence of a Brönsted acid catalyst without using any solvent (Figure 1). The yield of the reaction is reduced by the formation of the undesirable o,p'-DPA isomer byproduct, as it has been shown in the literature (Liu *et al.*, 2013), (Van de Vyver *et al.*, 2012) and (Yu *et al.*, 2008). The molar ratio of both isomers has a significant effect on important polycarbonate properties, i.e. color stability and crystallinity.

This study deals with the development and application of carbon-based heterogeneous acid catalysts for the synthesis of DPA from LA. This study bears a significant novelty as there are very few related studies in the literature

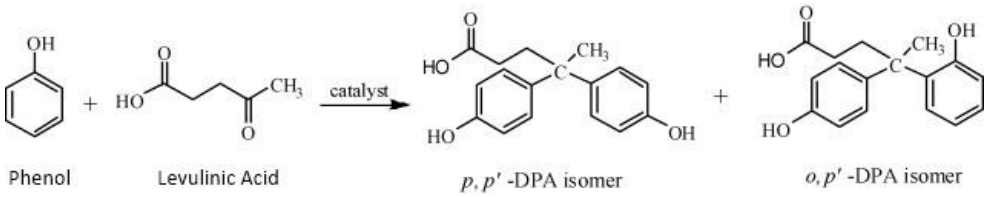


**FIGURE 1**: Condensation reaction of levulinic acid and phenol to obtain diphenolic acid.

## EXPERIMENTAL

Carbon materials used as catalysts have been obtained from almond shell by hydrothermal carbonization in mild conditions using either water or sulfuric acid solution, samples named ASW and ASS, respectively. The commercial SA-30 activated carbon (from MeadWestvaco) and Amberlyst 15DRY ion exchange resin (from Sigma-Aldrich) have been used as reference.

The ASW sample has been washed with acetone and treated with a 10M $H_2SO_4$ solution (10 mL solution/g carbon), with the aim of creating sulfonic groups and increasing its acidity. The treated sample is named ASW-a-s (*a* and *s* refer to acetone washing and treatment with $H_2SO_4$, respectively).

The DPA synthesis is carried out at 100 °C for 6 h in a glass reactor, under $N_2$ and stirring, using 360 µL LA, 900 µL phenol, 25 µL ethanethiol or 22 mg cysteine (co-catalyst) and 50 mg catalyst. The effect of not using a co-catalyst in the reaction has been comparatively studied. The reaction products are

analysed by HPLC using C8 column and UV-Vis detector (270 nm). The catalyst acidity was determined by potentiometric titration using 0.02M NaOH solution.

## RESULTS AND DISCUSSION

The catalytic results are presented in Table 1. DPA is not obtained neither in absence of catalyst, nor using SA-30 and ASW carbons, which do not contain sulfonic groups. In contrast, ASW-a-s and ASS carbons are active in the reaction, being the acidity of the second one about three times higher. These results show the importance of the presence of sulfonic groups. However, the TOF, referred to moles of acidic sites, is noticeably higher for ASW-a-s. The addition of ethanethiol is necessary to obtain a good yield of DPA, but it leads to a lower p,p':o,p' isomers ratio. The results obtained using Amberlyst 15DRY are comparable with those previously reported (Van de Vyver *et al.*, 2012), and it has been found that using cysteine instead of ethanethiol, the DPA yield is lower, revealing promotor steric effects influence (Van De Vyver *et al.*, 2012).

**TABLE 1:** Acid density in the catalysts and conditions and catalytic results in diphenolic acid synthesis.

| Catalyst | Acid density (mmol $H^+ \cdot g^{-1}$) | Additive | $Yield_{DPA}$ (%) | mol DPA/mol $H^+$ | TOF ($h^{-1}$)* | p,p':o,p'** |
|---|---|---|---|---|---|---|
| ASW-a-s | 0.56 | Ethanethiol | 1.86 | 6.85 | 1.14 | 0.5 |
| | | - | 0.11 | 0.36 | 0.07 | 0.7 |
| ASS | 1.51 | Ethanethiol | 0.17 | 0.23 | 0.04 | 0.2 |
| | | - | 0.01 | 0.01 | 0.002 | 0.3 |
| Amberlyst 15DRY | 4.22 | Ethanethiol | 25.18 | 12.20 | 2.03 | 6.0 |
| | | Cysteine | 0.16 | 0.08 | 0.01 | 0.4 |
| | | - | 6.45 | 3.13 | 0.52 | 8.0 |

**TOF ($h^{-1}$) calculated as moles of DPA/(moles $H^+ \cdot t(h)$); **Ratio of p,p'-DPA Isomer/o,p'-DPA Isomer*

## CONCLUSIONS

The biomass derived carbon-based heterogeneous catalysts have shown to be active for the synthesis of DPA from LA. The obtained results show that to achieve a high DPA yield, the carbon catalysts must contain sulfonic groups and a suitable acidity, and that a non-voluminous thiol promotor is necessary.


### ACKNOWLEDGEMENTS

The authors are grateful for the economic financing to PROMETEO/2018/076 (GV/Feder), RTI2018-095291-B-I00 and VIGROB-136 projects (University of Alicante). To Intrinsic Materials Ltd. and Meryem Bouchabou for providing IC-2, and ASW and ASS samples, respectively. E.G. Tane thanks the Spanish Catalysis Society (SECAT) for the 2021 Introduction to Investigation on Catalysis grant


### References


Liu, H. F. *et al.* (2013) 'Brønsted acidic ionic liquids catalyze the high-yield production of diphenolic acid/esters from renewable levulinic acid', *Green Chemistry*, 15(1), pp. 81–84. doi: 10.1039/c2gc36630d.

Van De Vyver, S. *et al.* (2012) 'Mechanistic insights into the kinetic and regiochemical control of the thiol-promoted catalytic synthesis of diphenolic acid', *ACS Catalysis*, 2(12), pp. 2700–2704. doi: 10.1021/cs300635r and 'Thiol-promoted catalytic synthesis of diphenolic acid with sulfonated hyperbranched poly(arylene oxindole)s', *Chemical Communications*, 48(29), pp. 3497–3499. doi: 10.1039/c2cc30239j.

Yu, X. *et al.* (2008) 'Catalytic synthesis of diphenolic acid from levulinic acid over cesium partly substituted Wells-Dawson type heteropolyacid', *Journal of Molecular Catalysis A: Chemical*, 290(1–2), pp. 44–53. doi: 10.1016/j.molcata.2008.04.023

20 C 22 arbon 2022

# Carbon materials for the catalytic transformation of levulinic acid

**Z. Ruiz-Bernal, M.A. Lillo-Ródenas and M.C. Román-Martínez**
MCMA research group, Department of Inorganic Chemistry, Faculty of Sciences and Materials Institute (IUMA). University of Alicante, Alicante, E-03080, Spain.
Email: zaira.ruiz@ua.es

**Keywords**
Carbon materials, surface oxygen groups, biomass, levulinic acid, gamma-valerolactone.

## INTRODUCTION

The depletion of fossil fuels and the environmental pollution derived from their use are promoting the use of renewable sources to obtain chemical products by means of environmentally friendly methods. In this context, the use of lignocellulosic biomass residues to generate high added-value products is a very interesting alternative (Seretis *et al.*, 2020). Hydrothermal carbonization of this biomass under acid conditions produces a carbonaceous material from which functional carbon materials can be prepared, and a solution with a relatively high concentration of levulinic acid (LA). LA can be catalytically transformed into other chemical compounds of interest for the chemical industry like, for example, gamma-valerolactone (GVL). Thus, the subject of the present study is the development and application of carbon supported Ru catalysts (1 wt. %) for the transformation of AL into GVL. Carbon materials of different nature and surface chemistry have been used, and the study aims to achieve high performance under mild reaction conditions. Analogous catalysts prepared using commercial $TiO_2$ as support have been also investigated.

## EXPERIMENTAL

The carbon materials used as catalyst supports are the following:

- Two carbons with spherical morphology (ø ~ 0.5 mm) prepared from a phenolic resin (Intrinsic Materials Ltd. (USA)), named IC-1 and IC-2 (IC-2 is an activated carbon).

- Two powdered activated carbons prepared from biomass residues using $H_3PO_4$, named ASC (from almond shell) and LC (from luffa cylindrica residues).

- A granular commercial activated carbon called A-1100 (MeadWestvaco (USA)), as received, and also subjected to thermal treatments in $N_2$ at 300, 600 and 900 °C to reduce the content of surface oxygenated groups. The treated samples are named A-1100(T), where T is the treatment temperature.

The supports and catalysts have been characterized by physical adsorption of gases ($N_2$ at -196 °C and $CO_2$ at 0 °C), programmed temperature desorption and reduction (TPD and TPR, respectively), and X-ray photoelectron spectroscopy (XPS). The reaction conditions are: 0.445 mL of AL, 0.130 g of catalyst, 15 bars of $H_2$, 1 h and 70 °C (moderate temperature, lower than the used in most reported studies (Song *et al.*, 2018), for the sake of sustainability).

## RESULTS

As shown in Table 1, all the prepared catalysts present developed surface area and porosity (all of them combine micro and mesopores). The catalysts prepared with A-1100(T) maintain the good textural properties and porosity of the pristine A-1100. The carbon materials used as supports show different content of surface oxygen groups (Table 1) and such content decrease upon the thermal treatment is well shown in the values included in Figure 1.

All the synthesized catalysts provide good activity and selectivity at 70°C, achieving in some cases GVL yields close to 70 %. In general, the catalysts prepared with the spherical-shaped supports, with lower content of surface oxygen complexes, lead to higher GVL yields. The influence of the surface chemistry on the catalytic activity is supported by the results obtained with the Ru/A-1100(T) series of samples (Figure 1). It is interesting to point out the high GVL yield obtained with the Ru/LC catalyst prepared from a biomass-derived support. The catalytic performance of Ru/IC-2 catalyst is similar to that for the titania-based one, Ru/P25 (72% GVL yield), whereas the highest yield, 90 %, is obtained with Ru/A-1100(900), as shown in Figure 1.

**TABLE 1**: Textural properties of Ru/C catalysts, total oxygen content of the carbon supports and GVL yield.

| Catalyst | $S_{BET}$ ($m^2/g$) | $V_{DR, N2}$ ($cm^3/g$) | $V_{meso}$ ($cm^3/g$) | $O_{TOTAL}$ (%) * | GVL yield (%) |
|---|---|---|---|---|---|
| **Ru/IC-1** | 554 | 0.22 | 0.12 | 2.3 | 63 |
| **Ru/IC-2** | 1777 | 0.78 | 0.08 | 0.6 | 69 |
| **Ru/ASC** | 1323 | 0.55 | 0.61 | 4.1 | 33 |
| **Ru/LC** | 1238 | 0.51 | 0.30 | 2.8 | 51 |
| **Ru/A-1100** | 1702 | 0.71 | 0.39 | 6.0 | 44 |

*$O_{TOTAL}$ (%) in the carbon materials, obtained with TPD experiments.

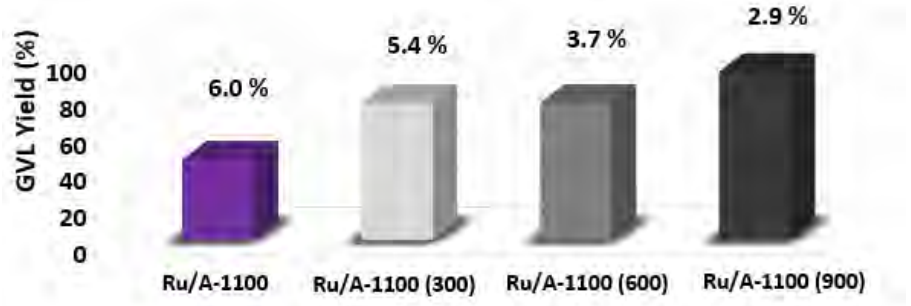


**FIGURE 1**: GVL yield and total oxygen content (%) of the carbon support.

## CONCLUSIONS

Ru catalysts supported on different carbon materials are active and selective at moderate reaction temperature (70°C). A large influence of the catalyst's properties, namely the support's nature and its surface chemistry, on the catalytic activity has been found. In general, supports with lower surface oxygen groups content lead to more efficient catalysts, and catalyst prepared with supports of spherical morphology provide very good catalytic results and are easy to handle. The suitable selection of the carbonaceous supports allows obtaining good catalytic results at moderate reaction temperature. It can be highlighted that up to 90 % of GVL yield was obtained with Ru/A-1100(900).

**Acknowledgements**

The authors thank the projects PROMETEO/2018/076 (GV/Feder), RTI2018-095291-B-I00 and VIGROB-136 (University of Alicante) for funding. Also, to Intrinsic Materials Ltd. for providing samples IC-1 and IC-2.

**References**

Seretis, A. *et al.* (2020) 'Recent Advances in Ruthenium-Catalyzed Hydrogenation Reactions of Renewable Biomass-Derived Levulinic Acid in Aqueous Media', *Frontiers in Chemistry*, 8, p. 221. doi: 10.3389/fchem.2020.00221.

Song, W. *et al.* (2018) 'New Insights in the Development of Carbon Supported Ruthenium Catalysts for Hydrogenation of Levulinic Acid', *Current Catalysis*, 7(2), pp. 129–137. doi: 10.2174/2211544707666180328162825.

20 C 22 arbon 2022

# Metal-free Activated Carbons for Deep Desulfurization of Model and Real Diesel Fuel

**Eleni D. Salonikidou[1], Dimitrios A. Giannakoudakis[1], Margaritis Kostoglou[1], Konstantinos S. Triantafyllidis[1,2], Eleni A. Deliyanni[1]**

[1] Department of Chemistry, Aristotle University of Thessaloniki, University Campus, Thessaloniki, Greece

[2] Center for Interdisciplinary Research and Innovation (CIRI-AUTH), Balkan Center, 10th km Thessaloniki-Thermi Rd, P.O. Box 8318, 57001 Thessaloniki, Greece

Email: elensalonikidou@gmail.com

**Keywords**
Deep desulfurization, activated porous carbons, oxidation treatment, effect of aromatics, real diesel fuel.

## INTRODUCTION

The ongoing demand for cleaner fuels in addition to the recent stringent regulations that establish the maximum sulfur content in diesel fuel to reach really low levels (even less than 5 ppmwS), has driven the research to alternative approaches to the commercially applied process of hydrodesulfurization (Triantafyllidis and Deliyanni, 2014; Svinterikos, Zuburtikudis and Al-Marzouqi, 2019). Adsorptive desulfurization utilizing nanoporous materials, such as activated carbons, as adsorbents is considered as a promising, economic, efficient and green-oriented method for the removal of refractory sulfur compounds from liquid fuels (Salonikidou *et al.*, 2022).

## SCOPE

In this work, several commercial metal-free activated carbons with different physicochemical characteristics, as it can be seen in **Figure 1**, were evaluated for the desulfurization of a model, as well as the real diesel fuel, under ambient conditions. Aiming at studying in depth which physicochemical properties (with emphasis on the surface chemistry heterogeneity and textural features) influence the desulfurization performance of the adsorbents, and in addition to further increasing their efficiency, four activated carbons (SX PLUS, SAE SUPER, BAX, CPL) with different porosity and surface acidities were chemically modified through treatment with $HNO_3$.

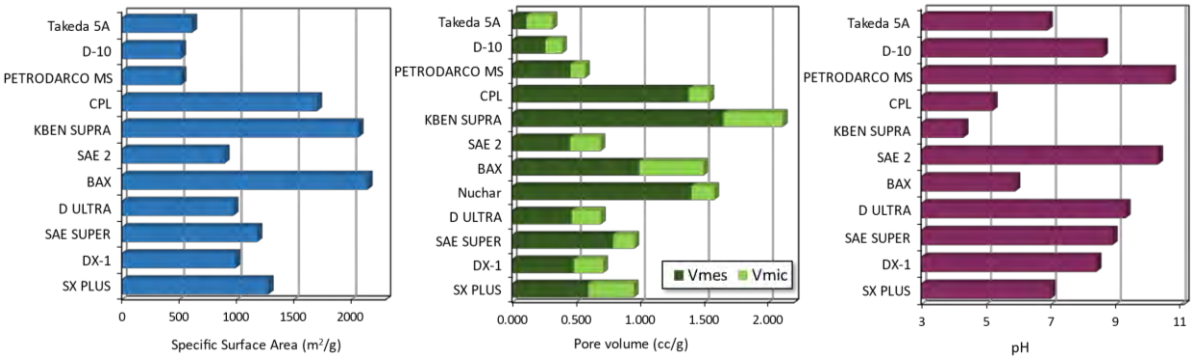


**FIGURE 1**: Specific surface area, porosity parameters and surface pH of the commercial activated carbons.

## RESULTS

Initially, the desulfurization capability of the activated carbons was evaluated for the adsorption of 4,6-dimethyldibenzothiophene (4,6-DMDBT) from hexadecane, starting from low initial sulfur

concentration (20 ppmwS). In an attempt to investigate the impact of the co-presence of aromatic compounds in the desulfurization process, various model diesel fuels were created, with the addition of benzene and naphthalene, in order to represent the mono- and di- aromatics in liquid fuels, respectively. The co-presence of another organosulfur molecule, dibenzothiophene (DBT), in the model fuel was additionally explored so as to provide information about the available active sites. The main outcome is that a complicated correlation exists between the desulfurization efficiency and specific physicochemical features, namely porosity and surface chemistry.

The results regarding the four carbons that were chosen for further oxidative treatment are presented in **Figure 2**. The first clear observation is that the oxidation treatment enhanced the adsorption capacity of the carbons, especially in the case of the carbons with moderate or low desulfurization performance, despite a decrease in porosity characteristics. Studying the antagonistic effect of the co-presence of aromatic compounds in the desulfurization efficiency of the activated carbons in low concentrations, it was demonstrated that the addition of aromatic components slightly reduced the adsorption capability of the activated carbons, revealing their limited competitive character in adsorptive desulfurization. On the other hand, the addition of aromatics in higher concentrations (not presented here), mimicking those of a real diesel fuel, significantly declined the adsorption efficiency of the carbons. Moreover, investigating the model fuel that contained both organosulfur molecules led to the conclusion that even though DBT and 4,6-DMDBT compete up to a certain extend with each other, the adsorption of the two thiophenic compounds mainly takes place at different adsorption active sites.

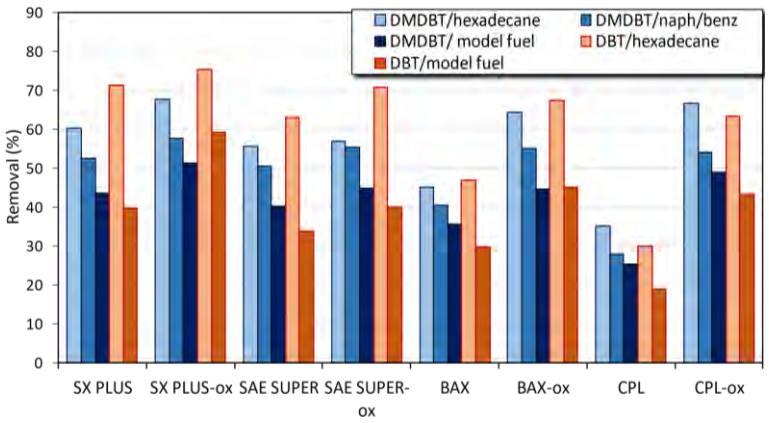


**FIGURE 2**: Adsorptive removal of 4,6-DMDBT and DBT in hexadecane with and without the presence of aromatic compounds for several activated carbons; conditions: 400 mL/g, 20 ppmwS 4,6-DMDBT + 20ppmwS DBT, T = 25 $^{o}$C, 170 rpm, t = 3 h, $n_{4,6\text{-DMDBT}}/n_{DBT}/n_{naph}/n_{benzene}$ =1/1/10/150, 801 ppmw naphthalene, 7323 ppmw benzene.

Moving the research to the next level, experiments were carried out with the real diesel fuel and a model diesel fuel that best represented the real, meaning low initial sulfur concentration (5.5 ppmwS) and very high concentration of aromatics. In an attempt to simulate industrial conditions, greater amount of adsorbent was utilized (30 mL fuel/ g adsorbent in comparison to 400 mL fuel/ g adsorbent used in the previous experiments). The results, presented in **Figure 3** as the adsorptive removal of sulfur from the model and the real diesel fuel, illustrate that activated carbons, and especially their oxidized counterparts were very effective adsorbents, since after adsorption the achieved remaining sulfur concentration was less than 0.2 ppmwS for the model fuel and less than 1 ppmwS for the real diesel fuel. It is also worth noticing that some activated carbons, like SX PLUS oxidized (SX PLUS-ox) and SAE SUPER-oxidized (SAE SUPER-ox), even though they exhibited excellent performance in the model fuel, they were incapable of desulfurizing the real diesel fuel.

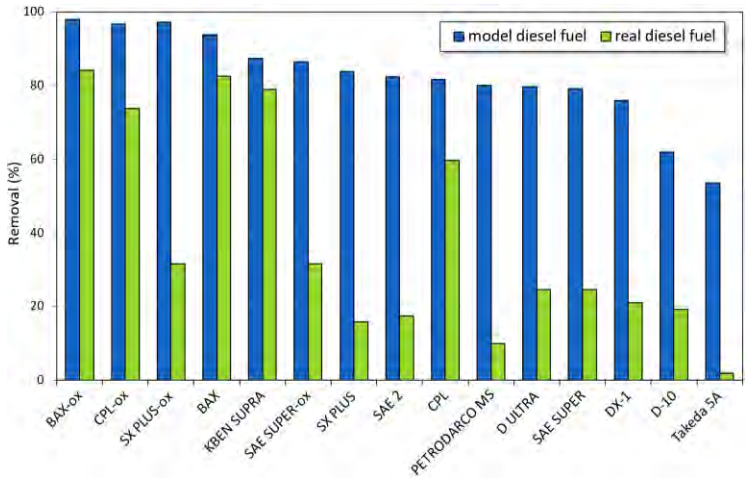


**FIGURE 3**: Adsorptive removal of sulfur from model and real diesel fuel for several activated carbons; conditions: 30 mL/g, 5.5 ppmwS (4,6-DMDBT + DBT), T = 25 °C, 170 rpm, t = 24 h, 19600 ppmw naphthalene, 184800 ppmw toluene.

## CONCLUSIONS

A few basic conclusions that can be exported from this work is that activated carbons and especially their oxidized forms were very effective adsorbent materials, since ultra-deep desulfurization was achieved, given that the remaining sulfur concentration in the real diesel fuel was less than 1 ppmwS after adsorption. The modification of the carbons had a positive impact on their desulfurization performance, suggesting that surface oxidation is an effective strategy for material's design. Lastly, it was also confirmed that there was a rather complicated correlation between the adsorptive capacity and the main physicochemical features of the carbons, with both porosity and especially surface chemistry to play a vital role.

**Acknowledgements**

This research has been co-financed by the European Regional Development Fund of the European Union and Greek national funds through the Operational Program Competitiveness, Entrepreneurship and Innovation (EPAnEK 2014-2020), under the Action "RESEARCH–CREATE–INNOVATE B' CALL" (Project: DESULFUR, code: T2EΔK-01976).

**References**

Salonikidou, E. D. et al. (2022). Deep desulfurization of model fuels by metal-free activated carbons: the impact of surface oxidation and antagonistic effects by mono- and poly-aromatics. Journal of Molecular Liquids, 351, p. 118661. doi: 10.1016/j.molliq.2022.118661.

Svinterikos, E., Zuburtikudis, I. and Al-Marzouqi, M. (2019). Carbon Nanomaterials for the Adsorptive Desulfurization of Fuels. Journal of Nanotechnology, 2019. doi: 10.1155/2019/2809867.

Triantafyllidis, K. S. and Deliyanni, E. A. (2014). Desulfurization of diesel fuels: Adsorption of 4,6-DMDBT on different origin and surface chemistry nanoporous activated carbons. Chemical Engineering Journal, 236, pp. 406–414. doi: 10.1016/j.cej.2013.09.099.

Carbon 2022

# Modification of lignocellulosic hydrochar to improve the As (V) adsorption

**I. Sanchis*, E. Diaz, J. J. Rodriguez, A. F. Mohedano**
Chemical Engineering Department, Faculty of Sciences, Universidad Autonoma de Madrid, 28049 Madrid, Spain
Email: ines.sanchis@uam.es

**Keywords**
Hydrothermal carbonization, As adsorption, biomass valorization

## INTRODUCTION

Hydrothermal carbonization (HTC) is a thermochemical process that operates in presence of water at temperatures within 180-250 °C and the corresponding saturation pressure, and residence times ranging from 5 min to 24 h. The main reaction product is a solid known as hydrochar, more stable and with a high carbon content than the raw biomass. The hydrochar has been previously tested for several applications, including the production of catalytic supports, soil amendment, fuels and as adsorbents of heavy metals (Mau et al. 2020, Capobianco et al. 2020). In this sense, the As adsorption seems to be influenced by textural properties, Fe content or the amount of oxygen surface groups of the adsorbent material (He et al. 2018). The aim of this work is the recovery of garden and park wastes (GPW) into As (V) adsorbents by means of hydrothermal carbonization and the modification of the resultant hydrochar (HC) by activation, oxidation and Fe impregnation.

## METHODOLOGY

Synthesized adsorbents were classified as non-oxidated and oxidated materials. On one hand, non-oxidated materials including plain hydrochar (230 ºC, 80 % of water, 16 h), hydrochar synthesized with Fe (230 ºC, 16 h, 80 % $H_2O$, 1;1 wt. $FeCl_3$:GPW), $N_2$ pyrolyzed hydrochar (750 ºC, 1 h, 10 ºC/min, 100 NmL $N_2$/min) and hydrochar activated with $FeCl_3$ (1:1 wt. $FeCl_3$:HC-GPW, 750 ºC, 1 h, 10 ºC/min, 100 NmL $N_2$/min). On the other hand, oxidated materials were prepared from $N_2$ pyrolyzed hydrochar, which was subjected to an oxidative treatment with $KMnO_4$, mixing 2 g of HC-GPW in 30 mL of 0.1 M $KMnO_4$ during 1 h, and impregnated by a Fe solution (1:1 wt. $FeCl_3$:HC-GPW-$KMnO_4$ in deionized water, 24 h, room temperature, 200 rpm). The materials were characterized by 77 K $N_2$ adsorption-desorption isotherms, ICP-OES and $pH_{slurry}$. Adsorbents were tested in batch adsorption experiments (0.4 g/L adsorbent, <100 µm, 100-1000 µg/L As (V), 20 ºC, 200 rpm). As concentration was determined by UV-Vis spectrophotometry (Dhar et al. 2004).

## RESULTS AND DISCUSSION

The most important adsorbent properties for the As adsorption proved to be Fe content, $pH_{slurry}$ and specific surface area (Table 1, Figure 1). The As adsorption was dominated both by electrostatic attraction, especially when the $pH_{slurry}$ of the material was higher than the pH of the solution (6.2), and by the Fe species on the adsorbent surface. The results obtained fitted the Langmuir equation ($R^2$ > 0.94). In the case of non-oxidated materials, the incorporation of Fe during the HTC process resulted in an increase of Fe content up to 2.2 % (wt.), enhancing the maximum adsorption capacity ($q_L$) from 142 to 513 µg/g. Moreover, the pyrolysis of the hydrochar synthesized with Fe increased the surface area from 34 to 507 $m^2$/g, which increased the $q_L$ to 730 µg/g. The higher Fe incorporation in the adsorbent was achieved by means of activation of hydrochar with $FeCl_3$ (35 % (wt.) of Fe), with which it was achieved the highest maximum adsorption capacity ($q_L$ = 2360 µg/g). In the case of the oxidated materials, the $KMnO_4$ oxidated adsorbents obtained maximum adsorption capacities within 1255-1543 µg/g, which were superior for pyrolyzed materials independent on the Fe content.

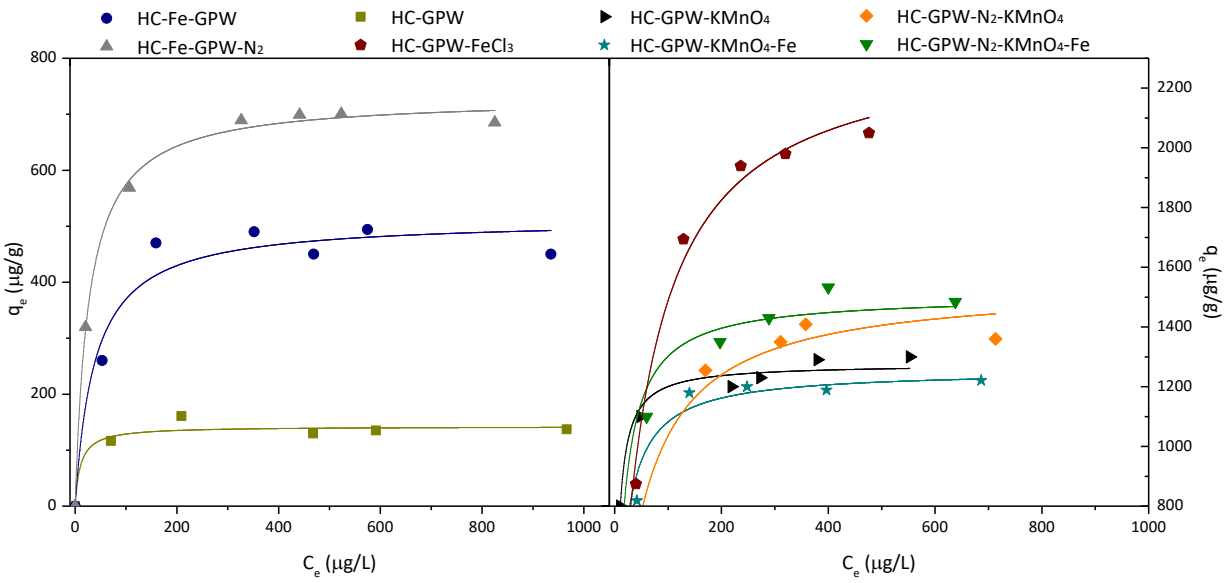


**FIGURE 1**: Adsorption isotherms of As(V) on prepared adsorbents (20 ºC, 200 rpm, 0.4 g/L adsorbent, pH 6.2). Symbols: experimental values; solid lines: fitting to the Langmuir equation.

**TABLE 1**: Main characterization results for the prepared adsorbents and the Langmuir model parameters.

| Adsorbents | Characterization of adsorbents | | | Langmuir parameters | | |
|---|---|---|---|---|---|---|
| | $A_{BET}$ ($m^2/g$) | Fe (%) | $pH_{slurry}$ | $q_L$ (µg/g) | $K_L$ (L/µg) | $R^2$ |
| HC-GPW | nd | <0.1 | 4.7 | 142 ± 10 | 0.096 ± 0.110 | 0.94 |
| HC-Fe-GPW | 34 | 2.2 | 2.3 | 513 ± 29 | 0.026 ± 0.010 | 0.95 |
| HC-Fe-GPW-$N_2$ | 507 | 1.6 | 7.9 | 730 ± 9 | 0.037 ± 0.003 | 1.00 |
| HC-GPW-$FeCl_3$ | 475 | 35.2 | 7.1 | 2360 ± 68 | 0.017 ± 0.002 | 0.99 |
| HC-GPW-$KMnO_4$ | nd | <0.1 | 7.5 | 1276 ± 18 | 0.160 ± 0.019 | 0.99 |
| HC-GPW-$KMnO_4$-Fe | nd | 2.2 | 4.9 | 1255 ± 34 | 0.063 ± 0.011 | 0.99 |
| HC-GPW-$N_2$-$KMnO_4$ | 316 | <0.1 | 7.0 | 1543 ± 48 | 0.021 ± 0.003 | 0.99 |
| HC-GPW-$N_2$-$KMnO_4$-Fe | 221 | 1.0 | 4.5 | 1505 ± 46 | 0.064 ± 0.016 | 0.99 |

## CONCLUSION

In conclusion, the activation of hydrochar using $FeCl_3$ gave rise to an appropriate material for As adsorption that complies a significant Fe content and a high specific surface area.

**Acknowledgements**

The authors wish to thank the Spanish MINECO (PID2019-108445RB-I00) and the Comunidad de Madrid (PEJD-265 2017-PRE/AMB-4616; S2018/EMT-4344) for their financial support.

**References**

Capobianco, L., Di Caprio, F., Altimari, P., Astolfi, M.L. and Pagnanelli, F. (2020) Production of an iron-coated adsorbent for arsenic removal by hydrothermal carbonization of olive pomace: Effect of the feedwater pH. *Journal of Environmental Management*, 273, 111164.

Dhar, R.K., Zheng, Y., Rubenstone, J., van Geen, A. (2004) A rapid colorimetric method for measuring arsenic concentrations in groundwater. *Analytica Chimica Acta*, 526, 203-209.

He, R., Peng, Z., Lyu, H., Huang, H., Nan, Q. and Tang, J. (2018) Synthesis and characterization of an iron-impregnated biochar for aqueous arsenic removal. *Science of the Total Environment*, 612, 1177-1186.

Mau, V., Arye, G. and Gross, A. (2020) Poultry litter hydrochar as an amendment for sandy soils. *Journal of Environmental Management*, 271, 110959.

Carbon 2022

# Circular Carbon Black Production from Tire Pyrolysis Oils

**Arndt Schinkel, Helmut Gromes, Dirk Rechenbach, David Deters**
Orion Engineered Carbons, Harry-Kloepfer-Str. 1, 50997 Cologne, Germany
Email: arndt-peter.schinkel@orioncarbons.com

**Keywords**
Sustainable carbon black, circular carbon black, Life cycle assessment

## INTRODUCTION

The demand on biogenic carbon and more sustainable production is growing rapidly. Therefore, the possible feedstock landscape is changing. In the frame of the EU-project black cycle we are looking into the recycle loop of tires and try to close this cycle by utilizing the liquids from the tire pyrolysis to produce carbon black. The characteristic of this new feedstock differs significantly from the typical carbon black feedstocks.
Nevertheless, it has been experimentally proven to produce N200, N300, and N500 series grades. Due to the natural rubber content the carbon black consists of approximately 40% biogenic carbon shown in Figure 1.

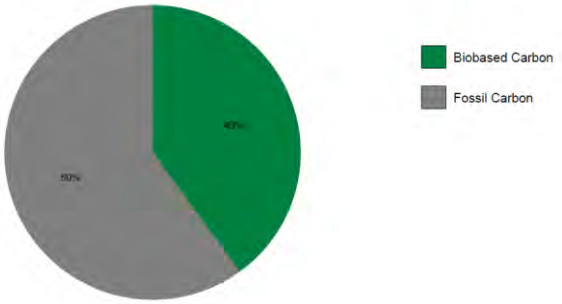


*Figure 1 Results of a N234 produced by heavy tire tar*

This is in the same range of the bionic carbon content of the heavy tire tar itself. In this paper the impact of the utilization of heavy tire tar is discussed on the overall fossil $CO_2$ equivalent emissions is discussed.

## EXPERIMENTS

The experiments have been performed on a pilot furnace reactor. The reactor was fired with natural gas. The air flow, air preheat, and a combustion ratio are 2700 $Nm^3/h$, 614 °C, 1.4 respectively. *Figure 2* shows the schematic of a furnace reactor.

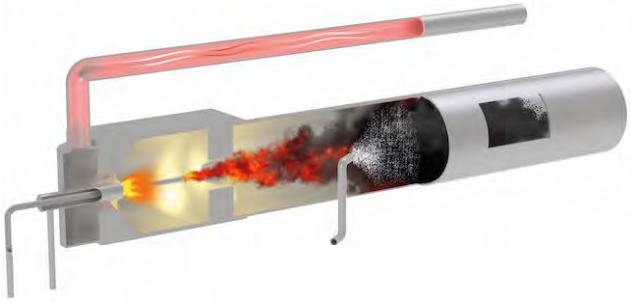

*Figure 2 Schematic of a furnace reactor*

The utilized feedstock is a heavy tire tar derived from a tire tar distillation process. These kinds of oils are significant different from standard carbon black oils like coal tar distillates, steam cracker tars or FCC bottoms. The heavy tire tar and FCC bottoms are analyzed by IR spectroscopy. Significant differences can be observed in the structure. Heavy tire tars have a high amount of benzene and mono subsidized aromatics. These kinds of structures are less suitable for carbon black formation as the standard feedstocks.
Figure 4 shows the relative fossil $CO_2$ emissions to produce a sustainable carbon black. In total we obtain a reduction of the $CO_2$ footprint. It is obvious that under these conditions a well operating electricity/heat production is of high importance.

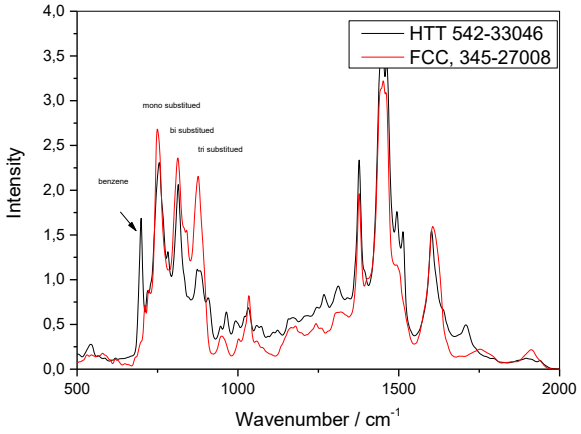


*Figure 3 IR spectrum of a heavy tire tar and a FCC bottom*

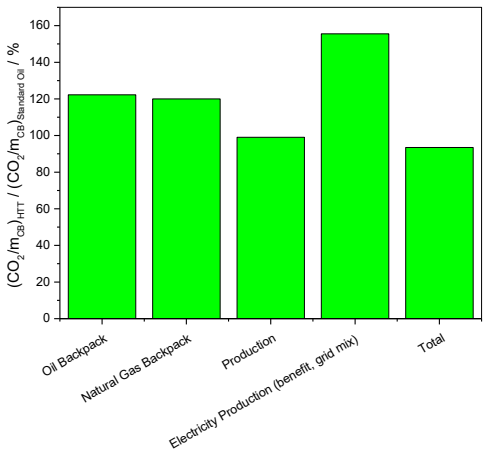


*Figure 4 Relative specific fossil $CO_2$ emission utilizing heavy tire tar as feedstock for carbon black production*

**CONCLUSION**

The experimental results show the possibility to produce carbon black for the tire industry using heavy tire tar. This approach is a step forward in the circular economy. Nevertheless, it demonstrates the challenges for the future to improve the efficiency of the process.

**ACKNOWLEDGEMENT**

This work has received funding from the European Union's Horizon 2020 research and innovation program under grant agreement No. 869625.

20 C 22 arbon 2022

# Ultrafast Electron Transfer in Carbon Nanodots-Nanotubes Composites

**Alice Sciortino[1,2] and Francesco Ferrante[1] and Simonpietro Agnello[1] and Marco Cannas[1] and Dario Duca[1] and Fabrizio Messina[1,2]**

[1]Dipartimento di Fisica e Chimica – Emilio Segrè, Università degli Studi di Palermo, Viale delle Scienze, Ed. 17, 90128, Palermo, Italy
[2]CHAB-ATeN Center, Università degli studi di Palermo, Viale delle Scienze, Ed. 18, 90128, Palermo, Italy
Email: alices.sciortino02@unipa.it

**Keywords**
Carbon nanodots, Carbon nanotubes, ultrafast electron transfer.

## INTRODUCTION

Carbon nanodots (CDs) are carbon nanoparticles characterized by intense and tunable absorption-emission in the visible range. Their optical response is combined with a great sensitivity to external agents. Besides, CDs display exceptional electron donating capabilities, interesting for several optoelectronic applications (Arcudi, 2017). Single-wall Carbon Nanotubes (SWCNTs) are probably one of the most iconic materials in nanoscience, endowed with a range of exceptional properties ultimately related to their 1D structure (Rahman, 2019).

Here, we electrostatically coupled carbon nanodots (CDs) with single walled carbon nanotubes (SWCNTs) in order to combine the behaviour of CDs as efficient light absorbers and electron donors, with the excellent electron accepting and electron transport properties of SWCNTs. We explore the photophysics of the CD-SWCNT nanohybrids by different optical techniques with temporal resolutions going from less than 100 fs to the steady state. The experiments have been supported by computational studies which confirmed the model.

## RESULTS & DISCUSSION

CDs have been synthesized as described in (Scialabba, 2019) and SWCNTs (with (7,6) nominal chirality) were purchased from Sigma Aldrich. We performed a complete optical analysis from the steady state to the femtosecond resolution to investigate the photophysics of the nanohybrids. As shown in Figure 1a, the characteristic CDs fluorescence is quenched in presence of SWCNTs, suggesting the formation of a complex and the occurrence of an electron transfer from the CD to the SWCNTs as already seen before with other CD-based nanocomplexes (Madonia, 2020). Nanosecond time-resolved measurements show (Figure 1b) that the decay kinetics in absence and in presence of SWCNTs do not change, demonstrating that the quenching is non-collisional, and, on the contrary, is due to stable CD-SWCNTs complexes interacting within a sub-nanosecond temporal range.

To learn more on the electronic properties of CD-SWCNT complexes, we performed density functional tight binding calculations (DFTB), focusing on a model of CD/s-SWCNT. The HOMO and LUMO levels of the CD are found at -3.94 eV (localized in the core) and at -0.98 eV (localized on the surface), respectively (Sciortino, 2021a). In regard to SWCNT(7,6), the HOMO is at -4.79 eV and the LUMO at -3.94 eV. We expect that the energy associated to the molecular orbitals of the nanocomposites does not change drastically if compared to the isolated counterparts. In fact, calculations on the CD-SWCNT nanocomposite identify a HOMO at -4.26 eV localized on CD, while the LUMO, at -3.85 eV, is delocalized on the central portion of SWCNT surface.

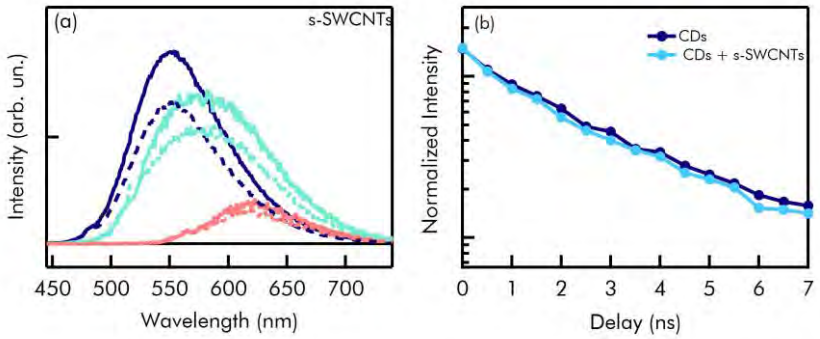


**FIGURE 1:** (a) Emission spectra of CDs (continuous lines) and of CDs+SWCNTs (dashed lines) excited at 480 nm (blue line), 520 nm (green line), 560 nm (pink line). (b) Decay kinetics of the fluorescence of bare CDs (blue line) and of CDs+SWCNTs (light blue line) excited at 540 nm.

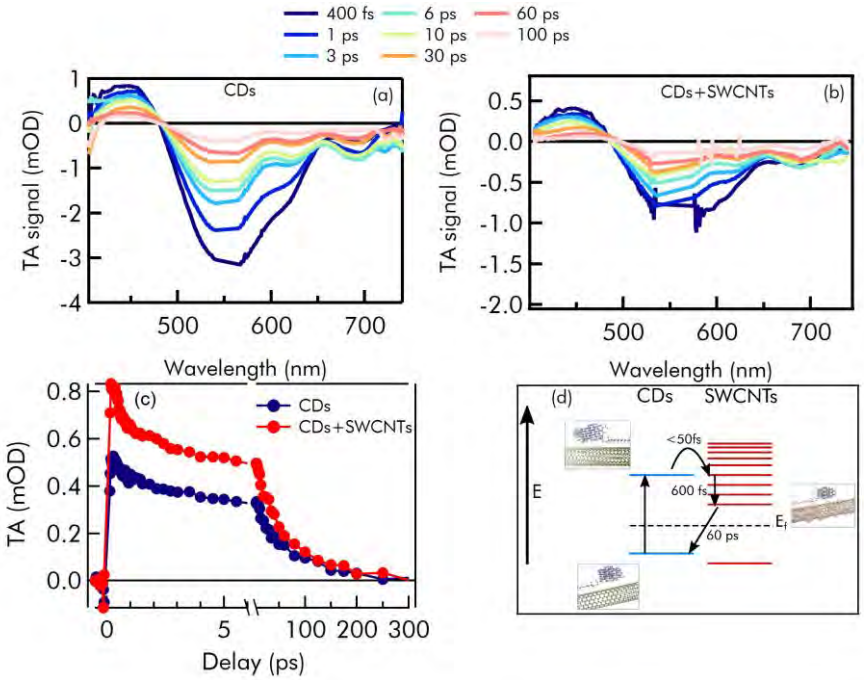


**FIGURE 2**: (a) Transient absorption spectra of CDs solution excited at 520 nm as a function of delay from the photoexcitation. (b) Transient absorption spectra of CDs+SWCNTs solution excited at 520 nm as a function of delay from the photoexcitation. (c) Transient absorption kinetics at 450 nm of bare CDs (blue curve) and of CDs+SWCNTs (red curve). (d) Schematized model of forward and back electron transfer from CDs to SWCNTs with the related timescales as obtained by fitting procedure.

To deeply investigate the dynamics of the nanohybrids on a faster time scale, we performed transient absorption (TA) measurements by pumping the samples with 50 fs laser pulses at 550 nm. The TA signal of CDs (Figure 2a) is dominated by a broad negative contribution around the excitation wavelength, which is already present at the earliest time delays, and can be ascribed to a combination of ground-state bleaching (GSB) and stimulated emission (SE) signals. There is also an excited-state absorption (ESA) signal at 450 nm, probably related to bi-excitonic electronic transitions. All the signal decay with an average lifetime of 3 ps. The same TA experiments were repeated on nanocomplexes (Figure 2b). Although the TA signal of the complexes is similar to the bare CDs signal, it displays a strong intensity reduction, already at the very earliest delays from photoexcitation. Hence, the electron transfer must have occurred during the 50 fs laser pulse. Although we are not capable of directly visualize such a quasi-instantaneous electron transfer, we are able to follow the subsequent dynamics comparing the decay kinetics between bare CDs and

CDs/SWCNTs complexes, after normalization at long time delays. This comparison (Figure 2c) reveals that in the signal of CD/SWCNTs nanocomplexes we can identify two new temporal components, with time scales of 600 fs and 50 ps, which are absent in isolated CDs. The former represents an internal relaxation of the complex after the electron transfer (Lauret, 2003), and the latter, considering the coincidence of the kinetics at longer times, represents a back electron transfer from the nanotube to the CD and, so, the end of the photocycle.

Based on these results, and considering the energy levels alignment, the dynamics of the CD-SWCNT nanohybrids is finally modelled as drawn in Figure 1d. Photoexcitation produces an electron transfer in less than 50 fs from the surface of the CDs to the SWCNTs. Then, an internal relaxation drives the electron in 600 fs to the bottom of the conduction band of SWCNTs. Finally, the electron goes back to CDs in 50 ps closing the photocycle.

## CONCLUSIONS

We succeeded in the synthesis of an "all-carbon" nanohybrids coupling CDs with SWCNTs (Sciortino, 2021b). Investigating the photocycle of these nanohybrids we showed that the complexes formation produces a quenching of CDs emission which is a consequence of the efficient photoinduced charge transfer from CDs to the neighbouring nanotubes, in less than 50 fs. Moreover, the electron transfer is followed by a back electron transfer to CDs in about 50-60 ps. Our results unravel the nature of CD-SWCNTs interactions which can be further exploited in several photo-electronic applications.

**Acknowledgements**

A.S. was supported by the "L'Oréal Italia Per le Donne e la Scienza" Program (17th edition). We thank the Italian Ministry of University and Research (MUR) for project PRIN2017 "CANDL2", grant number 2017W75RAE.

**References**

Arcudi, F., Dordevic, L., and Prato, L. (2017). Rationally Designed Carbon Nanodots towards Pure White-Light Emission. *Angewandte Chemie-International Edition*, 56 [40], 12097-12101. https://doi.org/10.1002/anie.201612160

Lauret, J. S., Voisin, C., Cassabois, G., Delalande, C., Roussignol, P., Jost, O. and Capes, L. (2003) Ultrafast Carrier Dynamics in Single-wall Carbon Nanotubes. *Phys. Rev. Lett.* 90, 057404. https://doi.org/10.1103/PhysRevLett.90.057404

Madonia, A., Martin-Sabi, M., Sciortino, A., Agnello, S., Cannas, M., Ammar, S., Messina, F. and Schaming, D. (2020) Highly Efficient Electron Transfer in a Carbon Dot−Polyoxometalate Nanohybrid. *J. Phys. Chem. Lett.* 11, 4379−4384. https://doi.org/10.1021/acs.jpclett.0c01078.

Rahman, G., Najaf, Z., Mehmood, A., Bilal, S., ul Haq Ali Shah, A., Mian, S. A. and Ali, G. (2019).An overview of the recent progress in the synthesis and application of carbon nanotubes. *C-Journal of Carbon Research*, 5 [1], 31. https://doi.org/10.3390/c5010003

Scialabba, C., Sciortino, A., Messina, F., Buscarino, G., Cannas, M., Roscigno, G., Condorelli, G., Cavallaro, G., Giammona, G. and Mauro, N. (2019) Highly Homogeneous Biotinylated Carbon Nanodots: Red-Emitting Nanoheaters as Theranostic Agents toward Precision Cancer Medicine. *ACS Appl. Mater. Interfaces*, 11, 19854−19866. https://doi.org/10.1021/acsami.9b04925.

Sciortino, A., Ferrante, F., Mauro, N., Buscarino, G., Sciortino, L., Giammona, G., Cannas, M., Duca, D. and Messina, F. (2021). Disclosing the Emissive Surface Traps in Green-Emitting Carbon Nanodots. *Carbon*, 173, 454−461. https://doi.org/10.1016/j.carbon.2020.11.030

Sciortino, A., Ferrante, F., Goncalves, G., Tobias, G., Popescu, R., Gerthsen, D., Mauro, N., Giammona, G., Buscarino, G., Gelardi, F. M., Agnello, S., Cannas, M., Duca, D. and Messina, F. (2021). Ultrafast interface charge separation in carbon nanodot-nanotube hybrids. *ACS Appl. Mater. Interfaces* 13 [41], 49232-49241. https://doi.org/10.1021/acsami.1c16929

Carbon 2022

# Functional nanocomposites obtained by electrostatic coupling of carbon dots to plasmonic metal nanoparticles

**A. Sciortino, M. Reale, G. Buscarino, A. Emanuele, M. Cannas and F. Messina**
Dipartimento di Fisica e Chimica "Emilio Segrè"
Università degli Studi di Palermo, Via Archirafi 36, 90123 Palermo,Italy
Email: fabrizio.messina@unipa.it

**Keywords**
Carbon dots, nanocomposites, fluorescence, photocatalysis.

## INTRODUCTION

Carbon nanodots (CDs) are a family of carbon nanomaterials displaying several interesting optical properties, such as a bright fluorescence and an ability to behave as photo-activated charge donors. CDs also display several advantages with respect to other optical nanomaterials, such as non-toxicity and ease of synthesis. Since their original discovery in 2006 (Sun, 2006), CDs are attracting a large research interest in nanoscience, and many groups are pursuing their application in multiple fields, such as optoelectronics, photocatalysis, bioimaging (Ragazzon, 2021). The nature of CDs as tunable light harvesters or light emitters, combined with their chemical versatility, makes them ideal building blocks for a variety of functional nanocomposites.

Nowadays, a great attention is being devoted in material science to designing nanohybrids exploiting the combination of different nanomaterials to obtain functional features generally absent in the individual components. Coupling CDs to plasmonic metal nanoparticles (MNPs) such as nano-silver or gold (AgNPs and AuNPs, respectively) has been investigated only by a few studies (Emam, 2017; Yuan, 2020), despite it may offer interesting routes to modulate the optical response of CDs in view of many possible applications. On the one hand, MNPs can behave as nano-antennas participating to bi-directional energy exchanges with nearby CDs. On the other hand, photoinduced charge transfer from CDs to coupled MNPs may lead to a strong charge separation, which paves the way to significant photocatalytic properties.

## RESULTS AND DISCUSSION

We investigated the photo-physical and -chemical response of hybrid nanomaterials obtained by coupling Carbon Dots (CDs) to gold (AuNPs) or silver (AgNPs) nanoparticles. AgNPs (50 nm average diameter) and AuNPs (20 nm average diameter) were synthesized by the Turkevich method, and then treated with cetyltrimethylammonium bromide (CTAB) which replaces surface citrate ions so as to impart a positive surface charge to the MNPs.

Two types of CDs (CD1 and CD2) were synthesized by hydrothermal routes described in previous papers (Sciortino, 2018; Scialabba, 2019). The size of both CD1 and CD2 is broadly distributed around an average diameter of 6 nm, while their surfaces are functionalized with carboxylic groups (CD1) or polyethylene glycol chains (CD2). Both CD1 and CD2 are strongly fluorescent, with peak emissions in the green (540 nm) and orange (620 nm) respectively. Interestingly, the maximum optical absorption of CD1 (410 nm) spectrally matches the plasmonic resonance of AgNPs, while CD2 absorb at 540 nm, which is close to the typical AuNP plasmonic peak. CD1 and CD2 were mixed in solution with controlled amounts to AgNPs and AuNPs respectively, in order to allow the formation of nanohybrids held together by electrostatic attraction. The resulting nanocomposites were characterized by steady-state, nanosecond-resolved and femtosecond-resolved optical spectroscopy in order to gain an extensive picture of the underlying interactions. For

both CD1 and CD2, we have strong evidence of the formation of CD-MNP nanocomposites, but the influence of MNPs on the optical response of CDs is very different in the two cases.

The successful formation of CD1-AgNP nanocomposites is highlighted by the quenching of CD fluorescence due to electron transfer from photoexcited CDs to the nearby MNPs (Figure 1a). This conclusion is also confirmed by femtosecond-resolved measurements (not shown here). Photoexcited electron transfer generates a charge-separated pair which imparts the nanocomposites with significant photocatalytic activity, as we demonstrate by the decomposition of methylene blue (inset of Figure 1a). Such a photocatalytic response is not observed with isolated CDs or MNPs. In fact, it is an emerging consequence of their excited-state interactions.

The behaviour of CD2-AuNPs composites is entirely different. Instead of fluorescence quenching, here we find that the interaction between CD2 and the coupled AuNP leads to a strong enhancement of the initial orange fluorescence of CDs, by up to a factor of 6 (Figure 1b). In-depth studies with nanosecond and femtosecond-resolved spectroscopy allow to understand this effect as a result of near-field enhancement of the photon absorption probability from CDs, due to their close proximity to the AuNPs nanoantennas. This result provides a promising route to overcome the low emission of CDs in the orange-red region, which is one of the main open problems in the field.

Overall, these experiments demonstrate different ways in which MNPs can be exploited to modulate the optical response of CDs and enhance their performance in multiple applications.

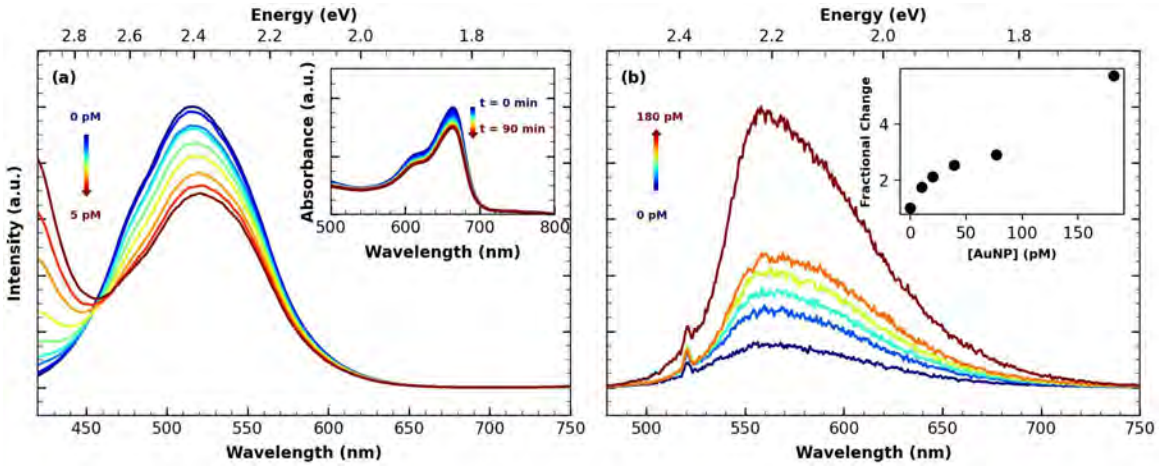


**FIGURE 1**: Panel (a): photoluminescence of carbon dots (CD1) as observed after the addition of increasing concentrations of AgNPs up to 5 pM. Inset: optical absorption spectra of methylene blue, continuously exposed to the light from a discharge lamp, in the presence of CD1-AgNPs nanocomposites. Panel (b): photoluminescence of carbon dots (CD2) as observed after the addition of increasing concentrations of AuNPs up to 180 pM. Inset: intensity enhancement of CD2 emission as a function of AuNP concentration.

## CONCLUSIONS

We demonstrated easy strategies to produce CD-AuNP and CD-AgNP nanocomposites through electrostatic self-assembly in solution phase, facilitated by surface and charge engineering of the two components. We demonstrate two interaction pathways between CDs and metal NPs, leading to different consequences on the optical response of the nanocomposites. In CD-AuNP nanocomposites, we achieve an enhancement of the orange-red emission of CDs through ultrafast energy transfer from photoexcited AuNPs. In CD-AgNP nanocomposites we show an emergent photocatalytic activity stemming from the ultrafast electron transfer from photoexcited CDs to coupled AgNPs. The results are very promising and encourage further studies to develop a new generation of CD-based functional nanocomposites for a range of applications such as light emitters, pollutant degradation, and water splitting.

**References**


Emam, A. N., Loutfy, S. A., Mostafa, A. A., Awad, H. and Mohamed, M. B (2017). Cyto-toxicity, biocompatibility and cellular response of carbon dots-plasmonic based nano-hybrids for bioimaging. *RSC Adv.* 7, 23502. https://doi.org/10.1039/C7RA01423F

Ragazzon, G., Cadranel, A., Ushakova, E. V., Wang, Y., Guldi, D. M., Rogach, A. L., Kotov, N. A., and Prato M. (2021). Optical processes in carbon nanocolloids. *Chem* 7, 606. https://doi.org/10.1016/j.chempr.2020.11.012

Sun, Y. P., Zhou, B., Lin, Y., Wang, W., Fernando, K. A. S., Pathak, P., Meziani, M. J., Harruff B. A. , Wang, X., Wang, H., Luo, P. G., Yang, H., Kose, M. E., Chen, B. (2006). Quantum-sized carbon dots for bright and colorful photoluminescence. *J. Am. Chem. Soc*. 128, 7756. https://doi.org/10.1021/ja062677d

Sciortino, A., Mauro, N., Buscarino, G., Sciortino, L., Popescu, R., Schneider, R., Giammona, G., Gerthsen, D., Cannas, M., Messina, F. (2018). β-$C_3N_4$ Nanocrystals: Carbon Dots with Extraordinary Morphological, Structural, and Optical Homogeneity. *Chem. Mater*. 30, 1695. https://doi.org/10.1021/acs.chemmater.7b05178

Scialabba, C., Sciortino, A., Messina, F., Buscarino, G., Cannas, M., Roscigno, G., Condorelli, G., Cavallaro, G., Giammona, G., Mauro, N. (2019). Highly Homogeneous Biotinylated Carbon Nanodots: Red-Emitting Nanoheaters as Theranostic Agents toward Precision Cancer Medicine. *ACS Appl. Mater. Interf.* 11, 19584. https://doi.org/10.1021/acsami.9b04925.

Yuan, K., Qui, R., Yu, J., Li, X., Li, L., Yang, X., Yu, Z., Lu, X. Liu, H. (2020). Effects of localized surface plasmon resonance of Ag nanoparticles on luminescence of carbon dots with blue, green and yellow emission. *Appl. Surf. Sci.* 502, 144277. https://doi.org/10.1016/j.apsusc.2019.144277.

Carbon 2022

# Cellulose as a Precursor of High-Performance Energy Storage Materials in Li-S Batteries and Supercapacitors

**Marta Sevilla, Noel Díez and Antonio B. Fuertes**
Instituto de Ciencia y Tecnología del Carbono (INCAR), CSIC, Francisco Pintado Fe 26, 33011 Oviedo, Spain
Email: martasev@incar.csic.es

**Keywords**
Porous carbon, Li-S battery, supercapacitor

## INTRODUCTION

To combat global warming and environmental pollution, the electrification of transportation is essential. However, full electrification relies on accomplishing significant advances in energy storage solutions, such as rechargeable batteries and supercapacitors. In both cases, enhancement of their performance strongly relies on improvements on the materials composing the electrodes. Besides, to tackle the expected large demand of such kind of materials without further compromising the environment, improvements in the synthesis processes are also necessary.

In this work, energy storage materials targeted for Li-S batteries and supercapacitors have been developed through a versatile, green and sustainable methodology. Specifically, sulfur/carbon composites or highly porous carbons have been successfully synthesized from cellulose or cellulose acetate, respectively, by chemical activation with sodium thiosulfate by simply modifying the washing procedure used after the high-temperature treatment.

## MATERIALS SYNTHESIS

### Synthesis of sulfur/carbon composites

Cellulose or cellulose acetate was mixed with KCl and $Na_2S_2O_3$, heat-treated under $N_2$ up to 800 $^oC$ (5 $^oC$ $min^{-1}$, 1 h). The solid product was then dispersed in 5 M HCl for 8 h under stirring. Finally, the S/carbon composite was collected by filtration, washed with distilled water, and dried at 90 $^oC$. The S/carbon composites obtained from cellulose were labelled CS-x, where x = $Na_2S_2O_3$/carbon precursor weight ratio used in the synthesis. Further details can be found in (Sevilla, 2021).

### Synthesis of porous carbon

Cellulose or cellulose acetate was mixed with KCl and $Na_2S_2O_3$, and heat-treated under $N_2$ up to 800 $^oC$ (5 $^oC$ $min^{-1}$, 1 h). The solid product was then washed with distilled water and the porous carbon particles were recovered by filtration and dried at 120 $^oC$. The porous carbons obtained from cellulose were designated as C-x and those from cellulose acetate as CA-x.

## RESULTS AND DISCUSSION

The synthesis procedure for both porous carbons and S/carbon composites from two abundant, biomass-derived substances cellulose (C) and cellulose acetate (CA) is illustrated in Scheme 1. The synthesis is based on a novel, green strategy developed by our group, consisting on the $Na_2S_2O_3$ activation assisted by KCl as the reaction medium. The key for the production of highly porous carbons or S/carbon composites lies on the subsequent washing procedure (Díez, 2019; Fuertes, 2018). Thus, when a mixture of a carbon precursor, $Na_2S_2O_3$ and KCl is heat-treated under an inert atmosphere, a porous carbon embedded in a mixture of sodium sulfide/polysulfides is obtained (Scheme 1). Depending on whether we want to synthesize a porous carbon or a S/carbon composite, we should follow two different procedures: a) immersion of the reaction product in water allows the dissolution of all the inorganic impurities (KCl and $Na_2S_x$) and the recovery of the porous carbon, and

b) immersion of the reaction product in an aqueous HCl solution leads to the dissolution of the inorganic species as well as the simultaneous production of a S/carbon composite as a result of the disproportionation of the polysulfide anions (Scheme 1). By analizing the relative proportion of $Na_2S_x$ and $Na_2S$ in the carbonization products, it is found that the use of C leads to the formation of a higher amount of $Na_2S_x$ compared to CA (60 *vs.* 38 %, for the same carbon yield). Accordingly, for the same amount of $Na_2S_2O_3$ (*e.g.*, $Na_2S_2O_3$/precursor = 1.7), C enables the production of S/carbon composites with a larger sulfur fraction (62 % S *vs*. 48 % for the S/CA composite).

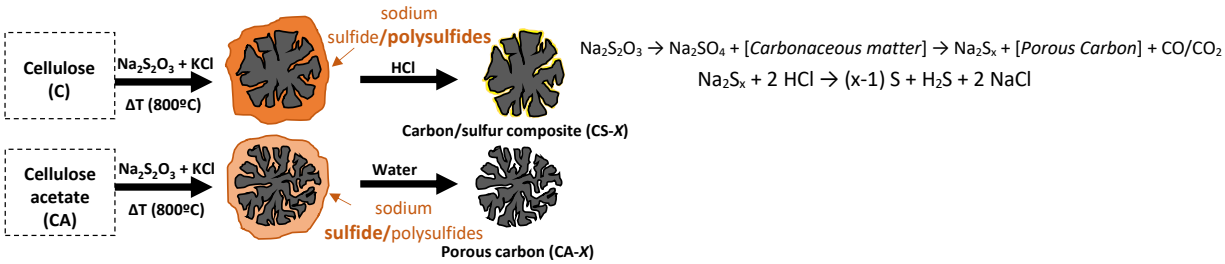


**SCHEME 1:** Synthesis strategy followed for the production of sulfur/carbon composites and porous carbons from cellulose-based materials.

## Physico-chemical properties of the cellulose-based S/carbon composites and their electrochemical performance as Li-S cathodes

S/carbon composites were successfully prepared from cellulose using different amounts of $Na_2S_2O_3$. By increasing the $Na_2S_2O_3$/cellulose weight ratio from 1.7 to 1.9, composites with S contents in the 62 to 75 wt % range are obtained, as determined by TGA (Table 1). In parallel to the introduction of elemental S inside the porous structure of the carbon, a certain amount of S atoms are also covalently bonded to the carbon framework as tiophenic moieties (determined by XPS) (Table 1). The analysis of the S/carbon composites by $N_2$ physisorption shows that S is mainly accommodated in the micropores when S = 62 %, while mesopores begin to be filled by sulfur for S $\geq$ 69 %.

These composites show a good electrochemical performance in Li-S batteries, with capacity values > 1000 mAh $g^{-1}$ S (0.1C) and still above 500 mAh $g^{-1}$ S at 2C for a S loading of 2 mg $cm^{-2}$ (Figure 1a). To evaluate the real potential of the materials, their electrochemical performance was also tested under high S loading conditions (75 % S and 5.4 mg $cm^{-2}$ S), providing a capacity of 7.4 mAh $cm^{-2}$ at 0.05C and 5.5 mAh $cm^{-2}$ at 0.2C, and still preserving 4.1 mAh $cm^{-2}$ after > 100 cycles (Figure 1b).

**TABLE 1:** Physico-chemical properties of the S/carbon composites and, in parenthesis, those of the corresponding porous carbon hosts.

| Material | Sample code | $S_{BET}$ [$m^2 \cdot g^{-1}$] | $V_p$ [$cm^3 \cdot g^{-1}$][a] | $V_{micro < 2\ nm}$ [$cm^3 \cdot g^{-1}$][b] | $S_{infiltrated}$ [wt %][c] | $S_{doped}$ [wt %][d] | Carbon yield [%] |
|---|---|---|---|---|---|---|---|
| S/carbon | CS-1.7 | 294 (2667) | 0.30 (1.87) | 0.067 (0.84) | 62 | 5.13 | 8.0 |
| | CS-1.8 | 72 (2641) | 0.08 (1.87) | 0.014 (0.84) | 69 | 6.23 | 7.1 |
| | CS-1.9 | 6 (2255) | 0.01 (1.58) | 0.002 (0.72) | 75 | 5.86 | 6.5 |

[a] Total pore volume was determined at $p/p_o$ ~0.95. [b] Volume of micropores was calculated by using the QSDFT pore size distribution. [c] Determined by TGA. [d] Percentage of S attached to the carbon framework, determined once the infiltrated S has been removed by elemental analysis.

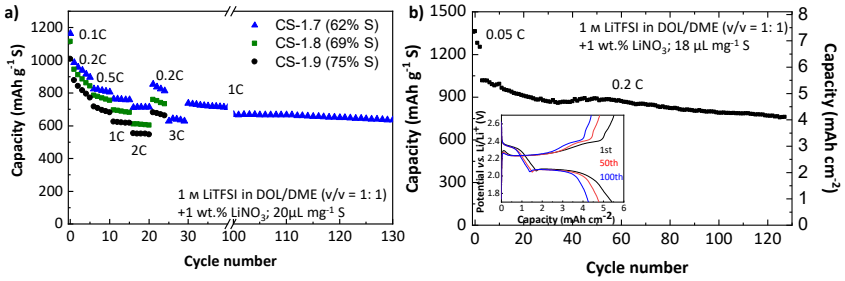


**FIGURE 1:** a) C-rate capability of the different cellulose-based S/carbon composites, b) long-term cycling stability at 0.2 C of CS-1.9 (inset: voltage profiles at different cycles at 0.2C).

**Physico-chemical properties of the cellulose acetate-derived porous carbons and their supercapacitor performance in ionic liquid electrolyte**

Even though cellulose acetate may not be a good precursor for the production of sulfur/carbon composites with high sulfur content, it is, however, an excellent precursor for the production of highly porous carbons with a micro–mesoporous structure (Figure 2a) and good electronic conductivity (Table 2).

**TABLE 2:** Physico-chemical properties of the porous carbons obtained from cellulose acetate.

| Sample code | $S_{BET}$ [$m^2 \cdot g^{-1}$] | $V_p$ [$cm^3 \cdot g^{-1}$] | $V_{micro < 2\ nm}$ [$cm^3 \cdot g^{-1}$] | $S_{doped}$ [wt%] | Carbon yield [%] | Electronic conductivity @ 7.1 MPa [S $cm^{-1}$] |
|---|---|---|---|---|---|---|
| CA-1 | 2484 | 1.26 | 0.96 | 0.36 | 13.5 | 5.8 |
| CA-1.5 | 2843 | 1.80 | 0.99 | 1.74 | 9.3 | 5.1 |
| CA-1.7 | 2570 | 1.73 | 0.88 | 4.24 | 7.9 | n.d. |

These porous carbons exhibit high capacitance values (Figure 2b) in EMImTFSI, good long-term stability (3 % capacitance loss after 8000 cycles at 3 A $g^{-1}$ and an additional 5 % after 75 h at 3 V), and low self-discharge (80 % of its voltage is kept after almost one day at open circuit). Figure 2c shows the Ragone plot of the supercapacitors. At low power, they can store up to ~50 Wh $kg^{-1}$ *vs.* 37-39 Wh $kg^{-1}$ stored using the conventional organic electrolyte $TEABF_4$/acetonitrile (cell voltage = 2.7 V).

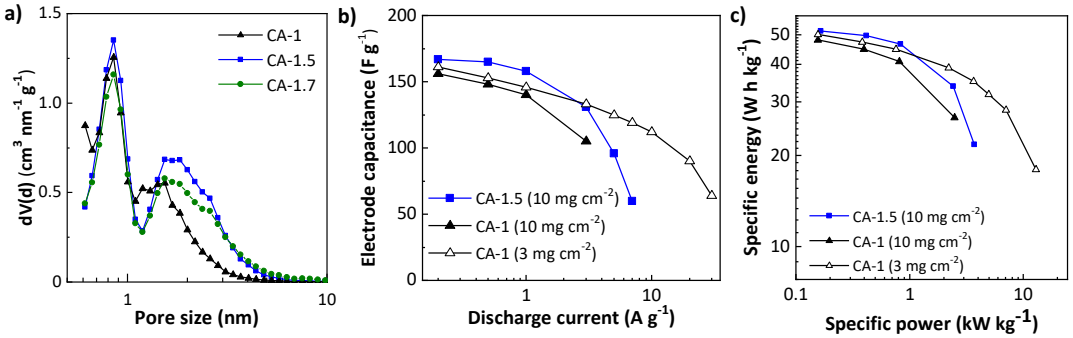


**FIGURE 2:** a) QSDFT pore size distribution, b) rate capability and c) Ragone plot of the porous carbons.

## CONCLUSIONS

Thiosulfate activation is a versatile process that allows the production of S/carbon composites or porous carbons depending on the washing procedure used after the high temperature treatment. The selection of an appropriate carbon precursor is key to synthesize highly porous carbons and to achieve composites with high S content at reasonable product yield and chemical reagents consumption. Cellulose has proven to be a good precursor for the production of S/carbon composites with a S content >60 wt% and a good electrochemical performance in Li-S batteries. Meanwhile, cellulose acetate has allowed the synthesis of highly micro-mesoporous carbons with a good and robust electrochemical performance as electrodes in ionic liquid-based supercapacitors.


### Acknowledgements

This research work was supported by projects RTI2018-093712-B-I00 (MCIU/AEI/FEDER, UE) and IDI/2018/000148 (regional GRUPIN2018).


### References


Díez, N., Ferrero, G.A., Sevilla, M. and Fuertes, A.B. (2019). A simple and general approach for *in situ* synthesis of sulfur–porous carbon composites for lithium–sulfur batteries. *Sustain. Energy Fuels.*, 3, 3498–3509. https://doi.org/10.1039/C9SE00722A

Fuertes, A.B., Ferrero, G.A., Diez, N. , Sevilla, M. (2018). A green route to high-surface area carbons by chemical activation of biomass-based products with sodium thiosulfate. *ACS Sustain. Chem. Eng.*, 6, 16323–16331. https://doi.org/10.1021/acssuschemeng.8b03264

Sevilla, M, Díez, N and Fuertes, A. B (2021). Cellulose as a precursor of high-performance energy storage materials in Li–S batteries and supercapacitors. *Energy Technol.*, 2100268. https://doi.org/10.1002/ente.202100268

Carbon 2022

# Effect of Solvent Component on the Anisotropic Texture and Mechanical Properties of Spinnable Mesophase Pitch

**Hiroki Shimanoe[1], Takashi Mashio[2], Taisei Tomaru[2], Young-Pyo Jeon[3], Koji Nakabayashi[1, 2], Jin Miyawaki[1, 2] and Seong-Ho Yoon[1, 2]**

[1]Institute for Materials Chemistry and Engineering, Kyushu University, Kasuga, 816-8580 Fukuoka, JAPAN

Email: h.shimanoe@cm.kyushu-u.ac.jp

[2]Interdisciplinary Graduate School of Engineering Science, Kyushu University, Kasuga, 816-8580 Fukuoka, JAPAN

[3]Center for C-Industry Incubation Korea Research Institute of Chemical Technology (KRICT), Daejeon, 34114, KOREA

**Keywords**

Lyotropic liquid crystal, Mesophase pitch, Solvent component

## INTRODUCTION

Spinnable mesophase pitches (SMPs) are known to be composed of mesogenic and solvent components. In our laboratory, SMPs, which were prepared by heat-treating mixtures of such mesogenic and solvent components in various ratios, have been examined by X-ray diffraction and polarized light microscopy (POM) to investigate the lyotropic liquid crystal properties of SMPs (Shimanoe, 2022). The results showed that, when the concentration ratio of the mesogenic/ solvent components was above the threshold, SMP was always 100 vol% anisotropic texture in both the solid and molten states, and the number of stacked (002) sheets was equal or greater than that of the mesogenic component. However, in order to understand the lyotropic liquid crystal properties of SMPs, it is necessary to investigate not only the correlation about the anisotropic texture and molecular stacking property of SMP the but also the nature and role of mesogenic and solvent components in detail. In this study, we focused on the solvent component of SMP. The effects of the molecular structure and molecular weight of the solvent components on the optical anisotropy of SMPs and on the graphitic and mechanical properties of the derived carbon fibers were investigated.

## METHODOLOGY

Tetrahydrofuran insoluble fraction (AR-THFI) prepared by fractionation of AR pitch, a naphthalene-derived SMP (Mochida, 1990), with THF at 50°C, was assumed to be the mesogenic component. Isotropic pitches derived from slurry oil (SO) and coal tar pitch (CTP) were prepared by distillation at 370°C for 3 h in an Ar atmosphere, followed by a thin-layer evaporation to adjust the softening point to 140°C and 180°C (SO140, CTP140 and CTP180). SMPs were then obtained by mixing AR-THFI and the prepared isotropic pitches at weight ratios of 7/3, 6/4, 5/5, and 4/6, and heat treatment at 350°C for 30 min in an $N_2$ atmosphere with stirring.

After melt spinning of the obtained pitch using a mono-hole melt-spinning apparatus, the mesophase pitch fibers were stabilized at 270°C without a holding time in an air atmosphere. The heating rate was 0.5°C/min. The stabilized fibers were carbonized at 1000°C for 30 min under vacuum, and the carbonized fibers were further graphitized at 2800°C for 10 min in an Ar atmosphere. The mechanical properties of the obtained fibers were measured according to the JIS R 7606:2000 method.

## RESULTS AND DISCUSSION

FIGURE 1 shows POM images of AR-THFI/SO140 (6/4), AR-THFI/CTP140 (6/4 and 4/6) and AR-THFI/CTP180 (4/6). AR-THFI/SO140 (6/4) had an anisotropic flow structure and an isotropic structure that contained many small anisotropic spheres. This indicates that the aromatic hydrocarbon component of SO140 allowed AR-THFI to be dispersed at high temperature but was incompatible with AR-THFI. On the other hand, AR-THFI/CTP140 (6/4) showed 100 vol% anisotropic texture. CTP140 had a broad molecular weight distribution and also contained various kinds of aromatic hydrocarbons. AR-THFI dissolved sufficiently in these hydrocarbons when melted at high temperature. Thus, AR-THFI/CTP140 (6/4) showed full anisotropy. Increasing the amount of CTP140, the matrix texture ultimately became isotropic (FIGURE 1(c)). However, AR-THFI/CTP180 showed over 90 vol% anisotropic texture even at the same mixing ratio of 4/6 (FIGURE 1(d)). CTP140 had larger variety and quantity of low molecular weight species than CTP180, and AR-THFI exhibited high dispersibility and solubility in the molten CTP140 at high temperature, forming anisotropic spheres. Thus, the differences in the solvent components affect the dispersion and solubility of mesogenic components. Based on the results, the molecular weight and molecular structure of solvent components affected the degree of development of anisotropic texture. The graphitic and mechanical properties of the carbon fibers derived from the prepared SMPs were compared with those of AR pitch-based carbon fiber (TABLE 1). Both carbon fibers showed comparable values. The graphitic and mechanical properties might be influenced by the mesogenic component.

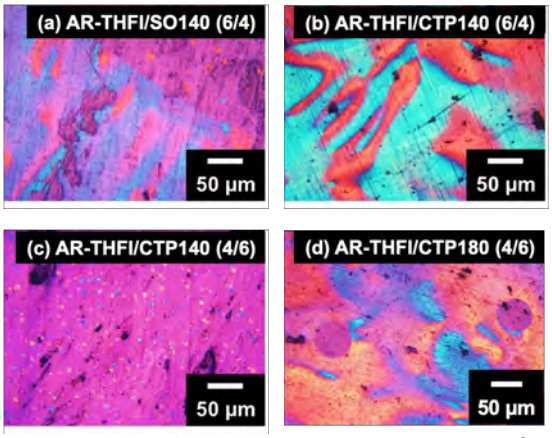


**FIGURE 1**: Polarized microscope images of pitches. (a) AR-THFI/SO140 (6/4), AR-THFI/CTP140 ((b) 6/4 and (c) 4/6) and (d) AR-THFI/CTP180 (4/6).

**TABLE 1**: The mechanical and graphitic properties of graphitized fibers of AR pitch and AR-THFI/CTP180 (4/6).

| | Diameter [μm] | Tensile strength [GPa] | Elongation ratio [%] | Young's modulus [GPa] | $d_{002}$ [nm] | Lc [nm] |
|---|---|---|---|---|---|---|
| AR pitch | 13.7±0.5 | 2.6±0.4 | 0.6±0.1 | 450±50 | 0.337 | 28.72 |
| AR-THFI/CTP180(4/6) | 14.0±1.0 | 2.7±0.3 | 0.6±0.1 | 470±70 | 0.338 | 24.04 |

## CONCLUSIONS

A CTP-derived isotropic pitch showed better solvent performance than a SO-derived in terms of anisotropic texture. An isotropic pitch which had many various kinds of aromatic hydrocarbons including polycyclic aromatic carbons was suitable as a solvent component. The molecular weight and structure of solvent component did not affect on the graphitic and mechanical properties.


### Acknowledgements

This work was supported by the JSPS KAKENHI grant number 20K15321 and the Technology Innovation Program (10082582; Development of petroleum-based high-quality MP and high-yield MP for premium carbon materials) funded by the Ministry of Trade, Industry, and Energy (MOTIE, Korea).


### References


Shimanoe H., Mashio T., Nakashima H., Ko S., Jeon Y.-P., Nakabayashi K., Miyawaki J. and Yoon S.-H. (2022). Correlation between molecular stacking and anisotropic texture in spinnable mesophase pitch. *Carbon*, 192, 395-404. https://doi.org/10.1016/j.carbon.2022.02.062

Mochida I., Shimizu K., Korai Y., Otsuka H., Sakai Y. and Fujiyama S. (1990). Preparation of mesophase pitch from aromatic hydrocarbons by the aid of HF/$BF_3$. *Carbon*, 28(2-3), 311-319. https://doi.org/10.1016/0008-6223(90)90005-J

Carbon 2022

# Correlation between the Anisotropic Texture and the Molecular Stacking Property in Spinnable Mesophase Pitch

**Hiroki Shimanoe[1], Takashi Mashio[2], Young-Pyo Jeon[3], Koji Nakabayashi[1, 2], Jin Miyawaki[1, 2] and Seong-Ho Yoon[1, 2]**

[1]Institute for Materials Chemistry and Engineering, Kyushu University, Kasuga, 816-8580 Fukuoka, JAPAN

Email: h.shimanoe@cm.kyushu-u.ac.jp

[2]Interdisciplinary Graduate School of Engineering Science, Kyushu University, Kasuga, 816-8580 Fukuoka, JAPAN

[3]Center for C-Industry Incubation Korea Research Institute of Chemical Technology (KRICT), Daejeon, 34114, KOREA

**Keywords**

Lyotropic liquid crystal, Mesogenic component, Mesophase pitch

**NOTICE**

This work was published in Carbon journal (Shimanoe, 2022).

## INTRODUCTION

Spinnable mesophase pitch (SMP) is a material that has the properties of lyotropic liquid crystals but has a molecular composition that differs from that of typical lyotropic liquid crystal materials. SMP is composed of both mesogenic and solvent components as same as typical lyotropic liquid crystals. Mesogenic and solvent components in SMP have similar molecular structures, but the molecular weight of mesogenic component is larger. The occurrence and shape of anisotropic texture in SMP depend on the ratio of solvent to mesogenic components. Soap, one of the typical lyotropic liquid crystals, has two specific molecules with two different functions, hydrophilic and lipophilic, in one molecule. On the other hand, SMP does not have two different functions in one molecule, but is composed of relatively planar molecules that can be easily stacked in the (002) direction. In other words, SMPs are not micelles, but exhibit similar molecular assemblies with soap molecules. So far, however, the correlation between molecular stacking and optical anisotropy texture has not been precisely understood. Therefore, in this study, we attempted to clarify the correlation between molecular stacking and optical anisotropy texture by researching the lyotropic liquid crystal properties of AR pitch, a SMP derived from naphthalene (Mochida, 1990), with changing the mesogenic/solvent components ratio.

## METHODOLOGY

AR pitch was solvent-fractionated with tetrahydrofuran (THF) at 50℃, and the THF-insoluble and the THF-soluble fractions of AR pitch were assumed as a mesogenic component (AR-THFI) and a solvent component (AR-THFS), respectively. AR-THFI/AR-THFS mixtures were prepared at various weight ratios, and the sample was measured with X-ray diffraction (XRD) calculation of interlayer spacing ($d_{002}$), molecular stacking height ($L_c$ (002)) and the number of molecular sheets using the Bragg and Scherrer equations and equation (1), respectively.

$$\text{Number of sheets} = \left(\frac{L_c(002)}{d_{002}}\right) + 1 \qquad (1)$$

The correlation between anisotropic structure and (002) molecular stacking properties was examined from the measured anisotropic content, $d_{002}$, $L_c$ (002) and the number of molecular sheets.

## RESULTS AND DISCUSSION

FIGUREs 1 and 2 show the number of stacking sheets and anisotropic texture of various AR-THFI/AR-THFS mixtures under room and high temperature conditions, respectively. Except for AR-THFS, all samples showed a decrease in the number of stacking sheets at higher temperatures. Polarized microscopy revealed that, with increasing the sample temperature, the anisotropic texture decreased and the pitch became isotropic. These changes are attributed to the increase in solubility of AR-THFI in AR-THFS with increasing temperature. If the concentration ratio of the mesogenic and solvent components exceeded a threshold value (*e.g.* AR-THFI/AR-THFS = 6/4, in this system), the number of molecular stacks in the (002) direction was equal to or greater than that of the mesogenic component and the isotropic pitch changed to 100 vol% anisotropic pitch.

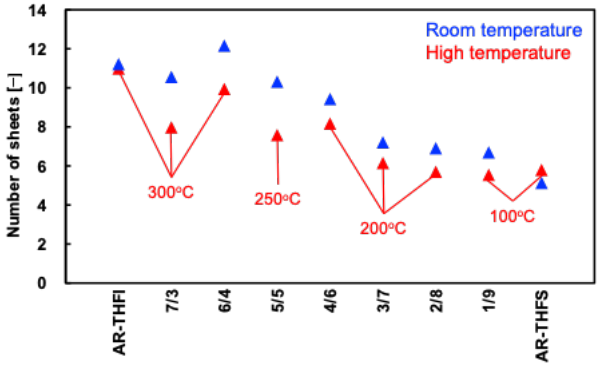


**FIGURE 1**: Number of stacked sheets of pitches derived from various AR-THFI/AR-THFS mixtures at room and high temperature conditions (Shimanoe, 2022).

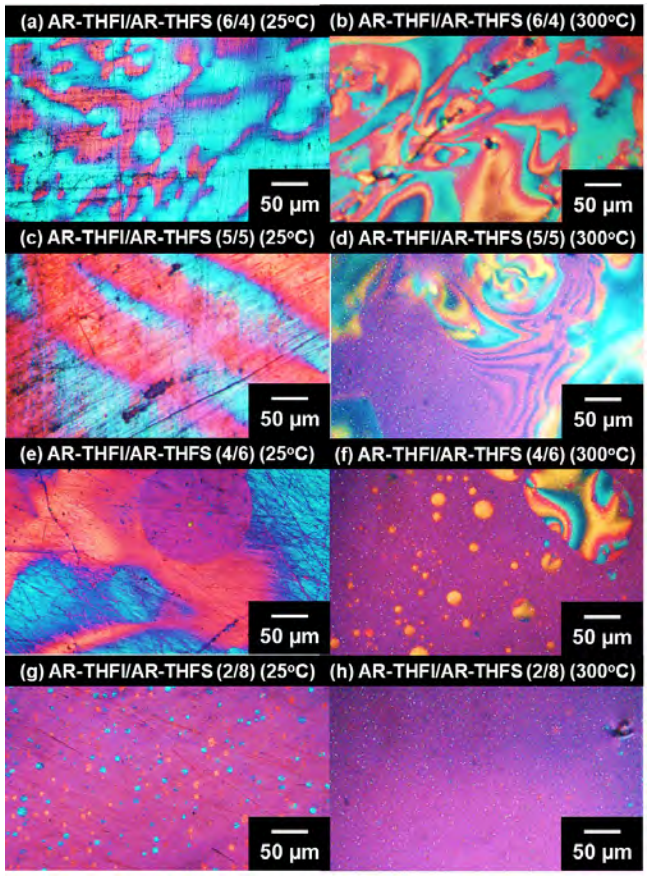


**FIGURE 2**: Polarized microscope images of pitches derived from various AR-THFI/AR-THFS mixtures at room temperature and in the melted state. AR-THFI/AR-THFS = 6/4 (w/w) at (a) 25°C and (b) 300°C, AR-THFI/AR-THFS = 5/5 (w/w) at (c) 25°C and (d) 300°C, AR-THFI/AR-THFS = 4/6 (w/w) at (e) 25°C and (f) 300°C, and AR-THFI/AR-THFS = 2/8 (w/w) at (g) 25°C and (h) 300°C (Shimanoe, 2022).

## CONCLUSIONS

When the concentration ratio of the mesogenic/ solvent components was above the threshold, SMP was always 100 vol% anisotropic texture in both the solid and molten states, and the number of stacked (002) sheets was equal or greater than that of the mesogenic component.


### Acknowledgements

This work was supported by the JSPS KAKENHI grant number 20K15321 and the Technology Innovation Program (10082582; Development of petroleum-based high-quality MP and high-yield MP for premium carbon materials) funded by the Ministry of Trade, Industry, and Energy (MOTIE, Korea).


### References


Shimanoe H., Mashio T., Nakashima H., Ko S., Jeon Y.-P., Nakabayashi K., Miyawaki J. and Yoon S.-H. (2022). Correlation between molecular stacking and anisotropic texture in spinnable mesophase pitch. *Carbon*, 192, 395-404. https://doi.org/10.1016/j.carbon.2022.02.062

Mochida I., Shimizu K., Korai Y., Otsuka H., Sakai Y. and Fujiyama S. (1990). Preparation of mesophase pitch from aromatic hydrocarbons by the aid of HF/$BF_3$. *Carbon*, 28(2-3), 311-319. https://doi.org/10.1016/0008-6223(90)90005-J

Carbon 2022

# Investigation of Stabilization Conditions on the Properties of Petroleum-derived Mesophase Pitch Carbon Fibers

**Priscila Sieira[1] [2]*, Caroline Guimarães[2], Arthur Braga[2], Maria Helena Pereira[2] and Luiz E. P. Borges[1]**
[1]*Seção de Química, Instituto Militar de Engenharia, Rio de Janeiro, Brasil*
[2]*Seção de Tecnologia de Materiais de Carbono, Centro Tecnológico do Exército, Rio de Janeiro, Brasil*

*Email: sieira.priscilla@ime.eb.br

**Keywords**
Petroleum pitch, pitch carbon fibers, carbon fibers stabilization.

## INTRODUCTION

The automotive industry's demand for carbon fibers has been growing in recent years. The required tensile strength of 1.72 GPa and tensile modulus of 172 GPa are lower than the properties achieved by several PAN-based carbon fibers. The current limitation in expanding the usage of those carbon fibers to structural automotive components is the high cost of PAN-derived fibers (Guo *et al*., 2020). On that concern, efforts on reducing the prices of carbon fibers have been the focus of many studies (Guo *et al*., 2020; Le *et al*., 2022; Peng *et al*., 2021; Saad *et al*., 2022; Shimanoe *et al*., 2019; Shimanoe *et al*., 2020). Two main approaches are commonly observed in those studies: reducing the cost of the final product by improving the manufacturing process or changing the precursor to a low-cost alternative. Pitch derived from heavy petroleum byproducts are cheaper precursors that represent a potential alternative to produce competitive lower-cost carbon fibers that meet those mechanical requirements.

Carbon fibers produced from petroleum pitches follow a continuous process that starts on the melt-spinning of the precursor and passes through stabilization and carbonization steps. Extruded filaments are led to the thermal treatments where their microstructures are perfected. The stabilization process transforms the green filament to a thermosetting material by creating oxygen bonds between the parallel graphene sheets. The stabilization is a cost and time-consuming part of the production (Shimanoe et al., 2020). Hence, stabilization conditions must be carefully planned to allow the fibers to undergo the carbonization step without compromising their structures. Tensile strength is very sensitive to cracks and voids that may happen if stabilization is performed inefficiently. The goal of this study is to investigate the effect of different stabilization conditions on the mechanical properties of the carbon fibers produced.

## MATERIALS AND METHODS

Petroleum-derived mesophase pitch filaments of 24.85±2.18 µm of diameter were used to test different stabilization conditions. The analyzed variables were the final temperature and the time held at that final stabilization temperature. The heating rate was initially set as 0.5°C/min. All filaments were carbonized at 1500°C. Tensile strength and modulus were obtained in a mechanical analysis equipment (LEX 810, Dia-stron) with a gauge length of 20 mm. The average of 15 tests with an error of less than 15% was adopted for each experiment. The diameters of the broken fibers were observed in a scanning electron microscope (SUPRA 40, ZEISS). Two experiments were added to the investigation: the first was done at a higher heating rate to minimize the stabilization time, while the second was the confirmation of those parameters in a sample of green filaments of smaller diameters.

**RESULTS AND DISCUSSION**

The experimental data of the tensile strength based on the stabilization parameters for green filaments of approximately 25µm is shown in table 1.

**TABLE 1**: Carbon Fibers produced with different stabilization conditions

| Exp n° | Temperature (°C) | Time (min) | Fiber diameter (µm) | Tensile Strength (GPa) |
|---|---|---|---|---|
| 1 | 265 | 130 | 21.78 ±1.06 | 1.12 ±0.23 |
| 2 | 265 | 230 | 19.41 ±1.32 | 1.29 ±0.12 |
| 3 | 312 | 180 | 20.18 ±1.75 | 1.03 ±0.16 |
| 4 | 312 | 80 | 21.88 ±1.44 | 1.01 ±0.11 |
| 5 | 265 | 30 | 21.61 ±1.52 | 1.26 ±0.18 |
| 6 | 218 | 80 | 19.98 ±1.90 | 1.47 ±0.22 |
| 7 | 218 | 180 | 21.51 ±2.01 | 1.28 ±0.12 |

Higher temperatures and slower rates are commonly used in stabilizations where the diffusion of oxygen is the controlling parameter. However, the results obtained in the experiments point towards the lower level of both time and temperature as better conditions. There is a chance that the exothermic nature of the reactions between oxygen and the carbon molecules are causing damage to the filament structure in the longer experiments. Probably, due to the low heating rate of 0.5°C/min, the total time of oxygen exposition might be more than enough to those filaments.

Experiment 6, that provided the higher response, was the shortest. An 8th experiment was performed with a heating rate of 5°C/min to 265°C with a total time of half of the experiment 6. The resulting fiber supported 1.43 ±0.12 GPa. The mean tensile strength obtained in those experiments are not statistically different from each other at a 99% level. That same stabilization condition was used in the 9th experiment with filaments under 20 µm. Figure 1 shows the radial microstructure of representative fibers from experiments 6 and 8.


**FIGURE 1**: Fibers from experiment 6 (left) and 8 (right)

Fibers from those experiments underwent a significant shrinkage between 20 and 25% from the precursor green filaments. Experiment 9 reached average tensile strength and modulus of 1.60 ±0.21 GPa and 170 ±19 GPa, respectively. The fibers filaments show radial alignment of the graphene sheets. There are no significant differences across the cross-section of those fibers and no visual evidence of defects introduced to their structures. Further carbonization and/or graphitization of fibers 6, 8 and 9 are expected to enhance the mechanical properties of the final fibers.

## CONCLUSIONS

Low-cost heavy fractions of petroleum can be used as a raw material to carbon fiber precursors mesophase pitches. In order to guarantee compatibility with the continuous process and that the process itself does not introduce excessive costs to the product, the stabilization of those pitch filaments must be carefully designed. In this work, the effect of time, temperature and temperature rate were explored over eight stabilization experiments. The best experiment produced fibers that reached tensile strengths of 1.60 GPa and modulus of 170 GPa, showing that petroleum mesophase pitches are promising precursors as its derived carbon fibers can potentially meet the desired properties and costs demanded by the automotive industry.

**Acknowledgements**

The authors thank the *Centro Tecnológico do Exército* and the *Instituto Militar de Engenharia*. The authors are indebted to CAPES and FAPERJ for the financial support to the *Instituto Militar de Engenharia*.

**References**

Guo, J., Li, X., Xu, H., Zhu, H., Li, B., Westwood, A., 2020. Molecular Structure Control in Mesophase Pitch via Co-Carbonization of Coal Tar Pitch and Petroleum Pitch for Production of Carbon Fibers with Both High Mechanical Properties and Thermal Conductivity. Energy & Fuels 34, 6474–6482. https://doi.org/10.1021/acs.energyfuels.0c00196

Le, N.D., Trogen, M., Varley, R.J., Hummel, M., Byrne, N., 2022. Chemically Accelerated Stabilization of a Cellulose-Lignin Precursor as a Route to High Yield Carbon Fiber Production. Biomacromolecules 23, 839–846. https://doi.org/10.1021/acs.biomac.1c01226

Peng, Y., Tan, R., Liu, Y., Yang, J., Li, Y., Li, J., Fan, Z., Shi, K., 2021. Mesophase pitch-based carbon fibers: Accelerated stabilization of pitch fibers under effective plasma irradiation-assisted modification. Materials (Basel). 14. https://doi.org/10.3390/ma14216382

Saad, S., Zeraati, A.S., Roy, S., Shahriar Rahman Saadi, M.A., Radović, J.R., Rajeev, A., Miller, K.A., Bhattacharyya, S., Larter, S.R., Natale, G., Sundararaj, U., Ajayan, P.M., Rahman, M.M., Kibria, M.G., 2022. Transformation of petroleum asphaltenes to carbon fibers. Carbon 190, 92–103. https://doi.org/10.1016/j.carbon.2022.01.011

Shimanoe, H., Ko, S., Jeon, Y.P., Nakabayashi, K., Miyawaki, J., Yoon, S.H., 2019. Shortening stabilization time using pressurized air flow in manufacturing mesophase pitch-based carbon fiber. Polymers (Basel). 11. https://doi.org/10.3390/polym11121911

Shimanoe, H., Mashio, T., Nakabayashi, K., Inoue, T., Hamaguchi, M., Miyawaki, J., Mochida, I., Yoon, S.-H., 2020. Manufacturing spinnable mesophase pitch using direct coal extracted fraction and its derived mesophase pitch based carbon fiber. Carbon 158, 922–929. https://doi.org/https://doi.org/10.1016/j.carbon.2019.11.082

# Graphene-based catalysts for water splitting technology

**Malgorzata Skorupska[1,*], Anna Ilnicka[1], Magdalena Tyc[1], Kinga Kowalska[1], Mariusz Szkoda[2,3], Jerzy P. Lukaszewicz[1,4]**

[1] Faculty of Chemistry, Nicolaus Copernicus University in Torun, Gagarina 7, 87-100 Torun, Poland

[2] Faculty of Chemistry, Department of Chemistry and Technology of Functional Materials, Gdańsk University of Technology, Narutowicza 11/12, 80-233 Gdańsk, Poland

[3] Advanced Materials Center, Gdańsk University of Technology, Narutowicza 11/12, 80-233 Gdańsk, Poland

[4] Centre for Modern Interdisciplinary Technologies, Nicolaus Copernicus University in Torun, Wilenska 4, 87-100 Torun, Poland

* m.skorupska@doktorant.umk.pl

## Introduction

Electrocatalytic water splitting driven by a renewable energy input used to produce clean $H_2$ has been widely viewed as a promising strategy of a future energy portfolio. Currently, the state-of-the-art electrocatalysts for water splitting in acidic solutions are $IrO_2$ or $RuO_2$ for the $O_2$ evolution reaction (OER), and Pt for the $H_2$ evolution reaction (HER). However, the realization of large-scale $H_2$ production from water splitting requires competent nonprecious electrocatalysts. The rational design of photocatalysts for efficient water splitting should employ hybrid systems.

The aim of the research was to propose an innovative synthesis of hybrid materials with graphene. The particular aim of this work was to establish effective synthesis conditions, including (a) the type of graphene materials, (b) the way to combine oxides of manganese, cobalt, cerium, or nickel with the previously prepared graphene material, (c) or the amount of the nitrogen-precursor (N-doping causes an increase in the electrocatalytic activity of the obtained materials).

## Materials and Methods

The research involves the preparation of hybrids which perform beneficially in OER and HER reactions using porous graphene material obtained either from commercial low-quality graphene or from natural porous carbon materials and carbon-embedded metal oxides. Two routes of synthesis were used to deposit oxide particles of appropriate metals: manganese (Mn), cobalt (Co), nickel (Ni), or cerium (Ce). One is based on the addition of carbon material at the stage of synthesizing appropriate components consisting of the metals above, while the other consists of mechanically mixing the obtained mixture of metal oxides with graphene. Afterwards, the materials undergo calcination at two temperatures of 500°C and 900°C in an inert gas flow.

Hybrid samples of graphene and metal oxides were characterized with XPS, SEM/EDX, HRTEM, and XRD analyses. The identification of the most electrocatalytically active electrodes was performed in electrochemical studies of OER and HER reactions in KOH and $H_2SO_4$ aqueous electrolytes.

## Results and Discussion

The morphology of the obtained hybrid materials was determined by scanning electron microscope analysis. Figure 1 shows the obtained materials at two different temperatures; figures 1a, 1b consist of distinct metal oxide structures uniformly dispersed on the graphene layer, carbonized at 500°C; figures 1c, 1d show the hybrid carbonized at 900°C, where clumped transition metal oxides are also uniformly dispersed on the carbon structure.

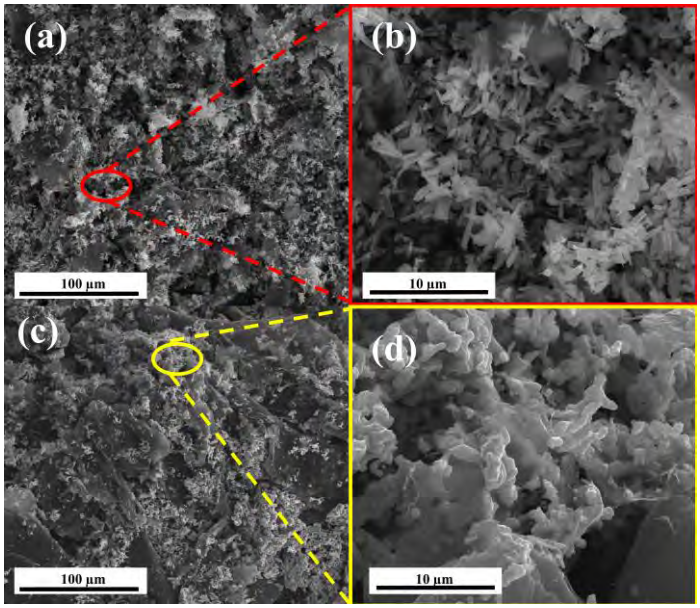


**Figure 1. SEM images of (a, b) GN-1-500, (c, d) GN-1-900.**

X-ray diffraction patterns (Figure 2a) show that the materials obtained at two different temperatures contain $Co_2MnO_4$. For samples GN-1-500 and GN-1-900, a cubic spinel structure was observed. The Bragg peaks at 111, 220, 311, 222, 400, 422, 333, 440 were assigned to $Co_2MnO_4$. An additional prominent peak located at about the angular value of 28° comes from graphene multilayer structures. The HER and OER studies presented in Figures 2b, 2c show the achieved overpotential required to reach a current density of 10 mA $cm^{-2}$, which is a key parameter in evaluating effective catalysts. The apparent improvement in the overpotential for the hybrids is evidence that the materials, when combined with graphene, show improved performance in HER and OER. Graphene achieves excellent conductivity at high temperatures, therefore a high carbonization temperature (900°C) is required to improve its activity.

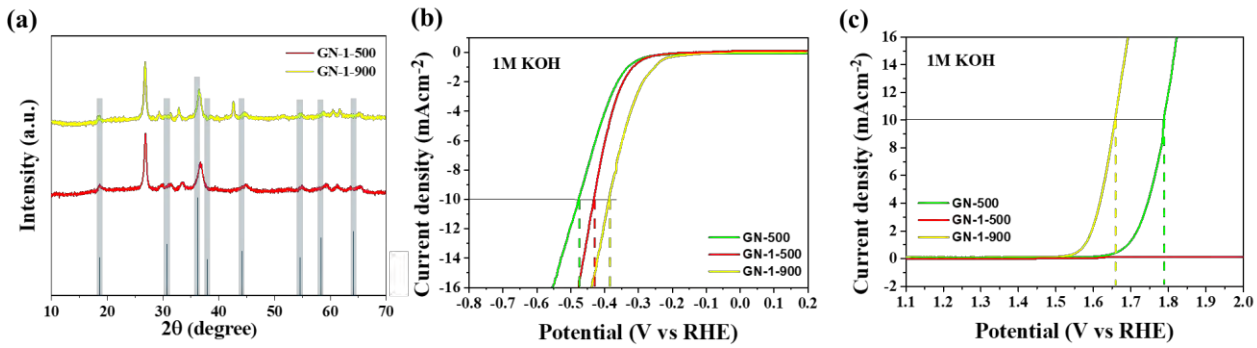


**Figure 2.** (a) X-ray diffraction spectra of GN-1-500 and GN-1-900; (b) Polarization curves for HER of samples: GN-500, GN-1-500, and GN-1-900 in 1M KOH with a scan rate of 1 mV $s^{-1}$; (c) Polarization curves for OER of samples: GN-500, GN-1-500, and GN-1-900 in 1M KOH with a scan rate of 1 mV $s^{-1}$.

## Conclusions

The obtained $Co_2MnO_4$ spinel structures on graphene were tested in HER and OER reactions, showing favourable properties for applications as electrodes for water splitting devices. The proposed preparation method leads to the efficient agglomeration of $Co_2MnO_4$ structures on carbon layers, thus improving conductivity. The obtained hybrids can successfully be used as electrocatalysts for effective green hydrogen production.

## Acknowledgment

This work was carried out as a result of the research project no. NOR/SGS/IL-HYDROGEN/0202/2020-00 financed by the National Centre for Research and Development, Poland.

# Modification of $TiO_2$ nanotubes by strontium and cobalt molybdate perovskite for efficient hydrogen evolution reaction in acid and alkaline media

**Malgorzata Skorupska[1,*], Mariusz Szkoda[2, 3], Anna Ilnicka[1], Jerzy P. Lukaszewicz[1,4]**

[1] Faculty of Chemistry, Nicolaus Copernicus University in Torun, Gagarina 7, 87-100 Torun, Poland

[2] Faculty of Chemistry, Department of Chemistry and Technology of Functional Materials, Gdańsk University of Technology, Narutowicza 11/12, 80-233 Gdańsk, Poland

[3] Advanced Materials Center, Gdańsk University of Technology, Narutowicza 11/12, 80-233 Gdańsk, Poland

[4] Centre for Modern Interdisciplinary Technologies, Nicolaus Copernicus University in Torun, Wilenska 4, 87-100 Torun, Poland

* m.skorupska@doktorant.umk.pl

## Introduction

Hydrogen is considered the most appropriate green energy source and water splitting (by electrochemical methods) is one of the effective ways for high purity $H_2$ production. To realize efficient production of hydrogen by means of such a technique, highly catalytic materials for hydrogen evolution reaction (HER) are usually required. One of them is platinum, but due to its high price, Pt as well as other precious metal catalysts cannot be used widely.

## Materials and Methods

Herein, we demonstrate that modification of $TiO_2$ nanotubes with strontium and cobalt molybdate perovskite can turn them into active electrocatalysts for HER. For this purpose, a simple method of hydrothermal synthesis of perovskites was developed directly on the $TiO_2$ nanotubes substrate. The obtained materials were characterized by transmission electron microscopy (TEM), scanning electron microscopy (SEM), Raman spectroscopy, X-ray diffraction analysis (XRD), and X-ray photoelectron spectroscopy (XPS). Catalytic properties were verified by electrochemical methods (linear voltammetry, chronopotentiometry). The obtained hybrids were characterized by much better catalytic properties towards hydrogen evolution reaction compared to $TiO_2$ and slightly worse than platinum.

## Results and Discussion

The detailed structural and morphological properties of the obtained materials were characterized by SEM analysis. Figure 1 exhibited the formation of porous morphology.

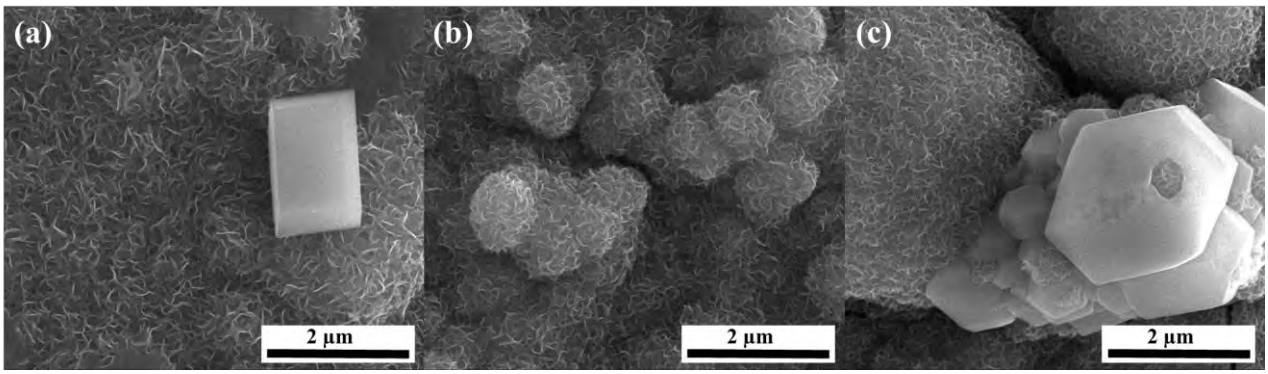


**Figure 1.** SEM images of samples: (a) $TiO_2/SrMoO_4$, (b) $TiO_2/CoMoO_4$, (c) $TiO_2/SrMoO_4/CoMoO_4$.

The X-ray diffraction patterns were reported to investigate the crystal structures and phase formation process of the synthesized materials. As displayed in Figure 2, all samples consist of $TiO_2$ and mainly incorporated $MoS_2$, $CoMoS_2$, or $SrMoO_4$.

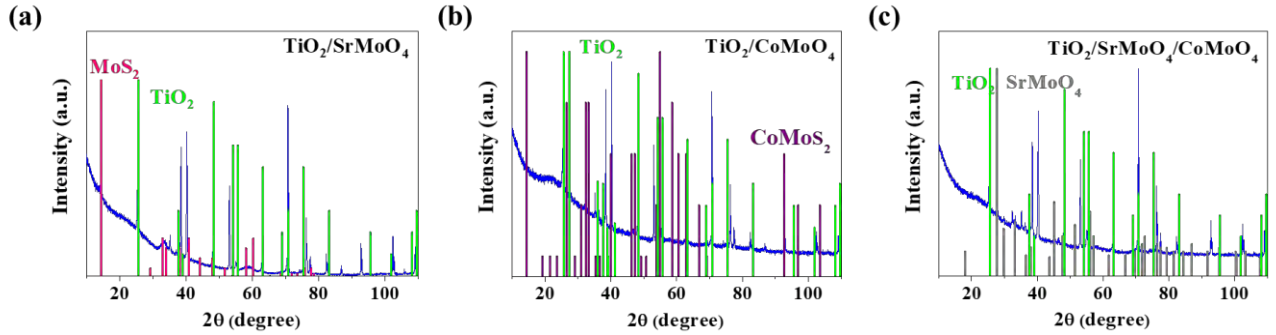


**Figure 2.** X-ray diffraction spectra of samples: (a) $TiO_2/SrMoO_4$, (b) $TiO_2/CoMoO_4$, (c) $TiO_2/SrMoO_4/CoMoO_4$.

The electrochemical HER performance of pristine Pt, $TiO_2$, and synthesized modified $TiO_2$ were examined by linear sweep voltammetry (LSV), Tafel-equation-based electrochemical analysis, and chronoamperometry in an acidic (0.2 M $H_2SO_4$) electrolyte. As illustrated in Figure 3a, the bare $TiO_2$ used in the test has negligible electrocatalytic activity. Other the obtained compounds are characterized by good electrochemical activity towards hydrogen evolution. For comparison, the platinum electrode was also presented (the best catalyst for HER). However, as can be seen, the composite $TiO_2/SrMoO_4/CoMoO_4$ shows the best electrocatalytic results while maintaining very good stability (Figure 3b) and is characterized by a low Tafel slope (Figure 3c).

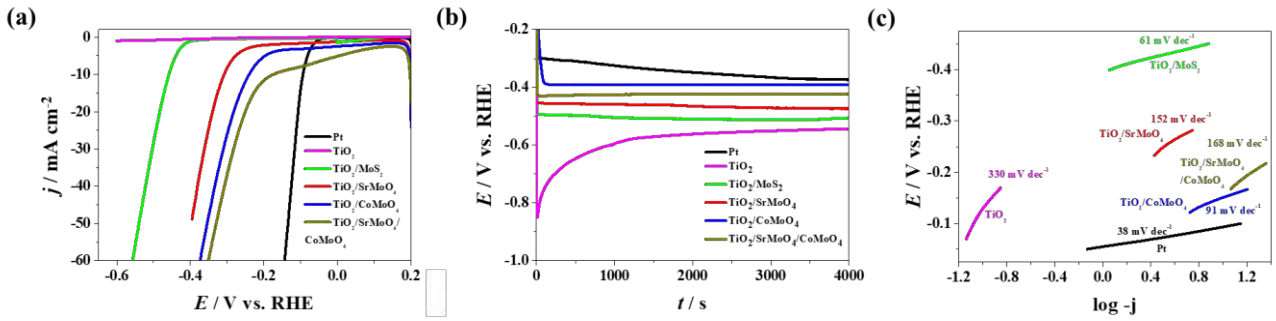


**Figure 3.** (a) HER LSV-polarization curves in 0.2 M $H_2SO_4$ electrolyte solution, (b) time-dependent chronoamperometry stability test, (c) corresponding Tafel plots of different electrocatalysts.

## Conclusions

In summary, our research results indicate that composites containing $TiO_2$ with mainly $MoS_2$, $CoMoS_2$, or $SrMoO_4$ were successfully synthesized and used as highly active electrocatalysts. The obtained composite $TiO_2/SrMoO_4/CoMoO_4$ showed an excellent HER activity and provided good stability. In the next step of our research, the obtained materials will be also synthesized with three-dimensional structured graphene to increase the application area also in the oxygen evolution reaction. This approach might be used to make different low-cost electrocatalysts, and thus applied for various cost-saving applications, such as energy conversion and water splitting devices.


## Acknowledgment

This work was carried out as a result of the research project no. NOR/SGS/IL-HYDROGEN/0202/2020-00 financed by the National Centre for Research and Development, Poland.

Carbon 2022

# Effect of Pore Discovery on the Evolution of Elastic Modulus in Nuclear Graphite Undergoing Oxidation in the Kinetic Regime

**James B. Spicer[1], Ryan M. Paul[2], Jose David Arregui-Mena[2], Ellen Berry[1], Cristian I. Contescu[2] and Nidia C. Gallego[2]**

[1]Department of Materials Science and Engineering, Johns Hopkins University, Baltimore, Maryland, USA 21218
Email: spicer@jhu.edu

[2]Carbon and Composites Group, Chemical Sciences Division, Oak Ridge National Laboratory, Oak Ridge, Tennessee, USA 37830

**Keywords**
Nuclear graphite, elastic modulus, oxidation.

## INTRODUCTION

Nuclear graphites in the as-manufactured, bulk state contain a range of defects that influence the physical properties of these materials. Among these defects, porosity plays a significant role in determining properties related to the elastic response, strength and toughness. It is well known that oxidation processes affect porosity and impact these properties as a result of the modification of the graphite porosity state. Under conditions associated with the kinetic regime for oxidation, porosity increases as a result of chemical reactions between graphite and gas phase species that occur at rates governed by the availability of reaction sites on basal planes and edge planes. These reactions occur in open pores where reactants arrive at these sites. During the oxidation process, closed pores become open and join the open pore population at a rate known as the pore discovery rate. The differences in reactivity between edge and basal plane sites reduces the connectivity of graphite crystallites sharing edges more rapidly than the junctions between other portions of the microstructure, and this has the effect of reducing stress transfer along basal planes. This work examines the effects of site reactivities along with the pore discovery rate to develop expressions for the dependence of elastic modulus on porosity in graphite. While the overall oxidation rate affects porosity generation, crystallite connectivity in open pores depends on oxidation rates at edge and basal planes while the discovery rate introduces pores to these processes. The net result is to produce a mean connectivity in the graphite microstructure that depends on site oxidation and pore discovery rates that affect the functional dependence of elastic modulus on porosity.

## PORE DISCOVERY AND ELASTIC MODULUS

Porosity in nuclear graphites directly affects elastic modulus, and oxidation processes that increase porosity decrease the modulus. Moreover, the differential rates of oxidation between basal planes and edge planes alters the distribution of stresses through the microstructure tending to increase Reuss-like behavior since edge plane connections are removed at a greater rate than those for basal planes. To account for the related effect on material stiffness, Young's modulus can be expressed as a weighted average of the Reuss and Voigt limits for an isotropic collection of graphite crystallites: $E = rE_{Reuss} + (1-r)E_{Voigt}$ where $r$ is a weighting factor that is called the Reuss parameter, $E_{Reuss}$ is Young's modulus in the Reuss limit and $E_{Voigt}$ is for the Voigt limit. Oxidation-induced variations of the Reuss parameter are associated with open porosity, $r_{open}$, since material at open pore surfaces will change while material at closed pore surfaces will not. The Reuss parameter in regions with open pores might take the following form:

$$r_{open} = [r_i + a\varphi_{open}][H(\varphi_{open}) - H(\varphi_{open} - \varphi_s)] + H(\varphi_{open} - \varphi_s) \quad [1]$$

where $r_i$ is the Reuss parameter for the microstructure before oxidation occurs, $a$ relates to the differential oxidation rate of edge and basal plane sites, $\varphi_{open}$ is the open porosity, $H(x)$ is the unit step function, and $\varphi_s$ is the porosity at which the Reuss parameter reaches unity. The Reuss parameter for the overall structure is a weighted average of those associated with open and closed porosity and can be expressed as:

$$r = f_{open}\left(r_{open} * \frac{d\varphi_{init}}{d\varphi_{open}}\right) / \varphi_{init} + (1 - f_{open}) r_i \quad [2]$$

where $f_{open}$ is the fraction of porosity that is open, the asterisk indicates a convolution operation with respect to open porosity, and the derivative is the open pore initiation rate that describes the rate at which pores become available for oxidation. This rate includes the initial open porosity along with porosity that is discovered during the oxidation process. If the pore discovery rate is constant, then the initiation rate can be written as:

$$\frac{d\varphi_{init}}{d\varphi_{open}} = \varphi_{open_i}\delta(\varphi_{open} - \varphi_{open_i}) + bH(\varphi_{open} - \varphi_{open_i}) \quad [3]$$

where $\varphi_{open_i}$ is the open porosity when oxidation begins, $\delta(x)$ is the Dirac delta function, and $b$ is a parameter reflecting the pore discovery rate. Using [3] with [2] and performing the indicated convolution yields a result where the Reuss parameter depends on $(\varphi_{open} - \varphi_{open_i})$. Figure 1(a) shows the variation of the Reuss parameter for different conditions of initially open porosity and pore discovery rate. Figure 1(b) provides the coresponding changes in modulus for $E_{Reuss} = 2.9$ GPa and $E_{Voigt} = 515.0$ GPa taking into account the overall effect of porosity on modulus.

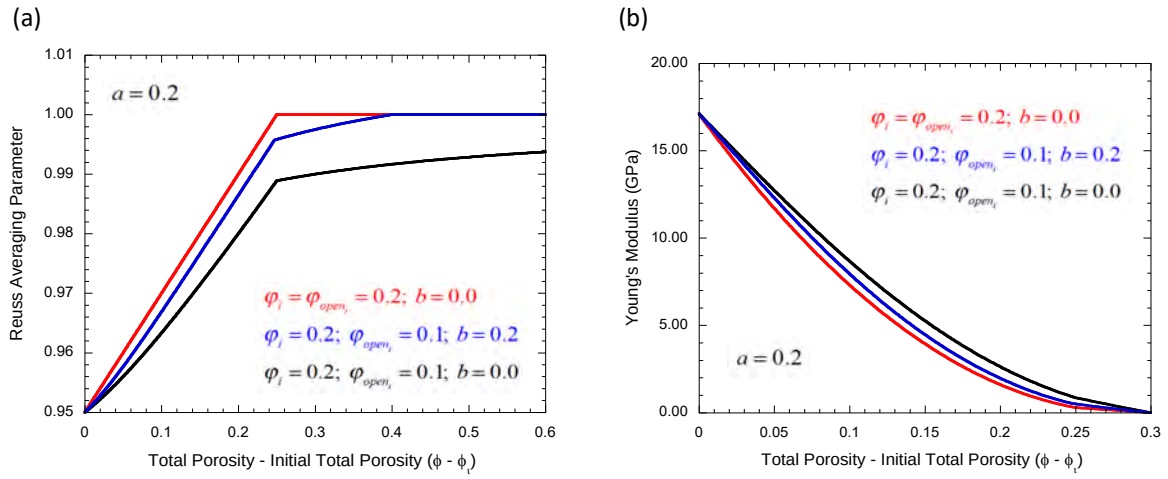


**FIGURE 1**: (a) Variation of the Reuss parameter with respect to porosity increase resulting from oxidation. (b) Changes in Young's modulus associated with oxidation-induced porosity increase for the conditions used in (a).

## CONCLUSIONS

Pore discovery is one aspect of oxidation-induced microstructural evolution that impacts elastic modulus in nuclear graphites. This work introduces a method for assessing the potential effects of pore discovery on modulus variation by associating it with changes in the elastic connectivity of graphite microstructure.

**Acknowledgements**

Research supported in part by the U.S. Department of Energy (DOE) through the Nuclear Energy University Program (NEUP) Contract No. 00118687.

20 C 22 arbon 2022

# Imide-derived Carbon Nanodots- a promising new approach as UV protectors

**Cornel Stan[1,2,3*], Hiba Idrissi[1], Guido Perrin[1*], Conchi O. Ania[1,2*]**
[1] CEMHTI, CNRS (UPR 3079), Université d'Orléans, Orléans, France
[2] TUIasi - Gheorghe Asachi Technical University of Iasi, Romania
[3] Le Studium Fellow, Loire Valley Institute of Advanced Studies, Tours & Orléans, France

Email: stancs@tuiasi.ro; guido.perrin@cnrs-orleans.fr; conchi.ania@cnrs-orleans.fr

**Keywords**
Carbon Dots ; photoluminescence ; UV protection.

## INTRODUCTION

The degradation occurring through long-term exposure to direct sunlight represents one of the most important issues of filmogen materials such as paints or varnishes. The long-time solar exposure leads to significant irreversible changes in gloss, reduced transparency and colour shifting. Such undesirable processes are due to the action of solar UV photons over the chemical structure of the polymers or pigments contained in the formulations of filmogen materials. To minimize them, photochemical stabilizers are required, being the class of HALS (hindered amines light stabilizers) and BUVS (benzotriazole UV stabilizers) most widely applied (Zakrzewski, 2000; Farkas 2010). However, these conventional UV additives present certain disadvantages as limited efficiency protection for many polymer matrices used in filmogen materials, relatively high costs and a negative impact on the environment or natural biological systems. Our approach is to explore the application of highly photoluminescent carbon nanodots as UV protectors of filmogen materials. Their incorporation in the formulation to filmogenic materials should provide the UV protection through the efficient translation of the incident UV radiation towards lower wavelengths due to the ability of CNDs to absorb UV photons.

## EXPERIMENTAL

The photoluminescent carbon nanodots (CDs) have been prepared using N- hydroxyphthalimide as precursor, following a low temperature thermal treatment reported elsewhere (Stan 2017). Several metallic ions have been incorporated upon ion-exchange to the precursor before the thermal treatment, to explore the impact in the absorption/emission features (Stan 2019). The filmogenic materials have been prepared upon dispersion of the resulting carbon nanodots in various polymer matrices (e.g., poly(2-hydroxy-ethylmethacrylate), poly(lactic-co-glycolic acid). The prepared CDs CDs/polymer composites were thoroughly characterized to obtain information about the structure, morphology and photoluminescence. Long term UV illumination exposure of the prepared filmogenic materials was carried out, and the changes in the materials were followed by the above-mentioned characterisation techniques.

## RESULTS AND DISCUSSION

The prepared carbon nanodots present a photoluminescence (PL) emission in the blue range of the visible spectrum when excited in the UV-B/UV-A range (300-400 nm). Photoluminescence quantum yield efficiencies of ca. 79% were obtained in the 410-470 nm emission range; the incorporation of metals in the precursor enabled to modify the PL emission profile of the CDs, shifting from blue emission in the pristine precursor to green emission in the presence of iron (III).

The CDs/polymer composite filmogens also displayed the photoluminescence properties of the pristine carbon dot, as seen in Figure 1.

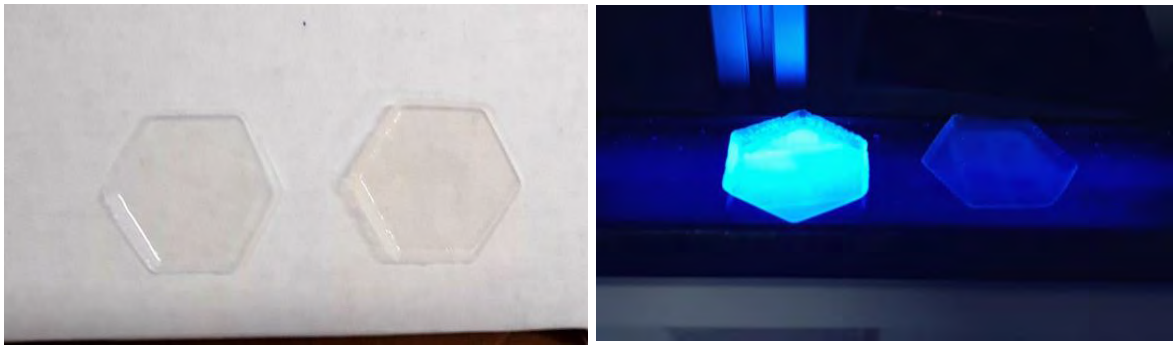

**FIGURE 1**. (a) Native polyacrylic film (right) and film with embedded carbon dots (left) ; (b) photoluminescence response of the films under UV-C exposure.

The long-term exposure to UV-C light provoked some changes in the prepared composites, as indicated by diffuse reflectance spectroscopy. This modification was significantly delayed for the CDs/polymer composite films, compared to the native films in the absence of the carbon nanodots. This behaviour demonstrates the protective role of the carbon nanodots due to their capacity to absorb the strong UV photons and convert them in less energetic photons in the visible.

## CONCLUSIONS

Carbon nanodots with varied photoluminescent response were prepared by the thermal treatment of N- hydroxyphthalimide. The optical response of the carbon dots was modulated in the presence of different metallic cations, with a shift from blue emission for the pristine carbon nanodots to a green emission in the presence of iron (III). The incorporation of carbon nanodot additives to several film materials provoked a remarkable delay in the UV modification of the composites upon long-term light exposure.

**Acknowledgements**

CS thanks Le Studium Fellowship for his internship in Orléans; the authors thank the financial support of the LEAP-RE program (NANOSOLARCELLS).

**References**

[1] Zakrzewski J, et al. (2000). Hydroxybenzophenone UV-absorbers containing 2,2,6,6-tetramethylpiperidine (HALS) group-benzoylation of corresponding phenol derivatives, *Polym. Degrad. Stab.,* 67, 279.

[2] Farkas R, et al. (2010). Synthesis of new 2-(2'-hydroxyaryl)benzotriazoles and evaluation of their photochemical behavior as potential UV-filters, *Molecules*, 15, 6205.

[3] Stan CS, et al. (2017). Facile preparation of highly luminescent composites by polymer embedding of carbon dots derived from N-hydroxyphthalimide, *J. Mater. Sci.* 52, 185.

[4] Stan CS, (2019). et al. Fe(III) doped carbon nanodots with intense green photoluminescence and dispersion medium dependent emission, *Nature-Sci. Rep.* 9, 18893.

20 C 22 arbon 2022

# Exploring the photocatalytic activity of solid-state carbon/carbon heterojunctions

**Tingwei Sun*, Encarnacion Raymundo-Pinero, Conchi Ania**
CEMHTI, CNRS (UPR 3079), Université d'Orléans, 45071 Orléans, France
Email: tingwei.sun@cnrs-orleans.fr

**Keywords**
Photocatalysts, bandgap, hybrid semiconductor/carbon.

## INTRODUCTION

The application of advanced oxidation processes for the remediation of wastewater has gained attention in recent years owing to the appearance of recalcitrant emerging pollutants that are not easily removed by conventional treatments (Deng, 2015). The use of carbon-based catalysts for these processes has become a largely investigated topic in many different types of approaches. As an example, in electroassisted treatments, carbon electrodes present the advantage of high electronic conductivity, high stability, and versatility since they may be used as either cathodes (e.g., in electrofenton reactions for due to the high overvoltage for hydrogen evolution) or as anodes (due to high overvoltage for oxygen evolution) upon an adequate selection of the physicochemical features of the carbon material (Meijide 2021; Maira 2021). In photocatalytic processes, some carbon materials have revealed to be efficient for the generation of radical species capable of promoting degradation of organic pollutants in solution (Gomis-Berenguer 2017; Carmona 2015). Indeed, a variety of carbon materials have been used for various AOPs in wastewater remediation, either alone or in combination with other catalysts, with excellent results with heterojunctions based on different carbon allotropes with semiconductors. In this work, we propose to build solid-state carbon/carbon heterojunctions as an approach to improve the charge separation efficiency of photogenerated electron-hole pairs.

## EXPERIMENTAL SECTION

Graphitic carbon nitride (g-$C_3N_4$) was prepared by directly heating melamine at 520 ◦C for 4 h. A series of binary carbon/carbon heterojunctions has been prepared by blending carbons with different pore features and photoactive sites (covering hydrochars, GO, rGO, polymeric carbons, activated carbons). **The hybrid CN/carbon photocatalysts were prepared by a hydrothermal method, using variable amounts of the carbon additive, ranging from 2 to 10 wt.%. Briefly, the carbon materials were mixed in water and sonicated for 15 min to assure a good dispersion. The suspension was transferred into a Teflon-lined stainless steel autoclave and maintained at 140 °C for 20 h. The precipitate was filtered, washed with distilled water and dried at 120 °C.** The optical properties of the catalysts were explored by UV–vis diffuse reflectance spectroscopy in a spectrophotometer equipped with an integrating sphere and using $BaSO_4$ as a reference. The measurements were recorded between 200-800 nm in the diffuse reflectance mode and transformed through the Kubelka-Munk function F(R∞) for the estimation of the energy band gap. Powders of the samples were pressed in holders of ca. 3 cm diameter and 5 mm depth.

## DISCUSSION AND RESULTS

The prepared carbon/carbon hybrid photocatalysts were initially characterized to evaluate their optical and photoelectrochemical features; data was compared to that of the pristine individual components of the hybrid composites. The diffuse reflectance features of the mixtures revealed that

the incorporation of low amounts of a carbon additive does not significantly alter the optical features of pristine $C_3N_4$. Most of the composites showed the wide band gap located at around 400 nm, similar to that of carbon nitride, with slight deviations towards lower wavelengths for the composites incorporating low amounts of carbon additives showing a strong light absorption (e.g., carbons prepared at high temperatures). No modifications were observed in the structural features of the main component, as inferred from XRD and XPS data.

On the other hand, the incorporation of the carbon additive had a marked impact in the photoelectrochemical characteristics of the hybrid photocatalysts, indicating the impact on the ability to separate the charge carriers generated upon exposure to light. For example, the open circuit potential of the hybrid composites under dark and illumination shifted towards more negative values, showing the electron donor character of the carbon materials. A similar behavior has been described for other semiconductor/carbon composites (e.g., $TiO_2$, ZnO, $Bi_2WO_6$).

This confirms that an adequate balance between the $\pi$-electron density, structural defects and electronic conductivity can be obtained in the hybrid photocatalysts, allowing their use as electron mediators under illumination. The efficiency of the prepared hybrid photocatalysts will be discussed in terms of the degradation efficiency of recalcitrant pollutants in water under artificial solar light and UV irradiation.

## CONCLUSIONS

We have investigated the effect of the use of carbon materials of varied origins as additives to carbon nitride, so as to obtain hybrid carbon/carbon composites with increased photocatalytic activity under solar illumination. We have observed that whereas the optical features of the catalysts remained rather unchanged, the nature of the carbon additive affects mostly the capacity of the resulting hybrid catalyst to separate the charge carriers. This is expected to have a large impact in the photocatalytic activity of the materials for the degradation of recalcitrant pollutants.

**Acknowledgements**

The financial support from Region Centre Val de Loire (APR-IA, PRESERVE grant), is acknowledged. TS thanks the funding of the China Scholarship Council CSC for a PhD fellowship in France (grant 202006460009).

**References**

Carmona, Rocio J., et al. Boosting the visible-light photoactivity of Bi2WO6 using acidic carbon additives. Applied Catalysis A: General 505 (2015) 467-477. https://doi.org/10.1016/j.apcata.2015.05.011

Deng, Yang, and Renzun Zhao. Advanced oxidation processes (AOPs) in wastewater treatment. Current Pollution Reports 1.3 (2015): 167-176. https://doi.org/10.1007/s40726-015-0015-z

Gomis-Berenguer, Alicia, et al. Photochemistry of nanoporous carbons: Perspectives in energy conversion and environmental remediation. Journal of Colloid and Interface Science 490 (2017) 879-901. https://doi.org/10.1016/j.jcis.2016.11.046

Meijide, Jessica, et al. Heterogeneous Electro-Fenton as “green” technology for pharmaceutical removal: a review. Catalysts 11.1 (2021): 85. https://doi.org/10.3390/catal11010085

Nair, Keerthi M., Vignesh Kumaravel, and Suresh C. Pillai. Carbonaceous cathode materials for electro-Fenton technology: Mechanism, kinetics, recent advances, opportunities and challenges. Chemosphere 269 (2021): 129325. https://doi.org/10.1016/j.chemosphere.2020.129325

20 C 22 arbon 2022

# Hydrogen addition to Small Cage Carbon Fullerenes

**Yuri Tanuma[1,2,3], Toru Maekawa[2], Chris Ewels[1]**
[1] Institut des Matériaux Jean Rouxel, CNRS/Université de Nantes, BP32229, 44322 Nantes, France
Email: chris.ewels@cnrs-imn.fr

[2]Graduate School of Interdisciplinary New Science, Toyo University, 2100 Kujirai, Kawagoe, Saitama 350-8585, Japan
[3]Center for Advanced Research of Energy and Materials, Hokkaido University, Kita 13 Nishi 8, Kitaku, Sapporo 060-8628, Japan, Hokkaido
[4] Bio-Nano Science Research Centre, Toyo University, 2100 Kujirai, Kawagoe, Saitama 350-8585, Japan

**Keywords**
Fullerenes, astrochemistry, DFT, modelling, $C_{60}$, growth.

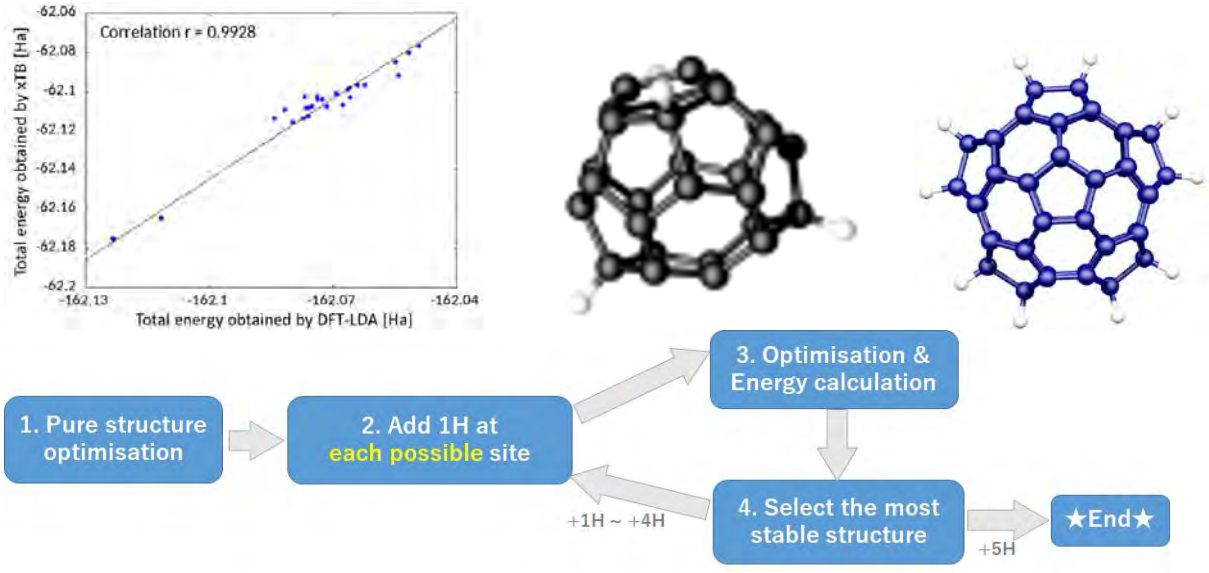


**Figure 1**: (left) Total energy correlation plot for isomers of $C_{28}H_5$ taken from (Tanuma 2021). (bottom) Schema of algorithm used to predict stable hydrogenation via sequential addition (i.e. with no H surface migration allowed). (right) Stable species such as $C_{28}H_4$ and $C_{50}H_{10}$ are readily identified by this method.

In order to understand fullerene formation, and fullerene behaviour in astrochemical environments, we have explored the family of hydrogenated small fullerenes ($C_n$, $n$ < 60). The problem of identifying the thermodynamically preferable species is computationally difficult, given the large number of small fullerene isomers, and even larger number of hydrogenated variants. We initially tested a variety of different semi-empirical methods to obtain reliable total energies. Of these, the new GFN2-xTB developed by the Grimme group (Bannwarth 2019) consistently gives highly accurate energy correlations ($r$ > 0.99) to full DFT-LDA calculations at a fraction of the computational cost. We then used this to explore hydrogenated cages from $C_{20}$ to $C_{58}$, identifying stable magic number hydrogenated small fullerenes, structures with high dipole moments, and explore potential hydrogen catalysed growth routes.

Essentially, we aimed to reduce the number of possible isomers to calculate, given that each calculation with GFN2-xTB takes of the order of 1-3 seconds on a 20 processor desktop machine. In order to explore all fullerene isomers from $C_{20}$ to $C_{58}$, and each from 1 to 12 hydrogen additions, would not be attainable with brute force methods. We nonetheless employed brute force for four example fullerenes, two isomers of $C_{28}H_n$ and two of $C_{40}H_n$ from n=1-4. This provided definitive low energy structures to benchmark against.

We next tried to use localised surface properties of a parent fullerene as a predictive tool to indicate preferential site for subsequent hydrogenation. However, when we attempted this using the localised pyramidalisation angle, sites with highest pyramidalisation angle, highest hybridisation value, and longest summation of bond lengths were not systematically the most favoured hydrogenation sites as found with the benchmarking. Neither were other geometric parameters such as various sum combinations of bond lengths. We also explored electronic structure, testing either the highest, lowest charging on the carbon atoms, or else using Fukai functions, adding or removing trace charge and seeing where this localised. None of these were able to systematically indicate the most stable subsequent hydrogenation site.

As a result we employed instead a sequential addition algorithm. In this case, all possible single hydrogenation sites were optimised, and hydrogen added at the most stable site. This hydrogen atom was thereafter considered fixed (immobile), and the process repeated for a second hydrogen atom, and so forth, up to 12 hydrogen atoms. This reduces massively the combinatorial options and allowed us to explore all species $C_nH_m$, $n$=20-58, $m$=0-12.

The results are currently being analysed, but certain known stable species, such as $C_{28}H_4$, are obtained via this method. Further analysis of growth routes will be published shortly.

**THE FULL PAPER ON THIS WORK IS AVAILABLE OPEN SOURCE FROM MDPI CRYSTALS (TANUMA 2021).**

The data presented in this study are openly available in Zenodo at 10.5281/zenodo.5615405. https://doi.org/10.5281/zenodo.5615404 (accessed on 27 October 2021)
including the most stable $C_{28}H_n$ and $C_{40}H_n$ structures and a complete library of GFN2-xTB optimised xyz files for all fullerene isomers from $C_{20}$ to $C_{80}$.

**Acknowledgements**
This research was funded by the Inoue Enryo Memorial Grant of Toyo University, C.E. and Y.T. acknowledge BI-FR/21-22-PROTEUS-003 project for funding, and Y.T. acknowledges financial support from French governmental bursary JP19-00207. Computing support was funded by Region Pays de la Loire “Paris Scientifiques 2017”, Grant Number 09375.

**References**

Bannwarth, C., Ehlert, S., Grimme, S., (2019). GFN2-xTB – An accurate and broadly parameterized self-consistent tight-bonding quantum chemical method with multipole electrostatics and density-dependent dispersion contributions. *J. Chem. Theory Comput.* 15 [**3**], 1652-1671. https://xtb-docs.readthedocs.io/en/latest/setup.html

Tanuma, Y., Maekawa, T., Ewels, C. (2021). Methodological Investigation for Hydrogen Addition to Small Cage Carbon Fullerenes. *MDPI* Crystals, 11 [11], 1334. https://doi.org/10.3390/cryst11111334

Carbon 2022

# Shining Carbon-based Hybrid Textile Supercapacitor: A Multifunctional Energy Storage/Fluorescent Device for Fashion and Safety Applications

**Joana S. Teixeira[1,2], André M. Pereira[2], Clara Pereira[1]**
[1] REQUIMTE/LAQV, Department of Chemistry and Biochemistry, Faculty of Sciences, University of Porto (FCUP), Porto, Portugal
[2] IFIMUP, Department of Physics and Astronomy, FCUP, Porto, Portugal
Email: joanafsteixeira@hotmail.com

**Keywords**
Carbon nanotubes, redox-active electrolyte, dual-functional textile supercapacitor, Mn-doped zinc sulfide

## INTRODUCTION

In the last decade, the consumers have been continuously motivated by new wearable electronic technologies, leading to a strong demand for miniaturized energy storage systems. Carbon-based textile supercapacitors (SCs) are considered a promising solution, due to their eco-friendly nature, high power density and cycling stability, also featuring the flexibility and lightness characteristic of textiles (Costa, 2021). These SCs have been extensively improved to be applied in diversified applications (*e.g.*, healthcare and military) (Rathinavel, 2021). However, the dark color of such devices often limits their application, compromising the visibility of nighttime users. As a solution, a multifunctional hybrid textile SC with simultaneous fluorescent properties and high energy storage ability was produced using carbon nanotubes (CNT)-coated textile electrodes and a shining redox-active solid-gel electrolyte (Teixeira, 2021).

## MATERIALS AND METHODS

The fabrication of the textile electrodes, electrolyte and SCs is described in detail in reference Teixeira, 2021. Briefly, textile electrodes (3.5×3.5 $cm^2$) were prepared by impregnation of a cotton fabric with an aqueous dispersion of CNTs, by dip-pad-dry process. The redox-active solid-gel electrolyte was prepared through the doping of poly(vinyl alcohol) (PVA)/$H_3PO_4$ with a fluorescent Mn-doped ZnS pigment (P). The fluorescent SC (SC_CNT_P) was fabricated using two textile electrodes sandwiching the redox-active solid-gel electrolyte (active area = 2.5 $cm^2$). For comparison, a SC based on undoped electrolyte was produced (SC_CNT). The P and CNTs were characterized by X-ray diffraction (XRD), scanning electron microscopy (SEM) and transmission electron microscopy (TEM). The electrochemical properties of the textile SCs was evaluated by electrochemical impedance spectroscopy, cyclic voltammetry and galvanostatic charge-discharge method (GCD).

## RESULTS AND DISCUSSION

The diffractogram of P was characteristic of a crystalline structure of ZnS in two different phases: cubic sphalerite (main) and hexagonal wurtzite ZnS phases (Figure 1A). The diffractogram of CNT confirmed the graphitic structure of the nanomaterial. The electron microscopy techniques revealed a rhombic morphology for P (particle size: 6–20 μm), while CNTs presented a tubular-like morphology (average outer and inner diameters of 14.3±1.2 and 3.9±0.7 nm, by TEM).

The CNT-based textile electrodes contained 6.7 wt% CNTs loading and presented an electrical resistance of 176 Ω (electrical resistivity: 3.17 Ω cm). Furthermore, the solid-gel P-doped electrolyte was successfully prepared and used to fabricate the dual-functional textile SC, exhibiting an orange fluorescent color in the action of UV light as a result of the doping of the crystal lattice of ZnS with $Mn^{2+}$ (confirmed by XPS and EDS).

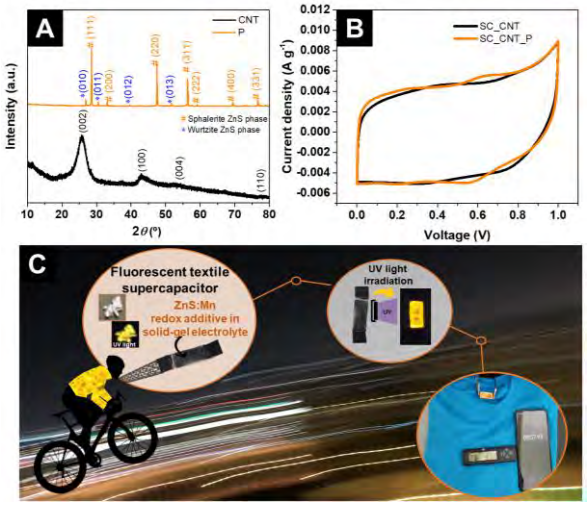


**FIGURE 1:** (A) Diffractograms of CNTs and P; (B) *i-V* cycles of SC_CNT and SC_CNT_P (1 mV $s^{-1}$); (C) Demonstration of the fluorescent properties of the SC_CNT_P and application to power an electronic sensor.

The *i-V* cycle of SC_CNT_P presented a rectangular shape and humps characteristic of redox reactions (Figure 1B), suggesting the simultaneous occurrence of pseudocapacitive and electrical double-layer energy storage mechanism. In contrast, the *i-V* cycle of SC_CNT was characteristic of electrical double layer capacitors (EDLC). The hybrid charge storage mechanism of SC_CNT_P led to 3.8% improvement of the specific capacitance relative to SC_CNT (4.37 F $g^{-1}$ *vs*. 4.21 F $g^{-1}$). Furthermore, SC_CNT_P presented 19.7% higher working potential (1.64 V *vs*. 1.37 V, determined by GCD), leading to up to 1.5× and 1.7× higher energy and power density (1.63 W h $kg^{-1}$ at 641.6 W $kg^{-1}$ *vs.* 1.10 W h $kg^{-1}$ at 369.2 W $kg^{-1}$) due to the redox-active nature of the electrolyte. Finally, SC_CNT_P presented 100% capacitance retention after 8000 cycles. In a practical application, SC_CNT_P was able to power a temperature/time sensor for almost 12 min, when charged for only 10 s (Figure 1C).

## CONCLUSIONS

A dual-functional textile SC with high-energy storage performance and remarkable fluorescence properties under UV light was produced using Mn-doped ZnS as redox additive in a solid-gel electrolyte. The SC_CNT_P exhibited improved electrochemical performance relative to SC_CNT based on the undoped electrolyte (20% and 48% higher working potential and energy density, respectively) and excellent cyclability. The shining device maintained an electronic sensor in operation for ~12 min (10 s charging time). This work demonstrated the usefulness of solid-gel electrolytes doped with inorganic redox-active compounds to develop shining energy storage textiles with enhanced performance for safety electronic clothing for nighttime users.

**Acknowledgements:** Work funded by Portuguese funds through FCT/MCTES (PTDC/CTM-TEX/4126/2021, UIDB/50006/2020 and UIDP/50006/2020). COST Action CA17107 – CONTEXT, supported by COST is acknowledged. JST thanks FCT for the PhD scholarship (SFRH/BD/145513/2019).

**References**

Rathinavel, S., Priyadharshini, K., Panda, D. (2021). A review on carbon nanotube: An overview of synthesis, properties, functionalization, characterization, and the application. *Materials Science & Engineering B*, 268, 115095. https://doi.org/10.1016/j.mseb.2021.115095

Costa, R. S., Soares, O. S. G. P., Vilarinho, R., Moreira, J. A., Pereira, M. F. R., Pereira, A. M., Pereira, C. (2021), Unveiling the role of oxidative treatments on the electrochemical performance of carbon nanotube-based cotton textile supercapacitors. *Carbon Trends*, 5, 100137. http://doi.org/10.1016/j.cartre.2021.100137

Teixeira, J. S., Trindade, A. M., Pereira, C. (2021). Smart dual-functional energy storage/fluorescent textile device based on a new redox-active Mn-doped ZnS solid-gel electrolyte. *Chemical Engineering Journal*, 426, 131274. http://doi.org/10.1016/j.cej.2021.131274

Carbon 2022

# In Situ Optical Studies of the Photobleaching and Recovery Kinetics of a Palette of Carbon Nanodots.

**A. Terracina, A. Armano[2], M. Meloni[3], M. Cannas[2], L. Malfatti[3], F. Messina[2]**
Dipartimento di Fisica e Chimica, Università degli Studi di Palermo, Via Archirafi 36, 90123 Palermo, Italy - Email: angela.terracina@unipa.it

[2]Dipartimento di Fisica e Chimica, Università di Palermo, Via Archirafi 36, 90123 Palermo, Italy
[3]Department of Chemistry and Pharmacy, Laboratory of Materials Science and Nanotechnology, CR-INSTM, University of Sassari, Via Vienna 2, 07100, Sassari, Italy

**Keywords**
Carbon nanodots, photobleaching, photoresistance, fluorescent nanoparticles.

## INTRODUCTION

Carbon dots (CDs) are a family of nanometer-sized particles displaying bright fluorescence and usually structured as quasi-spherical carbonaceous cores covered by a dense shell of chemical functional groups, typically containing significant amounts of oxygen and nitrogen. Their wide range of interesting properties make them attractive for many potential applications. There are still many different theories concerning the nature of CD fluorescence attributed sometimes to the formation of molecular fluorophores attached to the CDs surface, or even to side synthesis products consisting in free emitting small molecules like citrazinic acid (Sciortino, 2018; Xiong, 2018). Recently many works have evidenced even the occurrence of photobleaching (PB) effects. However, too few studies have been carried out under strong visible-light beams and furthermore only the net effect of the PB process is generally observed (Longo, 2020). In contrast, our work provides a systematic study conducted on a wide palette of different emitting CDs, observing their real time kinetics, and finding a relation between photostability and CDs optical features. Taking advantage of PB effects we have also extracted information about the nature of CD fluorescence.

## RESULTS

We have studied five different bottom-up CD types (synthesis already published: Mura, 2020; Ludmerczki, 2021). Five of them are hydrophilic: two blue-emitting CDs (BLUE1 and BLUE2), two green-emitting CDs (GREEN1 and GREEN2), one red-emitter (RED1).
Aiming to compare the photostability among CD samples, we collected FLIP (Fluorescence Loss In Photobleaching) data for all the samples. Such experiments consist in the in-situ pump-probe measurements by using an intense pulsed laser beam at a wavelength close to the excitation peak of the fluorescence transition of the specific sample (355 nm for blue-emitters, 410 for green-emitters, 532 for red-emitter). Similarly, we carried out FRAP (Fluorescence Recovery After Photobleaching) experiments, where CD samples were subjected to an initial bleaching stage and thereafter only probed to reveal possible recovery phenomena of the fluorescence over time. FRAP measurements have been carried out via both total-illumination (TI, the entire volume of the sample is involved) and partial-illumination (PI, only 25% of the whole volume) configuration.
The curves displayed in Figure 1a show the trend of the fluorescence on increasing the number of pulses (from 0 to $5 \cdot 10^4$) for each sample. CD fluorescence progressively fades with increasing the number of bleach pulses received by the samples, clearly indicating the destructive effect of intense illumination on the emission properties of the CDs. Despite strong heterogeneity in the resistance to PB among samples, a peculiar trend appears, consisting in a clear increase of the photo-resistance

from blue- to red-emitting CDs. In fact, the former CDs show the lowest photostability, typically losing 50% of the initial fluorescence within 2000 laser pulses or less; in contrast, PB of RED1 is the slowest we observe and its fluorescence halves after more $10^5$ pulses. Furthermore, CDs displaying almost identical absorption and emission properties (like GREEN1 and GREEN2) respond very differently to PB.

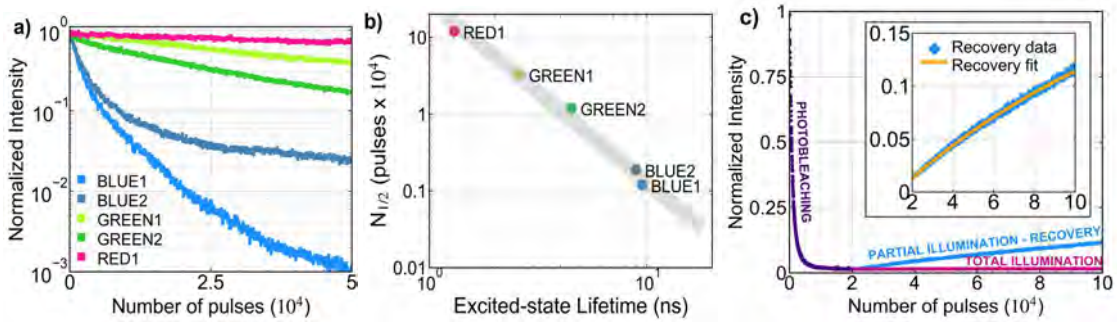


**FIGURE 1**: (a) Comparison of FLIP decay curves obtained for the palette of CDs. (b) The number of bleaching pulses necessary to halve the initial fluorescence intensity are plotted as a function on the excited-state lifetime of each sample (c) FRAP of BLUE1 sample performed in total illumination (TI) and partial illumination (PI). In the inset, the overlap between experimental data and fit for the recovery curve.

It is worth noting that, acquiring the time-decay of all the samples involved by time-resolved fluorescence experiments, the enhanced photo resistance observed when moving from blue- to red-emitting CDs reflects the decreasing of the excited-state lifetimes, resulting in a form of anti-correlation between photo-resistance and lifetime (Figure 1b).

The curves displayed in Figure 1c show FRAP experiment carried out on BLUE1. After the bleach laser is turned off (when $2{\cdot}10^4$ pulses have hit the sample), the evolution of fluorescence intensity is different in the two geometries: a progressive fluorescence recovery is revealed in PI geometry (blue points) but did not in TI geometry (pink points). This means that PB of our emitters is irreversible and fluorescence recovery phenomenon can be uniquely attributed to non-photobleached fluorophores diffusing from the non-illuminated (and not bleached) 75% volume of the sample. By using both random walk and Stokes-Einstein's equation as frequently done in literature, we were able to estimate the hydrodynamic radius of objects diffused in ~3 h of fluorescence probing, which resulted about 0.2-0.3 nm in all CD samples involved, and the percentage of such particles with respect to the full amount of emitters, which in no case exceed ~35%. This means that at least ~65% of the emitters consists in larger objects, presumably fluorophores attached to nanometer-CDs, and the contribution of smaller free-diffusing molecules is certainly minor although present.

## CONCLUSIONS

Our systematic comparative experiments on a palette of different CDs emitting across the whole visible spectrum revealed a general trend, consisting in the increasing of resistance to PB going from blue- to red-emitters and in an anti-correlation with the excited-state lifetime of the sample. Concerning the nature of the CD fluorescence, via FRAP experiments we found that embedded fluorophores are always a majority, in all types of CDs we studied, compared to free diffusing molecular-like emitters.

### References


Longo, A.V., Sciortino, A., Cannas, M. and Messina, F. (2020). UV photobleaching of carbon nanodots investigated by in situ optical methods. *Physical Chemistry Chemical Physics*, 22(24), pp.13398-13407. https://doi.org/10.1039/D0CP00952K

Ludmerczki, R., Malfatti, L., Stagi, L., Meloni, M., Carbonaro, C.M., Casula, M.F., Bogdán, D., Mura, S., Mándity, I.M. and Innocenzi, P. (2021). Polymerization-Driven Photoluminescence in Alkanolamine-Based C-Dots. *Chemistry–A European Journal*, 27(7), pp.2543-2550. https://doi.org/10.1002/chem.202004465

Mura, S., Ludmerczki, R., Stagi, L., Garroni, S., Carbonaro, C.M., Ricci, P.C., Casula, M.F., Malfatti, L. and Innocenzi, P. (2020). Integrating sol-gel and carbon dots chemistry for the fabrication of fluorescent hybrid organic-inorganic films. *Scientific reports*, 10(1), pp.1-12. https://doi.org/10.1038/s41598-020-61517-x

Sciortino, A., Cannizzo, A. and Messina, F. (2018). Carbon nanodots: a review—from the current understanding of the fundamental photophysics to the full control of the optical response. *C*, 4(4), p.67. https://doi.org/10.3390/c4040067

Xiong, Y., Schneider, J., Ushakova, E.V. and Rogach, A.L. (2018). Influence of molecular fluorophores on the research field of chemically synthesized carbon dots. *Nano Today*, 23, pp.124-139. https://doi.org/10.1016/j.nantod.2018.10.010

Carbon 2022

# Formation of Cesium Carbonate in Ion-Implanted Graphite, Examined with Dual-Source X-ray Photoelectron Spectroscopy, Density Functional Theory Calculations and Thermodynamic Modelling.

**Alex Theodosiou[1], Ben F. Spencer[2], Jonathan Counsell[3], Philippe Ouzilleau[4], Zhoutong He[5], Abbie N. Jones[1]**

Email: alex.theodosiou@manchester.ac.uk

[1] Nuclear Graphite Research Group (NGRG), The University of Manchester, Oxford Road, Manchester, M13 9PL, UK.

[2]Henry Royce Institute and Department of Materials, The University of Manchester, Oxford Road, Manchester, M13 9PL, UK.

[3]Kratos Analytical, Wharfside, Trafford Wharf Road, Manchester, M17 1GP, UK.

[4]Department of Mining and Materials Engineering, McGill University, Montreal H3A 0C5, Canada

[5]Shanghai Institute of Applied Physics, Chinese Academy of Sciences, Shanghai 201800,

P. R. China.

**Keywords**

Nuclear Graphite, Fission Products, X-ray Photoelectron Spectroscopy

A sample of HOPG was implanted with Cs+ ions in order to study the effect on the graphite matrix and the subsequent Cs/C interactions. The mean implantation depth was calculated to be ~ 22 nm, allowing for investigation with X-ray Photoelectron Spectroscopy, (XPS), where both a traditional Al Kα X-ray source and a higher energy Ag Lα source was used for an increased sampling depth deeper into the surface. A schematic of the ion implanted system is given in Figure 1.

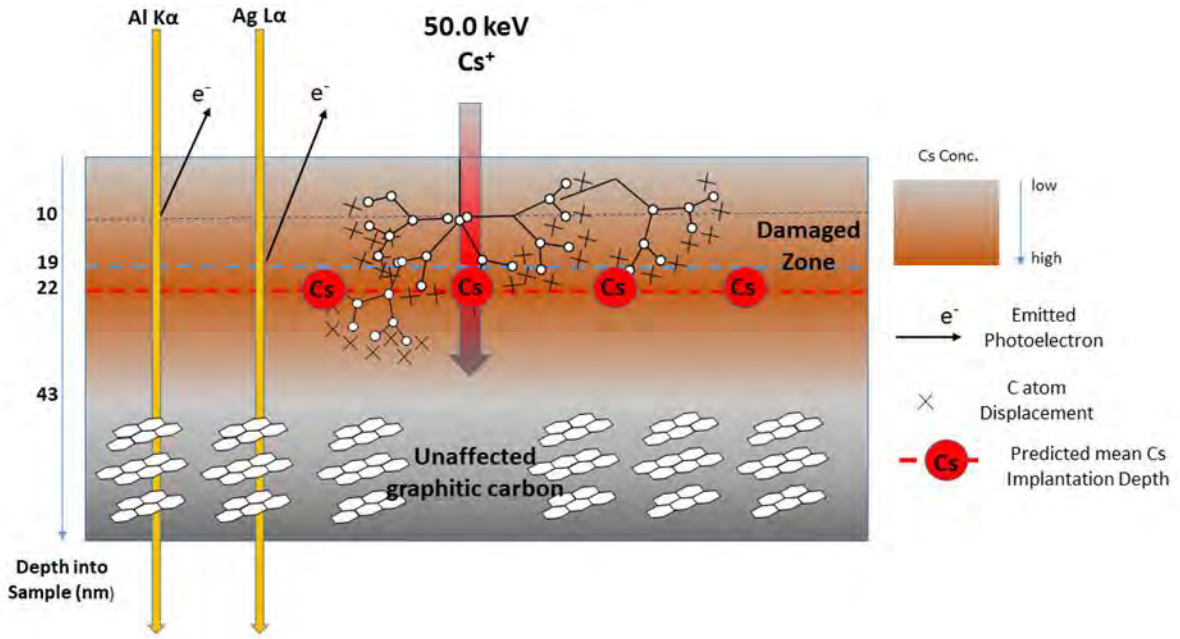


**FIGURE 1:** A schematic of the $Cs^+$ irradiation of HOPG.

Subsequent XPS analysis found that there was a reduction of $sp^2$ C-C bonding with increasing implantation dose, resulting in a total loss of $sp^2$ character at ~ 6 at% $Cs^+$. A striking increase in higher BE components (285.8 – 289.4 eV) in the C 1s spectra cannot be attributed solely to the presence of C-O species, instead indicating a dramatic re-ordering of the graphitic lattice to accommodate and neutralize the embedded Cs. At greater depths, in the region where the Cs became embedded, XPS analysis suggested the presence of carbonate species, which was reinforced through analysis of a reference $Cs_2CO_3$ sample. Parallel thermodynamic modelling and DFT calculations provided sufficient evidence to support the XPS findings and, along with degraphitised HOPG and oxygenated degraphitised HOPG, the $Cs_2CO_3$ was determined to be in thermodynamic equilibrium within the ion implanted sample. These findings highlight the usefulness of performing XPS with multiple photon energies which has provided valuable information on the effects of cesium implantation on graphite, and in particular the physio-chemical behaviour of the cesium within the graphite lattice. The methods outlined in this study may be applied to other research areas, such as energy storage, where ion-doped graphite is of interest.

20 C 22 arbon 2022

# Carbon Materials As a Support For TMD Based Supercapacitor Electrodes

**Maciej Tobis, Masoud Foroutan Koudahi, Andrii Kachmar, Sara Azmi, Elżbieta Frąckowiak**
Poznan University of Technology, Institute of Chemistry and Technical Electrochemistry, Poland
Email: elzbieta.frackowiak@put.poznan.pl

**Keywords**
Transition metal dichalcogenides, carbon supports, supercapacitors

## INTRODUCTION

Electrochemical capacitors (ECs) called supercapacitors are devices where the mechanism of energy storage is based on reversible adsorption of ions at the electrode/electrolyte interface. During polarization, charges are separated and ions are physically attracted towards oppositely signed electrodes. Such purely physical form of energy storage allows ECs to operate at high-frequency charge/discharge rates delivering high values of power density. Therefore, the performance of the ECs is mainly dependent on the type of the electrode material, as well as type of the electrolyte used. Thanks to the structural and textural tuning possibility, as well as diverse forms, carbons have become the most commonly used EC electrode materials. Usually, carbonaceous materials are able to provide satisfying cell performance in terms of specific capacitance and conductivity. Although, since the discovery of two-dimensional (2D) materials, the researchers are focusing on binding carbons with other components improving the performance of the ECs through incorporation of redox behaviour. Among many examples, particularly attractive are transition metal dichalcogenides (TMDs). They can be expressed by the formula of $MX_2$, where one layer of transition metal atoms M (e.g., Mo, Re, V, Ni, etc.) is sandwiched between two layers of chalcogen atoms X (e.g., S, Se, or Te). Thanks to their two-dimensionality and structural variety they gained a significant attention as attractive electrode materials in ECs. The aim of the presentation is to show how the electrochemical performance of the ECs changes dependent on the type of carbon support used for the synthesis of TMDs based composites. In our study, we have selected different types of carbon materials, such as three-dimensional graphene like structures (3DG), multiwalled carbon nanotubes (NTs), and reduced graphene oxide (rGO), for further modification with TMDs materials (i.e., $VS_2$, $ReS_2$ and $NiS_2$, accordingly) (Fig. 1). Dependent on the structural and textural properties of the support, loading content and type of the deposited TMD, ECs were able to reach improved energy and power response.

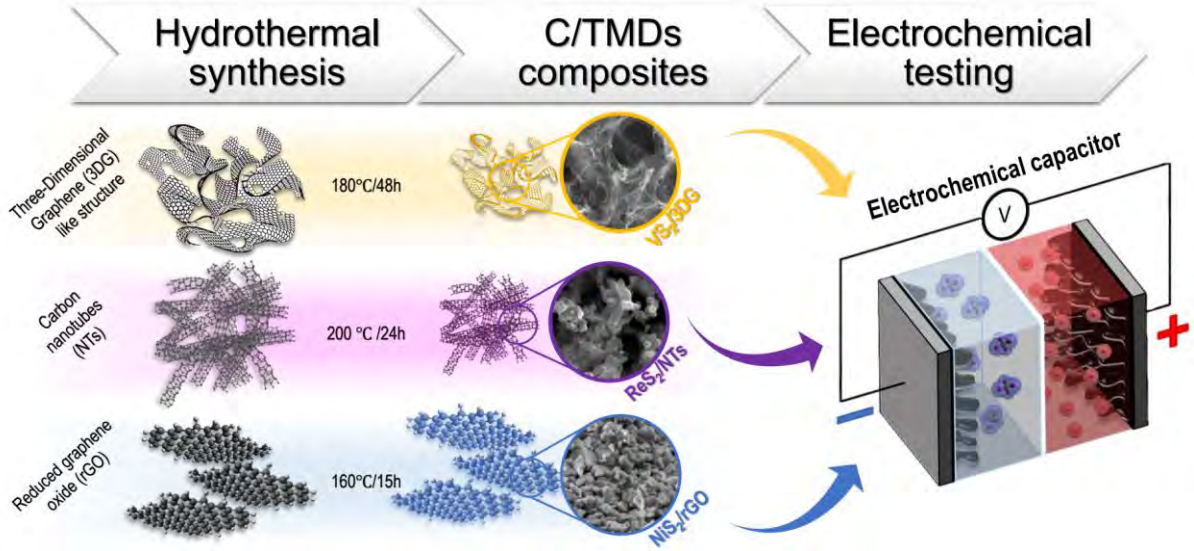


**FIGURE 1.** Graphical representation of composite synthesis and further EC investigation.

For example, the 3DG made from edge-free graphene walls is able to operate at 1.5 V giving 108 F $g^{-1}$ at 1 A $g^{-1}$. After deposition of layered $VS_2$ on the 3DG, the cell was able to extend its operational window to 1.8 V, reaching 161 F $g^{-1}$ at 1 A $g^{-1}$ with 80% of energetic efficiency. Surprisingly, the cell with composite was able to withstand high current density regime of 100 A $g^{-1}$ showing 110 F $g^{-1}$. The optimum porous edge-free structure with deposited $VS_2$ layers provided pseudocapacitive behaviour improving the energy and power response, minimized the possibility of the electrolyte decomposition, and allowed the cell to provide stable performance within wide voltage window [1]. Generally, 2D-TMD family consists of inert basal planes and active edge sites. Dependent on the number of exposed active edge sites, the TMDs will promote hydrogen evolution. For example, $ReS_2$ was deposited on the NTs surface, in the form of layered structure with exposed surface edge sites, improving the performance of the ECs (108 F $g^{-1}$ and 73 F $g^{-1}$, for composite and pristine $ReS_2$, respectively) while restricting the operational voltage to 0.8 V. Catalytic activity of exposed edge sites (or unsaturated sulfur atoms) is the reason for narrowing the voltage window of the cell. From operation of the negative electrode, it seems that the hydrogen storage does not proceed at all. On the contrary, hydrogen evolution reaction (HER) is observed. One of the reasons can be the mesoporous, edge-rich character of the NTs that exclude the possibility of the hydrogen storage [2]. What is also interesting, that the catalytic effect of TMDs has been observed regardless of the crystallographic structure (layered or cubic). For example, bulk $NiS_2$ deposited on the surface of the rGO limits the operating voltage window of the cell and decreases its specific capacitance due to rapid HER. Only asymmetric cell assembled in 6M KOH with rGO/$NiS_2$ working as the positive electrode and rGO as the negative one showed higher capacitance (165 F $g^{-1}$ at 0.2 A $g^{-1}$) than symmetric cell. Generally, electrolytes play the most important role for extension of the EC operating voltage. For example, during utilization of mesoporous carbon BP2000 and reline as an deep eutectic solvent type of electrolyte the high capacitance (157 F $g^{-1}$ at 1 A $g^{-1}$) of the cell has been achieved. Reline based ECs was able to withstand wide operating voltage window of 2.2 V proving its anticorrosive character. In addition, reline showed high capacitance retention of 88% for more than 25 000 cycles at 1 A $g^{-1}$ [3]. In a conclusion, the rational hybridization of the carbon support with pseudocapacitive materials is of paramount importance when designing new electrode material. Usually, the battery-like behaviour and catalytic activity of the dichalcogenides narrows the operational voltage windows and slows down the power response of the device. However, when properly design, electrode materials based on TMDs can be successfully employed in the ECs.

Acknowledgement: The authors would like to acknowledge the National Science Centre, Poland, for the financial support in the framework of the project 2018/31/B/ST4/01852.

**References**

[1] Koudahi, M. F. and Frąckowiak, E. (2022). Fast response supercapacitor based on carbon-$VS_2$ electrodes with a wide operating voltage range, Energy Storage Materials, 49, 255-267. https://doi.org/10.1016/j.ensm.2022.04.021

[2] Frąckowiak, E. , Koudahi, M. F., Tobis, M. (2021). Electrochemical Capacitor Performance of Nanotextured Carbon/Transition Metal Dichalcogenides Composites, Small, 17, 2006821. https://doi.org/10.1002/smll.202006821

[3] Azmi, S., Koudahi, M. F., Frąckowiak, E. (2022). Reline deep eutectic solvent as a green electrolyte for electrochemical energy storage applications, Energy & Environmental Science, 15, 1156-1171. https://doi.org/10.1039/D1EE02920G

Carbon 2022

# Preparation of Solvent Component of Spinnable Mesophase Pitch Using Ethylene Bottom Oil through the Bromination-debromination Reaction

**Taisei Tomaru[1], Takashi Mashio[1] Hiroki Shimanoe[1], Seung-Jae Ha[2], Young-Pyo Jeon[2], Koji Nakabayashi[1], Jin Miyawaki[1], Seong-Ho Yoon[1]**

[1]Interdisciplinary Graduate School of Engineering Science, Kyushu University, Kasuga, Fukuoka 816-8580, Japan.

[2]Center for C-Industry Incubation Korea Research Institute of Chemical Technology (KRICT), Daejeon, 34114, KOREA

E-mail: tomaru.taisei.827@s.kyushu-u.ac.jp

**Keywords**

Spinnable mesophase pitch, lyotropic liquid crystalline solution, bromination-dehydrobromination reaction

## INTRODUCTION

Spinnable mesophase pitch (SMP) are used as important precursors for fabricating advanced functional carbon such as carbon fiber. Recently, we proved that the AR pitch, which is one of SMPs and exhibits 100% optical anisotropy, is a lyotropic liquid crystalline solution. The AR pitch is composed of anisotropic mesogen and isotropic solvent components by the weight ratios of 70/30. In this study, we focused on the preparation of various ethylene bottom oil (EO)-based isotropic pitches as a solvent component for SMP by bromination-dehydrobromination of EO, to examine the decisive factor for controlling the characteristics of SMPs. For modifying the molecular structures of solvent components, coal tar (CT) or slurry oil (SO) was added to EO. Then, we examined anisotropic contents of the obtained SMPs that were prepared from the thermal-mixing of the mesogen and solvent components with different mixing ratios.

## MATERIALS AND METHODS

### Preparation of solvent components

**FIGURE 1** shows a scheme for preparing various solvent components. EO, CT and SO were solvent fractionated with hexane or tetrahydrofuran (THF), respectively, and the obtained hexane-soluble fraction of EO (EO-HS), THF-soluble fraction of CT (CT-THFS), and THF-soluble fraction of SO (SO-THFS) were used as raw materials. EO-HS and CT-THFS or SO-THFS were mixed at 10/0 and 7/3 of weight ratio, and the mixture was treated by pressurized heat treatment, bromination-dehydrobromination, vacuum distillation, and then thin layer evaporation (TLE). TLE was carefully repeated to obtain pitches with a softening point of 140 ± 3°C. The obtained solvent components were designated as shown in **FIGURE 1**.

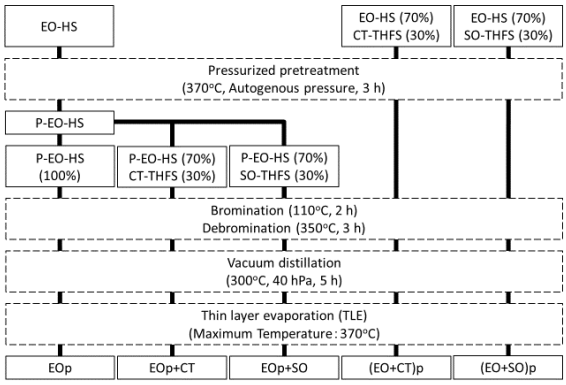


**FIGURE 1**: Preparation scheme of EO-based solvent components.

### Preparation of mesophase pitches

The obtained SMPs were prepared by thermal-mixing of each of the five prepared solvent components with mesogen one (THF-insoluble fraction of AR pitch: AR-THFI). AR-THFI and solvent

components were mixed by the weight ratios of 7/3, 6/4, 5/5, 4/6 and 3/7, respectively. The mixture was annealed at 370 °C for 10 min under the nitrogen atmosphere.

**Characterization of pitches**

The physical and chemical characteristics of the prepared EO-based isotropic pitches such as softening point (SP), elemental compositions, molecular structure and molecular weight distribution were measured by TMA, CHN elemental analysis, $^{1}$H-NMR, $^{13}$C-NMR and MALDI-TOF/MS, respectively. Anisotropic contents of pitches were evaluated using polarizing microscopy. Molecular stacking properties were analyzed by X-ray diffractometer (XRD).

## RESULTS AND DISCUSSION

**TABLE 1** shows the physical and chemical properties of the prepared solvent components together with those of THF-soluble fraction of AR pitch (AR-THFS). The addition of CT-THFS into EO-HS increased the pitch yield, molecular weight and aromaticity ($f_a$) of the obtained solvent pitches. The addition of SO-THFS also increased the pitch yield but decreased the aromaticity of the obtained pitches. Here, we assumed the mesogen concentration at which the obtained SMPs with more than 95% anisotropic texture was prepared as the threshold concentration (TC). All EO-based isotropic pitches showed higher TC than AR-THFS, suggesting that they have relatively lower solvent ability than that of AR-THFS. As shown in **FIGURE 2,** the EOp isotropic pitch prepared from only EO did not attain to TC at over the mixing ratios of 7/3 and could not express the 100% full anisotropy. The CT addition could improve the solvent ability: The EOp+CT and (EO+CT)p isotropic pitches showed the 100% full anisotropy at the mixing ratios of 7/3. However, the (EO+SO)p isotropic pitch showed less than 90% anisotropy even at the mixing ratio of 7/3, confirming the lower solvent ability. In this study, since the isotropic pitches were prepared by bromination-dehydrobromination, the all isotropic pitches had some amounts of methylene side chains, which made the solvent ability lower because of their difficulty of molecular stacking. It can be confirmed that the anisotropic textures of the obtained SMPs by the mixing ratios of 5/5~3/7 showed the difficulty to growing into large anisotropic texture through the coalescence with other anisotropic particles.

TABLE **1**: The properties of the solvent components.

| | Yield | TMA | Elemental analysis | | | | | TOF/MS | $^{1}$H-NMR | $^{13}$C-NMR |
|---|---|---|---|---|---|---|---|---|---|---|
| | | SP | C | H | N | O | H/C | AMW | $H_{ar}/H_{al}$ | $f_a$ |
| | [%] | [°C] | [%] | [%] | [%] | [%] | [at%/at%] | [-] | [-] | [-] |
| AR-THFS | - | 138.0 | 94.2 | 5.3 | 0.0 | 0.6 | 0.67 | 400 | 1.00 | 0.61 |
| EOp | 22.1 | 142.3 | 93.5 | 5.2 | 0.4 | 0.9 | 0.66 | 389 | 1.13 | 0.776 |
| EOp+CT | 26.4 | 139.9 | 93.5 | 4.9 | 0.7 | 0.9 | 0.63 | 403 | 1.54 | 0.829 |
| EOp+SO | 23.7 | 142.4 | 93.6 | 5.3 | 0.4 | 0.7 | 0.68 | 408 | 1.00 | 0.758 |
| (EO+CT)p | 28.9 | 141.4 | 93.4 | 5.0 | 0.7 | 0.9 | 0.63 | 405 | 1.58 | 0.829 |
| (EO+SO)p | 26.0 | 138.6 | 93.4 | 5.5 | 0.4 | 0.8 | 0.70 | 392 | 0.946 | 0.742 |

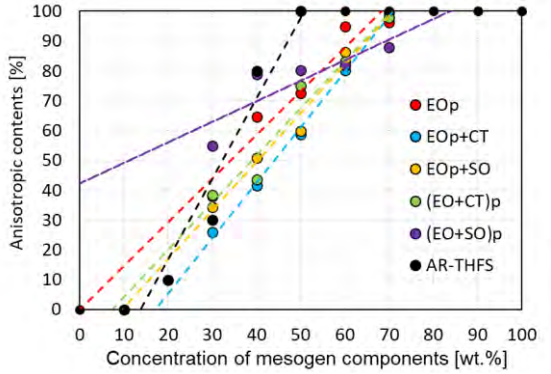


**FIGURE 2**: Anisotropic extents of the obtained SMPs according to mixing ratios of mesogen and solvent components.

## CONCLUSIONS

From the results, we became aware that the molecular structure of the solvent component was very important to express the full anisotropic texture. The increasing of carbon aromaticity by adding CT could improve such property of the solvent component.

**Acknowledgements**

This work was supported by the JSPS KAKENHI grant number 20K15321 and the Technology Innovation Program (10082582; Development of petroleum-based high-quality MP and high-yield MP for premium carbon materials) funded by the Ministry of Trade, Industry, and Energy (MOTIE, Korea).

**Reference**

Hiroki Shimanoe, Takashi Mashio, Hideki Nakashima, Seunghyun Ko, Young-Pyo Jeon, Koji Nakabayashi, Jin Miyawaki, Seong-Ho Yoon, (2022). Correlation between molecular stacking and anisotropic texture in spinnable mesophase pitch. *Carbon*, 192, 395-404. https://doi.org/10.1016/j.carbon.2022.02.062

Carbon 2022

# Tannin as Precursor for High-Performance Hard Carbon Anode in Sodium-Ion Batteries

**Hélène TONNOIR,[1] Da HUO,[1] Rafael L.S. CANEVESI,[2] Vanessa FIERRO,[2] Alain CELZARD[2] and Raphaël JANOT[1]**

[1]Laboratoire de Réactivité et Chimie des Solides, UMR7314 CNRS, Université de Picardie Jules Verne, Amiens, FRANCE

Email: helene.tonnoir@u-picardie.fr

[2]Institut Jean Lamour, UMR7198 CNRS, Université de Lorraine, Epinal, FRANCE

**Keywords**

Hard carbon, Sodium-ion batteries, Biomass

## CONTEXT

The energy transition is driving a sharp increase in demand for efficient and cheap electrochemical energy storage devices. The price of lithium carbonate, which is widely used for the production of lithium-ion battery, continues to rise: a 485% increase has been observed over 2021 (according to Benchmark Minerals). In this context, sodium-ion batteries (SIBs) present many advantages: with chemical properties similar to lithium, sodium is more abundant and evenly distributed on earth, which makes it less expensive. Thus, SIBs appear as a good alternative to lithium-ion batteries, especially for stationary applications.

Among all the different materials studied as anode for SIBs, hard carbons (HCs) have shown good electrochemical performances with reversible capacity between 250 and 300 mAh/g, low working potential (vs. $Na^+/Na$) and good cycling stability (Dou, 2019) (Daher, 2020). Moreover, these materials can be synthesized from various precursors, e.g. from biomass. In this study, we focused on tannins.

## RESULTS AND DISCUSSION

Tannins are polyphenolic molecules that are very abundant in nature. They present a similar reactivity to petrochemical molecules such as phenol and resorcinol (Tondi, 2009). Furthermore, they have quite low extraction costs. In our study, hard carbons were synthesized using tannin extracted from mimosa (Acacia mearnsii) bark. A tannin-based thermosetting resin was first produced as a rigid foam. This foam was then pyrolysed at four different temperatures (1000°C, 1200°C, 1400°C and 1600°C) under argon flow. The hard carbons obtained were characterized in terms of structure, texture and electrochemical properties in order to study the impact of the pyrolysis temperature on the characteristics of these materials.

Encouraging electrochemical performances have been obtained for the hard carbon pyrolysed at 1600°C: a reversible capacity ($Q_{rev}$) of 306 mAh/g and a coulombic efficiency at the first cycle ($CE1^{st}$) of 87 % at C/20 versus $Na^+/Na$ (Figure 1) (Tonnoir, 2022). These results are promising compared to other hard carbons derived from biomass precursors.

The galvanostatic profile of HCs can be divided into two parts: the sloping part corresponding to a decrease in potential down to 0.1 V; and the low-voltage plateau (< 0.1 V vs $Na^+/Na$). Each of these parts is related to the way sodium is stored in HC. Two main mechanisms have been proposed in the literature. The first one, proposed in 2000 by Stevens and Dahn (Stevens, 2000), associated the sloping

part with sodium intercalation between graphene layers in turbostratic domains, and the low-voltage plateau with micropores filling. In 2015, another mechanism was proposed by Bommier et al. (Bommier, 2015). They attributed the sloping part to sodium adsorption on structural defects and the plateau to sodium intercalation between graphene layers. Many studies have been conducted to confirm, refute and/or complement these mechanisms but no scientific consensus has been found. Nevertheless, all these studies show that three phenomena are involved in the storage of sodium in HC: intercalation of sodium ions between graphene layers, adsorption on structural defects and filling of micropores. In our case, the plateau region appears to be correlated with the filling of micropores by sodium.

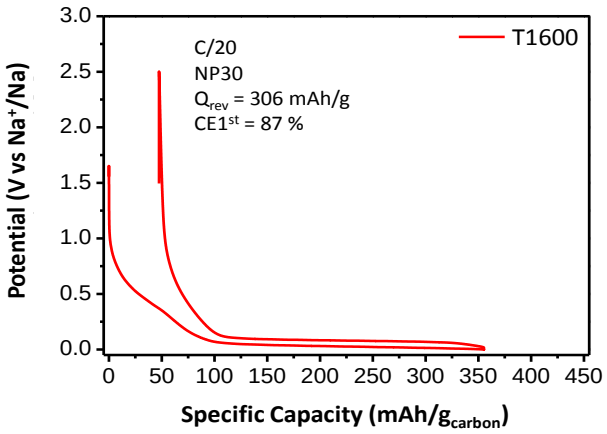


**FIGURE 1**: Galvanostatic profile at C/20 (18.6 mAh/$g_{carbon}$) of tannin-based HC pyrolyzed at 1600°C. Electrolyte: NP30 ($NaPF_6$ 1 mol/L in a mix of ethylene carbonate/dimethyl carbonate (mass ratio 1:1)).

## CONCLUSION

Through this presentation, we will demonstrate that the control of the synthesis conditions is a key factor for the optimization of the electrochemical performances of hard carbons, and we will discuss the impact of the structural and textural properties of the material on its electrochemical performance.

## References


Bommier, C., Surta, T. W., Dolgos, M., Ji, X. (2015) New Mechanistic Insights on Na-Ion Storage in Nongraphitizable Carbon. *Nano Lett.*, 15 (9), 5888–5892. https://doi.org/10.1021/acs.nanolett.5b01969.

Daher, N., Huo, D., Davoisne, C., Meunier, P., Janot, R. (2020) Impact of Preoxidation Treatments on Performances of Pitch-Based Hard Carbons for Sodium-Ion Batteries. *ACS Appl. Energy Mater.*, 3 (7), 6501–6510. https://doi.org/10.1021/acsaem.0c00727.

Dou, X., Hasa, I., Saurel, D., Vaalma, C., Wu, L., Buchholz, D., Bresser, D., Komaba, S., Passerini, S. (2019) Hard Carbons for Sodium-Ion Batteries: Structure, Analysis, Sustainability, and Electrochemistry. *Mater. Today*, 23, 87–104. https://doi.org/10.1016/j.mattod.2018.12.040

Stevens, D. A., Dahn, J. R. (2000) High Capacity Anode Materials for Rechargeable Sodium-Ion Batteries. *J. Electrochem. Soc.*, 147 (4), 1271. https://doi.org/10.1149/1.1393348.

Tondi, G., Fierro, V., Pizzi, A., Celzard, A. (2009) Tannin-Based Carbon Foams. *Carbon N. Y.*, 47 (6), 1480–1492. https://doi.org/10.1016/j.carbon.2009.01.041.

Tondi, G., Zhao, W., Pizzi, A., Du, G., Fierro, V., Celzard, A. (2009) Tannin-Based Rigid Foams: A Survey of Chemical and Physical Properties. *Bioresour. Technol.*, 100 (21), 5162–5169. https://doi.org/10.1016/j.biortech.2009.05.055.

Tonnoir, H., Huo, D., Canevesi, R. L. S., Fierro, V., Celzard, A., Janot, R. (2022) Tannin-Based Hard Carbons as High-Performance Anode Materials for Sodium-Ion Batteries. *Mater. Today Chem.*, 23, 100614. https://doi.org/10.1016/j.mtchem.2021.100614.

Carbon 2022

# Preparation of few-layered graphene by exfoliation of ternary interlayer compounds

**Masahiro Toyoda[1], Yuhei Zaizen[1], Hiroshi Yoshitani[2], Takuya Wada[2], Hiroji Fukui[2],**
[1]Graduate School of Engineering, Oita University, 700 Dannoharu, Oita 870-1192, Japan
[2]HSP Lab., SEKISUI CHEMICAL CO., LTD., Momoyama, Shimamoto-cho, Osaka 618-0021, Japan

Email: toyoda22@oita-u.ac.jp

**Keywords**
Graphene, Intercalation Componds, K-THF-GICs, Grafting

## INTRODUCTION

It is necessary to prepare graphene with a large area, few layers, and no oxidation. Thus far, we have determined that it is possible to prepare few-layer graphene without oxidation by synthesizing graphite intercalation compounds (GICs) and adding water to them [1], but only in a small area. Therefore, we investigated the addition of aldehydes (with different alkyl chain lengths containing electron-withdrawing groups, allowing the use of an electrophilic addition reaction on carbon hexagonal layers) to GICs to prepare few-layer graphene in a large area without oxidation. In this study, the solution method was used to synthesize stage 1 ternary graphite intercalation compounds (K-THF-GICs). Aldehyde solvents of different alkyl chain lengths were added to K-THF-GICs. Attempts have been made to prepare a few layers graphene with minimum oxidation. The results demonstrated that the addition of aldehyde containing an electron-withdrawing group to GICs promoted exfoliation with the electrophilic addition reaction in the carbon hexagonal layer forming few-layer graphene.

## MATERIAL AND METHOD

All the preparations of K-THF-GICs were performed in a glove box (Miwa, Model 1ADB-30AH, dew point of −80°C or less) in an atmosphere of high-purity Ar (purity 99.999%). The preparation of K-THF-GICs matrix was performed in a $50 \times 10^{-3}$ $dm^3$ sample bottle. A $20 \times 10^{-3}$ $dm^3$ tetrahydrofuran (THF, purity 99.5%, water content up to 0.001 wt%) was added, and $10 \times 10^{-3}$-mol naphthalene (Kishida Chemical) was dissolved in THF. Next, 0.5 g potassium metal (purity 99.5%) was added, and the mixture was stirred with a stirrer for 30 min. Therefore, 0.5 g host graphite with the particle size of 100 µm was immersed in the solution. The solution was stirred for 24 h to synthesize K-THF-GICs. The experimental conditions were optimized to prepare for stage 1 of K-THF-GIC. A stage 1 intercalation compound (K-THF-GIC) was used to obtain graphene through exfoliation. The obtained K-THF-GICs were washed twice with $20 \times 10^{-3}$ $dm^3$ THF. After THF washing, K-THF-GICs were weighed into a sample bottle, and butanal, heptanal, decanal, octadecanal, and decane solution were separately added and stirred for 72 h. Thus, few-layer graphene was prepared. After the reaction, the solution was separated into supernatant and sediment. The precipitate in the supernatant was recovered by repeatedly washing it with ethanol, THF, and water, followed by centrifugation to remove the alkali metal and solvent; the precipitate was then vacuum-dried at approximately 60°C to obtain few-layer graphene.

## RESULTS AND DISCUSSION

Fig. 1 shows the Raman spectra of graphite and few-layer graphene prepared using butanal, decanal, and octadecanal. The inset on the upper right side represents the result of peak separation after enlarging each two-dimensional (2D) (G') band; the broken line represents the peak after separation. In the Raman spectrum of graphite shown in Fig 1(a), a 2D (G') band was observed near 2726 $cm^{-1}$, and in butanal, a 2D (G') band was observed near 2725 $cm^{-1}$. There are no differences in the 2D (G') band of graphite and butanal.However, in decanal and octadecanal, 2D (G') bands were observed at approximately 2693 $cm^{-1}$

and 2695 $cm^{-1}$, respectively, and a redshift of the 2D (G') band was confirmed. It has been reported that a redshift of the 2D (G') band occurs in the Raman spectrum of graphite when the number of layers is less than five [2], implying the existence of graphene with less than five layers. When the areas of peaks on the low wavenumber side of the 2D (G') band are compared after the peak separation, the ratio of its peak area is approximately 42%, 39%, 57%, and 75% in graphite, butanal, decanal, and octadecanal, respectively, indicating that the addition of decanal and octadecanal produced few-layer graphene. Specifically, for octadecanal addition, the peak area on the low wavenumber side was the largest, and the exfoliation to form graphene occurred. Furthermore, comparing the D bands of graphite with those of decanal and octadecanal, the areas of the D bands of decanal and octadecanal increased. Therefore, the added aldehyde would be grafted onto the hexagonal layer of carbon. The images of few-layer graphene prepared using decanal and octadecanal are shown in Figs. 2(a) and (b), respectively; in addition, 002 lattice fringes of these graphene samples are shown in Figs. 2(c) and (d), respectively. Graphene with a surface area of several tens of $\mu m^2$ and two or three layers was confirmed. Specifically, graphene obtained from the addition of octadecanal produced a thin and large-area few-layer graphene, as observed in the black frame of the transmission electron microscopy (TEM) photograph (Fig. 2(b)). Thickness and area were calculated from the TEM images of 70 points of each sample, and the table shows the average value of the thickness and area of each sample. The results in Fig. 2(a) indicate that the thickness of few-layer graphene prepared with octadecanal is often thinner than that of the graphene prepared with decanal, implying that there are many sheets with thicknesses of 1–2 nm or less. In addition, it was confirmed that the proportion of sheets with a thickness of 2 nm or less was 74%. Moreover, the average thickness (decanal, 2.4 nm; octadecanal, 1.8 nm) for all samples was thinner than that of few-layer graphene (2.7 nm) prepared by adding water to K-THF-GICs [1] (Table).

## CONCLUSION

The addition of aldehyde containing an electron-withdrawing group to GICs promoted exfoliation with the electrophilic addition reaction in the carbon hexagonal layer forming few-layer graphene. According to Raman spectroscopy and TEM, graphene exfoliated by decanal as three and two layers, respectively, was minimally oxidized and demonstrated an area of several tens of $\mu m^2$. The grafting of few-layer graphene exfoliated using decane was possible. Such grafting may involve exfoliation. With little oxidation, few-layer graphene with a thickness of 2.0 nm and an average area of 100 $\mu m^2$ was obtained using decanal, which contains the longest alkyl chain among the solvents tested in this study.

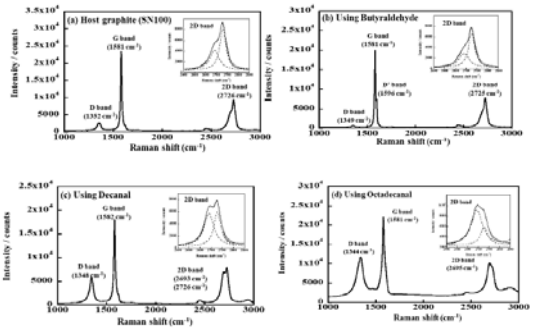


Fig.1. Raman spectra of (a) host graphite (SN100) and precipitate in a supernatant solution obtained by the addition of (b) butanal (c) decanal, and (d) octadecanal

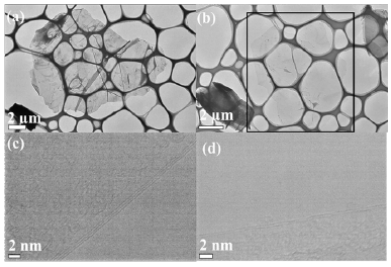


Fig. 2. TEM micrographs of the precipitate in a decanal supernatant solution (a) whole image and (c) 002 lattice, and in an octadecanal supernatant solution (b) whole image and (d) 002 lattic

Table Parameter of thickness and area of few-layered graphene

| | Thickness / nm | Area / $mm^2$ |
|---|---|---|
| Few-layerd graphene prepared using Decanal | 2.4 | 76 |
| Few-layerd graphene prepared using Octadecanal | 1.8 | 82 |
| Few-layerd graphene prepared using Water [20] | 2.7 | 6.2 |

References

[1] T. Wada, M. Toyoda et. al., J. Nano. Mater., vol. 2014, Article ID 925253
[2] A.C. Ferrai, J.C. Meyer, et. al., Phys. Rev. Lett. 97 (18) (2006) 187401.

Carbon 2022

# Correlation Of Structural Evolution And Electrochemical Behaviour Of Corncob Derived Non-Graphitizable Carbons

**Blaž Tratnik[a,b], Nigel Van de Velde[a], Gregor Kapun[a], Elena Tchernychova[a], Matija Tomšič[b], Andrej Jamnik[b], Boštjan Genorio[b], Alen Vizintin[a,*], Robert Dominko[a,b,c]**

[a] *National Institute of Chemistry, Hajdrihova 19, 1000, Ljubljana, Slovenia*
[b] *UL FKKT, Večna pot 113, 1000, Ljubljana, Slovenia*
[c] *ALISTORE-European Research Institute, CNRS FR 3104, Hub de l'Energie, Rue Baudelocque, 80039, Amiens Cedex, France*

Email: alen.vizintin@ki.si

**Keywords**
Hard carbons, Sodium-ion batteries, Structural evolution

Sodium ion batteries (SIBs) are considered as one of the promising candidates to displace lithium ion batteries (LIBs) in the large-scale energy storage application due to the abundance of raw materials and homogenous sodium distribution around the globe (Vaalma *et al.*, 2018; Liu *et al.*, 2019). A number of cathode materials have already been employed for SIBs (Fang *et al.*, 2015; Komaba *et al.*, 2019). Meanwhile, the research and development on the anodic side has faced more obstacles. Graphite, the anodic material in LIBs is not suitable for the use in SIBs. Therefore, due to its inability to form binary graphite intercalation compounds with sodium, non-graphitizable carbons are currently the most viable option as negative electrode materials in SIBs because of their low price, high storage capacity and cycling stability (Irisarri, Ponrouch and Palacin, 2015). Additionally, non-graphitizable carbons can be obtained through the pyrolysis process of waste biomass. In this regard, the waste biomass is incorporated into the circular economy, reducing the strain on the environment. However, the choice of the precursor (e.g. cellulose, lignin, etc.) for the non-graphitizable carbon synthesis plays a deciding role in the structural and morphological evolution during heat treatment, dictating the electrochemical performance of produced carbon materials.
In this study, corncob derived non-graphitizable carbons were prepared via two-step carbonization process. The second step was implemented to 1200°C, 1400°C and 1600°C, respectively. The obtained samples were denoted as Corn@900°C, Corn@1200°C, Corn@1400°C and Corn@1600°C. Structural, textural and morphological properties were determined by employing conventional characterization techniques (Raman spectroscopy, X-ray diffraction (XRD) and $N_2$ adsorption) and less frequently used ones (electron energy loss spectroscopy (EELS) and small and wide angle X-ray scattering (SWAXS)).
The concentration of defects was determined by Raman and the values decreased with increasing temperature of carbonization. However, Raman is recommended for the analysis of graphitic materials, while non-graphitizable carbons also exhibit amorphous domains. Therefore, the prepared materials were additionally investigated with EELS. EELS spectra provide important information on the degree of graphitization by determining the ratio of $sp^2/sp^3$ hybridization. In contrast to Raman, EELS unambiguously provides information on the graphitization degree, irrespective of the material studied. The $sp^2/sp^3$ ratio increases with the increasing temperature of carbonization, from 4.12 for Corn@900°C to 5.36 for Corn@1600°C. Additional information about the structure of the corncob derived carbons was obtained from the interlayer spacing, *d*, as determined from XRD. The values of *d* ranged from 0.376 nm to 0.367 nm. These values are sufficient for $Na^+$ ions to intercalate between the graphene sheets of corncob derived non-graphitizable carbons. Gas adsorption measurements were performed with $N_2$ to determine the

specific surface area and the volume and size of pores. All studied materials exhibited characteristics of non-porous materials as well as low surface areas ranging from 7.3 to 11.2 $m^2 g^{-1}$. The average open pore width decreased from 10.0 nm for Corn@900°C to 8.0 and 8.1 nm for Corn@1200°C and Corn@1400°C, respectively. However, the average pore width for Corn@1600°C increased to 9.6 nm. Yet the total open pore volume decreased from $3.5\times10^{-3}$ $cm^3 g^{-1}$ for Corn@900°C to $1.3\times10^{-3}$ $cm^3 g^{-1}$ for Corn@1600°C. Insights into the structure in different spatial resolutions were obtained by the use of SWAXS, a characterization technique not so commonly employed in the field of non-graphitizable carbons. Depending on different ranges of the length of the scattering vector *q*, the structural information on length scales ranging from approximately 2 Å up to approximately 79 nm can be extracted from the SWAXS data. It is a very useful technique to complement the shortcomings of other characterization techniques. For example, the total surface area of pores including closed pores can be determined by SWAXS, while it could not be determined by gas adsorption measurements, due to the inability of gas molecules to penetrate the closed pores. Additional parameters describing the porosity were determined, namely the pore volume fraction, the average pore width and the average width of the carbon matrix. On a more atomistic level, parameters describing the specific bending and curvature of the graphene layers in the non-graphitizable carbons were described. Parameters such as the distortion length beyond which the long-range order is lost, the length below which the layers can be considered as effectively flat and the distortion length which determines the layer-layer distance above which the long-range order is lost provide a detailed description of the carbon structure. Overall, the investigated materials followed a trend of increased ordering of the carbon structure with the increased final temperature of carbonization.

The electrochemical characterization of investigated materials was performed to establish correlations between the structural properties and electrochemical behavior. Initial Coulombic efficiencies (iCE) ranged from 62% to 73% with Corn@1400°C exhibiting the highest efficiency. iCE constituted a correlation with the total surface area of the materials – higher surface areas led to lower efficiencies. Capacity contributions were separated into two regions, namely the sloping region above 0.1V and the plateau region below 0.1V. The plateau contribution for Corn@900°C amounted to 44%, gradually increasing for other samples and finally reaching 74% for Corn@1600°C. Several parameters obtained from SWAXS i.e., the correlation length beyond which the long-range order is lost, the length beyond which the regions can be considered locally flat, and distortion length which determines the layer-layer distance above which the long-range order is lost, correlate well with the results on the capacity contribution of the plateau region. Long term cycling was also performed. Reversible capacities of 166.9 mAh $g^{-1}$, 204.9 mAh $g^{-1}$, 258.2 mAh $g^{-1}$ and 234.6 mAh $g^{-1}$ were achieved after 100 cycles for Corn@900°C, Corn@1200°C, Corn@1400°C and Corn@1600°C respectively.

Full cell experiment in a 3-electrode configuration was performed. Corn@1400°C was selected as the negative electrode and $Na_3V_2(PO_4)_2F_3$ (NVPF) was used as the positive electrode while sodium metal was used as the reference electrode. As a consequence of the irreversible loss of the active material, the positive electrode (NVPF) could not be fully sodiated at the end of the first cycle. Long term cycling was additionally performed with a two electrode full cell. The cell exhibited 85 mAh $g^{-1}$ after 100 cycles.

**References**

Fang, Y. *et al.* (2015) 'Hierarchical Carbon Framework Wrapped Na 3 V 2 (PO 4 ) 3 as a Superior High-Rate and Extended Lifespan Cathode for Sodium-Ion Batteries', *Advanced Materials*, 27(39), pp. 5895–5900. doi: 10.1002/adma.201502018.

Irisarri, E., Ponrouch, A. and Palacin, M. R. (2015) 'Review—Hard Carbon Negative Electrode Materials for Sodium-Ion Batteries', *Journal of The Electrochemical Society*. The Electrochemical Society, 162(14), pp. A2476–A2482. doi: 10.1149/2.0091514jes.

Komaba, S. *et al.* (2019) 'Electrochemically Reversible Sodium Intercalation of Layered NaNi0.5Mn0.5O2 and NaCrO2', *ECS Transactions*, 16(42), pp. 43–55. doi: 10.1149/1.3112727.

Liu, T. *et al.* (2019) 'Exploring competitive features of stationary sodium ion batteries for electrochemical energy storage', *Energy and Environmental Science*. Royal Society of Chemistry, 12(5), pp. 1512–1533. doi: 10.1039/c8ee03727b.
Vaalma, C. *et al.* (2018) 'A cost and resource analysis of sodium-ion batteries', *Nature Reviews Materials*. doi: 10.1038/natrevmats.2018.13.

Carbon 2022

# Bio-Based Carbon Fibers: Increasing Carbon Yield And Mechanical Performance

**Christoph Unterweger[1], Jiri Duchoslav[2], Alexander Lumetzberger[2], Igor Pasti[3], Stefan Breitenbach[1], David Stifter[2] and Christian Fürst[1]**

[1]Wood K plus – Kompetenzzentrum Holz GmbH, Altenberger Strasse 69, 4040 Linz, Austria
Email: c.unterweger@wood-kplus.at

[2]Johannes Kepler University Linz, Center for Surface and Nanoanalytics (ZONA), Altenberger Strasse 69, 4040 Linz, Austria

[3]University of Belgrade - Faculty of Physical Chemistry, Studentski trg 12-16, 11158 Belgrade, Serbia

**Keywords**
Cellulose Fibers, Carbonization, Process Optimization

## INTRODUCTION

Carbon fibers (CF) are used in composite applications because of their exceptional mechanical properties, especially when weight saving is important, for example in aerospace, sports, wind energy or defense. Larger application, especially in automotive, is hindered due to the high costs of CF, which can be mostly attributed to the precursor PAN, a fossil-based polymer. Thus, there is a demand for development of cheaper, more sustainable precursor fibers (Peijs, 2022). Novel low-cost carbon fibers should at least reach a strength of 1700 MPa and a corresponding elastic modulus of 170 GPa, as stated by the US Department of Energy. Promising bio-based precursors are lignin (Kadla, 2002), cellulose (Spörl, 2017) or even lignin-cellulose composite fibers (Bengtsson, 2020), but reaching the target values is still a challenge, especially the modulus values. While the carbon yield is significantly higher for lignin, cellulose fibers seem to be more promising at the moment, as commercial filaments are available and various methods for improving the low carbon yield and the mechanical performance are described in the literature (Vocht, 2022).

## MATERIALS AND METHODS

A viscose 1840 dtex multifilament yarn consisting of 1000 single fibers was used as precursor. Aqueous solutions of ammonium dihydrogen phosphate (ADP) and diammonium sulfate (DAS) were used as impregnating agents. The concentrations were evaluated in preliminary trials and set to 2.8 wt% for DAP and 6.5 wt% for DAS in order to achieve a loading of 1 wt% P/cellulose or 2 wt% S/cellulose, which were found as optimum loadings in a previous study (Scholz, 2019).

Three tube furnaces (FRHT-5-100/2500/300, FRHT-5-100/2500/1050, FRH-2-50/1000/1700 by Linn High Therm) were used for the continuous thermal conversion of cellulose to CF. For stabilization, all five heating zones were set to the same temperature. 220, 230 and 240 °C were tested, while stretching of approximately 3 % was applied. For low temperature (LT) carbonization, the following temperature profile was used: 300 – 340 – 380 – 570 – 900 °C. By variation of tension and residence time (2 – 8 min per heating zone), the mechanical performance of the resulting CF was optimized. For the subsequent high temperature (HT) carbonization, both heating zones were set to 1500 °C. All three process steps were carried out individually, in order to allow characterization of the intermediates.

For each process step, the yield was determined. The stabilized and carbonized fibers were characterized by single fiber tensile test. The change of carbon structure was evaluated by XRD.

## RESULTS AND DISCUSSION

Both impregnation agents lead to significant improvements compared to a non-impregnated filament. The yield is significantly improved and a continuous carbonization process could be established, when either of the two impregnation agents is used. However, the yield after stabilization and subsequent LT carbonization is significantly higher for ADP. In addition, stabilization was possible up to 240 °C, while for DAS, the filament broke when stabilized at this temperature. 230 °C was the optimum stabilization temperature for both impregnation agents and the mechanical performance of the fibers after subsequent LT carbonization was identical. Despite lower total yields (35.7 vs. 42.6 %), DAS was chosen for further optimization, as the mass loss during carbonization is lower, thus, resulting in a more stable process and allowing more flexibility in process optimization.

FIGURE 1 shows that increased residence during the LT carbonization step leads to improved strength and modulus of the resulting CF.

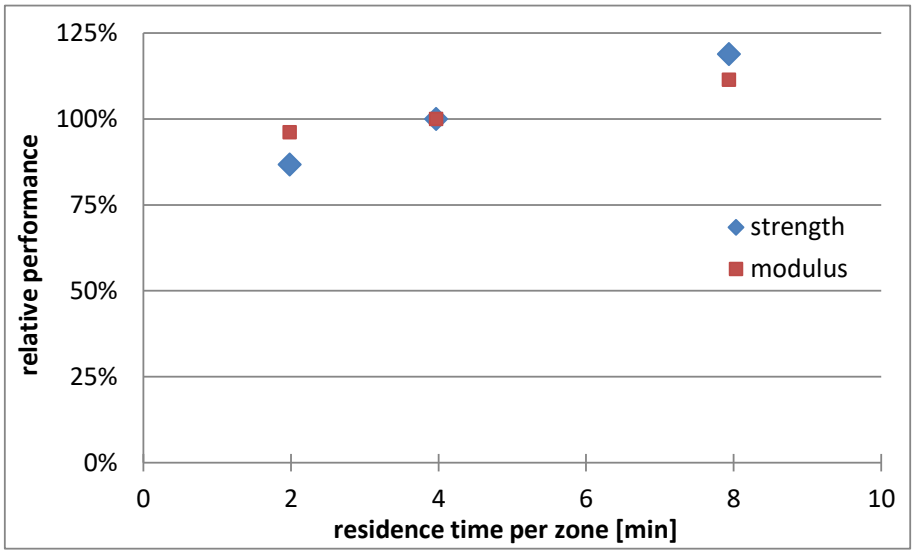


**FIGURE 1**: Influence of residence during LT carbonization on the mechanical performance of resulting CF

In a subsequent trial, the tension was varied during the carbonization steps. As can be seen in TABLE 1, both, strength and modulus, can be increased when higher tension is applied and the fiber is stretched during the LT process. By subsequent HT carbonization up to 1500 °C, the modulus can be further increased. This improvement is more pronounced for the fibers that were already stretched during the LT step and also higher tension can be applied during the HT step, leading to even higher tensile modulus of the resulting CF. The total yield after HT carbonization is 30 %. The best CF have an average strength of 1450 MPa strength and 85 GPa modulus. However, it has to be noted that the spread is quite large with the best single fiber even reaching 2250 MPa strength and 120 GPa modulus.

**TABLE 1**: Properties of CF in dependence of processing parameters

| process | tension | modulus [GPa] | strength [MPa] | elongation [%] | diameter [µm] |
|---|---|---|---|---|---|
| stab. | | 4.8 ± 0.5 | 165 ± 19 | 31.4 ± 5.8 | 10.6 ± 0.4 |
| stab.+LT | low | 48.3 ± 4.9 | 972 ± 146 | 2.0 ± 0.3 | 7.9 ± 0.2 |
| stab.+LT+HT | low+mid | 60.6 ± 5.2 | 1156 ± 194 | 1.8 ± 0.2 | 7.6 ± 0.3 |
| stab.+LT | high | 59.6 ± 2.9 | 1298 ± 179 | 2.1 ± 0.3 | 7.1 ± 0.2 |
| stab.+LT+HT | high+low | 71.7 ± 4.2 | 1007 ± 101 | 1.4 ± 0.1 | 7.0 ± 0.2 |
| stab.+LT+HT | high+mid | 77.2 ± 7.9 | 1216 ± 216 | 1.6 ± 0.2 | 6.6 ± 0.3 |
| stab.+LT+HT | high+high | 84.8 ± 9.8 | 1447 ± 185 | 1.7 ± 0.2 | 6.5 ± 0.3 |

XRD analysis revealed significant improvement of the carbon structure after each processing step, i.e. the calculated interlayer spacing is reduced with increasing temperature. In contrast to mechanical testing, no influence of the applied tension could be observed in the XRD spectra.

## CONCLUSIONS

A cellulose multifilament could be successfully converted to CF, when either ADP or DAS is used as impregnation agent before stabilization. The optimum stabilization temperature was found to be 230 °C. While the total yield is higher when using ADP, a more stable process is obtained when DAS is used. Longer residence time and higher tension during the LT process improve the mechanical performance of the resulting CF. Additional HT carbonization leads to further increase of the tensile modulus, especially when tension is applied, while no significant impact on the strength could be observed. A total yield after HT carbonization of 30 % can be achieved. The best results so far are:

- 1450 MPa strength and 85 GPa modulus (average from at least 20 single fibers)
- 2250 MPa strength and 120 GPa modulus (best single fiber)

**Acknowledgements**

This work was funded by the European Regional Development Fund (EFRE) and the province of Upper Austria through the program IWB 2014-2020 (project BioCarb-K).

**References**

Bengtsson, A., Hecht, P., Sommertune, J., Ek, M., Sedin, M., and Sjöholm, E. (2020). *ACS Sustainable Chemistry & Engineering*, 8 [17], 6826-6833. https://doi.org/10.1021/acssuschemeng.0c01734

Kadla, J.F., Kubo, S., Venditti, R. A., Gilbert, R. D., Compere, A. L., and Griffith, W. (2002). Lignin-based carbon fibers for composite fiber applications. *Carbon*, 40, [15], 2913-2920. https://doi.org/10.1016/S0008-6223(02)00248-8

Peijs, T., Kirschbaum, R., and Lemstra, P. J. (2022). Chapter 5: A critical review of carbon fiber and related products from an industrial perspective. *Advanced Industrial and Engineering Polymer Research*, 5, [2], 90-106. https://doi.org/10.1016/j.aiepr.2022.03.008

Scholz, R., Herbig, F., Beck, D., Spörl, J., Hermanutz, F., Unterweger, C. and Piana, F. (2019). Improvements in the carbonisation of viscose fibres. *Reinforced Plastics*, 63, [3], 146-150. https://doi.org/10.1016/j.repl.2018.10.002

Spörl, J. M., Beyer, R., Abels, F., Cwik, T., Müller, A., Hermanutz, F., and Buchmeiser, M. R. (2017). Cellulose-Derived Carbon Fibers with Improved Carbon Yield and Mechanical Properties. *Macromolecular Materials and Engineering*, 302, 1700195. https://doi.org/10.1002/mame.201700195

Vocht, M. P., Ota, A., Frank, E., Hermanutz, F., and Buchmeiser, M. R. (2022). Preparation of Cellulose-Derived Carbon Fibers Using a New Reduced-Pressure Stabilization Method. *Industrial & Engineering Chemistry Research*, 61, [15], 5191-5201. https://doi.org/10.1021/acs.iecr.2c00265

Carbon 2022

# The Advancing Uses of Agro-industrial Wastes: Potential Application In Drug Delivery Systems and Water Sanitation.

**Bernal Valentina [1] , Rodriguez-Estupiñan Jenny Paola [1] , Giraldo Liliana [1] , Moreno-Piraján Juan Carlos 2[2]**

Departamento de Química. Universidad Nacional de Colombia. Cra 30 No. 45-03, Bogotá, D. C.

Email: vbernalf@unal.edu.co

[2] Departamento de Química. Universidad de los Andes. Cra. 1a No. 18A- 10, Bogotá, D. C o

**Keywords**
Adsorption, graphene-based materials, activated carbon.

## INTRODUCTION

The circular economy is one of the most used concepts worldwide; it is defined as a new model of production and consumption. The main idea is to reduce waste to a minimum through practices such as recycling and reusing, etc (Stahel, 2016).
The food residues draw attention because large quantities of this waste are produced around the world; only the European Union produces around 88 million tonnes of food waste every year. In some cases, these residues can be revalued by becoming new materials after different processes (Scherhaufer, 2018).
The biomass (organic matter like fruit and vegetable peels) is made up of polymers with high carbon content such as cellulose, hemicellulose, lignin, and other carbohydrates. Which after chemical and physical processes (e.g. thermal treatments, metal salt impregnation) can be converted into carbonaceous materials such as graphene or activated carbon, high-cost materials (Reyes, 2021).

In this work, we prepared two carbonaceous materials from mangosteen shells. The physicochemical characteristics of the adsorbents were determined by Nitrogen isotherms at 77 K, SEM-EDS, FT-IR, and other techniques. Then, the materials were used to adsorb 5-Fluorouracil (5-FU) from an aqueous solution. This drug is an antineoplastic considered an emerging pollutant. The maximum drug adsorption was calculated from the isotherms at different temperatures. To evaluate the adsorbent-adsorbate affinity we performed immersion calorimetry in 5-FU solutions at 290 K.

## METHODOLOGY

### Activated carbon

The mangosteen shells were crushed, washed with hot water (363 K), and dried at 373 K. Then, the material was sieved (sieve 18, ASTM standard). 500 g of pre-conditioned material was immersed in $H_3PO_4$ solution (50%, 1L). The mixture was stirred for 24h at room temperature.

The sample was deposited in a quartz cell and subjected to thermal treatment at 723 K for 2h under a nitrogen atmosphere. The sample was called M-AC.

**Graphene-derived material**

On the other hand, another fraction of mangosteen peel was used SAG (Simultaneous Activation Graphitization) process. 3 g of mangosteen shells was mixed with of $ZnCl_2$ (9 g) in 50 mL of $FeCl_3$ solution (3 M). The mixture was evaporated at 363 K for 2 h under stirring. Then, the sample was dried at 373 K. Subsequently, the material was subjected to activation and graphitization. These processes were carried out in a THERMOLYNE furnace at 1173 K for 1 h under a nitrogen atmosphere. The sample was called M-GM.

**Adsorption test**

For the determination of paracetamol adsorption isotherms, 10 mg of each activated carbon was weighed in glass containers and 10 mL of 5-FU solution was added. The containers were stirred at 287 K until equilibrium was reached. Then, the solutions were filtered and the equilibrium concentration was determined by UV-vis spectrophotometry.

**RESULTS**

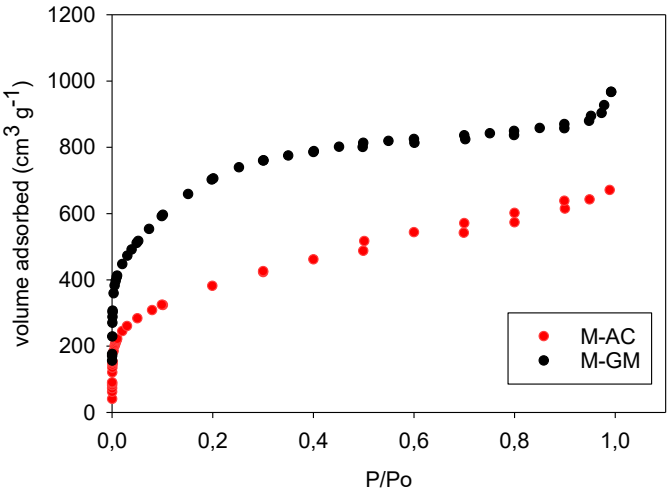


**FIGURE 1**: Nitrogen adsorption isotherms at 77K for the samples M-AC and M-GM.

Two materials were obtained from the mangosteen peel, the surface areas were 2531 and 1304 $m^2$ $g^{-1}$ for M-GM and M-AC, respectively.
At room temperature (287 K), the adsorption capacity of 5-FU was 1.94 mmol $g^{-1}$ on M-GM and 0.50 mmol $g^{-1}$ on M-AC.

**CONCLUSION**

Carbonaceous materials can be obtained from mangosteen peel using chemical activation with phosphoric acid and the SAG method. These adsorbents are useful for the adsorption of 5-FU. It is observed that the adsorption capacity of this compound increases proportionally with the surface area of the adsorbents.

**References**

Reyes, L., Abdelouahed, L., Mohabeer, C., Buvat, J. C., & Taouk, B. (2021). Energetic and exergetic study of the pyrolysis of lignocellulosic biomasses, cellulose, hemicellulose and lignin. Energy Conversion and Management, 244, 114459. https://doi.org/10.1016/j.enconman.2021.114459

Scherhaufer, S., Moates, G., Hartikainen, H., Waldron, K., & Obersteiner, G. (2018). Environmental impacts of food waste in Europe. Waste management, 77, 98-113. https://doi.org/10.1016/j.wasman.2018.04.038
Stahel, W. R. (2016). The circular economy. Nature, 531(7595), 435-438. https://doi.org/10.1038/531435a

Carbon 2022

# Fischer-Tropsch synthesis over lignin-derived cobalt-containing carbon fiber catalysts prepared in a single step by electrospinning

**María José Valero-Romero[1], Francisco José García-Mateos[1], Xiaohui Sun[2], Freek Kapteijn[2], José Rodríguez-Mirasol[1] and Tomás Cordero[1]**

Email: garciamateos@uma.es

[1]Departamento de Ingeniería Química, Escuela de Ingenierías, Universidad de Málaga, Andalucía Tech, Campus de Teatinos S/n, Málaga, 29071, Spain
[2] Catalysis Engineering, Department of Chemical Engineering, Delft University of Technology, Van der Maasweg 9, Delft, 2629, HZ, Netherlands

**Keywords**
Fischer-Tropsch synthesis, lignin, electrospinning, Co-containing carbon fibers

## INTRODUCTION

The growing concerns of greenhouse effects of using fossil resources have spurred worldwide interest in finding alternative feedstock for important petrochemical commodities and fuels. In this context, the development of efficient routes for the transformation of biomass into useful chemicals and fuels is of primary importance. Among possible options for the valorisation of biomass, gasification (followed by syngas cleaning) and Fischer-Tropsch synthesis (FTS) has received a renewed attention due to the growing attention to the use of sustainable energy and the implementation of more stringent environmental legislation on liquid fuels. In addition to this, biomass residues could be used to produce renewable FTS catalyst supports, and as a result both processes of biomass conversion have a positive environmental and economic impact (Valero-Romero, 2021).

In the present, work submicron-sized cobalt-containing lignin fibers have been prepared by the electrospinning technique, using Alcell lignin as carbon precursor, a low-cost co-product of the paper making industry. Carbon fibers were obtained by carbonization of Co-containing lignin fibers at different temperatures, yielding cobalt nanoparticles very well dispersed on the carbon fibers surface. These fibrillar catalysts were tested for Low-Temperature FTS using different $H_2$/CO ratios.

## EXPERIMENTAL

Cobalt-containing lignin-based submicron-sized fibers were synthesized in one step by electrospinning, in a coaxial configuration (Lallave, 2007), and using a cobalt nitrate-lignin-ethanol solution with a weight ratio of 0.17:1:1 (Co:lignin:ethanol). The lignin fibers were later thermostabilized in air at 200 ºC for 1 h to prevent lignin fibers from fusion during the following carbonization process at 500, 650 or 800 ºC for 1 h in inert atmosphere to obtain lignin-based cobalt-containing porous carbon submicrometer sized fibers. The cobalt-containing carbon fibers were denoted as Co@CF-T, where T indicates the heat-treatment temperature. The FTS catalysts were tested in a six-flow fixed-bed microreactor setup (Sartipi, 2013). Prior to the FTS reaction the catalysts were reduced *in-situ* by $H_2$ at 350 ºC for 3 h. The reaction conditions were 220 and 240 ºC, $H_2$/CO molar ratios of 1 or 2 and space velocities of 3.3, 4, 5.3 and 8 $m^3_{STP}\ kg_{cat}^{-1}\ h^{-1}$.

## RESULTS AND DISCUSSION

The Co-containing carbon fibers catalysts present a Co loading of 7, 8 and 12 *wt.* % for Co@CF-500, Co@CF-650 and Co@CF-800, respectively, due to the higher devolatilization of the Co-containing lignin fibers at higher heat-treatment temperatures. Furthermore, the catalysts present a well-developed

porosity ($S_{BET}$ = 418-460 $m^2$ $g^{-1}$), attributed to a self-induced carbon oxidation during the carbonization stage by the oxygen retained on the surface of the lignin fibers from the stabilization process, which may be catalyzed by the presence of Co. Figure 1a evidences the high flexibility of this type of carbon fibers, which allows them to be adapted as a catalytic fixed bed in a tubular reactor. The cobalt containing fibers have diameter sizes ranging from 0.25 µm to 2.0 µm (Figure 1b and 1c), smaller than lignin-derived carbon fibers heat-treated at similar conditions but without cobalt (1-4 µm) (Lallave, 2007). TEM images (Figures 1c and 1d) evidence the high dispersion of Co on the carbon fiber, whose particle sizes increased with carbonization temperature. The samples carbonized at 500 and 650 ºC present narrow cobalt particle size distributions with average particles between 6 to 13 nm, within the optimal range of Co-particle size for FTS (Bezemer, 2006). The carbon selectivity to the different product ranges over Co@CF-500 and Co@CF-650 is compared in Figure 2 at iso-conversion conditions. Co@CF-500 presents a relatively high selectivity to long chain hydrocarbons (C5+) and a lower selectivity to methane (C1). Raman and HR-TEM showed that higher pyrolysis temperature (> 500 ºC) led to Co-containing carbon fibers catalysts with larger metallic cobalt nanoparticle sizes encapsulated in graphitic-type carbon. This rendered them inaccessible for the FTS reactants, decreasing the activity and selectivity to C5+ hydrocarbons on these materials.

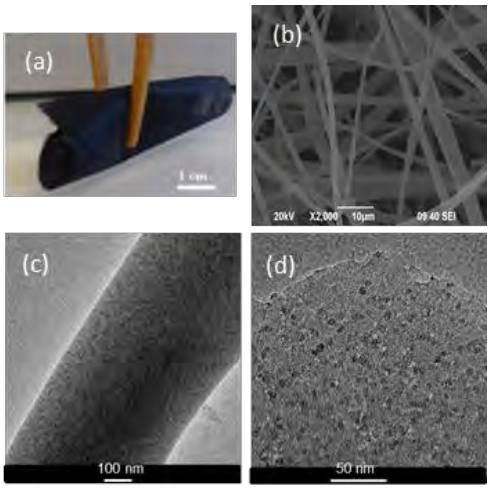


**FIGURE 1**: (a) photo of Co@CF-500 showing the catalyst flexibility, (b) SEM image, (c) TEM image and (d) HR-TEM image showing Co NPs for Co@CF-500.

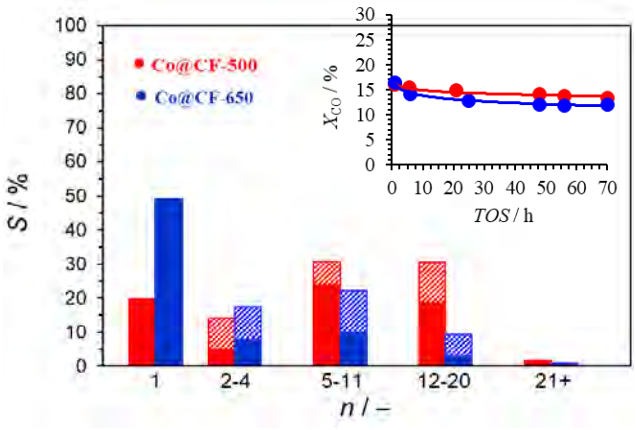


**FIGURE 2**: Carbon selectivity toward products of FTS at iso-conversion conditions after 70 h on stream; ▌: n-paraffins, ///: sum of isoparaffins and olefins. Reaction conditions: 513 K, 20 bar, $H_2/CO$ = 1 y GHSV / $m^3_{STP}$ $kg^{-1}_{cat}$ $h^{-1}$ = 4.5 and 6 for Co@CF-650 and Co@CF-500, respectively

**Acknowledgements**

The authors acknowledge the Spanish Ministry of Science, Innovation, and Universities (MICIU) and FEDER (Project RTI2018-097555-B-I00) and Junta de Andalucía (Project UMA18-FEDERJA-110 and P18-RT-4592).

**References**

Bezemer G. L., Bitter J. H., Herman Kuipers P.C.E.H, Oosterbeek H., Holewijn J. E., Xu S., Kapteijn F., Jos van Dillen J. and P. de Jong K. (2006). Cobalt particle size effects in the Fischer−Tropsch reaction studied with carbon nanofiber supported catalysts. *J. Am. Chem. Soc.*, 128, 3956–3964. https://doi.org/10.1021/ja058282w

Lallave M., Bedia, J., Ruiz-Rosas R., Rodríguez-Mirasol J., Cordero T., Otero J.C., Marquez M., Barrero A., Loscertales I.G. (2007). Filled and hollow carbon nanofibers by coaxial electrospining of Alcell lignin without binder polymers. *Advanced Materials*, 19, [23], 4292-4296. https://doi.org/10.1002/adma.200700963

Sartipi, S.; Jansma, H.; Bosma, D.; Boshuizen, B.; Makkee, M.; Gascon, J.; Kapteijn, F., Six-flow operations for catalyst development in Fischer-Tropsch synthesis: bridging the gap between high-throughput experimentation and extensive product evaluation. *Review of Scientific Instruments* **2013,** *84*, 124101-1-11 doi: http://dx.doi.org/10.1063/1.4834895.

Valero-Romero M. J., Rodríguez. Cano, M.A. Palomo, J. Rodríguez-Mirasol, J. Cordero T. (2021) Carbo-based materials as catalyst supports for Fischer-Tropsch synthesis: A Review. *Frontiers in Materials*, ISSN: 22968016. https://doi.org/10.3389/fmats.2020.617432

Carbon 2022

# Synthesis of Carbon Sorbents for CBR Protection: from Waste to Life Saver

**Leticia F. Velasco[1], Seitkhan Azat[2], Almagul Kerimkulova[2], Adrián Fernández Frías[1,3], Zulkhair Mansurov[2] and Peter Lodewyckx[1]**

[1]Department of Chemistry, Royal Military Academy, Avenue Renaissance 30, 1000 Brussels, Belgium
Email: leticia.fernandezvelasco@mil.be

[2]Institute of Combustion Problems, 172 Bogenbay batyr str, Almaty, Republic of Kazakhstan
[3]Autonomous University of Madrid, Ciudad Universitaria de Cantoblanco, 28049 Madrid

**Keywords**
Biomass waste, valorization, CBR protection

## INTRODUCTION

The increasing probability of both toxic industrial chemicals and chemical warfare agents being released to the atmosphere indicates the urgent need for highly efficient materials capable of protecting both military and civilian personnel. In this regard, the most common fillers currently used in gas mask canisters are impregnated activated carbons. However, it is still necessary to further develop them to properly afford broad spectrum protection. Moreover, growing industrial activities have led to waste biomass disposal problems. In this context, the valorization of these residues into high value-added carbon materials for CBR protection is of particular interest. Hence, and in order to face both problems at once, low-cost porous carbon sorbents have been synthesized from local waste biomass precursors and further impregnated following different strategies in order to confer suitable reactivity to their surface. The obtained materials were thoroughly characterized and their performance towards the removal of organic vapours and inorganic gases was assessed by breakthrough experiments performed in realistic conditions and compared to the one exhibited by commercial sorbents. Gathering and connecting these results allowed tailoring their textural, surface, physical and mechanical properties, in order to meet the operational requirements of the intended application and to optimize their efficiency.

## EXPERIMENTAL

First of all, the conditions for the synthesis of the raw sorbents were optimized in order to obtain a material with a developed and accessible porosity. For this purpose, several biomass wastes (including nutshell, rice husk and apricot stone) were used as precursors and different activation procedures were assessed.

Subsequently, the activated carbons with the desired properties were impregnated with metals (Cu, Co, Zn, Zr…) following different approaches including, among others, those proposed by Li (2016), Boutillara (2019) and Yang (2020).

The textural and surface properties of all the materials were studied by means of nitrogen, carbon dioxide and water vapour isotherms, thermogravimetric measurements, SEM-EDX… Their performance towards the sorption of both organic vapours and inorganic gases was evaluated by breakthrough time experiments. A screening of their efficiency was initially conducted at a small scale in a dynamic sorption analyzer (mixSorb S, 3P Instruments). Then, the most promising materials were tested at a real-scale in a specialized test rig. URC (Universal Respirator Carbon, Calgon Carbon Co) was used as a reference material.

## RESULTS AND DISCUSSION

Among the investigated precursors, nutshell revealed as the best option. Thus, a micro-mesoporous carbon with a BET specific surface area of 1325 $m^2/g$ and total and micro- pore volumes of 0.97 and 0.42 $cm^3/g$, respectively, was synthesized. These textural properties afford a high adsorption capacity for volatile organic compounds (VOCs) under different experimental conditions. Also, the material was grinded and sieved in order to have a proper particle size, especially for its use in respiratory filters.

Its subsequent impregnation with copper and cobalt salts led to reactive sorbents outperforming the reference material for the removal of ammonia and sulfur dioxide, respectively. Moreover, the sorbent impregnated with cobalt is a promising material for broad spectrum protection, since its performance towards ammonia retention is only slightly lower than the one of URC (Mansurov, 2022).

On the other hand, loading the raw carbon with a mixture of ZnO:MgO (0.8:0.2 wt. %) resulted on an enhanced removal efficacy towards ammonia, and almost the same removal capacity than URC for $H_2S$ in humid conditions (70% relative humidity).

The next step in this investigation is to combine two different materials with different removal affinities in the same air filtration setup. This approach is proving effective to develop a filter that offers a sufficient protection for a wide range of toxic chemicals.

## CONCLUSIONS

An activated carbon with the suitable textural properties, and therefore high physisorption capacity, has been developed from a biomass waste (nutshell). Moreover, its subsequent impregnation led to reactive sorbents with satisfactory performances for the removal of single and mixtures of VOCs and for single inorganic toxic industrial chemicals under different conditions of relative humidity and temperature. These reactive materials also show a high long-term stability, even when stored at high relative humidities.

**Acknowledgements**

This research was sponsored by the NATO Science for Peace and Security Programme under grant G5636.

**References**

Boutillara, Y., Tombeur, J.L., De Weireld, G., Lodewyckx, P. (2019). In-situ copper impregnation by chemical activation with $CuCl_2$ and its applications to $SO_2$ and $H_2S$ capture by activated carbons. *Chemical Engineering Journal*, 372, 631-637. https://doi.org/10.1016/j.cej.2019.04.183

Li, L., Li, K., Ma, L., and Luan, Z.Q. (2016). Activated carbon impregnated with zirconium hydroxide for toxic chemical removal. Material Science and Environmental Engineering – Chen (Ed.) Taylor & Francis Group, London, ISBN 978-1-138-02938-5.

Mansurov, Z.A., Lodewyckx, P., Velasco, L.F., Azat S. and Kerimkulova, A.R. (2022). Modified sorbents based on walnut shell for sorption of toxic gases. *Materials Today: Proceedings,* 49(6), 2521-2526. https://doi.org/10.1016/j.matpr.2020.12.948

Yang, C., Wang, Y., Fan, H., Falco, G., Yang S., Shangguan, J. and Bandosz, T.J. (2020). Bifunctional ZnO-MgO/activated carbon adsorbents boost H2S room temperature adsorption and catalytic oxidation. Applied Catalysis B: Environmental, 266, 118674. https://doi.org/10.1016/j.apcatb.2020.118674

Carbon 2022

# Increasing the Understanding of Water Adsorption in Nanoporous Carbons by Combining SAXs/WAXs and n-alkane Preadsorption

**Leticia F. Velasco[1], Yasmine Boutillara[2], Edouard Nadin[1] and Peter Lodewyckx[1]**
[1]Department of Chemistry, Royal Military Academy, Avenue Renaissance 30, 1000 Brussels, Belgium
Email: leticia.fernandezvelasco@mil.be

[2]Ecole Militaire Polytechnique, Unité d'Enseignement et de Recherche en Physico-chimie des Matériaux, B.P 17, Bordj El-Bahri, Algiers 16046, Algeria

**Keywords**
SAXs/WAXs, water adsorption, n-alkane preadsorption

## INTRODUCTION

The study of water adsorption on activated carbons (ACs) is of great importance for their applications. The presence of water vapour has a negative impact on the adsorption capacity of nanoporous carbons and limits their efficiency in humid environments. However, the fundamental understanding of water adsorption in carbon is still incomplete (Liu, 2017).

Related to this, the use of SAXs/WAXs has revealed to be a useful technique for gathering structural information about adsorbent–adsorbate systems in the nanometer scale range (László, 2010). Molecules adsorbed inside the pores modify the electronic contrast of their immediate surroundings. Thus, the SAXS signals constitute a means of monitoring pore filling, while WAXS provides complementary information on the adsorbed molecular layers. On the other hand, using an n-alkane to fill up the narrow micropore system of micro-mesoporous ACs with different surface chemistry, and subsequently measuring their water adsorption behaviour, revealed that water sorption in the narrow mesopores is highly dependent on the available surface oxygen groups (Velasco, 2017).

In order to further explore the mechanism of water adsorption in carbon pores and since any single technique only offers a one-sided view and partial understanding, it is desirable to tackle the problem from different approaches. Hence, in this work two different techniques were combined and SAXs/WAXs measurements on activated carbons preloaded with n-alkane and/or water vapour were performed.

## EXPERIMENTAL

Two commercial activated carbons (Norit® Cgran and R1), with different textural and surface properties, were powdered and preloaded with n-decane in order to fill the narrow pores. Cgran is a wood-based micro-mesoporous carbon obtained by chemical activation and therefore, with a high surface oxygen content. R1 is a mainly microporous activated carbon obtained by the physical activation of peat. N-decane was evaporated into a flow of air and passed through the carbon beds in a classical breakthrough installation.

The parent and n-alkane preloaded carbons were placed in boro-silicate capillary tubes (1.5 mm diameter) and exposed for a long time at given relative humidities (RHs), comprised between 0-90%. Performing the experiments with the raw and the n-alkane preloaded carbons at different RH helped to distinguish between the water and the n-alkane signal. At the end of the preparation, the capillary tubes were flame-sealed. The SAXs/WAXs experiments were performed with incident energy of 12.4 keV and exploring the wave vector range $0.01 \leq q \leq 7$ Å$^{-1}$.

## RESULTS AND DISCUSSION

The SAXs/WAXS profiles of the initial dry samples are typical of high surface area carbons with slight differences due to their distinct properties.

In the case of the samples exposed to water vapour, the upper and lower q-regions of the SAXs domain behave differently. In the macropore region (low q), the water adsorbed in the micropores enhances the macroscopic density of the carbon, and thus the contrast of the carbon with respect to air in the empty pores. On the contrary, in the micropore region the intensity decreases because the water reduces the contrast between the carbon matrix and its surroundings. This leads to a cross-over of the dry and wet curves. Moreover, with increasing relative humidity, the micropores gradually fill with water and the cross-over point steadily shifts to lower q. In the WAXs region the principal peak of the adsorbed water signal is gradually displaced to lower q with respect to bulk water. These results are in agreement with those of László (2010) and indicate that the structure of water changes as the water sorption process proceeds. This is also in line with the most accepted mechanism of water adsorption in carbon pores based on the growth and coalescence of water clusters.

Then, SAXs/WAXs measurements were carried out on the initial activated carbons (dry) preloaded with increasing amounts of n-decane. To attain this goal, the carbons were preloaded with n-decane and then, part of it was removed by thermal treatment and/or vacuum. Since n-decane is only filling the narrow micropores, the SAXs signals become only different at high values of q. Regarding the WAXs results, the maximum of the peaks of the preloaded samples is obtained at identical q values independently of their degree of pore filling.

Studying the SAXs/WAXs signals of the samples separately exposed to water and to n-decane, allows better understanding the results obtained when both adsorbates are simultaneously present in the carbon materials. The SAXs signals of R1 preloaded with n-decane and exposed to humidity are practically identical to that of the initial preloaded sample. This is attributable to both the microporous and hydrophobic character of this carbon, with most of the porosity occupied by the n-alkane, thus obstructing the subsequent sorption of water vapour in the small fraction of volume of bigger pores available. In the case of carbon Cg, differences in the signals are noted as the relative humidity is increased.

## CONCLUSIONS

Since water changes the intensity of SAXs/WAXs in a way that depends on how the pores are filled, the main goal of these experiments was to gain more knowledge about the state of water adsorbed in carbon pores. Moreover, by preloading an n-alkane in the porous structure, we were able to study the adsorbed state of water in pores of different sizes and exposing the samples to different relative humidities allowed us to qualitatively assess the progress of the water sorption mechanism.

**Acknowledgements**

The SAXs/WAXs experiments were performed at BL11 - NCD-SWEET beamline at ALBA Synchrotron with the collaboration of ALBA staff. We would especially like to thank the contribution of Dr. Eduardo Solano.

**References**

László, K., Czakkel, O., Dobos, G., Lodewyckx, P., Rochas C. and Geissler E. (2010). Water vapour adsorption in highly porous carbons as seen by small and wide angle X-ray scattering. *Carbon* 48, 1038-1048. https://10.1016/j.carbon.2009.11.023

Liu, L., Tan, S.J., Horikawa, T., Do, D.D., Nicholson, D. and Liu, J. (2017). Water adsorption on carbon - A review. *Advances in Colloid and Interface Science*, 250, 64-78. https://doi.org/10.1016/j.cis.2017.10.002

Velasco, L.F., Berezovska, I., Boutillara, Y. and Lodewyckx, P. (2017). The use of organic vapour preadsorption to understand water adsorption on activated carbons. *Microporous and Mesoporous Materials*, 241, 21-27. https://doi.org/10.1016/j.micromeso.2016.12.005

# Cobalt single atoms imbued sub-2 nm $Co_3O_4$ ultra-small nanoparticles interlace fibrous carbon for oxygen evolution from seawater

Sada Venkateswarlu, Jeon Young Hyun, Myung Jong Kim*

Department of Chemistry, Gachon University, Seongnam 13120, Republic of Korea

**Abstract**

Recently, electrochemical water splitting has emerged as a promising approach for converting electricity obtained from renewable sources into sustainable energy. Most importantly, the chemical free and noble metal free design of electrocatalysts is highly required. For the first time, we have applied a chemical free strategy to design highly reactive cobalt single atoms (Co SAs) imbued sub-2 nm $Co_3O_4$ ultra-small nanoparticles interlace fibrous carbon (FC) wrapped $Co_3O_4$ ultra-small nanoparticles (Co SAs@$Co_3O_4$/FC). The strategy is for the single green waste source (fibrous orange peel) to act as solvent and carbon precursor and multi applications (1+2+m) with zero waste generation. The green solvent with functional groups plays a crucial role to obtained Co SAs@$Co_3O_4$ ultra-small nanoparticles, which were further intertwined with the plethora of active sites that have fibrous carbon (FC). The HAADF-STEM indicates the presence of Co single atoms, in the structure of sub-2nm $Co_3O_4$ nanoparticles. Due to pivotal traits such as high surface area, mesoporosity, and active edge sites in the structure of Co SAs@$Co_3O_4$/FC shows an excellent electrocatalyst activity for oxygen evaluation reaction (OER) with an overpotential of 309 mV, 390 mV, and 410 mV at 10 mA $cm^{-2}$ and under deionized alkaline water, seawater, and wastewater. This synthesis strategy unveils the creation of eco-friendly nanostructures for energy conversion under different aqueous environments.

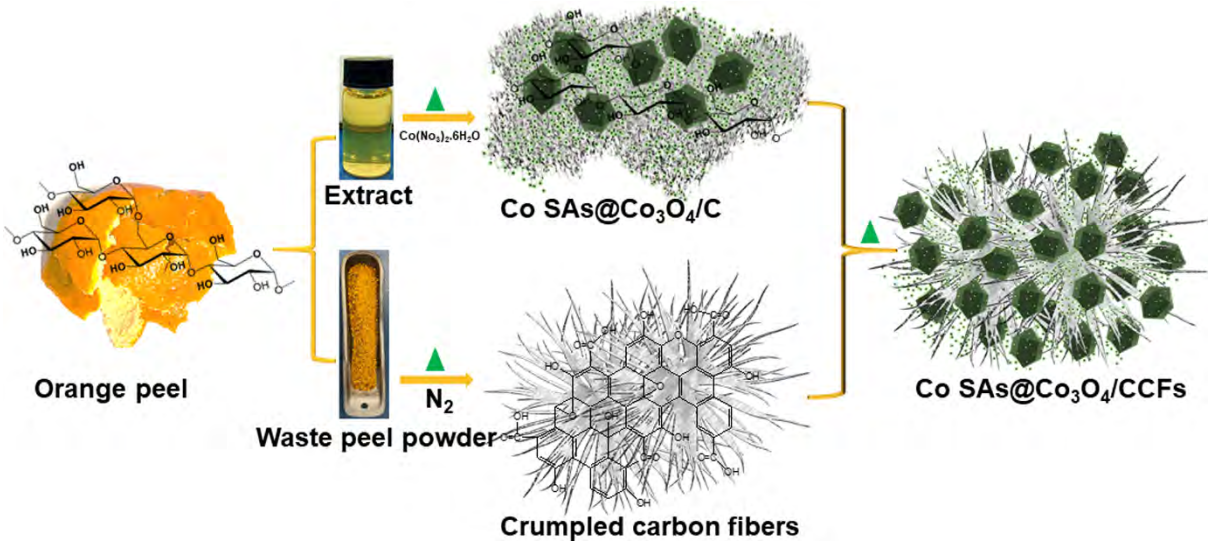

20 C 22 arbon 2022

# Manufacture of Carbon Materials with High Nitrogen Content

**David Villalgordo-Hernández[1], Aida Grau-Atienza[1], Antonio A. García-Marín[1], Enrique V. Ramos-Fernández [1] and Javier Narciso [1,2]***

[1]Laboratorio de Materiales Avanzados, Departamento de Química Inorgánica, Instituto Universitario de Materiales de Alicante, Universidad de Alicante, Alicante, Spain.
[2]Instituto de Investigación Sanitaria y Biomédica de Alicante (ISABIAL), Alicante, Spain.
Email: narciso@ua.es

**Keywords**
Activated carbon; $CO_2$ adsorption; N-doped porous carbon.

## INTRODUCTION

Currently the use of carbon materials has grown greatly in both electrochemistry and as a possible solution to reducing greenhouse effect by means of $CO_2$ capture. In both cases the presence of N is presented as essential. A recently published review (Quílez-Bermejo, J.; 2020) discusses about the importance of heteroatoms in carbon materials in their use for ORR (Oxygen Reduction Reaction).
Several works published show the preparation of carbon materials from various precursors such as acetonitrile (Mostazo-López, M.J.; 2018) or polyaniline (Silvestre-Albero, A.; 2015), which allow its obtention with a remarkable degree of % at. of N in its structure, though never greater than an 8 % at. Also we can find in literature authors reporting that the presence of N does favour $CO_2$ capture (Navarro Quirant, P.; 2020 or Silvestre-Albero, A.; 2014). Coming to the conclusion of the relevance of nitrogen in $CO_2$ capture, it is important to find synthetic methods that allow for the obtention of carbon materials with higher N content in order to increase its capture efficiency.
The main competitors of carbon for $CO_2$ capture are MOFs (Metallic Organic Frameworks), since their porosity and surface chemistry can be finely tuned (Ronda-Lloret. M.; 2021 and Ramos-Fernández, E.V.; 2020), however many of them are unstable under the conditions of application. Due to its easy manufacture and stability, UiO-66 (Cavka Hafizovic, J.; 2008) has become one of the most interesting MOFs, although not being the most suitable for $CO_2$ capture, a significant increase in its adsorption capacity can be achieved with the modification of its linker (using 2-aminoterephthalic acid instead of terephthalic acid) (Kandiah, M.; 2010). This result highlights the fact that the presence of N is essential in the capture of $CO_2$ where it is shown that it is possible to obtain carbons with a N content greater than 15% at. for its application in $CO_2$ capture, catalysis and electrocatalysis.
In this work, we have used MOFs containing N as a precursor of N doped carbons. For doing so, we have engineered a simple and cheap method to prepare ZIF-67 that will be further pyrolyzed in different conditions to obtain carbon materials.

## RESULTS AND DISCUSSION

In order to understand the pyrolysis procedure, TGA thermogravimetric experiments have been performed. In Figure 1A, the thermogram of the ZIF-67 in Ar atmosphere is shown, where a single weight loss is observed around 600 °C evidencing the great thermal stability of this MOF. This weight loss corresponds to the evolution of two characteristic 'm/z' of ZIF-67, which are 53 and 82; together with the evolution of $N_2$ (m/z = 28). Following the thermogram of the same sample but in an oxidizing atmosphere, as it is shown in Figure 1B, a weight loss around 270 °C can be observed, corresponding to the evolution of $CO_2$ (m/z = 44), NO (m/z = 30) and $NO_2$ (m/z = 46). It is also observed that the

evolution of NO is prolonged in time, which is indicative of the presence of different nitrogenous species.

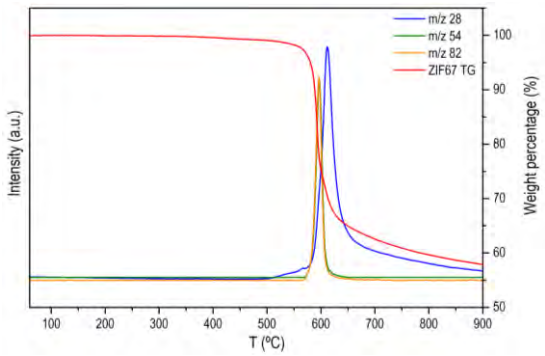


**FIGURE 1A:** ZIF-67 TG in inert atmosphere and mass spectrometry for its three main fragments.

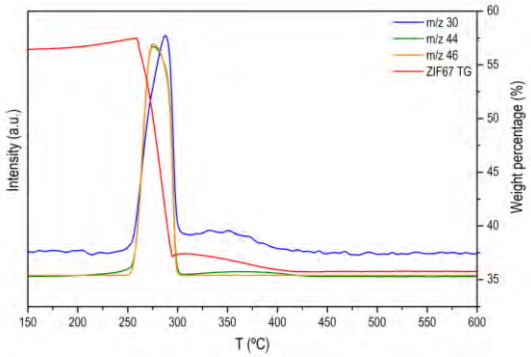


**FIGURE 1B:** ZIF-67 TG in oxidant atmosphere and mass spectrometry for its three main fragments.

An acid treatment has been carried out in order to eliminate part of the metal that remains in the carbon after ZIFs carbonization process, resulting in an increase in carbon's porosity since this is giving access to empty space that the metal had blocked. Thus, in Figure 2 it is shown the $N_2$ adsorption isotherms of some carbon ZIF-67 derived materials before and after being washed with an acid solution. The most remarkable thing is the change of porosity, increasing up to 70 % when the carbon derived from MOF is acid washed.

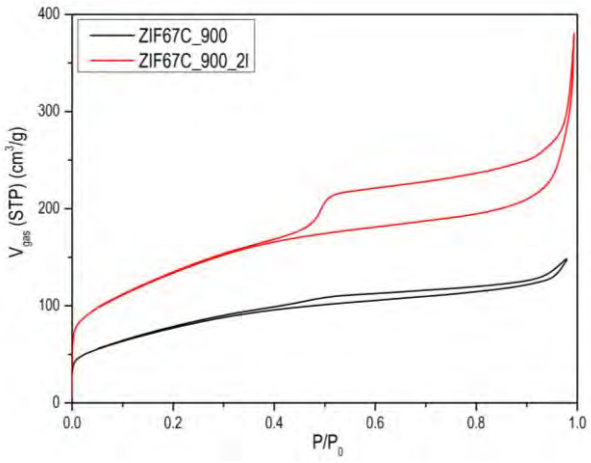


**FIGURE 2:** Nitrogen Adsorption Isotherm of a ZIF-67 carbonized at 900 °C and acid washed twice.

The SEM micrograph in Figure 3A shows a carbon material obtained by carbonization of ZIF-67 which maintains the original MOF morphology. Figure 3B shows the TEM micrograph of the sample acid treated where it clearly shows graphitic zones from where the cobalt has been eliminated. The appearance of these cavities, responsible for the development of porosity and thus resulting in these activated carbons.

The presence of cobalt nanoparticles with nitrogen functional groups (up to 20 % at.), makes these series of carbons to be very useful in several applications such as electrochemistry or catalysis.

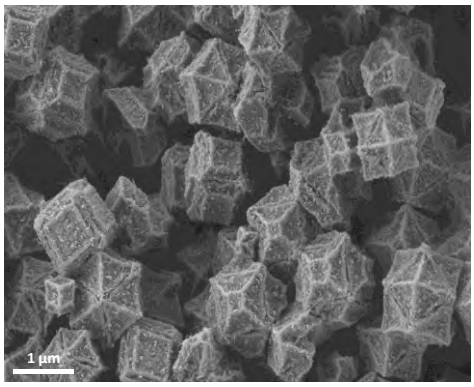


**FIGURE 3A:** SEM micrograph of a ZIF-67 carbonized at 900 °C.

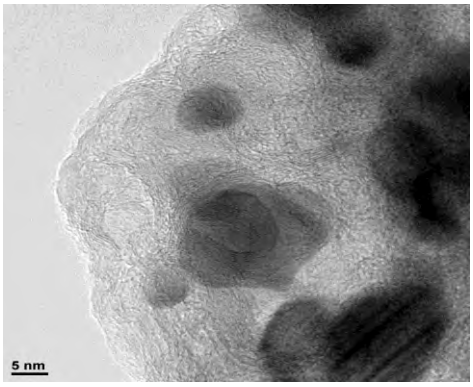


**FIGURE 3B:** TEM micrograph of a ZIF-67 carbonized at 900 °C and acid washed.

**Acknowledgements**
Authors acknowledge financial support by "Ministerio de Ciencia e Innovación" of Spain through the project PID2020-116998RB-I00.

**References**
Cavka Hafizovic, J.; Jakobsen, S.; Olsbye, U.; Guillou, N.; Lamberti, C.; Bordiga, S.; Lillerud Petter, K. A New Zirconium Inorganic Building Brick Forming Metal Organic Frameworks with Exceptional Stability. *J. Am. Chem. Soc.* **2008**, 130, 13850-13851.
Kandiah, M.; Hellner Nilsen, M.; Usseglio, S.; Jakobsen, S.; Olsbye, U.; Tilset, M.; Larabi, C.; Alessandra Quadrelli, E.; Bonino, F.; Petter Lillerud, K. Synthesis and Stability of Tagged UiO-66 Zr-MOFs. *Chem. Mater.* **2010**, 22, 6632-6640.
Mostazo-López, M.J.; Ruiz-Rosas, R.; Castro-Muñiz, A.; Nishihara, H.; Kyotani, T.; Morallón, E.; Cazorla-Amorós, D. Ultraporous nitrogen-doped zeolite-templated carbon for high power density aqueous-based supercapacitors. *Carbon* **2018**, 129, 510-519.
Navarro Quirant, P.; Cuadrado-Collados, C.; Romero-Anaya, A.J.; Silvestre Albero, J.; Martínez Escandell, M. Preparation of Porous Carbons from Petroleum Pitch and Polyaniline by Thermal Treatment for Methane Storage. *Ind. Eng. Chem. Res.* **2020**, 59, 5775-5785.
Quílez-Bermejo, J.; Morallón, E.; Cazorla-Amorós, D. Metal-free heteroatom-doped carbon-based catalysts for ORR: A critical assessment about the role of heteroatoms. *Carbon* **2020**, *165*, 434-454.
Ramos-Fernández, E.V.; Serrano-Ruiz, J.C.; Sepúlveda-Escribano, A.; Narciso, J.; Ferrando-Soria, J.; Pardo, E. Metal Organic Frameworks: From Material Chemistry to Catalytic Applications. Heterogeneous Catalysis for Energy Applications, **2020**, 235-303.
Ronda-Lloret. M.; Pellicer-Carreño, I.; Grau-Atienza, A.; Boada R.; Diaz-Moreno, S.; Narciso-Romero, J.; Serrano-Ruiz, J. C.; Sepúlveda-Escribano, A.; Ramos-Fernández, E. V. Mixed-valence Ce/Zr Metal-organic frameworks: Controlling the oxidation state of cerium in one-pot synthesis approach. *Adv. Funct. Mater*. **2021**, 31, 2102582.
Silvestre-Albero, A.; Silvestre-Albero, J.; Martínez-Escandell, M.; Molina-Sabio, M.; Kovacs, A.; Rodríguez-Reinoso, F. Novel synthesis of a micro-mesoporous nitrogen-doped nanostructured carbon from polyaniline. *Microporous Mesoporous Mater.* **2015**, 218, 199-205.
Silvestre-Albero, A.; Silvestre-Albero, J.; Martínez-Escandell, M.; Rodríguez-Reinoso, F. Micro/Mesoporous Activated Carbons Derived from Polyaniline: Promising Candidates for $CO_2$ Adsorption. *Ind. Eng. Chem. Res.* **2014**, 53, 15398-15405.

Carbon 2022

# Biomass-based Nitrogen-Doped Carbon Catalysts for Oxygen Reduction Reaction

**Aleksandrs Volperts[1], Ance Plavniece[1], Kätlin Kaare[2], Galina Dobele[1], Aivars Zhurinsh[1], Ivar Kruusenberg[2]**

[1]Latvian State Institute of Wood Chemistry, LV-1006 Riga, Latvia

Email: aleksandrs.volperts@kki.lv

[2]National Institute of Chemical Physics and Biophysics, 10213 Tallinn, Estonia

**Keywords**

Activated carbons, fuel cells, oxygen reduction reaction.

## INTRODUCTION

The energy consumption is constantly increasing and the development of the effective and cheap electrochemical power sources is gaining more and more attention. Fuel cells attract attention because of their high efficiency, grid-independency and longer operating times, in comparison to the battery. Power specifications and price of fuel cells are limited, besides other factors, by the expensive platinum-based catalysts, thus the development of materials aimed to replace platinum-group metals is one of the most important issues for the fuel cell design.

The application of biomass-derived, N-doped carbons as novel metal-free cathode catalysts for oxygen reduction reactions (ORR) to transform chemical energy into electricity is the current and prospective approach to the use of carbon materials (Bruno and Viva, 2014). The performance of N-doped activated carbons is attributed to various factors, including number of active sites, such as pyridinic N, the favorable three-dimensional porous structure and the large specific surface area (Jiang *et al.*, 2020). The most prospective way to obtain highly porous carbon materials with well-developed nanoporous structure is alkali activation. There are two possible ways to improve ORR kinetics using carbon materials doped either with transition metals and/or with heteroatoms as catalysts (Dombrovskis and Palmqvist, 2016). To achieve the desired structure of N-doped carbon nanomaterials the optimization of activation and pyrolysis processes are required, as well as appropriate sources of nitrogen (Liu *et al.*, 2011).

The goal of this research was to synthesise activated at various temperatures and nitrogen-doped porous nanocarbons with high specific surface area and adjustable pore size distribution using wood charcoal as precursor. The obtained carbons were tested as candidates for application as the ORR cathode catalysts in the alkaline media.

## MATERIALS AND METHODS

Activated carbons based on alder wood charcoal, were obtained using chemical activation method with NaOH (activator to precursor ratio 3:1) at temperatures 650, 700, 750 and 800 °C in argon atmosphere. After activation samples were demineralized with 10% HCl and deionized water. Nitrogen was introduced into the activated samples using dicyandiamide solution in dimethylformamide with mass ratio carbon material/DCDA 1:20. Doping was performed at 800 °C for 1 hour in argon atmosphere. Porosity, elementary composition, XPS tests, structural properties (XRD, Raman), as well as electrochemical tests with a standard three-electrode system using the rotating disk electrode (RDE) at various rotation speeds in 0.1 M KOH solution were used to study the properties of the synthesized samples.

**RESULTS**

The samples were tested using nitrogen sorption at 77K and the resulting isotherms are demonstrated in the Figure 1a. The shape of the isotherm for the sample synthesized at 650 °C belongs to Type I according to IUPAC classification [16], which points at the pre-dominant presence of very fine micropores, only few molecular dimeters wide. At the activation temperatures 700 and 750 °C volume of adsorbed gas increases and isotherms are accompanied with visible H4 type hysteresis, characteristic to capillary condensation and development of mesoporosity. At the activation temperature 800 °C the shape of the isotherm changes even further and can be classified as Type II, while the shape of hysteresis points at significant input of mesopores into the adsorption process. Figure 1b compares the pore size distributions of carbon materials (AC-N), depending on the activation temperature, calculated from the nitrogen adsorption isotherms at 77K (Figure 1a) using density functional theory. The increase in the activation temperature substantially influences micropore development, increasing their width. At lower activation temperatures (650 °C), pores in the size range of 1 to 2 nm are mainly formed, and their volume is relatively low. As the temperature increases, volume of micropores with a width of 1–2 nm increases and reaches a maximum at the activation temperature of 750 °C. As the activation temperature increases to 800 °C, micropore input into the total specific volume of the samples under study significantly decreases, and the volume of mesopores with a pore width of 2–5 nm increases. Porosity data, elemental composition and yield of nitrogen doped activated carbons are shown in the Table 1.

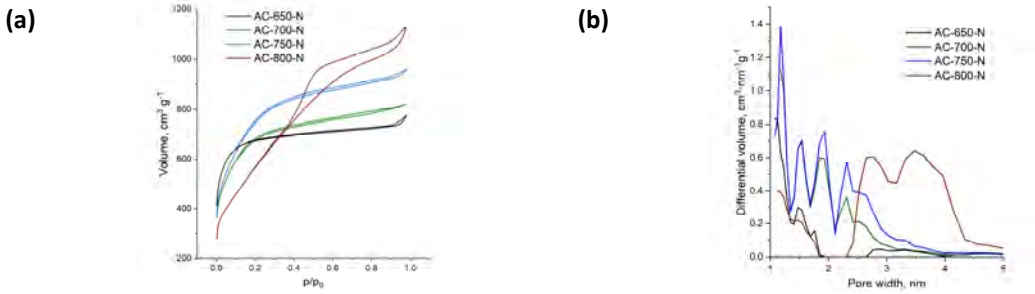


**FIGURE 1.** N-doped wood-based activated carbons nitrogen sorption isotherms at 77K (a) and pore size distributions (b) depending on activation temperature.

**Table 1.** Porosity, yield and elemental composition of nitrogen doped wood-based activated carbons.

| Samples | $T_{act.}$, °C | $S_{BET}$, $m^2 g^{-1}$ | $m^2 g^{-1}$ | $V_{micro}$, $cm^3 g^{-1}$ | $V_{meso}$, $cm^3 g^{-1}$ | Yield, % | N, % | C, % | H,% | O, % |
|---|---|---|---|---|---|---|---|---|---|---|
| AC-650-N | 650 | 2021 | 1582 | 0.94 | 0.26 | 31.2 | 7.52 | 89.53 | 0.68 | 2.27 |
| AC-700-N | 700 | 2435 | 1675 | 0.65 | 0.62 | 24.9 | 5.55 | 90.97 | 0.89 | 2.59 |
| AC-750-N | 750 | 2728 | 1764 | 0.86 | 0.63 | 20.2 | 3.42 | 93.08 | 0.72 | 2.78 |
| AC-800-N | 800 | 1924 | 1383 | 0.61 | 1.14 | 19.2 | 2.48 | 94.98 | 2.06 | 1.48 |

The surface chemical composition of AC-N was studied using (XPS). Peaks corresponding to C1s, O1s and N1s were recorded. The C1 peak consists mainly of $sp^2$ hybridized carbon. Four peaks were determined for nitrogen: pyridinic-N, pyrrolic-N, graphitic-N, pyridine-N-oxide. Most of the nitrogen was in the pyridinic form, which lowers the potential for oxygen reduction reactions (Lai *et al.*, 2012) the second most important form of nitrogen is graphite-N, which helps to achieve a higher diffusion limited current.

RDE tests were performed at 23 °C at rotation speeds 360, 610, 960, 1900, 3100, 4600 rpm. As the activation temperature increases from 650 to 800 °C, the onset and half-wave potentials become more positive, but at the same time, the diffusion-limited current density falls to slightly lower values. When the activation temperature is 800 °C, the curves almost coincide with the selected commercial 20% Pt/C catalyst samples (Figure 2a). the samples activated at lower temperatures, the current is under the mixed, kinetic-diffusional limitations, even in the case of overpotentials. However, the activity steadily increases with the increase in the activation temperature, and judging from Koutecky-Levich plots is practically only diffusion-limited. The changes in the number of transferred electrons, *n* (per $O_2$ molecule), depending on the mesopore volume ratio to total adsorbed volume, can be seen in Figure 2b. As the activation temperature increases, the total pore volume increases linearly, and

the mesopore volume and the number of transferred electrons increase as well, while the micropore volume decreases. More efficient electron transfer occurs when the volume of mesopores (size 2.5–5 nm) of the material is greater than the volume of micropores.

(**a**) (**b**)

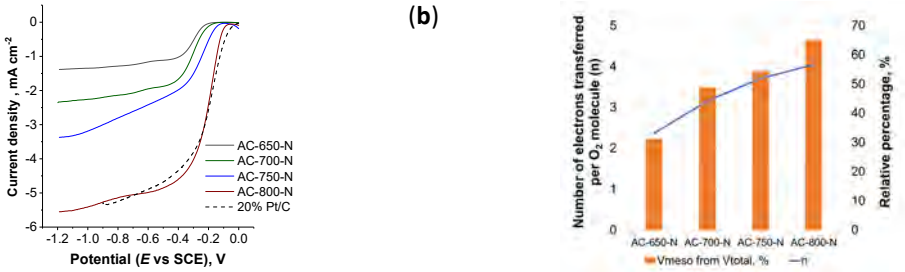


**FIGURE 2.** RDE polarization curves of glassy carbon electrodes modified with wood-based, nitrogen-doped activated carbons synthesized at various temperatures and commercial 20 % Pt/C in $O_2$ saturated 0.1 M KOH (v = 10 mV $s^{-1}$, $\omega$ = 1900 rpm) (a). Changes in the number of transferred electrons, n (per $O_2$ molecule), depending on the mesopore volume ratio (b).

## CONCLUSIONS

Nitrogen-doped activated carbons were synthesized using the chemical activation method with NaOH and studied as catalysts for oxygen reduction reactions in fuel cells. The dependence of porosity of carbons on the activation temperature was studied. It was found that with the increase in activation temperature from 650 to 800 °C, micropores walls collapse, leading to the higher input of mesopores into total specific volume. The ORR activity of the carbon material in the case of a nitrogen-doped sample activated at 800 °C wood char was comparable with commercial 20% Pt/C catalysts. Electrocatalytic activity of the synthesized nitrogen-doped, wood-based carbon catalysts may be associated with the highly developed surface area, favourable micro and mesoporous ratio and balance, high percentage of pyridinic nitrogen, and lack of stacking defects of graphene layers, as well as partial transformation into a more ordered structure. The results of this study demonstrate that the oxygen reduction reaction is influenced by the structure of the material and the pore size distribution and nitrogen-doped carbon activated at 800 °C is a promising material for application in fuel cells as cathode for the oxygen reduction reaction.

**Acknowledgements**

This research was funded by postdoc project “Nitrogen and phosphorus-containing biomass based activated carbons for fuel cells and supercapacitors” No. 1.1.1.2/VIAA/4/20/596 and by European Regional Development Fund "Emerging orders in quantum and nanomaterials" project No. TK134.

**References**

Bruno, M. M. and Viva, F. A. (2014) ‘Carbon Materials for Fuel Cells’, *Direct Alcohol Fuel Cells: Materials, Performance, Durability and Applications*. Springer, Dordrecht, 9789400777088, pp. 231–270. doi: 10.1007/978-94-007-7708-8_7.

Dombrovskis, J. K. and Palmqvist, A. E. C. (2016) ‘Recent Progress in Synthesis, Characterization and Evaluation of Non-Precious Metal Catalysts for the Oxygen Reduction Reaction’, *Fuel Cells*. WILEY-VCH Verlag, 16(1), pp. 4–22. doi: 10.1002/fuce.201500123.

Jiang, M. *et al.* (2020) ‘Optimization Strategies of Preparation of Biomass-Derived Carbon Electrocatalyst for Boosting Oxygen Reduction Reaction: A Minireview’, *Catalysts 2020, Vol. 10, Page 1472*. Multidisciplinary Digital Publishing Institute, 10(12), p. 1472. doi: 10.3390/CATAL10121472.

Lai, L. *et al.* (2012) ‘Exploration of the active center structure of nitrogen-doped graphene-based catalysts for oxygen reduction reaction’, *Energy & Environmental Science*. The Royal Society of Chemistry, 5(7), p. 7936. doi: 10.1039/c2ee21802j.

Liu, J. *et al.* (2011) ‘Simple pyrolysis of urea into graphitic carbon nitride with recyclable adsorption and photocatalytic activity’, *Journal of Materials Chemistry*. The Royal Society of Chemistry, 21(38), p. 14398. doi: 10.1039/c1jm12620b.

Zheng, Y. *et al.* (2012) ‘Nanostructured Metal-Free Electrochemical Catalysts for Highly Efficient Oxygen Reduction’, *Small*. WILEY-VCH Verlag, 8(23), pp. 3550–3566. doi: 10.1002/smll.201200861.

Carbon 2022

# Evolution of Threshold Displacement Energy with Dose Studied by Molecular Dynamics Simulations on Irradiated Graphite Models

**Filip Vukovic[1,2], Nigel A. Marks[2], Philippe Aurel[1] and Jean Marc Leyssale[1]**
[1]Institut des Sciences Moléculaires, Univ. Bordeaux – CNRS – IPB, 33400 Talence, France
Email: jean-marc.leyssale@u-bordeaux.fr

[2]Department of Physics and Astronomy, Curtin University, Perth, Western Australia 6845, Australia

**Keywords**
Graphite; Radiation damage; Molecular dynamics simulations

## INTRODUCTION

The threshold displacement energy ($E_d$) quantifies the minimum kinetic energy that a primary-knock-on-atom (PKA) needs to create a permanent defect in a material under irradiation. This fundamental quantity is used to determine the number of displacements per atom (dpa), also called "dose", created in the material. While both experiments and molecular dynamics (MD) simulations can be used for determining $E_d$, values reported so far for graphite are extremely scattered (10-70 eV) and always obtained from short time irradiation of pristine (also termed virgin) material, following the common assumption that $E_d$ is a constant. In this work, we use a robust statistical method, based on extensive molecular dynamics simulations of low energy PKA events, to determine $E_d$ for graphite, irradiated graphite and up to the limit of amorphous carbon (a-C).

## MATERIAL AND METHODS

Four atomistic models are considered: a monocrystal of hexagonal graphite of about 9 x 9 x 5 $nm^3$, two models of irradiated graphite at 0.2 and 1 dpa, and a model of amorphous graphite, the three latter having a size of about 5 x 5 x 5 $nm^3$. The two irradiated graphite models were constructed from a time series of HRTEM images of graphite under electron irradiation, using the time-dependent image-guided atomistic reconstruction technique (Farbos, 2017) and validated against various experimental data (HRTEM images, carbon K-edge electron-energy-loss spectra, dose rate, and stored energies), showing good overall agreement. The a-C model was obtained by annealing the 1 dpa graphite model at 8000 K, up to complete melting and then fast (0.1 ps) quenching to room temperature.

PKA events were simulated by selecting an atom at random and assigning to it a velocity, corresponding to the PKA energy, with random orientation. Interatomic interactions are described with the Carbon EDIP potential, switched to a Ziegler-Biersack-Littmack potential at low interatomic separations. 500 hundred independent simulations are performed at each energy, for each model.

## RESULTS

The main findings of this work are summarized in Figure 1, showing the evolutions of the displacement probability (DP) and average number of displacements ($N_d$) with PKA energy. In agreement with other recent studies, there is no single threshold above which a displacement is observed. Instead, we observe a continuous increase in DP and $N_d$ with increasing PKA energy for all four materials.

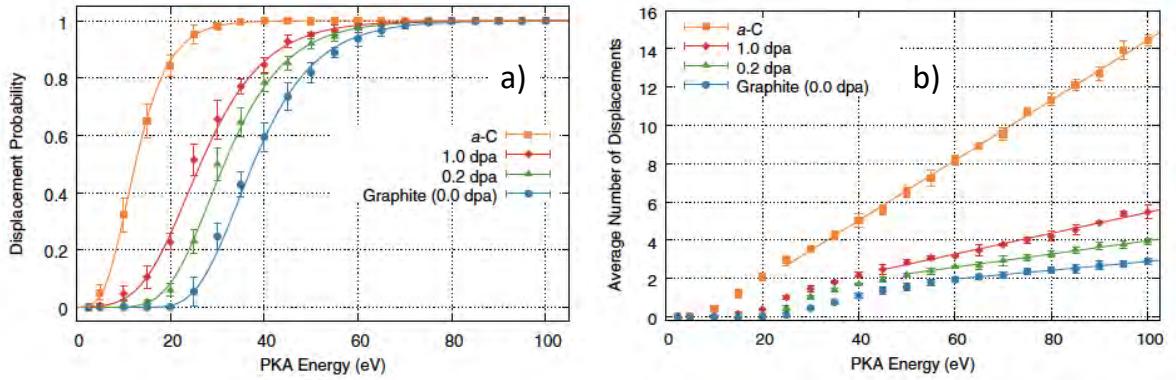


**FIGURE 1**: Evolution of (a) the displacement probability and (b) the average number of displacements as a function of the PKA energy (5-100 eV) for graphite at 0, 0.2 and 1 dpa and a-C.

Furthermore, the presence of damage, or structural defects, considerably increases DP and $N_d$ at a given PKA energy. For instance, the PKA energy required to have DP=50 % is 38 eV for pristine graphite, 31 eV at 0.2 dpa, 27 eV at 1 dpa and as less as 12 eV for a-C. Similarly, at a PKA energy of 100 eV, Nd reads 2.4 for pristine graphite, 4 at 0.2 dpa, 5.6 at 1 dpa and more than 14 for a-C. Despite the absence of a sharp threshold, we evaluated several possible definitions of $E_d$ and found three consistent definitions: i) the PKA energy at which DP = 10 %, ii) the intersection of the tangent of the DP curve at the inflexion point with the energy axis and iii) a definition based on the Kinchin-Pease model (Kinchin, 1955), predicting a linear evolution of $N_d$ with the PKA energy (E) at large E: $N_d = E/(2E_d)$. Predicted $E_d$ values read 24 eV (pristine), 18 eV (0.2 dpa), 13 eV (1 dpa) and 5 eV (a-C).

## CONCLUSIONS

Using MD simulations and a statistical approach we have been able to compute an accurate estimation of Ed for graphite, 24 eV, close to the most recent estimates for graphene (Susi, 2016). We have also shown that $E_d$ considerably decreases with increasing damage, dropping by nearly a factor of 2 at 1 dpa. While we agree that such damages can be annealed, in actual reactor graphite, this study show that the evolution of Ed with damage is an important missing element in current models of radiation dose estimations.


### Acknowledgements

Support from the French embassy in Australia as well as the access to the computing facilities of the France Grilles network and the Pawsey Supercomputing center are gratefully acknowledged.


### References


Farbos, B., Freeman, H., Hardcastle, T., Da Costa, J.-P., Brydson, R., Scott, A. J., Weisbecker, P., Germain, C., Vignoles, G. L. and Leyssale, J.-M. (2017). A time-dependent atomistic reconstruction of severe irradiation damage and associated property changes in nuclear graphite. *Carbon*, 120, 111-120. https://doi.org/10.1016/j.carbon.2017.05.009

Kinchin, G. H. and Pease, R. S. (1955). Displacement of Atoms in Solid by Radiation, Reports on Progress in Physics, 18, 1. https://doi.org/10.1088/0034-4885/18/1/301

Susi, T., Hofer, C., Argentero, G., Leuthner, G. T., Pennycook, T. J., Mangler, C., Meyer, J. C. and Kotakoski, J. (2016). Isotope analysis in the transmission electron microscope, *Nature Communications* 7, 1. https://doi.org/10.1038/ncomms13040

Vukovic, F., Leyssale, J.-M., Aurel, P. and Marks, N. A. (2018). Evolution of Threshold Displacement Energy in Irradiated Graphite. *Physical Review Applied*, 10, 064040. https://doi.org/10.1103/PhysRevApplied.10.064040

Carbon 2022

# Electrically conductive silicone-CNTs composite for electrical stimulation of cells

**Sebastian Wilk[1*], Krzysztof Pietryga[1,2], Marek Stencel[1], Alicja Martyniak[3], Jacek Stępniewski[3], Marcel Zambrzycki[1], Jacek Nizioł[1], Marta Gajewska[4], Józef Dulak[3], Aleksandra Benko[1]**

[1]AGH University of Science and Technology, Krakow, Poland
[2]Kardio-Med Silesia, Zabrze, Poland
[3]Jagiellonian University, Department of Medical Biotechnology, Faculty of Biochemistry, Biophysics and Biotechnology, Krakow, Poland
[4]Academic Centre for Materials and Nanotechnology AGH, Krakow, Poland
*Email: sewilk@agh.edu.pl

**Keywords**
Electroconductive silicon-carbon composites, regenerative medicine, carbon nanotubes

## INTRODUCTION

Myocardial tissue is characterized by one of the lowest regenerative potentials among all human tissues (Tzahor and Poss, 2017). Hence, materials that can affect cells like cardiomyocytes and heart fibroblasts, improving their viability and maturation in cell cultures, are of great importance in the area of regenerative medicine (Ashtari *et al.*, 2019). Elastic and electroconductive composites based on carbon nanotubes are particularly interesting, due to their versatility and facile processing into desired shapes (Distler *et al.*, 2021). Such materials can be used in designing modern electrostimulation chambers which, if biocompatible, can replace standard culture plates and dishes for use with cardiac cells or stem cells, possibly improving their proliferation, differentiation, maturation, and signaling (Rajendran *et al.*, 2021).

In this research, silicon-carbon type composite consisting of a commercially available, chemically cross-linked polydimethylsiloxane (PDMS, Sylgard 184) and multi-walled carbon nanotubes (MWCNTs) is presented. The aim of the study was to optimize the fabrication process of the composite to enhance its electrical properties and processability. The goal was to obtain electrically conductive, biocompatible material which can be easily formed into desired shapes, via 3D printing and moulding.

## MATERIALS AND METHODS

Multi-walled carbon nanotubes (3150 series) were purchased from Nanocyl Company. Two-component polydimethylsiloxane (PDMS): SYLGARD™ 184 silicone elastomer kit was purchased from Dow-Corning. Trimethylsiloxy terminated PDMS (MEP) was supplied by Gelest.

Materials were fabricated following a protocol by Kim et al. (Kim *et al.*, 2018), using a 1% wt. of MWCNTs.

The morphology of MWCNTs was evaluated with high-resolution transmission electron microscopy (Tecnai TF 20 X-TWIN, FEI), and dispersion of nanomaterials within polymer matrix was observed with the use of a Keyence digital microscope (VHX-900F). FTIR-ATR spectroscopy (Tensor 27, Bruker) was used to analyse the chemical composition of the obtained materials, while electrical properties were evaluated with the use of Ossila 4-point probe measurement and electrochemical impedance spectroscopy (EIS, PARSTAT 4000). Inspect Table universal testing machine (Hegewald - Peschke) was used to establish the effect of the addition of MWCNTs on the mechanical properties of composites. 3D printability of the mixture was assessed with the use of the CellInk BioX device. Finally, to evaluate biological performance, liquid extracts were prepared in accordance with an ISO 10993-5

standard. Unmodified PDMS served as a negative control, and an empty cell well was used as a blank. Cytocompatibility was established by MTT (Methylthiazolyldiphenyl-tetrazolium bromide, Sigma Aldrich) and LDH (lactate dehydrogenase, CytoTox 96®, Promega) tests, conducted on Human Embryonic Kidney 293 (HEK 293) cells and human Induced Pluripotent Stem Cell-derived cardiomyocytes (hIPSC-CM). MTT was dissolved in medium at 1 mg/ml concentration, added to cells in a 96-well plate and incubated for 2 h at 37 °C. Metabolically active cells converted the MTT to formazan crystals which were then dissolved in 100 µl DMSO 10% wt. SDS and 0,6% wt. acetic acid solution. The changes in colour were monitored at 579 nm, using 690 nm wavelength as a reference. The level of LDH was measured according to the manufacturer's instructions.

**RESULTS**

TEM images (FIGURE 1 A) revealed that the MWCNTs used in the study are long and tend to form aggregates. Despite this fact, the employed protocol (Kim *et al.*, 2018) allowed for their satisfactory dispersion in the matrix, yielding highly elastic and homogenous materials (FIGURE 1 B). The processability of the MWCNTs-sylgard composite was evaluated via 3D printing and moulding. The blends were found to be mouldable and easy to handle. The injectability was satisfactory, and the 3D printed materials were cohesive (FIGURE 1 C), maintaining their shape until fully crosslinked.


**FIGURE 1:** TEM image of MWCNTs which shows the tendency of nanomaterial to form agglomerate structures (A); image from the optical microscope that presents overall MWCNTs distribution in composite's volume (B); the photo of composite 3D printed with the use of CellInk BioX device (C).

FTIR-ATR spectroscopy revealed that the addition of carbon nanotubes did not affect the chemical composition of the silicone (FIGURE 2 A). However, the overall mechanical performance of the elastomer matrix was enhanced. Moreover, electrical measurements (FIGURE 2 B) revealed, that the obtained composites are electroconductive, with a resistance below 1kΩ. Kim et al. (Kim *et al.*, 2018) reported sheet resistance of 5225 ± 1755 Ω/sq for their PDMS matrix with the addition of 1% wt. of CNTs. Herein, we present a composite that is characterized by significantly higher conductivity, with the same amount of nanomaterial distributed in silicone mass.

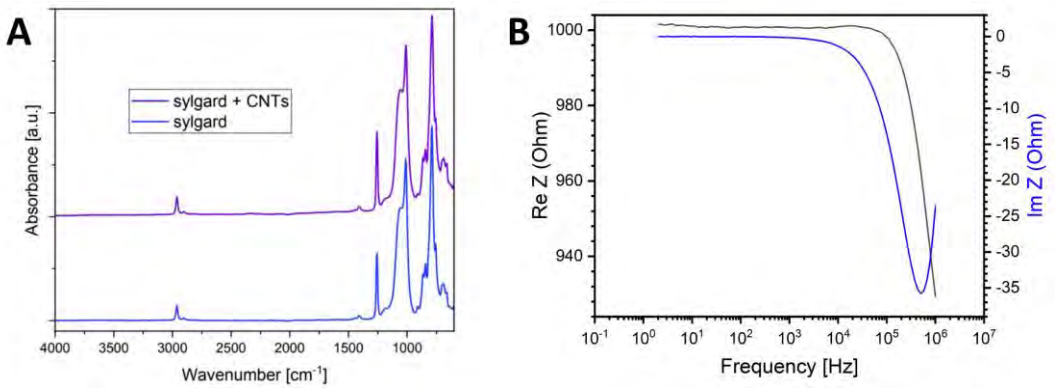

**FIGURE 2:** The results of FTIR-ATR spectroscopy analysis conducted on pure sylgard matrix and sylgard-MWCNTs composite (A); results from EIS measurement conducted on obtained composite at room temperature (B).

Finally, LDH assay, performed on both HEK 293 (FIGURE 3 A) and hIPSC-CM cells (FIGURE 3 B), revealed low cytotoxicity of all the tested materials, which was comparable to that of empty wells. Colorimetric MTT assay (Figure 3 C) showed that the materials did not affect the viability and proliferation of hIPSC-cardiomyocytes. Thus, the obtained composites are concluded to be cytocompatible.

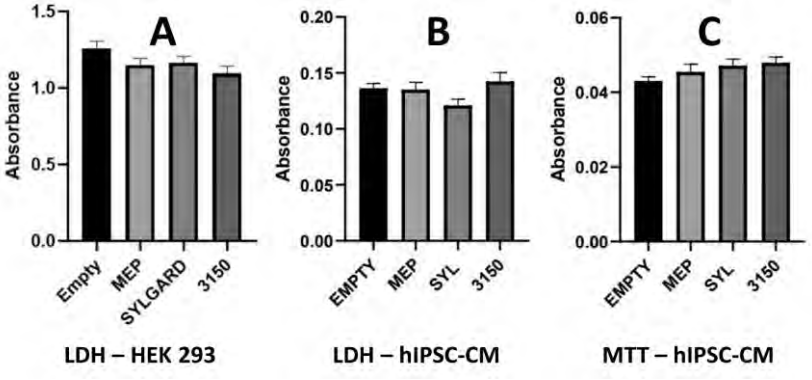


**FIGURE 3:** The results of cytotoxicity assays (A, B) and viability/proliferation assay (C), performed on HEK 293 (A) and hIPSC-CM cells (B,C).

## CONCLUSIONS

In our study, elastic, electroconductive, and biocompatible silicon-carbon composite was fabricated. Careful optimisation allowed to obtain a homogenous matrix with good dispersion of nanomaterial in elastomer volume. MWCNTs did not affect the chemical composition of the material, but increased mechanical properties and made the silicone electrically conductive. Viability and cytotoxicity assays performed with the use of HEK 293 and hIPSC-CM cells proved good cytocompatibility of all the compounds used in this study. It was also established that the MWCNTs-silicone mixture is 3D printable and mouldable. Thus, it is possible to create materials of more advanced shapes and morphologies, specifically tailored to meet the needs of regenerative medicine, wearable electronics, and various other fields of industry.

**Acknowledgements**

This study was supported by the National Science Centre, Poland, under grant no. UMO-2017/24/C/ST8/00400.

**References**

Ashtari, K. *et al.* (2019) 'Electrically conductive nanomaterials for cardiac tissue engineering', *Advanced Drug Delivery Reviews*, 144, pp. 162–179. doi: https://doi.org/10.1016/j.addr.2019.06.001.

Distler, T. *et al.* (2021) 'Electrically Conductive and 3D-Printable Oxidized Alginate-Gelatin Polypyrrole:PSS Hydrogels for Tissue Engineering', *Advanced Healthcare Materials*. John Wiley & Sons, Ltd, 10(9), p. 2001876. doi: https://doi.org/10.1002/adhm.202001876.

Kim, J. H. *et al.* (2018) 'Simple and cost-effective method of highly conductive and elastic carbon nanotube/polydimethylsiloxane composite for wearable electronics', *Scientific Reports*, 8(1), p. 1375. doi: 10.1038/s41598-017-18209-w.

Rajendran, S. B. *et al.* (2021) 'Electrical Stimulation to Enhance Wound Healing', *Journal of Functional Biomaterials* . doi: 10.3390/jfb12020040.

Tzahor, E. and Poss, K. D. (2017) 'Cardiac regeneration strategies: staying young at heart', *Science*. American Association for the Advancement of Science, 356(6342), pp. 1035–1039.

**Performance of Activated Carbon for Real World Environmental VOC Adsorption Applications**

Daryl Williams [1,2] Elwin Hunters-Sellers[2] and Luqman Hakim Mohd Azmi [2]

[1] Surface Measurement Systems Limited
[2] Department of Chemical Engineering, Imperial College London

ABSTRACT:

The adsorption performance of activated carbon (AC) was compared with standard adsorbents including 13X (MS13X), zeolite Y (A88Y), ZSM-5 zeolite (A14Z) and amorphous silica (AS) for a series of real-world environmental adsorption challenges. The sorption performance of these materials was ascertained against a series of common organic vapours, with the isotherms being characterized gravimetrically using the Dynamic Vapor Sorption method. Organic vapour sorption was also performed in the presence of high concentrations of humidity which can significantly impact sorbent performance. Figure 1 shows the superior vapour sorption performance of activated carbon in the presence of a single vapour components at 25C for water and toluene. This superior performance can be attributed to the innate surface hydrophobicity for AC as highlighted in Figure 2 which shows the extend of toluene adsorption for 5% $P/P_o$ as a function of background humidity. This figure confirms that even for high humidities, even above 50%RH, activated carbon is still an effective adsorbent for hydrophobic molecules such as toluene in the presence of humidity. This work confirms the importance of the innate hydrophobicity of AC for real world VOC capture.

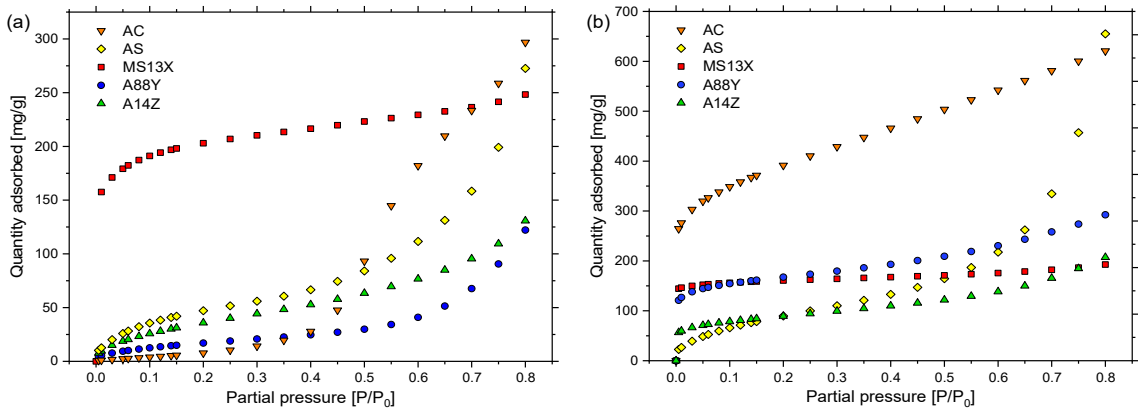


**Figure 1** Vapour adsorption isotherms of water (a), toluene (b) for activated charcoal, AC; amorphous silica, AS; molecular sieve 13X, MS13X; zeolite Y, A88Y; ZSM-5 zeolite, A14Z. T = 25˚C.

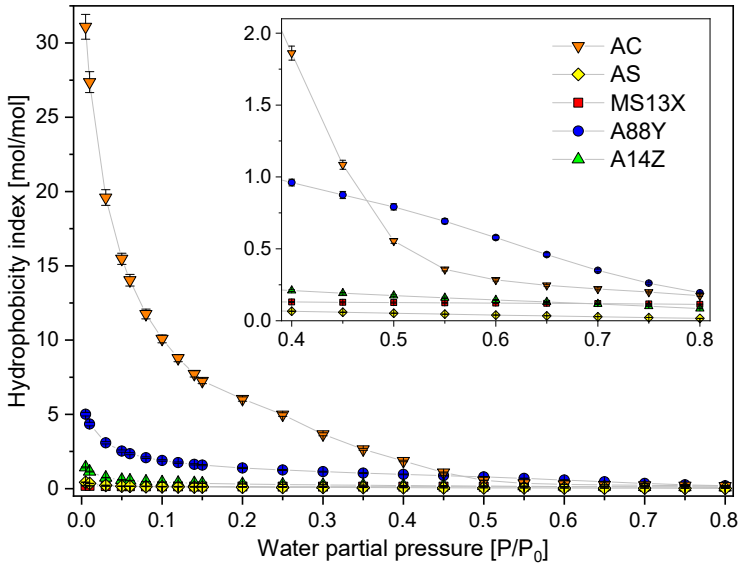


**Figure 2**: Hydrophobicity indexes versus humidity for adsorbents. $(P/P_0)_{toluene}$= 0.005, T =25˚C.

**References**

Adsorption of volatile organic compounds by industrial porous materials: Impact of relative humidity, *Microporous and Mesoporous Materials*, Volume 298, 2020, 110090, E. Hunter-Sellars, IP Parkin, DR Williams

20 C 22 arbon 2022

# Molecular modelling of biochars

**Rosie Wood[1*], Ondrej Masek[2] and Valentina Erastova[1]**
[1]School of Chemistry, University of Edinburgh, Edinburgh, UK, EH9 3FJ
*Email: rosie.wood@ed.ac.uk / s2125144@ed.ac.uk

[2]School of Geosciences, University of Edinburgh, Edinburgh, UK, EH9 3FJ

**Keywords**
Biochar, Molecular Dynamics, Charcoal

## INTRODUCTION

Biochars are black carbonaceous solids produced through the pyrolysis of biomass under conditions of little or no oxygen. For centuries, biochar-like materials have been used within agriculture as soil amendments; however, more recently, these materials have found use in water decontamination as economical and environmentally friendly adsorbents. This has led to an interest in their adsorption properties and the publication of numerous experimental studies focused on the optimisation of biochars for such applications (Ahmad et al., 2014). To this end, molecular modelling techniques offer many advantages. Molecular dynamics (MD) simulations, for example, have gained popularity in the study of structure-property relationships due to their ability to bring atomic-level insights into physicochemical processes such as adsorption. Nevertheless, very few MD studies of biochars can be found in literature, with those that can often based upon vastly oversimplified biochar models (e.g. (Chen et al., 2019)). Such models may fail to represent the true nature and properties of biochars. We believe this issue arises as a result of the complexity of biochars and lack of understanding of the molecular structures within them, thereby rendering the set-up of representative molecular models a challenge.

To remediate this, we used MD simulation to construct three molecular models representative of biochars produced from woody biomass at low (400ºC), medium (600ºC), and, high (800ºC) highest treatment temperatures (HTTs). We began by collecting experimental data from literature and used this to identify key physicochemical properties of these three biochar-types. We created molecular 'building blocks' with chemical properties aligned to those we had identified and used a simulated annealing procedure to condense our 'building blocks' into bulk systems representative of solid biochars. We compared the physical properties of our bulk systems to those identified from literature to validate the resulting structures. We then used these bulk systems to generate biochar layers with large, exposed surfaces ready for use in adsorption studies. These, along with the data used to develop them, will soon be made freely available via GitHub (https://github.com/Erastova-group/biochar_models.git).

Our subsequent work focuses on the optimisation of biochars for use in water decontamination. We used our molecular models to study the adsorption properties of biochars for a common pollutant, 2,4-dichlorophenoxyacetic acid (2,4-D). We used MD to simulate systems with a range of starting concentrations of 2,4-D. We were able to determine the key mechanisms through which 2,4-D adsorbed onto our biochars, as well as the effects of starting concentration upon this adsorption process. Our results suggest that 2,4-D adsorbs to biochars primarily through π-π and π-Cl interactions, with these functional groups found predominantly at distances of approximately 3-4 Å from the biochar surfaces. At low surface occupancies, 2,4-D preferentially adsorbed with its aromatic ring at

an angle of approximately 10º to the biochar surfaces, indicative of π-π stacking in the sandwich conformation. At higher surface occupancies this preference is reduced, potentially due to lack of available surface or interactions with other adsorbed 2,4-D molecules. When the starting concentration of 2,4-D was high, we observed aggregate formation and adsorption and, the formation of multilayers upon the biochar surfaces. These mechanisms did not appear to differ significantly between each of our biochar molecular models suggesting that all three biochar-types may be well suited to the adsorption of aromatic- and chlorine- containing pollutants.

Future work will focus on repeating these adsorption studies with pollutants comprising various functionalities, polarities and, charges. Our aim will be to gain insights into which types of pollutant may be eligible for adsorption with biochars and which biochar-types would be best suited for this purpose. We anticipate that this work will not only advance the understanding of these incredible materials as adsorbents, but also encourage the uptake of molecular modelling within the biochar research community as a whole.

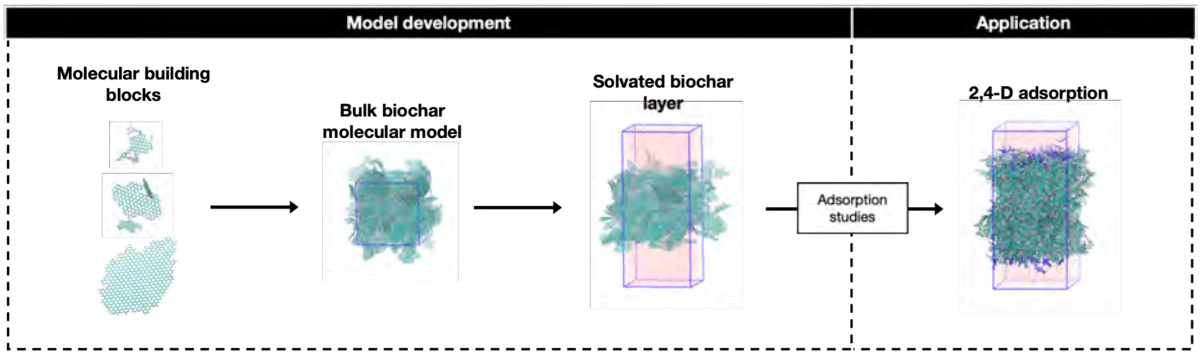


**FIGURE 1:** Schematic representation of research. From left to right: construction of molecular 'building blocks' with chemical properties aligned to those of each biochar-type, condensation of molecular 'building blocks' into bulk solids with physical properties aligned to those of each biochar-type, construction of biochar layer with large, exposed surfaces (soon available at https://github.com/Erastova-group/biochar_models.git) and, adsorption of 2,4-dichlorophenoxyacetic acid (2,4-D) onto biochar layer.

**References**

Ahmad, M. *et al.* (2014) 'Biochar as a sorbent for contaminant management in soil and water: A review', *Chemosphere*, 99, pp. 19–33. doi: 10.1016/j.chemosphere.2013.10.071.

Chen, Q. *et al.* (2019) 'Effect of carbon chain structure on the phthalic acid esters (PAEs) adsorption mechanism by mesoporous cellulose biochar', *Chemical Engineering Journal*, 362, pp. 383–391. doi: 10.1016/j.cej.2019.01.052.

# Influence of Nano-Sized Carbon on Chromium Based Electrochemical Coating Protection Properties

Gulmira Yar-Mukhamedova, Kanat Mukashev, Abyl Muradov, Aiman Kemelzanova

*Al-Farabi Kazakh National University, IETP, Almaty, Kazakhstan*

gulmira-alma-ata@mail.ru

## ABSTRACT

When develop new nano-structured composition electrochemical coatings (nano-CEC) carbon is one of the most perspective of components for improving functional properties. The report presents the results of experiments on introduction of nano-size particles of carbon C (11-100 nm) into chromium electrolytic coating and investigation of corrosion resistance in 3% NaCl solution. Nano-composition electrolytic coatings were obtained at the various density of current: 2-7 kA/m$^2$, temperature 303-343 K and nano-dispersion phase components' content. For testing of corrosion resistance of chromium-lamp soot nano-composition electrochemical coatings the experimental device for corrosion resistance determining by a weight method adjusted for coatings working conditions was developed, assembled and completed. The morphology of coating's surface was investigated by electron- and atom-force microscope before and after corrosion tests. It was established, that nanostructured composition electrolytic coatings, which were obtained in electrolytes contain 2-6 g/dm$^3$ C, temperature 303-343 K, density of current - 4-5 kA/m$^2$, have the highest corrosion resistance.

## Introduction

Electrochemical deposition of nano-structured composition coatings is an important and promising direction of electroplating on several grounds. Firstly, the list of metals that can be deposited from aqueous solutions is rather limited; therefore, electrolytic composition coatings are becoming increasingly important. Secondly, due to the combination of valuable qualities of individual metals, coatings with adding the nano-size particles [1–2] give the surface of products various chemical and physic-mechanical properties, the level of which can be quite easily varied. Third, at present, in practical electroplating, there is an almost no alternative transition to multicomponent and synergistic coatings, which are characterized by super-additive enhancement of functional properties with respect to the coating corrosion resistant [3-4], hard and wear resistant [5-6].

Among the practically important alloys, the main place is occupied by electrolytic compositions formed by the metals with different powders consisting of nano-size particles. One of the reasons for such attention is that, despite the extreme demand for mono-metallic coatings with different components. It is well known that individual coatings of metals have not the properly anticorrosion resistant, whereas with of the iron triad they can co-deposit into coatings [7-8].

Despite the great amount of investigation in the field of nano-structured metal materials, the main reasons of unique increasing functional properties have not discovered yet. Therefore the main goal of the research is investigating approaches of chromium-carbon electrolytic coatings obtaining.

## Materials and Methods

Electrolytic chromium, in comparison with other electrodeposit-able metals, is the most wear-resistant and has high hardness. Despite this, it is not protected surfaces against corrosion due to porosity. Deposition of composite electrolytic coatings (CEC) using appropriately dispersed particles can improve the anti-corrosion properties of electrolytic chromium. The protective ability of the coating depends on the amount, size, and dispersed phase in the metal matrix. We have chosen lamp soot as a second phase for our composite electrolytic coatings on chromium base.

We present the results of experiments on the introduction of nano-size particles of carbon C (11-100 nm) into chromium electrolytic coating and investigation of corrosion resistance in 3% NaCl

solution. Nano-composition electrolytic coatings were obtained at various densities of current: 2-7 kA/m$^2$, temperature 303-343 K, and nano-dispersion phase components' content. For testing of corrosion resistance of chromium-lamp soot nano-composition electrochemical coatings the experimental device for corrosion resistance determined by a weight method adjusted for coatings working conditions was developed, assembled, and completed.

**Results and Discussion**

To clarify the effect of temperature and concentration of nano-size carbon on the corrosion resistance of the composition electrolytic coatings, we were provided with three options that are inevitably associated with the deposition technology of any electrolytic coatings. The fact is that to obtain both electrolytic coatings and nanostructured electrolytic coatings there should be a sedimentation field of electrolyte - suspension, a nourishing process of electrolytic coatings deposition - dispersed parts regardless of the method of creating the sedimentation space of electrolyte - suspension: bags, airborne or ultrasonic, as in our case.

The most likely are three options for electrodeposition:

- in a quiet sedimentation field, not disturbed by any external influences, including ultrasound;

- in a sedimentation field periodically disturbed by an external influence, for example, by ultrasound;

- in the sedimentation field, which is under constant external influence, in our case - by ultrasound.

Since the coatings obtained in the mode of brilliant hard chrome plating have the greatest demand, electrodeposition of nano–composition electrolytic coatings was carried out at temperatures of 303-343 K, current density 3-7 kA / m$^2$, the concentration of carbon 20 g/l. For electrodeposition we used two variants of chromium-plating electrolytes, differing in the fact that one electrolyte contained strontium sulfate, in the other – without it.

The morphology of the coating's surface was investigated by electron- and atom-force microscope before and after corrosion tests. It was established, that nanostructured composition electrolytic coatings, which were obtained in electrolytes contain 2-6 g/dm$^3$ C, temperature 303-343 K, the density of current - 4-5 kA/m$^2$, have the highest corrosion resistance.

**Conclusions**

- Two electrolyte variants have been developed for the nano-CEC deposition of, chromium-silicon dioxide, characterized in that one contains strontium sulfate and the other does not.

- A test bench for corrosion resistance has been developed and created, which allows: conduct tests in various corrosive environments at temperatures from room temperature to 303-343 K.

- Quantitative assessment of the corrosion rate was carried out by a gravimetric method.

- Nano-composition electrolytic coatings Cr-C obtained from both electrolytes increase the corrosion resistance of steel St 3 in NaCl solutions up to 45-69 times.

**Acknowledgment**

This research has been funded by the Science Committee of the Ministry of Education and Science of the Republic of Kazakhstan (Grant № AP08855457)

**References**

1. Darisheva, A.M., Moldabaev, M., Karimova, I.S. *12nd Int.l Multidisc. Sc Geoconf. SGEM 2012. 12 (56), 2012.*
2. Karakurkchi, A., Sakhnenko, N., Atchibayev, R. *Materials Science and Engineering. P. 69-74. 2018.*
3. Ved', M., Sakhnenko, N., Yermolenko, I. *Euras. Chem-Techn. Journal. Vol.20, №3.- Pp. 145-152. (2018).*
4. Muradov, A., Mukashev, K. et al. *(2017). SGEM 2017. 201-208.*
5. Yar-Mukhamedova, G.Sh. (2017). Materials Science. 36(5). 752-754.
6. Belyaev, D. V., Mussabek, G., *SGEM 2017. 17 (61), 2017, Pp 233-240. 130800Fan.*
7. Ved, M.V., Sakhnenko, N.D. et al. *Eurasian Chemico-Technological Journal, № 20(2), p. 145-152. 2018.*
8. Muradov, A., Mukashev, K. *SGEM 2017. 17 (61), 2017, Pp 201-208. 130800.*

Carbon 2022

# Development of high-performance adsorption heat pump using pressurized physically activated carbon

**Hyeonseok Yi[1,2], Koji Nakabayashi[1,2], Seong-Ho Yoon[1,2], Jin Miyawaki[1,2]**
[1] Interdisciplinary Graduate School of Engineering Science, Kyushu University, Kasuga, Japan
[2] Institute of Materials Chemistry and Engineering, Kyushu University, Kasuga, Japan
Email: yi@cm.kyushu-u.ac.jp

**Keywords**
Activated carbon, Pressurized physical activation, Adsorption heat pump

## INTRODUCTION

The adsorption heat pump (AHP) is attracting great attentions as an environmentally-friendly heating and cooling system, which can be driven by low-temperature waste heat and solar heat. There are some combinations of refrigerant-adsorbent for AHP system. $NH_3$, water, $CO_2$, and alcohols are candidates for refrigerants, while porous materials such as silica gel, synthetic zeolite, and activated carbon (AC) are used as adsorbents. Synthetic zeolite–water pair is mostly used in commercial AHP systems. However, the zeolite–water pair is limited by the low adsorption capacity, and water cannot be driven below ice point. By these reasons, we are focusing on AC-ethanol pair. It has been reported that AC with pore size of 1.6 nm gave the maximum effective adsorption uptake of ethanol under an assumption of 283, 303, and 353 K for the cooling water, the surrounding environment, and regeneration temperatures, respectively (Miyazaki, 2017).
However, it is difficult to prepare AC having a large amount of 1.6 nm of pore structures by a conventional physical activation method using $CO_2$ or steam as an activation agent. On the other hand, chemical activation using KOH or the like as an activation agent can introduce a large number of micropores and mesopores; however, the requirements of anti-corrosion equipment and acid-washing as post-treatment step increase the production costs. Consequently, it is difficult to apply chemical AC as an AHP adsorbent. Recently, we have developed a new process called the pressurized physical activation method for highly porous AC production. This method enabled to impart a pore structure of about 1.6 nm even by the physical activation mechanism (Yi, 2021).
In this study, we investigated the applicability of AC having unique pore structure prepared by the pressurized physical activation method to AHP using ethanol as a refrigerant.

## EXPERIMENTAL

A spherical phenolic resin having a diameter of 8 µm was carbonized at 600°C. to obtain a spherical carbonized product (C6). AC was obtained by activating C6 at 900°C in a $CO_2$ flow of 0.1 MPa or 1.0 MPa (referred to as Physically Activated Carbon (PAC) and Pressurized Physically Activated Carbon (PPAC), respectively). In addition, AC prepared by chemical activation at 900°C using KOH is called Chemically Activated Carbon (CAC).
The pore structural parameters and pore size distribution of C6 and ACs were determined by the $\alpha_S$ plot analysis and the quenched solid density functional theory analysis of $N_2$ adsorption and desorption isotherms at 77 K, respectively. In addition, the effective adsorption uptake of ethanol was determined from the difference in the adsorption amounts at relative pressures ($P/P_0$) of 0.1 and 0.3 using the ethanol adsorption isotherm measured at 303 K.

## RESULTS AND DISCUSSION

**FIGURE 1 (a)** shows the pore size distributions, and **TABLE 1** shows the activation yield and pore structural parameters of C6 and ACs. PPAC prepared by the pressurized physical activation showed a high total pore volume more than twice of the PAC at the comparable activation yields (12-13%), and also shows a characteristic pore size distribution with a peak at about 1.6 nm. On the other hand, CAC showed higher total pore volume than PPAC even at high activation yield of 31%. As for the pore size distribution of CAC, it was found that mesopores were greatly developed along with micropores.

**FIGURE 1 (b)** shows ethanol adsorption–desorption isotherms measured at 303 K. PPAC exhibited a remarkably high effective ethanol uptake per unit volume of 220 mg/cm$^3$, whilst the value of CAC was only 120 mg/cm$^3$. The characteristic pore size distribution of PPAC, with an optimal pore size of 1.6 nm, provided high ethanol uptake at $P/P_0$ = 0.1–0.3 with high bulk density and thus showed the large effective adsorption uptake, despite its lower total pore volume than CAC.

**TABLE 1**: Activation yield and pore structural parameters of C6 and ACs.

| Sample | Activation yield [%] | Total pore volume [cm$^3$/g] | Micropore volume [cm$^3$/g] | Specific surface area [m$^2$/g] | Average pore width [nm] | Bulk density [g/cm$^3$] |
|---|---|---|---|---|---|---|
| C6 | - | 0.20 | 0.18 | 570 | 0.73 | 0.84 |
| PAC | 13 | 0.59 | 0.53 | 1650 | 0.72 | 0.57 |
| PPAC | 12 | 1.40 | 1.03 | 2630 | 1.34 | 0.39 |
| CAC | 31 | 2.41 | 1.10 | 3010 | 1.65 | 0.21 |

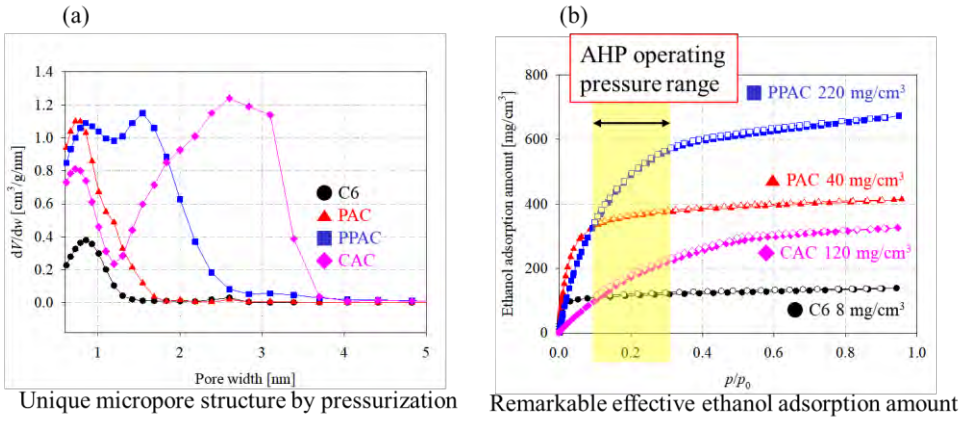


**FIGURE 1**: (a) Pore size distributions and (b) ethanol adsorption-desorption isotherms on a volume basis at 303 K of C6 and ACs.

## CONCLUSION

The pressurized physically activated carbon having characteristic pore structure showed outstanding effective adsorption uptake of ethanol on a volume basis, confirming a great potential of the pressurized physically activated carbon as an adsorbent for AHP system with ethanol refrigerant.


### Acknowledgements

This abstract was reproduced from *RSC Advances*, 12, 2558-2563. https://doi.org/10.1039/D1RA08395C with permission from the Royal Society of Chemistry. We acknowledge ASAHI YUKIZAI CORPORATION for providing spherical phenol resins.


### References


T. Miyazaki, J. Miyawaki, T. Ohba, S.–H. Yoon, B. B. Saha, and S. Koyama, (2017). Study toward high-performance thermally driven air-conditioning systems, *AIP Conference proceedings*, 1788, 020002. http://dx.doi.org/10.1063/1.4968250

H. Yi, K. Nakabayashi, S.-H. Yoon, and J. Miyawaki, (2021). Pressurized physical activation: A simple production method for activated carbon with a highly developed pore structure, *Carbon*, 183, 735-742. https://doi.org/10.1016/j.carbon.2021.07.061

20 C 22 arbon 2022

# High-temperature vacuum TPD analysis of nitrogen-doped carbon materials

**Takeharu Yoshii,[1] Ginga Nishikawa,[1] Rui Tang,[2] Eva Scholtzová,[3] Robert Szilagyi,[4] and Hirotomo Nishihara[1,2]**

[1]Institute of Multidisciplinary Research for Advanced Materials, Tohoku University, Sendai, Miyagi, Japan, 980-8577
Email: takeharu.yoshii.b3@tohoku.ac.jp
[2]Advanced Institute for Materials Research (WPI-AIMR), Tohoku University, Sendai, Miyagi, Japan, 980-8577
[3]Institute of Inorganic Chemistry, Slovak Academy of Sciences, Bratislava, Slovakia, 84536
[4]Department of Chemistry, UBC Okanagan, Kelowna, BC, Canada, V1V 1V7

**Keywords**
TPD measurement, N-doped carbon, High-sensitivity analysis

## INTRODUCTION

Nitrogen-doped (N-doped) carbon materials are attracting attention in various fields, such as catalysis for oxygen reduction reaction. (Nakamura et al., 2016) N-doping can be achieved in various processes and from diverse set of precursors. (Inagaki et al., 2018) CHN elemental analysis and XPS were conventionally used for analysis of N species, but their measurement accuracy is about 0.1 wt%. (Boudou et al., 2006) Thus, a technique for detailed qualitative and quantitative analysis of N species is desired. Herein, we propose high-temperature vacuum temperature-programmed desorption (TPD) as a new high-sensitivity analytical method for N-doped carbons.

## METHODS

Prior to the TPD measurement, N-containing mesoporous carbons were obtained by chemical vapor deposition of $CH_3CN$ on the $Al_2O_3$ nanoparticle templates, followed by a removal of the template using hydrofluoric acid. Since the mesopore wall is composed of about one layer of graphene sheets, the TPD results are consistent with the surface sensitive XPS analysis. TPD measurements were carried out from room temperature up to 1800 °C under high vacuum. XPS and CHN elemental analysis were performed on samples heat-treated at designated temperatures for comparison with TPD measurements. Density functional theory (DFT)-based fragmentation simulations were employed for molecular cluster and periodic boundary models to support the assignment of thermal decomposition processes.

## RESULTS AND DISCUSSION

In TPD result, thermal fragmentation followed by desorption of N-containing gases, $NH_3$, HCN, and $N_2$, was observed in a wide temperature range of 300-1800 °C. The nitrogen content calculated from the total amount of desorbed gas was 7.9 wt%, which is in close agreement to the CHN analysis (8.0 wt%) and XPS analysis (8.5 wt%).

Next, the results of the TPD analysis were compared with those of the XPS analysis. The XPS spectrum of the sample before the heat treatment was fit using three components: graphitic-N, pyrrolic-N, and pyridinic-N. In the sample heat-treated at 1000 °C, the amount of graphitic-N was almost unchanged, while the amount of pyridinic-N, and pyrrolic-N decreased. Further heat treatment at 1400 °C resulted in an overall decrease in N content and the disappearance of pyrrolic-N. Since $NH_3$ completely desorbed at around 1400 °C in the TPD measurement, it was suggested that $NH_3$ was caused by the desorption of pyrrolic-N in the sample. On the other hand, $N_2$

desorbed at high temperatures above 1400 °C was attributed to graphitic-N. From the detailed analysis, it was concluded that the pyrrolic-N was desorbed as $NH_3$ and HCN in a temperature range of 300-1200 °C and pyridinic-N was desorbed as HCN and $N_2$ at around 1000 °C. The thermally stable graphitic-N was desorbed as $N_2$ in the high temperature region above 1200 °C. DFT-based fragmentation simulations employing molecular cluster and periodic boundary models explains well the experimental TPD results and support the assignment of thermal decomposition processes. These results indicate that the amount of each N-environment can be quantitatively determined from TPD measurements.

Furthermore, TPD analysis was performed on a sample with a very small amount of N content and showed a high quantitative accuracy of the order of 10 ppm (0.001 wt%). On the other hand, 0.1 wt% was the lower limit of detection using XPS and CHN elemental analysis, indicating that TPD analysis can analyze nitrogen with higher sensitivity than conventional methods.

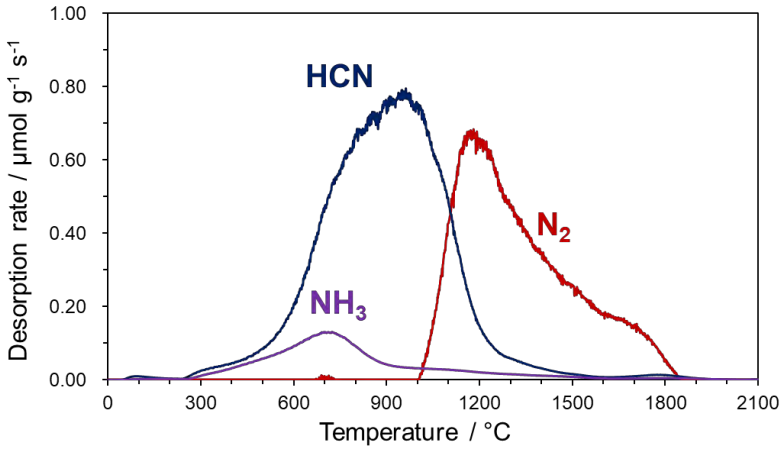


**FIGURE 1**: TPD profile of N-containing mesoporous carbon for $NH_3$, HCN, and $N_2$.

## CONCLUSIONS

In this study, a high-temperature vacuum TPD measurement method was developed to analyze N species in carbon materials. Three N-containing gases, $NH_3$, HCN and $N_2$, desorbed in the temperature range of 300-1800°C, and all N species in the material could be determined by this method. Combined with the results of XPS and DFT calculations, the thermal decomposition process to each desorbed gas species was suggested. These results demonstrate that TPD analysis is a promising new method for chemical speciation and quantitative analysis of N species in carbon materials with high sensitivity.

**Acknowledgements**

The AtomDec Consortium (V4-Japan/JRP/2021/96/AtomDeC) is supported by the Visegrad Group-Japan 2021 Joint Call on Advanced Materials in cooperation with the International Visegrad Fund. It is funded by the Japan Science and Technology Agency (JST SICORP Grant No. JPMJSC2112 (Japan) and Slovak Academy of Sciences (Slovakia).

**References**

D. Guo, R. Shibuya, C. Akiba, S. Saji, T. Kondo, J. Nakamura, Active sites of nitrogen-doped carbon materials for oxygen reduction reaction clarified using model catalysts, *Science*, 351, 361-365 (2016).

M. Inagaki, M. Toyoda, Y. Soneda, T. Morishita, Nitrogen-doped carbon materials, *Carbon*, 132, 104-140 (2018).

J.P. Boudou, Ph. Parent, F. Suarez-Garcia, S. Villar-Rodil, A. Martinez-Alonso, J.M.D. Tascon, Nitrogen in aramid-based activated carbon fibers by TPD, XPS and XANES, *Carbon*, 44, 2452-2462 (2006).

Carbon 2022

# Influence of Carbon Cathode Edge Sites on Li-$O_2$ Batteries

**Wei Yu, Takeharu Yoshii, Zhengze Pan, Rui Tang and Hirotomo Nishihara**
Advanced Institute for Materials Research (WPI-AIMR), Tohoku University, Sendai, Miyagi, Japan, 980-8577
Email: yu.wei.a3@tohoku.ac.jp

**Keywords**
Carbon edge sites, Li-air battery, Graphene mesosponge

## INTRODUCTION

The Li-$O_2$ battery, with an extremely high theoretical energy density (> 3500 Wh/kg), has attracted much attention in recent years, and is considered one of the most promising candidates for next-generation energy storage. (Kwak et al., 2020) However, as researchers continue to explore rechargeable Li-$O_2$ batteries, they have found that there are several problems with this complex electrochemical device involving gas. For example, the sluggish kinetics of both the oxygen reduction reaction (ORR) and the oxygen evolution reaction (OER) in a typical nonaqueous Li-$O_2$ battery, especially the OER during charging, usually leads to a large overpotential and low energy efficiency; the formation of highly reactive reduced oxides such as lithium superoxide ($LiO_2$), singlet oxygen ($^1O_2$) and even the discharge product lithium peroxide ($Li_2O_2$) triggers the degradation of electrolytes and cathodes. (Mahne et al., 2017)

Since the Li-$O_2$ battery was first proposed, carbon materials have always been considered as promising cathode materials. However, due to the harsh operating conditions of Li-$O_2$ batteries, current carbon materials are far from an ideal cathode. (Ottakam Thotiyl et al., 2013) For example, the cathode is always exposed to oxygen and other reactive intermediates during ORR/OER reactions. (Itkis et al., 2013) In addition, the cathode withstands a higher potential during the charging process. In fact, carbon has been found to undergo oxidation reactions under Li-$O_2$ battery operating conditions. Although the reactivity of the carbon was thought to be caused by edge-sites or defects, there are no reports that clarify the influence of different carbon edge sites on the performance of Li-$O_2$ batteries.

## RESULTS AND DISCUSSION

To investigate the influence of different carbon edge-sites, 3-D model carbon materials, carbon mesosponge (CMS) and graphene mesosponge (GMS), were synthesized by chemical vapor deposition method and treated at different temperatures. (Nishihara et. al., 2016) FIGURE 1a shows the gas evolution of $H_2$, CO, $CO_2$, and $H_2O$ during advanced temperature programmed desorption measurement (TPD) up to 1800 °C for CMS. As shown in FIGURE 1b, the evolution at different temperatures corresponds to the decomposition of different edge-sites. Four different temperatures (600 °C, 900 °C, 1350 °C and 1800 °C) were selected to synthesize GMS with different types of edge-sites (FIGURE 1c-f). As shown in FIGURE 1c, GMS-600 should contain a large amount of quinones formed by the CVD process or the decomposition of carboxyls. Although phenols may be present in GMS-600, the amount should be quite small due to the very limited $H_2O$ evolution at above 600 °C. As can be seen in FIGURE 1d, GMS-900 should contain some quinines and a large amount of H-terminated edge-sites. GMS-1350 still has a small amount of H-terminated edge-sites (FIGURE 1e). After treatment at 1800 °C, GMS-1800 should be almost an edge-site-free carbon (FIGURE 1f), as evidenced by the very low gas evolution in the TPD measurement towards GMS-1800. (Nishihara et. al., 2016) The cycling performance of Li-$O_2$ batteries with cathodes

CMS-CP, GMS-600-CP, GMS-900-CP, GMS-1350-CP, and GMS-1800-CP was investigated at a current density of 0.1 mA with a limited capacity of 0.25 mAh. It was found that the removal of H-containing edge-sites, carboxyls and phenols from CMS to GMS-600 and H-terminated edge-sites from GMS-900 to GMS-1350 and then to GMS-1800 can contribute to the improvement of carbon cathode stability. However, the removal of O-only edge-sites such as quinones does not contribute to the improvement of carbon cathode stability in Li-$O_2$ battery.

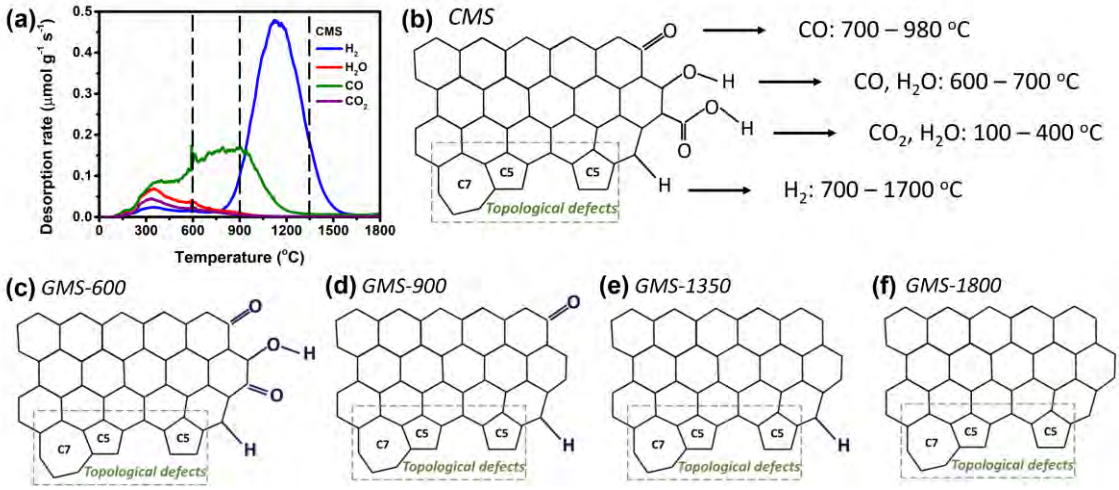


**FIGURE 1:** (a) Gas evolution of $H_2$, CO, $CO_2$, and $H_2O$ during the TPD measurements for CMS. (b-f) Schematic carbon structures of CMS/GMS treated at different temperatures.

## CONCLUSIONS

In this work, the influence of different carbon edge-sites were investigated by comparing the performance of Li-$O_2$ batteries based on 3-D template carbons, CMS/GMS. Advanced TPD was used to determine the type and number of edge-sites in the CMS cathodes treated at different temperatures. Our results demonstrate that it is H-containing edge-sites that lead to carbon corrosion and Li-$O_2$ battery failure. This work will provide a guide for the development of stable carbon cathodes for Li-$O_2$ batteries on an atomic basis.


### Acknowledgements

The work was supported by JST ALCA-SPRING, Japan (grant no. JPMJAL1301), JSPS KAKENHI (grant nos. 22K14757 and 21K14490), the “Five-star Alliance” in “NJRC Mater. & Dev.”, Japan Association for Chemical Innovation, V4-Japan 2021 Jiont Call on Advanced Materials (V4-Japan/JRP/2021/96AtomDeC) and JST SICORP Grant no. JPMJSC2112.


### References


Kwak, W. J., Sharma, R., Sharon, D., Xia, C., Kim, H., Johnson, L., Bruce, P., Nazar, L., Sun, Y.-K., Frimer, A., Noked, M., Freunberger, S. A. & Arubach, D. (2020). Lithium–Oxygen Batteries and Related Systems: Potential, Status, and Future. *Chem. Rev.,* 120**,** 6626-6683.

Mahne, N., Schafzahl, B., Leypold, C., Leypold, M., Grumm, S., Leitgeb, A., Strohmeier, Gernot A., Wilkening, M., Fontaine, O., Kramer, D., Slugovc, C., Borisov, Sergey M. & Freunberger, S. A. (2017). Singlet oxygen generation as a major cause for parasitic reactions during cycling of aprotic lithium–oxygen batteries. *Nat. Energy,* 2**,** 17036.

Ottakam Thotiyl, M. M., Freunberger, S. A., Peng, Z. & Bruce, P. G. 2013. The Carbon Electrode in Nonaqueous Li-$O_2$ Cells. *J. Am. Chem. Soc.,* 135**,** 494-500.

Itkis, D. M., Semenenko, D. A., Kataev, E. Y., Belova, A. I., Neudachina, V. S., Sirotina, A. P., Hvecker, M., Teschner, D., Knop-Gericke, A., Dudin, P., Barinov, A., Goodilin, E. A., Shao-Horn, Y. & Yashina, L. V. 2013. Reactivity of Carbon in Lithium–Oxygen Battery Positive Electrodes. *Nano Lett.,* 13**,** 4697-4701.

Nishihara, H., Simura, T., Kobayashi, S., Nomura, K., Berenguer, R., Ito, M., Uchimura, M., Iden, H., Arihara, K., Ohma, A., Hayasaka, Y. & Kyotani, T. 2016. Oxidation-Resistant and Elastic Mesoporous Carbon with Single-Layer Graphene Walls. *Adv. Funct. Mater.,* 26**,** 6418-6427.

Carbon 2022

# A COMPOSITE MAGNETIC SORBENT BASED ON THE EXPANDED GRAPHITE

**Yuriy L. Zabulonov, Vadim M. Kadoshnikov, Tetyana I. Melnychenko and Oleksandr V. Pugach**
Institute of Environmental Geochemistry of National Academy of Sciences of Ukraine
Email: 1952zyl@gmail.com

**Keywords**
Thermally expanded graphite, oil spillage, metal-carbon nanosorbent

## INTRODUCTION

Oil spillages often happen during oil extraction and transportation. They cause significant pollution of large coastal and sea water areas, agricultural lands, and other territories. Oil pollution of aqueous environment is particularly damaging. According to Zamparas (2020), 25% of oil spillages come from ships, 25% from oil terminals, 20% from tankers, 15% from barges and 15% from platforms.

A number of physical, chemical, thermal and biological methods are used to combat oil spills. Among them, sorption is considered to be efficient in removing thin oil films from water surface. A multitude of organic and mineral sorbents have been tested in this application, such as synthetic and natural porous materials – ash, coke, peat, silica gel, alumina gel, natural and modified clays, foam polymers, foam glass, and aerogels made of various industrial and agricultural wastes (Huang, 2022; Roulia, 2022; Zamparas, 2020). To be efficient, such sorbents should be both oleophilic and hydrophobic, have minimal water sorption capacity, good buoyancy, low toxicity and cause no negative impact on the environment.

Clays and zeolites are high density materials, which precipitate and form sediments affecting the biochemical processes at the bottom of water basins. Spent oil sorbents of natural origin are ecologically safe and could be utilised, however they exhibit insufficient sorption capacity due to their low hydrophobicity (Zamparas, 2020). Recently, thermally expanded (exfoliated) graphite, TEG, has been added to the list of sorbents capable of removing oil spills. TEG has high oil sorption capacity and buoyancy due to its structure and high hydrophobicity of its surface. The mineral composition of water has little effect on its buoyancy and sorption properties, which allows using TEG in sea waters (Vocciante, 2022). However its low bulk density causes high windage of TEG upon spraying over the water surface and collecting after its use. Having a sorbent with magnetic properties would facilitate its separation from the water but TEG is a very hydrophobic material which makes it difficult to combine with magnetic components.

## PURPOSE OF THE STUDY

The aim of this study was to design a TEG-based composite magnetic sorbent for oil removal which has low windage and stable positive buoyancy.

## MATERIALS AND METHODS

We used TEG and metal-carbon nanosorbent (MCN) obtained from UkrGraphite (Zaporizhzhya, Ukraine), and crude oil from the “Naftokhimik Prykarpattya” Oil Refinery (Ivano-Frankivs’k, Ukraine). MCN was characterised using thermal gravimetry and scanning electron microscopy (SEM), JEOL JSM-6490LV (JEOL Ltd., Japan). Elemental analysis was carried out using EDX-SEM method.

## RESULTS AND DISCUSSION

The magnetic TEG sorbent was synthesised using MCN. The properties of metal-carbon composites depend on their chemical composition and structure, particle size and shape. The metal-carbon

interaction determines the electronic and vibrational properties of the nanostructure (Trineeva, 2012). It has been determined that MCN contains carbon (70-75%), iron (9-20%) and iron oxides (5-21%). According to EDX-SEM analysis, the magnetic core of the nanosorbent comprises a Fe-Mn-Co-Ni alloy with total content of nonferrous metals less than 2%, and iron oxides. The disaggregated particle size of the metal phase was 1.5 micron and 1.4 micron of the oxide phase (Fig. 1).

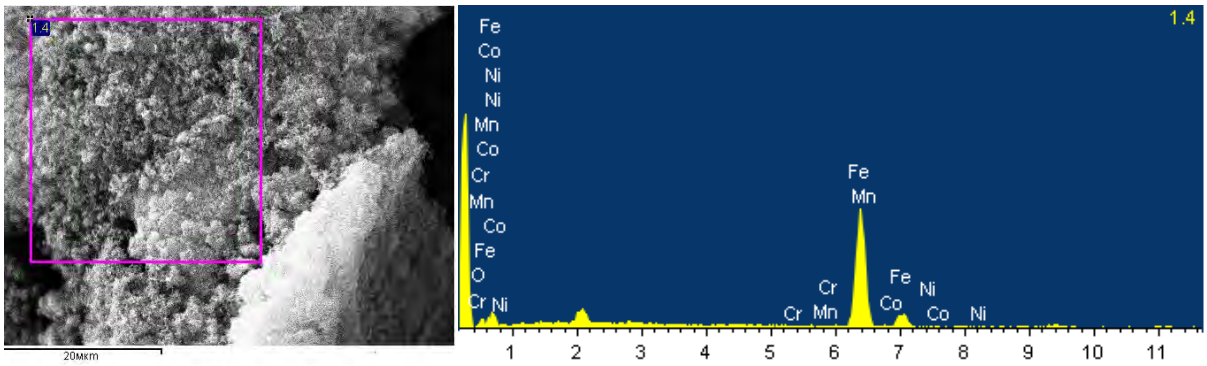


**FIGURE 1**: SEM analysis of the metal-carbon nanosorbent.
Left – SEM micrograph of the sorbent particles, right - EDX elemental analysis.

The composite magnetic TEG sorbent was made by coating TEG with nanoparticles of MCN. TEG particles have high affinity with the MCN coating via intermolecular forces (Zabulonov, 2021). Taking into account that MCN has a metallic core and negative buoyancy, and TEG particles have high positive buoyancy, we carried out experiments which enabled us to determine the optimal TEG:MCN ratio between (2:1) and (10:1) w/w. Within this range, the composite sorbent retained good buoyancy and had low windage.

The spent sorbent was separated from the surface of water by an external magnetic field. When the magnetic field was applied, the sorbent particles formed agglomerates which were easily collected from the water surface by magnetic separation. In our experiments, up to 95% efficiency of removing oil and oil product spills was achieved with composite magnetic TEG sorbents (Fig. 2).

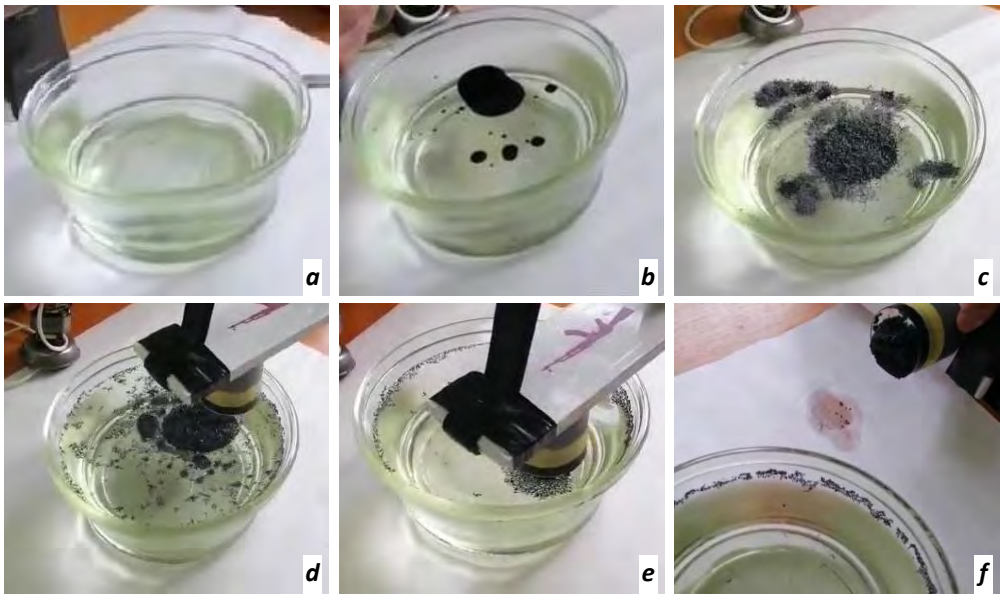


**FIGURE 2**: Oil spillage removal by sorption followed by magnetic separation of the composite magnetic sorbent from the water surface (a – f). a – clean water; b - oil spillage; c – magnetic sorbent sprayed over the water surface; d – external magnetic field applied; e – magnetised sorbent particles lifted from the water surface; f – sorbent particles removed and water surface is clean.

## CONCLUSIONS

1. A novel composite magnetic sorbent based on thermally expanded graphite (TEG) and metal-carbon nanosorbent (MCN) has been synthesised. High affinity between the TEG core and MCN coating is ensured by intermolecular forces.
2. The new sorbent has advantageous features such as stable positive buoyancy, low windage and high sorption capacity for oil and oil spillage products.
3. The spent sorbent can be easily separated and removed from water surface by applying an external magnetic field.

**Acknowledgements**

This work was funded by the National Academy of Sciences of Ukraine.

**References**

Huang, J., Li, D., Huang, L., Tan, S. and Liu, T. (2022). Bio-based aerogel based on bamboo, waste paper, and reduced graphene oxide for oil/water separation. *Langmuir*, 38 [10], 3064–3075.

Roulia, M., Koukouza, K., Stamatakis, M. and Vasilatos, C. (2022). Fly-ash derived Na-P1, natural zeolite tuffs and diatomite in motor oil retention. *Cleaner Materials*, 4, 100063.

Trineeva, V.V., Bakhrushina, M.A., Bulatov, D.L. and Kodolov, V.I. (2012). [Obtaining metal/carbon nanocomposites and studying their structural features]. *Nanotechnics*, 4 [32], 18–20 (in Russian).

Vocciante, M., De Folly D'Auris, A. and Reverberi, A.P. (2022). A novel graphite-based sorbent for oil spill cleanup. *Materials*, 15 [2], 609.

Zabulonov, Y.L., Kadoshnikov, V.M., Melnychenko, T.I., Pugach, O.V., Lytvynenko, Y.V., Shkapenko, V.V. and Odukalets, L.A. (2021). Method of removal of non-polar organic liquids from the surface of natural reservoirs and from man-made polluted waters using a complex magnetically sensitive nanosorbent. *UA Patent 145971U*. https://sis.ukrpatent.org/uk/search/detail/1472524/.

Zamparas, M., Tzivras, D., Dracopoulos, V. & Ioannides, T. (2020). Application of sorbents for oil spill cleanup focusing on natural-based modified materials: A review. *Molecules,* 25 [19], 4522.